

The public reporting burden for this collection of information is estimated to average 1 hour per response, including the time for reviewing instructions, searching existing data sources, gathering and maintaining the data needed, and completing and reviewing the collection of information. Send comments regarding this burden estimate or any other aspect of this collection of information, including suggestions for reducing this burden, to Washington Headquarters Services, Directorate for Information Operations and Reports, 1215 Jefferson Davis Highway, Suite 1204, Arlington VA, 22202-4302. Respondents should be aware that notwithstanding any other provision of law, no person shall be subject to any penalty for failing to comply with a collection of information if it does not display a currently valid OMB control number.
PLEASE DO NOT RETURN YOUR FORM TO THE ABOVE ADDRESS.

1. REPORT DATE (DD-MM-YYYY) 29-05-2021	2. REPORT TYPE Final Report	3. DATES COVERED (From - To) 1-Oct-2016 - 30-Sep-2020
---	--------------------------------	--

4. TITLE AND SUBTITLE Final Report: Multisensory Integration by Circadian Clocks - Area 3 Mathematics (Biomathematics) and Area 8 Life Sciences (Neurophysiology)	5a. CONTRACT NUMBER W911NF-16-1-0584
	5b. GRANT NUMBER
	5c. PROGRAM ELEMENT NUMBER 611102

6. AUTHORS	5d. PROJECT NUMBER
	5e. TASK NUMBER
	5f. WORK UNIT NUMBER

7. PERFORMING ORGANIZATION NAMES AND ADDRESSES Northwestern University Evanston Campus 1801 Maple Avenue Evanston, IL 60201 -3149	8. PERFORMING ORGANIZATION REPORT NUMBER
--	--

9. SPONSORING/MONITORING AGENCY NAME(S) AND ADDRESS (ES) U.S. Army Research Office P.O. Box 12211 Research Triangle Park, NC 27709-2211	10. SPONSOR/MONITOR'S ACRONYM(S) ARO
	11. SPONSOR/MONITOR'S REPORT NUMBER(S) 67885-MA.8

12. DISTRIBUTION AVAILABILITY STATEMENT
Approved for public release; distribution is unlimited.

13. SUPPLEMENTARY NOTES
The views, opinions and/or findings contained in this report are those of the author(s) and should not be construed as an official Department of the Army position, policy or decision, unless so designated by other documentation.

14. ABSTRACT

15. SUBJECT TERMS

16. SECURITY CLASSIFICATION OF:			17. LIMITATION OF ABSTRACT UU	15. NUMBER OF PAGES	19a. NAME OF RESPONSIBLE PERSON Ravi Allada
a. REPORT UU	b. ABSTRACT UU	c. THIS PAGE UU			19b. TELEPHONE NUMBER 847-491-2809

RPPR Final Report
as of 28-Jul-2021

Agency Code: 21XD

Proposal Number: 67885MA

Agreement Number: W911NF-16-1-0584

INVESTIGATOR(S):

Name: Ravi Allada
Email: r-allada@northwestern.edu
Phone Number: 8474912809
Principal: Y

Organization: **Northwestern University Evanston Campus**

Address: 1801 Maple Avenue, Evanston, IL 602013149

Country: USA

DUNS Number: 160079455

EIN: 362167817

Report Date: 31-Dec-2020

Date Received: 29-May-2021

Final Report for Period Beginning 01-Oct-2016 and Ending 30-Sep-2020

Title: Multisensory Integration by Circadian Clocks - Area 3 Mathematics (Biomathematics) and Area 8 Life Sciences (Neurophysiology)

Begin Performance Period: 01-Oct-2016

End Performance Period: 30-Sep-2020

Report Term: 0-Other

Submitted By: Ravi Allada

Email: r-allada@northwestern.edu

Phone: (847) 491-2809

Distribution Statement: 1-Approved for public release; distribution is unlimited.

STEM Degrees: 1

STEM Participants: 3

Major Goals: Task 1. From Gene to Neuron: Integrating Transcriptomics, Optical Imaging, and RNA Interference
Task 2. From Neuron to Circuit: Applying Connectomics and Network Modeling
Task 3. Determining How Information from Multiple Sensory Modalities Are Integrated to Align the Clock to Environmental Cycles.

Accomplishments: Big Wins:

1. Advancement of data assimilation algorithms to solve the inverse problem of constructing conductance-based neuronal models directly from voltage traces (published and submitted)
2. Development of an automated peak finder that will detect action potentials in electrophysiological datasets dramatically speeding up the analysis of "big data" (to be submitted)
3. Discovery of novel molecular and circuit pathways controlling membrane excitability important for circadian sleep-wake cycles and sensory responses to environmental temperature (published and to be submitted)

A PDF document will be uploaded containing manuscripts published and submitted

Training Opportunities: The grant funded the scientific in lab training for 3 graduate students and 4 postdoctoral fellows.

RPPR Final Report

as of 28-Jul-2021

Results Dissemination: Publications:

Moye M and Diekman CO (2018). Data assimilation methods for neuronal state and parameter estimation. The Journal of Mathematical Neuroscience, Accepted.

Belle M and Diekman CO (2018). Neuronal oscillations on an ultra-slow timescale: daily rhythms in electrical activity and gene expression in the mammalian master circadian clockwork. European Journal of Neuroscience, doi: 10.1111/ejn.13856.

Diekman CO and Bose A (2018). Reentrainment of the circadian pacemaker during jet lag: East-west asymmetry and the effects of north-south travel. Journal of Theoretical Biology, 437:261-285.

Moye M and Diekman CO (2018). Data assimilation methods for neuronal state and parameter estimation. The Journal of Mathematical Neuroscience. 8(11):1-38. doi: 10.1186/s13408-018-0066-8. Published August 9, 2018.

Kaur M, Ng A, Kim P, Diekman C, and Kim YI (2019). CikA Modulates the Effect of KaiA on the Period of the Circadian Oscillation in KaiC Phosphorylation. Journal of Biological Rhythms. 34(2):218-223. doi: 10.1177/0748730419828068

Jeong YM, Dias C, Diekman C, Brochon H, Kim P, Kaur M, Kim YS, Jang HI, and Kim YI (2019). Magnesium Regulates the Circadian Oscillator in Cyanobacteria. Journal of Biological Rhythms. 34(4):380-390. doi: 10.1177/0748730419851655.

Alpert MH, Frank DD, Kaspi E, Flourakis M, Zaharieva EE, Allada R, Para A, Gallio M (2020). A Circuit Encoding Absolute Cold Temperature in Drosophila. Curr Biol. 30(12):2275-2288.e5. doi: 10.1016/j.cub.2020

Presentations

- CO Diekman. Society for Research on Biological Rhythms, Amelia Island, FL. May 13, 2018. "Beyond the limits of circadian entrainment: computational modeling and analysis of shift work, social jet lag, and non-24-hour sleep-wake disorder"
- CO Diekman. Computational Neuroscience Initiative Seminar, University of Pennsylvania, Philadelphia, PA. May 1, 2018. "Computational modeling of circadian rhythms: gene expression, membrane excitability, and jet lag"
- M Moye. Institute for Brain and Neuroscience Research Showcase, NJIT, Newark, NJ. March 29, 2018. "Data assimilation methods for neuronal state and parameter estimation"
- CO Diekman. Biomathematics Seminar, North Carolina State University, Raleigh, NC. October 17, 2017. "Circadian Regulation of Electrical Activity in Neurons and Cardiomyocytes"
- CO Diekman. Applied Mathematics Colloquium, University of Cincinnati, Cincinnati, OH. September 15, 2017. "Circadian Regulation of Electrical Activity in Neurons and Cardiomyocytes"

Honors and Awards: Nothing to Report

Protocol Activity Status:

Technology Transfer: Nothing to Report

PARTICIPANTS:

Participant Type: Co PD/PI

Participant: Ravi Allada

Person Months Worked: 5.00

Project Contribution:

National Academy Member: N

Funding Support:

Participant Type: Co PD/PI

Participant: Casey Diekman

RPPR Final Report
as of 28-Jul-2021

Person Months Worked: 5.00
Project Contribution:
National Academy Member: N

Funding Support:

Participant Type: Co-Investigator
Participant: William Kath

Person Months Worked: 3.00
Project Contribution:
National Academy Member: N

Funding Support:

Participant Type: Postdoctoral (scholar, fellow or other postdoctoral position)

Participant: Evrim Yildirim

Person Months Worked: 12.00
Project Contribution:
National Academy Member: N

Funding Support:

Participant Type: Postdoctoral (scholar, fellow or other postdoctoral position)

Participant: Jack Curran

Person Months Worked: 15.00
Project Contribution:
National Academy Member: N

Funding Support:

Participant Type: Postdoctoral (scholar, fellow or other postdoctoral position)

Participant: Matthieu Flourakis

Person Months Worked: 4.00
Project Contribution:
National Academy Member: N

Funding Support:

Participant Type: Graduate Student (research assistant)

Participant: Eric Johnson

Person Months Worked: 12.00
Project Contribution:
National Academy Member: N

Funding Support:

Participant Type: Graduate Student (research assistant)

Participant: Matthew Moye

Person Months Worked: 2.00
Project Contribution:
National Academy Member: N

Funding Support:

Participant Type: Graduate Student (research assistant)

Participant: Emel Khan

Person Months Worked: 1.00
Project Contribution:

Funding Support:

RPPR Final Report

as of 28-Jul-2021

National Academy Member: N

Participant Type: Postdoctoral (scholar, fellow or other postdoctoral position)

Participant: Aushra Abuzeid

Person Months Worked: 3.00

Funding Support:

Project Contribution:

National Academy Member: N

ARTICLES:

Publication Type: Journal Article Peer Reviewed: Y **Publication Status:** 1-Published

Journal: The Journal of Mathematical Neuroscience

Publication Identifier Type: DOI

Publication Identifier: 10.1186/s13408-018-0066-8

Volume: 8

Issue: 1

First Page #:

Date Submitted: 6/27/19 12:00AM

Date Published: 8/1/18 4:00AM

Publication Location:

Article Title: Data Assimilation Methods for Neuronal State and Parameter Estimation

Authors: Matthew J. Moye, Casey O. Diekman

Keywords: Data assimilation; Neuronal excitability; Conductance-based models; Parameter estimation

Abstract: This tutorial illustrates the use of data assimilation algorithms to estimate unobserved variables and unknown parameters of conductance-based neuronal models. Modern data assimilation (DA) techniques are widely used in climate science and weather prediction, but have only recently begun to be applied in neuroscience. The two main classes of DA techniques are sequential methods and variational methods. We provide computer code implementing basic versions of a method from each class, the Unscented Kalman Filter and 4D-Var, and demonstrate how to use these algorithms to infer several parameters of the Morris-Lecar model from a single voltage trace. We conclude by discussing extensions of these DA algorithms that have appeared in the neuroscience literature.

Distribution Statement: 3-Distribution authorized to U.S. Government Agencies and their contractors

Acknowledged Federal Support: Y

Publication Type: Journal Article Peer Reviewed: Y **Publication Status:** 1-Published

Journal: European Journal of Neuroscience

Publication Identifier Type: DOI

Publication Identifier: 10.1111/ejn.13856

Volume: 48

Issue: 8

First Page #: 2696

Date Submitted: 6/27/19 12:00AM

Date Published: 10/1/18 4:00AM

Publication Location:

Article Title: Neuronal oscillations on an ultra-slow timescale: daily rhythms in electrical activity and gene expression in the mammalian master circadian clockwork

Authors: Mino D. C. Belle, Casey O. Diekman

Keywords: circadian rhythms; clock genes; electrical activity; mathematical modelling; neuronal oscillations; suprachiasmatic nuclei

Abstract: Neuronal oscillations of the brain, such as those observed in the cortices and hippocampi of behaving animals and humans, span across wide frequency bands, from slow delta waves (0.1 Hz) to ultra-fast ripples (600 Hz). Here, we focus on ultra-slow neuronal oscillators in the hypothalamic suprachiasmatic nuclei (SCN), the master daily clock that operates on interlocking transcription-translation feedback loops to produce circadian rhythms in clock gene expression with a period of near 24 h (< 0.001 Hz). In this review, we emphasise the circadian processes that drive daily electrical oscillations in SCN neurons, and highlight how mathematical modelling contributes to our increasing understanding of circadian rhythm generation, synchronisation and communication within this hypothalamic region and across other brain circuits.

Distribution Statement: 3-Distribution authorized to U.S. Government Agencies and their contractors

Acknowledged Federal Support: Y

RPPR Final Report as of 28-Jul-2021

Publication Type: Journal Article Peer Reviewed: Y **Publication Status:** 1-Published

Journal: Journal of Theoretical Biology

Publication Identifier Type: DOI

Publication Identifier: 10.1016/j.jtbi.2017.10.002

Volume: 437

Issue:

First Page #: 261

Date Submitted: 6/27/19 12:00AM

Date Published: 1/1/18 12:00AM

Publication Location:

Article Title: Reentrainment of the circadian pacemaker during jet lag: East-west asymmetry and the effects of north-south travel

Authors: Casey O. Diekman, Amitabha Bose

Keywords: Biological rhythms; Entrainment; Circadian oscillator; Light-dark cycles; Poincaré map; Translatitudinal travel

Abstract: The normal alignment of circadian rhythms with the 24-h light-dark cycle is disrupted after rapid travel between home and destination time zones, leading to sleep problems, indigestion, and other symptoms collectively known as jet lag. Using mathematical and computational analysis, we study the process of reentrainment to the light-dark cycle of the destination time zone in a model of the human circadian pacemaker. We calculate the reentrainment time for travel between any two points on the globe at any time of the day and year. We construct one-dimensional entrainment maps to explain several properties of jet lag, such as why most people experience worse jet lag after traveling east than west. Our techniques could be used to provide advice to travelers on how to minimize jet lag on trips involving multiple destinations and a combination of transmeridian and translatitudinal travel.

Distribution Statement: 3-Distribution authorized to U.S. Government Agencies and their contractors
Acknowledged Federal Support: Y

Publication Type: Journal Article Peer Reviewed: Y **Publication Status:** 1-Published

Journal: Journal of Biological Rhythms

Publication Identifier Type: DOI

Publication Identifier: 10.1177/0748730419828068

Volume: 34

Issue: 2

First Page #: 218

Date Submitted: 6/27/19 12:00AM

Date Published: 2/1/19 12:00AM

Publication Location:

Article Title: CikA Modulates the Effect of KaiA on the Period of the Circadian Oscillation in KaiC Phosphorylation

Authors: Manpreet Kaur, Amy Ng, Pyonghwa Kim, Casey Diekman, Yong-Ick Kim

Keywords: CikA, cyanobacteria, Circadian clock, input pathway, in vitro

Abstract: Cyanobacteria contain a circadian oscillator that can be reconstituted in vitro. In the reconstituted circadian oscillator, the phosphorylation state of KaiC oscillates with a circadian period, spending about 12 h in the phosphorylation phase and another 12 h in the dephosphorylation phase. Although some entrainment studies have been performed using the reconstituted oscillator, they were insufficient to fully explain entrainment mechanisms of the cyanobacterial circadian clock due to the lack of input pathway components in the in vitro oscillator reaction mixture. Here, we investigate how an input pathway component, CikA, affects the phosphorylation state of KaiC in vitro. Our findings give insight into how to reconstitute the cyanobacterial circadian clock in vitro by the addition of an input pathway component, and explain how this affects circadian oscillations by directly interacting with the oscillator components.

Distribution Statement: 3-Distribution authorized to U.S. Government Agencies and their contractors
Acknowledged Federal Support: Y

RPPR Final Report
as of 28-Jul-2021

Publication Type: Journal Article Peer Reviewed: Y **Publication Status:** 1-Published

Journal: Journal of Biological Rhythms

Publication Identifier Type: DOI

Publication Identifier: 10.1177/0748730419851655

Volume: Issue:

First Page #: 074873041

Date Submitted: 6/27/19 12:00AM

Date Published: 6/1/19 12:00AM

Publication Location:

Article Title: Magnesium Regulates the Circadian Oscillator in Cyanobacteria

Authors: Young M. Jeong, Cristiano Dias, Casey Diekman, Helene Brochon, Pyonghwa Kim, Manpreet Kaur, Yor

Keywords: circadian cloc; KaiC; phosphorylation; hourglass; autokinase; PhoQ

Abstract: The circadian clock controls 24-h biological rhythms in our body, influencing many time-related activities such as sleep and wake. The simplest circadian clock is found in cyanobacteria, with the proteins KaiA, KaiB, and KaiC generating a self-sustained circadian oscillation of KaiC phosphorylation and dephosphorylation. KaiA activates KaiC phosphorylation by binding the A-loop of KaiC, while KaiB attenuates the phosphorylation by sequestering KaiA from the A-loop. Structural analysis revealed that magnesium regulates the phosphorylation and dephosphorylation of KaiC by dissociating from and associating with catalytic Glu residues that activate phosphorylation and dephosphorylation, respectively. High magnesium causes KaiC to dephosphorylate, whereas low magnesium causes KaiC to phosphorylate. We suggest that a magnesium-based hourglass timekeeping system may have been used by ancient cyanobacteria before magnesium homeostasis was established.

Distribution Statement: 3-Distribution authorized to U.S. Government Agencies and their contractors

Acknowledged Federal Support: Y

Partners

I certify that the information in the report is complete and accurate:

Signature: Ravi Allada

Signature Date: 5/29/21 11:51AM

Neuronal oscillations on an ultra-slow timescale: daily rhythms in electrical activity and gene expression in the mammalian master circadian clockwork

Mino D. C. Belle¹  and Casey O. Diekman^{2,3} 

¹Institute of Clinical and Biomedical Sciences, University of Exeter Medical School, University of Exeter, Exeter, EX4 4PS, UK

²Department of Mathematical Sciences, New Jersey Institute of Technology, Newark, NJ, USA

³Institute for Brain and Neuroscience Research, New Jersey Institute of Technology, Newark, NJ, USA

Keywords: circadian rhythms, clock genes, electrical activity, mathematical modelling, neuronal oscillations, suprachiasmatic nuclei

Abstract

Neuronal oscillations of the brain, such as those observed in the cortices and hippocampi of behaving animals and humans, span across wide frequency bands, from slow delta waves (0.1 Hz) to ultra-fast ripples (600 Hz). Here, we focus on ultra-slow neuronal oscillators in the hypothalamic suprachiasmatic nuclei (SCN), the master daily clock that operates on interlocking transcription-translation feedback loops to produce circadian rhythms in clock gene expression with a period of near 24 h (< 0.001 Hz). This intracellular molecular clock interacts with the cell's membrane through poorly understood mechanisms to drive the daily pattern in the electrical excitability of SCN neurons, exhibiting an up-state during the day and a down-state at night. In turn, the membrane activity feeds back to regulate the oscillatory activity of clock gene programs. In this review, we emphasise the circadian processes that drive daily electrical oscillations in SCN neurons, and highlight how mathematical modelling contributes to our increasing understanding of circadian rhythm generation, synchronisation and communication within this hypothalamic region and across other brain circuits.

Introduction

Neuronal oscillations or rhythms are integral to normal brain function and underlie the ever-evolving landscape of brain activity, brain states and behaviour (Engel *et al.*, 2001; Buzsaki & Draguhn, 2004; Buzsaki, 2015). These perpetual oscillations can be monitored from the scalp as electroencephalogram (EEG) and depict the synchronous activity of neurons that spans a number of brain region-specific frequency bands, from less than 0.2 Hz to frequencies in excess of 500 Hz (Lopes da Silva, 2013; Buzsaki, 2015). Intriguingly, these myriad rhythms can interact with one another through cross-frequency coupling, where oscillations with slower frequency drive and modulate the amplitude of faster local oscillatory events, while broadcasting to and recruiting larger networks of neuronal ensemble across the brain (Steriade, 2001; Csicsvari *et al.*, 2003; Sirota *et al.*, 2003; Buzsaki & Draguhn, 2004; Buzsaki *et al.*, 2012). Our increasing understanding is that these oscillations and their interactions shape and manage information flow in the brain,

and are critical for healthy brain function (Basar-Eroglu *et al.*, 1996; Herrmann & Demiralp, 2005; Buzsaki *et al.*, 2012; Basar, 2013; Buzsaki, 2015).

This article focuses on the neuronal oscillations of the mammalian master circadian clock, the suprachiasmatic nuclei (SCN), which by comparison influence brain activity at a much slower frequency with a circadian period of near 24 h. We discuss some of the ionic, inter- and intracellular signalling, and molecular clockwork mechanisms driving the rhythmic excitability states of SCN neurons across the day–night cycle. In addition, we indicate how mathematical modelling is complementing and guiding some of the experimental work. This maturing synergy between experimental and computational methods is providing circadian biologists with invaluable insights into some of the circadian processes and mechanisms that otherwise would be impenetrable (Gonze, 2011b; Pauls *et al.*, 2016).

The SCN is a network of approximately 20 000 heterogeneous neurons coupled through chemical synapses, paracrine signalling and electrical gap junctions. A hallmark feature of SCN neurons, and one that is paramount to their collective functioning as the master circadian clock, is that their electrical activity shows spontaneous oscillation across the day–night cycle (Brown & Piggins, 2007; Colwell, 2011; Belle, 2015; Allen *et al.*, 2017); see Fig. 1. That is, these neurons are significantly more active during the day [an up-

Correspondence: Dr Mino D. C. Belle, as above. E-mail: m.d.c.belle@exeter.ac.uk

Received 16 October 2017, revised 16 January 2018, accepted 28 January 2018

Edited by John Foxe. Reviewed by Michael Antle, University of Calgary, Canada and Iliia Karatsoreos, Washington State University, USA

All peer review communications can be found with the online version of the article.

state with depolarised resting membrane potential (RMP) and generally discharging action potentials (APs) at $\sim 4\text{--}6$ Hz) than at night (a down-state with hyperpolarised RMP, firing at $\sim 0.1\text{--}2$ Hz or completely hyperpolarised-silent and not spiking; Fig. 1). Even when dissociated from the SCN network and dispersed *in vitro*, most SCN neurons retain their ability to generate this daily oscillation in excitability states for several days [e.g., see (Welsh *et al.*, 1995; Herzog *et al.*, 1998; Honma *et al.*, 1998; Shirakawa *et al.*, 2000; Aton & Herzog, 2005; Webb *et al.*, 2009)]. This indicates that most individual SCN neurons are intrinsic circadian oscillators, and while synaptic communication between the neurons is needed for synchronisation, it is largely not necessary for rhythms at the single-cell level. To achieve such evolving spontaneity in excitability across the circadian day, several intrinsic ionic membrane currents must interact (Bean, 2007; Llinas, 2014). Importantly, the magnitude of these currents and their interactions must also be appropriately tuned and sculpted across the 24-h period. The prevailing view is that these are achieved through the coordinated and cooperative activity of the molecular and membrane clocks (Colwell, 2011; Belle, 2015), see Fig. 2 and Modelling section 1.

The drive to peak excitation during the day

The depolarised RMP during the day (on average at ~ -45 mV) results from membrane excitation driven by several voltage-sensitive cation currents, including inward conductance provided both by sodium and calcium channels (Thomson, 1984; Wheal & Thomson, 1984; Thomson & West, 1990; Akasu *et al.*, 1993; Huang, 1993;

Pennartz *et al.*, 1997; De Jeu *et al.*, 2002; Cloues & Sather, 2003; Jackson *et al.*, 2004; Kononenko & Dudek, 2004; Kononenko *et al.*, 2004; Paul *et al.*, 2016). Recently, through combined modelling and experimental work, a voltage-independent sodium channel (NALCN) was also identified as a positive driver for the SCN neuronal up-state (Clay, 2015; Flourakis *et al.*, 2015). Reduced global potassium channel activity during the day also contributes to the depolarised RMP (Jiang *et al.*, 1997; Kuhlman & McMahon, 2004). In particular, inhibition of the voltage-insensitive small-conductance calcium-activated potassium channels (SK_{Ca}) forces some SCN neurons to become hyperexcited (severely depolarised) and enter depolarisation blockade, a membrane state too positive (~ -30 mV) for AP generation (Belle *et al.*, 2009; Scott *et al.*, 2010; Diekman *et al.*, 2013; Belle, 2015; Paul *et al.*, 2016; Wegner *et al.*, 2017). Thus, these neurons either become completely silent or generate 2–7 Hz TTX-resistant, L-type calcium channel-dependent, depolarised low-amplitude membrane oscillations (DLAMOs) (Belle *et al.*, 2009; Diekman *et al.*, 2013; Belle & Piggins, 2017). Although the neurophysiological function of DLAMOs remains unknown, similar low-amplitude membrane oscillations are seen at moderate RMPs (~ -45 mV) when TTX-sensitive sodium channels are pharmacologically blocked [TTX-LAMOs: see (Diekman *et al.*, 2013)]. These TTX-LAMOs arguably provide the underlying membrane rhythm for pacemaking activity in some SCN neurons (Jiang *et al.*, 1997; de Jeu *et al.*, 1998; Pennartz *et al.*, 2002; Jackson *et al.*, 2004). Indeed, mathematical modelling of experimental data shows that DLAMOs and TTX-LAMOs share similar neurophysiological characteristics and that the daily drive to hyperexcitation in SCN

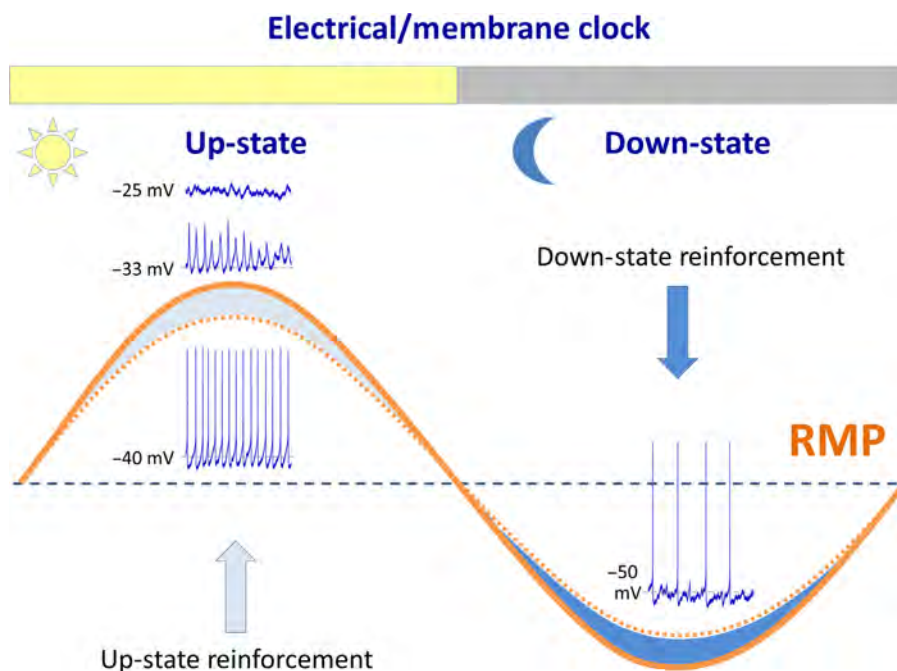


FIG. 1. A schematic overview of the excitability profile/waveform of suprachiasmatic nuclei (SCN) neurons over the day–night cycle. SCN neurons show overt oscillation in their resting membrane potential (RMP), traversing through points of neutral rest state (indicated by where the dashed blue line crosses the orange dashed and solid lines). The RMP of SCN neurons is depolarised (up-state) during the day and hyperpolarised (down-state) at night. In some neurons, the increased RMP elicits action potential (AP) discharge. In others, the RMP becomes too positive (~ -33 mV) to sustain AP production. These neurons display depolarised low-amplitude membrane oscillations (DLAMOs: ~ -33 mV) or become silent by depolarisation blockade (~ -25 mV). At night, the RMP reduces (~ -55 mV) causing SCN neurons to generate APs at lower rates or become completely silent by severe hyperpolarisation (~ -70 mV, not shown). Top yellow and grey bars represent the daytime and night-time, respectively. The blue arrow during the day represents extrinsic signals reinforcing SCN electrical up-state, and at night, the blue arrow represents physiological signals reinforcing SCN down-state (hypoexcitability). The light- and dark-blue shading areas, under and over the curve, show the differences in waveform amplitude between autonomous SCN activity (dashed line) and during appropriate daily reinforcement inputs.

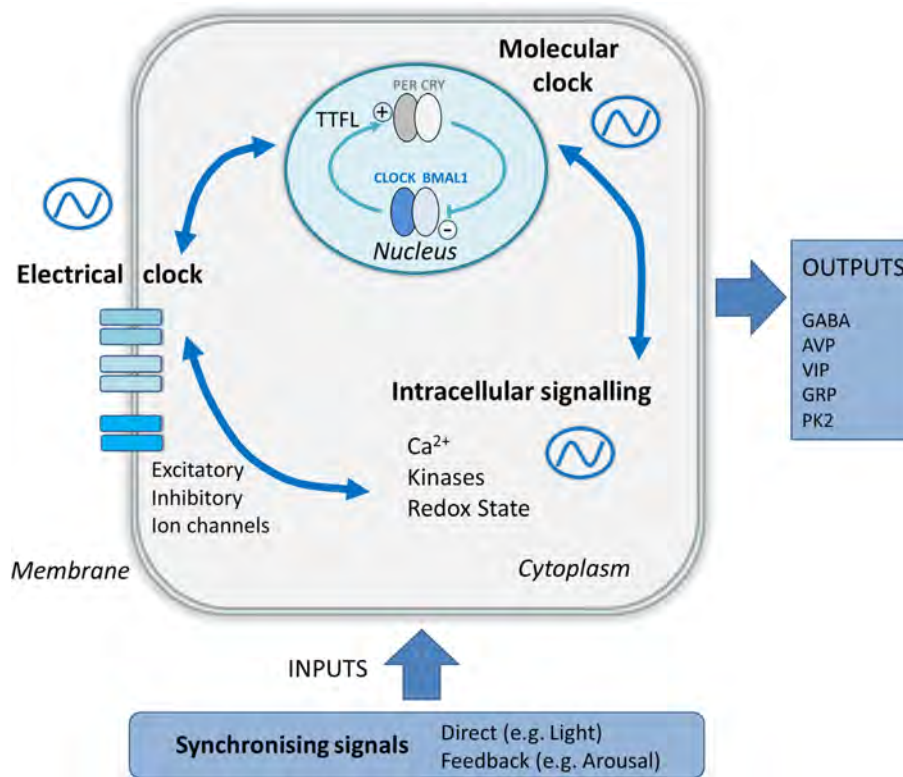


FIG. 2. A simplified schematic view of the intricate collaborative relationship between the molecular and electrical/membrane clocks for generating circadian rhythms/oscillations in the suprachiasmatic nuclei (SCN), and beyond. Within SCN neurons, autonomous molecular timekeeping signals generated by the transcription-translation feedback loop (TTFL) appropriately drive daily excitability and electro-responsiveness of the proximal membrane via intracellular signalling modulation of ion channel activity. Changes in membrane electrical activity feed back to sculpt and stabilise the molecular clockwork. This molecular/genetic-electrical interplay is dynamic and changes over the circadian cycle, temporally integrating time-adjusting cues from the light–dark cycle, physiology and behaviour. Thin intracellular blue arrows indicate direction of signal flow. Input and output signals to and from the SCN clockwork, respectively, are shown by extracellular thick blue arrows.

neurons may be paramount for circadian rhythm generation, maintenance and communication in this hypothalamic region (Diekmann *et al.*, 2013; DeWoskin *et al.*, 2015).

In response to these moderately depolarised RMPs during the day, most SCN neurons generate 4–6 h of sustained spiking activity (Schaap *et al.*, 2003a; Welsh *et al.*, 2010). At the population level, this firing activity pattern collectively extends across the entire light phase of the circadian cycle, with peak firing frequency occurring in the middle of the day, around zeitgeber time 6–7 (ZT6–7, ZT0; time of lights on). This profile of activity has been measured extracellularly *in vitro* and in freely moving animals in several pioneering studies (Inouye & Kawamura, 1979; Green & Gillette, 1982; Groos & Hendriks, 1982; Shibata *et al.*, 1982; Gillette *et al.*, 1995; Schaap *et al.*, 2003b; VanderLeest *et al.*, 2007; Lucassen *et al.*, 2012), and in more recent years, with whole-cell electrophysiology and voltage-sensing genetic probe imaging (Morin & Allen, 2006; Brown & Piggins, 2007; Colwell, 2011; Belle, 2015; Allen *et al.*, 2017; Brancaccio *et al.*, 2017; Enoki *et al.*, 2017a, 2017b). To support the elevated firing frequency during the day, the activity and gating characteristics of several action potential-shaping potassium channels are appropriately regulated. This includes upregulation of the fast delayed rectifier (FDR) and A-type channels, and downregulation/modulation of the large-conductance calcium-activated potassium (BK_{Ca}) channel activity (Cloues & Sather, 2003; Itri *et al.*, 2005, 2010; Pitts *et al.*, 2006; Granados-Fuentes *et al.*, 2012; Montgomery & Meredith, 2012; Montgomery *et al.*, 2013; Whitt *et al.*, 2016).

Night-time silencing

Towards the end of the light phase, SCN neurons begin to traverse to the hypoactive down-state where most of these cells reduce their firing rate or become hyperpolarised-silent, ceasing spiking activity (Fig. 1). In some neurons, this represents an impressive 20–30 mV migration in RMP, when daytime and night-time rest state values are compared (Kuhlman & McMahon, 2004, 2006; Belle *et al.*, 2009; Paul *et al.*, 2016). Potassium channel activity is the main driver for this night-time silencing. For example, the outward conductance of potassium channels, such as BK_{Ca}, is known to increase during the night (Jiang *et al.*, 1997; Pitts *et al.*, 2006; Flourakis *et al.*, 2015; Whitt *et al.*, 2016). Further, SCN neurons show activity for the two-tandem pore domain potassium (K2P) channels (Wang *et al.*, 2012; Belle *et al.*, 2014). Although no biophysical and electrophysiological measurements of K2P channel activity are reported in SCN neurons across the day–night cycle, transcripts for these channels peak during the night (Panda *et al.*, 2002; Lein *et al.*, 2007). These voltage-independent potassium ‘leak’ channels contribute to RMP setting in neurons (Mathie, 2007). Thus, their activity in the SCN at night will contribute to membrane hyperpolarisation, placing SCN neurons into the down-state (see possible reinforcement by orexin-K2P channel activity below).

As a result, the average excitability waveform of the SCN neuronal ensemble across the day–night cycle is sinusoidal with a peak during the day and a trough at night, traversing two neutral rest states at dawn and dusk (Fig. 1). Incredibly, the overall timing and

half-width of this peak and trough in electrical activity follow day length/photoperiod, endowing the SCN with the additional ability to time and regulate important aspects of the body's seasonal rhythms, such as neuro-hormone secretion during the short winter and long summer days (Mrugala *et al.*, 2000; VanderLeest *et al.*, 2007; Welsh *et al.*, 2010; Coomans *et al.*, 2014).

The molecular clockwork: demonstrated as the driver of SCN electrical oscillations

Compared with some of the high-frequency rhythms that are measured elsewhere in the brain, SCN neurons are exceedingly slow oscillators. This is because the daily excitability cycle of SCN neurons is driven by an internal molecular clock which functions as an interlocking transcription-translation feedback loop (TTFL). Much is known about the intricate inner working of the TTFL molecular machinery which shares remarkable homology across species studied so far, from plants to insects, fish and mammals (Hastings & Maywood, 2000; Reppert & Weaver, 2002; Ko & Takahashi, 2006; Guilding & Piggins, 2007; Takahashi *et al.*, 2008; Glossop, 2011; Mohawk & Takahashi, 2011; Mohawk *et al.*, 2012; Buhr & Takahashi, 2013; O'Neill *et al.*, 2013; Partch *et al.*, 2014). At its core, the molecular clock in mammals includes a dynamic interplay between the protein products of canonical clock genes, such as *Period1/2* (*Per1/2*), *Cryptochrome 1/2* (*Cry1/2*), *Clock* and *Bmal1* (Fig. 2). The TTFL-clockwork is excellently reviewed in the above references and therefore will be fleetingly mentioned here. The 'positive arm' of the clock begins with the nuclear transcription and cytoplasmic translation of the proteins CLOCK and BMAL1. Once accumulated in the cytoplasm, they dimerise and the CLOCK/BMAL1 heterodimer then enters the nucleus and binds to the promoter regions of the *Per1/2* and *Cry1/2* genes, activating their transcription (Fig. 2). The negative loop occurs when PER/CRY proteins dimerise, get phosphorylated by casein kinase 1 and translocated into the nucleus to suppress the CLOCK/BMAL1 activity, thereby terminating their own transcription. The overall interaction of these feedforward feedback loops drives perpetual rhythms in *Per1/2* and *Cry1/2* expression, with a peak during the day and a nadir at night, while *Bmal1* peaks at night and trough during the day [e.g. see Fig. 2 in (Guilding & Piggins, 2007)]. During the day phase of the cycle, the *Rev-erb α* gene is also transcribed and its protein product, REV-ERB α , acts in the nucleus to inhibit *Bmal1* transcription, forming an additional negative loop. Eventually, this *Bmal1* inhibition is lifted through PER/CRY suppression of *Rev-erb α* transcription, permitting BMAL1 to again slowly accumulate in the cytoplasm during the night phase.

Linking TTFL activity with excitability and behavioural rhythms

Although the mechanistic nature of the intracellular signals that interweave the molecular clockwork and membrane excitability in the SCN is still poorly understood, there is compelling evidence linking the activity of the molecular clock with membrane excitability oscillations in SCN neurons. The strongest indications come from studies assessing the effects of molecular clock mutations on the SCN temporal excitability profile. There is a clear relationship in wild-type animals between the period of the molecular clockwork, neuronal rhythms in the SCN and the animal's daily locomotor activity cycle. This link is highlighted/exposed when the activity of the molecular clock is astutely manipulated genetically. For example, in hamsters, a mutation in casein kinase 1 (the *Tau* mutation)

shortens the period of neuronal oscillations (accelerates the speed of the clock) in the SCN, as measured by the timing in the daily peak of electrical activity (Liu *et al.*, 1997). This mutation also accelerates the locomotor activity rhythms in these animals (measured by wheel-running activity) by a factor that is representative of the period change in the SCN's electrical oscillations (Liu *et al.*, 1997). In mice, heterozygous *Clock* mutation lengthens behavioural and peak firing activity rhythms in the SCN (Herzog *et al.*, 1998; Nakamura *et al.*, 2002). Elimination of *Cry1* or *Cry2* activity lengthens and shortens the electrical and behavioural rhythms, respectively (Maywood *et al.*, 2011a; Anand *et al.*, 2013), while animals with *Cry1/2*, *Per1/2*, *Bmal1* deletion or homozygous mutations for *Clock* are completely arrhythmic with severe alterations in electrical firing patterns in the SCN (Herzog *et al.*, 1998; van der Horst *et al.*, 1999; Vitaterna *et al.*, 1999; Bunge *et al.*, 2000; Nakamura *et al.*, 2002; Bae & Weaver, 2007; van der Veen *et al.*, 2008; Pfeffer *et al.*, 2009). Further, delaying the degradation of CRY1 and CRY2 in mice lengthens the periods of the molecular clock, excitability rhythms in the SCN, and locomotor activity (Godinho *et al.*, 2007; Guilding *et al.*, 2013; Wegner *et al.*, 2017), whereas the *Tau* mutation of casein kinase 1 accelerates the clock and behavioural rhythms in these animals (Lowrey *et al.*, 2000; Meng *et al.*, 2008).

Further evidence linking the activity of the molecular clock with membrane excitability oscillations in the SCN comes from studies showing that the transcription activity and conductivity of several ion channels expressed by SCN neurons, such as L- and T-type calcium, BK_{Ca}, K2P, and voltage-gated and passive 'leak' sodium channels, are under circadian control (Panda *et al.*, 2002; Brown & Piggins, 2007; Colwell, 2011; Belle, 2015; Flourakis *et al.*, 2015; Whitt *et al.*, 2016; Allen *et al.*, 2017). Also, ion channel activity can be directly regulated by the TTFL components, such as the REV-ERB α regulation of L-type calcium channel activity (Schmutz *et al.*, 2014). In support, disruption in the activity of circadian clock's key molecular components perturbs ion channel function, leading to altered electrical activity in SCN neurons (Albus *et al.*, 2002; Colwell, 2011; Granados-Fuentes *et al.*, 2012). And finally, several intracellular signalling molecules that are associated with modulating membrane excitability in SCN neurons, such as cAMP, are also rhythmically regulated in the SCN (O'Neill *et al.*, 2008; Doi *et al.*, 2011).

The slow daily TTFL and electrical oscillations in SCN neurons are fundamental for providing appropriate circadian timing in physiology and behaviour, such as the sleep/wake cycle, feeding, hormone synthesis and secretion, and cardiovascular output (Kalsbeek *et al.*, 2006; Bechtold & Loudon, 2013; Miller & Takahashi, 2013; Belle, 2015). Having such a daily timer arms organisms with the capacity to predict recurring changes in the environment, an ability that is critical for survival; maximising feeding and reproduction while avoiding predation, for example (Pittendrigh & Minis, 1972; Saunders, 1972; Ouyang *et al.*, 1998; DeCoursey *et al.*, 2000; Spoelstra *et al.*, 2016). Indeed, for most species, the most relevant recurrent environmental change is the light-dark (LD) cycle, emerging from the earth's daily rotation about its axis.

Synchronisation and reinforcement of SCN neuronal oscillations by the environment and physiology

Although the daily excitability waveform of SCN neurons persists in the absence of external time cues (endogenous/free-running), their activity has to be synchronised and aligned with the animal's LD cycle. This ensures that the circadian timing signals communicated to the brain and body are in accordance with the external environment (see Modelling section 2). Our current understanding is that

under natural conditions, these neurons are entrained/synchronised by information on the intensity and spectral composition of ambient daylight (Walmsley *et al.*, 2015; Brown, 2016). This light information is conveyed directly to SCN neurons by the glutamatergic retino-hypothalamic tract (Lokshin *et al.*, 2015; Fernandez *et al.*, 2016) through the activity of specialised melanopsin-containing retinal ganglion cells (Meijer & Rietveld, 1989; Schmidt *et al.*, 2011; Lucas *et al.*, 2014). Although not all SCN neurons respond to light, a large proportion of cells are excited by this photic signal (Groos & Mason, 1978; Meijer *et al.*, 1989; Jiao *et al.*, 1999; Saeb-Parsy & Dyball, 2003b; Drouyer *et al.*, 2007; Brown *et al.*, 2011; Walmsley & Brown, 2015; Walmsley *et al.*, 2015; Tsuji *et al.*, 2016). Therefore, besides synchronising SCN activity, this extrinsic excitatory photic drive may also act to reinforce the TTFL-driven up-state of SCN neurons during the day.

Several internal physiological signals emerging from the body's arousal/wakefulness and homeostatic brain circuits feedback to influence circadian timing in the SCN [(Mrosovsky, 1996; Hut & Van der Zee, 2011; Hughes & Piggins, 2012; Belle, 2015; Meijer & Michel, 2015); see next section below]. These non-photoc inputs include neuropeptide Y (NPY) neurons of the thalamic intergeniculate leaflet (IGL) which send axonal projections through the geniculate-hypothalamic tract (GHT), the serotonergic system of the raphe nuclei (Harrington, 1997; Morin, 2013), the basal forebrain cholinergic system (Bina *et al.*, 1993; Yamakawa *et al.*, 2016), as well as the arousal-promoting orexinergic neurons of the lateral hypothalamus (Mieda & Sakurai, 2012) which projects in the vicinity of SCN neurons (Date *et al.*, 1999; Belle *et al.*, 2014). In nocturnal rodents, a dark-pulse during the daytime causes increased locomotor activity together with a reduction of c-fos expression in the SCN (Marston *et al.*, 2008). This suggests that brain activity during arousal and wakefulness can feed back to suppress excitability in SCN neurons. Indeed, electrical recordings in behaving nocturnal rodents revealed that bouts of prolonged behavioural activity are associated with the immediate suppression of action potential discharge in the SCN, which remained stably suppressed throughout the duration of the behavioural activity (Yamazaki *et al.*, 1998; Schaap & Meijer, 2001; van Oosterhout *et al.*, 2012). It is therefore probable that in nocturnal animals, activity during wakefulness at night may serve as reinforcement for the TTFL-driven electrical down-state of SCN neurons. This is likely mediated through behavioural-dependent release of NPY and orexins in the SCN (Biello *et al.*, 1994; Belle *et al.*, 2014).

In support, exogenous application of NPY, serotonin, agonists for the acetylcholine receptors or orexins to SCN slices robustly suppress clock gene expression and excitability in SCN neurons (Liou & Albers, 1991; Shibata *et al.*, 1992; Prosser *et al.*, 1994b; van den Pol *et al.*, 1996; Cutler *et al.*, 1998; Gribkoff *et al.*, 1998; Farkas *et al.*, 2002; Brown *et al.*, 2008; Klisch *et al.*, 2009; Yang *et al.*, 2010; Besing *et al.*, 2012; Belle *et al.*, 2014; Belle & Piggins, 2017). Fittingly, when applied to SCN slices during the subjective night, orexin-A recruits the activity of potassium 'leak' channels to strongly suppress the RMP and spiking activity of SCN *Per1*-EGFP+ve neurons (Belle *et al.*, 2014); see also night-time silencing section above.

Despite differences in their temporal niche preference, clock gene expression and electrical activity in the SCN of diurnal and nocturnal animals show similar patterns of circadian oscillations (Kubota *et al.*, 1981; Schwartz *et al.*, 1983; Sato & Kawamura, 1984; Bae *et al.*, 2001; Mrosovsky *et al.*, 2001; Yan & Okamura, 2002; Caldeas *et al.*, 2003; Otolara *et al.*, 2013). This suggests that mechanisms acting downstream from the SCN are involved in determining

animal's chronotype (Smale *et al.*, 2003). Nevertheless, results from the above studies make tantalising conjectures that suppressive behavioural inputs into the SCN are important in nocturnal animals to reinforce the night-time electrical down-state, while in diurnal species, up-state SCN activity is reinforced by excitatory photic inputs during the day.

To date, the effects of behavioural activity on SCN electrical output in diurnal species have not been comprehensively investigated. However, from our knowledge of the electrical rhythms in diurnal rodent SCNs we hypothesize that wakefulness and locomotor activity in these animals should provide excitatory inputs to SCN neurons. Under laboratory conditions, unlike in the wild, nocturnal animals are continuously exposed to ambient light during the day. It is therefore likely that, at least under laboratory conditions, light can act to reinforce SCN excitability during the day both in diurnal and nocturnal SCNs. The locomotor activity, on the other hand, reinforces SCN suppression in nocturnal animals at night while possibly supporting SCN excitability in diurnal species during the day.

Overall, these external and internal reinforcements are vital for normal SCN function as they collaborate with TTFL activity to ensure high-amplitude circadian oscillations in SCN excitability (van Oosterhout *et al.*, 2012), a neurophysiological requirement for good health, well-being and cognition (Ramkisoensing & Meijer, 2015). Indeed, this necessity for neuronal oscillation bolstering in the SCN by extrinsic signals is exposed during the ageing process. Here, the age-related dampening of SCN electrical rhythms, due to diminished TTFL outputs and neurochemical signalling, can be restored by daily voluntary exercise and exposure to bright light during the day (Schroeder & Colwell, 2013).

Glial reinforcement of SCN neuronal oscillations

Brain function occurs largely through the intricate and balanced synergistic relationship between neurons and neuroglia. In recent years, the role of glia in neuronal function has received renewed recognition with the discovery that astrocytes respond, synthesise and release many of the neurochemicals (known as 'gliotransmitters') that are pertinent in neuronal information processing (Cornell-Bell *et al.*, 1990; Fiacco *et al.*, 2009; Halassa *et al.*, 2009; Santello *et al.*, 2012; Verkhratsky *et al.*, 2012b). This raises the possibility that, besides maintaining homeostatic processes of the brain (sustaining energy balance, modulating synaptic/neurotransmitter activity and providing metabolic support), glial cells may have a more direct involvement in brain communication processes. Indeed, glial cells show fast intracellular calcium oscillations and can signal through vast network by gap junctions, shaping neuronal activity in the process (Verkhratsky & Kettenmann, 1996; Nedergaard & Verkhratsky, 2010; Nedergaard *et al.*, 2010; Verkhratsky *et al.*, 2012a). In the context of neuronal oscillations, recent pioneering studies have undeniably revealed a surprising role for astrocytes in information processing and cognitive behaviour. These studies found that astrocytic activity in the cortices of behaving animals shapes neuronal rhythm features in these brain areas to influence aspects of learning and memory (Lee *et al.*, 2014), and to appropriately switch cortical circuit rhythms into a synchronous sleep-like state (Poskanzer & Yuste, 2016).

The SCN have an elaborate astrocytic cell network (Guldner, 1983), which exhibits daily rhythms in glial fibrillary acidic protein (Lavialle & Serviere, 1993; Moriya *et al.*, 2000; Gerics *et al.*, 2006; Becquet *et al.*, 2008; Lindley *et al.*, 2008; Canal *et al.*, 2009; Womac *et al.*, 2009; Burkeen *et al.*, 2011), and metabolic activity (Schwartz & Gainer, 1977; van den Pol *et al.*, 1992; Lavialle &

Serviere, 1993; Womac *et al.*, 2009; Burkeen *et al.*, 2011). This SCN GFAP oscillation is sensitive to light, suggesting a possible role for glial involvement in SCN photic information processing. In support, the genetic disruption of GFAP activity in animals maintained under constant light conditions (LL) elicited profound alteration in locomotor activity (Moriya *et al.*, 2000). In addition, several lines of evidence suggest that astrocytes may influence the phase-resetting effects of light in the SCN by putative modulation of glutamatergic transmission at the retinal terminals (van den Pol *et al.*, 1992; Lavialle & Serviere, 1995; Tamada *et al.*, 1998; Moriya *et al.*, 2000; Lavialle *et al.*, 2001; Girardet *et al.*, 2010). Astrocytes are also known to rhythmically affiliate with dendrites of vasoactive intestinal polypeptide (VIP) and arginine vasopressin (AVP) SCN neurons across the day (Becquet *et al.*, 2008). Activity of these neurons promotes cell-to-cell synchronisation and circadian communication within the SCN, and beyond (see section below). Therefore, this daily fluctuation in glial-VIP/AVP neuronal contact may shape electrical activity in these neurons and, thus, supports circadian-relevant information processing in the SCN. In turn, VIP can dose-dependently influence the phase and amplitude of astrocytic rhythms (Marpegan *et al.*, 2009), and pharmacological blockade of metabolic activity in astrocytes alters electrical rhythms in the SCN (Prosser *et al.*, 1994a). Together, these results support that functional signalling between neurons and glia occurs in the SCN, but the role of glial communication in circadian timekeeping still needs in-depth investigation (Jackson, 2011).

Importantly, several studies have reported intrinsic daily oscillations in clock gene/protein expression in SCN astrocytes (Prolo *et al.*, 2005; Cheng *et al.*, 2009; Yagita *et al.*, 2010; Duhart *et al.*, 2013; Brancaccio *et al.*, 2017). This raises the possibility that the daily variation in SCN astrocytic clock activity contributes to overall circadian rhythm generation and communication in the SCN. Indeed, genetic disruption/manipulation of GFAP [(Moriya *et al.*, 2000), but only under LL] and circadian clock gene (Brancaccio *et al.*, 2017) activities in SCN astrocytes produced profound alteration in locomotor activity, and in SCN neuronal clock gene and intracellular calcium oscillations (Barca-Mayo *et al.*, 2017; Brancaccio *et al.*, 2017; Tso *et al.*, 2017). Remarkably, clock gene expression in SCN astrocytes oscillates in antiphase to the rhythm in SCN neurons, peaking during the subjective night in astrocytes (Brancaccio *et al.*, 2017). This night-time peak in SCN astrocytic clock activity is associated with elevated extracellular glutamate level, which may favour an increase in inhibitory GABAergic tone in the SCN, primarily in the dorsal aspect (Brancaccio *et al.*, 2017). Novel mechanisms through which astrocyte activity transforms glutamatergic excitation into tonic GABAergic inhibition have been described elsewhere in the brain (Heja *et al.*, 2012). Such glial-dependent tonic inhibitory GABAergic activity may provide further reinforcement for the electrical down-state in the SCN at night.

Collectively, these studies provide strong evidence supporting a collaborative role for glia and neurons in circadian rhythm generation and communication in the SCN, and, likely, beyond. Further, as in the cortices, glial activity in the SCN may have the additional function in shaping neuronal oscillation features to promote/favour appropriate circadian information processing across the circadian day, such as entrainment, synchronisation and brain-wide/body-wide circadian rhythm communication.

Intra- and intercellular signalling

Elsewhere in the nervous system, oscillations in intracellular calcium signalling underlie most of the fast rhythms in neuronal excitability

(Berridge, 1998, 2014). In SCN neurons, steady-state intracellular calcium $[Ca^{2+}]_i$ concentration/level oscillates in a circadian manner, peaking during the day and entering a nadir at night [(Colwell, 2000; Ikeda *et al.*, 2003a; Irwin & Allen, 2010; Enoki *et al.*, 2012; Hong *et al.*, 2012; Brancaccio *et al.*, 2013; Belle *et al.*, 2014; Ikeda & Ikeda, 2014; Noguchi *et al.*, 2017); but see (Ikeda *et al.*, 2003b)]. This peak in global SCN $[Ca^{2+}]_i$ anticipates the peak in electrical activity (Ikeda *et al.*, 2003a; Enoki *et al.*, 2017b), raising the possibility that the initial source of $[Ca^{2+}]_i$ in SCN neurons is largely through clock-operated intracellular calcium store release (COi-CaSR), and not through depolarised RMP- and action potential-evoked membrane calcium entry via voltage-gated calcium channels (VGCCs). In support, pharmacological blockade of VGCCs and voltage-gated TTX-sensitive sodium channels diminished the amplitude (by ~30%) but does not completely abolish circadian rhythms in $[Ca^{2+}]_i$ (Ikeda *et al.*, 2003a; Enoki *et al.*, 2012).

Activation of the ryanodine receptors (RyR1 and RyR2) represents one of the key signalling pathways by which calcium is released from intracellular stores (Berridge, 1998). The transcripts and proteins for both receptor types are expressed by SCN neurons with RyR2 transcript and protein showing higher levels during the subjective day than at night (Diaz-Munoz *et al.*, 1999; Pfeffer *et al.*, 2009). Interestingly, pharmacological disruption of RyR function abolishes circadian rhythms in $[Ca^{2+}]_i$ level, electrical activity and behaviour (Ikeda *et al.*, 2003a; Mercado *et al.*, 2009), suggesting that this is a key link between the molecular and electrical oscillations in SCN neurons. Indeed, members of the molecular clock, *Bmal1* and *Cry1*, interact to modulate the activity of the RyR2 transcription (Pfeffer *et al.*, 2009; Ikeda & Ikeda, 2014), while pharmacological activation of the RyRs causes excitation in SCN neurons (Aguilar-Roblero *et al.*, 2007, 2016). Together, this suggests that clock-operated intracellular calcium store release contributes to the up-state of SCN neurons during the day.

As in all neurons, the depolarised RMP and increased action potential firing during the up-state cause further calcium influx in SCN neurons through VGCCs (Jackson *et al.*, 2004; Irwin & Allen, 2007). Pharmacological blockade of this TTX-sensitive extracellular calcium source interrupts the molecular clock and electrical oscillations (McMahon & Block, 1987; Yamaguchi *et al.*, 2003; Lundkvist & Block, 2005; Lundkvist *et al.*, 2005; Myung *et al.*, 2012; Enoki *et al.*, 2017b), suggesting that calcium entry through VGCCs also contributes to circadian rhythm generation in the SCN.

Suprachiasmatic nuclei neurons are neurochemically and functionally heterogeneous, forming distinct peptidergic clusters within the ventral, medio-lateral and dorsal aspects of the SCN. Broadly, ventral SCN neurons synthesise VIP, while cells in the medio-lateral region produce gastrin releasing peptide (GRP), and dorsal neurons contain and release AVP (Antle & Silver, 2005; Morin & Allen, 2006; Golombek & Rosenstein, 2010). Some SCN neurons also contain prokineticin 2 (PK2), cardiotrophin-like cytokine and the transforming growth factor α (Kalsbeek & Buijs, 1992; Kalsbeek *et al.*, 1993; Kramer *et al.*, 2001; Cheng *et al.*, 2002, 2005; Kraves & Weitz, 2006; Li *et al.*, 2006; Burton *et al.*, 2016). Collectively, most SCN neurons produce the neurotransmitter GABA and express GABA_A receptors (Abrahamson & Moore, 2001; Belenky *et al.*, 2008). Here, GABA acts primarily on the GABA_A receptors to cause excitation or inhibition in the SCN [see (Albers *et al.*, 2017) for a comprehensive review], presumably coreleased by the SCN peptidergic neurons. As demonstrated by most forms of neuronal synchronisation in the central nervous system, GABA-GABA_A receptor signalling in the SCN acts to synchronise the activity of its neurons (Liu & Reppert, 2000; Shirakawa *et al.*, 2000; Aton &

Herzog, 2005; Evans *et al.*, 2013; DeWoskin *et al.*, 2015; Myung *et al.*, 2015). Signalling from VIP, GRP and AVP neurons intermingles with GABAergic activity across the day–night cycle, through poorly understood mechanisms, to organise and sustain the overall neuronal oscillation architecture of the SCN (see Modelling section 3), such as the phase relationship of its neurons (Harmar *et al.*, 2002; Albus *et al.*, 2005; Aton & Herzog, 2005; Brown *et al.*, 2005; Maywood *et al.*, 2006, 2011a; Hughes *et al.*, 2008; Kalsbeek *et al.*, 2010; Welsh *et al.*, 2010; Evans *et al.*, 2013; Freeman *et al.*, 2013; Fan *et al.*, 2015; Mieda *et al.*, 2015). This phase relationship is dynamic with tremendous plasticity, and varies with environmental conditions (VanderLeest *et al.*, 2007; Lucassen *et al.*, 2012). The GABAergic-neuropeptidergic communication conduits also act cooperatively with the light-input pathway to integrate and align the SCN's daily pattern of oscillations with external environmental signals and feedback inputs from physiology and behaviour. Together, this ensures that, at the population level, SCN neurons produce coherent and high-amplitude circadian rhythms that are representative of the animal's solar cycle and internal physiological demands. Such integrated outputs are in turn necessary for driving robust circadian rhythms across the brain and body.

Function of neuronal oscillations in the SCN

Despite running at a much slower pace, circadian neuronal oscillations in the SCN share some common underlying principles and functions with neuronal oscillators studied elsewhere in the brain. For example, neuronal oscillators have an inherent capacity to appropriately 'gate' or 'vary' their sensitivity to synchronising signals, otherwise known as 'bias input selection' [see (Hutcheon & Yarom, 2000)]. Similarly, SCN neurons show variation across the day in their sensitivity to inputs, such as environmental light and internal physiological signals. Pioneering studies investigating the effects of light on nocturnal rodents, for example, established that light exposure in the early night delays subsequent cycles in locomotor activity, during the late night advances locomotor rhythms, and light during the day has no shifting effect on behavioural rhythm phase (Decoursey, 1960, 1964; Daan & Pittendrigh, 1976). These patterns of temporal sensitivity to light can also be observed in diurnal species, including humans [(Hoban & Sulzman, 1985; Kas & Edgar, 2000; Mahoney *et al.*, 2001; Khalsa *et al.*, 2003); see also Fig. 1 in (Brown, 2016)]. Application of pharmacological mimics of the light-input pathways to living SCN slices, such as glutamate or the glutamate receptor agonists AMPA and NMDA, also causes phase shifts in the electrical rhythms that imitate the light-induced shifts in locomotor activity (Colwell & Menaker, 1992; Shibata *et al.*, 1994; Biello *et al.*, 1997; Ding *et al.*, 1998; Moriya *et al.*, 2000, 2003). Similarly, optogenetic manipulation of SCN activity causes phase shifts in electrical and gene expression rhythms both *in vivo* and *in vitro* (Jones *et al.*, 2015). This phase adjustment by light allows daily resynchronisation of SCN cells to the external light–dark cycle (see section above) and, in extreme situations, permits realignment of the circadian system following a drastic shift in the LD cycle, as is the case in humans when flying across time zones. Albeit, the SCN's slow oscillation means that resynchronisation to the new LD cycle takes several cycles to accomplish (Reddy *et al.*, 2002; Nagano *et al.*, 2003; Yan & Silver, 2004; Nakamura *et al.*, 2005; Davidson *et al.*, 2009).

By contrast, non-photic inputs produce phase shifts in the SCN that differ significantly from those produced by light [see Fig. 1 in (Albers *et al.*, 2017)]. These signals produce large phase advances in behavioural rhythms during the day and small phase delays

during the night (Mrosovsky, 1988; Reeb & Mrosovsky, 1989; Mead *et al.*, 1992; Hastings *et al.*, 1998; Lone & Sharma, 2011; Polidaro *et al.*, 2011). These non-photic phase shifts of the circadian system have also been studied in humans (Redlin & Mrosovsky, 1997; Mistlberger & Skene, 2005). As with the glutamatergic agonist mimics of the light-input pathway, when the SCN are treated during the day with neurochemicals that are linked with non-photic signalling in this structure, such as NPY, large phase advances are seen in locomotor behaviour or SCN firing rate rhythms *in vitro* (Albers & Ferris, 1984; Huhman & Albers, 1994; Biello & Mrosovsky, 1996; Golombek *et al.*, 1996; Biello *et al.*, 1997; Besing *et al.*, 2012). Remarkably, excitatory photic and suppressive non-photic signals can interact with each other at the level of the SCN. Cancellation of non-photic resetting effects occurs during the day if the non-photic signal is followed by a light pulse, or glutamatergic receptor agonists (Biello & Mrosovsky, 1995; Biello *et al.*, 1997; Gamble *et al.*, 2004). Similarly, the phase-shifting effects of light or glutamatergic receptor agonists at night are attenuated if the light pulse or glutamatergic agonist application is followed by non-photic-associated signals (Ralph & Mrosovsky, 1992; Mistlberger & Antle, 1998; Yannielli & Harrington, 2000, 2001; Yannielli *et al.*, 2004).

These inputs modulate rather than dictate SCN function, and this amenability to appropriate phase modulation by external signals represents a canonical property of neuronal oscillators of the brain and one that is central to their function. The capacity for SCN neurons to maintain temporal sensitivity and phase-adjust their electrical rhythms to pharmacological mimics of the light and non-photic input pathways *in vitro* suggests that the mechanisms involved are largely confined within the SCN circuits. Emerging evidence also suggests that these processes are determined both by the molecular and excitability states of SCN neurons (Ding *et al.*, 1998; Pfeffer *et al.*, 2009; Belle & Piggins, 2017). Therefore, the daily oscillatory excitability patterns or waveform of the SCN (up-state during the day and down-state at night, see Fig. 1) determines when and how excitatory and inhibitory inputs are likely to cause significant adjustments to the SCN phase. Such gating properties are crucial, providing a mechanistic neuronal substrate that permits the animals to appropriately respond to potentially competing external and internal signals in order to organise physiology and behaviour.

SCN outputs: communicating circadian rhythms across the brain

Circadian rhythms generated by SCN neurons are communicated across the brain through a broad array of synaptic and paracrine neurochemical signalling, such as VIP, GABA, AVP and PK2 (Ralph *et al.*, 1990; Silver *et al.*, 1990, 1996; Tousson & Meissl, 2004; Morin & Allen, 2006; Maywood *et al.*, 2011b; Morin, 2013; Silver & Kriegsfeld, 2014; Belle, 2015). Many of the downstream targets, including cortical, thalamic, epithalamic and hypothalamic areas, also express clock genes with some showing semi-autonomous variation in clock activity (Guilding & Piggins, 2007; Guilding *et al.*, 2009, 2010; Mohawk *et al.*, 2012; Bano-Otalora & Piggins, 2017). Indeed, electrical activity measurement in some of these brain regions also shows daily patterns in neuronal firing rate that are linked with the molecular clock activity (Sakhi *et al.*, 2014a, 2014b). Arguably, this demonstrates that the influence of the molecular clock on neuronal excitability is not a unique feature of SCN neurons, but extends to other neuronal populations across the brain. Notably, the phasing of clock gene expression in some of these extra-SCN oscillators is aligned with the animal's locomotor

patterns and not with the SCN's phase. Ideal examples for this can be seen in the hippocampi of dual-phasing rodents, such as the *Octodon degus* and diurnal grass rat, *Arvicanthis niloticus*. In these dual-phasing species, hippocampal circadian gene activity peaks in phase with the animal's behavioural rhythm, that is coincidentally in phase with SCN activity when the animals show a diurnal activity pattern, but establish an antiphase relationship when these animals shift their activity phase preference to the night (Ramanathan *et al.*, 2010; Otolara *et al.*, 2013). Indeed, hippocampal and SCN clock gene oscillations in nocturnal species occur out of phase, with hippocampal clock gene expression consistently peaking during the animal's active phase at night (Wakamatsu *et al.*, 2001; Wang *et al.*, 2009). This supports the view that extra-SCN oscillators provide brain region-specific circadian timing in neurophysiology, aligning appropriate neuronal activity rhythms with behavioural and physiological demands (Martin-Fairey & Nunez, 2014), such as for the support of hippocampal memory formation and persistence (Eckel-Mahan, 2012; Wardlaw *et al.*, 2014). Indeed, these semi-autonomous clocks form part of an extended brain-wide circadian timing circuit in which the SCN are the master pacemakers (Green *et al.*, 2008; Morin, 2013). Accordingly, some of these SCN target areas receive direct neuronal projections from the SCN, and collectively, they express receptors for the neurochemicals that are endogenous to SCN neurons, including receptors for VIP (VPAC2), AVP (V1a/b) and PK2 (Zhou & Cheng, 2005; Cheng *et al.*, 2006; Morin & Allen, 2006; Guilding & Piggins, 2007; Mohawk *et al.*, 2012; Sakhi *et al.*, 2014b; Belle, 2015; Burton *et al.*, 2016). The intricate neurophysiological processes and mechanisms through which SCN neurons dynamically sustain/shape circadian rhythms in these extra-SCN clocks, however, remain poorly understood (Fig. 3). Sadly, this knowledge gap is now hampering progress in our understanding of how chronodisruption impacts ailments, such as mental health, metabolic syndrome, Alzheimer's disease and cancer.

Indeed, in several of these brain regions, rhythms that occur at the circadian timescale coexist with neuronal oscillations happening at much faster rates. Good examples for this can be measured in hippocampal and thalamic neuronal ensembles, where exceedingly fast oscillations (at 0.1 to 500 Hz) are interlaced with rhythms sustaining a near 24-h periodicity (Colavito *et al.*, 2015; Loh *et al.*, 2015; Besing *et al.*, 2017; Chen *et al.*, 2017). It is noteworthy that at the population level, neurons of the SCN, and those of the IGL and dorsolateral geniculate nuclei, also produce faster-than-24-h isoperiodic, ultradian or fast narrowband oscillations in electrical activity (Groos & Hendriks, 1979; Miller & Fuller, 1992; Walsh *et al.*, 1992; Bina *et al.*, 1993; Zhang *et al.*, 1995; Pennartz *et al.*, 1998; Aggelopoulos & Meissl, 2000; Lewandowski *et al.*, 2000; Saeb-Parsy & Dyball, 2003a; Brown *et al.*, 2008; Sakai, 2014; Tsuji *et al.*, 2016; Storchi *et al.*, 2017). Recent work has also described neuronal discharge in the SCN with a harmonic distribution close to 30 Hz (Tsuji *et al.*, 2016), oscillations that normally frequent the thalamocortical systems. Remarkably, even when dispersed in culture, SCN neurons can sustain faster-than-24-h oscillations in firing rate at the single-cell level [firing burst rhythms of ~10 min in duration with interburst intervals of 20 to 60 min (Kononenko *et al.*, 2013)]. Elsewhere in the brain, when neighbouring neuronal rhythms with contrasting frequency bands occur within the same anatomical structure, they are normally associated with different brain states. Indeed, these oscillations can appropriately compete or interact with one another (Klimesch, 1999; Kopell *et al.*, 2000; Engel *et al.*, 2001; Steriade, 2001; Csicsvari *et al.*, 2003). In the SCN, how these neighbouring rhythms interact and whether they coalesce to influence circadian rhythm generation and

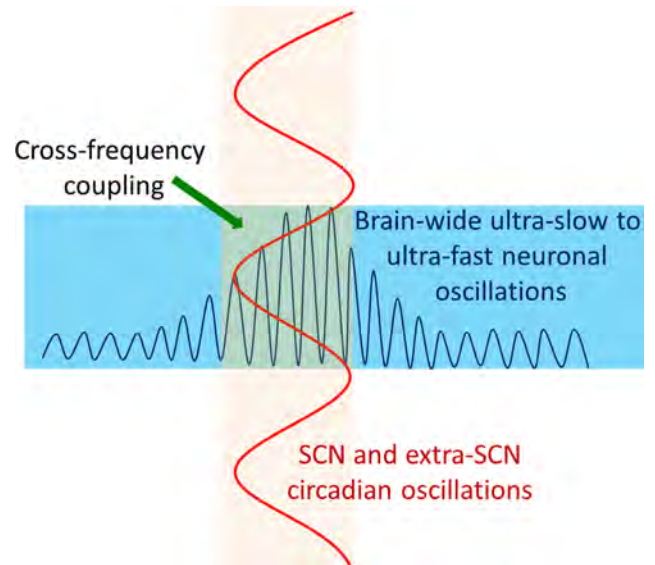


FIG. 3. A conceptualised schematic view of possible interactions between circadian rhythms and much faster neuronal oscillations in the brain, such as the fast rhythms of the hippocampus. The slow near 24-h rhythms generated by the suprachiasmatic nuclei (SCN) and/or extra-SCN oscillators interact with faster neuronal oscillations through cross-frequency coupling. This interaction influences the rhythm features, such as rhythm amplitude, of these faster brain oscillators. The detailed mechanisms involved remain elusive, but the concept presented here is based on our current understanding of neuronal rhythms interactions in the brain, and the circadian influence on ultradian corticosterone pulsatile release. Together, these may provide a glimpse into how these oscillations interact in the CNS in order to organise physiology and behaviour.

communication in this hypothalamic structure are unknown and warrant detailed investigations.

Nevertheless, the interesting observation that these faster ultradian and beta/gamma rhythms are more prominent during photopic than scotopic conditions suggests that they may play important roles in broadcasting and modulating environmental light information across the SCN circuits, and beyond. Indeed, many of the body's hormonal secretion profiles follow an ultradian rhythm (Bonfont, 2010; Fitzsimons *et al.*, 2016). Our recent understanding of the intricate relationship between circadian and ultradian rhythms in daily corticosterone pulsatile release and activity provides a glimpse, perhaps, into how these oscillations may interact in the SCN and the brain for normal physiology [(Spiga *et al.*, 2014; Fitzsimons *et al.*, 2016); see Fig. 3 for a hypothesis]. As demonstrated elsewhere in the 'rhythm' fields, mathematical modelling will no doubt play a crucial role in shaping our understanding of such interactions and their physiological and behavioural relevance (see Modelling section 4).

Modelling section 1: mathematical modelling of the circadian clock at the single-cell level

One of the earliest models of biochemical oscillations incorporating the regulation of gene expression was introduced by Goodwin (Goodwin, 1965). This three-variable model, consisting of delayed negative feedback to a single gene, has been used by many researchers as a simple model of the mammalian molecular clock; see Fig. 4A (Ruoff *et al.*, 1999; Locke *et al.*, 2008; Woller *et al.*, 2013). The basic mathematical concept underlying these models is that delayed negative feedback can destabilise a steady state and

give rise to stable limit cycle oscillations through Hopf bifurcation (Forger, 2017). The only nonlinearity in the Goodwin model is the sigmoidal Hill function that characterises repression of transcription. Griffith showed that limit cycle oscillations are only possible in the Goodwin model with a Hill exponent $n > 8$ (Griffith, 1968). While such a large Hill exponent is unlikely to arise from cooperative binding of the repressor to the promoter (the typical interpretation for using $n = 3$ or 4 in enzyme kinetics) alone, other processes, such as multisite phosphorylation/dephosphorylation, could contribute to the sharpness of the protein activation function (Gonze & Abou-Jaoude, 2013; Woller *et al.*, 2014). Following the identification of several core clock genes, Leloup–Goldebeter and Forger–Peskin introduced detailed models incorporating these genes and their protein products (Forger & Peskin, 2003; Leloup & Goldebeter, 2003). The Leloup–Goldebeter retained the Hill function formulation of transcriptional regulation, whereas the Forger–Peskin model replaced Hill functions with first-order mass action kinetics. This results in a higher-dimensional model (73 differential equations in Forger–Peskin versus 16 in Leloup–Goldebeter), but fewer phenomenological parameters (such as Hill exponents) to estimate since all parameters now represent reaction rates. Development of new molecular models in both of these styles has continued as additional clock components and processes are characterised (Mirsky *et al.*, 2009; Relógio *et al.*, 2011; Kim & Forger, 2012; Jolley *et al.*, 2014; Woller *et al.*, 2016); see (Podkolodnaya *et al.*, 2017) for a recent review of this line of work. These models have made testable predictions that were validated experimentally, such as the short-period effect of the *Tau* mutation in hamsters (Gallego *et al.*, 2006). Detailed predictive models can provide insight into circadian clock mechanisms and evaluate competing hypotheses. For example, the Kim–Forger model has been used to argue that the key mechanism of transcriptional regulation in the mammalian clock is sequestration, and not multisite phosphorylation, of the repressor protein (Kim & Forger, 2012; Kim, 2016).

In comparison with the molecular clock, the electrical activity of mammalian clock neurons has received less attention from modellers. The first electrophysiological model of SCN neurons was developed by Sim and Forger (Sim & Forger, 2007) using the Hodgkin–Huxley formalism. The basic concept underlying conductance-based models is an electrical equivalent circuit representation of the cell membrane; see Fig. 4B. The Sim–Forger model was fit primarily to voltage-clamp data from dissociated SCN neurons (Jackson *et al.*, 2004), and included three voltage-gated currents (I_{Na} , I_{Ca} and I_K) and a passive ‘leak’ current (I_L). This model suggested that SCN neurons may enter depolarisation blockade at a certain time of day, a prediction that has since been validated experimentally (Belle *et al.*, 2009). Several authors have extended the Sim–Forger model to study various aspects of SCN neuronal activity, such as interspike interval variability due to stochastic openings of subthreshold voltage-dependent cation (SVC) channels (Kononenko & Berezetskaya, 2010), calcium-dependent inhibition of calcium influx through RNA editing of L-type calcium channels (Huang *et al.*, 2012) and nonlinear dependence of I_{Ca} on the Ca^{2+} driving force (Clay, 2015).

There are many ways in which the molecular clock may affect membrane excitability, such as by regulating the activation or inactivation properties of voltage-gated ionic channels. For example, Kononenko & Berezetskaya (2010) assumed that a circadian-regulated protein decreases the closed-time distribution of SVC channels (Kononenko & Berezetskaya, 2010). However, the most common way of connecting molecular and membrane models is to translate rhythms in mRNA levels of ion channel transcripts to rhythms in

maximal conductances. As circadian changes in gene expression and protein abundance happen on a much slower timescale than the dynamics of action potential generation, one can model the electrical activity of SCN neurons over a short time interval by treating the gene and protein levels as parameters rather than dynamical variables. To simulate electrical activity at different times of day, the gene and protein parameters can be set in accordance with the phase of their daily rhythms. Viewed in this context, the maximal conductances of a Hodgkin–Huxley-type model become natural bifurcation parameters, and dynamical systems tools can be used to study transitions in SCN electrical activity over the course of the day. This strategy was used to interpret the DLAMOs observed in a subset of SCN neurons as evidence of the cells approaching a supercritical Hopf bifurcation due to increased g_{Ca} and decreased g_K (Belle *et al.*, 2009). The circadian variation in firing rate and resting membrane potential exhibited by SCN neurons is likely due to circadian variation in the conductance of several different types of ion channels (Kim & Jeong, 2008; Colwell, 2011). Flourakis *et al.* (2015) used a combination of experiments and modelling to show that antiphase rhythms in voltage-independent passive ‘leak’ currents, with sodium leak upregulated during the day and potassium leak upregulated at night, could reproduce the observed circadian variations in firing rate of SCN neurons. Furthermore, this ‘bicycle’ mechanism of anti-phase regulation appears to be conserved in flies and mice.

A few models have dynamically integrated gene regulation and electrical activity at the single-cell level. Vasalou and Henson combined the Leloup–Goldebeter model of the molecular clock with an electrophysiology model based on the integrate-and-fire formalism (Vasalou & Henson, 2010). In this framework, circadian variation in ionic conductances leads to daily rhythms in variables representing RMP and firing rate. However, the model evolves on a timescale of minutes rather than milliseconds and therefore does not actually produce individual spike events (action potentials). Diekman *et al.* (2013) combined a modified version of the Sim–Forger model of action potential generation with a Goodwin-like model of gene regulation. In both the Vasalou–Henson and Diekman *et al.* models, intracellular calcium serves as the link between membrane dynamics and gene expression. The additional layer of feedback that comes from coupling membrane excitability to transcription can induce circadian oscillations in gene expression in a model of the molecular clock with parameters set such that it does not oscillate in the absence of excitation–transcription coupling (see Figs. 4C and 5). This supports the notion that SCN electrical activity may not just be a circadian output signal but also part of the clock’s timekeeping mechanism, conceptualised here as the membrane clock.

Modelling section 2: mathematical modelling of circadian entrainment

There is a long history of mathematical modelling to aid understanding of how circadian oscillators (with periods near but not equal to 24 h) entrain to 24-h environmental cycles (Pavlidis, 1978; Winfree, 2001; Gonze, 2011a). Models predating the discovery of the suprachiasmatic nuclei and the transcriptional–translation feedback loops underlying the molecular clock were necessarily phenomenological rather than mechanistic. Wever used a modified version of the van der Pol oscillator to study re-entrainment of circadian rhythms following phase shifts of the light–dark cycle (Wever, 1966). Kronauer and colleagues further modified the van der Pol model to match experimental data on human circadian rhythms (Kronauer, 1990; Forger *et al.*, 1999). Variants of the Kronauer model are still being used to explain properties of jet-lag and to

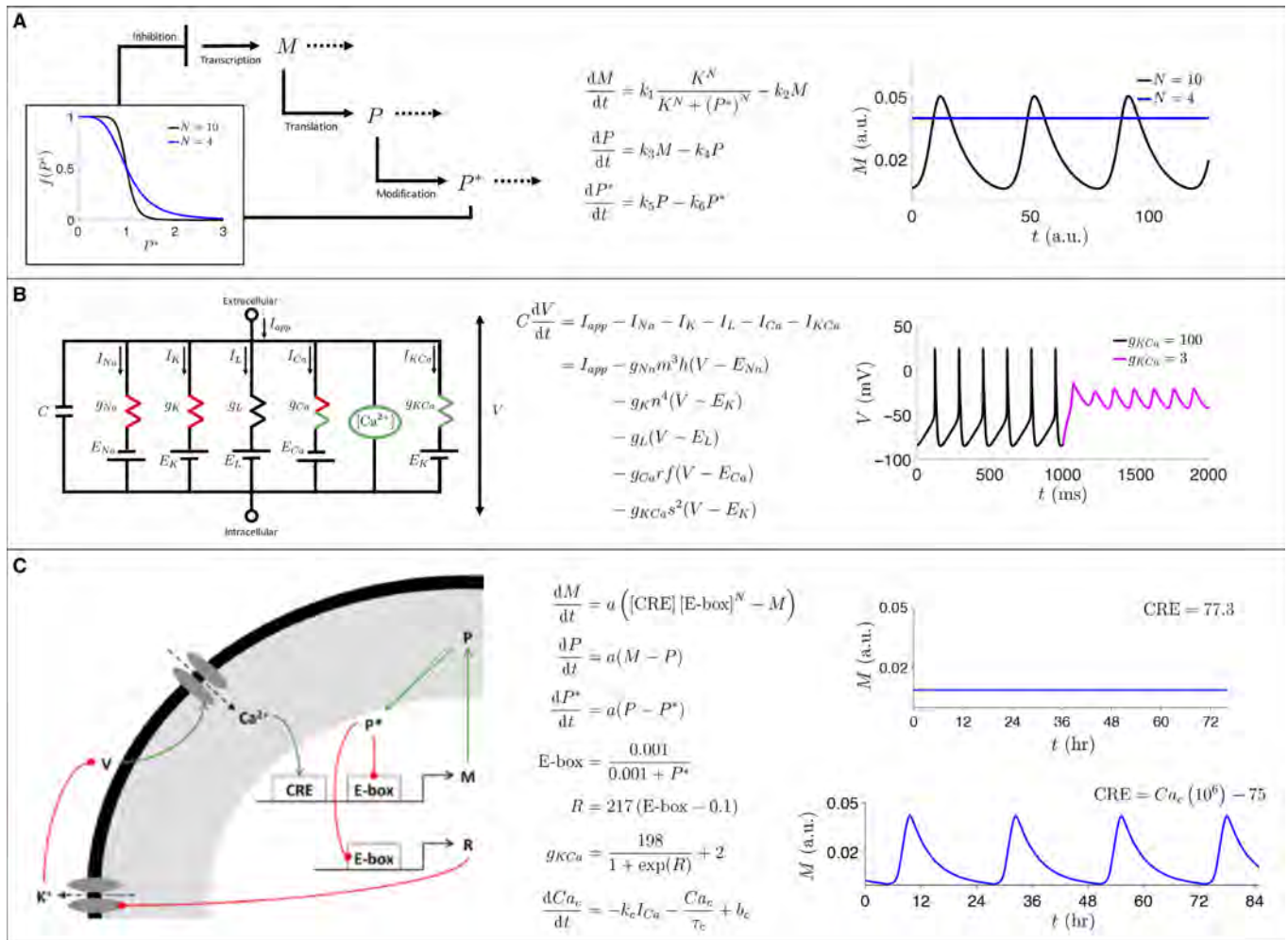


FIG. 4. Schematic overview, main equations and sample output for models of the molecular circadian clock (A), the electrophysiology of suprachiasmatic nuclei (SCN) neurons (B), and the interaction between circadian gene expression and SCN electrical activity (C). A: Goodwin model of gene regulation. A gene is transcribed into mRNA (M) and translated into protein (P), which undergoes posttranslational modifications (P^*) and is imported back into the nucleus where it inhibits production of M . This negative feedback loop can lead to oscillations in mRNA and protein levels if the Hill exponent (N) in the transcription repression function $f(P^*)$ is large enough. The dashed arrows represent mRNA and protein degradation. B: Hodgkin-Huxley-type model of neuronal excitability. The membrane voltage (V) is governed by a current-balance equation involving the cell capacitance (C) and ionic currents (I_x for ion x), described by a conductance (g_x) multiplied by a driving force ($V - E_x$), where E_x is the reversal potential of the ion channel. The sodium (Na), potassium (K) and calcium (Ca) channels are voltage-gated, with activation (m , n , r) and inactivation (h) gating variables that open/close as functions of voltage (red resistors). The activation gating variable (s) of the calcium-dependent potassium channel (KCa), as well as the inactivation gating variable of the calcium channel (f), are functions of intracellular calcium concentration $[Ca^{2+}]_i$ (green resistors). The conductance of the leak channel (L) is passive, that is, not voltage- or calcium-dependent (black resistor). The differential equations describing the dynamics of the gating variables are not shown. This system of ordinary differential equations (ODEs) simulates how membrane voltage evolves over time and can produce both repetitive firing of action potentials ($g_{KCa} = 100$ nS) and depolarised low-amplitude membrane oscillations (DLAMOs; $g_{KCa} = 3$ nS). C: Extended gene regulation model incorporating electrophysiology. Another gene product (R) is under the control of the same enhancer (E-box) found in the promoter region of the circadian clock gene that is transcribed into M . R downregulates the activity of potassium channels, which depolarises the membrane potential (V), leading to calcium influx through I_{Ca} . Higher levels of intracellular calcium (Ca_c) can activate transcription through the cAMP response element (CRE) pathway. Modelling CRE-dependent transcription as a function of Ca_c (bottom right inset) provides an additional layer of feedback control from membrane excitability onto gene expression and induces oscillations in mRNA concentration (M , arbitrary units), whereas modelling CRE activity as constant (top right inset) does not produce oscillations. In both cases, the Hill exponent representing cooperativity of repression at the E-box is set at $N = 4$.

design optimal schedules for fast re-entrainment following trans-meridian travel (Serkh & Forger, 2014; Diekmann & Bose, 2017). The process of re-entrainment has also been studied in more detailed models of the SCN network (Kingsbury *et al.*, 2016), and hierarchical systems with internal desynchrony between the SCN and clocks in peripheral organs (Leise & Siegelmann, 2006). An area requiring further work in the context of re-entrainment is the incorporation of homeostatic sleep drive and the gating of light input due to sleep (Booth *et al.*, 2017; Skeldon *et al.*, 2017). Classical dynamical

systems tools such as phase response curves and Arnold tongues (Bordyugov *et al.*, 2015), along with the more recently developed methods of velocity response curves (Taylor *et al.*, 2010), macroscopic reduction of coupled phase oscillators (Hannay *et al.*, 2015; Lu *et al.*, 2016), and entrainment maps (Diekmann & Bose, 2016), can provide insight into how entrainment properties of circadian oscillators depend on internal and external parameters, such as the oscillator's endogenous period, the environmental light intensity and daylength.

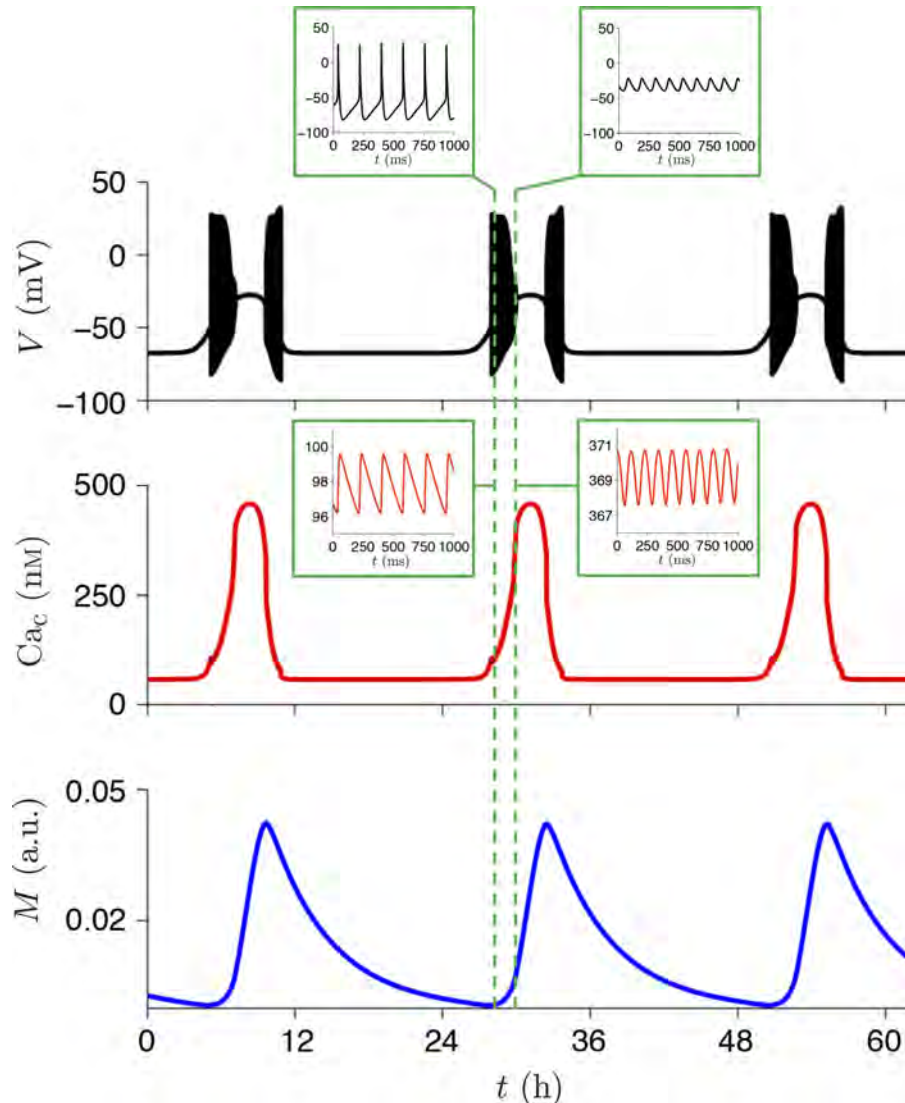


FIG. 5. Computer simulations of a multiscale mathematical model of suprachiasmatic nuclei (SCN) neurons integrating membrane excitability, intracellular calcium dynamics and gene regulation (see Fig. 4C). The membrane potential (V , thick black trace) exhibits a daily oscillation traversing several different electrical states on the timescale of hours. Embedded within the daily rhythm are oscillations on a much faster timescale (milliseconds), such as repetitive firing of action potentials at 6 Hz (top left inset) and DLAMOs (top right inset). These rhythms in RMP drive oscillations in intracellular calcium concentration (Ca_c) on both the daily (thick red trace) and millisecond (above left and right insets) timescales. The calcium rhythm induces a daily oscillation in gene expression [mRNA concentration M (arbitrary units), thick blue trace]. In turn, the gene expression rhythm regulates ion channel conductances that coordinate to produce the daily oscillation in membrane potential. This figure is adapted from (Diekmann *et al.*, 2013).

Modelling section 3: mathematical modelling of the circadian clock at the network level

How the neurons within the SCN form a tissue-level clock capable of entraining to 24-h environmental rhythms and communicating this time-of-day information to other parts of the brain and body remains a fundamental question in the circadian field. As is the case for single-cell models, network models of the SCN exist at varying levels of biophysical detail. On the abstract end of the spectrum are models that view the SCN as a weakly coupled network of phase oscillators (Liu *et al.*, 1997). However, generic amplitude-phase oscillators may be more appropriate than pure phase models (Bordyugov *et al.*, 2011), as it has been shown that the amplitude of circadian oscillations can affect entrainment behaviour (VanderLeest *et al.*, 2009). Networks of modified van der Pol oscillators

with local coupling (Kunz & Achermann, 2003), or daily inputs from non-rhythmic 'gate' cells (Antle *et al.*, 2003), have also been explored. Gonze *et al.* (2005) studied a network of Goodwin-like genetic oscillators globally coupled by a generic neurotransmitter. Many network models have since been developed incorporating more detailed descriptions of clock gene regulation, intercellular signalling cascades, and coupling architecture [for a review, see (Henson, 2013)]. For example, To *et al.* (2007) employed the Leloup-Goldbeter model of the TTFL, then added VIP/VPAC2 signalling, and a network with coupling strengths inversely proportional to the distance between cells. Bernard *et al.* (2007) used a molecular clock model that produces damped oscillations in the absence of coupling (Becker-Weimann *et al.*, 2004) and tested the effects of random sparse coupling, nearest-neighbour coupling, and an SCN-like combination of random sparse and nearest-neighbour connections. The

Vasalou–Herzog–Henson model included both VIP and GABA signalling, and mimicked the spatial organisation of the SCN by using small-world coupling for the ventral core region and nearest-neighbour coupling for the dorsal shell region (Vasalou *et al.*, 2011). This model also included an electrophysiology component that accounted for the effect of various ion channels and synaptic currents on each cell's firing rate, but did not simulate individual action potentials. Similarly, Bush and Siegelman used the leaky integrate-and-fire formalism and a two-variable model of the molecular clock to investigate the interaction of gene expression and firing rate in a small-world SCN network (Bush & Siegelman, 2006). Diekman and Forger modelled action potential generation in the SCN network with Hodgkin–Huxley-type neurons and GABA synapses. However, this model did not include dynamics of the molecular clock (Diekman & Forger, 2009). DeWoskin *et al.* (2015) developed the first network model of the SCN that resolves individual action potentials and intracellular molecular clock mechanisms. This model predicts that tonic GABA release at depolarised resting membrane potentials (during hyperexcitation) can phase shift the molecular rhythms and affects SCN synchrony. This highlights the importance of hyperexcitation in SCN neurons during the day.

Modelling section 4: future directions for mathematical modelling of the circadian system

In contrast to the prevalence of phenomenological and molecular models of the circadian clock, electrophysiological modelling of the SCN network is relatively nascent. The mechanisms by which the release of GABA, VIP, and other neurotransmitters and neuropeptides coordinate the daily electrical and gene expression rhythms of SCN neurons in the dorsal shell and ventral core are still poorly understood. Multiscale models of the SCN have the potential to generate experimentally testable predictions regarding rhythm generation across the network, inspired by the role that the interaction of modelling and experiment has played in distinguishing the ING (interneuronal network gamma) and PING (pyramidal-interneuronal network gamma) mechanisms of gamma oscillations (Whittington *et al.*, 2000; Tiesinga & Sejnowski, 2009; Wang & Buzsáki, 2012; Börgers, 2017).

In this review, we have primarily discussed models consisting of deterministic systems of ordinary differential equations (ODEs). Figure 6 provides a visual summary of the degree to which detailed molecular clock and electrophysiological mechanisms were incorporated into each of these models. Stochastic single-cell and network models have also been developed (Forger & Peskin, 2005; Ko *et al.*, 2010; An *et al.*, 2013) to explore the robustness of circadian rhythms to intrinsic and extrinsic sources of noise, but these have yet to be combined with electrophysiological models. ODE models, whether deterministic or stochastic, also neglect the spatial aspect of mRNA and protein molecules moving throughout the cell. Thus, partial differential equation (PDE) models incorporating reaction-diffusion may be useful for making quantitative predictions about spatial dynamics of the molecular clock. Nonetheless, ODE models have been able to explain certain features of spatial patterning in the SCN, such as why clock gene expression in the dorsal region phase leads the ventral region (Myung *et al.*, 2012). Aside from dynamical modelling, machine-learning algorithms have also been used to analyse how the spatial architecture of the SCN contributes to robust rhythm generation (Pauls *et al.*, 2014).

Beyond circadian rhythms, other biological oscillations involve the feedback between gene expression and electrical activity, for example the pulsatile release of GnRH every 90 minutes. Lightman and colleagues (Spiga *et al.*, 2015) have developed mathematical

models to explore the interaction between the circadian clock and this ultradian endocrine rhythm. Furthermore, a mathematical modelling study of pancreatic islet β -cells has shown that calcium-dependent transcription can adjust potassium channel activity to rescue electrical bursting and insulin oscillations (Yildirim & Bertram, 2017). Circadian rhythms also modulate cortical excitability and EEG synchrony (Ly *et al.*, 2016). Chellappa *et al.* (2016) used neural mass modelling and the dynamic causal modelling (DCM) framework to demonstrate a strong circadian influence on cortical excitation/inhibition balance and gamma oscillations. Recent modelling and experimental work has also suggested that the circadian phase distribution of neurons in the hippocampus can support memory formation (Eckel-Mahan, 2012; Damineli, 2014). Damineli coined the term 'Tau wave' to describe the temporarily coherent phase clusters with an approximately 24-hour period that emerged in his model of memory trace formation. As *Tau* is often used to denote the intrinsic period of a circadian oscillator, this term nicely emphasises the commonality between brain rhythms on the ultra-slow timescale and faster neuronal oscillations, such as alpha, beta, gamma, delta, mu and theta waves/oscillations. Future work integrating circadian components into models of neuronal oscillations on faster timescales could reveal new insights into daily regulation of a variety of brain functions.

Conclusion and perspectives

Neuronal oscillations in the master mammalian daily clock generate and broadcast circadian timing across the brain and body. These synchronising signals shape the spatiotemporal architecture of physiology and behaviour, aligning their respective processes and activity with the prevailing light–dark cycle and the animal's internal physiological demands. To provide such timing signals, SCN neurons vary their membrane excitability state, so that their RMPs are generally more depolarised during the day than at night. In some SCN neurons, action potential discharge patterns are in phase with the day–night RMP rhythm, firing at higher rates during the day than at night. In others, the daytime RMP becomes too depolarised for spiking, and the neurons enter a silent state of depolarisation blockade or generate 2–7 Hz DLAMOs during the afternoon, before traversing to the hypoexcited night state. These RMP and firing rate excursions produce a sinusoidal excitability waveform in the SCN that peaks during the day and troughs at night, sustaining a neuronal oscillation with a near 24-h period or wavelength (Fig. 1).

In most SCN neurons, the drive to peak excitation during the day and hypoexcitation at night results from the activity of an internal molecular clockwork, where perpetual daily oscillations in clock gene expression regulate intracellular signalling cascades, ion channel activity and neurotransmitter release. Despite our formidable knowledge of the cell-autonomous processes that cause daily oscillations in clock gene expression, our understanding of how the molecular clockwork interacts with the membrane to regulate excitability of SCN neurons is severely lacking. Feedback cues from the environment and internal physiology also signal to SCN neurons, adjusting the timing precision of their internal molecular clockwork. This raises an interesting conundrum, because to influence the activity of the clock these resetting cues must first signal through the plasma membrane (Fig. 2). The mechanisms involved in this electrical-genetic interaction remain elusive, but emerging evidence, both in mammals and *Drosophila* clocks, supports the concept that the plasma membrane is not merely the proximal target of the molecular clockwork, but its excitability is integral to the functioning of the clock (Nitabach *et al.*, 2002, 2006; Lundkvist & Block, 2005;

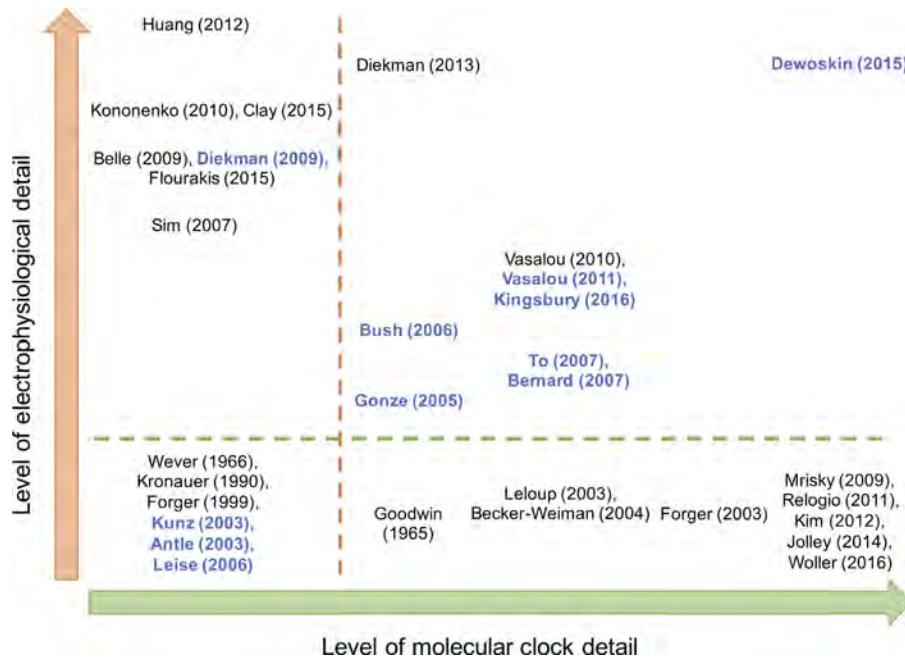


FIG. 6. Visual summary of the level of molecular clock and electrophysiological detail of 31 circadian models in the literature. Models below the green line are purely molecular, and models to the left of the orange line are purely electrophysiological. Models in the lower left quadrant are phenomenological (i.e., neither molecular nor electrophysiological), and models in the upper right quadrant have both molecular and electrophysiological components. Models in black font are single-cell models, and models in blue font are network models.

Lundkvist *et al.*, 2005; Wu *et al.*, 2008; Diekman *et al.*, 2013; Granados-Fuentes *et al.*, 2015), conceptualised here as the membrane clock (Fig. 2). An ingenious study in flies by Mizrak and colleagues established that the membrane clock can indeed feedback to impose time-of-day stamps onto the molecular clock transcriptome, acting as an internal *zeitgeber* (time-giver; Mizrak *et al.*, 2012). Alternatively, intercellular signals could also influence the activity of the molecular clock in manners that are independent of membrane excitability. For example, VIP could directly activate clock gene transcription through its effects on intracellular calcium and cAMP signalling (Akiyama *et al.*, 2001; Travnickova-Bendova *et al.*, 2002; Itri & Colwell, 2003; Irwin & Allen, 2010). Indeed, calcium entry through glutamatergic receptors activation could also have similar direct modulating effects on clock gene transcription alongside or independent of electrical excitation. Remarkably, therefore, the circadian clock functions through an autonomous and intricate genetic-electrical interplay which dynamically regulates, integrates and processes converging inputs at multiple cellular and network levels, while simultaneously broadcasting circadian signals across the brain and body.

Undeniably, neuronal rhythms are a widespread phenomenon, spanning across several brain regions and a wide range of frequency bands, from 0.05 to 600 Hz. In some of these structures, such as the hippocampus and cortex, these fast rhythms coexist alongside the much slower circadian oscillations. Interestingly, even in the SCN, faster ultradian and beta/gamma rhythms are found embedded within the slower circadian cycle. Uncovering the relationship between these brain-wide neuronal oscillators is a daunting challenge, but a necessary task if we are to understand how the all-important timing in physiology and behaviour is dynamically shaped and organised at multiple timescales (see Fig. 3). Across the forebrain regions, slow rhythms are known to influence the amplitude of oscillations with higher frequencies, synchronise large spatial domains and temporally link neurons into assemblies. Thus,

taking all this into account, circadian rhythms must therefore be studied in the context of other brain oscillations if we are to understand their roles in shaping faster global brain events. In support, despite the wide distribution of neuronal oscillators along the frequency spectrum, the frequencies of these oscillations form a linear progression on the natural logarithmic scale (Freeman *et al.*, 2000; Penttonen & Buzsaki, 2003), perhaps mathematically underscoring their brain-wide interconnection. In the context of circadian timing, it is therefore conceivable that neuronal oscillations in the SCN at the circadian, ultradian and faster timescales represent the critical ‘middle ground’, linking single neuron activity, at the microsecond and millisecond timescales of ion channel conductance, action potential firing and synaptic release, to circadian pattern generation in physiology and behaviour.

Indeed, as demonstrated across the neuroscience disciplines and beyond, mathematical modelling has become an indispensable companion for driving our hypotheses, guiding our experiments and clarifying our understanding. This alliance between the two fields will no doubt be central in our strive to unravel some of the idiosyncratic processes in brain operation, physiology and behaviour that otherwise would be impenetrable.

Acknowledgements

We thank Dr. Beatriz Baño Otálora for producing some of the figures and for her critical comments. We also extend our gratitude to Dr. Mark Humphries for his invaluable comments. M.D.C.B is supported by the University of Exeter Medical School (UEMS). C.O.D’s work was partially supported by the National Science Foundation under grant nos. DMS-1412877 and DMS-155237, and the U.S. Army Research Laboratory and the U.S. Army Research Office under Grant No. W911NF-16-1-0584.

Conflict of interest

The authors have no conflict of interests to declare.

Author contributions

MDCB conceived and wrote the physiological data section. COD conceived and wrote the computational modelling section. MDCB and COD edited the manuscript and approved the submission of the final version.

Abbreviations

AMPA, α -amino-3-hydroxy-5-methyl-4-isoxazole-propionic acid; APs, action potentials; AVP, arginine vasopressin; BK_{Ca} , large-conductance calcium-activated potassium channels; *Bmal1*, brain and muscle Arnt-like gene-1; BMAL1, brain and muscle Arnt-like protein-1; $[Ca^{2+}]_i$, intracellular calcium; cAMP, cyclic adenosine monophosphate; CLOCK/BMAL1, CLOCK and BMAL1 heterodimer; *Clock*, circadian locomotor output cycles Kaput gene; CLOCK, circadian locomotor output cycles Kaput protein; COiCaSR, clock-operated intracellular calcium store release; *Cry1*, *cryptochrome 1* gene; CRY1, cryptochrome 1 protein; *Cry2*, *cryptochrome 2* gene; CRY2, cryptochrome 2 protein; DCM, dynamic causal modelling; DLAMOs, depolarised low-amplitude membrane oscillations; EEG, electroencephalogram; EGFP, enhanced green fluorescent protein; FDR, fast delayed rectifier; GABA, gamma-aminobutyric acid; g_{Ca} , calcium conductance; GFAP, glial fibrillary acidic protein; geniculohypothalamic tract; g_K , potassium conductance; GRP, gastrin releasing peptide; I_{Ca} , calcium current; IGL, intergeniculate leaflet; I_K , potassium current; I_L , voltage 'leak' current; I_{Na} , sodium current; K2P, two-tandem pore domain potassium channels; LAMOs, low-amplitude membrane oscillations; LD, light-dark cycle; LL, light-light cycle or constant light conditions; NACLN, voltage-insensitive nonselective cation channel; NMDA, N-methyl-D-aspartate; NPY, neuropeptide Y; ODEs, ordinary differential equations; PDE, partial differential equation; PER/CRY, PER/CRY proteins heterodimer; *Per1*, *Period1* gene; PER1, Period1 protein; *Per2*, *Period2* gene; PER2, Period2 protein; PK2, prokineticin 2; PKR2, receptor for PK2; *Rev-erba*, gene; REV-ERB α , protein; RHT, retino-hypothalamic tract; RMP, resting membrane potential; RyR1, ryanodine receptor type 1; RyR2, ryanodine receptor type 2; RyRs, ryanodine receptors; SCN, suprachiasmatic nuclei; SK_{Ca} , small-conductance calcium-activated potassium channels; SVC, subthreshold voltage-gated cation channels; TGF α , transforming growth factor α ; TTFL, transcription-translation feedback loop; TTX, tetrodotoxin; V1a/b, receptors for AVP; VGCCs, voltage-gated calcium channels; VIP, vasoactive intestinal polypeptide; VPAC2, receptor for VIP; ZT, zeitgeber time (time-giver).

References

Abrahamson, E.E. & Moore, R.Y. (2001) Suprachiasmatic nucleus in the mouse: retinal innervation, intrinsic organization and efferent projections. *Brain Res.*, **916**, 172–191.

Aggelopoulos, N.C. & Meissl, H. (2000) Responses of neurons of the rat suprachiasmatic nucleus to retinal illumination under photopic and scotopic conditions. *J. Physiol.*, **523**(Pt 1), 211–222.

Aguilar-Roblero, R., Mercado, C., Alamilla, J., Laville, A. & Diaz-Munoz, M. (2007) Ryanodine receptor Ca^{2+} -release channels are an output pathway for the circadian clock in the rat suprachiasmatic nuclei. *Eur. J. Neurosci.*, **26**, 575–582.

Aguilar-Roblero, R., Quinto, D., Baez-Ruiz, A., Chavez, J.L., Belin, A.C., Diaz-Munoz, M., Michel, S. & Lundkvist, G. (2016) Ryanodine-sensitive intracellular Ca^{2+} channels are involved in the output from the SCN circadian clock. *Eur. J. Neurosci.*, **44**, 2504–2514.

Akasu, T., Shoji, S. & Hasuo, H. (1993) Inward rectifier and low-threshold calcium currents contribute to the spontaneous firing mechanism in neurons of the rat suprachiasmatic nucleus. *Pflug. Arch.*, **425**, 109–116.

Akiyama, M., Minami, Y., Nakajima, T., Moriya, T. & Shibata, S. (2001) Calcium and pituitary adenylate cyclase-activating polypeptide induced expression of circadian clock gene *mPer1* in the mouse cerebellar granule cell culture. *J. Neurochem.*, **78**, 499–508.

Albers, H.E. & Ferris, C.F. (1984) Neuropeptide Y: role in light-dark cycle entrainment of hamster circadian rhythms. *Neurosci. Lett.*, **50**, 163–168.

Albers, H.E., Walton, J.C., Gamble, K.L., McNeill, J.K.T. & Hummer, D.L. (2017) The dynamics of GABA signaling: revelations from the circadian pacemaker in the suprachiasmatic nucleus. *Front. Neuroendocrinol.*, **44**, 35–82.

Albus, H., Bonnefont, X., Chaves, I., Yasui, A., Doczy, J., van der Horst, G.T. & Meijer, J.H. (2002) Cryptochrome-deficient mice lack circadian electrical activity in the suprachiasmatic nuclei. *Curr. Biol.*, **12**, 1130–1133.

Albus, H., Vansteensel, M.J., Michel, S., Block, G.D. & Meijer, J.H. (2005) A GABAergic mechanism is necessary for coupling dissociable ventral

and dorsal regional oscillators within the circadian clock. *Curr. Biol.*, **15**, 886–893.

Allen, C.N., Nitabach, M.N. & Colwell, C.S. (2017) Membrane currents, gene expression, and circadian clocks. *CSH Perspect. Biol.*, **9**, a027714.

An, S., Harang, R., Meeker, K., Granados-Fuentes, D., Tsai, C.A., Mazuski, C., Kim, J., Doyle F.J. *et al.* (2013) A neuropeptide speeds circadian entrainment by reducing intercellular synchrony. *Proc. Natl. Acad. Sci. USA*, **110**, E4355–E4361.

Anand, S.N., Maywood, E.S., Chesham, J.E., Joynson, G., Banks, G.T., Hastings, M.H. & Nolan, P.M. (2013) Distinct and separable roles for endogenous CRY1 and CRY2 within the circadian molecular clockwork of the suprachiasmatic nucleus, as revealed by the *Fbx13*(*Afh*) mutation. *J. Neurosci.*, **33**, 7145–7153.

Antle, M.C. & Silver, R. (2005) Orchestrating time: arrangements of the brain circadian clock. *Trends Neurosci.*, **28**, 145–151.

Antle, M.C., Foley, D.K., Foley, N.C. & Silver, R. (2003) Gates and oscillators: a network model of the brain clock. *J. Biol. Rhythms*, **18**, 339–350.

Aton, S.J. & Herzog, E.D. (2005) Come together, right... now: synchronization of rhythms in a mammalian circadian clock. *Neuron*, **48**, 531–534.

Bae, K. & Weaver, D.R. (2007) Transient, light-induced rhythmicity in *mPer*-deficient mice. *J. Biol. Rhythms*, **22**, 85–88.

Bae, K., Jin, X., Maywood, E.S., Hastings, M.H., Reppert, S.M. & Weaver, D.R. (2001) Differential functions of *mPer1*, *mPer2*, and *mPer3* in the SCN circadian clock. *Neuron*, **30**, 525–536.

Bano-Otalora, B. & Piggins, H.D. (2017) Contributions of the lateral habenula to circadian timekeeping. *Pharmacol. Biochem. Behav.*, **162**, 46–54.

Barca-Mayo, O., Pons-Espinal, M., Follert, P., Armirotti, A., Berdondini, L. & De Pietri Tonelli, D. (2017) Astrocyte deletion of *Bmal1* alters daily locomotor activity and cognitive functions via GABA signalling. *Nat. Commun.*, **8**, 14336.

Basar, E. (2013) Brain oscillations in neuropsychiatric disease. *Dialogues Clin. Neurosci.*, **15**, 291–300.

Basar-Eroglu, C., Struber, D., Schurmann, M., Stadler, M. & Basar, E. (1996) Gamma-band responses in the brain: a short review of psychophysiological correlates and functional significance. *Int. J. Psychophysiol.*, **24**, 101–112.

Bean, B.P. (2007) The action potential in mammalian central neurons. *Nat. Rev. Neurosci.*, **8**, 451–465.

Bechtold, D.A. & Loudon, A.S. (2013) Hypothalamic clocks and rhythms in feeding behaviour. *Trends Neurosci.*, **36**, 74–82.

Becker-Weimann, S., Wolf, J., Herzog, H. & Kramer, A. (2004) Modeling feedback loops of the mammalian circadian oscillator. *Biophys. J.*, **87**, 3023–3034.

Becquet, D., Girardet, C., Guillaumond, F., Francois-Bellan, A.M. & Bosler, O. (2008) Ultrastructural plasticity in the rat suprachiasmatic nucleus. Possible involvement in clock entrainment. *Glia*, **56**, 294–305.

Belenky, M.A., Yarom, Y. & Pickard, G.E. (2008) Heterogeneous expression of gamma-aminobutyric acid and gamma-aminobutyric acid-associated receptors and transporters in the rat suprachiasmatic nucleus. *J. Comp. Neurol.*, **506**, 708–732.

Belle, M.D. (2015) Circadian tick-talking across the neuroendocrine system and suprachiasmatic nuclei circuits: the enigmatic communication between the molecular and electrical membrane clocks. *J. Neuroendocrinol.*, **27**, 567–576.

Belle, M.D. & Piggins, H.D. (2017) Circadian regulation of mouse suprachiasmatic nuclei neuronal states shapes responses to orexin. *Eur. J. Neurosci.*, **45**, 723–732.

Belle, M.D., Diekman, C.O., Forger, D.B. & Piggins, H.D. (2009) Daily electrical silencing in the mammalian circadian clock. *Science*, **326**, 281–284.

Belle, M.D., Hughes, A.T., Bechtold, D.A., Cunningham, P., Pierucci, M., Burdakov, D. & Piggins, H.D. (2014) Acute suppressive and long-term phase modulation actions of orexin on the mammalian circadian clock. *J. Neurosci.*, **34**, 3607–3621.

Bernard, S., Gonze, D., Cajavec, B., Herzog, H. & Kramer, A. (2007) Synchronization-induced rhythmicity of circadian oscillators in the suprachiasmatic nucleus. *PLoS Comput. Biol.*, **3**, 667–679.

Berridge, M.J. (1998) Neuronal calcium signaling. *Neuron*, **21**, 13–26.

Berridge, M.J. (2014) Calcium regulation of neural rhythms, memory and Alzheimer's disease. *J. Physiol.*, **592**, 281–293.

Besing, R.C., Hablitz, L.M., Paul, J.R., Johnson, R.L., Prosser, R.A. & Gamble, K.L. (2012) Neuropeptide Y-induced phase shifts of PER2:LUC rhythms are mediated by long-term suppression of neuronal excitability in a phase-specific manner. *Chronobiol. Int.*, **29**, 91–102.

- Besing, R.C., Rogers, C.O., Paul, J.R., Hablitz, L.M., Johnson, R.L., McMahon, L.L. & Gamble, K.L. (2017) GSK3 activity regulates rhythms in hippocampal clock gene expression and synaptic plasticity. *Hippocampus*, **27**, 890–898.
- Biello, S.M., Janik, D. & Mrosovsky, N. (1994) Neuropeptide Y and behaviorally induced phase shifts. *Neuroscience*, **62**, 273–279.
- Biello, S.M. & Mrosovsky, N. (1995) Blocking the phase-shifting effect of neuropeptide Y with light. *P. Roy. Soc. B-Biol. Sci.*, **259**, 179–187.
- Biello, S.M. & Mrosovsky, N. (1996) Phase response curves to neuropeptide Y in wildtype and tau mutant hamsters. *J. Biol. Rhythms*, **11**, 27–34.
- Biello, S.M., Golombek, D.A. & Harrington, M.E. (1997) Neuropeptide Y and glutamate block each other's phase shifts in the suprachiasmatic nucleus *in vitro*. *Neuroscience*, **77**, 1049–1057.
- Bina, K.G., Rusak, B. & Semba, K. (1993) Localization of cholinergic neurons in the forebrain and brainstem that project to the suprachiasmatic nucleus of the hypothalamus in rat. *J. Comp. Neurol.*, **335**, 295–307.
- Bonnefont, X. (2010) Circadian timekeeping and multiple timescale neuroendocrine rhythms. *J. Neuroendocrinol.*, **22**, 209–216.
- Booth, V., Xique, I. & Diniz Behn, C.G. (2017) A one-dimensional map for the circadian modulation of sleep in a sleep-wake regulatory network model for human sleep. *SIAM J. Appl. Dyn. Syst.*, **16**, 1089–1112.
- Bordyugov, G., Granada, A.E. & Herzog, H. (2011) How coupling determines the entrainment of circadian clocks. *Eur. Phys. J. B*, **82**, 227–234.
- Bordyugov, G., Abraham, U., Granada, A., Rose, P., Imkeller, K., Kramer, A. & Herzog, H. (2015) Tuning the phase of circadian entrainment. *J. R. Soc. Interface*, **12**, 20150282.
- Börgers, C. (2017). *An Introduction to Modeling Neuronal Dynamics*. Springer, Cham.
- Brancaccio, M., Maywood, E.S., Chesham, J.E., Loudon, A.S. & Hastings, M.H. (2013) A Gq-Ca²⁺ axis controls circuit-level encoding of circadian time in the suprachiasmatic nucleus. *Neuron*, **78**, 714–728.
- Brancaccio, M., Patton, A.P., Chesham, J.E., Maywood, E.S. & Hastings, M.H. (2017) Astrocytes control circadian timekeeping in the suprachiasmatic nucleus via glutamatergic signaling. *Neuron*, **93**(1420–1435), e1425.
- Brown, T.M., Hughes, A.T. & Piggins, H.D. (2005) Gastrin-releasing peptide promotes suprachiasmatic nuclei cellular rhythmicity in the absence of vasoactive intestinal polypeptide-VPAC2 receptor signaling. *J. Neurosci.*, **25**, 11155–11164.
- Brown, T.M. & Piggins, H.D. (2007) Electrophysiology of the suprachiasmatic circadian clock. *Prog. Neurobiol.*, **82**, 229–255.
- Brown, T.M. (2016) Using light to tell the time of day: sensory coding in the mammalian circadian visual network. *J. Exp. Biol.*, **219**, 1779–1792.
- Brown, T.M., Coogan, A.N., Cutler, D.J., Hughes, A.T. & Piggins, H.D. (2008) Electrophysiological actions of orexins on rat suprachiasmatic neurons *in vitro*. *Neurosci. Lett.*, **448**, 273–278.
- Brown, T.M., Wynne, J., Piggins, H.D. & Lucas, R.J. (2011) Multiple hypothalamic cell populations encoding distinct visual information. *J. Physiol.*, **589**, 1173–1194.
- Buhr, E.D. & Takahashi, J.S. (2013) Molecular components of the mammalian circadian clock. *Handb. Exp. Pharmacol.*, **217**, 3–27.
- Bunger, M.K., Wilsbacher, L.D., Moran, S.M., Clendenen, C., Radcliffe, L.A., Hogenesch, J.B., Simon, M.C., Takahashi, J.S. *et al.* (2000) Mop3 is an essential component of the master circadian pacemaker in mammals. *Cell*, **103**, 1009–1017.
- Burke, J.F., Womac, A.D., Earnest, D.J. & Zoran, M.J. (2011) Mitochondrial calcium signaling mediates rhythmic extracellular ATP accumulation in suprachiasmatic nucleus astrocytes. *J. Neurosci.*, **31**, 8432–8440.
- Burton, K.J., Li, X., Li, B., Cheng, M.Y., Urbanski, H.F. & Zhou, Q.Y. (2016) Expression of prokineticin 2 and its receptor in the macaque monkey brain. *Chronobiol. Int.*, **33**, 191–199.
- Bush, W.S. & Siegelman, H.T. (2006) Circadian synchrony in networks of protein rhythm driven neurons. *Complexity*, **12**, 67–72.
- Buzsáki, G. & Draguhn, A. (2004) Neuronal oscillations in cortical networks. *Science*, **304**, 1926–1929.
- Buzsáki, G., Anastassiou, C.A. & Koch, C. (2012) The origin of extracellular fields and currents—EEG, ECoG, LFP and spikes. *Nat. Rev. Neurosci.*, **13**, 407–420.
- Buzsáki, G. (2015) Hippocampal sharp wave-ripple: a cognitive biomarker for episodic memory and planning. *Hippocampus*, **25**, 1073–1188.
- Caldelas, I., Poiré, V.J., Sicard, B., Pevet, P. & Challet, E. (2003) Circadian profile and photic regulation of clock genes in the suprachiasmatic nucleus of a diurnal mammal *Arvicantha ansorgei*. *Neuroscience*, **116**, 583–591.
- Canal, M.M., Mohammed, N.M. & Rodriguez, J.J. (2009) Early programming of astrocyte organization in the mouse suprachiasmatic nuclei by light. *Chronobiol. Int.*, **26**, 1545–1558.
- Chellappa, S.L., Gaggioni, G., Ly, J.Q., Papachilleos, S., Borsu, C., Brzozowski, A., Rosanova, M., Sarasso, S. *et al.* (2016) Circadian dynamics in measures of cortical excitation and inhibition balance. *Sci. Rep.*, **6**, 33661.
- Chen, L., Serdyuk, T., Yang, B., Wang, S., Chen, S., Chu, X., Zhang, X., Song, J. *et al.* (2017) Abnormal circadian oscillation of hippocampal MAPK activity and power spectrums in NF1 mutant mice. *Mol. Brain*, **10**, 29.
- Cheng, M.Y., Bullock, C.M., Li, C., Lee, A.G., Bermak, J.C., Belluzzi, J., Weaver, D.R., Leslie, F.M. *et al.* (2002) Prokineticin 2 transmits the behavioural circadian rhythm of the suprachiasmatic nucleus. *Nature*, **417**, 405–410.
- Cheng, M.Y., Bittman, E.L., Hattar, S. & Zhou, Q.Y. (2005) Regulation of prokineticin 2 expression by light and the circadian clock. *BMC Neurosci.*, **6**, 17.
- Cheng, M.Y., Leslie, F.M. & Zhou, Q.Y. (2006) Expression of prokineticins and their receptors in the adult mouse brain. *J. Comp. Neurol.*, **498**, 796–809.
- Cheng, H.Y., Alvarez-Saavedra, M., Dziema, H., Choi, Y.S., Li, A. & Oribetan, K. (2009) Segregation of expression of mPeriod gene homologs in neurons and glia: possible divergent roles of mPeriod1 and mPeriod2 in the brain. *Hum. Mol. Genet.*, **18**, 3110–3124.
- Clay, J.R. (2015) Novel description of ionic currents recorded with the action potential clamp technique: application to excitatory currents in suprachiasmatic nucleus neurons. *J. Neurophysiol.*, **114**, 707–716.
- Cloues, R.K. & Sather, W.A. (2003) After hyperpolarization regulates firing rate in neurons of the suprachiasmatic nucleus. *J. Neurosci.*, **23**, 1593–1604.
- Colavite, V., Tesoriero, C., Wirtu, A.T., Grassi-Zucconi, G. & Bentivoglio, M. (2015) Limbic thalamus and state-dependent behavior: the paraventricular nucleus of the thalamic midline as a node in circadian timing and sleep/wake-regulatory networks. *Neurosci. Biobehav. R.*, **54**, 3–17.
- Colwell, C.S. & Menaker, M. (1992) NMDA as well as non-NMDA receptor antagonists can prevent the phase-shifting effects of light on the circadian system of the golden hamster. *J. Biol. Rhythms*, **7**, 125–136.
- Colwell, C.S. (2000) Circadian modulation of calcium levels in cells in the suprachiasmatic nucleus. *Eur. J. Neurosci.*, **12**, 571–576.
- Colwell, C.S. (2011) Linking neural activity and molecular oscillations in the SCN. *Nat. Rev. Neurosci.*, **12**, 553–569.
- Coomans, C.P., Ramkisoensing, A. & Meijer, J.H. (2014) The suprachiasmatic nuclei as a seasonal clock. *Front. Neuroendocrin.*, **37**, 29–42.
- Cornell-Bell, A.H., Finkbeiner, S.M., Cooper, M.S. & Smith, S.J. (1990) Glutamate induces calcium waves in cultured astrocytes: long-range glial signaling. *Science*, **247**, 470–473.
- Csicsvari, J., Jamieson, B., Wise, K.D. & Buzsáki, G. (2003) Mechanisms of gamma oscillations in the hippocampus of the behaving rat. *Neuron*, **37**, 311–322.
- Cutler, D.J., Piggins, H.D., Selbie, L.A. & Mason, R. (1998) Responses to neuropeptide Y in adult hamster suprachiasmatic nucleus neurons *in vitro*. *Eur. J. Pharmacol.*, **345**, 155–162.
- Daan, S. & Pittendrigh, C. (1976) A functional analysis of circadian pacemakers in nocturnal rodents: II. The variability of phase response curves. *J. Comp. Physiol.*, **106**, 253–266.
- Damineli, D.S.C. (2014) Synchronization properties of multi-oscillator circadian systems: Biological functions beyond time-keeping. PhD Dissertation. Universidade Nova de Lisboa, Portugal.
- Date, Y., Ueta, Y., Yamashita, H., Yamaguchi, H., Matsukura, S., Kangawa, K., Sakurai, T., Yanagisawa, M. *et al.* (1999) Orexins, orexigenic hypothalamic peptides, interact with autonomic, neuroendocrine and neuroregulatory systems. *Proc. Natl. Acad. Sci. USA*, **96**, 748–753.
- Davidson, A.J., Castanon-Cervantes, O., Leise, T.L., Molyneux, P.C. & Harrington, M.E. (2009) Visualizing jet lag in the mouse suprachiasmatic nucleus and peripheral circadian timing system. *Eur. J. Neurosci.*, **29**, 171–180.
- de Jeu, M., Hermes, M. & Pennartz, C. (1998) Circadian modulation of membrane properties in slices of rat suprachiasmatic nucleus. *NeuroReport*, **9**, 3725–3729.
- De Jeu, M., Geurtsen, A. & Pennartz, C. (2002) A Ba(2+)-sensitive K(+) current contributes to the resting membrane potential of neurons in rat suprachiasmatic nucleus. *J. Neurophysiol.*, **88**, 869–878.
- Decourcy, P.J. (1960) Phase control of activity in a rodent. *Cold Spring Harb. SYM*, **25**, 49–55.
- Decourcy, P.J. (1964) Function of a light response rhythm in hamsters. *J. Cell. Compar. Physiol.*, **63**, 189–196.
- DeCoursey, P.J., Walker, J.K. & Smith, S.A. (2000) A circadian pacemaker in free-living chipmunks: essential for survival? *J. Comp. Physiol. A.*, **186**, 169–180.

- DeWoskin, D., Myung, J., Belle, M.D., Piggins, H.D., Takumi, T. & Forger, D.B. (2015) Distinct roles for GABA across multiple timescales in mammalian circadian timekeeping. *Proc. Natl. Acad. Sci. USA*, **112**, E3911–E3919.
- Diaz-Munoz, M., Dent, M.A., Granados-Fuentes, D., Hall, A.C., Hernandez-Cruz, A., Harrington, M.E. & Aguilar-Roblero, R. (1999) Circadian modulation of the ryanodine receptor type 2 in the SCN of rodents. *NeuroReport*, **10**, 481–486.
- Diekman, C.O. & Forger, D.B. (2009) Clustering predicted by an electrophysiological model of the suprachiasmatic nucleus. *J. Biol. Rhythm.*, **24**, 322–333.
- Diekman, C.O. & Bose, A. (2016) Entrainment maps: a new tool for understanding properties of circadian oscillator models. *J. Biol. Rhythm.*, **31**, 598–616.
- Diekman, C.O. & Bose, A. (2017) Reentrainment of the circadian pacemaker during jet lag: east-west asymmetry and the effects of north-south travel. *J. Theor. Biol.*, **437**, 261–285.
- Diekman, C.O., Belle, M.D., Irwin, R.P., Allen, C.N., Piggins, H.D. & Forger, D.B. (2013) Causes and consequences of hyperexcitation in central clock neurons. *PLoS Comput. Biol.*, **9**, e1003196.
- Ding, J.M., Buchanan, G.F., Tischkau, S.A., Chen, D., Kuriashkina, L., Faiman, L.E., Alster, J.M., McPherson P.S. *et al.* (1998) A neuronal ryanodine receptor mediates light-induced phase delays of the circadian clock. *Nature*, **394**, 381–384.
- Doi, M., Ishida, A., Miyake, A., Sato, M., Komatsu, R., Yamazaki, F., Kimura, I., Tsuchiya S. *et al.* (2011) Circadian regulation of intracellular G-protein signalling mediates intercellular synchrony and rhythmicity in the suprachiasmatic nucleus. *Nat. Commun.*, **2**, 327.
- Drouyer, E., Rieux, C., Hut, R.A. & Cooper, H.M. (2007) Responses of suprachiasmatic nucleus neurons to light and dark adaptation: relative contributions of melanopsin and rod-cone inputs. *J. Neurosci.*, **27**, 9623–9631.
- Duhart, J.M., Leone, M.J., Paladino, N., Evans, J.A., Castanon-Cervantes, O., Davidson, A.J. & Golombek, D.A. (2013) Suprachiasmatic astrocytes modulate the circadian clock in response to TNF- α . *J. Immunol.*, **191**, 4656–4664.
- Eckel-Mahan, K.L. (2012) Circadian oscillations within the hippocampus support memory formation and persistence. *Front. Mol. Neurosci.*, **5**, 46.
- Engel, A.K., Fries, P. & Singer, W. (2001) Dynamic predictions: oscillations and synchrony in top-down processing. *Nat. Rev. Neurosci.*, **2**, 704–716.
- Enoki, R., Ono, D., Hasan, M.T., Honma, S. & Honma, K. (2012) Single-cell resolution fluorescence imaging of circadian rhythms detected with a Nipkow spinning disk confocal system. *J. Neurosci. Meth.*, **207**, 72–79.
- Enoki, R., Oda, Y., Mieda, M., Ono, D., Honma, S. & Honma, K.I. (2017a) Synchronous circadian voltage rhythms with asynchronous calcium rhythms in the suprachiasmatic nucleus. *Proc. Natl. Acad. Sci. USA*, **114**, E2476–E2485.
- Enoki, R., Ono, D., Kuroda, S., Honma, S. & Honma, K.I. (2017b) Dual origins of the intracellular circadian calcium rhythm in the suprachiasmatic nucleus. *Sci. Rep.*, **7**, 41733.
- Evans, J.A., Leise, T.L., Castanon-Cervantes, O. & Davidson, A.J. (2013) Dynamic interactions mediated by nonredundant signaling mechanisms couple circadian clock neurons. *Neuron*, **80**, 973–983.
- Fan, J., Zeng, H., Olson, D.P., Huber, K.M., Gibson, J.R. & Takahashi, J.S. (2015) Vasoactive intestinal polypeptide (VIP)-expressing neurons in the suprachiasmatic nucleus provide sparse GABAergic outputs to local neurons with circadian regulation occurring distal to the opening of postsynaptic GABA_A ionotropic receptors. *J. Neurosci.*, **35**, 1905–1920.
- Farkas, B., Vilagi, I. & Detari, L. (2002) Effect of orexin-A on discharge rate of rat suprachiasmatic nucleus neurons *in vitro*. *Acta Biol. Hung.*, **53**, 435–443.
- Fernandez, D.C., Chang, Y.T., Hattar, S. & Chen, S.K. (2016) Architecture of retinal projections to the central circadian pacemaker. *Proc. Natl. Acad. Sci. USA*, **113**, 6047–6052.
- Fiacco, T.A., Agulhon, C. & McCarthy, K.D. (2009) Sorting out astrocyte physiology from pharmacology. *Annu. Rev. Pharmacol.*, **49**, 151–174.
- Fitzsimons, C.P., Herbert, J., Schouten, M., Meijer, O.C., Lucassen, P.J. & Lightman, S. (2016) Circadian and ultradian glucocorticoid rhythmicity: implications for the effects of glucocorticoids on neural stem cells and adult hippocampal neurogenesis. *Front. Neuroendocrin.*, **41**, 44–58.
- Flourakis, M., Kula-Eversole, E., Hutchison, A.L., Han, T.H., Aranda, K., Moose, D.L., White, K.P., Dinner A.R. *et al.* (2015) A conserved bicycle model for circadian clock control of membrane excitability. *Cell*, **162**, 836–848.
- Forger, D.B. & Peskin, C.S. (2003) A detailed predictive model of the mammalian circadian clock. *Proc. Natl. Acad. Sci. USA*, **100**, 14806–14811.
- Forger, D.B. & Peskin, C.S. (2005) Stochastic simulation of the mammalian circadian clock. *Proc. Natl. Acad. Sci. USA*, **102**, 321–324.
- Forger, D.B. (2017). *Biological Clocks, Rhythms, and Oscillations: the Theory of Biological Timekeeping*. The MIT Press, Cambridge, MA.
- Forger, D.B., Jewett, M.E. & Kronauer, R.E. (1999) A simpler model of the human circadian pacemaker. *J. Biol. Rhythm.*, **14**, 532–537.
- Freeman, W.J., Rogers, L.J., Holmes, M.D. & Silbergeld, D.L. (2000) Spatial spectral analysis of human electrocorticograms including the alpha and gamma bands. *J. Neurosci. Meth.*, **95**, 111–121.
- Freeman, G.M. Jr, Krock, R.M., Aton, S.J., Thaben, P. & Herzog, E.D. (2013) GABA networks destabilize genetic oscillations in the circadian pacemaker. *Neuron*, **78**, 799–806.
- Gallego, M., Eide, E.J., Woolf, M.F., Virshup, D.M. & Forger, D.B. (2006) An opposite role for tau in circadian rhythms revealed by mathematical modeling. *Proc. Natl. Acad. Sci. USA*, **103**, 10618–10623.
- Gamble, K.L., Novak, C.M. & Albers, H.E. (2004) Neuropeptide Y and N-methyl-D-aspartic acid interact within the suprachiasmatic nuclei to alter circadian phase. *Neuroscience*, **126**, 559–565.
- Gerics, B., Szalay, F. & Hajos, F. (2006) Glial fibrillary acidic protein immunoreactivity in the rat suprachiasmatic nucleus: circadian changes and their seasonal dependence. *J. Anat.*, **209**, 231–237.
- Gillette, M.U., Medanic, M., McArthur, A.J., Liu, C., Ding, J.M., Faiman, L.E., Weber, E.T., Tchong T.K. *et al.* 1995. Intrinsic neuronal rhythms in the suprachiasmatic nuclei and their adjustment. *Ciba F. Symp.*, **183**, 134–144; discussion 144–153.
- Girardet, C., Becquet, D., Blanchard, M.P., Francois-Bellan, A.M. & Bosler, O. (2010) Neuroglial and synaptic rearrangements associated with photic entrainment of the circadian clock in the suprachiasmatic nucleus. *Eur. J. Neurosci.*, **32**, 2133–2142.
- Glossop, N.R. (2011) Circadian timekeeping in *Drosophila melanogaster* and *Mus musculus*. *Essays Biochem.*, **49**, 19–35.
- Godinho, S.I., Maywood, E.S., Shaw, L., Tucci, V., Barnard, A.R., Busino, L., Pagano, M., Kendall R. *et al.* (2007) The after-hours mutant reveals a role for Fbx13 in determining mammalian circadian period. *Science*, **316**, 897–900.
- Golombek, D.A. & Rosenstein, R.E. (2010) Physiology of circadian entrainment. *Physiol. Rev.*, **90**, 1063–1102.
- Golombek, D.A., Biello, S.M., Rendon, R.A. & Harrington, M.E. (1996) Neuropeptide Y phase shifts the circadian clock *in vitro* via a Y2 receptor. *NeuroReport*, **7**, 1315–1319.
- Gonze, D. (2011a) Modeling circadian clocks: from equations to oscillations. *Open Life Sci.*, **6**, 699.
- Gonze, D., Bernard, S., Waltermann, C., Kramer, A. & Herzog, H. (2005) Spontaneous synchronization of coupled circadian oscillators. *Biophys. J.*, **89**, 120–129.
- Gonze, D. (2011b) Modeling circadian clocks: roles, advantages, and limitations. *Open Life Sci.*, **6**, 712–729.
- Gonze, D. & Abou-Jaoude, W. (2013) The Goodwin model: behind the Hill function. *PLoS ONE*, **8**, e69573.
- Goodwin, B.C. (1965) Oscillatory behavior in enzymatic control processes. *Adv. Enzyme Regul.*, **3**, 425–438.
- Granados-Fuentes, D., Norris, A.J., Carrasquillo, Y., Nerbonne, J.M. & Herzog, E.D. (2012) IA channels encoded by Kv1.4 and Kv4.2 regulate neuronal firing in the suprachiasmatic nucleus and circadian rhythms in locomotor activity. *J. Neurosci.*, **32**, 10045–10052.
- Granados-Fuentes, D., Hermansteyne, T.O., Carrasquillo, Y., Nerbonne, J.M. & Herzog, E.D. (2015) IA channels encoded by Kv1.4 and Kv4.2 regulate circadian period of PER2 expression in the suprachiasmatic nucleus. *J. Biol. Rhythm.*, **30**, 396–407.
- Green, D.J. & Gillette, R. (1982) Circadian rhythm of firing rate recorded from single cells in the rat suprachiasmatic brain slice. *Brain Res.*, **245**, 198–200.
- Green, C.B., Takahashi, J.S. & Bass, J. (2008) The meter of metabolism. *Cell*, **134**, 728–742.
- Gribkoff, V.K., Pieschl, R.L., Wisialowski, T.A., van den Pol, A.N. & Yocca, F.D. (1998) Phase shifting of circadian rhythms and depression of neuronal activity in the rat suprachiasmatic nucleus by neuropeptide Y: mediation by different receptor subtypes. *J. Neurosci.*, **18**, 3014–3022.
- Griffith, J.S. (1968) Mathematics of cellular control processes. I. Negative feedback to one gene. *J. Theor. Biol.*, **20**, 202–208.
- Groos, G. & Mason, R. (1978) Maintained discharge of rat suprachiasmatic neurons at different adaptation levels. *Neurosci. Lett.*, **8**, 59–64.

- Groos, G.A. & Hendriks, J. (1979) Regularly firing neurones in the rat suprachiasmatic nucleus. *Experientia*, **35**, 1597–1598.
- Groos, G. & Hendriks, J. (1982) Circadian rhythms in electrical discharge of rat suprachiasmatic neurones recorded *in vitro*. *Neurosci. Lett.*, **34**, 283–288.
- Guilding, C. & Piggins, H.D. (2007) Challenging the omnipotence of the suprachiasmatic timekeeper: are circadian oscillators present throughout the mammalian brain? *Eur. J. Neurosci.*, **25**, 3195–3216.
- Guilding, C., Hughes, A.T., Brown, T.M., Namvar, S. & Piggins, H.D. (2009) A riot of rhythms: neuronal and glial circadian oscillators in the mediobasal hypothalamus. *Mol. Brain*, **2**, 28.
- Guilding, C., Hughes, A.T. & Piggins, H.D. (2010) Circadian oscillators in the epithalamus. *Neuroscience*, **169**, 1630–1639.
- Guilding, C., Scott, F., Bechtold, D.A., Brown, T.M., Wegner, S. & Piggins, H.D. (2013) Suppressed cellular oscillations in after-hours mutant mice are associated with enhanced circadian phase-resetting. *J. Physiol.*, **591**, 1063–1080.
- Guldner, F.H. (1983) Numbers of neurons and astroglial cells in the suprachiasmatic nucleus of male and female rats. *Exp. Brain Res.*, **50**, 373–376.
- Halassa, M.M., Fellin, T. & Haydon, P.G. (2009) Tripartite synapses: roles for astrocytic purines in the control of synaptic physiology and behavior. *Neuropharmacology*, **57**, 343–346.
- Hannay, K.M., Booth, V. & Forger, D.B. (2015) Collective phase response curves for heterogeneous coupled oscillators. *Phys. Rev. E*, **92**, 022923.
- Harmar, A.J., Marston, H.M., Shen, S., Spratt, C., West, K.M., Sheward, W.J., Morrison, C.F., Dorin, J.R. *et al.* (2002) The VPAC(2) receptor is essential for circadian function in the mouse suprachiasmatic nuclei. *Cell*, **109**, 497–508.
- Harrington, M.E. (1997) The ventral lateral geniculate nucleus and the intergeniculate leaflet: interrelated structures in the visual and circadian systems. *Neurosci. Biobehav. R.*, **21**, 705–727.
- Hastings, M.H., Duffield, G.E., Smith, E.J., Maywood, E.S. & Ebling, F.J. (1998) Entrainment of the circadian system of mammals by nonphotic cues. *Chronobiol. Int.*, **15**, 425–445.
- Hastings, M. & Maywood, E.S. (2000) Circadian clocks in the mammalian brain. *BioEssays*, **22**, 23–31.
- Heja, L., Nyitrai, G., Kekesi, O., Dobolyi, A., Szabo, P., Fiath, R., Ulbert, I., Pal-Szenthe B. *et al.* (2012) Astrocytes convert network excitation to tonic inhibition of neurons. *BMC Biol.*, **10**, 26.
- Henson, M.A. (2013) Multicellular models of intercellular synchronization in circadian neural networks. *Chaos Soliton. Fract.*, **50**, 48–64.
- Herrmann, C.S. & Demiralp, T. (2005) Human EEG gamma oscillations in neuropsychiatric disorders. *Clin. Neurophysiol.*, **116**, 2719–2733.
- Herzog, E.D., Takahashi, J.S. & Block, G.D. (1998) Clock controls circadian period in isolated suprachiasmatic nucleus neurons. *Nat. Neurosci.*, **1**, 708–713.
- Hoban, T.M. & Sulzman, F.M. (1985) Light effects on circadian timing system of a diurnal primate, the squirrel monkey. *Am. J. Physiol.*, **249**, R274–R280.
- Hong, J.H., Jeong, B., Min, C.H. & Lee, K.J. (2012) Circadian waves of cytosolic calcium concentration and long-range network connections in rat suprachiasmatic nucleus. *Eur. J. Neurosci.*, **35**, 1417–1425.
- Honma, S., Shirakawa, T., Katsuno, Y., Namihira, M. & Honma, K. (1998) Circadian periods of single suprachiasmatic neurons in rats. *Neurosci. Lett.*, **250**, 157–160.
- Huang, R.C. (1993) Sodium and calcium currents in acutely dissociated neurons from rat suprachiasmatic nucleus. *J. Neurophysiol.*, **70**, 1692–1703.
- Huang, H., Tan, Bao Z., Shen, Y., Tao, J., Jiang, F., Sung, Ying Y., Ng, Choon K., Raida M. *et al.* (2012) RNA editing of the IQ domain in Cav1.3 channels modulates their Ca²⁺-dependent inactivation. *Neuron*, **73**, 304–316.
- Hughes, A.T. & Piggins, H.D. (2012) Feedback actions of locomotor activity to the circadian clock. *Prog. Brain Res.*, **199**, 305–336.
- Hughes, A.T., Guilding, C., Lennox, L., Samuels, R.E., McMahon, D.G. & Piggins, H.D. (2008) Live imaging of altered *period1* expression in the suprachiasmatic nuclei of *Vipr2*^{-/-} mice. *J. Neurochem.*, **106**, 1646–1657.
- Huhman, K.L. & Albers, H.E. (1994) Neuropeptide Y microinjected into the suprachiasmatic region phase shifts circadian rhythms in constant darkness. *Peptides*, **15**, 1475–1478.
- Hut, R.A. & Van der Zee, E.A. (2011) The cholinergic system, circadian rhythmicity, and time memory. *Behav. Brain Res.*, **221**, 466–480.
- Hutcheon, B. & Yarom, Y. (2000) Resonance, oscillation and the intrinsic frequency preferences of neurons. *Trends Neurosci.*, **23**, 216–222.
- Ikeda, M. & Ikeda, M. (2014) Bmal1 is an essential regulator for circadian cytosolic Ca²⁺ rhythms in suprachiasmatic nucleus neurons. *J. Neurosci.*, **34**, 12029–12038.
- Ikeda, M., Sugiyama, T., Wallace, C.S., Gompf, H.S., Yoshioka, T., Miyawaki, A. & Allen, C.N. (2003a) Circadian dynamics of cytosolic and nuclear Ca²⁺ in single suprachiasmatic nucleus neurons. *Neuron*, **38**, 253–263.
- Ikeda, M., Yoshioka, T. & Allen, C.N. (2003b) Developmental and circadian changes in Ca²⁺ mobilization mediated by GABAA and NMDA receptors in the suprachiasmatic nucleus. *Eur. J. Neurosci.*, **17**, 58–70.
- Inouye, S.T. & Kawamura, H. (1979) Persistence of circadian rhythmicity in a mammalian hypothalamic “island” containing the suprachiasmatic nucleus. *Proc. Natl. Acad. Sci. USA*, **76**, 5962–5966.
- Irwin, R.P. & Allen, C.N. (2007) Calcium response to retinohypothalamic tract synaptic transmission in suprachiasmatic nucleus neurons. *J. Neurosci.*, **27**, 11748–11757.
- Irwin, R.P. & Allen, C.N. (2010) Neuropeptide-mediated calcium signaling in the suprachiasmatic nucleus network. *Eur. J. Neurosci.*, **32**, 1497–1506.
- Itri, J. & Colwell, C.S. (2003) Regulation of inhibitory synaptic transmission by vasoactive intestinal peptide (VIP) in the mouse suprachiasmatic nucleus. *J. Neurophysiol.*, **90**, 1589–1597.
- Itri, J.N., Michel, S., Vansteensel, M.J., Meijer, J.H. & Colwell, C.S. (2005) Fast delayed rectifier potassium current is required for circadian neural activity. *Nat. Neurosci.*, **8**, 650–656.
- Itri, J.N., Vosko, A.M., Schroeder, A., Dragich, J.M., Michel, S. & Colwell, C.S. (2010) Circadian regulation of a-type potassium currents in the suprachiasmatic nucleus. *J. Neurophysiol.*, **103**, 632–640.
- Jackson, A.C., Yao, G.L. & Bean, B.P. (2004) Mechanism of spontaneous firing in dorsomedial suprachiasmatic nucleus neurons. *J. Neurosci.*, **24**, 7985–7998.
- Jackson, F.R. (2011) Glial cell modulation of circadian rhythms. *Glia*, **59**, 1341–1350.
- Jiang, Z.G., Yang, Y., Liu, Z.P. & Allen, C.N. (1997) Membrane properties and synaptic inputs of suprachiasmatic nucleus neurons in rat brain slices. *J. Physiol.*, **499**(Pt 1), 141–159.
- Jiao, Y.Y., Lee, T.M. & Rusak, B. (1999) Photic responses of suprachiasmatic area neurons in diurnal degus (*Octodon degus*) and nocturnal rats (*Rattus norvegicus*). *Brain Res.*, **817**, 93–103.
- Jolley, C.C., Ukai-Tadenuma, M., Perrin, D. & Ueda, H.R. (2014) A mammalian circadian clock model incorporating daytime expression elements. *Biophys. J.*, **107**, 1462–1473.
- Jones, J.R., Tackenberg, M.C. & McMahon, D.G. (2015) Manipulating circadian clock neuron firing rate resets molecular circadian rhythms and behavior. *Nat. Neurosci.*, **18**, 373–375.
- Kalsbeek, A. & Buijs, R.M. (1992) Peptidergic transmitters of the suprachiasmatic nuclei and the control of circadian rhythmicity. *Prog. Brain Res.*, **92**, 321–333.
- Kalsbeek, A., Teclemariam-Mesbah, R. & Pevet, P. (1993) Efferent projections of the suprachiasmatic nucleus in the golden hamster (*Mesocricetus auratus*). *J. Comp. Neurol.*, **332**, 293–314.
- Kalsbeek, A., Perreau-Lenz, S. & Buijs, R.M. (2006) A network of (autonomic) clock outputs. *Chronobiol. Int.*, **23**, 201–215.
- Kalsbeek, A., Fliers, E., Hofman, M.A., Swaab, D.F. & Buijs, R.M. (2010) Vasopressin and the output of the hypothalamic biological clock. *J. Neuroendocrinol.*, **22**, 362–372.
- Kas, M.J. & Edgar, D.M. (2000) Photic phase response curve in *Octodon degus*: assessment as a function of activity phase preference. *Am. J. Physiol.-Reg. I.*, **278**, R1385–R1389.
- Khalsa, S.B., Jewett, M.E., Cajochen, C. & Czeisler, C.A. (2003) A phase response curve to single bright light pulses in human subjects. *J. Physiol.*, **549**, 945–952.
- Kim, H. & Jeong, J. (2008) Computational modeling of circadian rhythms in suprachiasmatic nucleus neurons. *ICONIP*, **2007**, 930–939.
- Kim, J.K. & Forger, D.B. (2012) A mechanism for robust circadian time-keeping via stoichiometric balance. *Mol. Syst. Biol.*, **8**, 630.
- Kim, J.K. (2016) Protein sequestration versus Hill-type repression in circadian clock models. *IET Syst. Biol.*, **10**, 125–135.
- Kingsbury, N.J., Taylor, S.R. & Henson, M.A. (2016) Inhibitory and excitatory networks balance cell coupling in the suprachiasmatic nucleus: a modeling approach. *J. Theor. Biol.*, **397**, 135–144.
- Klimesch, W. (1999) EEG alpha and theta oscillations reflect cognitive and memory performance: a review and analysis. *Brain Res. Rev.*, **29**, 169–195.
- Klisch, C., Inyushkin, A., Mordel, J., Karnas, D., Pevet, P. & Meissl, H. (2009) Orexin A modulates neuronal activity of the rodent suprachiasmatic nucleus *in vitro*. *Eur. J. Neurosci.*, **30**, 65–75.
- Ko, C.H. & Takahashi, J.S. (2006) Molecular components of the mammalian circadian clock. *Hum. Mol. Genet.*, **15**(Suppl. 2), R271–R277.

- Ko, C.H., Yamada, Y.R., Welsh, D.K., Buhr, E.D., Liu, A.C., Zhang, E.E., Ralph, M.R., Kay S.A. *et al.* (2010) Emergence of noise-induced oscillations in the central circadian pacemaker. *PLoS Biol.*, **8**, e1000513.
- Kononenko, N.I. & Dudek, F.E. (2004) Mechanism of irregular firing of suprachiasmatic nucleus neurons in rat hypothalamic slices. *J. Neurophysiol.*, **91**, 267–273.
- Kononenko, N.I. & Berezetskaya, N.M. (2010) Modeling the spontaneous activity in suprachiasmatic nucleus neurons: role of cation single channels. *J. Theor. Biol.*, **265**, 115–125.
- Kononenko, N.I., Medina, I. & Dudek, F.E. (2004) Persistent subthreshold voltage-dependent cation single channels in suprachiasmatic nucleus neurons. *Neuroscience*, **129**, 85–92.
- Kononenko, N.I., Honma, S. & Honma, K. (2013) Fast synchronous oscillations of firing rate in cultured rat suprachiasmatic nucleus neurons: possible role in circadian synchronization in the intact nucleus. *Neurosci. Res.*, **75**, 218–227.
- Kopell, N., Ermentrout, G.B., Whittington, M.A. & Traub, R.D. (2000) Gamma rhythms and beta rhythms have different synchronization properties. *Proc. Natl. Acad. Sci. USA*, **97**, 1867–1872.
- Kramer, A., Yang, F.C., Snodgrass, P., Li, X., Scammell, T.E., Davis, F.C. & Weitz, C.J. (2001) Regulation of daily locomotor activity and sleep by hypothalamic EGF receptor signaling. *Science*, **294**, 2511–2515.
- Kraves, S. & Weitz, C.J. (2006) A role for cardiotrophin-like cytokine in the circadian control of mammalian locomotor activity. *Nat. Neurosci.*, **9**, 212–219.
- Kronauer, R.E. (1990) A quantitative model for the effects of light on the amplitude and phase of the deep circadian pacemaker, based on human data. In Horne, J. (Ed.), *Sleep'90, Proceedings of the Tenth European Congress on Sleep Research*. Pontenagel Press, Düsseldorf, pp. 306–309.
- Kubota, A., Inouye, S.T. & Kawamura, H. (1981) Reversal of multiunit activity within and outside the suprachiasmatic nucleus in the rat. *Neurosci. Lett.*, **27**, 303–308.
- Kuhlman, S.J. & McMahon, D.G. (2004) Rhythmic regulation of membrane potential and potassium current persists in SCN neurons in the absence of environmental input. *Eur. J. Neurosci.*, **20**, 1113–1117.
- Kuhlman, S.J. & McMahon, D.G. (2006) Encoding the ins and outs of circadian pacemaking. *J. Biol. Rhythm.*, **21**, 470–481.
- Kunz, H. & Achermann, P. (2003) Simulation of circadian rhythm generation in the suprachiasmatic nucleus with locally coupled self-sustained oscillators. *J. Theor. Biol.*, **224**, 63–78.
- Lavialle, M. & Serviere, J. (1993) Circadian fluctuations in GFAP distribution in the Syrian hamster suprachiasmatic nucleus. *NeuroReport*, **4**, 1243–1246.
- Lavialle, M. & Serviere, J. (1995) Developmental study in the circadian clock of the golden hamster: a putative role of astrocytes. *Brain Res. Dev. Brain Res.*, **86**, 275–282.
- Lavialle, M., Begue, A., Papillon, C. & Vilaplana, J. (2001) Modifications of retinal afferent activity induce changes in astroglial plasticity in the hamster circadian clock. *Glia*, **34**, 88–100.
- Lee, H.S., Ghetti, A., Pinto-Duarte, A., Wang, X., Dziewczapolski, G., Galimi, F., Huitron-Resendiz, S., Pina-Crespo J.C. *et al.* (2014) Astrocytes contribute to gamma oscillations and recognition memory. *Proc. Natl. Acad. Sci. USA*, **111**, E3343–E3352.
- Lein, E.S., Hawrylycz, M.J., Ao, N., Ayres, M., Bensinger, A., Bernard, A., Boe, A.F., Boguski M.S. *et al.* (2007) Genome-wide atlas of gene expression in the adult mouse brain. *Nature*, **445**, 168–176.
- Leise, T. & Siegelmann, H. (2006) Dynamics of a multistage circadian system. *J. Biol. Rhythm.*, **21**, 314–323.
- Leloup, J.-C. & Goldbeter, A. (2003) Toward a detailed computational model for the mammalian circadian clock. *Proc. Natl. Acad. Sci. USA*, **100**, 7051–7056.
- Lewandowski, M.H., Blasiak, T., Domszowski, J. & Wolkowska, A. (2000) Ultradian rhythmic neuronal oscillation in the intergeniculate leaflet. *NeuroReport*, **11**, 317–321.
- Li, J.D., Hu, W.P., Boehmer, L., Cheng, M.Y., Lee, A.G., Jilek, A., Siegel, J.M. & Zhou, Q.Y. (2006) Attenuated circadian rhythms in mice lacking the prokineticin 2 gene. *J. Neurosci.*, **26**, 11615–11623.
- Lindley, J., Deurveilher, S., Rusak, B. & Semba, K. (2008) Transforming growth factor-alpha and glial fibrillary acidic protein in the hamster circadian system: daily profile and cellular localization. *Brain Res.*, **1197**, 94–105.
- Liou, S.Y. & Albers, H.E. (1991) Single unit response of neurons within the hamster suprachiasmatic nucleus to neuropeptide Y. *Brain Res. Bull.*, **27**, 825–828.
- Liu, C. & Reppert, S.M. (2000) GABA synchronizes clock cells within the suprachiasmatic circadian clock. *Neuron*, **25**, 123–128.
- Liu, C., Weaver, D.R., Strogatz, S.H. & Reppert, S.M. (1997) Cellular construction of a circadian clock: period determination in the suprachiasmatic nuclei. *Cell*, **91**, 855–860.
- Llinas, R.R. (2014) Intrinsic electrical properties of mammalian neurons and CNS function: a historical perspective. *Front. Cell Neurosci.*, **8**, 320.
- Locke, J.C.W., Westermarck, P.O., Kramer, A. & Herzog, H. (2008) Global parameter search reveals design principles of the mammalian circadian clock. *BMC Syst. Biol.*, **2**, 22.
- Loh, D.H., Jami, S.A., Flores, R.E., Truong, D., Ghiani, C.A., O'Dell, T.J. & Colwell, C.S. (2015) Misaligned feeding impairs memories. *eLife*, **4**, e09460.
- Lokshin, M., LeSauter, J. & Silver, R. (2015) Selective distribution of retinal input to mouse SCN revealed in analysis of sagittal sections. *J. Biol. Rhythm.*, **30**, 251–257.
- Lone, S.R. & Sharma, V.K. (2011) Timekeeping through social contacts: social synchronization of circadian locomotor activity rhythm in the carpenter ant *Camponotus paria*. *Chronobiol. Int.*, **28**, 862–872.
- Lopes da Silva, F. (2013) EEG and MEG: relevance to neuroscience. *Neuron*, **80**, 1112–1128.
- Lowrey, P.L., Shimomura, K., Antoch, M.P., Yamazaki, S., Zemenides, P.D., Ralph, M.R., Menaker, M. & Takahashi, J.S. (2000) Positional syntenic cloning and functional characterization of the mammalian circadian mutation tau. *Science*, **288**, 483–492.
- Lu, Z., Klein-Cardena, K., Lee, S., Antonsen, T.M., Girvan, M. & Ott, E. (2016) Resynchronization of circadian oscillators and the east-west asymmetry of jet-lag. *Chaos*, **26**, 094811.
- Lucas, R.J., Peirson, S.N., Berson, D.M., Brown, T.M., Cooper, H.M., Czeisler, C.A., Figueiro, M.G., Gamlin P.D. *et al.* (2014) Measuring and using light in the melanopsin age. *Trends Neurosci.*, **37**, 1–9.
- Lucassen, E.A., van Diepen, H.C., Houben, T., Michel, S., Colwell, C.S. & Meijer, J.H. (2012) Role of vasoactive intestinal peptide in seasonal encoding by the suprachiasmatic nucleus clock. *Eur. J. Neurosci.*, **35**, 1466–1474.
- Lundkvist, G.B. & Block, G.D. (2005) Role of neuronal membrane events in circadian rhythm generation. *Methods Enzymol.*, **393**, 623–642.
- Lundkvist, G.B., Kwak, Y., Davis, E.K., Tei, H. & Block, G.D. (2005) A calcium flux is required for circadian rhythm generation in mammalian pacemaker neurons. *J. Neurosci.*, **25**, 7682–7686.
- Ly, J.Q., Gaggioni, G., Chellappa, S.L., Papachilleos, S., Brzozowski, A., Borsu, C., Rosanova, M., Sarasso S. *et al.* (2016) Circadian regulation of human cortical excitability. *Nat. Commun.*, **7**, 11828.
- Mahoney, M., Bult, A. & Smale, L. (2001) Phase response curve and light-induced fos expression in the suprachiasmatic nucleus and adjacent hypothalamus of *Arvicantis niloticus*. *J. Biol. Rhythm.*, **16**, 149–162.
- Marpegan, L., Krall, T.J. & Herzog, E.D. (2009) Vasoactive intestinal polypeptide entrains circadian rhythms in astrocytes. *J. Biol. Rhythm.*, **24**, 135–143.
- Marston, O.J., Williams, R.H., Canal, M.M., Samuels, R.E., Upton, N. & Piggins, H.D. (2008) Circadian and dark-pulse activation of orexin/hypocretin neurons. *Mol. Brain*, **1**, 19.
- Martin-Fairey, C.A. & Nunez, A.A. (2014) Circadian modulation of memory and plasticity gene products in a diurnal species. *Brain Res.*, **1581**, 30–39.
- Mathie, A. (2007) Neuronal two-pore-domain potassium channels and their regulation by G protein-coupled receptors. *J. Physiol.*, **578**, 377–385.
- Maywood, E.S., Reddy, A.B., Wong, G.K., O'Neill, J.S., O'Brien, J.A., McMahon, D.G., Harmor, A.J., Okamura H. *et al.* (2006) Synchronization and maintenance of timekeeping in suprachiasmatic circadian clock cells by neuropeptidergic signaling. *Curr. Biol.*, **16**, 599–605.
- Maywood, E.S., Chesham, J.E., Meng, Q.J., Nolan, P.M., Loudon, A.S. & Hastings, M.H. (2011a) Tuning the period of the mammalian circadian clock: additive and independent effects of CK1epsilonTau and Fbx13Afl mutations on mouse circadian behavior and molecular pacemaking. *J. Neurosci.*, **31**, 1539–1544.
- Maywood, E.S., Chesham, J.E., O'Brien, J.A. & Hastings, M.H. (2011b) A diversity of paracrine signals sustains molecular circadian cycling in suprachiasmatic nucleus circuits. *Proc. Natl. Acad. Sci. USA*, **108**, 14306–14311.
- McMahon, D.G. & Block, G.D. (1987) The Bulla ocular circadian pacemaker. I. Pacemaker neuron membrane potential controls phase through a calcium-dependent mechanism. *J. Comp. Physiol. A*, **161**, 335–346.
- Mead, S., Ebling, F.J., Maywood, E.S., Humby, T., Herbert, J. & Hastings, M.H. (1992) A nonphotic stimulus causes instantaneous phase advances of the light-entrainable circadian oscillator of the Syrian hamster but does not induce the expression of c-fos in the suprachiasmatic nuclei. *J. Neurosci.*, **12**, 2516–2522.

- Meijer, J.H. & Rietveld, W.J. (1989) Neurophysiology of the suprachiasmatic circadian pacemaker in rodents. *Physiol. Rev.*, **69**, 671–707.
- Meijer, J.H., Rusak, B. & Harrington, M.E. (1989) Photically responsive neurons in the hypothalamus of a diurnal ground squirrel. *Brain Res.*, **501**, 315–323.
- Meijer, J.H. & Michel, S. (2015) Neurophysiological analysis of the suprachiasmatic nucleus: a challenge at multiple levels. *Methods Enzymol.*, **552**, 75–102.
- Meng, Q.J., Logunova, L., Maywood, E.S., Gallego, M., Lebiecki, J., Brown, T.M., Sladek, M., Semikhodskii A.S. *et al.* (2008) Setting clock speed in mammals: the CK1 epsilon tau mutation in mice accelerates circadian pacesetters by selectively destabilizing PERIOD proteins. *Neuron*, **58**, 78–88.
- Mercado, C., Diaz-Munoz, M., Alamilla, J., Valderrama, K., Morales-Tlalpan, V. & Aguilar-Roblero, R. (2009) Ryanodine-sensitive intracellular Ca²⁺ channels in rat suprachiasmatic nuclei are required for circadian clock control of behavior. *J. Biol. Rhythm.*, **24**, 203–210.
- Mieda, M. & Sakurai, T. (2012) Overview of orexin/hypocretin system. *Prog. Brain Res.*, **198**, 5–14.
- Mieda, M., Ono, D., Hasegawa, E., Okamoto, H., Honma, K., Honma, S. & Sakurai, T. (2015) Cellular clocks in AVP neurons of the SCN are critical for interneuronal coupling regulating circadian behavior rhythm. *Neuron*, **85**, 1103–1116.
- Miller, J.D. & Fuller, C.A. (1992) Isoperiodic neuronal activity in suprachiasmatic nucleus of the rat. *Am. J. Physiol.*, **263**, R51–R58.
- Miller, B.H. & Takahashi, J.S. (2013) Central circadian control of female reproductive function. *Front. Endocrinol. (Lausanne)*, **4**, 195.
- Mirsky, H.P., Liu, A.C., Welsh, D.K., Kay, S.A. & Doyle, F.J. (2009) A model of the cell-autonomous mammalian circadian clock. *Proc. Natl. Acad. Sci. USA*, **106**, 11107–11112.
- Mistlberger, R.E. & Antle, M.C. (1998) Behavioral inhibition of light-induced circadian phase resetting is phase and serotonin dependent. *Brain Res.*, **786**, 31–38.
- Mistlberger, R.E. & Skene, D.J. (2005) Nonphotic entrainment in humans? *J. Biol. Rhythm.*, **20**, 339–352.
- Mizrak, D., Ruben, M., Myers, G.N., Rhrissorakkrai, K., Gunsalus, K.C. & Blau, J. (2012) Electrical activity can impose time of day on the circadian transcriptome of pacemaker neurons. *Curr. Biol.*, **22**, 1871–1880.
- Mohawk, J.A. & Takahashi, J.S. (2011) Cell autonomy and synchrony of suprachiasmatic nucleus circadian oscillators. *Trends Neurosci.*, **34**, 349–358.
- Mohawk, J.A., Green, C.B. & Takahashi, J.S. (2012) Central and peripheral circadian clocks in mammals. *Annu. Rev. Neurosci.*, **35**, 445–462.
- Montgomery, J.R. & Meredith, A.L. (2012) Genetic activation of BK currents *in vivo* generates bidirectional effects on neuronal excitability. *Proc. Natl. Acad. Sci. USA*, **109**, 18997–19002.
- Montgomery, J.R., Whitt, J.P., Wright, B.N., Lai, M.H. & Meredith, A.L. (2013) Mis-expression of the BK K(+) channel disrupts suprachiasmatic nucleus circuit rhythmicity and alters clock-controlled behavior. *Am. J. Physiol. Cell Physiol.*, **304**, C299–C311.
- Morin, L.P. & Allen, C.N. (2006) The circadian visual system, 2005. *Brain Res. Rev.*, **51**, 1–60.
- Morin, L.P. (2013) Neuroanatomy of the extended circadian rhythm system. *Exp. Neurol.*, **243**, 4–20.
- Moriya, T., Yoshinobu, Y., Kouzu, Y., Katoh, A., Gomi, H., Ikeda, M., Yoshioka, T., Itohara S. *et al.* (2000) Involvement of glial fibrillary acidic protein (GFAP) expressed in astroglial cells in circadian rhythm under constant lighting conditions in mice. *J. Neurosci. Res.*, **60**, 212–218.
- Moriya, T., Ikeda, M., Teshima, K., Hara, R., Kuriyama, K., Yoshioka, T., Allen, C.N. & Shibata, S. (2003) Facilitation of alpha-amino-3-hydroxy-5-methylisoxazole-4-propionate receptor transmission in the suprachiasmatic nucleus by aniracetam enhances photic responses of the biological clock in rodents. *J. Neurochem.*, **85**, 978–987.
- Mrosovsky, N. (1988) Phase response curves for social entrainment. *J. Comp. Physiol. A*, **162**, 35–46.
- Mrosovsky, N. (1996) Locomotor activity and non-photic influences on circadian clocks. *Biol. Rev. Camb. Philos.*, **71**, 343–372.
- Mrosovsky, N., Edelman, K., Hastings, M.H. & Maywood, E.S. (2001) Cycle of period gene expression in a diurnal mammal (*Spermophilus tridecemlineatus*): implications for nonphotic phase shifting. *J. Biol. Rhythm.*, **16**, 471–478.
- Mrugala, M., Zlomanczuk, P., Jagota, A. & Schwartz, W.J. (2000) Rhythmic multiunit neural activity in slices of hamster suprachiasmatic nucleus reflect prior photoperiod. *Am. J. Physiol.-Reg. I.*, **278**, R987–R994.
- Myung, J., Hong, S., Hatanaka, F., Nakajima, Y., De, S.E. & Takumi, T. (2012) Period coding of Bmal1 oscillators in the suprachiasmatic nucleus. *J. Neurosci.*, **32**, 8900–8918.
- Myung, J., Hong, S., DeWoskin, D., De Schutter, E., Forger, D.B. & Takumi, T. (2015) GABA-mediated repulsive coupling between circadian clock neurons in the SCN encodes seasonal time. *Proc. Natl. Acad. Sci. USA*, **112**, E3920–E3929.
- Nagano, M., Adachi, A., Nakahama, K., Nakamura, T., Tamada, M., Meyer-Bernstein, E., Sehgal, A. & Shigeyoshi, Y. (2003) An abrupt shift in the day/night cycle causes desynchrony in the mammalian circadian center. *J. Neurosci.*, **23**, 6141–6151.
- Nakamura, W., Honma, S., Shirakawa, T. & Honma, K. (2002) Clock mutation lengthens the circadian period without damping rhythms in individual SCN neurons. *Nat. Neurosci.*, **5**, 399–400.
- Nakamura, W., Yamazaki, S., Takasu, N.N., Mishima, K. & Block, G.D. (2005) Differential response of Period 1 expression within the suprachiasmatic nucleus. *J. Neurosci.*, **25**, 5481–5487.
- Nedergaard, M. & Verkhratsky, A. (2010) Calcium dyshomeostasis and pathological calcium signalling in neurological diseases. *Cell Calcium*, **47**, 101–102.
- Nedergaard, M., Rodriguez, J.J. & Verkhratsky, A. (2010) Glial calcium and diseases of the nervous system. *Cell Calcium*, **47**, 140–149.
- Nitabach, M.N., Blau, J. & Holmes, T.C. (2002) Electrical silencing of *Drosophila* pacemaker neurons stops the free-running circadian clock. *Cell*, **109**, 485–495.
- Nitabach, M.N., Wu, Y., Sheeba, V., Lemon, W.C., Strumbos, J., Zelensky, P.K., White, B.H. & Holmes, T.C. (2006) Electrical hyperexcitation of lateral ventral pacemaker neurons desynchronizes downstream circadian oscillators in the fly circadian circuit and induces multiple behavioral periods. *J. Neurosci.*, **26**, 479–489.
- Noguchi, T., Leise, T.L., Kingsbury, N.J., Diemer, T., Wang, L.L., Henson, M.A. & Welsh, D.K. (2017) Calcium circadian rhythmicity in the suprachiasmatic nucleus: cell autonomy and network modulation. *eNeuro*, **4**, ENEURO.0160-17.2017.
- O'Neill, J.S., Maywood, E.S., Chesham, J.E., Takahashi, J.S. & Hastings, M.H. (2008) cAMP-dependent signaling as a core component of the mammalian circadian pacemaker. *Science*, **320**, 949–953.
- O'Neill, J.S., Maywood, E.S. & Hastings, M.H. (2013) Cellular mechanisms of circadian pacemaking: beyond transcriptional loops. *Handb. Exp. Pharmacol.*, **217**, 67–103.
- Otalora, B.B., Hagenauer, M.H., Rol, M.A., Madrid, J.A. & Lee, T.M. (2013) Period gene expression in the brain of a dual-phasing rodent, the *Octodon degus*. *J. Biol. Rhythm.*, **28**, 249–261.
- Ouyang, Y., Andersson, C.R., Kondo, T., Golden, S.S. & Johnson, C.H. (1998) Resonating circadian clocks enhance fitness in cyanobacteria. *Proc. Natl. Acad. Sci. USA*, **95**, 8660–8664.
- Panda, S., Antoch, M.P., Miller, B.H., Su, A.I., Schook, A.B., Straume, M., Schultz, P.G., Kay S.A. *et al.* (2002) Coordinated transcription of key pathways in the mouse by the circadian clock. *Cell*, **109**, 307–320.
- Partch, C.L., Green, C.B. & Takahashi, J.S. (2014) Molecular architecture of the mammalian circadian clock. *Trends Cell Biol.*, **24**, 90–99.
- Paul, J.R., DeWoskin, D., McMeekin, L.J., Cowell, R.M., Forger, D.B. & Gamble, K.L. (2016) Regulation of persistent sodium currents by glycogen synthase kinase 3 encodes daily rhythms of neuronal excitability. *Nat. Commun.*, **7**, 13470.
- Pauls, S., Foley, N.C., Foley, D.K., LeSauter, J., Hastings, M.H., Maywood, E.S. & Silver, R. (2014) Differential contributions of intra-cellular and inter-cellular mechanisms to the spatial and temporal architecture of the suprachiasmatic nucleus circadian circuitry in wild-type, cryptochrome-null and vasoactive intestinal peptide receptor 2-null mutant mice. *Eur. J. Neurosci.*, **40**, 2528–2540.
- Pauls, S.D., Honma, K., Honma, S. & Silver, R. (2016) Deconstructing circadian rhythmicity with models and manipulations. *Trends Neurosci.*, **39**, 405–419.
- Pavlidis, T. (1978) What do mathematical models tell us about circadian clocks? *B. Math. Biol.*, **40**, 625–635.
- Pennartz, C.M., Bierlaagh, M.A. & Geurtsen, A.M. (1997) Cellular mechanisms underlying spontaneous firing in rat suprachiasmatic nucleus: involvement of a slowly inactivating component of sodium current. *J. Neurophysiol.*, **78**, 1811–1825.
- Pennartz, C.M., De Jeu, M.T., Geurtsen, A.M., Sluiter, A.A. & Hermes, M.L. (1998) Electrophysiological and morphological heterogeneity of neurons in slices of rat suprachiasmatic nucleus. *J. Physiol.*, **506**(Pt 3), 775–793.
- Pennartz, C.M., de Jeu, M.T., Bos, N.P., Schaap, J. & Geurtsen, A.M. (2002) Diurnal modulation of pacemaker potentials and calcium current in the mammalian circadian clock. *Nature*, **416**, 286–290.
- Penttonen, M. & Buzsáki, G. (2003) Natural logarithmic relationship between brain oscillators. *Thalamus Related Syst.*, **2**, 145.


- Pfeffer, M., Muller, C.M., Mordel, J., Meissl, H., Ansari, N., Deller, T., Korf, H.W. & von Gall, C. (2009) The mammalian molecular clockwork controls rhythmic expression of its own input pathway components. *J. Neurosci.*, **29**, 6114–6123.
- Pittendrigh, C.S. & Minis, D.H. (1972) Circadian systems: longevity as a function of circadian resonance in *Drosophila melanogaster*. *Proc. Natl. Acad. Sci. USA*, **69**, 1537–1539.
- Pitts, G.R., Ohta, H. & McMahon, D.G. (2006) Daily rhythmicity of large-conductance Ca²⁺-activated K⁺ currents in suprachiasmatic nucleus neurons. *Brain Res.*, **1071**, 54–62.
- Podkolodnaya, O.A., Tverdokhlebov, N.N. & Podkolodnyy, N.L. (2017) Computational modeling of the cell-autonomous mammalian circadian oscillator. *BMC Syst. Biol.*, **11**, 27–42.
- Polidarova, L., Sladek, M., Sotak, M., Pacha, J. & Sumova, A. (2011) Hepatic, duodenal, and colonic circadian clocks differ in their persistence under conditions of constant light and in their entrainment by restricted feeding. *Chronobiol. Int.*, **28**, 204–215.
- Poskanzer, K.E. & Yuste, R. (2016) Astrocytes regulate cortical state switching *in vivo*. *Proc. Natl. Acad. Sci. USA*, **113**, E2675–E2684.
- Prolo, L.M., Takahashi, J.S. & Herzog, E.D. (2005) Circadian rhythm generation and entrainment in astrocytes. *J. Neurosci.*, **25**, 404–408.
- Prosser, R.A., Edgar, D.M., Heller, H.C. & Miller, J.D. (1994a) A possible glial role in the mammalian circadian clock. *Brain Res.*, **643**, 296–301.
- Prosser, R.A., Heller, H.C. & Miller, J.D. (1994b) Serotonergic phase advances of the mammalian circadian clock involve protein kinase A and K⁺ channel opening. *Brain Res.*, **644**, 67–73.
- Ralph, M.R., Foster, R.G., Davis, F.C. & Menaker, M. (1990) Transplanted suprachiasmatic nucleus determines circadian period. *Science*, **247**, 975–978.
- Ralph, M.R. & Mrosovsky, N. (1992) Behavioral inhibition of circadian responses to light. *J. Biol. Rhythm.*, **7**, 353–359.
- Ramanathan, C., Stowie, A., Smale, L. & Nunez, A.A. (2010) Phase preference for the display of activity is associated with the phase of extra-suprachiasmatic nucleus oscillators within and between species. *Neuroscience*, **170**, 758–772.
- Ramkisoensing, A. & Meijer, J.H. (2015) Synchronization of biological clock neurons by light and peripheral feedback systems promotes circadian rhythms and health. *Front. Neurol.*, **6**, 128.
- Reddy, A.B., Field, M.D., Maywood, E.S. & Hastings, M.H. (2002) Differential resynchronization of circadian clock gene expression within the suprachiasmatic nuclei of mice subjected to experimental jet lag. *J. Neurosci.*, **22**, 7326–7330.
- Redlin, U. & Mrosovsky, N. (1997) Exercise and human circadian rhythms: what we know and what we need to know. *Chronobiol. Int.*, **14**, 221–229.
- Reebs, S.G. & Mrosovsky, N. (1989) Effects of induced wheel running on the circadian activity rhythms of Syrian hamsters: entrainment and phase response curve. *J. Biol. Rhythm.*, **4**, 39–48.
- Relógio, A., Westermarck, P.O., Wallach, T., Schellenberg, K., Kramer, A. & Herzog, H. (2011) Tuning the mammalian circadian clock: robust synergy of two loops. *PLoS Comput. Biol.*, **7**, 1–18.
- Reppert, S.M. & Weaver, D.R. (2002) Coordination of circadian timing in mammals. *Nature*, **418**, 935–941.
- Ruoff, P., Vinsjevnik, M., Monnerjahn, C. & Rensing, L. (1999) The Goodwin oscillator: on the importance of degradation reactions in the circadian clock. *J. Biol. Rhythm.*, **14**, 469–479.
- Saeb-Parsy, K. & Dyball, R.E. (2003a) Defined cell groups in the rat suprachiasmatic nucleus have different day/night rhythms of single-unit activity *in vivo*. *J. Biol. Rhythm.*, **18**, 26–42.
- Saeb-Parsy, K. & Dyball, R.E. (2003b) Responses of cells in the rat suprachiasmatic nucleus *in vivo* to stimulation of afferent pathways are different at different times of the light/dark cycle. *J. Neuroendocrinol.*, **15**, 895–903.
- Sakai, K. (2014) Single unit activity of the suprachiasmatic nucleus and surrounding neurons during the wake-sleep cycle in mice. *Neuroscience*, **260**, 249–264.
- Sakhi, K., Belle, M.D., Gossan, N., Delagrange, P. & Piggins, H.D. (2014a) Daily variation in the electrophysiological activity of mouse medial habenula neurons. *J. Physiol.*, **592**, 587–603.
- Sakhi, K., Wegner, S., Belle, M.D., Howarth, M., Delagrange, P., Brown, T.M. & Piggins, H.D. (2014b) Intrinsic and extrinsic cues regulate the daily profile of mouse lateral habenula neuronal activity. *J. Physiol.*, **592**, 5025–5045.
- Santello, M., Cali, C. & Bezzi, P. (2012) Gliotransmission and the tripartite synapse. *Adv. Exp. Med. Biol.*, **970**, 307–331.
- Sato, T. & Kawamura, H. (1984) Circadian rhythms in multiple unit activity inside and outside the suprachiasmatic nucleus in the diurnal chipmunk (*Eutamias sibiricus*). *Neurosci. Res.*, **1**, 45–52.
- Saunders, D.S. (1972) Circadian control of larval growth rate in *Sarcophaga argyrostoma*. *Proc. Natl. Acad. Sci. USA*, **69**, 2738–2740.
- Schaap, J. & Meijer, J.H. (2001) Opposing effects of behavioural activity and light on neurons of the suprachiasmatic nucleus. *Eur. J. Neurosci.*, **13**, 1955–1962.
- Schaap, J., Albus, H., VanderLeest, H.T., Eilers, P.H., Detari, L. & Meijer, J.H. (2003a) Heterogeneity of rhythmic suprachiasmatic nucleus neurons: implications for circadian waveform and photoperiodic encoding. *Proc. Natl. Acad. Sci. USA*, **100**, 15994–15999.
- Schaap, J., Pennartz, C.M. & Meijer, J.H. (2003b) Electrophysiology of the circadian pacemaker in mammals. *Chronobiol. Int.*, **20**, 171–188.
- Schmidt, T.M., Do, M.T., Dacey, D., Lucas, R., Hattar, S. & Matynia, A. (2011) Melanopsin-positive intrinsically photosensitive retinal ganglion cells: from form to function. *J. Neurosci.*, **31**, 16094–16101.
- Schmutz, I., Chavan, R., Ripperger, J.A., Maywood, E.S., Langwieser, N., Jurik, A., Stauffer, A., Delorme J.E. *et al.* (2014) A specific role for the REV-ERB α -controlled L-type voltage-gated calcium channel CaV1.2 in resetting the circadian clock in the late night. *J. Biol. Rhythm.*, **29**, 288–298.
- Schroeder, A.M. & Colwell, C.S. (2013) How to fix a broken clock. *Trends Pharmacol. Sci.*, **34**, 605–619.
- Schwartz, W.J. & Gainer, H. (1977) Suprachiasmatic nucleus: use of 14C-labeled deoxyglucose uptake as a functional marker. *Science*, **197**, 1089–1091.
- Schwartz, W.J., Reppert, S.M., Eagan, S.M. & Moore-Ede, M.C. (1983) *In vivo* metabolic activity of the suprachiasmatic nuclei: a comparative study. *Brain Res.*, **274**, 184–187.
- Scott, F.F., Belle, M.D., Delagrange, P. & Piggins, H.D. (2010) Electrophysiological effects of melatonin on mouse Per1 and non-Per1 suprachiasmatic nuclei neurones *in vitro*. *J. Neuroendocrinol.*, **22**, 1148–1156.
- Serkh, K. & Forger, D.B. (2014) Optimal schedules of light exposure for rapidly correcting circadian misalignment. *PLoS Comput. Biol.*, **10**, e1003523.
- Shibata, S., Oomura, Y., Kita, H. & Hattori, K. (1982) Circadian rhythmic changes of neuronal activity in the suprachiasmatic nucleus of the rat hypothalamic slice. *Brain Res.*, **247**, 154–158.
- Shibata, S., Tsuneyoshi, A., Hamada, T., Tominaga, K. & Watanabe, S. (1992) Phase-resetting effect of 8-OH-DPAT, a serotonin1A receptor agonist, on the circadian rhythm of firing rate in the rat suprachiasmatic nuclei *in vitro*. *Brain Res.*, **582**, 353–356.
- Shibata, S., Watanabe, A., Hamada, T., Ono, M. & Watanabe, S. (1994) N-methyl-D-aspartate induces phase shifts in circadian rhythm of neuronal activity of rat SCN *in vitro*. *Am. J. Physiol.*, **267**, R360–R364.
- Shirakawa, T., Honma, S., Katsuno, Y., Oguchi, H. & Honma, K.I. (2000) Synchronization of circadian firing rhythms in cultured rat suprachiasmatic neurons. *Eur. J. Neurosci.*, **12**, 2833–2838.
- Silver, R., LeSauter, J., Tresco, P.A. & Lehman, M.N. (1996) A diffusible coupling signal from the transplanted suprachiasmatic nucleus controlling circadian locomotor rhythms. *Nature*, **382**, 810–813.
- Silver, R. & Kriegsfeld, L.J. (2014) Circadian rhythms have broad implications for understanding brain and behavior. *Eur. J. Neurosci.*, **39**, 1866–1880.
- Silver, R., Lehman, M.N., Gibson, M., Gladstone, W.R. & Bittman, E.L. (1990) Dispersed cell suspensions of fetal SCN restore circadian rhythmicity in SCN-lesioned adult hamsters. *Brain Res.*, **525**, 45–58.
- Sim, C.K. & Forger, D.B. (2007) Modeling the electrophysiology of suprachiasmatic nucleus neurons. *J. Biol. Rhythm.*, **22**, 445–453.
- Sirota, A., Csicsvari, J., Buhl, D. & Buzsáki, G. (2003) Communication between neocortex and hippocampus during sleep in rodents. *Proc. Natl. Acad. Sci. USA*, **100**, 2065–2069.
- Skeldon, A.C., Phillips, A.J.K. & Dijk, D.-J. (2017) The effects of self-selected light-dark cycles and social constraints on human sleep and circadian timing: a modeling approach. *Sci. Rep.*, **7**, 45158.
- Smale, L., Lee, T. & Nunez, A.A. (2003) Mammalian diurnality: some facts and gaps. *J. Biol. Rhythm.*, **18**, 356–366.
- Spiga, F., Walker, J.J., Terry, J.R. & Lightman, S.L. (2014) HPA axis-rhythms. *Compr. Physiol.*, **4**, 1273–1298.
- Spiga, F., Walker, J.J., Gupta, R., Terry, J.R. & Lightman, S.L. (2015) Glucocorticoid dynamics: insights from mathematical, experimental and clinical studies. *J. Endocrinol.*, **226**, T55–T66.
- Spoelstra, K., Wikelski, M., Daan, S., Loudon, A.S. & Hau, M. (2016) Natural selection against a circadian clock gene mutation in mice. *Proc. Natl. Acad. Sci. USA*, **113**, 686–691.
- Steriade, M. (2001) Impact of network activities on neuronal properties in corticothalamic systems. *J. Neurophysiol.*, **86**, 1–39.

- Storchi, R., Bedford, R.A., Martial, F.P., Allen, A.E., Wynne, J., Montemurro, M.A., Petersen, R.S. & Lucas, R.J. (2017) Modulation of fast narrowband oscillations in the mouse retina and dLGN according to background light intensity. *Neuron*, **93**, 299–307.
- Takahashi, J.S., Hong, H.K., Ko, C.H. & McDearmon, E.L. (2008) The genetics of mammalian circadian order and disorder: implications for physiology and disease. *Nat. Rev. Genet.*, **9**, 764–775.
- Tamada, Y., Tanaka, M., Munekawa, K., Hayashi, S., Okamura, H., Kubo, T., Hisa, Y. & Ibata, Y. (1998) Neuron-glia interaction in the suprachiasmatic nucleus: a double labeling light and electron microscopic immunocytochemical study in the rat. *Brain Res. Bull.*, **45**, 281–287.
- Taylor, S.R., Webb, A.B., Smith, K.S., Petzold, L.R. & Doyle, F.J. (2010) Velocity response curves support the role of continuous entrainment in circadian clocks. *J. Biol. Rhythms*, **25**, 138–149.
- Thomson, A.M. (1984) Slow, regular discharge in suprachiasmatic neurones is calcium dependent, in slices of rat brain. *Neuroscience*, **13**, 761–767.
- Thomson, A.M. & West, D.C. (1990) Factors affecting slow regular firing in the suprachiasmatic nucleus *in vitro*. *J. Biol. Rhythms*, **5**, 59–75.
- Tiesinga, P. & Sejnowski, T.J. (2009) Cortical enlightenment: are attentional gamma oscillations driven by ING or PING? *Neuron*, **63**, 727–732.
- To, T.-L., Henson, M.A., Herzog, E.D. & Doyle, F.J. (2007) A molecular model for intercellular synchronization in the mammalian circadian clock. *Biophys. J.*, **92**, 3792–3803.
- Tousson, E. & Meissl, H. (2004) Suprachiasmatic nuclei grafts restore the circadian rhythm in the paraventricular nucleus of the hypothalamus. *J. Neurosci.*, **24**, 2983–2988.
- Travnickova-Bendova, Z., Cermakian, N., Reppert, S.M. & Sassone-Corsi, P. (2002) Bimodal regulation of mPeriod promoters by CREB-dependent signaling and CLOCK/BMAL1 activity. *Proc. Natl. Acad. Sci. USA*, **99**, 7728–7733.
- Tso, C.F., Simon, T., Greenlaw, A.C., Puri, T., Mieda, M. & Herzog, E.D. (2017) Astrocytes regulate daily rhythms in the suprachiasmatic nucleus and behavior. *Curr. Biol.*, **27**, 1055–1061.
- Tsujii, T., Tsujii, C., Ludwig, M. & Leng, G. (2016) The rat suprachiasmatic nucleus: the master clock ticks at 30 Hz. *J. Physiol.*, **594**, 3629–3650.
- van den Pol, A.N., Finkbeiner, S.M. & Cornell-Bell, A.H. (1992) Calcium excitability and oscillations in suprachiasmatic nucleus neurons and glia *in vitro*. *J. Neurosci.*, **12**, 2648–2664.
- van den Pol, A.N., Obrietan, K., Chen, G. & Belousov, A.B. (1996) Neuropeptide Y-mediated long-term depression of excitatory activity in suprachiasmatic nucleus neurons. *J. Neurosci.*, **16**, 5883–5895.
- van der Horst, G.T., Muijtjens, M., Kobayashi, K., Takano, R., Kanno, S., Takao, M., de Wit, J., Verkerk, A. *et al.* (1999) Mammalian Cry1 and Cry2 are essential for maintenance of circadian rhythms. *Nature*, **398**, 627–630.
- van der Veen, D.R., Mulder, E.G., Oster, H., Gerkema, M.P. & Hut, R.A. (2008) SCN-AVP release of mPer1/mPer2 double-mutant mice *in vitro*. *J. Circadian Rhythms*, **6**, 5.
- van Oosterhout, F., Lucassen, E.A., Houben, T., vanderLeest, H.T., Antle, M.C. & Meijer, J.H. (2012) Amplitude of the SCN clock enhanced by the behavioral activity rhythm. *PLoS ONE*, **7**, e39693.
- VanderLeest, H.T., Houben, T., Michel, S., Deboer, T., Albus, H., Vansteensel, M.J., Block, G.D. & Meijer, J.H. (2007) Seasonal encoding by the circadian pacemaker of the SCN. *Curr. Biol.*, **17**, 468–473.
- VanderLeest, H.T., Rohling, J.H.T., Michel, S. & Meijer, J.H. (2009) Phase shifting capacity of the circadian pacemaker determined by the SCN neuronal network organization. *PLoS ONE*, **4**, e4976.
- Vasalou, C. & Henson, M.A. (2010) A multiscale model to investigate circadian rhythmicity of pacemaker neurons in the suprachiasmatic nucleus. *PLoS Comput. Biol.*, **6**, e1000706.
- Vasalou, C., Herzog, E.D. & Henson, M.A. (2011) Multicellular model for intercellular synchronization in circadian neural networks. *Biophys. J.*, **101**, 12–20.
- Verkhatsky, A. & Kettenmann, H. (1996) Calcium signalling in glial cells. *Trends Neurosci.*, **19**, 346–352.
- Verkhatsky, A., Rodriguez, J.J. & Parpura, V. (2012a) Calcium signalling in astroglia. *Mol. Cell. Endocrinol.*, **353**, 45–56.
- Verkhatsky, A., Rodriguez, J.J. & Parpura, V. (2012b) Neurotransmitters and integration in neuronal-astroglial networks. *Neurochem. Res.*, **37**, 2326–2338.
- Vitaterna, M.H., Selby, C.P., Todo, T., Niwa, H., Thompson, C., Fruechte, E.M., Hitomi, K., Thresher R.J. *et al.* (1999) Differential regulation of mammalian period genes and circadian rhythmicity by cryptochromes 1 and 2. *Proc. Natl. Acad. Sci. USA*, **96**, 12114–12119.
- Wakamatsu, H., Yoshinobu, Y., Aida, R., Moriya, T., Akiyama, M. & Shibata, S. (2001) Restricted-feeding-induced anticipatory activity rhythm is associated with a phase-shift of the expression of mPer1 and mPer2 mRNA in the cerebral cortex and hippocampus but not in the suprachiasmatic nucleus of mice. *Eur. J. Neurosci.*, **13**, 1190–1196.
- Walmsley, L. & Brown, T.M. (2015) Eye-specific visual processing in the mouse suprachiasmatic nuclei. *J. Physiol.*, **593**, 1731–1743.
- Walmsley, L., Hanna, L., Moulard, J., Martial, F., West, A., Smedley, A.R., Bechtold, D.A., Webb, A.R. *et al.* (2015) Colour as a signal for entraining the mammalian circadian clock. *PLoS Biol.*, **13**, e1002127.
- Walsh, I.B., van den Berg, R.J., Marani, E. & Rietveld, W.J. (1992) Spontaneous and stimulated firing in cultured rat suprachiasmatic neurons. *Brain Res.*, **588**, 120–131.
- Wang, L.M., Dragich, J.M., Kudo, T., Odom, I.H., Welsh, D.K., O'Dell, T.J. & Colwell, C.S. (2009) Expression of the circadian clock gene *Period2* in the hippocampus: possible implications for synaptic plasticity and learned behaviour. *ASN Neuro.*, **1**, e00012.
- Wang, X.-J. & Buzsáki, G. (2012) Mechanisms of gamma oscillations. *Annu. Rev. Neurosci.*, **35**, 203–225.
- Wang, T.A., Yu, Y.V., Govindaiah, G., Ye, X., Artinian, L., Coleman, T.P., Sweedler, J.V., Cox C.L. *et al.* (2012) Circadian rhythm of redox state regulates excitability in suprachiasmatic nucleus neurons. *Science*, **337**, 839–842.
- Wardlaw, S.M., Phan, T.X., Saraf, A., Chen, X. & Storm, D.R. (2014) Genetic disruption of the core circadian clock impairs hippocampus-dependent memory. *Learn Memory*, **21**, 417–423.
- Webb, A.B., Angelo, N., Huettner, J.E. & Herzog, E.D. (2009) Intrinsic, nondeterministic circadian rhythm generation in identified mammalian neurons. *Proc. Natl. Acad. Sci. USA*, **106**, 16493–16498.
- Wegner, S., Belle, M.D.C., Hughes, A.T.L., Diekmann, C.O. & Piggins, H.D. (2017) Delayed cryptochrome degradation asymmetrically alters the daily rhythm in suprachiasmatic clock neuron excitability. *J. Neurosci.*, **37**, 7824–7836.
- Welsh, D.K., Logothetis, D.E., Meister, M. & Reppert, S.M. (1995) Individual neurons dissociated from rat suprachiasmatic nucleus express independently phased circadian firing rhythms. *Neuron*, **14**, 697–706.
- Welsh, D.K., Takahashi, J.S. & Kay, S.A. (2010) Suprachiasmatic nucleus: cell autonomy and network properties. *Annu. Rev. Physiol.*, **72**, 551–577.
- Wever, R. (1966) The duration of re-entrainment of circadian rhythms after phase shifts of the Zeitgeber A theoretical investigation. *J. Theor. Biol.*, **13**, 187–201.
- Wheal, H.V. & Thomson, A.M. (1984) The electrical properties of neurones of the rat suprachiasmatic nucleus recorded intracellularly *in vitro*. *Neuroscience*, **13**, 97–104.
- Whitt, J.P., Montgomery, J.R. & Meredith, A.L. (2016) BK channel inactivation gates daytime excitability in the circadian clock. *Nat. Commun.*, **7**, 10837.
- Whittington, M.A., Traub, R.D., Kopell, N., Ermentrout, B. & Buhl, E.H. (2000) Inhibition-based rhythms: experimental and mathematical observations on network dynamics. *Int. J. Psychophysiol.*, **38**, 315–336.
- Winfree, A.T. 2001. *The Geometry of Biological Time*. Springer Science & Business Media, Berlin.
- Woller, A., Gonze, D. & Erneux, T. (2013) Strong feedback limit of the Goodwin circadian oscillator. *Phys. Rev. E*, **87**, 1–8.
- Woller, A., Gonze, D. & Erneux, T. (2014) The Goodwin model revisited: Hopf bifurcation, limit-cycle, and periodic entrainment. *Phys. Biol.*, **11**, 045002.
- Woller, A., Duez, H., Staels, B. & Lefranc, M. (2016) A mathematical model of the liver circadian clock linking feeding and fasting cycles to clock function. *Cell Rep.*, **17**, 1087–1097.
- Womac, A.D., Burkeen, J.F., Neuendorff, N., Earnest, D.J. & Zoran, M.J. (2009) Circadian rhythms of extracellular ATP accumulation in suprachiasmatic nucleus cells and cultured astrocytes. *Eur. J. Neurosci.*, **30**, 869–876.
- Wu, Y., Cao, G., Pavlicek, B., Luo, X. & Nitabach, M.N. (2008) Phase coupling of a circadian neuropeptide with rest/activity rhythms detected using a membrane-tethered spider toxin. *PLoS Biol.*, **6**, e273.
- Yagita, K., Yamanaka, I., Emoto, N., Kawakami, K. & Shimada, S. (2010) Real-time monitoring of circadian clock oscillations in primary cultures of mammalian cells using Tol2 transposon-mediated gene transfer strategy. *BMC Biotechnol.*, **10**, 3.
- Yamaguchi, S., Isejima, H., Matsuo, T., Okura, R., Yagita, K., Kobayashi, M. & Okamura, H. (2003) Synchronization of cellular clocks in the suprachiasmatic nucleus. *Science*, **302**, 1408–1412.

- Yamakawa, G.R., Basu, P., Cortese, F., MacDonnell, J., Whalley, D., Smith, V.M. & Antle, M.C. (2016) The cholinergic forebrain arousal system acts directly on the circadian pacemaker. *Proc. Natl. Acad. Sci. USA*, **113**, 13498–13503.
- Yamazaki, S., Kerbeshian, M.C., Hocker, C.G., Block, G.D. & Menaker, M. (1998) Rhythmic properties of the hamster suprachiasmatic nucleus *in vivo*. *J. Neurosci.*, **18**, 10709–10723.
- Yan, L. & Okamura, H. (2002) Gradients in the circadian expression of *Per1* and *Per2* genes in the rat suprachiasmatic nucleus. *Eur. J. Neurosci.*, **15**, 1153–1162.
- Yan, L. & Silver, R. (2004) Resetting the brain clock: time course and localization of mPER1 and mPER2 protein expression in suprachiasmatic nuclei during phase shifts. *Eur. J. Neurosci.*, **19**, 1105–1109.
- Yang, J.J., Wang, Y.T., Cheng, P.C., Kuo, Y.J. & Huang, R.C. (2010) Cholinergic modulation of neuronal excitability in the rat suprachiasmatic nucleus. *J. Neurophysiol.*, **103**, 1397–1409.
- Yannielli, P.C. & Harrington, M.E. (2000) Neuropeptide Y applied *in vitro* can block the phase shifts induced by light *in vivo*. *NeuroReport*, **11**, 1587–1591.
- Yannielli, P.C. & Harrington, M.E. (2001) Neuropeptide Y in the mammalian circadian system: effects on light-induced circadian responses. *Pep-tides*, **22**, 547–556.
- Yannielli, P.C., Brewer, J.M. & Harrington, M.E. (2004) Blockade of the NPY Y5 receptor potentiates circadian responses to light: complementary *in vivo* and *in vitro* studies. *Eur. J. Neurosci.*, **19**, 891–897.
- Yildirim, V. & Bertram, R. (2017) Calcium oscillation frequency-sensitive gene regulation and homeostatic compensation in pancreatic [Formula: see text]-cells. *B. Math. Biol.*, **79**, 1295–1324.
- Zhang, L., Aguilar-Roblero, R., Barrio, R.A. & Maini, P.K. (1995) Rhythmic firing patterns in suprachiasmatic nucleus (SCN): the role of circuit interactions. *Int. J. Biomed. Comput.*, **38**, 23–31.
- Zhou, Q.Y. & Cheng, M.Y. (2005) Prokineticin 2 and circadian clock output. *FEBS J.*, **272**, 5703–5709.



Data Assimilation Methods for Neuronal State and Parameter Estimation

Matthew J. Moyer¹ · Casey O. Diekman¹ 

Received: 16 February 2018 / Accepted: 11 July 2018 / Published online: 09 August 2018

© The Author(s) 2018. This article is distributed under the terms of the Creative Commons Attribution 4.0 International License (<http://creativecommons.org/licenses/by/4.0/>), which permits unrestricted use, distribution, and reproduction in any medium, provided you give appropriate credit to the original author(s) and the source, provide a link to the Creative Commons license, and indicate if changes were made.

Abstract This tutorial illustrates the use of data assimilation algorithms to estimate unobserved variables and unknown parameters of conductance-based neuronal models. Modern data assimilation (DA) techniques are widely used in climate science and weather prediction, but have only recently begun to be applied in neuroscience. The two main classes of DA techniques are sequential methods and variational methods. We provide computer code implementing basic versions of a method from each class, the Unscented Kalman Filter and 4D-Var, and demonstrate how to use these algorithms to infer several parameters of the Morris–Lecar model from a single voltage trace. Depending on parameters, the Morris–Lecar model exhibits qualitatively different types of neuronal excitability due to changes in the underlying bifurcation structure. We show that when presented with voltage traces from each of the various excitability regimes, the DA methods can identify parameter sets that produce the correct bifurcation structure even with initial parameter guesses that correspond to a different excitability regime. This demonstrates the ability of DA techniques to perform nonlinear state and parameter estimation and introduces the geometric structure of inferred models as a novel qualitative measure of estimation success. We conclude by discussing extensions of these DA algorithms that have appeared in the neuroscience literature.

Keywords Data assimilation · Neuronal excitability · Conductance-based models · Parameter estimation

Electronic supplementary material The online version of this article (<https://doi.org/10.1186/s13408-018-0066-8>) contains supplementary material.

✉ C.O. Diekman
diekman@njit.edu

M.J. Moyer
mjm83@njit.edu

¹ Department of Mathematical Sciences & Institute for Brain and Neuroscience Research, New Jersey Institute of Technology, Newark, USA

List of Abbreviations

DA	data assimilation
PDE	partial differential equation
4D-Var	4D-Variational
EKF	Extended Kalman Filter
UKF	Unscented Kalman Filter
SNIC	saddle-node on invariant circle
EnKF	Ensemble Kalman Filter
LETK	Local Ensemble Transform Kalman Filter

1 Introduction

1.1 The Parameter Estimation Problem

The goal of conductance-based modeling is to be able to reproduce, explain, and predict the electrical behavior of a neuron or networks of neurons. Conductance-based modeling of neuronal excitability began in the 1950s with the Hodgkin–Huxley model of action potential generation in the squid giant axon [1]. This modeling framework uses an equivalent circuit representation for the movement of ions across the cell membrane:

$$C \frac{dV}{dt} = I_{\text{app}} - \sum_{\text{ion}} I_{\text{ion}}, \quad (1)$$

where V is membrane voltage, C is cell capacitance, I_{ion} are ionic currents, and I_{app} is an external current applied by the experimentalist. The ionic currents arise from channels in the membrane that are voltage- or calcium-gated and selective for particular ions, such sodium (Na^+) and potassium (K^+). For example, consider the classical Hodgkin–Huxley currents:

$$I_{\text{Na}} = g_{\text{Na}} m^3 h (V - E_{\text{Na}}), \quad (2)$$

$$I_{\text{K}} = g_{\text{K}} n^4 (V - E_{\text{K}}). \quad (3)$$

The maximal conductance g_{ion} is a parameter that represents the density of channels in the membrane. The term $(V - E_{\text{ion}})$ is the driving force, where the equilibrium potential E_{ion} is the voltage at which the concentration of the ion inside and outside of the cell is at steady state. The gating variable m is the probability that one of three identical subunits of the sodium channel is “open”, and the gating variable h is the probability that a fourth subunit is “inactivated”. Similarly, the gating variable n is the probability that one of four identical subunits of the potassium channel is open. For current to flow through the channel, all subunits must be open and not inactivated. The rate at which subunits open, close, inactivate, and de-inactivate depends on the voltage. The dynamics of the gating variables are given by

$$\frac{dx}{dt} = \alpha_x(V)(1 - x) + \beta_x(V)x, \quad (4)$$

where $\alpha_x(V)$ and $\beta_x(V)$ are nonlinear functions of voltage with several parameters.

The parameters of conductance-based models are typically fit to voltage-clamp recordings. In these experiments, individual ionic currents are isolated using pharmacological blockers and one measures current traces in response to voltage pulses. However, many electrophysiological datasets consist of current-clamp rather than voltage-clamp recordings. In current-clamp, one records a voltage trace (e.g., a series of action potentials) in response to injected current. Fitting a conductance-based model to current-clamp data is challenging because the individual ionic currents have not been measured directly. In terms of the Hodgkin–Huxley model, only one state variable (V) has been observed, and the other three state variables (m , h , and n) are unobserved. Conductance-based models of neurons often contain several ionic currents and, therefore, more unobserved gating variables and more unknown or poorly known parameters. For example, a model of HVC neurons in the zebra finch has 9 ionic currents, 12 state variables, and 72 parameters [2]. An additional difficulty in attempting to fit a model to a voltage trace is that if one performs a least-squares minimization between the data and model output, then small differences in the timing of action potentials in the data and the model can result in large error [3]. Data assimilation methods have the potential to overcome these challenges by performing state estimation (of both observed and unobserved states) and parameter estimation simultaneously.

1.2 Data Assimilation

Data assimilation can broadly be considered to be the optimal integration of observations from a system to improve estimates of a model output describing that system. Data assimilation (DA) is used across the geosciences, e.g., in studying land hydrology and ocean currents, as well as studies of climates of other planets [4–6]. An application of DA familiar to the general public is its use in numerical weather prediction [7]. In the earth sciences, the models are typically high-dimensional partial differential equations (PDEs) that incorporate dynamics of the many relevant governing processes, and the state system is a discretization of those PDEs across the spatial domain. These models are nonlinear and chaotic, with interactions of system components across temporal and spatial scales. The observations are sparse in time, contaminated by noise, and only partial with respect to the full state-space.

In neuroscience, models can also be highly nonlinear and potentially chaotic. When dealing with network dynamics or wave propagation, the state-space can be quite large, and there are certainly components of the system for which one would not have time course measurements [8]. As mentioned above, if one has a biophysical model of a single neuron and measurements from a current-clamp protocol, the only quantity in the model that is actually measured is the membrane voltage. The question then becomes: how does one obtain estimates of the full system state?

To begin, we assume we have a model to represent the system of interest and a way to relate observations we have of that system to the components of the model. Additionally, we allow, and naturally expect, there to be errors present in the model and measurements. To start, let us consider first a general model with linear dynamics and a set of discrete observations which depend linearly on the system components:

$$x_{k+1} = Fx_k + \omega_{k+1}, \quad x_k \in \mathbb{R}^L \quad (5)$$

$$y_{k+1} = Hx_{k+1} + \eta_{k+1}, \quad y_{k+1} \in \mathbb{R}^M. \tag{6}$$

In this state-space representation, x_k is interpreted as the state of the system at some time t_k , and y_k are our observations. For application in neuroscience, we can take $M \ll L$ as few state variables of the system are readily observed. F is our model which maps states x_k between time points t_k and t_{k+1} . H is our observation operator which describes how we connect our observations y_{k+1} to our state-space at t_{k+1} . The random variables ω_{k+1} and η_{k+1} represent model error and measurement error, respectively. A simplifying assumption is that our measurements are diluted by Gaussian white noise, and that the error in the model can be approximated by Gaussian white noise as well. Then $\omega_k \sim \mathcal{N}(0, Q_k)$ and $\eta_k \sim \mathcal{N}(0, R_k)$, where Q_k is our model error covariance matrix and R_k is our measurement error covariance matrix. We will assume these distributions for the error terms for the remainder of the paper.

We now have defined a stochastic dynamical system where we have characterized the evolution of our states and observations therein based upon assumed error statistics. The goal is now to utilize these transitions to construct methods to best estimate the state x over time. To approach this goal, it may be simpler to consider the evaluation of *background* knowledge of the system compared to what we actually observe from a measuring device. Consider the following cost function [9]:

$$C(x) = \frac{1}{2} \|y - Hx\|_R^2 + \frac{1}{2} \|x - x^b\|_{P^b}^2, \tag{7}$$

where $\|z\|_A^2 = z^T A^{-1} z$. P^b acts to give weight to certain background components x^b , and R acts in the same manner to the measurement terms. The model or background term acts to regularize the cost function. Specifically, trying to minimize $\frac{1}{2} \|y - Hx\|_R^2$ is underdetermined with respect to the observations unless we can observe the full system, and the model term aims to inform the problem of the unobserved components. We are minimizing over state components x . In this way, we balance the influence of what we think we know about the system, such as from a model, compared to what we can actually observe. The cost function is minimized from

$$\nabla C = (H^T R^{-1} H + (P^b)^{-1})x^a - (H^T R^{-1} y + (P^b)^{-1} x^b) = 0. \tag{8}$$

This can be restructured as

$$x^a = x^b + K(y - Hx^b), \tag{9}$$

where

$$K = P^b H^T (H P^b H^T + R)^{-1}. \tag{10}$$

The optimal Kalman gain matrix K acts as a weighting of the confidence of our observations to the confidence of our background information given by the model. If the background uncertainty is relatively high or the measurement uncertainty is relatively low, K is larger, which more heavily weights the *innovation* $y - Hx^b$.

The solution of (7) can be interpreted as the solution of a single time step in our state-space problem (5)–(6). In the DA literature, minimizing this cost function independent of time is referred to as 3D-Var. However, practically we are interested in

problems resembling the following:

$$C(x) = \frac{1}{2} \sum_{k=0}^N \|y_k - Hx_k\|_{R_k}^2 + \frac{1}{2} \sum_{k=0}^{N-1} \|x_{k+1} - Fx_k\|_{P_k^b}^2, \tag{11}$$

where formally the background component x^b has now been replaced with our model. Now we are concerned with minimizing over an observation window with $N + 1$ time points. *Variational methods*, specifically “weak 4D-Var”, seek minima of (11) either by formulation of an adjoint problem [10], or directly from numerical optimization techniques.

Alternatively, *sequential data assimilation* approaches, specifically *filters*, aim to use information from previous time points t_0, t_1, \dots, t_k , and observations at the current time t_{k+1} , to optimally estimate the state at t_{k+1} . The classical Kalman filter utilizes the form of (10), which minimizes the trace of the posterior covariance matrix of the system at step $k + 1$, P_{k+1}^a , to update the state estimate and system uncertainty.

The Kalman filtering algorithm takes the following form. Our *analysis* estimate, \hat{x}_k^a from the previous iteration, is mapped through the linear model operator F to obtain our *forecast* estimate \hat{x}_{k+1}^f :

$$\hat{x}_{k+1}^f = F_k \hat{x}_k^a. \tag{12}$$

The observation operator H is applied to the forecast estimate to generate the measurement estimate \hat{y}_{k+1}^f :

$$\hat{y}_{k+1}^f = H_{k+1} \hat{x}_{k+1}^f. \tag{13}$$

The forecast estimate covariance P_{k+1}^f is generated through calculating the covariance from the model and adding it with the model error covariance Q_k :

$$P_{k+1}^f = F_k P_k^a F_k^T + Q_k. \tag{14}$$

Similarly, we can construct the measurement covariance estimate by calculating the covariance from our observation equation and adding it to the measurement error covariance R_k :

$$P_{k+1}^y = H_{k+1} P_{k+1}^f H_{k+1}^T + R_k. \tag{15}$$

The Kalman gain is defined analogously to (10):

$$K_{k+1} = P_{k+1}^f H_{k+1}^T (P_{k+1}^y)^{-1}. \tag{16}$$

The covariance and the mean estimate of the system are updated through a weighted sum with the Kalman gain:

$$P_{k+1}^a = (I - K_{k+1} H_{k+1}) P_{k+1}^f \tag{17}$$

$$\hat{x}_{k+1}^a = \hat{x}_{k+1}^f + K_{k+1} (y_{k+1} - \hat{y}_{k+1}^f). \tag{18}$$

These equations can be interpreted as a predictor–corrector method, where the predictions of the state estimates are \hat{x}_{k+1}^f with corresponding uncertainties P_{k+1}^f in the *forecast*. The correction, or *analysis*, step linearly interpolates the forecast predictions with observational readings.

In this paper we only consider filters, however *smoothers* are another form of sequential DA that also use observational data from future times t_{k+2}, \dots, t_{k+l} to estimate the state at t_{k+1} .

2 Nonlinear Data Assimilation Methods

2.1 Nonlinear Filtering

For nonlinear models, the Kalman equations need to be adapted to permit nonlinear mappings in the forward operator and the observation operator:

$$x_{k+1} = f(x_k) + \omega_{k+1}, \quad \omega_k \in \mathbb{R}^L, \quad (19)$$

$$y_{k+1} = h(x_{k+1}) + \eta_{k+1}, \quad \eta_{k+1} \in \mathbb{R}^M. \quad (20)$$

Our observation operator for voltage data remains linear: $h(x) = Hx = [\mathbf{e}_1 0 \dots 0]x$, where \mathbf{e}_j is the j th elementary basis vector, is a projection onto the voltage component of our system. Note that $h(x)$ is an operator, not to be confused with the inactivation gate in (2). Our nonlinear model update, $f(x)$ in (19), is taken as the forward integration of the dynamical equations between observation times.

Multiple platforms for adapting the Kalman equations exist. The most straightforward approach is the extended Kalman filter (EKF) which uses local linearizations of the nonlinear operators in (19)–(20) and plugs these into the standard Kalman equations. By doing so, one preserves Gaussianity of the state-space. Underlying the data assimilation framework is the goal of understanding the distribution, or statistics of the distribution, of the states of the system given the observations:

$$p(x|y) \propto p(y|x)p(x). \quad (21)$$

The Gaussianity of the state-space declares the posterior conditional distribution $p(x|y)$ to be a normal distribution by the product of Gaussians being Gaussian, and the statistics of this distribution lead to the Kalman update equations [10]. However, the EKF is really only suitable when the dynamics are nearly linear between observations and can result in divergence of the estimates [11].

Rather than trying to linearize the transformation to preserve Gaussianity, where this distributional assumption is not going to be valid for practical problems anyway, an alternative approach is to preserve the nonlinear transformation and try to estimate the first two moments of transformed state [11]. The Unscented Kalman Filter (UKF) approximates the first two statistics of $p(x_k|y_0 \dots y_k)$ by calculating sample means and variances, which bypasses the need for Gaussian integral products. The UKF uses an ensemble of deterministically selected points in the state-space whose collective mean and covariance are that of the state estimate and its associated covariance at

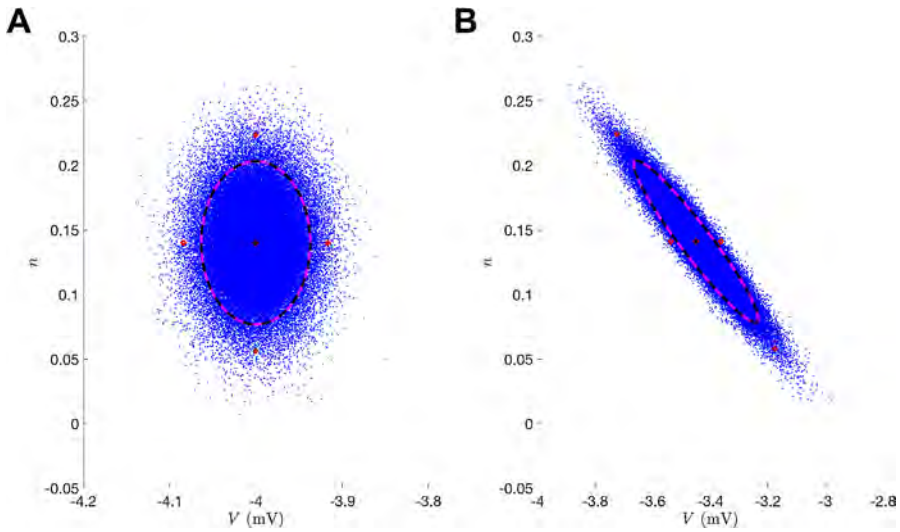


Fig. 1 Unscented transformation. (A) Initial data where blue corresponds to sampling points from a normal distribution of the V, n state-space and the red circles are the sigma points. Black corresponds to the true uncertainty and mean of the sampled distribution. Magenta corresponds to the statistics of the sigma points. (B) Illustrates the forward operator $f(x)$ acting on each element of the left panel where $f(x)$ is the numerical integration of the Morris–Lecar equations (42)–(46) between observation times

some time. The forward operator $f(x)$ is applied to each of these *sigma points*, and the mean and covariance of the transformed points can then be computed to estimate the nonlinearly transformed mean and covariance. Figure 1 depicts this “unscented” transformation. The sigma points precisely estimate the true statistics both initially (Fig. 1(A)) and after nonlinear mapping (Fig. 1(B)).

In the UKF framework, as with all DA techniques, one is attempting to estimate the states of the system. The standard set of states in conductance-based models includes the voltage, the gating variables, and any intracellular ion concentrations not taken to be stationary. To incorporate parameter estimation, parameters θ to be estimated are promoted to states whose evolution is governed by the model error random variable:

$$\theta_{k+1} = \theta_k + \omega_{k+1}^\theta, \quad \omega_k^\theta \in R^D. \tag{22}$$

This is referred to as an “artificial noise evolution model”, as the random disturbances driving deviations in model parameters over time rob them of their time-invariant definition [12, 13]. We found this choice to be appropriate for convergence and as a tuning mechanism. An alternative is to zero out the entries of Q_k corresponding to the parameters in what is called a “persistence model” where $\theta_{k+1} = \theta_k$ [14]. However, changes in parameters can still occur during the analysis stage.

We declare our augmented state to be comprised of the states in the dynamical system as well as parameters θ of interest:

$$\text{Augmented State: } \mathbf{x} = (V, \mathbf{q}, \theta)^\top, \quad \mathbf{q} \in \mathbb{R}^{L-1}, \theta \in \mathbb{R}^D, \tag{23}$$

where q represents the additional states of the system besides the voltage. The filter requires an initial guess of the state \hat{x}_0 and covariance P_{xx} . An implementation of this algorithm is provided as Supplementary Material with the parent function *UKFML.m* and one time step of the algorithm computed in *UKF_Step.m*.

An ensemble of σ points are formed and their position and weights are determined by λ , which can be chosen to try to match higher moments of the system distribution [11]. Practically, this algorithmic parameter can be chosen to spread the ensemble for $\lambda > 0$, shrink the ensemble for $-N < \lambda < 0$, or to have the mean point completely removed from the ensemble by setting it to zero. The ensemble is formed on lines 80-82 of *UKF_Step.m*. The individual weights can be negative, but their cumulative sum is 1.

$$\begin{aligned} \sigma \text{ Points: } & X_j = \hat{x}_k^a \pm (\sqrt{(N + \lambda)P_{xx}})_j, \quad j = 1, \dots, 2N, \quad X_0 = \hat{x}_k^a, \\ \text{Weights: } & W_j = \frac{1}{2(N + \lambda)}, \quad j = 1, \dots, 2N, \quad W_0 = \frac{\lambda}{N + \lambda}. \end{aligned} \tag{24}$$

We form our background estimate \hat{x}_{k+1}^b by applying our map $f(x)$ to each of the ensemble members

$$\tilde{X}_j = f(X_j) \tag{25}$$

and then computing the resulting mean:

$$\text{Forecast Estimate: } \hat{x}_{k+1}^b = \sum_{j=0}^{2N} W_j \tilde{X}_j. \tag{26}$$

We then propagate the transformed sigma points through the observation operator

$$\tilde{Y}_j = h(\tilde{X}_j) \tag{27}$$

and compute our predicted observation \hat{y}_{k+1}^b from the mapped ensemble:

$$\text{Measurement Estimate: } \hat{y}_{k+1}^b = \sum_{j=0}^{2N} W_j \tilde{Y}_j. \tag{28}$$

We compute the background covariance estimate by calculating the variance of the mapped ensemble and adding the process noise Q_k :

$$\text{Background Cov. Est.: } P_{xx}^f = \sum_{j=0}^{2N} W_j (\tilde{X}_j - \hat{x}_{i+k}^b)(\tilde{X}_j - \hat{x}_{i+k}^b)^T + Q_k \tag{29}$$

and do the same for the predicted measurement covariance with the addition of R_k :

$$\text{Predicted Meas. Cov.: } P_{yy} = \sum_{j=0}^{2N} W_j (\tilde{Y}_j - \hat{y}_{k+1}^b)(\tilde{Y}_j - \hat{y}_{k+1}^b)^T + R_{k+1}. \tag{30}$$

The Kalman gain is computed by matrix multiplication of the cross-covariance:

$$\text{Cross-Cov. : } P_{xy} = \sum_{j=0}^{2N} W_j (\tilde{X}_j - \hat{x}_{k+1}^b) (\tilde{Y}_j - \hat{y}_{k+1}^b)^T \tag{31}$$

with the predicted measurement covariance:

$$\text{Kalman Gain : } K = P_{xy} P_{yy}^{-1}. \tag{32}$$

When only observing voltage, this step is merely scalar multiplication of a vector. The gain is used in the *analysis*, or update step, to linearly interpolate our background statistics with measurement corrections. The update step for the covariance is

$$P_{xx}^a = P_{xx}^f - K P_{xy}^T, \tag{33}$$

and the mean is updated to interpolate the background estimate with the deviations of the estimated measurement term with the observed data y_{k+1} :

$$\hat{x}_{k+1}^a = \hat{x}_{k+1}^b + K (y_{k+1} - \hat{y}_{k+1}^b). \tag{34}$$

The analysis step is performed on line 124 of *UKF_Step.m*. Some implementations also include a redistribution of the sigma points about the forecast estimate using the background covariance prior to computing the cross-covariance P_{xy} or the predicted measurement covariance P_{yy} [15]. So, after (29), we redefine \tilde{X}_j, \tilde{Y}_j in (25) as follows:

$$\begin{aligned} \tilde{X}_j &= \hat{x}_{k+1}^b \pm (\sqrt{(N + \lambda) P_{xx}})_j, \quad j = 1, \dots, 2N, \\ \tilde{Y}_j &= h(\tilde{X}_j). \end{aligned}$$

The above is shown in lines 98–117 in *UKF_Step*. A particularly critical part of using a filter, or any DA method, is choosing the process covariance matrix Q_k and the measurement covariance matrix R_k . The measurement noise may be intuitively based upon knowledge of one’s measuring device, but the model error is practically impossible to know *a priori*. Work has been done to use previous innovations to simultaneously estimate Q and R during the course of the estimation cycle [16], but this becomes a challenge for systems with low observability (such as is the case when only observing voltage). Rather than estimating the states and parameters simultaneously as with an augmented state-space, one can try to estimate the states and parameters separately. For example, [17] used a shooting method to estimate parameters and the UKF to estimate the states. This study also provided a systematic way to estimate an optimal covariance inflation Q_k . For high-dimensional systems where computational efficiency is a concern, an implementation which efficiently propagates the square root of the state covariance has been developed [18].

Figure 2 depicts how the algorithm operates. Between observation times, the previous analysis (or best estimate) point is propagated through the model to come up with the predicted model estimate. The Kalman update step interpolates this point with observations weighted by the Kalman gain.

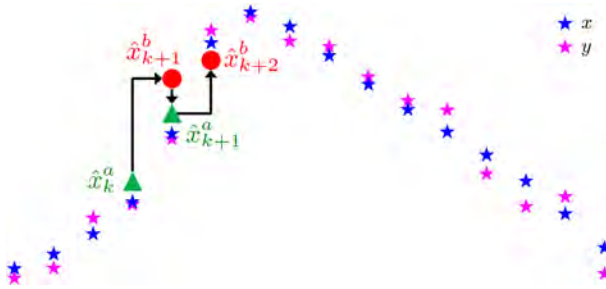


Fig. 2 Example of iterative estimation in UKF. The red circles are the result of forward integration through the model using the previous best estimates. The green are the estimates after combining these with observational data. The blue stars depict the true system output (without any noise), and the magenta stars are the noisy observational data with noise generated by (48) and $\varepsilon = 0.1$

2.2 Variational Methods

In continuous time, variational methods aim to find minimizers of functionals which represent approximations to the probability distribution of a system conditioned on some observations. As our data is available only in discrete measurements, it is practical to work with a discrete form similar to (7) for nonlinear systems:

$$C(x) = \frac{1}{2} \sum_{k=0}^N \|y_k - h(x_k)\|_{R_k}^2 + \frac{1}{2} \sum_{k=0}^{N-1} \|x_{k+1} - f(x_k)\|_{P_k^b}^2. \tag{35}$$

We assume that the states follow the state-space description in (19)–(20) with $\omega_k \sim \mathcal{N}(0, Q)$ and $\eta_k \sim \mathcal{N}(0, R)$, where Q is our model error covariance matrix and R is our measurement error covariance matrix. As an approximation, we impose Q, R to be diagonal matrices, indicating that there is assumed to be no correlation between errors in other states. Namely, Q , contains only the assumed model error variance for each state-space component, and R is just the measurement error variance of the voltage observations. These assumptions simplify the cost function to the following:

$$C(x) = \frac{1}{2} \sum_{k=0}^N R^{-1}(y_k - V_k)^2 + \frac{1}{2} \sum_{l=1}^L \sum_{k=0}^{N-1} Q_{l,l}^{-1}(x_{l,k+1} - f_l(x_k))^2, \tag{36}$$

where $V_k = x_{1,k}$. For the current-clamp data problem in neuroscience, one seeks to minimize equation (36) in what is called the “weak 4D-Var” approach. An example implementation of weak 4D-Var is provided in *w4DvarML.m* in the Supplementary Material. An example of the cost function with which to minimize over is given in the child function *w4dvarobjfun.m*. Each of the x_k is mapped by $f(x)$ on line 108. Alternatively, “strong 4D-Var” forces the resulting estimates to be consistent with the model $f(x)$. This can be considered the result of taking $Q \rightarrow \mathbf{0}$, which yields the nonlinearly constrained problem

$$C(x) = \frac{1}{2} \sum_{k=0}^N R^{-1}(y_k - V_k)^2 \tag{37}$$

such that

$$x_{k+1} = f(x_k), \quad k = 0, \dots, N. \quad (38)$$

The rest of this paper will be focused on the weak case (36), where we can define the argument of the optimization as follows:

$$\mathbf{x} = [x_{1,1}, x_{1,2}, \dots, x_{1,N}, x_{2,1}, \dots, x_{L,N}, \theta_1, \theta_2, \dots, \theta_D] \quad (39)$$

resulting in an $(N + 1)L + D$ -dimensional estimation problem. An important aspect of the scalability of this problem is that the Hessian matrix

$$\mathbf{H}_{i,j} = \frac{\partial^2 C}{\partial x_i \partial x_j} \quad (40)$$

is sparse. Namely, each state at each discrete time has dependencies based upon the model equations and the chosen numerical integration scheme. At the heart of many gradient-based optimization techniques lies a linear system, involving the Hessian and the gradient $\nabla C(\mathbf{x}_n)$ of the objective function, that is used to solve for the next candidate point. Specifically, Newton's method for optimization is

$$\mathbf{x}_{n+1} = \mathbf{x}_n - \mathbf{H}^{-1} \nabla C(\mathbf{x}_n). \quad (41)$$

Therefore, if $(N + 1)L + D$ is large, then providing the sparsity pattern is advantageous when numerical derivative approximations, or functional representations of them, are being used to perform minimization with a derivative-based method. One can calculate these derivatives by hand, symbolic differentiation, or automatic differentiation.

A feature of the most common derivative-based methods is assured convergence to local minima. However, our problem is non-convex due to the model term, which leads to the development of multiple local minima in the optimization surface as depicted in Fig. 3. For the results in this tutorial, we will only utilize local optimization tools, but see Sect. 5 for a brief discussion of some global optimization methods with stochastic search strategies.

3 Application to Spiking Regimes of the Morris–Lecar Model

3.1 Twin Experiments

Data assimilation is a framework for the incorporation of system observations into an estimation problem in a systematic fashion. Unfortunately, the methods themselves do not provide a great deal of insight into the tractability of unobserved system components of specific models. There may be a certain level of redundancy in the model equations and degeneracy in the parameter space leading to multiple potential solutions [19]. Also, it may be the case that certain parameters are non-identifiable if, for instance, a parameter can be completely scaled out [20]. Some further work on identifiability is ongoing [21, 22].

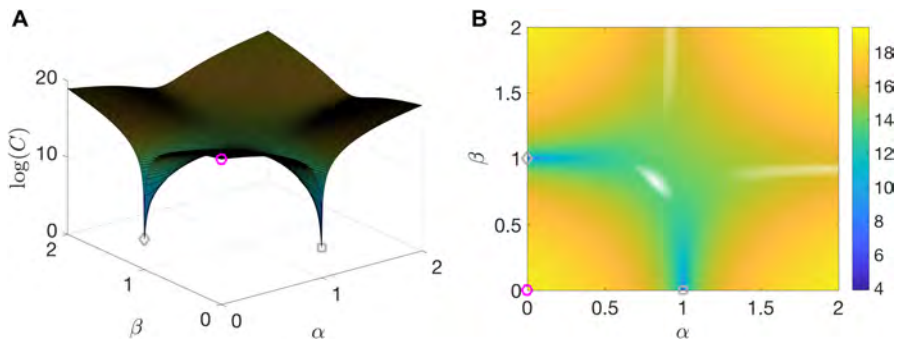


Fig. 3 Example cost function for 4D-Var. (A) Surface generated by taking the logarithm of $C(\alpha, \beta)$, where $C(\alpha, \beta) = C(\mathbf{x}_0(1 - \alpha)(1 - \beta) + \alpha x_{\min,d} + \beta x_{\min,s})$ so that at $\alpha = \beta = 0$, $\mathbf{x} = \mathbf{x}_0$ (magenta circle), and at $\alpha = 1$ and $\beta = 0$, $\mathbf{x} = x_{\min,d}$ for the deeper minima (gray square), and similarly for the shallower minima (gray diamond). (B) Contour plot of the surface shown in (A)

Before applying a method to data from a real biological experiment, it is important to test it against simulated data where the ground truth is known. In these experiments, one creates simulated data from a model and then tries to recover the true states and parameters of that model from the simulated data alone.

3.2 Recovery of Bifurcation Structure

In conductance-based models, as well as in real neurons, slight changes in a parameter value can lead to drastically different model output or neuronal behavior. Sudden changes in the topological structure of a dynamical system upon smooth variation of a parameter are called *bifurcations*. Different types of bifurcations lead to different neuronal properties, such as the presence of bistability and subthreshold oscillations [23]. Thus, it is important for a neuronal model to accurately capture the bifurcation dynamics of the cell being modeled [24]. In this paper, we ask whether or not the models estimated through data assimilation match the bifurcation structure of the model that generated the data. This provides a qualitative measure of success or failure for the estimation algorithm. Since bifurcations are an inherently nonlinear phenomenon, our use of topological structure as an assay emphasizes how nonlinear estimation is a fundamentally distinct problem from estimation in linear systems.

3.3 Morris–Lecar Model

The Morris–Lecar model, first used to describe action potential generation in barnacle muscle fibers, has become a canonical model for studying neuronal excitability [25]. The model includes an inward voltage-dependent calcium current, an outward voltage-dependent potassium current, and a passive leak current. The activation gating variable for the potassium current has dynamics, whereas the calcium current activation gate is assumed to respond instantaneously to changes in voltage. The calcium current is also non-inactivating, resulting in a two-dimensional model. The model exhibits multiple mechanisms of excitability: for different choices of model parameters, different bifurcations from quiescence to repetitive spiking occur as the applied

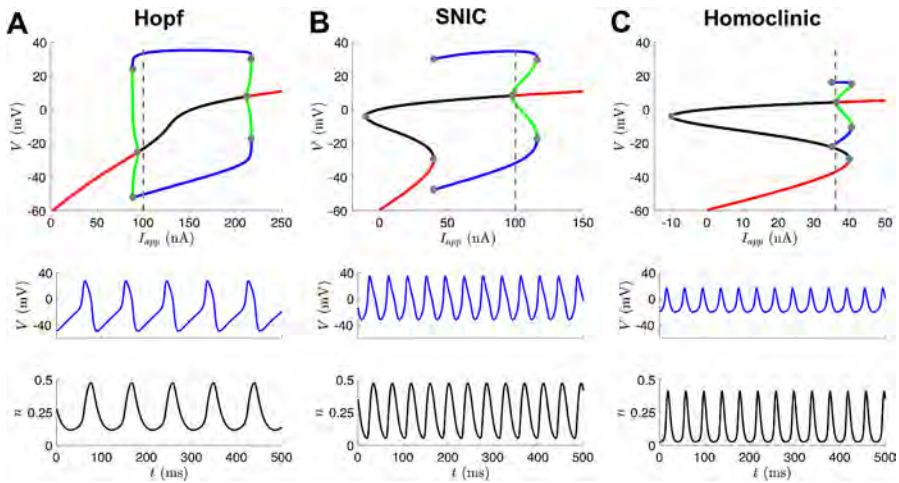


Fig. 4 Three different excitability regimes of the Morris–Lecar model. The bifurcation diagrams in the top row depict stable fixed points (red), unstable fixed points (black), stable limit cycles (blue), and unstable limit cycles (green). Gray dots indicate bifurcation points, and the dashed gray lines indicate the value of I_{app} corresponding to the traces shown for V (middle row) and n (bottom row). (A) As I_{app} is increased from 0 or decreased from 250 nA, the branches of stable fixed points lose stability through subcritical Hopf bifurcation, and unstable limit cycles are born. The branch of stable limit cycles that exists at $I_{app} = 100$ nA eventually collides with these unstable limit cycles and is destroyed in a saddle-node of periodic orbits (SNPO) bifurcation as I_{app} is increased or decreased from this value. (B) As I_{app} is increased from 0, a branch of stable fixed points is destroyed through saddle-node bifurcation with the branch of unstable fixed points. As I_{app} is decreased from 150 nA, a branch of stable fixed points loses stability through subcritical Hopf bifurcation, and unstable limit cycles are born. The branch of stable limit cycles that exists at $I_{app} = 100$ nA is destroyed through a SNPO bifurcation as I_{app} is increased and a SNIC bifurcation as I_{app} is decreased. (C) Same as (B), except that the stable limit cycles that exist at $I_{app} = 36$ nA are destroyed through a homoclinic orbit bifurcation as I_{app} is decreased

Table 1 Morris–Lecar parameter values. For all simulations, $C = 20$, $E_{Ca} = 120$, $E_K = -84$, and $E_L = -60$. For the Hopf and SNIC regime, $I_{app} = 100$; for the homoclinic regime, $I_{app} = 36$

	Hopf	SNIC	Homoclinic
ϕ	0.04	0.067	0.23
g_{Ca}	4	4	4
V_3	2	12	12
V_4	30	17.4	17.4
g_K	8	8	8
g_L	2	2	2
V_1	-1.2	-1.2	-1.2
V_2	18	18	18

current is increased [23]. Three different bifurcation regimes—Hopf, saddle-node on an invariant circle (SNIC), and homoclinic—are depicted in Fig. 4 and correspond to the parameter sets in Table 1. For a given applied current in the region where a stable limit cycle (corresponding to repetitive spiking) exists, each regime displays a distinct firing frequency and action potential shape.

The equations for the Morris–Lecar model are as follows:

$$\begin{aligned}
 C_m \frac{dV}{dt} &= I_{\text{app}} - g_L(V - E_L) - g_K n(V - E_K) \\
 &\quad - g_{\text{Ca}} m_\infty(V)(V - E_{\text{Ca}}) \\
 &= f_V^*(V, n; \boldsymbol{\theta}),
 \end{aligned}
 \tag{42}$$

$$\frac{dn}{dt} = \phi(n_\infty(V) - n)/\tau_n(V) = f_n^*(V, n; \boldsymbol{\theta}),
 \tag{43}$$

with

$$m_\infty = \frac{1}{2} [1 + \tanh((V - V_1)/V_2)],
 \tag{44}$$

$$\tau_n = 1/\cosh((V - V_3)/2V_4),
 \tag{45}$$

$$n_\infty = \frac{1}{2} [1 + \tanh((V - V_3)/V_4)].
 \tag{46}$$

The eight parameters that we will attempt to estimate from data are g_L , g_K , g_{Ca} , ϕ , V_1 , V_2 , V_3 , and V_4 . We are interested in whether the estimated parameters yield a model with the desired mechanism of excitability. Specifically, we will conduct twin experiments where the observed data is produced by a model with parameters in a certain bifurcation regime, but the data assimilation algorithm is initialized with parameter guesses corresponding to a different bifurcation regime. We then assess whether or not a model with the set of estimated parameters undergoes the same bifurcations as the model that produced the observed data. This approach provides an additional qualitative measure of estimation accuracy, beyond simply comparing the values of the true and estimated parameters.

3.4 Results with UKF

The UKF was tested on the Morris–Lecar model in an effort to simultaneously estimate V and n along with the eight parameters in Table 1. Data was generated via a modified Euler scheme at observation points every 0.1 ms, where we take the step-size Δt as 0.1 as well:

$$\begin{aligned}
 \tilde{x}_{k+1} &= x_k + \Delta t f^*(t_k, x_k), \\
 x_{k+1} &= x_k + \frac{\Delta t}{2} (f^*(t_k, x_k) + f^*(t_{k+1}, \tilde{x}_{k+1})) \\
 &= f(x_k).
 \end{aligned}
 \tag{47}$$

The UKF is a particularly powerful tool when a lot of data is available; the computational complexity in time is effectively the same as the numerical scheme of choice, whereas the additional operations at each time point are $O((L + D)^3)$ [26]. $f(x)$ in (19) is taken to be the Morris–Lecar equations (42)–(43), acting as $f^*(t_k, x_k)$, integrated forward via modified Euler (47), and is given on line 126 of *UKFML.m*. The

function *fXaug.m*, provided in the Supplementary Material, represents our augmented vector field. Our observational operator H is displayed on line 136 of *UKFML.m*. To reiterate, the states to be estimated in the Morris–Lecar model are the voltage and the potassium gating variable. The eight additional parameters are promoted to the members of state-space with trivial dynamics resulting in a ten-dimensional estimation problem.

These examples were run using 20 seconds of data which is 200,001 time points. During this time window, the Hopf, SNIC, and homoclinic models fire 220, 477, and 491 spikes, respectively. Such a computation for a ten-dimensional model takes only a few minutes on a laptop computer. R can be set to 0 when one believes the observed signal to be completely noiseless, but even then it is commonly left as a small number to try to mitigate the development of singularities in the predicted measurement covariance. We set our observed voltage to be the simulated output using modified Euler with additive white noise at each time point:

$$V_{\text{obs}}(t) = V_{\text{true}}(t) + \eta(t), \quad (48)$$

where $\eta \sim \mathcal{N}(0, (\varepsilon\sigma_{\text{true}})^2)$ is a normal random variable whose variance is equal to the square of the standard deviation of the signal scaled by a factor ε , which is kept fixed at 0.01 for these simulations. R is taken as the variance of η . The initial covariance of the system is $\alpha_I I$, where I is the identity matrix and α_I is 0.001. The initial guess for n is taken to be 0. Q is fixed in time as a diagonal matrix with diagonal $10^{-7} [\max(V_{\text{obs}}) - \min(V_{\text{obs}}), 1, |\theta_0|]$, where θ_0 represents our initial parameter guesses. We set $\lambda = 5$; however, this parameter was not especially influential for the results of these runs, as discussed further below. These initializations are displayed in the body of the parent function *UKFML.m*.

Figure 5 shows the state estimation results when the observed voltage is from the SNIC regime, but the UKF is initialized with parameter guess corresponding to the Hopf regime. Initially, the state estimate for n and its true, unobserved dynamics have great disparity. As the observations are assimilated over the estimation window, the states and model parameters adjust to produce estimates which better replicate the observed, and unobserved, system components. In this way, information from the observations is transferred to the model. The evolution of the parameter estimates for this case is shown in the first column of Fig. 6, with ϕ , V_3 , and V_4 all converging to close to their true values after 10 seconds of observations. The only difference in parameter values between the SNIC and homoclinic regimes is the value of the parameter ϕ . The second column of Fig. 6 shows that when the observed data is from the homoclinic regime but the initial parameter guesses are from the SNIC regime, the estimates of V_3 and V_4 remain mostly constant near their original (and correct) values, whereas the estimate of ϕ quickly converges to its new true value. Finally, the third column of Fig. 6 shows that all three parameter estimates evolve to near their true values when the UKF is presented with data from the Hopf regime but initial parameter estimates from the homoclinic regime.

Table 2 shows the parameter estimates at the end of the estimation window for all of the nine possible twin experiments. Promisingly, a common feature of the results is the near recovery of the true value of each of the parameters. However, the estimated parameter values alone do not necessarily tell us about the dynamics of the inferred

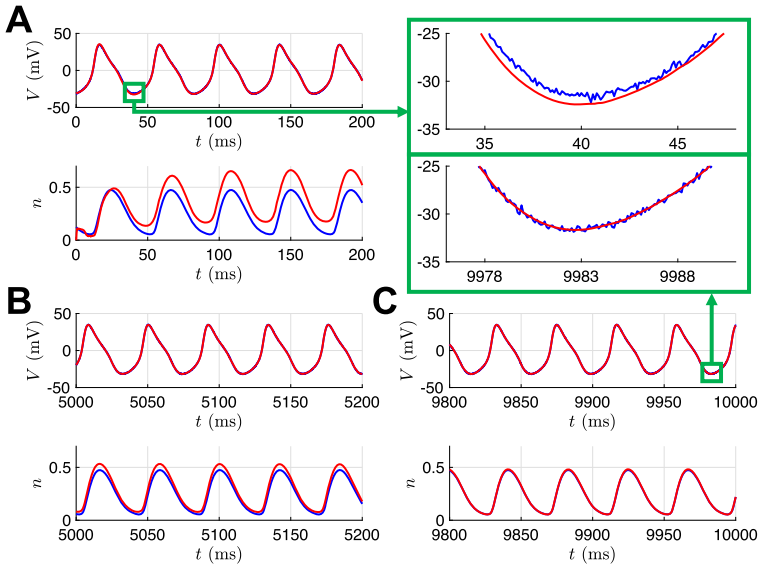


Fig. 5 State estimates for UKF. This example corresponds to initializing with parameters from the HOPF regime and attempting to correctly estimate those of the SNIC regime. The noisy observed voltage V and true unobserved gating variable n are shown in blue, and their UKF estimates are shown in red

Table 2 UKF parameter estimates at end of estimation window, with observed data from bifurcation regime ‘ t ’ and initial parameter guesses corresponding to bifurcation regime ‘ g ’

	t:HOPF			t:SNIC			t:HOMO		
	g:HOPF	g:SNIC	g:HOMO	g:HOPF	g:SNIC	g:HOMO	g:HOPF	g:SNIC	g:HOMO
ϕ	0.040	0.40	0.040	0.067	0.040	0.067	0.237	0.224	0.224
g_{Ca}	4.017	4.019	4.025	4.001	4.000	4.001	4.112	3.874	3.877
V_3	1.612	1.762	1.660	11.931	11.937	11.912	11.751	11.784	11.772
V_4	29.646	29.832	29.771	17.343	17.337	17.342	17.739	16.806	16.815
g_K	7.895	7.926	7.892	7.970	7.971	7.958	7.929	7.854	7.850
g_L	2.032	2.027	2.033	2.003	2.004	2.003	2.025	1.967	1.968
V_1	-1.199	-1.195	-1.189	-1.193	-1.193	-1.190	-1.064	-1.346	-1.341
V_2	18.045	18.053	18.067	17.991	17.991	17.991	18.179	17.734	17.740

model. To assess the inferred models, we generate bifurcation diagrams using the estimated parameters and compare them to the bifurcation diagrams for the parameters that produced the observed data. Figure 7 shows that the SNIC and homoclinic bifurcation diagrams were recovered quite exactly. The Hopf structure was consistently recovered, but with shifted regions of spiking and quiescence and minor differences in spike amplitude.

To check the consistency of our estimation, we set 100 initial guesses for n across its dynamical range as samples from $\mathcal{U}(0, 1)$. Figure 8 shows that the state estimates

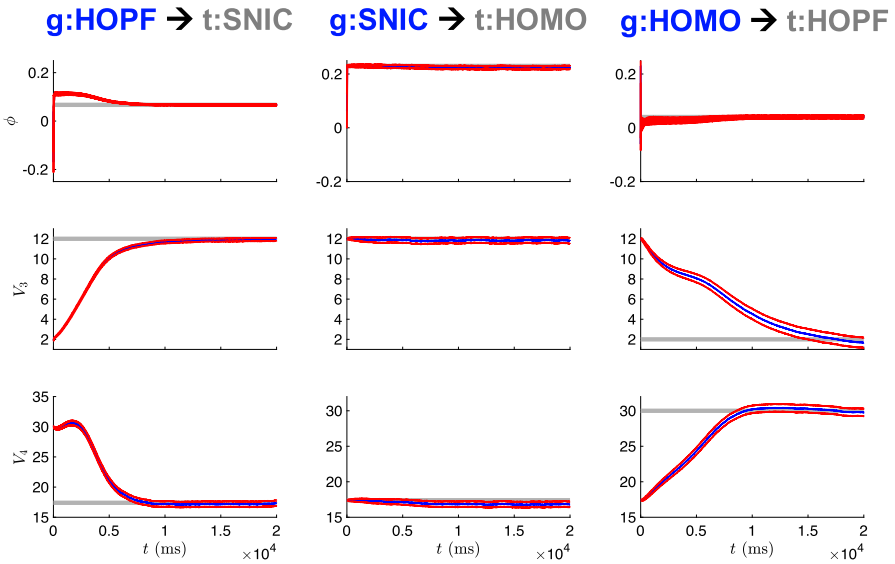


Fig. 6 Parameter estimates for UKF. This example corresponds to initializing with parameters from the HOPF, SNIC, and HOMO regimes and attempting to correctly estimate those of the SNIC, HOMO, and HOPF regimes (left to right column, respectively). The blue curves are the estimates from the UKF, with ± 2 standard deviations from the mean (based on the filter estimated covariance) shown in red. The gray lines indicate the true parameter values

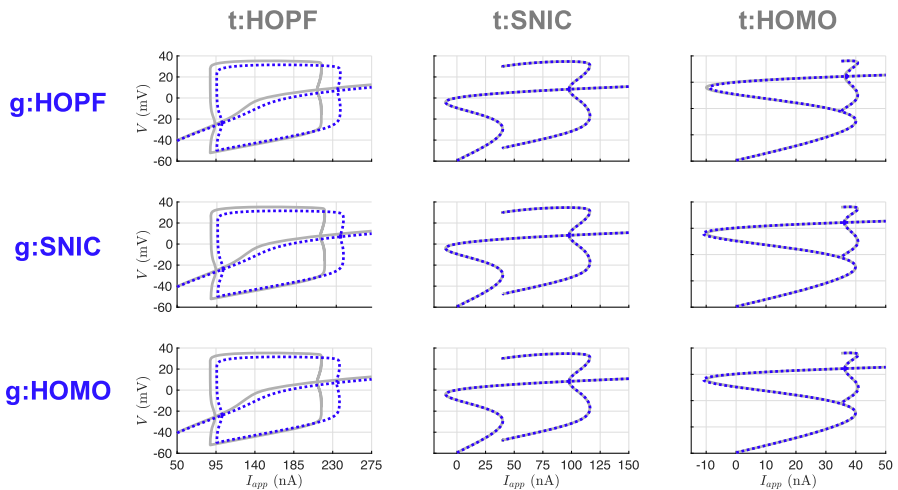
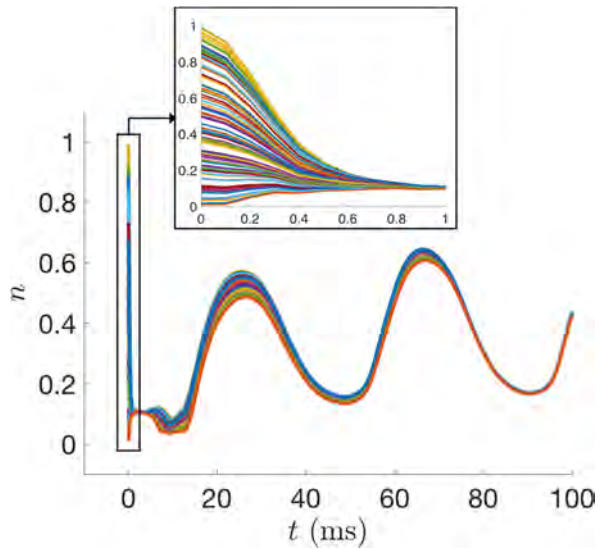


Fig. 7 Bifurcation diagrams for UKF twin experiments. The gray lines correspond to the true diagrams, and the blue dotted lines correspond to the diagrams produced from the estimated parameters in Table 2

for n across these initializations quickly approached very similar trajectories. We confirmed that after the estimation cycle was over, the parameter estimates for all 100 initializations were essentially identical to the values shown in Table 2. In this

Fig. 8 UKF state estimates of n for the Morris–Lecar model with 100 different initial guesses of the state sampled from $\mathcal{U}(0, 1)$, with all other parameters held fixed



paper, we always initialized the UKF with initial parameter values corresponding to the various bifurcation regimes and did not explore the performance for randomly selected initial parameter guesses. For initial parameter guesses that are too far from the true values, it is possible that the filter would converge to incorrect parameter values or fail outright before reaching the end of the estimation window. Additionally, we investigated the choices of certain algorithmic parameters for the UKF, namely λ and α_I . Figure 9(A) shows suitable ranges of these parameters, with the color indicating the root mean squared error of the parameters at the end of the cycle compared to their true values. We found this behavior to be preserved across our nine twin experiment scenarios. Notably, this shows that our results in Table 2 were generated using an initial covariance $\alpha_I = 0.001$ that was smaller than necessary. By increasing the initial variability, the estimated system can converge to the true dynamics more quickly, as shown for $\alpha_I = 0.1$ in Fig. 9(B). The value of λ does not have a large impact on these results, except for when $\alpha_I = 1$. Here the filter fails before completing the estimation cycle, except for a few cases where λ is small enough to effectively shrink the ensemble spread and compensate for the large initial covariance. For example, with $\lambda = -9$, we have $N - 9 = 1$ and, therefore, the ensemble spread in (24) is simply $X_j = \hat{x}_k^a \pm \sqrt{P_{xx}}$. For even larger initial covariances ($\alpha_I > 1$), the filter fails regardless of the value of λ . We noticed that in many of the cases that failed, the parameter estimate for ϕ was becoming negative (which is unrealistic for a rate) or quite large ($\phi > 1$), and that the state estimate for n was going outside of its biophysical range of 0 to 1. When the gating variable extends outside of its dynamical range it can skew the estimated statistics and the filter may be unable to recover. The standard UKF framework does not provide a natural way of incorporating bounds on parameter estimates, and we do not apply any for the results presented here. However, we did find that we can modify our numerical integration scheme to prevent the filter from failing in many of these cases, as shown in Fig. 9(C). Specifically, if n becomes negative or exceeds 1 after the update step, then artificially setting n to 0 or 1 in the

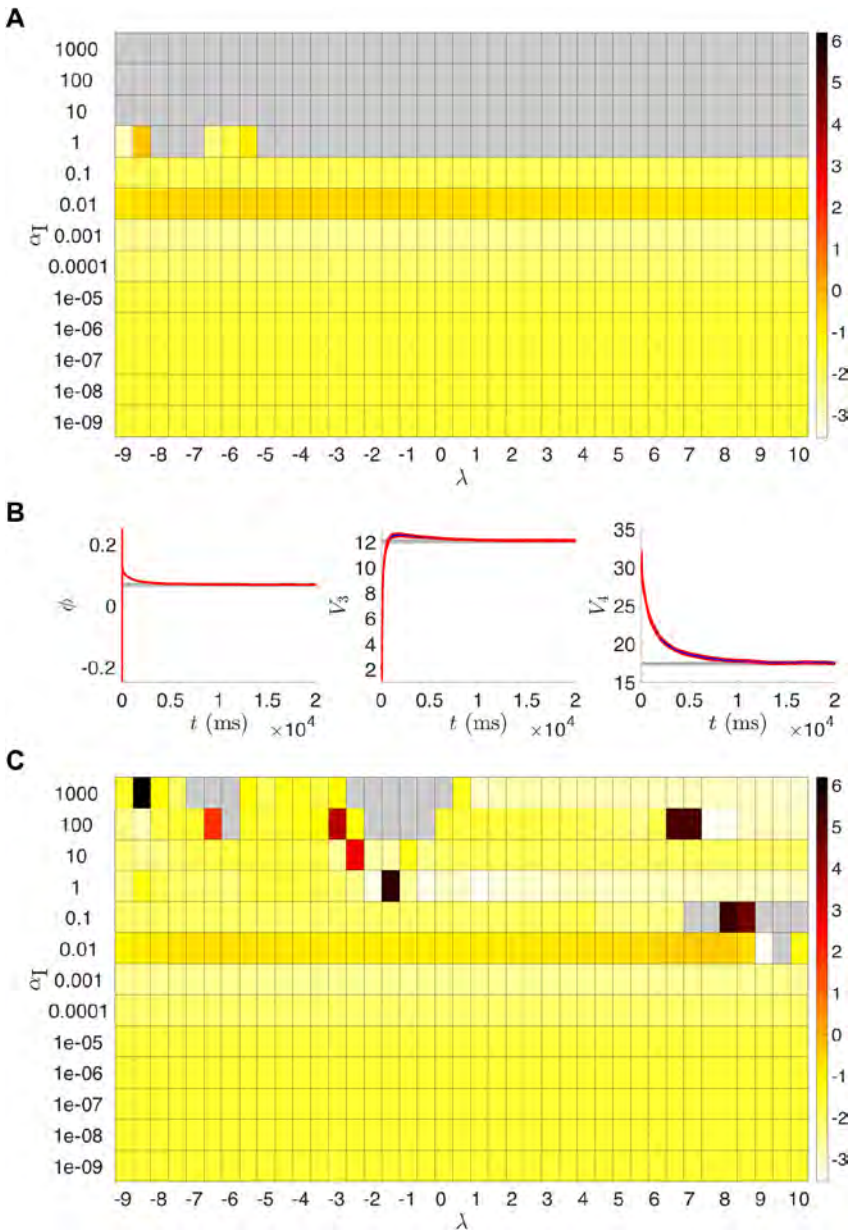


Fig. 9 (A) UKF results from runs of the t:SNIC/g:HOPF twin experiment for various parameter combinations of λ and α_I . The color scale represents the root mean squared error of the final parameter values at $T = 200,001$ from the parameters of the SNIC bifurcation regime. Gray indicates the filter failed outright before reaching the end of the estimation window. (B) Parameter estimates over time for the run with $\lambda = 5$, $\alpha_I = 0.1$. The parameters (especially ϕ and V_3) approach their true values more quickly than corresponding runs with smaller initial covariances; see column 1 of Fig. 6 for parameter estimates with $\lambda = 5$, $\alpha_I = 0.001$. C: Same as (A), but with a modification to the numerical integration scheme that restricts the gating variable n to remain within its biophysical range of 0 to 1

modified Euler method (47) before proceeding can enable the filter to reach the end of the estimation window and yield reasonable parameter estimates.

3.5 Results with 4D-Var

The following results illustrate the use of weak 4D-Var. One can minimize the cost function (36) using a favorite choice of optimization routine. For the following examples, we will consider a local optimizer by using interior point optimization with MATLAB's built-in solver *fmincon*. At the heart of the solver is a Newton-step which uses information about the Hessian, or a conjugate gradient step using gradient information [27–29]. The input we are optimizing over conceptually takes the form of

$$\mathbf{x} = [V_0, V_1, \dots, V_N, n_0, n_1, \dots, n_N, \theta_1, \theta_2, \dots, \theta_D] \quad (49)$$

resulting in an $(N + 1)L + D$ -dimensional estimation problem where $L = 2$. There are computational limitations with memory storage and the time required to sufficiently solve the optimization problem to a suitable tolerance for reasonable parameter estimates. Therefore, we cannot be cavalier with using as much data with 4D-Var as we did with the UKF, as that would result in a $(200,001)2 + 8 = 400,010$ dimensional problem. Using Newton's method (41) on this problem would involve inverting a Hessian matrix of size $(400,010)^2$, which according to a rough calculation would require over 1 TB of RAM. Initialization of the optimization is shown on line 71 of *w4DVarML.m*.

The estimated parameters are given in Table 3. These results were run using $N = 2001$ time points. To simplify the search space, the parameter estimates were constrained between the bounds listed in Table 4. These ranges were chosen to ensure that the maximal conductances, the rate ϕ , and the activation curve slope V_2 all remain positive. We found that running 4D-Var with even looser bounds (Table A1) yielded less accurate parameter estimates (Tables A2 and A3). The white noise perturbations for the 4D-Var trials were the same as those from the UKF examples. Initial guesses for the states at each time point are required. For these trials, V is initialized as V_{obs} , and n is initialized as the result of integration of its dynamics forced with V_{obs} using the initial guesses for the parameters, i.e., $n = \int f_n(V_{\text{obs}}, n; \theta_0)$. The initial guesses are generated beginning on line 38 of *w4DvarML.m*. We impose that Q^{-1} in (36) is a diagonal matrix with entries $\alpha_Q[1, 100^2]$ to balance the dynamical variance of V and n . The scaling factor α_Q represents the relative weight of the model term compared to the measurement term. Based on preliminary tuning experiments, we set $\alpha_Q = 100$ for the results presented.

Figure 10 depicts the states produced by integrating the model with the estimated parameters across different iterations within the interior-point optimization. Over iteration cycles, the geometry of spikes as well as the spike time alignments eventually coincide with the noiseless data V_{true} . Figure 11 shows the evolution of the parameters across the entire estimation cycle. For the UKF, the “plateauing” effect of the parameter estimates seen in Fig. 6 indicates confidence that they are conforming to being constant in time. With 4D-Var, and in a limiting sense of the UKF, the plateauing effect indicates the parameters are settling into a local minimum of the cost function.

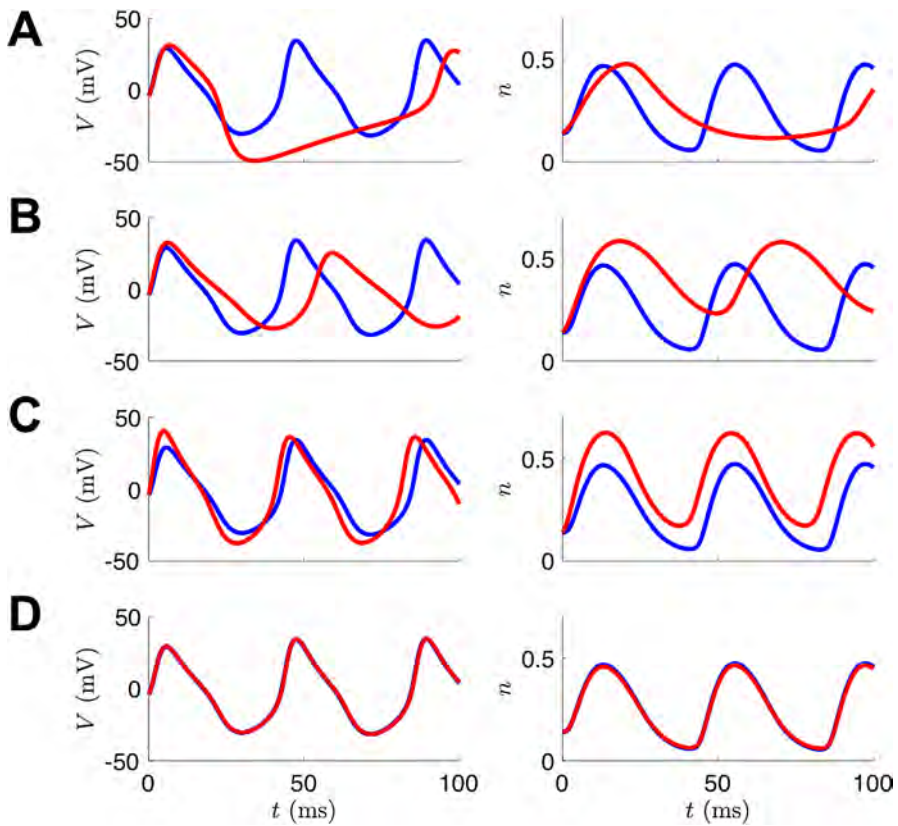


Fig. 10 Example of 4D-Var assimilation initializing with parameters from the Hopf regime but observational data from the SNIC regime. The blue traces are noiseless versions of the observed voltage data (left column) or the unobserved variable n (right column) from the model that produced the data. The red traces are the result of integrating the model with the estimated parameter sets at various points during the course of the optimization. **(A)** Initial parameter guesses. **(B)** Parameter values after 1000 iterations. **(C)** Parameter values after 1000 iterations. **(D)** Parameter values after 30,000 iterations (corresponds to t :SNIC/g:HOPF column of Table 3)

In Fig. 12 we show the bifurcation diagrams of the estimated models from our 4D-Var trials. Notice, and shown explicitly in Table 3, when initializing with the true parameters, the correct model parameters are recovered as our optimization routine is confidently within the basin of attraction of the global minimum. In the UKF, comparatively, there is no sense of stopping at a local minimum. Parameter estimates may still fluctuate even when starting from their true values, unless the variances of the state components fall to very low values and the covariance Q_k can be tuned to have a baseline variability in the system. The parameter sets for the SNIC and homoclinic bifurcation regimes only deviate in the ϕ parameter, and so our optimization had great success estimating one from the other. The kinetic parameters (V_3 and V_4) for the Hopf regime deviate quite a bit from the SNIC or homoclinic. Still, the recovered bifurcation structures from estimated parameters associated with trials involving HOPF remained consistent with the true structure.

Table 3 4D-Var parameter estimates at the end of the optimization for each bifurcation regime. The parameter bounds in Table 4 were used for these trials. Hessian information was not provided to the optimizer

	t:HOPF			t:SNIC			t:HOMO		
	g:HOPF	g:SNIC	g:HOMO	g:HOPF	g:SNIC	g:HOMO	g:HOPF	g:SNIC	g:HOMO
ϕ	0.040	0.037	0.039	0.069	0.067	0.066	0.414	0.218	0.230
g_{Ca}	4.000	3.890	3.976	4.024	4.000	4.045	9.037	3.813	3.999
V_3	2.000	3.404	3.241	12.695	12.000	12.076	7.458	13.022	12.004
V_4	30.000	29.085	30.122	18.759	17.400	16.990	28.365	17.165	17.403
g_K	8.000	8.386	8.287	8.284	8.000	8.009	9.817	8.472	8.002
g_L	2.000	2.016	2.021	1.930	2.000	2.071	3.140	1.941	2.000
V_1	-1.200	-1.335	-1.250	-1.078	-1.200	-1.179	2.872	-1.419	-1.202
V_2	18.000	17.619	17.911	18.091	18.000	18.162	24.769	17.712	18.000

Table 4 Bounds used during 4D-Var estimation for the results shown in Tables 3 and A4

	Lower bound	Upper bound
ϕ	0	1
g_{Ca}	0	10
V_3	-20	20
V_4	0.1	35
g_K	0	10
g_L	0	5
V_1	-10	20
V_2	0.1	35

A drawback of the results shown in Table 3 is that for the default tolerances in *fmincon*, some runs took more than two days to complete on a dedicated core. Figure 11 shows that the optimal solution had essentially been found after 22,000 iterations; however, the optimizer kept running for several thousand more iterations before the convergence tolerances were met. Rather than attempting to speed up these computations by adjusting the algorithmic parameters associated with this solver for this specific problem, we decided to try to exploit the dynamic structure of the model equations using automatic differentiation (AD). AD deconstructs derivatives of the objective function into elementary functions and operations through the chain rule. We used the MATLAB AD tool ADiGator, which performs source transformation via operator overloading and has scripts available for simple integration with various optimization tools, including *fmincon* [30]. For the same problem scenario and algorithmic parameters, we additionally passed in the generated gradient and Hessian functions to the solver. For this problem, the Hessian structure is shown in Fig. 13. Note that we are using a very simple scheme in the modified Euler method (47) to perform numerical integration between observation points, and the states at $k + 1$ only have dependencies upon those at k and on the parameters. Higher order methods, including implicit methods, can be employed naturally since the system is being

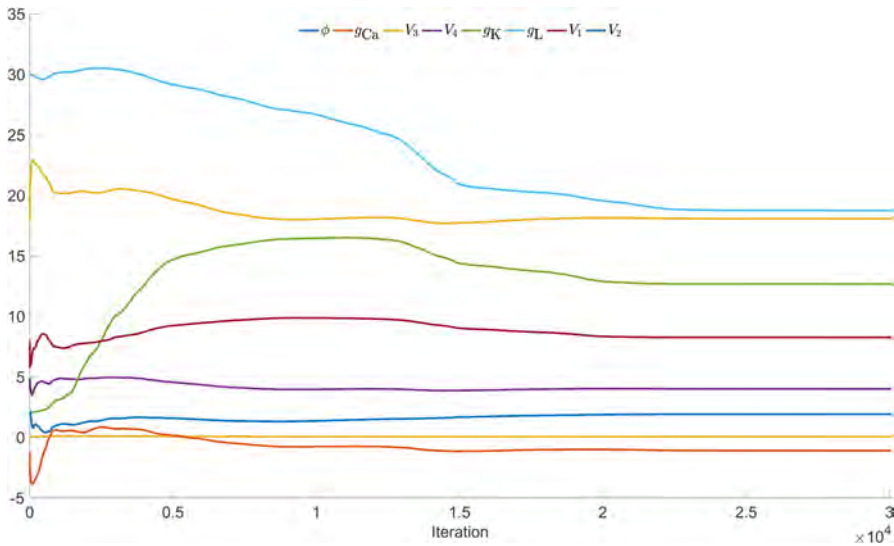


Fig. 11 Example parameter estimation with 4D-Var initializing with Hopf parameter regime and estimating parameters of SNIC regime

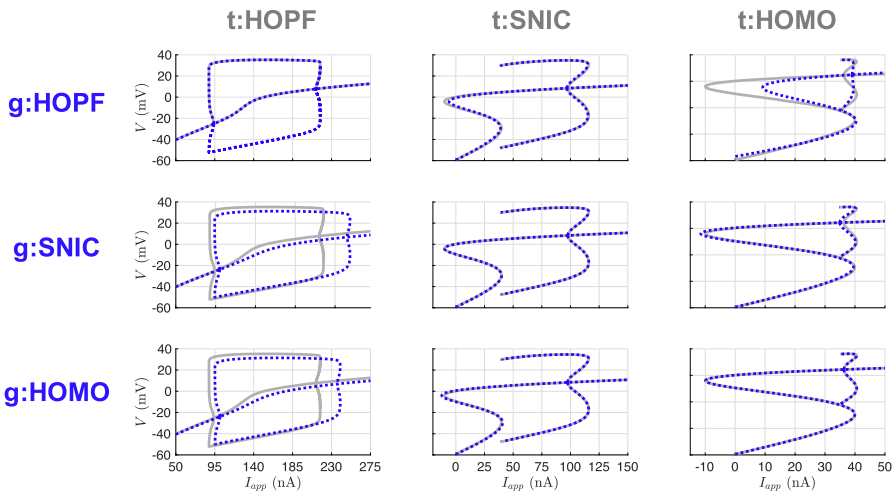


Fig. 12 Bifurcation diagrams for 4D-Var twin experiments. The gray lines correspond to the true diagrams, and the blue dotted lines correspond to the diagrams produced from the estimated parameters in Table 3

estimated simultaneously. A tutorial specific to collocation methods for optimization has been developed [31].

The results are shown in Table A4. Each twin experiment scenario took, at most, a few minutes on a dedicated core. These trials converged to the optimal solution in much fewer iterations than the trials without using the Hessian. Since convergence

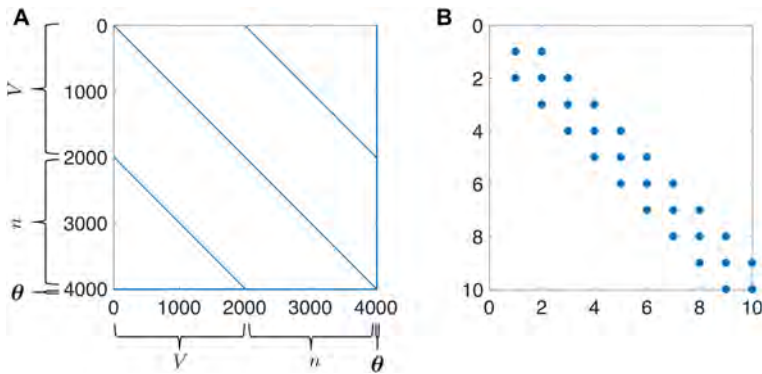


Fig. 13 (A) Sparsity pattern for the Hessian of the cost function for the Morris–Lecar equations for $N + 1 = 2001$ time points. The final eight rows (and symmetrically the last eight columns) depict how the states at each time depend upon the parameters. (B) The top left corner of the Hessian shown in (A)

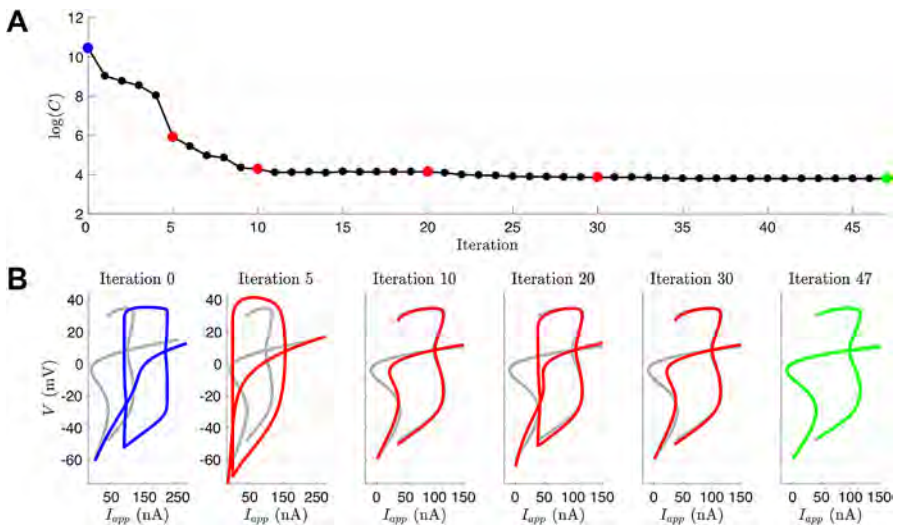


Fig. 14 (A) Logarithm of the value of the cost function for a twin experiment initialized with parameters from the Hopf regime but observational data from the SNIC regime. The iterates were generated from *fmincon* with provided Hessian and gradient functions. (B) Bifurcation diagrams produced from parameter estimates for selected iterations. The blue is the initial bifurcation structure, the gray is the true bifurcation structure for the parameters that generated the observed data, the red is the bifurcation structure of the iterates, and the green is the bifurcation structure of the optimal point determined by *fmincon*

was achieved within a few dozen iterations, we decided to inspect how the bifurcation structure of the estimated model evolved throughout the process for the case of HOPF to SNIC. Figure 14 shows that by Iteration 10, the objective function value has decreased greatly, and parameters that produce a qualitatively correct bifurcation structure have been found. The optimization continues for another 37 iterations and explores other parts of parameter space that do not yield the correct bifurcation structure before converging very close to the true parameter values.

Again, these results, at best, can reflect only locally optimal solutions of the optimization manifold. The 4D-Var framework has been applied to neuroscience using a more systematic approach to finding the global optimum. In [32], a population of initial states \mathbf{x} is optimized in parallel with an outer loop that incorporates an *annealing* algorithm. The annealing parameter relates the weights of the two summations in (36), and the iteration proceeds by increasing the weight given to the model error compared to the measurement error.

We also wished to understand more about the sensitivity of this problem to initial conditions. We initialized the system with the voltage states as those of the observation, the parameters as those of the initializing guess bifurcation regime, and the gating variable $[n_0, n_1, \dots, n_N]$ to be i.i.d. from $\mathcal{U}(0, 1)$. The results confirm our suspicions that multiple local minima exist. For 100 different initializations of n , for the problem of going from SNIC to HOPF, 63 were found to fall into a deeper minima, yielding better estimates and a smaller objective function value, while 16 fell into a shallower minima, and the rest into three different even shallower minima. While one cannot truly visualize high-dimensional manifolds, one can try to visualize a subset of the surface. Figure 3 shows the surface that arises from evaluating the objective function on a linear combination of the two deepest minima and an initial condition \mathbf{x}_0 , which eventually landed in the shallower of the two minima as points in 4010-dimensional space.

4 Application to Bursting Regimes of the Morris–Lecar Model

Many types of neurons display burst firing, consisting of groups of spikes separated by periods of quiescence. Bursting arises from the interplay of fast currents that generate spiking and slow currents that modulate the spiking activity. The Morris–Lecar model can be modified to exhibit bursting by including a calcium-gated potassium (K_{Ca}) current that depends on slow intracellular calcium dynamics [33]:

$$C_m \frac{dV}{dt} = I_{app} - g_L(V - E_L) - g_K n(V - E_K) - g_{Ca} m_\infty(V)(V - E_{Ca}) - g_{KCa} z(V - E_K), \tag{50}$$

$$\frac{dn}{dt} = \phi(n_\infty(V) - n) / \tau_n(V), \tag{51}$$

$$\frac{dCa}{dt} = \varepsilon(-\mu I_{Ca} - Ca), \tag{52}$$

$$z = \frac{Ca}{Ca + 1}. \tag{53}$$

Bursting can be analyzed mathematically by decomposing models into fast and slow subsystems and applying geometric singular perturbation theory. Several different types of bursters have been classified based on the bifurcation structure of the fast subsystem. In square-wave bursting, the active phase of the burst is initiated at a saddle-node bifurcation and terminates at a homoclinic bifurcation. In elliptic bursting, spiking begins at a Hopf bifurcation and terminates at a saddle-node of periodic

Table 5 Parameters for bursting in the modified Morris–Lecar model. For square-wave bursting $I_{\text{app}} = 45$, and for elliptic bursting $I_{\text{app}} = 120$. All other parameters are the same as in Table 1

	Square-wave	Elliptic
ϕ	0.23	0.04
g_{Ca}	4	4.4
V_3	12	2
V_4	17.4	30
g_{K}	8	8
g_{L}	2	2
V_1	-1.2	-1.2
V_2	18	18
g_{KCa}	0.25	0.75
ε	0.005	0.005
μ	0.02	0.02

orbits bifurcation. The voltage traces produced by these two types of bursting are quite distinct, as shown in Fig. 15.

4.1 Results with UKF

We conducted a set of twin experiments for the bursting model to address the same question as we did for the spiking model: from a voltage trace alone, can DA methods estimate parameters that yield the appropriate qualitative dynamical behavior? Specifically, we simulated data from the square-wave (elliptic) bursting regime, and then initialized the UKF with parameter guesses corresponding to elliptic (square-wave) bursting (these parameter values are shown in Table 5). As a control experiment, we also ran the UKF with initial parameter guesses corresponding to the same bursting regime as the observed data. The observed voltage trace included additive white noise generated following the same protocol as in previous trials. We used 200,001 time points with observations at every 1 ms. Between observations, the system was integrated forward using substeps of 0.025 ms. For the square-wave burster, this included 215 bursts with 4 spikes per burst, and 225 bursts with 2 spikes for the elliptic burster.

The small parameters ε and μ in the calcium dynamics equation were assumed to be known and were not estimated by the UKF. Thus, for the bursting model, we are estimating one additional state variable (Ca) and one additional parameter (g_{KCa}) compared to the case for the spiking model. Table 6 shows the UKF parameter estimates after initialization with either the true parameters or the parameters producing the other type of bursting. The results for either case are quite consistent and fairly close to their true values for both types of bursting. Since small changes in parameter values can affect bursting dynamics, we also computed bifurcation diagrams for these estimated parameters and compared them to their true counterparts. Figure 16 shows that in all four cases, the estimated models have the same qualitative bifurcation structure as the models that produced the data. The recovered parameter estimates were insensitive to the initial conditions for n and Ca , with 100 different initializations for these state variables sampled from $\mathcal{U}(0, 1)$ and $\mathcal{U}(0, 5)$, respectively. Note, most

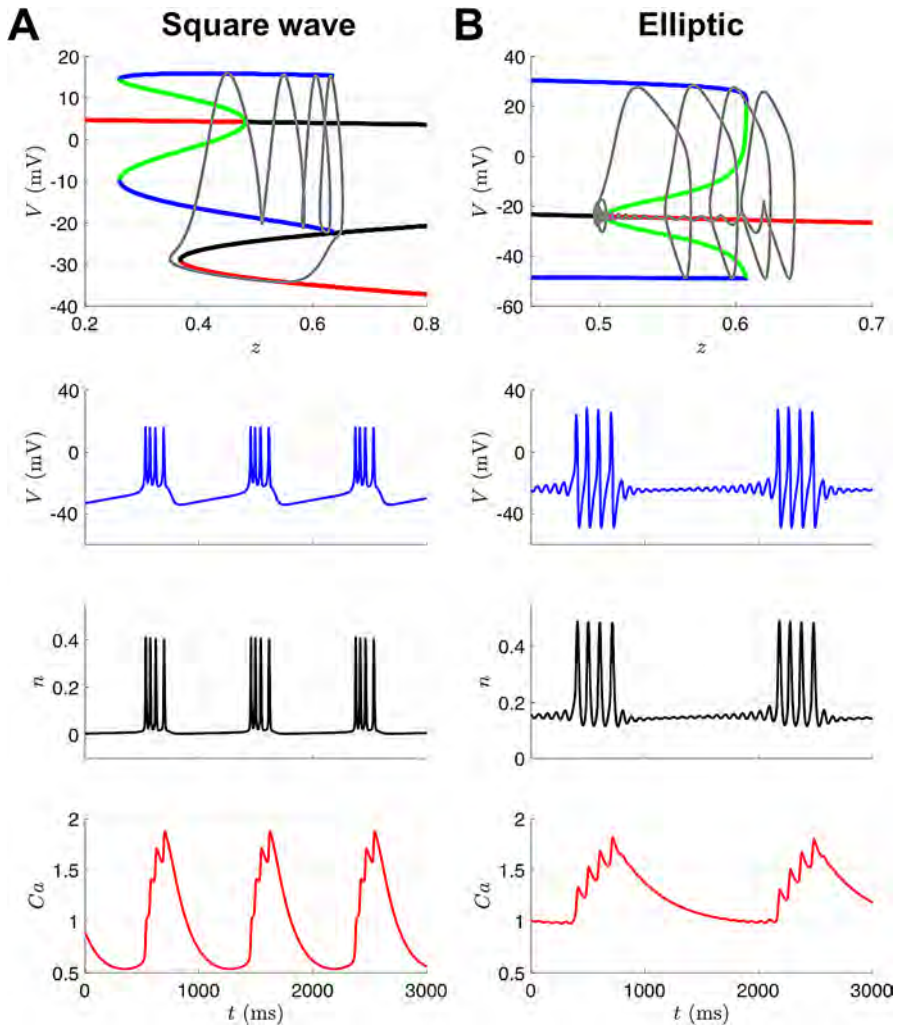


Fig. 15 Bursting model bifurcation diagrams and trajectories. The bifurcation diagrams (top row) depict stable fixed points (red), unstable fixed points (black), stable limit cycles (blue), and unstable limit cycles (green) of the fast subsystem (V, n) with bifurcation parameter z . The gray curves are the projection of the 3-D burst trajectory (V, n, Ca) onto the (V, z) plane, where z is a function of Ca . **(A)** During the quiescent phase of the burst, Ca and therefore z are decreasing and the trajectory slowly moves leftward along the lower stable branch of fixed points until reaching the saddle-node bifurcation or “knee”, at which point spiking begins. During spiking, Ca and z are slowly increasing and the trajectory oscillates while traveling rightward until the stable limit cycle is destroyed at a homoclinic bifurcation and spiking ceases. **(B)** During the quiescent phase of the burst, z is decreasing and the trajectory moves leftward along the branch of stable fixed points with small-amplitude decaying oscillations until reaching the Hopf bifurcation, at which point the oscillations grow in amplitude to full spikes. During spiking, z is slowly increasing and the trajectory oscillates while traveling rightward until the stable limit cycle is destroyed at a saddle-node of periodic orbits bifurcation and spiking ceases

Table 6 UKF parameter estimates for each bursting regime

	t:Square-wave		t:Elliptic	
	g:Square-wave	g:Elliptic	g:Square-wave	g:Elliptic
ϕ	0.214	0.215	0.040	0.040
g_{Ca}	3.758	3.767	4.396	4.398
V_3	12.045	12.023	1.603	1.685
V_4	16.272	16.316	29.582	29.639
g_K	7.955	7.952	7.866	7.889
g_L	1.974	1.972	2.015	2.017
V_1	-1.514	-1.511	-1.120	-1.199
V_2	17.640	17.624	18.010	18.015
g_{KCa}	0.251	0.251	0.767	0.763

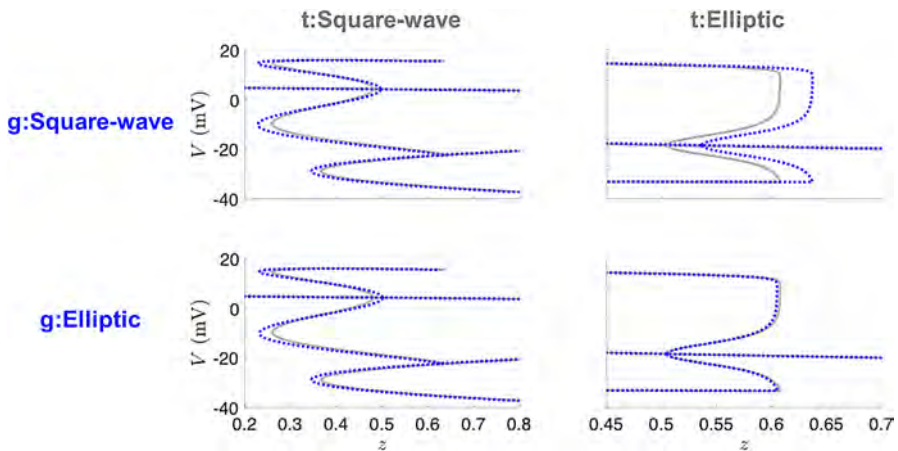


Fig. 16 Bifurcation diagrams for UKF twin experiments for the bursting Morris–Lecar model. The gray lines correspond to the true diagrams, and the blue dotted lines correspond to the diagrams produced from the estimated parameters in Table 6

predominantly in the top right panel, the location of the bifurcations is relatively sensitive to small deviations in certain parameters, such as g_{KCa} . Estimating g_{KCa} is challenging due to the algebraic degeneracy of estimating both terms involved in the conductance $G_{KCa} = g_{KCa}Ca/(Ca + 1)$, and the inherent time-scale disparity of the Ca dynamics compared to V and n . If one had observations of calcium, or full knowledge of its dynamical equations, this degeneracy would be immediately alleviated. To address difficulties in the estimation of bursting models, an approach that separates the estimation problem into two stages based on timescales—first estimating the slow dynamics with the fast dynamics blocked and then estimating the fast dynamics with the slow parameters held fixed—has been developed [34].

Table 7 4D-Var parameter estimates for each bursting regime

	t:Square-wave		t:Elliptic	
	g:Square-wave	g:Elliptic	g:Square-wave	g:Elliptic
ϕ	0.230	0.260	0.037	0.040
g_{Ca}	4.009	4.509	4.244	4.412
V_3	12.009	11.920	6.667	1.971
V_4	17.437	19.581	32.605	30.026
g_K	8.006	8.244	9.485	8.002
g_L	2.003	2.068	1.979	2.009
V_1	-1.187	-0.627	-1.307	-1.172
V_2	18.029	18.754	17.469	18.049
g_{KCa}	0.250	0.237	0.554	0.741

4.2 Results with 4D-Var

We also investigated the utility of variational techniques to recover the mechanisms of bursting. For these runs, we took our observations to be coarsely sampled at 0.1 ms, and our forward mapping is taken to be one step of modified Euler between observation times, as was the case for our previous 4D-Var Morris–Lecar results. We used 10,000 time points, which is one burst for the square wave burster, and one full burst plus another spike for the elliptic burster. We used the *L-BFGS-B* method [35], as we found it to perform faster for this problem than *fmincon*. This method approximates the Broyden–Fletcher–Goldfarb–Shanno (BFGS) quasi-Newton algorithm using a limited memory (L) inverse Hessian approximation, with an extension to handle bound constraints (B). It is available for Windows through the OPTI toolbox [36] or through a nonspecific operating system MATLAB MEX wrapper [37]. We supplied the gradient of the objective function, but allowed the solver to define the limited-memory Hessian approximation for our 30,012-dimensional problem. The results are captured in Table 7. We performed the same tests with providing the Hessian; however, there was no significant gain in accuracy or speed. The value for g_{KCa} for initializing with the square wave parameters and estimating the elliptical parameters is quite off, which reflects our earlier assessment for the value in observing calcium dynamics. Figure 17 shows that we are still successful in recovering the true bifurcation structure.

5 Discussion and Conclusions

Data assimilation is a framework by which one can optimally combine measurements and a model of a system. In neuroscience, depending on the neural system of interest, the data we have may unveil only a small subset of the overall activity of the system. For the results presented here, we used simulated data from the Morris–Lecar model with distinct activity based upon different choices for model parameters. We assumed access only to the voltage and the input current, which corresponds to the expected data from a current-clamp recording.

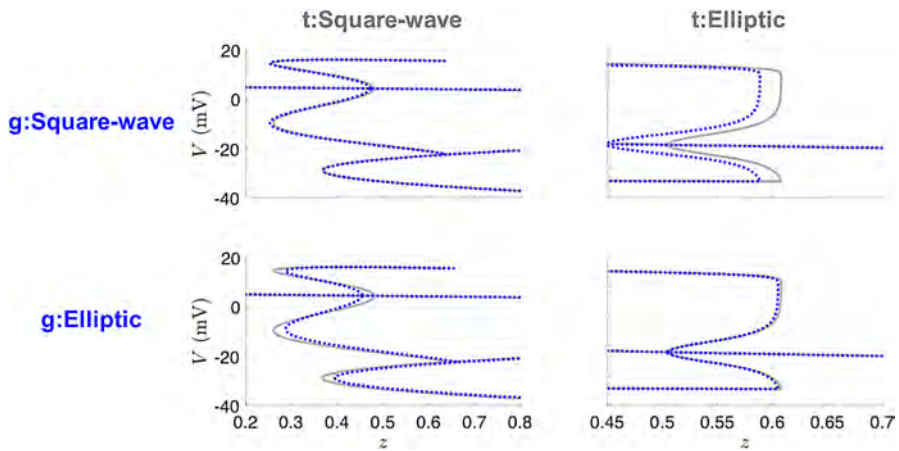


Fig. 17 Bifurcation diagrams for 4D-Var twin experiments for the bursting Morris–Lecar model. The gray lines correspond to the true diagrams, and the blue dotted lines correspond to the diagrams produced from the estimated parameters in Table 7

We showed the effectiveness of standard implementations of the Unscented Kalman Filter and weak 4D-Var to recover spiking behavior and, in many circumstances, near-exact parameters of interest. We showed that the estimated models undergo the same bifurcations as the model that produced the observed data, even when the initial parameter guesses do not. Additionally, we are also provided with estimates of the states and uncertainties associated with each state and parameter, but for sake of brevity these values were not always displayed. The methods, while not insensitive to noise, have intrinsic weightings of measurement deviations to account for the noise of the observed signal. Results were shown for mild additive noise. We also extended the Morris–Lecar model to exhibit bursting activity and demonstrated the ability to recover these model parameters using the UKF.

The UKF and 4D-Var approaches implemented here both attempt to optimally link a dynamic model of a system to observed data from that system, with error statistics assumed to be Gaussian. Furthermore, both approaches try to approximate the mean (and for the UKF also the variance) of the underlying, unassumed system distributions. The UKF is especially adept at estimating states over long time courses, and if the algorithmic parameters such as the model error can be tuned, then the parameters can be estimated simultaneously. Therefore, if one has access to a long series of data, then the UKF (or an Unscented Kalman Smoother, which uses more history of the data for each update step) is a great tool to have at one's disposal. However, sometimes one only has a small amount of time series data, or the tuning of initial covariance, the spread parameter λ , and the process noise Q_k associated with the augmented state and parameter system becomes too daunting. The 4D-Var approach sets the states at each time point and the parameters as optimization variables, transitioning the estimation process from the one which iterates in time to the one which iterates up to a tolerance in a chosen optimization routine. The only tuning parameters are those associated with the chosen optimization routine, and the weights $Q_{l,l}^{-1}$, $l \in [1 \dots L]$, for the model uncertainty of the state components at each

Table 8 Comparison of the sequential (UKF) and variational (4D-Var) approaches to data assimilation

	UKF	4D-Var
Implementation choices	initial covariance ($P_{x,x}$) sigma points (λ) process covariance matrix (Q)	model uncertainty (Q^{-1}) type of optimizer/optimizer settings state and parameter bounds
Data requirements	Pro: can handle a large amount of data Con: may not find a good solution with a small amount of data	Pro: may find a good solution with a small amount of data Con: cannot handle a large amount of data
Run time	Minutes	Days, hours, or minutes depending on choice of optimizer and settings
Scalability to larger models	Harder to choose Q EnKF may use a smaller number of ensemble members	Search dimension is $(N + 1)L + D$ Sparse Hessian can be exploited during optimization

time. There are natural ways to provide parameter bounds in the 4D-Var framework, whereas this is not the case for the UKF. However, depending upon the implementation choices and the dimension of the problem (which is extremely large for long time series data), the optimization may take a computing time scale of days to yield reasonable estimates. Fortunately, derivative information can be provided to the optimizer to speed up the 4D-Var procedure. Both the UKF and 4D-Var can provide estimates of the system uncertainty in addition to estimates of the system mean. The UKF provides mean and variance estimates at each iteration during the analysis step. In 4D-Var, one seeks mean estimates by minimization of a cost function. It has been shown that for cost functions of the form (36), the system variance can be interpreted as the inverse of the Hessian evaluated at minima of (36), and scales roughly as Q for large Q^{-1} [32]. The pros and cons of implementing these two DA approaches are summarized in Table 8.

The UKF and 4D-Var methodologies welcome the addition of any observables of the system, but current-clamp data may be all that is available. With this experimental data in mind, for a more complex system, the number of variables increases, while the total number of observables will remain at unity. Therefore, it may be useful to assess *a priori* which parameters are structurally identifiable and the sensitivity of the model to parameters of interest in order to reduce the estimation state-space [38]. Additionally, one should consider what manner of applied current to use to aid in state and parameter estimation. In the results presented above, we used a constant applied current, but work has been done which suggests the use of complex time-varying currents that stimulate as many of the model's degrees of freedom as possible [39].

The results we presented are based on MATLAB implementations of the derived equations for the UKF and weak 4D-Var. Sample code is provided in the Supplementary Material. Additional data assimilation examples in MATLAB can be found in [40]. The UKF has been applied to other spiking neuron models such as the FitzHugh–Nagumo model [41]. A sample of this code can be found in [42], as well as further exploration of the UKF in estimating neural systems. The UKF has been used

on real data from pyramidal neurons to track the states and externally applied current [43], the connectivity of cultured neuronal networks sampled by a microelectrode array [44], to assimilate seizure data from hippocampal OLM interneurons [15], and to reconstruct mammalian sleep dynamics [17]. A comparative study of the efficacy of the EKF and UKF on conductance-based models has been conducted [45].

The UKF is a particularly good framework for the state dimensions of a single compartment conductance based model as the size of the ensemble is chosen to be $2(L + D) + 1$. When considering larger state dimensions, as is the case for PDE models, a more general Ensemble Kalman Filter (EnKF) may be appropriate. An introduction to the EnKF can be found in [46, 47]. An adaptive methodology using past innovations to iteratively estimate the model and measurement covariances Q and R has been developed for use with ensemble filters [16]. The Local Ensemble Transform Kalman Filter (LETKF) [48] has been used to estimate the states associated with cardiac electrical wave dynamics [8]. Rather than estimating the mean and covariance through an ensemble, particle filters aim to fully construct the posterior density of the states conditioned on the observations. A particle filter approach has been applied to infer parameters of a stochastic Morris–Lecar model [49], to assimilate spike train data from rat layer V cortical neurons into a biophysical model [50], and to assimilate noisy, model-generated data for other states to motivate the use of imaging techniques when available [51].

An approach to the variational problem which tries to uncover the global minima more systematically has been developed [32]. In this framework, comparing to (36), they define for diagonal entries of Q^{-1} that

$$Q^{-1} = Q_0^{-1} \alpha^\beta$$

for $\alpha > 1$ and $\beta \geq 0$. The model term is initialized as relatively small, and over the course of an annealing procedure, β is incremented resulting in a steady increase of the model term's influence on the cost function. This annealing schedule is conducted in parallel for different initial guesses for the state-space. The development of this variational approach can be found in [52], and it has been used to assimilate neuronal data from HVC neurons [34] as well as to calibrate a neuromorphic very large scale integrated (VLSI) circuit [53]. An alternative to the variational approach is to frame the assimilation problem from a probabilistic sampling perspective and use Markov chain Monte-Carlo methods [54].

A closely associated variational technique, known as “nudging”, augments the vector field with a control term. If we only have observations of the voltage, this manifests as follows:

$$\frac{dV}{dt} = f_V^*(V, \mathbf{q}; \boldsymbol{\theta}) + u(V_{\text{obs}} - V).$$

The vector field with the observational coupling term is now passed into the strong 4D-Var constraints. The control parameter u may remain fixed, or be estimated along with the states [55, 56]. More details on nudging can be found [57]. A similar control framework has been applied to data from neurons of the stomatogastric ganglion [58].

Many other approaches outside the framework of data assimilation have been developed for parameter estimation of neuronal models, see [59] for a review. A prob-

lem often encountered when fitting models to a voltage trace is that phase shifts, or small differences in spike timing, between model output and the data can result in large root mean square error. This is less of an issue for data assimilation methods, especially sequential algorithms like UKF. Other approaches to avoid harshly penalizing spike timing errors in the cost function are to consider spikes in the data and model-generated spikes that occur within a narrow time window of each other as coincident [60], or to minimize error with respect to the dV/dt versus V phase-plane trajectory rather than $V(t)$ itself [59]. Another way to avoid spike mismatch errors is to force the model with the voltage data and perform linear regression to estimate the linear parameters (maximal conductances), and then perhaps couple the problem with another optimization strategy to access the nonlinearly-dependent gating parameters [3, 61, 62].

A common optimization strategy is to construct an objective function that encapsulates important features derived from the voltage trace, and then use a genetic algorithm to stochastically search for optimal solutions. These algorithms proceed by forming a population of possible solutions and applying biologically inspired evolution strategies to gradually increase the fitness (defined with respect to the objective function) of the population across generations. Multi-objective optimization schemes will generate a “Pareto front” of optimal solutions that are considered equally good. A multi-objective non-dominated sorting genetic algorithm (NSGA-II) has recently been used to estimate parameters of the pacemaker PD neurons of the crab pyloric network [63, 64].

In this paper, we compared the bifurcation structure of models estimated by DA algorithms to the bifurcation structure of the model that generated the data. We found that the estimated models exhibited the correct bifurcations even when the algorithms were initiated in a region of parameter space corresponding to a different bifurcation regime. This type of twin experiment is a useful addition to the field that specifically emphasizes the difficulty of nonlinear estimation and provides a qualitative measure of estimation success or failure. Prior literature on parameter estimation that has made use of geometric structure includes work on bursting respiratory neurons [65] and “inverse bifurcation analysis” of gene regulatory networks [66, 67].

Looking forward, data assimilation can complement the growth of new recording technologies for collecting observational data from the brain. The joint collaboration of these automated algorithms with the painstaking work of experimentalists and model developers may help answer many remaining questions about neuronal dynamics.

Acknowledgements We thank Tyrus Berry and Franz Hamilton for helpful discussions about the UKF and for sharing code, and Nirag Kadakia and Paul Rozdeba for helpful discussions about 4D-Var methods and for sharing code. MM also benefited from lectures and discussions at the Mathematics and Climate Summer Graduate Program held at the University of Kansas in 2016, which was sponsored by the Institute for Mathematics and its Applications and the Mathematics and Climate Research Network.

Funding This work was supported in part by NSF grants DMS-1412877 and DMS-1555237, and U.S. Army Research Office grant W911NF-16-1-0584. The funding bodies had no role in the design of the study and collection, analysis, and interpretation of data and in writing the manuscript should be declared.

Availability of data and materials The MATLAB code used in this study is provided as Supplementary Material.

Ethics approval and consent to participate Not applicable.

Competing interests The authors declare that they have no competing interests.

Consent for publication Not applicable.

Authors' contributions MM wrote the computer code implementing the data assimilation algorithms. MM and CD conceived of the study, performed simulations and analysis, wrote the manuscript, and read and approved the final version of the manuscript.

Appendix

Table A1 Bounds used during 4D-Var estimation for the results shown in Tables A2 and A3

	Lower Bound	Upper Bound
ϕ	0	∞
g_{Ca}	0	∞
V_3	$-\infty$	∞
V_4	0.1	∞
g_K	0	∞
g_L	0	∞
V_1	$-\infty$	∞
V_2	0.1	∞

Table A2 4D-Var parameter estimates at the end of the optimization for each bifurcation regime. The loose parameter bounds in Table A1 were used for these trials. Hessian information was not provided to the optimizer

	t:HOPF			t:SNIC			t:HOMO		
	g:HOPF	g:SNIC	g:HOMO	g:HOPF	g:SNIC	g:HOMO	g:HOPF	g:SNIC	g:HOMO
ϕ	0.040	0.041	0.040	0.066	0.067	0.066	0.406	0.225	0.229
g_{Ca}	4.011	3.959	3.989	4.016	4.035	4.040	8.623	3.992	3.983
V_3	2.210	13.479	6.284	12.497	12.176	12.102	7.453	14.333	12.197
V_4	29.917	37.854	32.748	17.589	17.342	16.998	27.569	18.593	17.464
g_K	8.046	10.857	8.989	8.192	8.057	8.021	9.543	9.213	8.092
g_L	2.026	1.806	1.959	2.009	2.038	2.067	3.029	1.960	1.990
V_1	-1.222	-1.188	-1.208	-1.171	-1.165	-1.188	2.604	-1.198	-1.212
V_2	18.030	17.921	17.979	18.087	18.126	18.148	24.260	18.089	17.985

Table A3 4D-Var parameter estimates at the end of the optimization for each bifurcation regime. The loose parameter bounds in Table A1 were used for these trials. Hessian information was provided to the optimizer

	t:HOPF			t:SNIC			t:HOMO		
	g:HOPF	g:SNIC	g:HOMO	g:HOPF	g:SNIC	g:HOMO	g:HOPF	g:SNIC	g:HOMO
ϕ	0.039	0.039	0.039	0.066	0.066	0.066	0.571	0.560	0.549
g_{Ca}	3.889	3.889	3.889	4.002	4.002	4.002	831.907	911.887	913.350
V_3	1.971	1.971	1.971	11.825	11.825	11.825	826.608	896.717	822.366
V_4	29.533	29.533	29.533	17.071	17.071	17.071	1695.018	1816.501	1813.829
g_K	8.050	8.050	8.050	7.923	7.923	7.923	847.999	932.249	885.392
g_L	1.928	1.928	1.928	2.027	2.027	2.027	0.024	0.026	0.118
V_1	-1.301	-1.301	-1.301	-1.232	-1.232	-1.232	53.706	54.172	53.913
V_2	17.600	17.600	17.600	18.004	18.004	18.004	75.855	76.135	76.111

Table A4 4D-Var parameter estimates at the end of the optimization for each bifurcation regime. The parameter bounds in Table 4 were used for these trials. Hessian information was provided to the optimizer

	t:HOPF			t:SNIC			t:HOMO		
	g:HOPF	g:SNIC	g:HOMO	g:HOPF	g:SNIC	g:HOMO	g:HOPF	g:SNIC	g:HOMO
ϕ	0.039	0.039	0.039	0.066	0.067	0.066	0.230	0.230	0.230
g_{Ca}	3.889	3.889	3.889	4.002	4.035	4.002	4.014	4.019	4.014
V_3	1.971	1.971	1.971	11.825	12.176	11.825	12.321	12.320	12.320
V_4	29.533	29.533	29.533	17.071	17.342	17.071	17.615	17.633	17.616
g_K	8.050	8.050	8.050	7.923	8.057	7.923	8.157	8.158	8.157
g_L	1.928	1.928	1.928	2.027	2.038	2.027	1.996	1.997	1.996
V_1	-1.301	-1.301	-1.301	-1.232	-1.165	-1.232	-1.154	-1.148	-1.153
V_2	17.600	17.600	17.600	18.004	18.126	18.004	18.050	18.057	18.050

Publisher's Note

Springer Nature remains neutral with regard to jurisdictional claims in published maps and institutional affiliations.

References

- Hodgkin AL, Huxley AF. A quantitative description of membrane current and its application to conduction and excitation in nerve. *Bull Math Biol.* 1990;52(1–2):25–71.
- Meliza CD, Kostuk M, Huang H, Nogaret A, Margoliash D, Abarbanel HD. Estimating parameters and predicting membrane voltages with conductance-based neuron models. *Biol Cybern.* 2014;108:495–516.
- Lepora NF, Overton PG, Gurney K. Efficient fitting of conductance-based model neurons from somatic current clamp. *J Comput Neurosci.* 2012;32(1):1–24.
- Carton JA, Giese BS. A reanalysis of ocean climate using simple ocean data assimilation (SODA). *Mon Weather Rev.* 2008;136(8):2999–3017. <https://doi.org/10.1175/2007MWR1978.1>.

5. Greybush SJ, Wilson RJ, Hoffman RN, Hoffman MJ, Miyoshi T, Ide K, et al. Ensemble Kalman filter data assimilation of thermal emission spectrometer temperature retrievals into a mars GCM. *J Geophys Res, Planets*. 2012;117(11):1–17.
6. Reichle RH. Data assimilation methods in the Earth sciences. *Adv Water Resour*. 2008;31(11):1411–8. <https://doi.org/10.1016/j.advwatres.2008.01.001>.
7. Bauer P, Thorpe A, Brunet G. The quiet revolution of numerical weather prediction. *Nature*. 2015;525(7567):47–55.
8. Hoffman MJ, LaVigne NS, Scorse ST, Fenton FH, Cherry EM. Reconstructing three-dimensional reentrant cardiac electrical wave dynamics using data assimilation. *Chaos, Interdiscip J Nonlinear Sci*. 2016;26(1):013107. <https://doi.org/10.1063/1.4940238>.
9. Apte A. An Introduction to data assimilation. In: Sarkar S, Basu U, De S, editors. *Applied mathematics. Springer proceedings in mathematics & statistics*. 2015. p. 31–42.
10. Asch M, Bocquet M, Nodet M. *Data assimilation: methods, algorithms, and applications. Fundamentals of algorithms*. Philadelphia: SIAM; 2016. <https://doi.org/10.1137/1.9781611974546>
11. Julier SJ, Uhlmann JK. Unscented filtering and nonlinear estimation. In: *Proceedings of the IEEE*. vol. 92. 2004. p. 401–22. <https://doi.org/10.1109/JPROC.2003.823141>.
12. Gordon NJ, Salmond DJ, Smith AFM. Novel approach to nonlinear/non-Gaussian Bayesian state estimation. *IEE Proc F, Commun Radar Signal Process*. 1993;140(2):107–13.
13. Liu J, West M. Combined parameter and state estimation in simulation-based filtering. In: Doucet A, Freitas N, Gordon N, editors. *Sequential Monte Carlo methods in practice. Statistics for engineering and information science*. New York: Springer; 2001. p. 197–223.
14. DelSole T, Yang X. State and parameter estimation in stochastic dynamical models. *Physica D*. 2010;239(18):1781–8.
15. Ullah G, Schiff SJ. Assimilating seizure dynamics. *PLoS Comput Biol*. 2010;6(5):e1000776. <https://doi.org/10.1371/journal.pcbi.1000776>.
16. Berry T, Sauer T. Adaptive ensemble Kalman filtering of non-linear systems. *Tellus, Ser A Dyn Meteorol Oceanogr*. 2013;65(1):2031. <https://doi.org/10.3402/tellusa.v65i0.20331>
17. Sedigh-Sarvestani M, Schiff SJ, Gluckman BJ. Reconstructing mammalian sleep dynamics with data assimilation. *PLoS Comput Biol*. 2012;8(11):e1002788. <https://doi.org/10.1371/journal.pcbi.1002788>.
18. Van der Merwe R, Wan EA. The square-root unscented Kalman filter for state and parameter estimation. In: 2001 IEEE international conference on acoustics, speech, and signal processing. *Proceedings (Cat. No. 01CH37221)*. vol. 6. New York: IEEE Press; 2001. p. 3461–4. <https://doi.org/10.1109/ICASSP.2001.940586>
19. Rotstein HG, Olarinre M, Galowasch J. Dynamic compensation mechanism gives rise to period and duty-cycle level sets in oscillatory neuronal models. *J Neurophysiol*. 2016;116(5):2431–52. <https://doi.org/10.1152/jn.00357.2016>
20. Walch OJ, Eisenberg MC. Parameter identifiability and identifiable combinations in generalized Hodgkin–Huxley models. *Neurocomputing*. 2016;199:137–43.
21. Stanhope S, Rubin JE, Swigon D. Identifiability of linear and linear-in-parameters dynamical systems from a single trajectory. *SIAM J Appl Dyn Syst*. 2014;13(4):1792–815. <https://doi.org/10.1137/130937913>.
22. Stanhope S, Rubin JE, Swigon D. Robustness of solutions of the inverse problem for linear dynamical systems with uncertain data. *SIAM/ASA J Uncertain Quantificat*. 2017;5(1):572–97. <https://doi.org/10.1137/16M1062466>.
23. Ermentrout GB, Terman DH. *Mathematical foundations of neuroscience. Interdisciplinary applied mathematics*. vol. 35. New York: Springer; 2010. <https://doi.org/10.1007/978-0-387-87708-2>.
24. Izhikevich E. *Dynamical systems in neuroscience: the geometry of excitability and bursting*. Cambridge: MIT Press; 2007.
25. Morris C, Lecar H. Voltage oscillations in the barnacle giant muscle fiber. *Biophys J*. 1981;35(1):193–213.
26. Wan EA, Van Der Merwe R. The unscented Kalman filter for nonlinear estimation. In: *Proceedings of the IEEE 2000 adaptive systems for signal processing, communications, and control symposium, AS-SPCC 2000 (Cat. No. 00EX373)*. 2000. p. 153–8. <https://doi.org/10.1109/ASSPCC.2000.882463>
27. Byrd RH, Hribar ME, Nocedal J. An interior point algorithm for large-scale nonlinear programming. *SIAM J Optim*. 1999;9(4):877–900.
28. Byrd RH, Gilbert JC, Nocedal J. A trust region method based on interior point techniques for nonlinear programming. *Math Program, Ser A*. 2000;89:149–85.

29. Waltz RA, Morales JL, Nocedal J, Orban D. An interior algorithm for nonlinear optimization that combines line search and trust region steps. *Math Program, Ser. A.* 2006;107:391–408.
30. Weinstein MJ, Rao AV. Algorithm 984: ADiGator, a toolbox for the algorithmic differentiation of mathematical functions in MATLAB using source transformation via operator overloading. *ACM Trans Math Softw.* 2017;44(2):1–25. <https://doi.org/10.1145/3104990>
31. Kelly M. An introduction to trajectory optimization: how to do your own direct collocation. *SIAM Rev.* 2017;59(4):849–904.
32. Ye J, Rey D, Kadakia N, Eldridge M, Morone UI, Rozdeba P, et al. Systematic variational method for statistical nonlinear state and parameter estimation. *Phys Rev E, Stat Nonlinear Soft Matter Phys.* 2015;92(5):052901. <https://doi.org/10.1103/PhysRevE.92.052901>.
33. Rinzel J, Ermentrout GB. Analysis of neural excitability and oscillations. In: Koch C, Segev I, editors. *Methods in neuronal modeling: from synapses to networks.* Cambridge: MIT Press; 1989. p. 135–69.
34. Kadakia N, Armstrong E, Breen D, Morone U, Daou A, Margoliash D, et al. Nonlinear statistical data assimilation for HVC_{RA} neurons in the avian song system. *Biol Cybern.* 2016;110(6):417–34. <https://doi.org/10.1007/s00422-016-0697-3>.
35. Zhu C, Byrd RH, Lu P, Nocedal J. Algorithm 778: L-BFGS-B: Fortran subroutines for large-scale bound-constrained optimization. *ACM Trans Math Softw.* 1997;23(4):550–60.
36. Nocedal J. OPTI Toolbox: a free MATLAB toolbox for optimization. 2018. <https://www.inverseproblem.co.nz/OPTI/index.php/Solvers/L-BFGS-B>. Accessed 2018-06-26.
37. Becker S. L-BFGS-B-C. 2018. <https://github.com/stephenbecker/L-BFGS-B-C>. Accessed 2018-06-26.
38. Olufsen MS, Ottesen JT. A practical approach to parameter estimation applied to model predicting heart rate regulation. *J Math Biol.* 2013;67(1):39–68. <https://doi.org/10.1007/s00285-012-0535-8>.
39. Abarbanel HDI, Shirman S, Breen D, Kadakia N, Rey D, Armstrong E, Margoliash D. A unifying view of synchronization for data assimilation in complex nonlinear networks. *Chaos.* 2017;27(12):126802. <https://doi.org/10.1063/1.5001816>.
40. Law K, Stuart A, Zygalkis K. Data assimilation: a mathematical introduction. In *texts in applied mathematics*. vol. 62. Cham: Springer; 2015. <https://doi.org/10.1007/978-3-319-20325-6>.
41. Voss HU, Timmer J, Kurths J. Nonlinear dynamical system identification from uncertain and indirect measurements. *Int J Bifurc Chaos.* 2004;14(06):1905–33. <https://doi.org/10.1142/S0218127404010345>.
42. Schiff SJ. Neural control engineering: the emerging intersection between control theory and neuroscience. In: *Computational neuroscience.* Cambridge: MIT Press; 2012. <https://books.google.com/books?id=P9UvTQtnqKwC&pgis=1>.
43. Wei Y, Ullah G, Parekh R, Ziburkus J, Schiff SJ. Kalman filter tracking of intracellular neuronal voltage and current. In: *Proceedings of the IEEE conference on decision and control.* 2011. p. 5844–9.
44. Hamilton F, Berry T, Peixoto N, Sauer T. Real-time tracking of neuronal network structure using data assimilation. *Physical Review E.* 2013;88(5):052715. <https://doi.org/10.1103/PhysRevE.88.052715>.
45. Lankarany M, Zhu WP, Swamy MNS. Joint estimation of states and parameters of Hodgkin-Huxley neuronal model using Kalman filtering. *Neurocomputing.* 2014;136:289–99. <https://doi.org/10.1016/j.neucom.2014.01.003>.
46. Evensen G. The ensemble Kalman filter for combined state and parameter estimation. *IEEE Control Syst Mag.* 2009;29(3):83–104. <http://ieeexplore.ieee.org/document/4939313/>.
47. Evensen G. Data assimilation: the ensemble Kalman filter. Berlin: Springer; 2009. <https://doi.org/10.1007/978-3-642-03711-5>.
48. Hunt BR, Kostelich EJ, Szunyogh I. Efficient data assimilation for spatiotemporal chaos: a local ensemble transform Kalman filter. *Phys D: Nonlinear Phenom.* 2007;230(1–2):112–26.
49. Ditlevsen S, Samson A. Estimation in the partially observed stochastic Morris–Lecar neuronal model with particle filter and stochastic approximation methods. *Ann Appl Stat.* 2014;8(2):674–702. <http://projecteuclid.org/euclid.aoas/1404229510>.
50. Meng L, Kramer MA, Middleton SJ, Whittington MA, Eden UT. A unified approach to linking experimental, statistical and computational analysis of spike train data. *PLoS ONE.* 2014;9(1):e85269. <https://doi.org/10.1371/journal.pone.0085269>.
51. Huys QJM, Paninski L. Smoothing of, and parameter estimation from, noisy biophysical recordings. *PLoS Comput Biol.* 2009;5(5):e1000379. <https://doi.org/10.1371/journal.pcbi.1000379>.
52. Abarbanel H. Predicting the future: completing models of observed complex systems. *Understanding complex systems.* New York: Springer; 2013. <https://books.google.com/books?id=Vne5BQAAQBAJ>.

53. Wang J, Breen D, Akinin A, Broccard F, Abarbanel HDI, Cauwenberghs G. Assimilation of biophysical neuronal dynamics in neuromorphic VLSI. *IEEE Trans Biomed Circuits Syst.* 2017;11(6):1258–70.
54. Kostuk M, Toth BA, Meliza CD, Margoliash D, Abarbanel HDI. Dynamical estimation of neuron and network properties II: path integral Monte Carlo methods. *Biol Cybern.* 2012;106(3):155–67.
55. Toth BA, Kostuk M, Meliza CD, Margoliash D, Abarbanel HDI. Dynamical estimation of neuron and network properties I: variational methods. *Biol Cybern.* 2011;105(3–4):217–37. <https://doi.org/10.1007/s00422-011-0459-1>.
56. Abarbanel HDI, Creveling DR, Farsian R, Kostuk M. Dynamical state and parameter estimation. *SIAM J Appl Dyn Syst.* 2009;8(4):1341–81. <https://doi.org/10.1137/090749761>.
57. Lakshmiarahan S, Lewis JM. Nudging methods: a critical overview. In: Park SK, Xu L, editors. *Data assimilation for atmospheric, oceanic and hydrologic applications*, vol. II. Berlin: Springer; 2013. p. 27–57. https://doi.org/10.1007/978-3-642-35088-7_2.
58. Brookings T, Goeritz ML, Marder E. Automatic parameter estimation of multicompartmental neuron models via minimization of trace error with control adjustment. *J Neurophysiol.* 2014;112(9):2332–48. <https://doi.org/10.1152/jn.00007.2014>.
59. Van Geit W, De Schutter E, Achard P. Automated neuron model optimization techniques: a review. *Biol Cybern.* 2008;99(4–5):241–51.
60. Rossant C. Automatic fitting of spiking neuron models to electrophysiological recordings. *Front Neuroinformatics.* 2010;4:2. <https://doi.org/10.3389/neuro.11.002.2010>.
61. Huys QJM. Efficient estimation of detailed single-neuron models. *J Neurophysiol.* 2006;96(2):872–90. <https://doi.org/10.1152/jn.00079.2006>.
62. Hauffer D, Morin F, Lacaillie JC, Skinner FK. Parameter estimation in single-compartment neuron models using a synchronization-based method. *Neurocomputing.* 2007;70(10–12):1605–10.
63. Deb K, Pratap A, Agarwal S, Meyarivan T. A fast and elitist multiobjective genetic algorithm: NSGA-II. *IEEE Trans Evol Comput.* 2002;6(2):182–97.
64. Fox DM, Tseng HA, Smolinski TG, Rotstein HG, Nadim F. Mechanisms of generation of membrane potential resonance in a neuron with multiple resonant ionic currents. *PLoS Comput Biol.* 2017;13(6):1–30.
65. Tien JH, Guckenheimer J. Parameter estimation for bursting neural models. *J Comput Neurosci.* 2006;24:359–73.
66. Lu J, Engl HW, Schuster P. Inverse bifurcation analysis: application to simple gene systems. *Algorithms Mol Biol.* 2006;1:11. <https://doi.org/10.1186/1748-7188-1-11>.
67. Engl HW, Flamm C, Kügler P, Lu J, Müller S, Schuster P. Inverse problems in systems biology. *Inverse Probl.* 2009;25:1–51.

Entrainment Dynamics of Forced Hierarchical Circadian Systems Revealed by 2-Dimensional Maps*

Guangyuan Liao[†], Casey Diekman[†], and Amitabha Bose[†]

Abstract. The ability of a circadian system to entrain to the 24-hour light-dark cycle is one of its most important properties. A new tool, called the entrainment map, was recently introduced to study this process for a single oscillator. Here we generalize the map to study the effects of light-dark forcing in a hierarchical system consisting of a central circadian oscillator that drives a peripheral circadian oscillator. We develop techniques to reduce the higher-dimensional phase space of the coupled system to derive a generalized two-dimensional entrainment map. Determining the nature of various fixed points, together with an understanding of their stable and unstable manifolds, leads to conditions for existence and stability of periodic orbits of the circadian system. We use the map to investigate how various properties of solutions depend on parameters and initial conditions including the time to and direction of entrainment. We show that the concepts of phase advance and phase delay need to be carefully assessed when considering hierarchical systems.

Key words. circadian rhythm, limit cycle, Poincaré map, coupled oscillators

AMS subject classifications. 37E10, 92B25

DOI. 10.1137/19M1307676

1. Introduction. Circadian rhythms refer to a variety of oscillatory processes that occur over a roughly 24-hour time period. Circadian oscillations are found in a variety of animal and plant species [5]. Within humans a common example involves our core body temperature which shows a local minimum typically in the early morning hours ($\sim 4:00$ AM) and a local maximum roughly twelve hours later [25]. Similarly, concentrations of certain hormone levels within our bodies oscillate over the course of a day [12]. In the absence of any explicit forcing from naturally occurring light-dark cycles, circadian oscillators possess endogenous periods of roughly 24 hours. Their ability to also entrain to 24-hour periodic cycles of light and dark is one of their most important properties.

The entrainment of circadian oscillators has been mathematically analyzed using a variety of techniques. Often this involves describing the circadian oscillator with a reduced phase description such as that given by a Kuramoto oscillator [7, 27]. The problem then reduces to studying periodically forced Kuramoto systems. Other approaches include deriving model equations that retain more of their connection to the underlying biological process [36, 41]. Recently Diekman and Bose [13] introduced a novel tool called the entrainment map to de-

*Received by the editors December 18, 2019; accepted for publication (in revised form) by J. Rubin July 2, 2020; published electronically September 15, 2020.

<https://doi.org/10.1137/19M1307676>

Funding: The work of the second author was partially supported by NSF grant DMS-1555237 and U.S. Army Research Office grant W911NF-16-1-0584.

[†]Department of Mathematical Sciences, New Jersey Institute of Technology, Newark, NJ 07102 (g192@njit.edu, casey.o.diekman@njit.edu, bose@njit.edu).

termine whether a circadian oscillator can entrain to the 24-hour light-dark cycle and, if so, at what phase. The derived map is equivalent to a 1-dimensional (1-D) Poincaré map that tracks the phase of light onset of the light-dark forcing on a cycle-by-cycle basis. In principle, the dimension of the underlying circadian oscillator model is not relevant. Diekman and Bose derived entrainment maps for the 2-dimensional (2-D) Novák–Tyson model [41, 36], the 3-dimensional (3-D) Gonze model [18], and the 180-D Kim–Forger model [22]. In general, the map can be used to estimate both entrainment times and whether entrainment occurs through phase advance or delay with respect to the daily onset of lights.

There are several scenarios in which circadian oscillators do not directly receive light-dark forcing [18, 20, 29]. Instead they are part of hierarchical systems in which, as “peripheral” oscillators, they are periodically forced by other “central” circadian oscillators that do directly receive light input. Cells within major organs in our bodies fall into this category. Several natural questions arise about the entrainment process of these peripheral oscillators. For example, do they entrain through phase advance or phase delay as central oscillators do? To what extent is their entrainment time dependent on the entrainment process of the central oscillator from which they receive forcing? To study such questions, here we generalize the entrainment map to a 2-D map where we track from the perspective of the peripheral oscillator both the phase of the central oscillator as well as the phase of light onset.

In this paper, we first consider the situation in which a single central oscillator receives light-dark input. In turn, this central oscillator sends input to a single peripheral oscillator. To focus on the mathematical aspects of the derivation and analysis of the 2-D entrainment map, we will utilize the planar Novák–Tyson model [36] for both the central and peripheral oscillators. The phase space for this problem is 5-dimensional (5-D), two for each of the oscillators and a fifth that accounts for the light-dark forcing. We will define a Poincaré section transversal to the flow allowing us to derive a 2-D map that determines the phase of light and the phase of the central oscillator at each cycle when the peripheral oscillator lies on the Poincaré section. We analyze the map by extending techniques first introduced in Akcay, Bose, and Nadim [1] and Akcay et al. [2]. We will show that for a range of parameter values, the map possesses four fixed points: one asymptotically stable and three unstable fixed points, two of which are saddle points. All of these fixed points are related to actual periodic orbits of the flow. By numerically calculating entrainment times (defined precisely later in the text), we are able to uncover how the stable and unstable manifolds of the saddle points organize the iterates of the map, determine the direction of entrainment, and give rise to a rich set of dynamics. The findings of the map are then validated by comparing them to direct simulations of the model equations. We also extend the analysis to the case of a semihierarchical system that consists of a second central oscillator that receives less light input than the first central oscillator.

Analysis of the map reveals several important insights into the entrainment and reentrainment process. First, bounds on important parameters, such as the intensity of light input and the strength of the coupling from the central oscillator that lead to entrainment, are easily identified. We are able to determine which kinds of perturbations lead to faster or slower reentrainment, e.g., whether perturbations that desynchronize only the peripheral oscillator but not the central one lead to quick reconvergence. Interestingly, we find that the straightforward notion of convergence via phase advance or phase delay needs to be generalized. Indeed, the peripheral oscillator can converge by a combination of phase advance and delay while the central

oscillator typically converges by either phase advancing or delaying. This result has implications for recovery from jet lag and abrupt changes in sleep-wake schedules. In experimental studies of aircrews, some subjects experienced internal dissociation with different components of the circadian system converging in opposite directions [23]. Specifically, after an eastbound flight across 9 time zones, activity rhythms reentrained through phase advances while body temperature reentrained through phase delays. In hospital studies, a 12-hour phase shift of sleep time results in a phase advance of urinary potassium but a phase delay in urinary hydrocorticosteroids [31]. Aschoff [4] referred to this behavior as “reentrainment by partition” and suggested that it may impact health and contribute to the degradation of psychomotor performance observed on postflight days. The saddle fixed points of our map provide a dynamical explanation for the partitioning phenomenon, as will be elaborated upon in the discussion.

2. Models and methods. Our model is based on the Novák–Tyson (NT) model [41] for the molecular circadian clock in the fruit fly *Drosophila*. The NT model can be written in the following form:

$$(1) \quad \begin{aligned} \frac{1}{\phi} \frac{dP}{dt} &= M - k_f h(P) - k_D P - k_L f(t)P, \\ \frac{1}{\phi} \frac{dM}{dt} &= \epsilon (g(P) - M), \end{aligned}$$

where $g(P) = \frac{1}{1+P^4}$, and $h(P) = \frac{P}{0.1+P+2P^2}$. The M variable represents mRNA concentration, and P variable represents the protein concentration. The parameter ϵ is small, which separates P and M into fast and slow variables. The parameter ϕ will directly affect the period of the solutions of this system; smaller values imply longer endogenous periods. The function $f(t)$ describes the light-dark (LD) forcing, which is defined by a 24-hour periodic step function, $f(t) = 1$ when lights are on and $f(t) = 0$ when lights are off. We consider for convenience a 12:12 photoperiod. There is no difficulty in extending to other photoperiods, though a minimum amount of light per day is needed for entrainment; see [13] for a detailed assessment of how entrainment depends on photoperiod and light intensity. In *Drosophila*, there is protein degradation during darkness, and light increases the degradation. So k_D represents the degradation rate during darkness, and k_L represents the additional degradation rate which is caused by light. The parameter k_f is a combination of two variables in the original Tyson et al. paper [41]. In [13], the entrainment of a single NT oscillator to a 24-hour period LD forcing was studied. The ensuing solution was denoted as an LD-entrained solution.

2.1. Coupled NT model. The coupled NT (CNT) model is given by the following equations:

$$(2) \quad \begin{aligned} \frac{1}{\phi_1} \frac{dP_1}{dt} &= M_1 - k_f h(P_1) - k_D P_1 - k_{L_1} f(t)P_1, \\ \frac{1}{\phi_1} \frac{dM_1}{dt} &= \epsilon [g(P_1) - M_1], \\ \frac{1}{\phi_2} \frac{dP_2}{dt} &= M_2 - k_f h(P_2) - k_D P_2 - k_{L_2} f(t)P_2, \\ \frac{1}{\phi_2} \frac{dM_2}{dt} &= \epsilon [g(P_2) - M_2 + \alpha_1 M_1 g(P_2)]. \end{aligned}$$



Figure 1. (a) Model with strict hierarchical coupling. (b) Semihierarchical model when both oscillators receive light input, but the light into O_2 is much weaker than the light into O_1 .

The parameters and variables have the same meaning as the original NT model. We introduce a coupling term $\alpha_1 M_1 g(P_2)$, from oscillator 1 (O_1) to oscillator 2 (O_2). The parameter α_1 is a nonnegative real number which denotes the coupling strength. We placed the coupling factor into the second equation of O_2 based on Roberts et al. [39], who suggest that coupling occurs between the mRNA production rates.

We mainly study the case with strict hierarchical coupling, which is shown in Figure 1(a). In this case, the LD forcing is applied only on O_1 , which then has feedforward coupling onto O_2 . We fix the value of parameter $k_{L_2} = 0$. Figure 1(b) shows the semihierarchical CNT model when both oscillators receive light forcing, but the effect of light into O_2 is taken to be less intense than that into O_1 ; in other words, $k_{L_2} < k_{L_1}$.

2.2. The entrainment map. When attempting to determine the existence of periodic solutions using Poincaré maps, one has to decide where in phase space to place the section. Often in circadian models, the Poincaré section is placed on the 24-hour LD forcing, leading to a stroboscopic map that determines the state of the system every 24 hours. In [13], Diekman and Bose instead placed the section in the phase space of the circadian oscillator and backed out the phase of light when the oscillator was at the section. Here, we follow that approach when building the 2-D map. The Poincaré section is chosen at a location in the flow that O_2 will be shown to cross. In this section, we first introduce the original 1-D map, and then generalize it to our 2-D map.

The entrainment map $\Pi(y)$ for the original NT model was introduced as a 1-D map in [13]. To define $\Pi(y)$, Diekman and Bose take a Poincaré section \mathcal{P} as a 1-D line segment which intersects the LD-entrained solution of a single periodically forced NT oscillator. The section is placed along a portion of an attracting 1-D slow manifold where all trajectories of the NT oscillator pass. A phase variable y is defined to be the amount of time that has passed since the beginning of the most recent LD cycle. When the trajectory first returns to \mathcal{P} , the map $\Pi(y)$ is defined to be the amount of time that has passed since the onset of the most recent LD cycle, which is the new phase of the light forcing. The domain and range of $\Pi(y)$ are both $(0, 24]$. The domain is actually homeomorphic to the unit circle \mathbb{S}^1 , so $y = 0$ and $y = 24$ are equivalent. The map is written as $y_{n+1} = \Pi(y_n)$, where

$$(3) \quad \Pi(y_n) = (\rho(y_n) + y_n) \bmod 24.$$

$\rho(y)$ is a return time map that measures the time a trajectory starting on \mathcal{P} takes to return

to \mathcal{P} . It is continuous and periodic at its endpoints $\rho(0^+) = \rho(24^-)$. If $\rho(y) < 24 - y$, then $\Pi(x) = \rho(y) + y$, because the trajectory will return back to \mathcal{P} within the same LD cycle which it started. If $24 - y < \rho(y) < 48 - y$, then $\Pi(y) = \rho(y) + y - 24$, because the trajectory will return in the next LD cycle and so on.

If there exists a y_s such that $y_s = \Pi(y_s)$ and $|\Pi'(y_s)| < 1$, then y_s is a stable fixed point of the map $\Pi(y)$, and it also determines a 1:1 phase locked solution. The phenomenon of 1:1 phase locking in this case occurs when the oscillator has one return to the Poincaré section for every one period of the LD forcing. When a stable solution exists, the map $\Pi(y)$ quite accurately calculates the time to approach the stable solution starting from any initial condition of y . Numerically we use the concept of entrainment to evaluate the convergence time. Suppose y_j is a sequence of iterates of the map, then we say the solution is entrained if there exists m , such that for all $j \geq m$, $|y_s - y_j| < 0.5$. The entrainment time is then $\sum_{i=1}^m \rho(y_i)$.

The 1-D O_1 -entrained map for the CNT system. The 1-D map for the NT system cannot be directly applied to the CNT system because the second oscillator will have additional free variables to determine, meaning that the entrainment map for the CNT system will be higher dimensional. However, for the hierarchical CNT system, if we assume that O_1 is already entrained, then the chain $LD \Rightarrow O_1 \Rightarrow O_2$ is reduced to O_1 -entrained $\Rightarrow O_2$. The system can be rewritten in the following manner:

$$(4) \quad \begin{aligned} \frac{1}{\phi_2} \frac{dP_2}{dt} &= M_2 - k_f h(P_2) - k_D P_2, \\ \frac{1}{\phi_2} \frac{dM_2}{dt} &= \epsilon [g(P_2) - M_2 + \alpha_1 M_1 g(P_2)]. \end{aligned}$$

In the O_1 -entrained case, O_2 is continuously forced by the coupling from O_1 . This differs from the coupling due to direct light input into O_1 which is a discontinuous square wave. We place a Poincaré section that intersects the entrained O_2 limit cycle solution at $\mathcal{P} : P_2 = 1.72, |M_2 - 0.1289| < \delta$ such that $P_2' < 0$, where δ is a small control parameter. In the results section, we will explain why trajectories are funneled into a region that forces them to cross this choice of Poincaré section. Along the section \mathcal{P} , P_2 is fixed, and M_2 is bounded by δ , so the only free variable is the phase of light. We define the 1-D O_1 -entrained map by

$$(5) \quad y_{n+1} = \Pi_{O_1}(y_n) = (y_n + \rho(y_n; \gamma(y_n))) \bmod 24,$$

where $y \in (0, 24]$ is defined to be the phase of the LD forcing, which has the same meaning as the 1-D entrainment map in [13]. We define $\gamma(t) := \varphi_t(X_0)$ to be the LD-entrained limit cycle of O_1 , where X_0 is a chosen reference point on $\gamma(t)$. We denote the set of points that lie on the limit cycle of O_1 by Γ_{O_1} . At X_0 , the lights just turn on for O_1 . In the O_1 -entrained case, the location of O_1 only depends on y_n and can be denoted by $\gamma(y_n)$. Based on the above definition, $\gamma(y_n)$ means a point on the limit cycle of O_1 when the light has been turned on for y_n hours. $\rho(y_n)$ measures the return time when O_2 first returns \mathcal{P} .

Notice that in the definition of the O_1 -entrained map, the phase of O_1 is determined by y (the phase of the LD forcing), since it is O_1 -entrained. This makes the O_1 -entrained map a 1-D map, and most of the properties of the NT model's 1-D map carry over to the O_1 -entrained

map. For example, if there is a point y_s , such that $y_s = \Pi_{O_1}(y_s)$ and $|\Pi'_{O_1}(y_s)| < 1$, then y_s is a stable fixed point of the O_1 -entrained map. The fixed points of the map also determine 1:1 phase locked solutions of the coupled system.

The general 2-D entrainment map. In the case of the O_1 -entrained map, the initial location of O_1 when O_2 lies on \mathcal{P} is always determined by y , the phase of the LD cycle. But in general, the initial location of O_1 doesn't always depend on y , rather it could lie arbitrarily in its phase space. To limit the possibilities, we restrict the initial location of O_1 to lie anywhere along its own limit cycle Γ_{O_1} . This restriction will therefore only introduce one new free variable and motivates us to generalize the map to two dimensions:

$$(x_{n+1}, y_{n+1}) = \Pi(x_n, y_n) = (\Pi_1(x_n, y_n), \Pi_2(x_n, y_n)).$$

We keep the definition of y_n and the location of the Poincaré section \mathcal{P} the same as in the O_1 -entrained map. We now introduce a new variable x to determine O_1 's position in phase space relative to its own LD-entrained solution. The detailed definition is explained using a phase angle.

Defining Π_1 using a phase angle. According to the O_1 -entrained map, the trajectory of O_1 always remains on Γ_{O_1} . However, if O_1 is not already entrained, then its trajectory may not lie on Γ_{O_1} but will instead approach it asymptotically. Thus we need a new independent variable to determine the position of O_1 for this situation. From the O_1 -entrained case, the position of O_1 can always be described as $\gamma(t)$, where $t \in (0, 24]$. The idea is to define a new independent phase variable x equivalent to the time variable t that is obtained by projecting the real location of O_1 onto its limit cycle Γ_{O_1} , while keeping the error small. We define the phase angle in the following steps:

(1) Transform the coordinate system appropriately: Shift the origin to the intersection point of the uncoupled O_1 's two nullclines. Then connect the origin and the point X_0 and expand the line segment as the x -axis of the new coordinate system. The y -axis is determined automatically to be orthogonal to the x -axis, as in Figure 2(a).

(2) Define x in terms of the phase angle: Consider the phase plane as a complex plane \mathbb{C} . Let's call the point X_0 as $z_0 = r_0 e^{i\theta_0} \in \mathbb{C}$, where $\theta_0 = 0$ after the coordinate system transformation. We can then represent any point on the limit cycle $\gamma(t)$ as a complex number $z = r e^{i\theta}$, where we define $\theta \in (0, 2\pi]$. Then x is defined to be the phase of O_1 when choosing X_0 as the reference point. In other words, $z = \gamma(x) = r e^{i\theta}$. Notice that x is homeomorphic to the unit circle \mathbb{S}^1 , because $\theta = \text{Arg}(\gamma(x))$; see Figure 2(a). The domain of x is also $\tilde{\mathbb{S}}^1 = (0, 24]$.

(3) Define the map Π_1 . Suppose we start integrating the system with any initial condition (x_n, y_n) (see Figure 2(a), lower panel as an example). After the time $\rho(x_n, y_n)$, O_2 returns to the Poincaré section, the new location of O_1 is now

$$\Psi_{\rho(x_n, y_n)}(\gamma(x_n)) = r_{n+1} e^{i\theta_{n+1}},$$

where $\Psi_t(X)$ is the flow of O_1 , and the phase angle is θ_{n+1} . We then find the unique point \hat{x} lying on Γ_{O_1} such that the phase angle of $\Psi_{\rho(x_n, y_n)}(\gamma(x_n))$ matches the angle associated with $\gamma(\hat{x})$. That is we choose \hat{x} such that $\text{Arg}(\gamma(\hat{x})) = \theta_{n+1}$. Geometrically, we are simply choosing \hat{x} as the associated value at which the ray passing through $\Psi_{\rho(x_n, y_n)}(\gamma(x_n))$ intersects $\gamma(t)$.

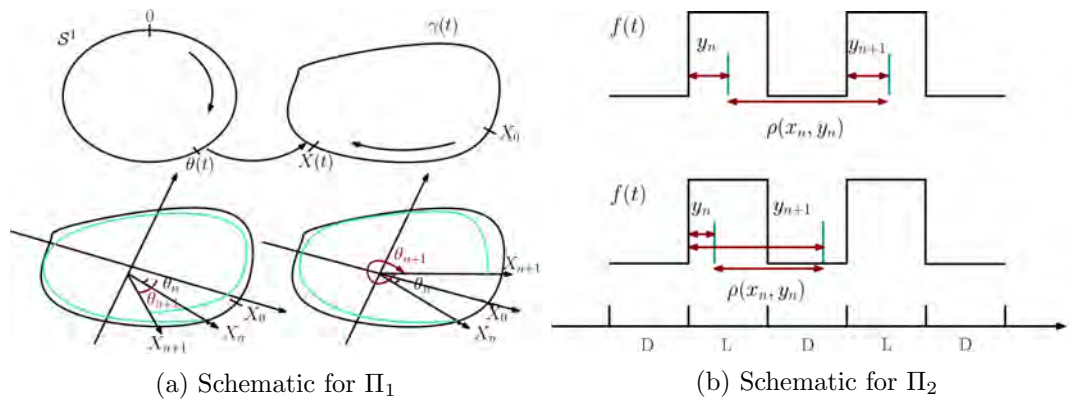


Figure 2. (a) The upper panel shows a schematic of the homeomorphism from the unit circle \mathbb{S}^1 to Γ_{O_1} . The lower panel shows how we construct the map in two different conditions; the left one shows the case when the phase angle θ associated with the trajectory of O_1 rotates through more than 2π , the right one is where the rotation is less than 2π . (b) In both panel schematics, the first blue vertical line segment denotes where we chose the initial phase of light. After time $\rho(x_n, y_n)$, the trajectory returns to \mathcal{P} , and the new phase of light is y_{n+1} . For the upper panel, $y_n + \rho(x_n, y_n) > 24$, so $y_{n+1} = y_n + \rho(x_n, y_n) - 24$. For the lower panel, $y_n + \rho(x_n, y_n) < 24$, so $y_{n+1} = y_n + \rho(x_n, y_n)$. The black square wave $f(t)$ in both panels represents the LD forcing.

We define $x_{n+1} = \hat{x}$. We can then write Π_1 as the following:

$$(6) \quad x_{n+1} = \Pi_1(x_n, y_n) = \{\hat{x} \in [0, 24) : \text{Arg}(\gamma(\hat{x})) = \theta_{n+1}\}.$$

(4) To numerically compute the map Π_1 , we integrate an initial condition where O_1 lies along its limit cycle and O_2 at \mathcal{P} , and integrate the system until O_2 returns to the section. We then use a linear map to shift the new location of O_1 to the coordinate system we set up in step 1. We transform the point into a complex number, and then use the built-in MATLAB function `angle()` to find the phase angle. Using this angle, we locate a point on the limit cycle of O_1 , that we had previously partitioned, with the same phase angle.

The definition of Π_2 is straightforward. We just mimic the construction of the O_1 -entrained map. The only difference is that the return time function ρ depends on both x and y , because O_1 is no longer O_1 -entrained:

$$(7) \quad y_{n+1} = \Pi_2(x_n, y_n) = y_n + \rho(x_n, y_n) \bmod 24,$$

where $y \in \tilde{\mathbb{S}}^1 = (0, 24]$ is defined on a homeomorphism of the unit circle \mathbb{S}^1 , $y = h(\theta) = \frac{12}{\pi} \times \theta$.

The schematic Figure 2(b) depicts a way to understand the definition of Π_2 . The first blue vertical line segment signifies the initial phase y_n of the lights when O_2 starts on \mathcal{P} . After time $\rho(x_n, y_n)$, the trajectory returns to \mathcal{P} , signified by the second blue vertical line segment, with the lights having turned on y_{n+1} hours ago. In the upper panel, $\rho(x_n, y_n) > 24 - y_n$, therefore, the trajectory does not return to \mathcal{P} within the same LD cycle. In the lower panel, $\rho(x_n, y_n) < 24 - y_n$, therefore, the trajectory does return to \mathcal{P} within the same LD cycle.

3. Results. In this section, we first show simulations demonstrating the entrainment of the strictly hierarchical CNT model. We then define and analyze a 1-D map in which O_1 is

assumed to already be entrained. We call this the O_1 -entrained map. Understanding the 1-D map will facilitate the definition and analysis of the 2-D entrainment map. Finally, we extend the results to the semihierarchical case.

3.1. The entrained solutions of the CNT model. To find the entrained solutions and understand the geometry of the strictly hierarchical CNT system in the presence of the LD cycle, the nullclines of each oscillator play an important role. The nullclines are the set of points where the right-hand sides of (2) equal zero and will be different for each of the oscillators. For O_1 , there are two different P -nullclines corresponding to the dark or light condition manifested through the square-wave forcing $f(t)$ and a single M -nullcline:

$$(8) \quad \begin{aligned} N_{P_D} : M_1 &= k_f h(P_1) + k_D P_1, \\ N_{P_L} : M_1 &= k_f h(P_1) + (k_D + k_L) P_1, \\ N_{M_1} : M_1 &= g(P_1). \end{aligned}$$

For O_2 , there is a single P -nullcline (since $k_{L_2} = 0$), but a family of M -nullclines since the coupling from O_1 is continuous rather than discrete:

$$(9) \quad \begin{aligned} N_P : M_2 &= k_f h(P_2) - k_D P_2, \\ N_{M_2} : M_2 &= g(P_2) + \alpha_1 M_1 g(P_2). \end{aligned}$$

Each P -nullcline is a cubic shaped curve. Note that N_{P_D} and N_{P_L} are independent of the variables P_2 and M_2 . In the four-dimensional space (P_1, M_1, P_2, M_2) they actually correspond to hypersurfaces. But since the equations governing the evolution of O_1 are independent of O_2 , we simply project and view N_{P_D} and N_{P_L} as curves in (P_1, M_1) space (Figure 3(a)). We similarly view the sigmoidal nullcline N_{M_1} as a curve in this phase plane. We project the nullclines of O_2 onto the (P_2, M_2) space (Figure 3(c)). Note that N_{M_2} now represents a continuum of sigmoidal shaped curves that vary depending on the value of M_1 . When O_1 is entrained, along its limit cycle, the M_1 value is bounded between $\min |M_1(t)|$ and $\max |M_1(t)|$. Thus N_{M_2} can oscillate between $N_M^{\min} : M_2 = g(P_2) + \alpha_1 \min |M_1(t)| g(P_2)$ and $N_M^{\max} : M_2 = g(P_2) + \alpha_1 \max |M_1(t)| g(P_2)$. We assume that any intersection between N_P and N_M occurs on the middle branch of the corresponding cubic nullclines. This will guarantee that any ensuing fixed points of the CNT system are unstable and will allow oscillations to exist.

We plot the entrained solution of the CNT by direct simulation. In our simulations, we take a specific set of parameters for (2), i.e., $\phi_1 = \phi_2 = 2.1$, $\epsilon_1 = \epsilon_2 = 0.05$, $k_D = 0.05$, $k_{L_1} = 0.05$, $k_{L_2} = 0$, $k_f = 1$, $\alpha_1 = 2$. In Figure 3(a), the periodic solutions of O_1 are presented for different light conditions. The dashed black (red) limit cycle denotes the stable solution of O_1 in DD (LL) conditions. The solid red-black limit cycle denotes the LD-entrained solution of O_1 , with hourly markings shown by green open circles. We also show various nullclines and note that the M nullcline (yellow curve) is unique, but the P -nullcline (red and blue curves) varies between $M_1 = (k_D + k_L)P + k_f h(P)$ and $M_1 = k_D P + k_f h(P)$. The corresponding time courses are shown for the P_1 variable in Figure 3(b).

In Figure 3(c), we show the entrained solutions of O_2 when O_1 is in different light conditions. The color convention is the same as in Figure 3(a). Here, we note that the P -nullcline (blue curve) is unique, but the M -nullcline (red and yellow curves) varies between

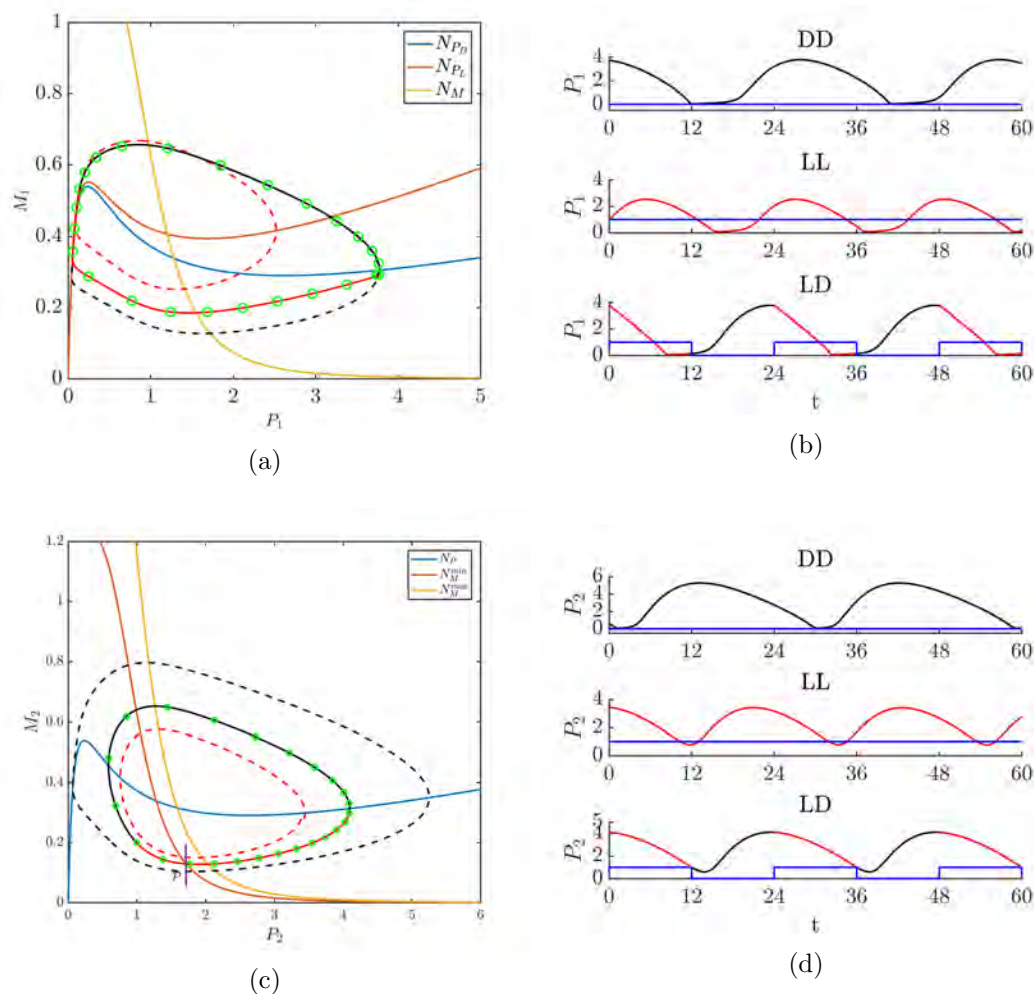


Figure 3. (a) The periodic solutions of O_1 in DD, LL, and LD conditions. The dashed black trajectory represents the DD limit cycle ($f(t) \equiv 0$), the dashed red trajectory represents the LL limit cycle ($f(t) \equiv 1$). The solid trajectory represents the LD solution with green hourly markers. The two different P_1 nullclines, N_{P_D} and N_{P_L} and the single M_1 nullcline, N_{M_1} , are shown. Note that for panels (a) and (c) the horizontal scale is much larger than the vertical scale. (b) The time course plots: P_1 versus t in all three cases (blue line lies at 0, 1, or is a square wave for DD, LL, or LD, respectively). (c) The periodic solutions of O_2 when O_1 is in DD, LL, and LD conditions. Same color scheme as in (a). The Poincaré section is represented at $P_2 = 1.72$ by a small vertical line segment. Note that only the maximal and minimal sigmoidal M_2 nullclines, N_M^{\min} and N_M^{\max} , are shown that bound the family of nullclines that exist for this case. (d) The time course plots: P_2 versus t in DD, LL, and LD conditions.

$M_2 = (1 + \alpha_1 \min |M_1(t)|)g(P_2)$ and $M_2 = (1 + \alpha_1 \max |M_1(t)|)g(P_2)$. We also show the time course plots related to the same condition in Figure 3(d). The time course plots show that the period of the DD solution is longer than that of LD, and the period of the LL solution is shorter than that of LD. In particular, we found that the period of the DD cycle is 28.9 h, which is the same as the DD cycle of O_1 , and the period of the LL cycle is 21.6 h, which

is also the same as the LL cycle of O_1 . This is not surprising, because when the coupling is strong enough, O_2 is entrained by O_1 .

The nullclines shown in Figure 3(c), together with the dashed LL and DD O_2 limit cycles, are useful to explain our choice of the Poincaré section at $P_2 = 1.72$, centered at $M_2 = 0.1289$. It is straightforward to use the vector field and phase plane analysis to show that any trajectory starting on \mathcal{P} will evolve clockwise and cross the right branch of N_P with $P_2 > 3$. Because of the difference in scaling of the vertical and horizontal components of that phase plane it may not be so obvious that the M_2 value does not vary much for points along the right branch between where the LL (dashed red) and DD (dashed blue) limit cycles intersect it. In the LD situation, a trajectory will intersect the right branch of the N_P nullcline somewhere between a neighborhood of each of these points. We now show that any two trajectories with initial conditions lying on this nullcline in that region remain close in their M_2 value. Suppose we have a trajectory cross the right branch of N_P at $(\tilde{P}_2, \tilde{M}_2)$, where $\tilde{P}_2 > 3$, so that

$$\tilde{M}_2 = H(P_2) = k_f h(\tilde{P}_2) + k_D \tilde{P}_2.$$

Taking a derivative of the function on the right-hand side and, for convenience, using x to represent the P_2 variable, yields

$$H'(x) = k_f h'(x) + k_D = k_f \frac{0.1 - x^2}{(0.1 + x + x^2)^2} + k_D.$$

When x is large, $H'(x) \rightarrow k_D$, implying $H(x) \approx k_D x$, where k_D is a small parameter. So when $\tilde{P}_2 > 3$,

$$H(x_1) - H(x_2) \approx k_D(x_1 - x_2).$$

Thus the difference of M_2 between two points on the right branch of N_P is small. Next we show that those points have approximately the same dynamics in the M_2 direction. When P_2 is large, $g(P_2) \rightarrow 0$, the second equation of (4) is approximately

$$\begin{aligned} \frac{dM_2}{dt} &= -\phi_2 \epsilon M_2, \\ M_2(t) &= \tilde{M}_2 e^{-\phi_2 \epsilon t}. \end{aligned}$$

The main point here is that the effect of M_1 is gone, so trajectories evolve largely independent of the coupling. Since any initial points lying on the region of the right branch of the N_P nullcline are close in their M_2 value, it is an easy application of Gronwall's inequality to show that they remain close until P_2 becomes sufficiently smaller. Thus those trajectories are funneled into the small region between the LL and DD limit cycles and cross the Poincaré section.

We note that our choice of Poincaré section is dictated by the funneling effect. For example, choosing the section elsewhere, say $P_2 = 3$, $|M_2 - 0.521| < \delta$, $\delta > 0$ but small, would not guarantee that trajectories cross through this section again. Trajectories will, of course, cross $P_2 = 3$ with $P_2' > 0$, but won't necessarily do so in a small neighborhood of the LD-entrained solution.

3.2. The O_1 -entrained map. The O_1 -entrained map we obtained from (5) has similar properties as the entrainment map Diekman and Bose constructed in their paper [13]. Figure 4 shows that there are two fixed points which correspond to different types of periodic solutions for the CNT system. The lower one with $y_{n+1} = y_n = 10.2$ is a stable fixed point of the map, which represents a stable periodic solution. The upper one with $y_{n+1} = y_n = 17.2$ is an unstable fixed point of the map.

We classify the direction of entrainment as occurring through phase advance or phase delay. Suppose $y_{n+1} = \Pi_{O_1}(y_n)$, and the return time needed from y_n to y_{n+1} is less than 24 hours. We call this a phase advance. Alternatively, if the return time is greater than 24 hours, we call it a phase delay. The unstable fixed point of the map plays an important role in determining this direction. For example, pick two different initial conditions ($y_0 = 16.5, 18$) near the unstable fixed point and use the cobweb method to observe how different directions of entrainment can occur. For $y_0 = 16.5$, the iterates move to the left and converge to the stable solution by phase advance. For $y_0 = 18$, however, the iterates move to the right and converge to the stable solution by phase delay. In Figure 4(b), we compare the iterates with simulations; the green curve corresponds to $y_0 = 16.5$ and the magenta curve corresponds to $y_0 = 18$. The black curve is the entrained solution for O_2 . The direction of entrainment from the simulations agrees with the calculations obtained from the map.

In our model system, there are two parameters of interest, the coupling strength α_1 and the intrinsic period of O_2 governed by ϕ_2 . In Figure 4(c), we decrease α_1 from 2.5 to 1.4, so that the coupling strength is weaker. As a result, the return time $\rho(y)$ increases. This makes the map move up, and the stable and unstable fixed points get closer to each other. At $\alpha_1 = 1.51$, the two fixed points collide at a saddle-node bifurcation. In Figure 4(d), we increase the intrinsic period of O_2 by decreasing ϕ_2 from 2.3 to 1.9, so that the difference between the intrinsic period and the 24-h forcing increases, which increases the return time to the Poincaré section. Hence the map moves up. When $\phi_2 = 1.91$, the map passes through the saddle-node bifurcation value. The disappearance of the stable fixed point means that in the full system 1:1 entrainment is lost and replaced by higher order periodic behavior. The details of this kind of behavior are interesting in their own right, but an investigation of this behavior is beyond the scope of this work.

Notice that the O_1 -entrained map we construct is not monotonic, which makes it different from the 1-D entrainment map found in [13]. To understand this nonmonotonicity, we take two initial conditions ($y_0 = 6$ and $y_0 = 8$) near the local maximum of the map in Figure 5(a), and analyze the dynamics of the system. Associated with the return time plot in Figure 5(b), we found that the return time is between 28 and 29 when y is less than the local maximum point. But when it crosses that point, the return time decreases quickly with the derivative $\rho'(y) < -1$. In Figure 5(c), we plot the trajectories with the two initial conditions. The trajectory for $y_0 = 6$ flows to the left branch of the P -nullcline, which increases the return time since evolution near this branch is slow. Alternatively, the trajectory for $y_0 = 8$ doesn't flow near the left branch and thus has a shorter return time. A minor consequence of this nonmonotonicity is that some solutions converge to the stable fixed point by initially phase delaying, but then ultimately phase advancing. For example, in Figure 5(d), we take $y_0 = 18$ then cobweb the map. We find that the first four iterates initially phase delay. The fourth iterate lands near the local maximum of the map, which lies above the value of the fixed point.

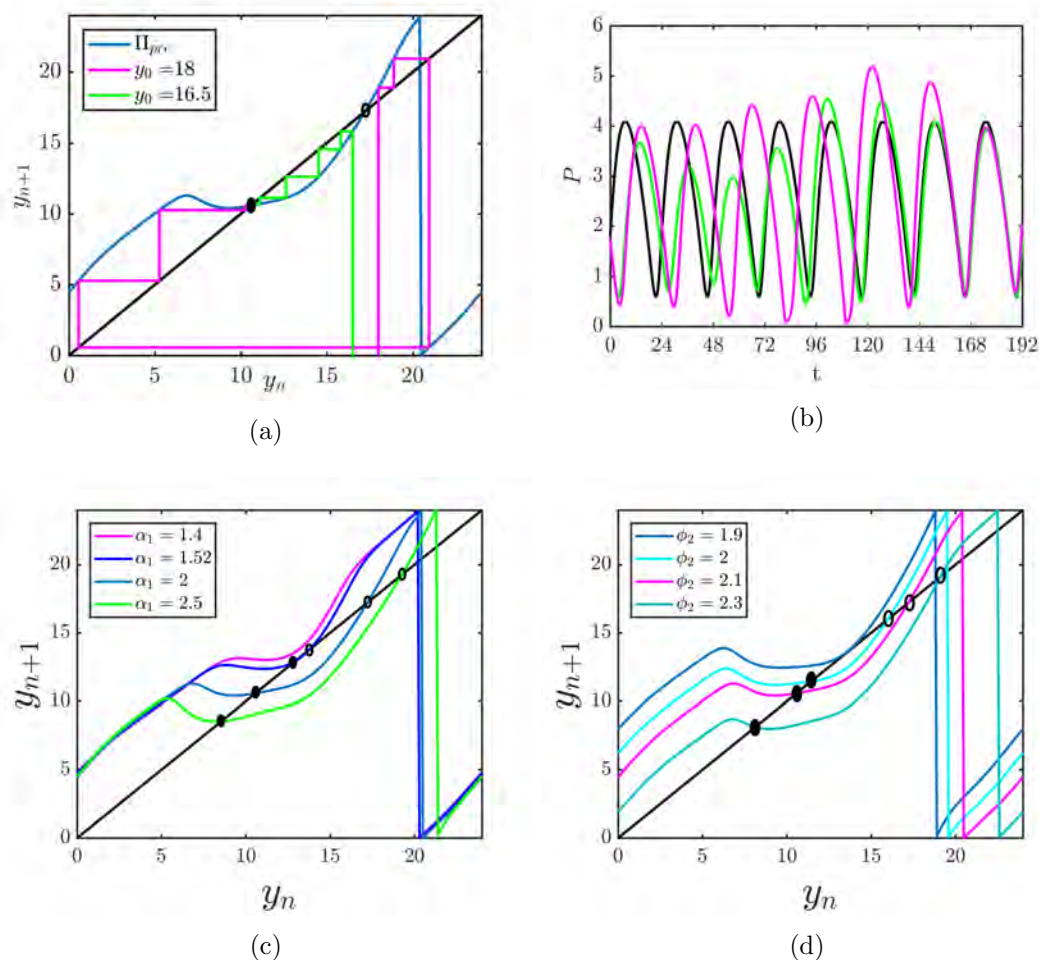


Figure 4. (a) The cobweb diagram for the O_1 -entrained map. We pick two different initial conditions and show how the iterates move to the stable fixed point. (b) The approach to the stable solution (black curve) in the t versus P plane; the colors correspond to the two initial conditions in (a). (c) The map displays a saddle-node bifurcation by decreasing α_1 . (d) Decreasing the intrinsic period of O_2 by decreasing ϕ_2 also leads the map to display a saddle-node bifurcation. Fixed points shown as open circles are unstable, and those shown with solid circles are stable.

This causes subsequent iterates to phase advance. This nonmonotonicity foreshadows a more complicated picture that arises under the dynamics of the 2-D map.

3.3. The results of the general 2-D map. In this section, the analysis of the 2-D map is presented. We follow ideas first derived by Akcay, Bose, and Nadim [1] and followed up on in [2] to find fixed points of the map via a geometric method. The entrainment time and the direction of entrainment are analyzed by iterating the map. We also compare these results with simulations. At the end of this section, we show that the map is also applicable to the semihierarchical model.

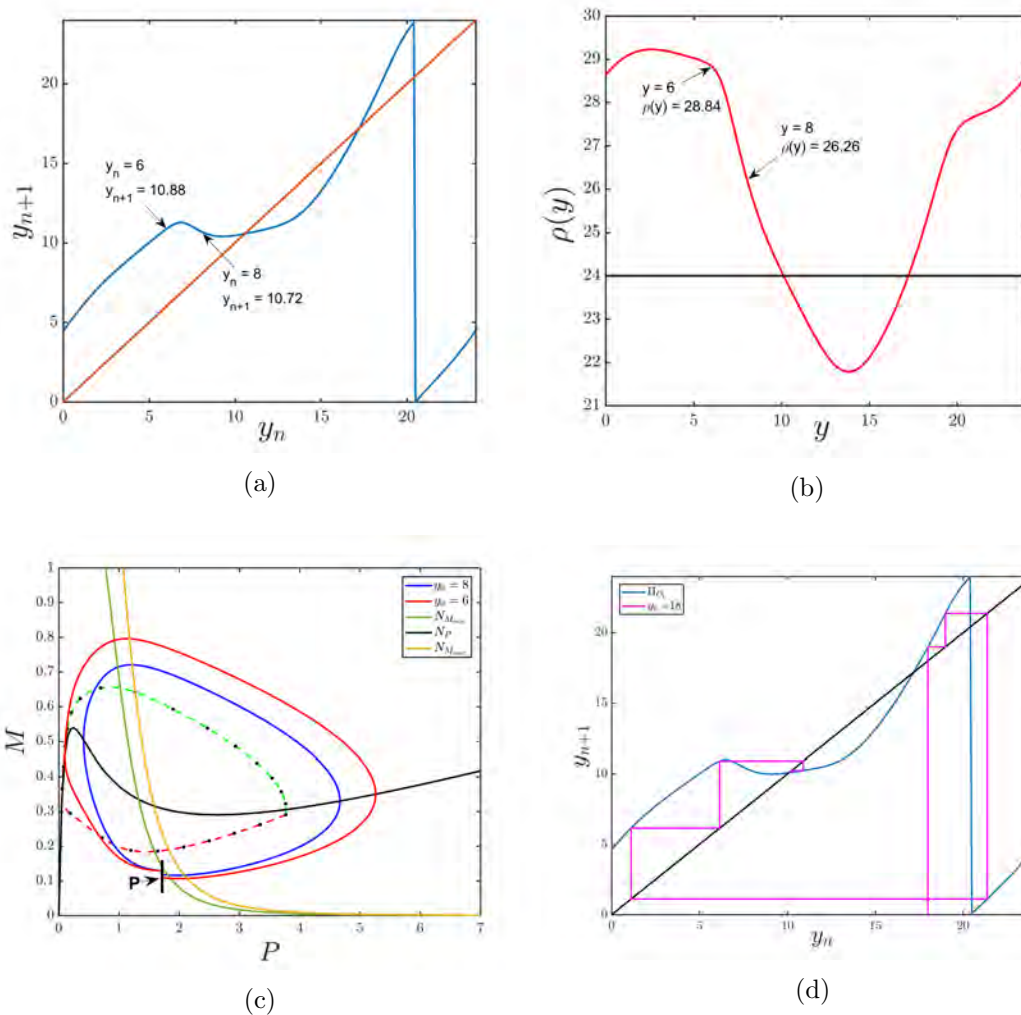


Figure 5. Nonmonotonicity in the entrainment map leads to convergence initially due to phase delay but ultimately due to phase advance. (a) The nonmonotone O_1 -entrained map and two choices of initial conditions near the local maximum. Note that the local maximum lies above the value of the fixed point of the map. (b) The return time plot associated with the two initial conditions. (c) The corresponding phase plane. The solid blue trajectory for $y_0 = 8$ does not approach the left branch of N_P , while the solid red trajectory for $y_0 = 6$ does, causing its evolution to slow down. (d) Starting with an initial condition $y_0 = 18$, the first four iterates phase delay. The fourth iterate lands near the local max of the map, and subsequent iterates then phase advance.

Basic results from the map. Both parts of the 2-D map Π_1 and Π_2 are surfaces in relevant 3-D spaces. Because of the mod 24 operation, each surface will contain discontinuities. In Figures 6(a) and 6(b), we project the surface onto the x - y plane. For Π_1 , the purple part of the surface is points lying above the diagonal plane $z = x$, in other words, $x_{n+1} > x_n$. The red part of the surface of Π_2 is points lying above the diagonal plane $z = y$, i.e., $y_{n+1} > y_n$. The points of gray color denote all points that are below the diagonal planes, $x_{n+1} < x_n$ and

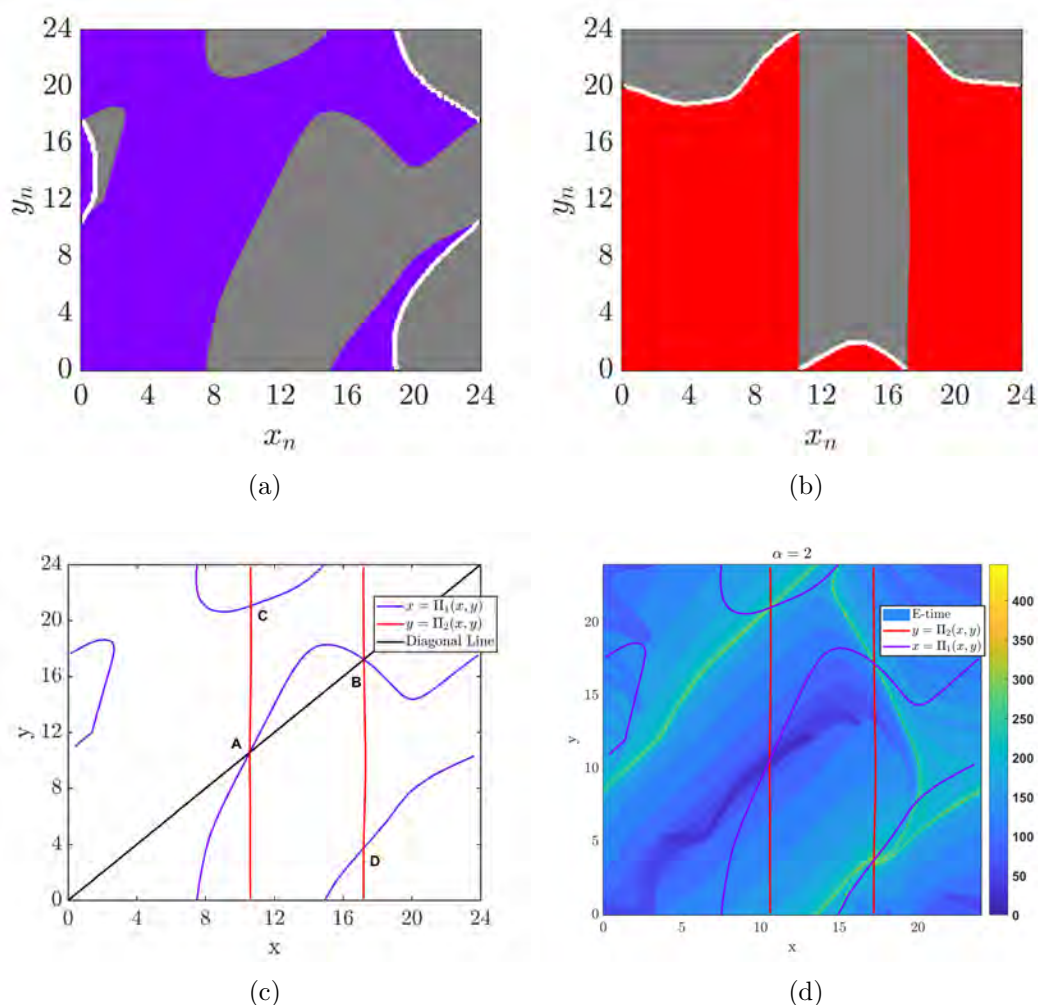


Figure 6. (a) and (b) The 2-D entrainment map is plotted as two separate maps Π_1 and Π_2 , and projected onto the domain space (x_n, y_n) . The purple and red color in both maps denote all points that are above the diagonal plane. The gray color denotes points that are below the diagonal plane. The white curves denote the discontinuity. (c) The purple curves denote points of Π_1 's nullcline N_x , where $x = \Pi_1(x, y)$, the red curves denote points of Π_2 's nullcline N_y , where $y = \Pi_2(x, y)$. Their intersections are the four fixed points of the map. (d) The entrainment time is plotted with a heatmap. The color denotes the entrainment time starting from a specific initial condition. The light green curves locate $W^s(B)$ and $W^s(C)$ from near which the longest entrainment times occur.

$y_{n+1} < y_n$. The white curves indicate locations of discontinuity of the map. The separation of the two different colors consists of curves which indicate the points where $x = \Pi_1(x, y)$ and $y = \Pi_2(x, y)$. Here we define those curves as nullclines of the map:

$$N_x = \{(x, y) : x = \Pi_1(x, y)\}, \quad N_y = \{(x, y) : y = \Pi_2(x, y)\},$$

which are plotted in Figure 6(c). The purple curves denote N_x . Similarly, the red curves

Table 1

Numerical computation of the eigenvalues of the map at the four fixed points. Eigenvalues with modulus less than one correspond to stable directions, while those with modulus greater than one correspond to unstable directions.

	x	y	Eigenvalue	Stability
A	10.6	10.6	0.1609, 0.4453	sink
B	17.2	17.2	2.0858, 0.4238	saddle
C	10.6	21.1	2.325, 0.2734	saddle
D	17.2	3.7	1.595+0.77i, 1.595-0.77i	source

denote N_y . Their intersections are four fixed points of the map. We numerically calculated the Jacobian at those fixed points and found the eigenvalues of the linearization. These values and the corresponding stability of each fixed point are shown in Table 1. From the results of the O_1 -entrained map, points A and B lying on the diagonal line correspond to the stable solution of O_1 . For O_2 , point A corresponds to the stable solution. For point B, the trajectory of O_2 returns to the Poincaré section after 24 hours but corresponds to the unstable solution of the O_1 -entrained map. At the fixed point C, O_1 lies on its own unstable periodic orbit. This can be inferred from and agrees with the calculation of Diekman and Bose [13] who showed that the original 1-D entrainment map has an unstable fixed point that corresponds to an unstable periodic orbit. Thus O_1 is entrained to a 24-hour LD cycle and provides a 24-hour forcing to O_2 . From simulation, we found that the trajectory of O_2 stays for several cycles near what appears to be a stable limit cycle, though it is different from the limit cycle corresponding to point A since O_1 is unstable and the forcing signal to O_2 is different. At point D, if we check the difference between C and D, we can see that

$$(x_D, y_D) = (x_C, y_C) + 6.6 \text{ mod } 24,$$

so O_1 is still on its unstable periodic orbit. That is, points C and D represent conditions where the forcing $M_1(t)$ is identical, but just phase shifted by 6.6 hours. Thus O_2 still receives 24-hour forcing so we also expect there to exist an unstable O_2 limit cycle for this case.

One advantage of the map is its ability to estimate the entrainment time. Starting from different initial conditions, we iterate the map $(x_{n+1}, y_{n+1}) = \Pi(x_n, y_n)$ until $\|(x_{n+1}, y_{n+1}) - (x_s, y_s)\| < 0.5$, where point A has coordinates (x_s, y_s) . The entrainment time is the sum of the return times corresponding to each iterate. In Figure 6(d), we show the entrainment times corresponding to different initial conditions on the torus expanded as a square. We also plot the nullclines N_x and N_y on top of it for illustrative purposes. The color for each point on the square denotes the entrainment time needed for that initial point.

Notice that, in Figure 6(d), there are two light green curves. Along these curves, the entrainment time is much longer than other regions. Additionally, they appear to connect the two saddle points B, C with the unstable source D. Though not proven here, we believe that these curves locate where the stable manifolds of the saddle points B and C ($W^s(B)$ and $W^s(C)$) are. To completely understand the dynamics of the entrainment map, it is useful to numerically find the stable and unstable manifolds.

The algorithm we used to find the manifolds of the entrainment map are based on the following results. For the unstable manifold, Krauskopf and Osinga [26] introduced a growing

method to calculate the unstable manifold point by point. They initially iterate points chosen in a neighborhood of the fixed point along the associated unstable eigenvector and accept new points as lying on the unstable manifold if they satisfy specific constraints. For the stable manifold, the search circle (SC) method introduced by England, Krauskopf, and Osinga [16] utilizes the stable eigenvector to find points within a certain radius that iterate onto a segment of the stable eigenvector. The SC method has the advantage that it does not require the inverse of the map to exist, which is important for us since our map is noninvertible. Both of these methods are constructed for planar nonperiodic domains. In our case, the map lives on a torus, but is graphically shown on a square. Whenever an iterated point exceeds the boundary of the square, we use the modulus operation to define the correct value within the square. Thus we develop our algorithm to account for this discontinuity. Another difference is that the terminating conditions for both the growing and SC methods rely on calculating the arc length of the manifolds up to a certain predetermined length. However, in our map, the stable manifolds of points B and C are generated from the source point D, while their unstable manifolds terminate at point A. Thus our algorithm terminates when these manifolds enter prescribed neighborhoods of those corresponding fixed points D and A.

In Figure 7(a), we choose initial points ranging from $0 < x < 24, 0 < y < 24$, and iterate ten times for each initial point. The arrow on each coordinate is pointing to its own next iterate. The obtained vector field give us another visualization of the map. In Figure 7(b), the numerical result of stable and unstable manifolds of B and C are plotted (also overlaid in panel (a) for easier comparison). $W^s(B)$ and $W^s(C)$ agree with the light green curves in Figure 6(d). $W^u(B)$ is exactly the diagonal line of the phase plane, which is not surprising. Because the diagonal line corresponds to the O_1 -entrained case, if an iterate starts on the diagonal line, it stays on it. The numerical calculation of the eigenvector of $E^u(B)$ is approximately $(0.7, 0.7)$ on the diagonal line, which means $W^u(B) = E^u(B)$. $W^u(C)$ also matches the darkest region in Figure 7(a). Indeed, these dark regions indicate the location of the unstable manifolds of points B and C. The located manifolds are also helpful for understanding the direction of entrainment of 2-D maps. In the case of the 1-D map, the direction of entrainment is essentially either phase advance or delay, and the longest entrainment times happen for initial conditions lying near the unstable fixed point. In the case of the 2-D map, the direction of entrainment need no longer be monotonic. The manifolds associated with the saddle points B and C appear to behave like a separatrix, despite this being a map and not a flow. To classify the direction of entrainment in the 2-D map, we consider phase delays and advances in the x and y directions separately. For the x direction, if the rotated angle from x_n to x_{n+1} is greater than 2π , we call it phase delay, otherwise we call it phase advance. For the y direction, we use the same definition as in the O_1 -entrained map. To illustrate different directions of entrainment, we pick several initial conditions near the stable manifolds, then iterate the map. We also run simulations with the same initial conditions for comparison. For Figure 8(a), in the left panel, we pick an initial point slightly above $W^s(C)$. It entrains to the stable solution by phase delay in the y direction, and phase delay-advance-delay in the x direction. In the right panel, the initial point is slightly below $W^s(C)$, but the entrainment is through phase delay-advance in y , and phase delay-advance in x . The corresponding simulations in Figure 8(b) agree with the direction of entrainment found through the map and demonstrate the sensitivity to initial conditions.

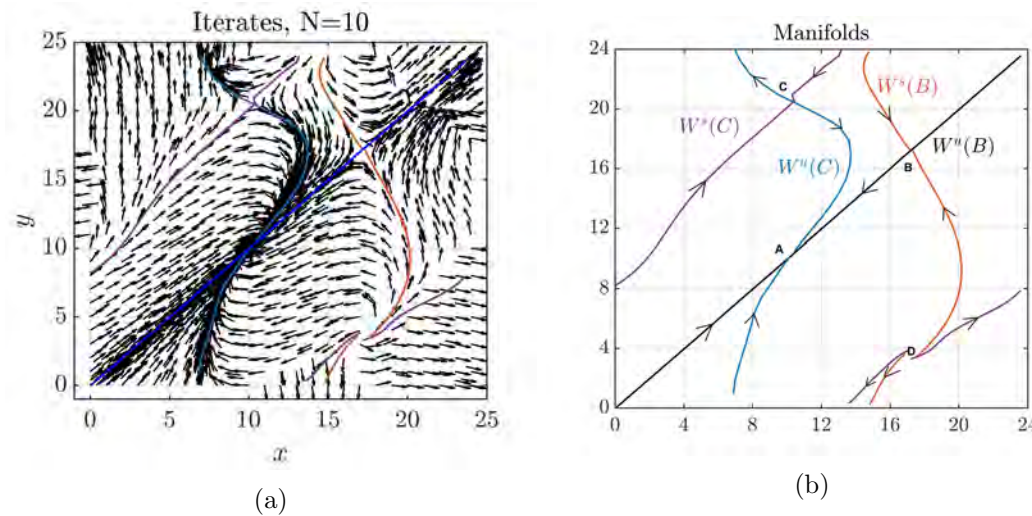


Figure 7. (a) $N = 10$ iterates from various initial points are shown. The arrow at each coordinate point is in the direction of the next iterate. The vector field indicates that there may exist a separatrix type structure at both points B and C . (b) Stable and unstable manifolds of B and C as generated through the generalization of the search circle and growing methods (see text) which are also overlayed in panel (a). The labeled manifolds do appear to provide a separatrix type behavior despite this being a map and not a flow.

Parameter dependence of the map. In the section on the O_1 -entrained map, we calculated the O_1 -entrained map for four different values of α_1 , and found the system will lose entrainment if the coupling strength is too small. Now we calculate the 2-D map at different values of α_1 to see how the fixed points and the entrainment time depend on α_1 . In Figures 9(a) and 9(b), we show the x and y nullclines for three different α_1 values; the points with a solid circle are the stable fixed points, the points with open circles are the unstable fixed points, and the starred points are saddle points. In Figure 9(c), we show the heatmap of entrainment times for $\alpha_1 = 1.52$. In Figures 9(d), we show the heatmap of entrainment times for $\alpha_1 = 2.5$. Note that $\alpha_1 = 2$ is our canonical case, and was presented before in Figure 6(d). Increasing α_1 , in general, decreases the entrainment time as can be observed from the color scale values (yellow max value ≈ 700 for $\alpha_1 = 1.52$) versus 400 for $\alpha_1 = 2.5$. In other words, stronger coupling between the central to peripheral oscillator speeds up entrainment.

The 2-D map for the semihierarchical case. For the strictly hierarchical model with only one feedforward connection from O_1 to O_2 , we have shown how to construct both the O_1 -entrained map and the general 2-D entrainment map. Here we will show that the 2-D map can be derived for the model when $0 < k_{L_2} < k_{L_1}$. In this case, O_1 is still dominant, allowing us to keep a semihierarchical structure.

We take $k_{L_2} = 0.025$, and keep the values of other parameters the same, so that O_1 and O_2 both receive light forcing. We define the Poincaré section $\mathcal{P} : P_2 = 1.72, |M_2 - 0.1548| < \delta$. We then obtained a 2-D map for this model. In Figures 10(a) and 10(b), the top view of Π_1 and Π_2 are presented. In Figure 10(c), we similarly obtained 4 fixed points (A,B,C,D) as in the strictly hierarchical case. Compared to the strictly hierarchical model, we found that the additional light forcing into O_2 accelerates the entrainment process, so that the time to

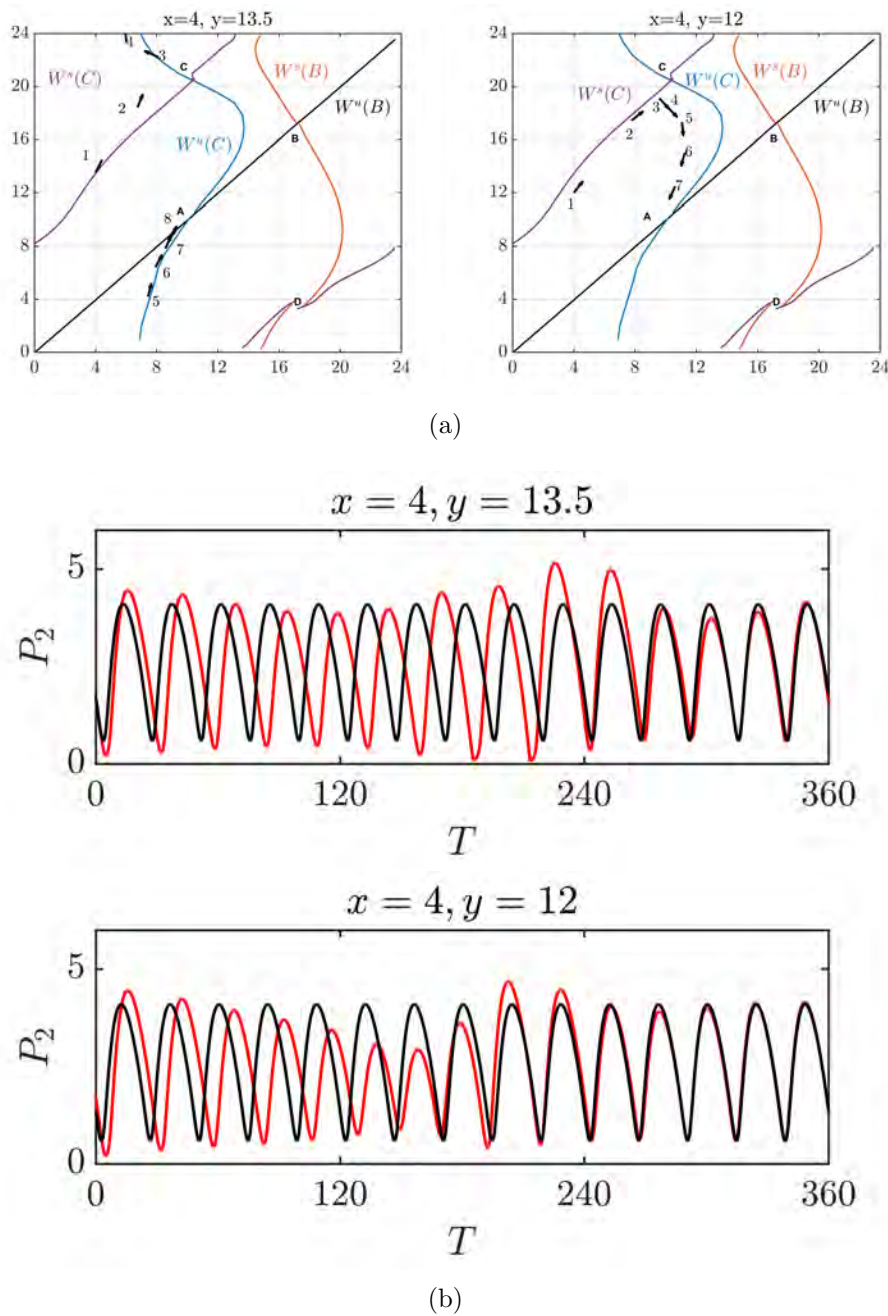


Figure 8. Direction of entrainment depends sensitively on initial conditions. (a) The initial point (labeled 1) in the left panel lies above $W^s(C)$, while the similarly labeled point in the panel to the right lies below $W^s(C)$. Numbers indicate iterates. As shown, the direction of entrainment differs significantly. (b) Corresponding simulations agree with the iterates. Note the top panel shows that O_2 (red time course) entrains through phase delay to the entrained solution (black time course); the lower panel shows O_2 entraining through phase advance.

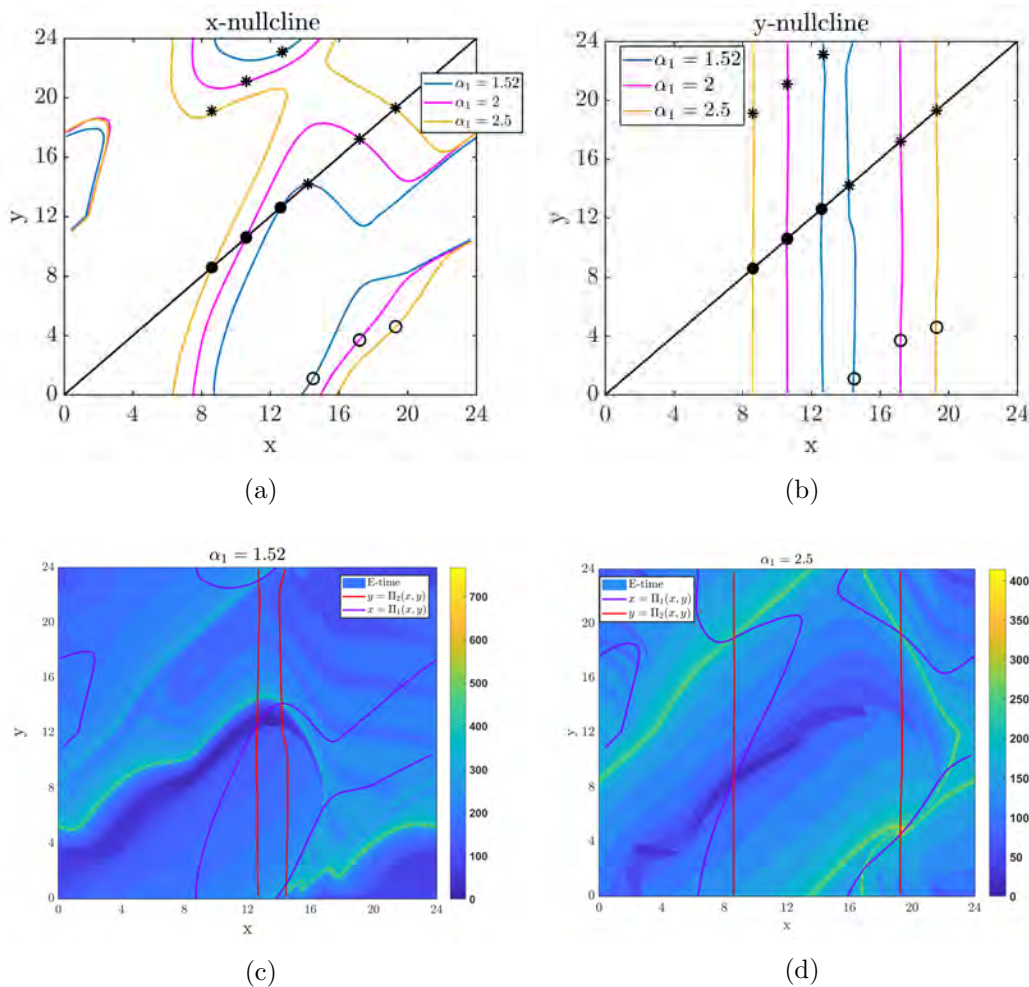


Figure 9. (a)–(b) The x and y nullclines under different α_1 values. Solid circles denote stable fixed points, open circles unstable fixed points, and stars saddle points. (c)–(d) The heatmap of entrainment times for different values of α_1 . Note the difference in numeric value of the maximum value of the color scale.

return to \mathcal{P} is decreased. Thus the whole surface shifts down, which causes A to move to the left of the diagonal, and B to move to the right of the diagonal. For points C and D , the limit cycle of O_2 is now determined by both O_1 and the light forcing, which changes the location of C and D . In Figure 10(d), we calculated the first 10 iterates of each initial point. Comparing these results with the strictly hierarchical case, the stability of each fixed point remains unchanged, but their location has changed. Further, the entrainment time required for each initial condition is reduced because of the LD forcing into O_2 .

4. Discussion. Circadian oscillations exist from the subcellular level involving genes, proteins, and mRNA up to whole body variations in core body temperature. These oscillations are typically entrained to the 24-hour LD cycle. Additionally, food, exercise, exterior temperature, and social interactions can also act as entraining agents in certain species [34]. In

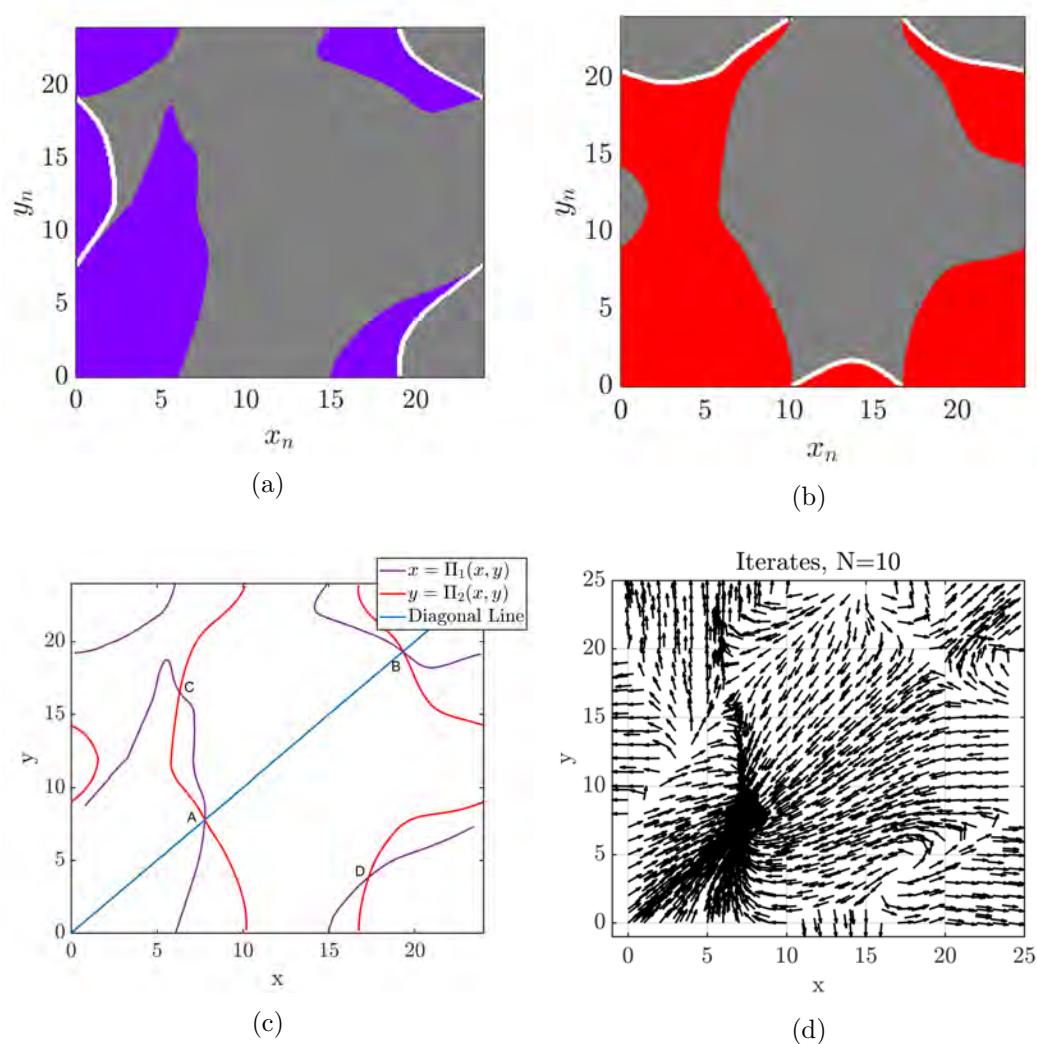


Figure 10. 2-D semihierarchical case. (a)–(b) The top view of Π_1 and Π_2 are presented; see Figures 6(a) and 6(b) for an explanation of color coding. (c) We obtained 4 fixed points (A,B,C,D) with similar stability of the canonical model. (d) Ten iterates of each point. The vector field looks qualitatively similar to the strictly hierarchical case shown in Figure 7(a).

these cases, various pathways in each species exist which carry the entraining information to relevant parts of the circadian system. In this paper, we refer to the set of oscillators that first receive this input as central circadian oscillators. In turn, these central oscillators send signals about the time of day to other peripheral oscillators. When viewed in this manner, we obtain a hierarchical circadian system. For example, in the strictly hierarchical model (Figure 1(a)), the central oscillator O_1 could represent the suprachiasmatic nucleus (SCN), the master pacemaker in the hypothalamus of mammals. The peripheral oscillator O_2 that does not receive light input could represent circadian clocks in organs such as the heart or

kidney. Alternatively, O_1 could represent the part of the SCN that directly receives light input (the ventral core), and O_2 could then represent the part of the SCN that does not (the dorsal shell) [21]. For the semihierarchical model (Figure 1(b)), O_1 and O_2 could represent the central and peripheral clocks in *Drosophila*, since in flies the clock protein cryptochrome is a photoreceptor and thus even peripheral organs receive some direct light input [11]. The main goal of this paper has been to develop a low-dimensional method to study the basic properties of hierarchical systems such as the existence and stability of entrained solutions, together with how the phase and direction of entrainment of the constituent oscillators depend on important parameters.

In this work, we have focused on how a hierarchical circadian system entrains to an external 24-hour LD cycle. To do so, we developed a method, partly analytic and partly computational, to assess the existence and stability of the entrained solution. Generalizing the approach of Diekmann and Bose [13], we derived a Poincaré map by placing a section in the phase space of the peripheral oscillator O_2 . The phase of O_1 with respect to a reference point on its own limit cycle, x , and of lights y , was then determined to derive the 2-D map. With this approach, we were able to determine that over a large set of parameters, the 2-D map possesses four fixed points, each of which corresponds to a periodic orbit of the hierarchical circadian system. Only one of these fixed points is asymptotically stable. The other three fixed points are unstable. We showed how one of them, labeled D in Figures 6(c), 7(b), and 10(c), is a source from which iterates emerge, including the stable manifolds of the two saddle points B and C. These manifolds appear to act as separatrices in the x - y domain of the map in the sense that, although they are for a map and not a flow, the manifolds separate the direction of convergence towards the stable fixed point A. Perhaps this is not so surprising as the saddle structure of the fixed points implies the existence of a saddle structure of the periodic orbits associated with points B and C. In the full 5-D phase space of the flow, each of the corresponding 1-D stable and unstable manifolds from the map become 3-D; the motion along the O_1 and O_2 limit cycles provide the additional two dimensions. This would be enough to form a separatrix in the 5-D phase space.

There are several findings of our work that are readily revealed through the 2-D map. First, in a strictly hierarchical system, central oscillators typically entrain first. This can be seen quite clearly from Figure 7(a) which shows that iterates of the map congregate along the diagonal line, which represents the O_1 -entrained subset of the 2-D map. This figure also shows that the peripheral oscillators may entrain in a different direction than the central oscillator or may in fact change their direction of entrainment during the transient. Given that direct light input speeds up entrainment, it is intuitively clear to see why entrainment times are, in general, less for semihierarchical compared to strictly hierarchical systems; see Figure 10. A second finding involves the stable and unstable manifolds of the fixed points. Despite this being a map, these manifolds help to organize the iterate structure. In particular, the stable manifolds of the unstable saddle points create a tubular neighborhood of initial conditions that lead to very long entrainment times, as seen in Figure 6(d). Determining that the unstable node and saddle points of the map actually exist is yet another important consequence of our map-based approach. Simulations alone would be unlikely to reveal either the existence or the role of these fixed points. Finally, effects of changing relevant parameters are readily explained

using the map. For example, the limits on parameters of entrainment are readily observed if the coupling to the peripheral oscillator is too weak or if that oscillator is intrinsically too slow (Figure 4). Alternatively, stronger coupling from central to peripheral oscillators speeds up entrainment as shown in Figure 9.

Related work. The mechanisms of communication between clock neurons is a topic of much ongoing research in the circadian field. The neuropeptide pigment-dispersing factor (PDF) is thought to act as the main synchronizing agent in the fly circadian neural network [32]. The analogue of PDF in the mammalian circadian system is vasoactive intestinal peptide (VIP), which plays a major role in synchronizing SCN neurons [33]. Although it is clear from studies with mutants that these neuropeptides provide important signals to synchronize circadian cells, the manner in which the signals interact with the molecular clock is not well understood [15]. Mathematical modeling can be used to explore the effect of different coupling mechanisms on clock network synchronization. In our model, we have assumed that production of the synchronizing factor is induced by activation of the clock gene in oscillator 1 (M_1), and that the effect of the synchronizing factor is to directly increase transcription of the clock gene in oscillator 2 (M_2). This type of coupling is similar to how Gonze et al. [18] modeled the action of VIP in the mammalian clock network; however, in the Gonze model they included a linear differential equation for the production and decay of the coupling agent. Thus, in their model the coupling agent is a delayed version of the clock gene activity. In the Roberts et al. [39] model of the fly clock network, the coupling signal is also increased by clock gene activity. As in our model, the coupling signal then instantaneously increases the clock gene transcription rate in other oscillators. In addition, the Roberts model included a second type of coupling where the coupling signal depends on clock protein levels, rather than clock gene activity, and the effect of the coupling signal is to instantaneously reduce the clock gene transcription rate in other oscillators. Their simulations suggested that networks with both coupling types promoted synchrony and entrainment better than networks with either type of coupling alone. In a more detailed model of the fly clock network, Risau-Gusman and Gleiser [38] explored 21 different coupling mechanisms and found that synchronization of the network can only be achieved with a few of them. In future work, it would be interesting to use generalized entrainment maps to try to gain insight into why certain types of coupling promote synchrony and entrainment better than others.

Several prior modeling studies on entrainment of circadian oscillators exist. Bordyugov et al. [7] used the Kuramoto phase model and found, via Arnold tongue analysis, that the forcing strength and the oscillator amplitude both affect the entrainment speed. As noted in their work, a limitation of the method is that it only works for relatively weak coupling. An et al. [3] found that large doses of VIP reduce the synchrony in the SCN, which then reduces the amplitude of circadian rhythms in the SCN. In turn, they show that this leads to faster reentrainment of the oscillators in a jet lag scenario. Lee et al. [28] directly introduced a linear phase model to study the entrainment processes. They found that the period of the central and peripheral oscillators are not the only predictors of the entrained phase. The intensity of light forcing to the central oscillator and the strength of coupling from the central to the peripheral oscillator also play a role in determining the stable phase. Their results are consistent with what we found for the O_1 -entrained map shown in Figure 4. Roberts et al. [39] studied a population of coupled, modified, heterogeneous Goodwin oscillators under DD

and single light pulse conditions. Their model simulations of a semihierarchical system show that because of heterogeneity, a single light pulse can desynchronize and phase disperse the oscillators. This can lead to a change in the coupling strength between oscillators which in turn leads to a new periodic solution of different amplitude than before the light pulse. Although they didn't consider 24-hour LD forcing, Roberts et al. suggests that this desynchrony can be an important component in assessing reentrainment of semihierarchical networks after jet lag. Our 2-D entrainment shows that this is indeed true. Namely, a shift in the light phasing that retains synchrony between O_1 and O_2 is equivalent to changing the initial y -value of our map, but keeping x fixed. Whereas a shift of light phasing accompanied by a desynchronization is equivalent to changing both x and y from the stable fixed point. As our simulations show (Figure 10(d)), the reentrainment process can be quite different in these two cases.

There are two modeling papers of hierarchical systems that are quite relevant to our work. In Leise and Siegelman [29], the authors consider a multistage hierarchical system to assess properties of jet lag. They utilized a 2-D circadian model due to olde Scheper et al. [37] to show that the direction of entrainment of peripheral oscillators need not follow that of the central oscillator. This is referred to as reentrainment by partition. To understand this idea more clearly, consider the concepts of orthodromic and antidromic reentrainment which are studied in the context of a time zone shift as in jet lag. Orthodromic reentrainment is defined as the oscillator shifting in the same direction as the forcing signal (e.g., advancing in response to an advance of the LD cycle) and antidromic reentrainment is when the oscillator shifts in the opposite direction as the forcing signal (e.g., delaying in response to an advance of the LD cycle). The situation is more complicated for hierarchical systems where different parts of the system may shift in different directions. For example, when Leise and Siegelman simulated a jet lag scenario involving a phase advance of 6 hours, they found that the pacemaker oscillator responded by phase advancing but the intermediate and peripheral oscillators responded by phase delaying. Similarly to Leise and Siegelman, we also observe reentrainment by partition in our model. With the parameter values that we used in this paper, a 6-hour phase advance leads to orthodromic reentrainment in our model with both oscillators responding by phase advancing. However, simulating a 10-hour phase delay of the LD cycle places the initial condition in the vicinity of the saddle fixed point C, leading to reentrainment through partition depending on the exact location relative to C. Our results are consistent with those of Leise and Siegelman, as they note that in their model reentrainment by partition can also be observed in response to phase delays of the LD cycle for certain values of the coupling strength between the master pacemaker and the intermediate component. The qualitative similarity in our results suggests that our findings can be used to infer that the Leise-Siegelman multistage model also possesses unstable saddle fixed points whose properties govern the reentrainment process. A second more recent paper due to Kori, Yamaguchi, and Okamura [24] developed a hierarchical Kuramoto model to study the entrainment of circadian systems. They applied the model to predict the reentrainment time after two types of phase shifts, a single eight-hour shift versus a two-step shift with 4-hour shifts in each step. It turns out the latter requires fewer days to recover. In our paper, this can be related to the properties of stable manifolds of B or C. For example, in Figure 6(d), for a single eight-hour shift near the fixed point A, the new point will stay close to $W^s(C)$, which makes the reentrainment time longer. For two successive four-hour shifts,

the new point will be further from $W^s(C)$, which decreases the reentrainment time. This result generalizes findings from Diekman and Bose [14] and Kori, Yamaguchi, and Okamura [24].

Regarding the numerical methods that we used to find stable and unstable manifolds, we basically applied the search circle for stable manifolds [16] and the growing method [26] for unstable manifolds. One difference between those methods and ours is the domain of the map, \mathbb{R}^2 versus a torus \mathbb{T}^2 in our case. Instead of growing one curve, our manifold is cut off when it hits the boundary of the domain. We then restart the calculation at the equivalent periodic point of the domain, e.g., $x = 24$ is reset to $x = 0$. Another difference is the terminating criteria for both growing and SC methods rely on calculating the arc length to a predetermined length. However, in our map, the manifolds are generated from a certain point (the source D or the sink A), thus our algorithm terminates when those manifolds enter a neighborhood of the corresponding fixed points D and A.

Recently Castejón and Guillamon derived a different 2-D entrainment map [9]. This map applies to a single oscillator (not necessarily a circadian oscillator), subject to pulsed periodic input. The variables of their map are the phase and amplitude of the oscillator. They use phase-response curve type methods to show that their 2-D map is more accurate in tracking the phase-locking dynamics as compared to a 1-D map of simply phase. While they use the term 2-D entrainment map, it appears that their method applies to a class of problems that are different than the ones considered in this paper.

Advantages and disadvantages of our method. The methods derived in this paper have the following advantages. Aside from allowing us to calculate entrainment times and directions as discussed above, the method provides a clear geometric description of why these results arise. Namely, the unstable manifolds of various fixed points organize the iterate structure of the dynamics. Our method does not specifically require the LD forcing to be weak in amplitude or short in duration. This is in contrast to methods that use phase response curves and thus require weak coupling or short duration perturbations [8, 35].

Second, the dimension on which we perform analysis is significantly reduced from five to two dimensions. The classical Poincaré map can reduce the dimension of the original system by one. For example, Tsumoto et al. [40] construct a Poincaré map for the 10-dimensional Leloup and Goldbeter model of the *Drosophila* molecular clock [30], reducing the dimension to 9. The phase reduction techniques of Brown, Moehlis, and Holmes [8] can reduce the dimension of limit cycle oscillators to 1 dimension, however, this method is not accurate for strong coupling.

There are some disadvantages of the map. First, the map only works to study local behavior near the stable limit cycle solutions. This is because we restrict the type of perturbations that we are considering to allow only for a shift of the LD cycle or a shift of the central oscillator along its own limit cycle. In particular, we don't know if there is an unstable or stable structure outside the basin of attraction of the stable entrained solution without additional analysis. Second, the phase angle method works well with 2-D systems. For higher-dimensional systems, it would require additional assumptions.

Open questions and future directions. This work is based in part on analysis and in part on simulations. We have not proved that the correspondence of the findings of the 2-D map, e.g., existence and stability of fixed points, actually exist for the hierarchical system of

ODEs. We would like to use a 1-D phase model, for example a Kuramoto model [27] for each oscillator, to see if this proof can be made. Alternatively, we believe this method of mapping should be applicable to other models, such as Goodwin [19], Gonze et al. [18], or Forger, Jewett, and Kronauer [17] oscillators which are all higher dimensional. Verifying this, at the moment, would have to rely on checking agreement with simulations. The 2-D entrainment map should also be applicable to understanding the interaction of circadian and sleep-wake rhythms to generalize the findings of Booth, Xique, and Diniz Behn [6].

A necessary condition of our method is the existence of limit cycle solutions of the forced system, so that we can map any point in the phase plane to a point on the limit cycle. Light input is not the only forcing signal that a circadian oscillator receives. For instance, exercise, the intake of meals, and taking melatonin can also be considered as an external forcing. We would like to develop the entrainment map for multiple forcing signals. Another possible direction for future work involves generalization of model reduction techniques. Most reduction techniques are based on weak coupling, such as phase reduction [8]. We would like to develop a technique for a system with strong coupling. This part could potentially be done by deriving a Floquet normal form [10] in phase and amplitude space. For the circadian oscillators that we studied in this paper, it remains open how to derive the Floquet normal form.

REFERENCES

- [1] Z. AKCAY, A. BOSE, AND F. NADIM, *Effects of synaptic plasticity on phase and period locking in a network of two oscillatory neurons*, J. Math. Neurosci., 4 (2014), 8.
- [2] Z. AKCAY, X. HUANG, F. NADIM, AND A. BOSE, *Phase-locking and bistability in neuronal networks with synaptic depression*, Phys. D, 364 (2018), pp. 8–21.
- [3] S. AN, R. HARANG, K. MEEKER, D. GRANADOS-FUENTES, C. A. TSAI, C. MAZUSKI, J. KIM, F. J. DOYLE, L. R. PETZOLD, AND E. D. HERZOG, *A neuropeptide speeds circadian entrainment by reducing intercellular synchrony*, Proc. Natl. Acad. Sci. USA, 110 (2013), pp. E4355–E4361.
- [4] J. ASCHOFF, *Problems of re-entrainment of circadian rhythms: Asymmetry effect, dissociation and partition*, in Environmental Endocrinology, Springer, Berlin, 1978, pp. 185–195.
- [5] R. BEN-SHLOMO AND B. KYRIACOU, *Circadian rhythm entrainment in flies and mammals*, Cell Biochem. Biophys., 37 (2002), pp. 141–156.
- [6] V. BOOTH, I. XIQUE, AND C. G. DINIZ BEHN, *One-dimensional map for the circadian modulation of sleep in a sleep-wake regulatory network model for human sleep*, SIAM J. Appl. Dyn. Syst., 16 (2017), pp. 1089–1112.
- [7] G. BORDYUGOV, U. ABRAHAM, A. GRANADA, P. ROSE, K. IMKELLER, A. KRAMER, AND H. HERZEL, *Tuning the phase of circadian entrainment*, J. R. Soc. Interface, 12 (2015), 20150282.
- [8] E. BROWN, J. MOEHLIS, AND P. HOLMES, *On the phase reduction and response dynamics of neural oscillator populations*, Neural Comput., 16 (2004), pp. 673–715.
- [9] O. CASTEJÓN AND A. GUILLAMON, *Phase-amplitude dynamics in terms of extended response functions: Invariant curves and Arnold tongues*, Commun. Nonlinear Sci. Numer. Simul., 81 (2020), 105008.
- [10] R. CASTELLI, J.-P. LESSARD, AND J. D. MIRELES JAMES, *Parameterization of invariant manifolds for periodic orbits I: Efficient numerics via the floquet normal form*, SIAM J. Appl. Dyn. Syst., 14 (2015), pp. 132–167.
- [11] R. CHAUHAN, K.-F. CHEN, B. A. KENT, AND D. C. CROWTHER, *Central and peripheral circadian clocks and their role in alzheimer's disease*, Dis. Models Mechanisms, 10 (2017), pp. 1187–1199.
- [12] C. A. CZEISLER AND E. B. KLERMAN, *Circadian and sleep-dependent regulation of hormone release in humans.*, Recent Progr. Horm. Res., 54 (1999), pp. 97–130.

- [13] C. O. DIEKMAN AND A. BOSE, *Entrainment maps: A new tool for understanding properties of circadian oscillator models*, *J. Biol. Rhythms*, 31 (2016), pp. 598–616.
- [14] C. O. DIEKMAN AND A. BOSE, *Reentrainment of the circadian pacemaker during jet lag: East-west asymmetry and the effects of north-south travel*, *J. Theoret. Biol.*, 437 (2018), pp. 261–285.
- [15] C. DUBOWY AND A. SEHGAL, *Circadian rhythms and sleep in drosophila melanogaster*, *Genetics*, 205 (2017), pp. 1373–1397.
- [16] J. P. ENGLAND, B. KRAUSKOPF, AND H. M. OSINGA, *Computing one-dimensional stable manifolds and stable sets of planar maps without the inverse*, *SIAM J. Appl. Dyn. Syst.*, 3 (2004), pp. 161–190.
- [17] D. B. FORGER, M. E. JEWETT, AND R. E. KRONAUER, *A simpler model of the human circadian pacemaker*, *J. Biol. Rhythms*, 14 (1999), pp. 533–538.
- [18] D. GONZE, S. BERNARD, C. WALTERMANN, A. KRAMER, AND H. HERZEL, *Spontaneous synchronization of coupled circadian oscillators*, *Biophys. J.*, 89 (2005), pp. 120–129.
- [19] B. GOODWIN, *Oscillatory behavior in enzymatic control processes*, *Adv. Enzyme Regul.*, 3 (1965), pp. 425–428.
- [20] C. GU, H. YANG, AND Z. RUAN, *Entrainment range of the suprachiasmatic nucleus affected by the difference in the neuronal amplitudes between the light-sensitive and light-insensitive regions*, *Phys. Rev. E*(3), 95 (2017), 042409.
- [21] S. HONMA, *The mammalian circadian system: A hierarchical multi-oscillator structure for generating circadian rhythm*, *J. Physiol. Sci.*, 68 (2018), pp. 207–219.
- [22] J. KIM AND D. FORGER, *A mechanism for robust circadian timekeeping via stoichiometric balance*, *Mol. Syst. Biol.*, 8 (2012), 630.
- [23] K. E. KLEIN, R. HERRMANN, P. KUKLINSKI, AND H.-M. WEGMANN, *Circadian performance rhythms: Experimental studies in air operations*, in *Vigilance*, Plenum, New York, 1977, pp. 111–132.
- [24] H. KORI, Y. YAMAGUCHI, AND H. OKAMURA, *Accelerating recovery from jet lag: Prediction from a multi-oscillator model and its experimental confirmation in model animals*, *Sci. Rep.*, 7 (2017), 46702.
- [25] K. KRÄUCHI, *How is the circadian rhythm of core body temperature regulated?*, *Clin. Auton. Res.*, 12 (2002), pp. 147–149.
- [26] B. KRAUSKOPF AND H. OSINGA, *Growing 1d and quasi-2d unstable manifolds of maps*, *J. Comput. Phys.*, 146 (1998), pp. 404–419.
- [27] Y. KURAMOTO, *Chemical Oscillations, Waves, and Turbulence*, Springer, Heidelberg, 1984.
- [28] K. LEE, P. SHIVA KUMAR, S. MCQUADE, J. Y. LEE, S. PARK, Z. AN, AND B. PICCOLI, *Experimental and mathematical analyses relating circadian period and phase of entrainment in neurospora crassa*, *J. Biol. Rhythms*, 32 (2017), pp. 550–559.
- [29] T. LEISE AND H. SIEGELMANN, *Dynamics of a multistage circadian system*, *J. Biol. Rhythms*, 21 (2006), pp. 314–323.
- [30] J.-C. LELOUP AND A. GOLDBETER, *A model for circadian rhythms in drosophila incorporating the formation of a complex between the per and tim proteins*, *J. Biol. Rhythms*, 13 (1998), pp. 70–87.
- [31] H. LEVINE, *Health and work shifts*, in *Shift Work and Health*, P. G. Rentos and R. D. Shephard, eds., US Department of Health, Education, and Welfare, Washington, DC, 1976, pp. 57–69.
- [32] Y. LIN, G. D. STORMO, AND P. H. TAGHERT, *The neuropeptide pigment-dispersing factor coordinates pacemaker interactions in the drosophila circadian system*, *J. Neurosci.*, 24 (2004), pp. 7951–7957.
- [33] C. MAZUSKI AND E. D. HERZOG, *Circadian rhythms: To sync or not to sync*, *Curr. Biol.*, 25 (2015), pp. R337–R339.
- [34] R. E. MISTLBERGER AND D. J. SKENE, *Nonphotic entrainment in humans?*, *J. Biol. Rhythms*, 20 (2005), pp. 339–352.
- [35] H. NAKAO, *Phase reduction approach to synchronisation of nonlinear oscillators*, *Contemp. Phys.*, 57 (2016), pp. 188–214.
- [36] B. NOVÁK AND J. J. TYSON, *Design principles of biochemical oscillators*, *Nat. Rev. Mol. Cell Biol.*, 9 (2008), pp. 981–991.
- [37] T. OLDE SCHEPER, D. KLINKENBERG, C. PENNARTZ, AND J. VAN PELT, *A mathematical model for the intracellular circadian rhythm generator*, *J. Neurosci. Res.*, 19 (1999), pp. 40–47.
- [38] S. RISAU-GUSMAN AND P. M. GLEISER, *A mathematical model of communication between groups of circadian neurons in drosophila melanogaster*, *J. Biol. Rhythms*, 29 (2014), pp. 401–410.

- [39] L. ROBERTS, T. L. LEISE, D. K. WELSH, AND T. C. HOLMES, *Functional contributions of strong and weak cellular oscillators to synchrony and light-shifted phase dynamics*, *J. Biol. Rhythms*, 31 (2016), pp. 337–351.
- [40] K. TSUMOTO, T. YOSHINAGA, H. IIDA, H. KAWAKAMI, AND K. AIHARA, *Bifurcations in a mathematical model for circadian oscillations of clock genes*, *J. Theoret. Biol.*, 239 (2006), pp. 101–122.
- [41] J. J. TYSON, C. I. HONG, C. D. THRON, AND B. NOVAK, *A simple model of circadian rhythms based on dimerization and proteolysis of per and tim*, *Biophys. J.*, 77 (1999), pp. 2411–2417.

Daily electrical activity in the master circadian clock of a diurnal mammal

Beatriz Bano-Otalora^{1,2,#}, Matthew J. Moye^{3,4,#}, Timothy M. Brown^{1,5},
Robert J. Lucas^{1,2,*}, Casey O. Diekman^{3,6,*}, Mino D. C. Belle^{7,*}

¹Centre for Biological Timing, Faculty of Biology Medicine & Health, University of Manchester, Manchester, Manchester, UK.

²Division of Neuroscience and Experimental Psychology, Faculty of Biology Medicine and Health, University of Manchester, Manchester, UK.

³Department of Mathematical Sciences, New Jersey Institute of Technology, Newark, NJ, USA.

⁴Department of Quantitative Pharmacology & Pharmacometrics (QP2) at Merck & Co. Inc., Kenilworth, New Jersey, USA.

⁵Division of Diabetes, Endocrinology and Gastroenterology, Faculty of Biology Medicine and Health, University of Manchester, Manchester, UK.

⁶EPSRC Centre for Predictive Modelling in Healthcare, Living Systems Institute, University of Exeter, Exeter, UK.

⁷Institute of Biomedical and Clinical Sciences, University of Exeter Medical School, University of Exeter, Exeter, UK.

#Authors contributed equally to this work.

*Corresponding Authors: m.d.c.belle@exeter.ac.uk, casey.o.diekman@njit.edu and robert.lucas@manchester.ac.uk

Abstract

Daily or circadian rhythms in mammals are orchestrated by a master circadian clock within the hypothalamic suprachiasmatic nuclei (SCN). Here, cell-autonomous oscillations in gene expression, intrinsic membrane properties, and synaptic communication shape the electrical landscape of the SCN across the circadian day, rendering SCN neurons overtly more active during the day than at night. This well-accepted hallmark bioelectrical feature of the SCN has overwhelmingly emerged from studies performed on a small number of nocturnal rodent species. Therefore, for the first time, we investigate the spontaneous and evoked electrical activity of SCN neurons in a diurnal mammal. To this end, we measured the electrical activity of individual SCN neurons during the day and at night in brain slices prepared from the diurnal murid rodent *Rhabdomys pumilio* and then developed cutting-edge data assimilation and mathematical modelling approaches to uncover the underlying ionic mechanisms. We find that *R. pumilio* SCN neurons were more excited in the day than at night, recapitulating the prototypical pattern of SCN neuronal activity previously observed in nocturnal rodents. By contrast, the evoked activity of *R. pumilio* neurons included a prominent suppressive response that is not present in the SCN of nocturnal rodents. Our computational modelling

approaches reveal transient subthreshold A-type potassium channels as the primary determinant of the suppressive response and highlight a key role for this ionic mechanism in tuning excitability of clock neurons and optimising SCN function to accommodate *R. pumilio*'s diurnal niche.

Keywords: diurnality, circadian rhythms, suprachiasmatic nucleus, electrical activity, mathematical modelling, data assimilation

INTRODUCTION

The mammalian master circadian clock is localized within the hypothalamic suprachiasmatic nucleus (SCN), where nearly 20,000 neurons synchronize their daily activity with the light-dark cycle to orchestrate circadian rhythms in physiology and behaviour (Reppert & Weaver, 2002). SCN neurons are electrically and chemically heterogeneous. Most, if not all, SCN neurons contain an internal molecular clock that operates on a transcription-translation feedback loop (TTFL) (Ko & Takahashi, 2006). Activity of the TTFL drives circadian rhythms in electrical activity, with SCN neurons notably more active during the day (up-state) than at night (down-state). This excitability landscape within the SCN is reinforced by the appropriate synaptic integration of extrinsic signals, which includes photic information from the retina and behavioural feedback reflecting arousal state (Belle & Diekmann, 2018).

Our current understanding of SCN neurophysiology comes overwhelmingly from electrophysiological recordings on a small number of nocturnal rodent species (mice, rats and hamsters) (Colwell, 2011; Belle & Diekmann, 2018; Harvey *et al.*, 2020). A handful of studies have confirmed that the daytime peak in spontaneous activity (as reflected in extracellular electrical activity or deoxyglucose uptake) is retained in the SCN of diurnal species (Sato & Kawamura, 1984; Schwartz, 1991; Ruby & Heller, 1996). However, there has been no whole-cell recording of SCN neurons from a diurnal species, and the question of how, or if, SCN neurophysiology is altered to accommodate a diurnal niche remains unanswered. *Rhabdomys pumilio* (the four striped mouse) represents an excellent opportunity to address this question. This species is strongly diurnal (Dewsbury & Dawson, 1979; Schumann *et al.*, 2005; Bano-Otalora *et al.*, 2020) and is a murid rodent, facilitating comparison with established findings from closely related nocturnal species (mice and rats).

We adopted a parallel approach of experimental recording and advanced computational modelling to understand the *R. pumilio* SCN. First, we address the lack of data on single-cell physiology in diurnal SCN by using whole-cell recordings to describe spontaneous electrical states and their daily variation. We then determined the evoked membrane properties of these diurnal SCN neurons by recording their responses to inputs. We then turned to cutting-edge data assimilation and modelling approaches to gain insight into the cellular and ionic mechanisms underlying passive and evoked electrical states. Our results revealed similarities in SCN neurophysiology between the *R. pumilio* and other rodent species, but also exposed fundamental differences which may serve to accommodate SCN functioning to a diurnal niche.

RESULTS

SCN neuropeptidergic organization in the diurnal *Rhabdomys pumilio*.

Prior to assaying single-cell electrical properties in the *R. pumilio* SCN, we first described the anatomical and neuropeptidergic organization of the SCN in this species. This provided us with a practical guide to ensure only neurons within the SCN were targeted for electrophysiology since no brain atlas yet exists for this species. To this end, we performed immunofluorescence labelling for nuclear DNA with DAPI, vasoactive intestinal polypeptide (VIP), arginine vasopressin (AVP), and gastrin-releasing peptide (GRP) (Fig.1).

The gross neuroanatomy of the *R. pumilio* SCN across the rostral-caudal axis is broadly similar to other rodent species (Smale & Boverhof, 1999; Abrahamson & Moore, 2001)

(Fig.1A). Immunofluorescence labelling for the main neuropeptides showed that the *R. pumilio* SCN contains VIP, AVP, and GRP, and importantly, the neuroanatomical localization of these neuropeptides was broadly similar to the distribution found in other rodent species (Smale & Boverhof, 1999; Abrahamson & Moore, 2001), AVP-positive cell bodies were mainly localized in the dorsomedial aspect (sometimes termed “shell” (Fig.1B)), while VIP-positive somas were localized throughout the ventral region or “core”, with VIP immunoreactive axonal processes extended into the dorsal SCN (Fig.1C). By contrast, GRP-positive neurons were localized in the central SCN (Fig.1D).

Diurnal changes in the spontaneous electrical activity of *Rhabdomys pumilio* SCN neurons.

The day-night electrical activity and membrane excitability states of SCN neurons at the single-cell level are well characterized in nocturnal animals (Colwell, 2011; Belle & Diekman, 2018; Harvey *et al.*, 2020), but thus far there are no such measurements performed in the SCN of diurnal mammals. We therefore set out to describe the intrinsic electrical states of *R. pumilio* SCN neurons with respect to the cell’s passive membrane properties (resting membrane potential (RMP), spontaneous firing rate (SFR), and input or membrane resistance (R_{input})), and how these change across the day and at night, using *in vitro* whole-cell patch clamp electrophysiology.

Recording (Fig.2A) from a total of 111 SCN neurons (from 8 animals) over the day-night cycle revealed four spontaneous excitability states in *R. pumilio* (Fig.2B), similar to previous descriptions in mice (Belle *et al.*, 2009; Diekman *et al.*, 2013; Paul *et al.*, 2016; Collins *et al.*, 2020). Thus, some SCN neurons were resting at moderate RMPs (-43.9 ± 0.41 mV, $n=94/111$) and firing action potentials (APs). Other neurons were severely depolarized or “hyperexcited” (-32.7 ± 2.36 , $n=6/111$), to the extent that rather than generating APs, they became depolarized-silent or exhibited depolarized low-amplitude membrane oscillations (DLAMOs). The final category of neurons were hyperpolarized-silent, having RMPs too negative to sustain firing (-50.5 ± 2.29 mV, $n=11/111$).

SCN neurons were overall more excited during the day than at night (Fig.2C-E), with hyperpolarized-silent neurons only appearing at night, and the daytime state being characterized by firing and depolarized cells, indicating a time-of-day control on these cellular electrical states ($\chi^2=21.498$, $p<0.001$; Fig.2C). Accordingly, RMP and SFR showed a robust circadian variation (Fig.2D-E). During the day, SCN neurons were overall resting at more depolarized RMP, generating APs at a higher rate. This indicates that, as in nocturnal species (Belle *et al.*, 2009; Belle & Piggins, 2017), cellular RMP in the diurnal *R. pumilio* SCN is a strong determinant of electrical states and SFR. To directly test this, we subjected depolarized-silent SCN neurons to progressive steps of steady-state suppressive (negative) currents (from 0 to ~ -16 pA; driving RMP from -32 mV to -60 mV), to see if we could elicit the range of spontaneous electrical behaviours seen in SCN neurons. Indeed, *R. pumilio* SCN neurons could be easily driven to transit from the depolarized- through to hyperpolarized-silent states, switching to DLAMOs and firing activity at appropriate RMPs in the process (Fig. 2G).

Measurement of R_{input} values showed a range from 0.84 to 4.23 G Ω , skewed towards high values, as reported in other species (Pennartz *et al.*, 1998; Jackson *et al.*, 2004; Kuhlman & McMahan, 2004; Belle *et al.*, 2009). However, we found neither a significant day-night variation in this measure (Mann-Whitney U=1966, $p>0.05$, Fig.2F) nor a correlation with RMP ($R^2 = 0.0305$, $p>0.05$), which stands in contrast to measurements in the SCN of nocturnal animals (de Jeu *et al.*, 1998; Kuhlman & McMahan, 2004; Belle *et al.*, 2009). This represents the first substantial difference between *R. pumilio* and mouse or rat SCN.

Diversity in the evoked electrical responses of *Rhabdomys pumilio* SCN neurons.

In addition to the daily variation in intrinsic electrical activity, SCN clock function also critically relies on the integrated activity of excitatory and inhibitory synaptic signals (Albers *et al.*, 2017). These inputs originate both from within the SCN (e.g. excitation or inhibition via GABA-GABA_A receptor signalling) and from other brain circuits (e.g. excitation or inhibition via glutamate, or GABA signalling). Mimicking these fast signals by depolarizing and hyperpolarizing current pulses elicits diverse electrical responses in the SCN of nocturnal animals and is useful for characterizing SCN neurons (Pennartz *et al.*, 1998; Belle *et al.*, 2009; Harvey *et al.*, 2020). Therefore, we next investigated the spiking responses of *R. pumilio* SCN neurons to inputs by challenging the cells with brief current pulses (see Methods).

When subjected to depolarizing pulses, *R. pumilio* SCN neurons exhibited electrical responses similar to those of nocturnal species: a small proportion of cells (21/102) responded with a sustained and regular train of action potentials, with no, or marginal, spike-frequency adaptation (non-adapting cells, Fig.3A). The remaining neurons (81/102) showed some degree of frequency adaptation (Fig. 3B&C). These cells either progressively slowed firing rate and exhibited increased spike shape broadening and amplitude reduction during the pulse (adapting-firing, Fig. 3B), or fired only a few APs during the initial phase of the depolarization before entering a silent state (adapting-to-silent, Fig. 3C). We found non-adapting and adapting cells resting at similar RMPs, indicating that cellular RMP was not the determinant of response type (e.g. Fig. 3A vs C). The proportion of cells displaying each of these responses did not vary across the day-night cycle ($\chi^2=0.324$, $p>0.05$, Fig. 3D). This suggests that, as in the mouse SCN (Belle *et al.*, 2009; Belle & Piggins, 2017), these different types of spiking behaviour likely reflect “hardwire” differences between SCN neurons, rather than time-of-day dependent variations in physiological state.

We next mimicked the effect of inhibitory signals by injecting hyperpolarizing current pulses (Fig.3E&F). In all cases, spike firing ceased during these hyperpolarizing currents. Upon pulse termination, 67% (69/103) of *R. pumilio* SCN neurons immediately resumed normal firing or showed rebound depolarization spiking before resuming normal pre-pulse level of firing (Fig. 3E), as previously reported for mouse and rat SCN (Thomson & West, 1990; Pennartz *et al.*, 1998; Kuhlman & McMahon, 2004; Belle *et al.*, 2009). The remaining 33% (34/103) of units displayed a low-threshold spike (LTS) followed by a rebound hyperpolarization which produced a prominent delay, ranging from 160 to 1430 msec, before firing resumed (Fig. 3Fi-ii, 6H). A high proportion of cells in this second group (73.5%; 25/34) also showed an inward rectification or depolarization “sag” (Fig. 3F) during the pulse, an electrical response that is associated with H-current activation (I_H , (Pennartz *et al.*, 1998; Atkinson *et al.*, 2011)). The hyperpolarization-evoked delay to fire and LTS response (Fig. 3Fi-ii) have not previously been reported for SCN neurons, and thus represents another significant point of divergence in SCN neurophysiology between *R. pumilio* and, previously studied, nocturnal species.

We termed *R. pumilio* neurons with rebound firing Type-A cells (Fig. 3E), and those with delays Type-B neurons (Fig. 3Fi-ii), to be consistent with nomenclatures previously used to identify neurons with those distinct electrical characteristics elsewhere in the brain (Burdakov & Ashcroft, 2002; Burdakov *et al.*, 2004). The relative abundance of Type-A and -B cells did not change across the day-night cycle ($\chi^2=$, $p>0.05$, Fig.3G), indicating that these response properties are determined by cell-type rather than time-of-day.

Ionic mechanisms underlying evoked electrical responses.

A comprehensive understanding of SCN neurophysiology would encompass an appreciation of the ionic mechanisms and channel parameters responsible for the electrophysiological properties revealed in our whole-cell recordings (Belle & Diekmann, 2018; Harvey *et al.*, 2020). Capturing this ionic information from current-clamp data has only recently become feasible due to advances in data assimilation (DA) techniques (Abarbanel, 2013). Here, we

developed a state-of-the-art DA algorithm (see Methods section for a detailed description) and applied it to build detailed computational models of *R. pumilio* SCN neurons (Fig.S1 & S2). This modelling approach reproduced the voltage trajectory and nuances of action potentials and subthreshold electrical activity generated during spontaneous and evoked firing of SCN neurons in remarkable detail (Fig. 4 and S2), providing confidence that the ionic currents and parameters estimated by our DA algorithm, and their dynamical relationship in the models, are indeed a close match to their biological values and activity.

Through simulations of the model, we first assessed how ionic conductances interact with each other to produce AP firing and other electrical behaviours (information that could never be obtained experimentally since current-clamp and voltage-clamp cannot be simultaneously performed). We applied this approach to compare the conductances underlying spontaneous AP generation in the *R. pumilio* SCN model (Fig.4A) to our previously published model of mouse SCN neurons (Belle *et al.*, 2009) containing the same sets of ionic currents (voltage-dependent transient sodium I_{Na} , voltage-dependent transient calcium I_{Ca} , voltage-dependent potassium I_K , and voltage-independent leak, I_L). We found that the overall profile of how these currents contribute to AP generation is similar across the two species (Fig.S3). In addition, the types of bifurcations at the transitions between rest states and spiking are the same in both models (subcritical Hopf from hyperpolarized silent to spiking, and supercritical Hopf from depolarized-silent to spiking), suggesting the qualitative dynamics that lead to repetitive AP firing are similar across the two species (Fig. S4A). Furthermore, the *R. pumilio* model can produce all the electrical behaviours observed across the day-night cycle (depolarized-silent, DLAMOs, fast-firing, slow-firing, and hyperpolarized-silent, Fig. S4B-F) through an antiphase circadian rhythm in sodium and potassium leak currents, consistent with the “bicycle model” proposed for the circadian regulation of electrical activity in mice and flies (Flourakis *et al.*, 2015).

We next used the model to gain insight into the mechanisms responsible for the adapting versus non-adapting firing behaviours observed in response to depolarizing pulses. Our DA algorithm yielded models that faithfully reproduced the voltage traces and spike shapes from non-adapting, adapting-firing, and adapting-to-silent cells (Fig. 5A-B). By inspecting the ionic currents flowing during the simulated voltage traces, we assessed the role of voltage-gated sodium I_{Na} , calcium I_{Ca} , and potassium I_K currents in producing these responses (Fig. 5C).

Our models revealed that frequency adaptation in SCN neurons in response to excitation resulted from the progressive inactivation of sodium channels. Indeed, the adapting-firing model indicated a much smaller amount of I_{Na} available for the APs during the depolarizing pulse (peak I_{Na} = -80pA, Fig. 5Cii), and a greater reduction in sodium conductance G_{Na} (26 nS before vs 1.5 nS during the pulse, Fig. 5Dii) compared with the non-adapting model (peak I_{Na} = -580 pA; G_{Na} = 27 nS before vs 13 nS during the pulse, Fig. 5Ci & Di). Remarkably however, increased sodium channel inactivation (h_{Na} close to 0) could not be ascribed to intrinsic differences in the sodium channel properties themselves between the non-adapting and adapting-firing models as the kinetic parameters of the sodium activation and inactivation gating variables were similar (Fig.5F-G). Rather, the difference was due to differing properties of the potassium channels. A combination of a flattened steady-state potassium activation (n_{∞}) curve (Fig. 5H) and the lower g_K value (Fig. 5I), led to a smaller I_K and reduced G_K during AP firing in the adapting-firing compared to the non-adapting model (250 pA, 3 nS vs 900 pA, 11 ns, respectively) (Fig.5C-D i-ii). Since I_K is an outward current, this means that the adapting-firing model does not repolarize as strongly after the peak of an AP, and therefore, the membrane does not hyperpolarize enough to de-inactivate the sodium channels. Thus, in the adapting-firing model, the inability of a weak I_K to sufficiently repolarize the membrane is what ultimately leads to the reduced I_{Na} and low-amplitude APs. The I_K is even smaller in the adapting-to-silent model (Fig. 5Ciii), failing to repolarize the membrane, and leads to sustained inactivation of the sodium channel (Fig. 5Eiii), negligible sodium conductance (Fig. 5Diii) and ultimately the inability to repeatedly fire APs during the

pulse (Fig. 5Biii). In summary, our models support progressive sodium channel inactivation as the mechanism of frequency adaptation (consistent with experimental observation in neurons elsewhere in the brain (Fleidervish *et al.*, 1996; Jung *et al.*, 1997; Kimm *et al.*, 2015) and our previously published model of mouse SCN neurons (Belle *et al.*, 2009)), while indicating that this is primarily a consequence of a weak I_K .

We next interrogated our models for the key ionic origins of Type-A vs Type-B responses to inhibition (Fig. 3E&F). In both cell types, hyperpolarizing pulses drove the membrane potential in the real and model cells below the firing threshold, which suppressed firing activity during the pulse (Fig. 6A-B, i-ii). Model analysis showed that in the Type-A cell, the I_{Na} and I_{Ca} currents were larger during the first AP immediately following the pulse than during the APs before the pulse (Fig. 6D), leading to a high-amplitude rebound spike. The rebound spiking was due to sodium and calcium ion channels becoming completely de-inactivated (h_{Na} and h_{Ca} both approach 1) at the hyperpolarized membrane potential reached during the pulse (Fig. 6F). The time scale of calcium ion channel inactivation causes I_{Ca} to remain elevated for a few hundred milliseconds after the pulse, resulting in a transient after-depolarization and a short burst of firing before returning to the baseline pre-pulsed spike rate (Fig. 6A).

Similar I_{Na} and I_{Ca} dynamics were present in the Type-B neuron model. However, the rebound hyperpolarization and prominent delay-to-fire after the pulse observed in Type-B neurons (Fig. 3F and 6Bi-ii), was not possible to reproduce using our existing basic model (Fig. 4A), consistent with the failure to observe such behaviour in the mouse SCN. It is well established in neurons elsewhere in the brain that the inhibitory actions of the transient subthreshold activating A-type (I_A) voltage-gated potassium channels (Kv) underpin such delay-to-fire activity (Schoppa & Westbrook, 1999; Saito & Isa, 2000; Burdakov & Ashcroft, 2002; Burdakov *et al.*, 2004; Nadin & Pfaffinger, 2010). Another feature of Type-B activity that could not be recreated with our basic model was the prominent depolarization “sag” seen in the voltage trace during the pulse (Fig. 3F and 6Bi). Such behaviour could be produced by activation of an I_H current by the hyperpolarizing pulse. We therefore added I_A , as well as a hyperpolarization-activated (I_H) current, to our mouse SCN model in an attempt to recreate the voltage trace and biophysical condition of the Type-B neuron (Fig. 6C).

The expanded model revealed a larger I_A current during the first APs after the delay (480 pA) than during a typical spike (220 pA, Fig. 6E). Importantly, there was also 15 pA of I_A current flowing during the delay itself (Fig. 6E inset). It is noteworthy that this was greater than the 5 pA of I_A current that flows during the inter-spike interval. This enhanced I_A current following the pulse was due to de-inactivation of the A-type channel (h_A approaches 1) during the hyperpolarizing pulse (Fig. 6G), rendering the I_A channel fully available upon release of the pulse, an observation that is consistent with experimental findings (Burdakov *et al.*, 2004). The I_A current then inactivates slowly and, until this outward current decays sufficiently, the cell cannot reach threshold to fire, thereby prolonging inhibition. This inhibition-supportive action of I_A is consistent with observations made elsewhere in the brain (Burdakov & Ashcroft, 2002; Burdakov *et al.*, 2004), and previous simulations (Rush & Rinzel, 1995; Patel *et al.*, 2012).

It has previously been shown that variation in cellular I_A conductances and inactivation time constant can impact time to fire (e.g. (Saito & Isa, 2000)), and this may explain the broad range in the delay-to-fire, from 160 to 1430 msec, seen in our Type-B neurons (Fig. 6H). Indeed, this was the case in our model. By varying the maximal I_A conductance (Fig. 6I&J) and inactivation time constant (Fig. 6M & N) parameters, we were able to capture the full range of latency to fire seen in Type-B cells, with higher conductances and longer inactivation time constants producing longer delays. Complete removal of the I_A conductance eliminated the delay and produced a Type-A response (Fig. 6Ji-iii), reinforcing the different ionic composition of these two cell types.

In summary, our revised model was able to mirror all the electrical features observed in *R. pumilio* SCN neurons in response to extrinsic inputs, and identified transient subthreshold A-type potassium channels as playing a key role in evoked-suppression firing in simulated SCN neurons.

I_A currents suppress firing under physiological simulation.

We finally interrogated our model to understand how the I_A conductances required to explain SCN responses to hyperpolarizing pulses may impact firing activity in a more realistic neurophysiological setting. To this end, we first subjected the model to simulated synaptic conductances recorded from *R. pumilio* SCN neurons (Fig. S5). To account for the ability of the SCN's major neurotransmitter (GABA) to be either inhibitory or excitatory (Albers *et al.*, 2017), we applied GABAergic synaptic conductances of either polarity (g_{syn-I} and g_{syn-E}). Our simulations showed that overall, in the absence of GABAergic synaptic conductance ($g_{syn-I} = 0$ nS), I_A led to a suppression of spontaneous firing rate in model SCN neurons (Fig. 7 A&B, *a1 vs a4*). This observation is consistent with previous experimental work (Granados-Fuentes *et al.*, 2012; Hermanstynne *et al.*, 2017). This effect was retained following inclusion of synaptic input of either polarity (Fig.7A-B, compare *a2 vs a5*, and *a3 vs a6*), with the suppressive effect of g_{syn-I} especially augmented by high I_A (Fig.7B).

Having observed such effects of I_A on intrinsic activity and cellular response to inputs, we next investigated its effects on the spontaneous activity exhibited by SCN neurons across the circadian day. Here, we simulated the different resting states of *R. pumilio* SCN neurons and day-night changes in spontaneous firing rate (as in the neurons, Fig. 2B&E, respectively) by subjecting the model to a range of leak currents. Specifically, we varied the scaling factor for the ratio of potassium leak (g_{LK}) to sodium leak (g_{LNa}) from 0.85 to 1.15 (Fig. 7C). This was motivated by previous work showing that sodium leak current is higher during the day than at night in mouse SCN neurons (Flourakis *et al.*, 2015). Furthermore, it has been suggested that potassium leak currents are lower during the day and higher at night. According to this “bicycle” model, a g_{LK}/g_{LNa} scaling factor less than 1 corresponds to a daytime “up-state”, and a scaling factor greater than 1 to a night-time “down-state”. Simulating this variation in leak currents indeed transited the spontaneous RMP and firing rate of the model cells from the daytime depolarized state to night-time suppressed state (as in the neurons, Fig. 2B&G; Fig. S4B-F). We then tested the influence of I_A on firing rate at each of these electrical states. As reported above, our results revealed that, overall, I_A conductances suppressed spontaneous firing activity (Fig. 7C, *c1-c3*), but the extent of this suppression was magnified in slow firing and more hyperpolarized cells (Fig. 7C, *c3*), such as those frequently recorded at night.

Altogether, these observations are consistent with experimental findings in the SCN, and elsewhere in the brain, that I_A conductances assist suppressive signals. We therefore conclude that in the *R. pumilio* SCN, I_A conductances may act as a “break” to modulate (tone down) excitation during the day in depolarized excited cells, and promote inhibition at night in more hyperpolarized slow-firing neurons.

DISCUSSION

We have applied whole-cell recordings, advanced data assimilation and modelling approaches to provide the first comprehensive description of spontaneous, and evoked, electrical activity of individual SCN neurons in a diurnal species. Our approach reveals strong similarities with the SCN of closely related nocturnal species, but also notable differences.

Similarities with the nocturnal SCN

Most importantly, the fundamental daily rhythm in electrical excitability ('upstate' during the day and a 'downstate' at night (Allen *et al.*, 2017; Belle & Diekman, 2018; Harvey *et al.*, 2020)) reported for nocturnal species is retained in *R. pumilio*. This reinforces the current view that mechanisms of rhythm generation and regulation are broadly retained across mammalian species with different circadian niches. Moreover, the response of *R. pumilio* SCN neurons to depolarizing inputs and the underlying ionic mechanisms were similar to that of nocturnal rodents (Belle *et al.*, 2009). In further support of this view, our modelling revealed similar action potential generation mechanisms in the *R. pumilio* SCN to those in the mouse and rat SCN (Jackson *et al.*, 2004; Belle *et al.*, 2009).

Novel properties of the *Rhabdomys pumilio* SCN

The most obvious point of divergence between the *R. pumilio* SCN and that of closely related nocturnal species was its response to hyperpolarizing pulses. Thus, we found that a substantial fraction of *R. pumilio* neurons showed a prominent delay-to-fire (for several hundreds of milliseconds in some cells) following inhibitory pulses. This sort of electrical reaction to inhibition has been observed in neurons elsewhere in the brain (Schoppa & Westbrook, 1999; Saito & Isa, 2000; Burdakov & Ashcroft, 2002; Burdakov *et al.*, 2004; Nadin & Pfaffinger, 2010), but to the best of our knowledge has never before been reported in SCN neurons (Thomson & West, 1990; Pennartz *et al.*, 1998; Kuhlman & McMahon, 2004; Belle *et al.*, 2009; Gamble *et al.*, 2011; Belle & Piggins, 2017). The appearance of such 'Type-B' neurons in the SCN is thus a novel property of *R. pumilio*.

What causes delay-to-fire activity in *R. pumilio* neurons (and why are they absent from the nocturnal SCN)? Our computational models identified the activity of the transient subthreshold A-type potassium channels (I_A) as the likely determinant of this suppressive bioelectrical effect, with the I_A conductance density (which presumably represents the number of functional I_A channels), defining the delay-to-fire latency. The implication, that cells with higher I_A conductances show longer delay-to-fire latencies, finds support from experimental findings elsewhere in the brain (Schoppa & Westbrook, 1999; Saito & Isa, 2000; Burdakov & Ashcroft, 2002; Burdakov *et al.*, 2004; Nadin & Pfaffinger, 2010).

The pore-forming (α) subunits of I_A channels (Kv1.4, 4.1, 4.2 and 4.3) are present in nocturnal rodent (rat, mouse and hamster) SCN neurons, and have been implicated in regulating electrical activity and supporting core clock function (Huang *et al.*, 1993; Bouskila & Dudek, 1995; Alvado & Allen, 2008; Itri *et al.*, 2010; Granados-Fuentes *et al.*, 2012; Granados-Fuentes *et al.*, 2015; Hermanstynne *et al.*, 2017). Their failure to produce the delay-to-fire phenotype in those nocturnal species therefore likely reflects some quantitative variation in their function. A likely possibility, consistent both with known features of I_A physiology and our modelling of the *R. pumilio* SCN, is variation in inactivation time constant (timescale over which a channel becomes inactivated following de-inactivation). Elsewhere in the brain it has been shown experimentally that cells expressing I_A channels with faster inactivation time constants (close to 12 ms) show rebound firing, while slower inactivation time constants (~140 ms) produce delay-to-fire activity (Saito & Isa, 2000; Burdakov *et al.*, 2004). Interestingly, the I_A inactivation time constant measured in mouse and hamster SCN neurons showed relatively fast gating variables (below 22 ms: (Alvado & Allen, 2008; Itri *et al.*, 2010)), consistent, therefore, with the presence of rebound but not delay-to-fire characteristics in SCN neurons of these species. In agreement, to fully model the range of delay-to-fire behaviours observed in *R. pumilio* SCN neurons, our original mouse model had to be supplemented with I_A channels with a slow inactivation time constant (near 140 ms) (Fig. 6C,J&N). Variation in delay-to-fire appeared due to alteration in I_A conductances (Fig. 6I&J), however, the range of delay latencies observed in our recordings could also be produced by varying the inactivation time constant while holding the I_A conductance constant (Fig. 6M&N). The inactivation time constants returned by this modelling fall within physiological ranges, and values required to produce delay-to-fire responses are similar to

experimentally determined values in other parts of the brain (Saito & Isa, 2000; Burdakov *et al.*, 2004).

The functional properties of the I_A channel family (Kv4), specifically inactivation time constant and current density, can be influenced by two classes of auxiliary proteins known as Kv channel-interacting proteins (KChIP1–4) and dipeptidyl peptidase-like proteins (DPLPs; DPP6 and DPP10) (Jerng & Pfaffinger, 2014). When associated with the various complements of these proteins, the I_A channel inactivation time constant can vary from a few ms to several hundred ms (depending on their expression pattern and the nature of interaction with the channels), reversibly transforming rebound firing to delay firing cells (Shibata *et al.*, 2000; Holmqvist *et al.*, 2002; Jerng *et al.*, 2004; Jerng *et al.*, 2005; Jerng *et al.*, 2007; Amarillo *et al.*, 2008; Maffie *et al.*, 2009; Nadin & Pfaffinger, 2010). The transcripts for these auxiliary proteins are expressed brain-wide across different mammals, including in the SCN of nocturnal rodents (Wen *et al.*, 2020) and the diurnal baboon (Mure *et al.*, 2018), and have been implicated in circadian control mechanisms in other excitable cell types (Jeyaraj *et al.*, 2012).

A plausible explanation for the range of delay-to-fire activity in the *R. pumilio* SCN, therefore, is variation in activity of KChIP and DPLP proteins producing diversity in inactivation time constants. Interestingly, such a mechanism could also account for the other notably unusual feature of the *R. pumilio* SCN - the absence of a clear relationship between RMP and R_{input} (Figure 2F). These I_A auxiliary proteins are known to regulate the input resistance (R_{input}) of neurons without changing resting membrane potential (RMP) and capacitance (Nadin & Pfaffinger, 2010). Thus, variation in KChIP and DPLP activity across the population of *R. pumilio* SCN neurons could both produce diversity in delay-to-fire activity and disrupt the link between RMP and R_{input} across neurons observed in nocturnal species (Kuhlman & McMahon, 2004; Belle *et al.*, 2009).

Putative functional significance

We applied modelling to determine how I_A channels may regulate excitability in *R. pumilio* SCN neurons in the face of spontaneous (circadian) variations in intrinsic neuronal properties and synaptic input. Experimental results in nocturnal SCN (Granados-Fuentes *et al.*, 2012; Hermansteyne *et al.*, 2017) and elsewhere in the brain (Connor & Stevens, 1971; Rudy, 1988; Liss *et al.*, 2001; Baranauskas, 2007; Khaliq & Bean, 2008) reveal that I_A channels can suppress spontaneous firing rate. Our modelling returned a similar impact of I_A in *R. pumilio*, while revealing aspects of this effect that could be especially relevant for a diurnal species. Thus, in general, I_A reduced the effect of intrinsic or synaptically-driven increases in excitability on firing, while enhancing the impact of inhibitory currents (Fig. 7). The weight of this effect though fell differently across the circadian cycle.

In our model, the weight of the imposed suppression of firing by I_A conductances was stronger at night (in hyperpolarized low-firing neurons) than in the day (in more depolarized fast-firing neurons) (Fig. 7). In this way, I_A would reinforce the SCN's 'down-state' at night. In nocturnal species, the intrinsic reduction in SCN activity at night is augmented by the appearance of inhibitory inputs associated with activity and arousal at this circadian phase (van Oosterhout *et al.*, 2012). Such inhibitory inputs are presumably reduced in diurnal species such as *R. pumilio*, in which activity occurs predominantly during the day. The biophysical properties of I_A channels (conductance active at the subthreshold range of the RMP and progressively becoming available with hyperpolarization), together with its sensitivity to neurotransmitters (Aghajanian, 1985; Yang *et al.*, 2001; Burdakov & Ashcroft, 2002), could provide an opportunity for the *R. pumilio* SCN to compensate for the reduction in inhibitory inputs at night. Accordingly, our modelling evidence favours the interpretation that I_A acts to amplify suppressive signals at night to maintain the low electrical activity in the SCN at this time of day.

The I_A conductance may also be an important response to enhanced excitatory inputs during the day in diurnal species. Day-active animals are exposed to daytime light (the most important excitatory input to the SCN) to an extent that nocturnal species are not. The ability of I_A to reduce the impact of such excitatory inputs, and perhaps augment the effect of inhibitory inputs from the thalamus, lateral hypothalamus or retina (Belle *et al.*, 2014; Sonoda *et al.*, 2020) or intrinsic to the SCN (Hannibal *et al.*, 2010), would apply an appropriate 'brake' on daytime activity of the SCN.

In summary, our whole-cell recordings and computational modelling highlight the potential importance of I_A in tuning excitability in the *R. pumilio* SCN. This may be an important step in accommodating SCN activity to diurnal living while maintaining the day/night contrast in electrical activity necessary for health and wellbeing.

Applying the data assimilation method to physiology

Our results demonstrate that data assimilation (DA) is a powerful tool for developing conductance-based models. Our state-of-the-art DA algorithm was able to reliably perform state and parameter estimation for *R. pumilio* SCN neuron models from current-clamp recordings without the use of voltage-clamp and pharmacological agents to isolate specific currents, and without the injection of custom-designed stimulus waveforms as used in other DA approaches (Meliza *et al.*, 2014). Rather, we made judicious use of the voltage traces resulting from standard depolarizing and hyperpolarizing current steps. This is an important step forward for the practicality of applying DA methodology in the neuroscience context, as it enables model-building from the plethora of past, present, and future current-clamp recordings obtained by electrophysiology labs using classical current-step protocols.

METHODS

Animals

All animal use was in accordance with the UK Animals, Scientific Procedures Act of 1986, and was approved by the University of Manchester Ethics committee. Adult *R. pumilio* (male and female, age 3-9 months) were housed under a 12:12h light dark cycle (14.80 Log Effective photon flux/cm²/s for melanopsin or Melanopic EDI (equivalent daylight illuminance) of 1941.7 lx) and 22°C ambient temperature in light tight cabinets. Food and water were available *ad libitum*. Cages were equipped with running wheels for environmental enrichment. Zeitgeber Time (ZT) 0 corresponds to the time of lights on, and ZT12 to lights off.

Brain slice preparation for electrophysiological recordings

Following sedation with isoflurane (Abbott Laboratories), animals were culled by cervical dislocation during the light phase (beginning of the day or late day). Brains were immediately removed and mounted onto a metal stage. Brain slices were prepared as described previously (Hanna *et al.*, 2017). 250µm coronal slices containing mid-SCN levels across the rostro-caudal axis were cut using a Campden 7000smz-2 vibrating microtome (Campden Instruments, Loughborough, UK). Slices were cut in an ice-cold (4°C) sucrose-based incubation solution containing the following (in mM): 3 KCl, 1.25 NaH₂PO₄, 0.1 CaCl₂, 5 MgSO₄, 26 NaHCO₃, 10 D-glucose, 189 sucrose, oxygenated with 95% O₂, 5%CO₂. After slicing, tissue was left to recover at room temperature in a holding chamber with continuously gassed incubation solution for at least 20 min before transferring into recording aCSF. Recording aCSF has the following composition (mM): 124 NaCl, 3 KCl, 24 NaHCO₃, 1.25 NaH₂PO₄, 1 MgSO₄, 10 D-Glucose and 2 CaCl₂, and 0 sucrose; measured osmolarity of 300-310 mOsmol/kg. Slices were allowed to rest for at least 90 min before starting electrophysiological recordings.

Whole-cell patch clamp recordings

SCN brain slice electrophysiology was performed as previously described (Belle *et al.*, 2014). SCN coronal brain slices were placed in the bath chamber of an upright Leica epifluorescence microscope (DMLFS; Leica Microsystems Ltd) equipped with infra-red video-enhanced differential interference contrast (IR/DIC) optics. Brain slices were kept in place with an anchor grid, and continuously perfused with aCSF by gravity (~2.5ml/min). Recordings were performed from neurons located across the whole SCN during the day and at night (Fig. 2A). SCN neurons were identified and targeted using a 40x water immersion UV objective (HCX APO; Leica) and a cooled Teledyne Photometrics camera (Retiga Electro), specifically designed for whole-cell electrophysiology. Photographs of the patch pipette sealed to SCN neurons were taken at the end of each recording for accurate confirmation of anatomical location of the recorded cell within the SCN.

Patch pipettes (resistance 7–10M Ω) were fashioned from thick-walled borosilicate glass capillaries (Harvard Apparatus) pulled using a two-stage micropipette puller (PB-10; Narishige). Recording pipettes were filled with an intracellular solution containing the following (in mM): 120 K-gluconate, 20 KCl, 2 MgCl₂, 2 K₂-ATP, 0.5 Na-GTP, 10 HEPES, and 0.5 EGTA, pH adjusted to 7.3 with KOH, measured osmolality 295–300 mOsmol/kg).

An Axopatch Multiclamp 700A amplifier (Molecular Devices) was used for voltage-clamp and current-clamp recordings. Pipette tip potential was zeroed before establishing membrane-pipette giga-ohm seal, and cell membrane was ruptured under voltage-clamp mode at -70 mV using minimal negative pressure. Signals were sampled at 25 kHz and appropriately acquired in gap-free or episodic stimulation mode using pClamp 10.7 (Molecular Devices). Series resistance (typically 10–30 M Ω) was corrected using bridge-balance in current-clamp experiments and was not compensated during voltage-clamp recordings. Access resistance for the cells used for analysis was <30 M Ω . Post-synaptic currents (PSCs) were measured under voltage-clamp mode while holding the cells at -70mV. Measurement of spontaneous activity in current-clamp mode was performed with no holding current (I=0). All data acquisition and protocols were generated through a Digidata 1322A interface (Molecular Devices). Recordings were performed at room temperature (~ 23°C). A portion of the data appearing in this study also contributed to the investigation of the impact of daytime light intensity on the neurophysiological activity and circadian amplitude in the *R. pumilio* SCN (Bano-Otalora *et al.*, 2020)

Membrane properties of SCN neurons

Resting membrane potential (RMP), spontaneous firing rate (SFR) and input resistance (R_{input}) were determined within 5 min of membrane rupture. Average SFR in firing cells was calculated as the number of action potentials per second within a 30s window of stable firing using a custom-written Spike2 script, and average RMP was measured as the mean voltage over a 30s window. R_{input} was estimated using Ohm's law ($R=V/I$) where V represents the change in voltage induced by a hyperpolarizing current pulse (-30pA for 500 ms) as previously described (Belle *et al.*, 2009). The neurone's response to excitatory and inhibitory stimuli was identified by a series of depolarizing and hyperpolarizing current pulses (from -30 to +30pA in 5pA steps, duration 1s).

Immunohistochemistry

R. pumilio were culled during the light phase and brains were fixed in 4% PFA, followed by 5 days in 30% sucrose. 35 μ m brain sections were cut using a freezing sledge microtome (Bright Instruments, Huntingdon, UK). Immunofluorescence staining was performed as previously described (Timothy *et al.*, 2018). Briefly, slices were washed in 0.1M PBS and 0.1% TritonX-100 in PBS before incubation with blocking solution (5% donkey serum (Jackson ImmunoResearch, Pennsylvania, US) in 0.05% Triton-X100 in 0.1M PBS). After 60 min, sections were incubated for 48h at 4°C with primary antibodies (AVP Rabbit, Millipore AB1565, 1:5000; VIP Rabbit, Enzo, VA1280-0100, 1:1000; GRP Rabbit, Enzo GA1166-0100, 1:5000). Following washes, slices were incubated overnight with secondary antibodies

(1:800; Donkey anti-rabbit Cy3, Jackson ImmunoResearch). Slices were finally mounted onto gelatine coated slides and cover-slipped using DAPI-containing Vectashield anti-fade media (Vector Laboratories, Peterborough, UK). Digital photos were taking using a Leica DFC365 FX camera connected to a Leica DM2500 microscope using Leica Microsystems LAS AF6000 software.

Data analysis

Current-clamp data were analysed using Spike2 software (Cambridge Electronic Design, CED). Non-normal distributed electrophysiological data from different time-of-day were compared using Mann-Whitney U Test. All statistical analyses were performed using SPSS version 23 (SPSS Inc., Chicago, IL, USA) and GraphPad Prism 7.04 (GraphPad Software Inc., CA, USA). For all tests, statistical significance was set at $p < 0.05$. Data are expressed as mean \pm SEM. Sample sizes are indicated throughout the text and figure legends. Percentages of cells in the different electrophysiological states and responses to depolarizing and hyperpolarizing pulses during the day and at night were analysed using Chi-Squared test.

Model estimation strategy

Traditionally, conductance-based (or Hodgkin-Huxley-type) models of neurons are constructed using voltage-clamp (VC) measurements of individual ionic currents. While VC can provide accurate descriptions of certain channel properties, its execution is experimentally labour intensive, and by measuring each current in isolation VC protocols do not capture the dynamical interplay between the many active channels that drive complex and integrated electrical behaviours in mammalian neurons. Furthermore, it is not feasible to use VC to measure all the ionic currents of interest from the same cell, due to the limited amount of time available to perform patch-clamp recordings before the cell dialyzes (approximately 5 to 10 minutes) and the need to wash out the pharmacological agents used to isolate and measure one current before isolating and measuring the next. Thus, a model constructed using VC data is not a representation of the currents active in a single cell, but rather is a combination of currents measured across several different cells (Golowasch *et al.*, 2002).

The advantage of current-clamp (CC) protocols is that the recorded voltage trace reflects the natural interaction of all the ionic conductances within that cell. The challenge for constructing a model based on CC data is that only one of the state variables of the model, the membrane voltage, has been measured directly; the gating variables that represent the opening and closing of ion channels are unobserved. Each ionic current has several parameters associated with it that are typically not known a priori and must also be estimated from the data.

Data assimilation is widely used in fields such as geoscience and numerical weather prediction but has only recently begun to be applied in neuroscience. One of the main classes of DA algorithms are variational methods such as 4D-Var that seek solutions through optimization over a time window and are able to deal more effectively with a large number of unobserved state variables and unknown parameters. Since our *R. pumilio* SCN model has many parameters that are not known a priori we chose to employ the variational approach in this study.

A variational data assimilation algorithm was used to perform model fitting. We used current-clamp data from multiple protocols (Fig. S1) simultaneously to inform the estimated model of robust responses to changes in the applied current. We initially used a set of channels in our *R. pumilio* model similar to that previously used for a mouse SCN model (Belle *et al.*, 2009) (Fig.4A), but permitted each of the parameters in the model the freedom to be distinct for each individual cell that we fit. We started the estimation algorithm for each cell using over

50 initial guesses for the parameters and state variables, and performed model selection by assessing a Pareto frontier consisting of the DA cost function evaluation and the mismatch in firing rate between the model output and the data for simulations the resulting model under various current-clamp conditions. These simulations were preformed using the ode15s and ode45 solvers in MATLAB.

Data assimilation algorithm

Here we briefly describe the variational DA algorithm employed in this paper (see (Moye, 2020) for further details). We represent the neuronal recordings using the following state-space description:

$$\begin{aligned}x_{k+1} &= f(x_k) + \omega_{k+1}, & x_k &\in R^L \\y_{k+1} &= V_{k+1} + \eta_{k+1}, & y_k &\in R^1\end{aligned}$$

where x_k is interpreted as the state of the neuron at some time t_k and y_k are our observations (i.e. the voltage measurements). The random variables ω_k and η_k represent model error and measurement error, respectively. We assume that $\omega_k \sim \mathcal{N}(0, Q)$ and $\eta_k \sim \mathcal{N}(0, R)$, where Q and R are the model error and measurement error covariance matrices, and that these have no cross-covariance.

Strong 4d-var forces our observations to be consistent with the model, f . This can be considered the result of taking $Q \rightarrow 0$, which yields the nonlinearly constrained problem:

$$C(x) = \frac{1}{2} \sum_{k=0}^N R^{-1} (y_k - V_k)^2$$

such that

$$x_{k+1} = f(x_k), \quad k = 0 \dots N$$

where R^{-1} can now be scaled out completely.

In the cost function, the estimated voltage is expected to be consistent with the dynamics for large model weighting Q^{-1} , but the dynamics cannot possibly reproduce the irregularity in the data.

Dynamical State and Parameter Estimation (DSPE) is a technique described by Abarbanel et al. (2009) (Abarbanel, 2009), with the premise being to stabilise the synchronization manifold of data assimilation problems by adding a control or “nudging” term u . The cost function then becomes:

$$C(x) = \frac{1}{2} \sum_{k=0}^N R^{-1} (y_k - V_k)^2 + \sum_{k=0}^N u_k^2$$

This synchronization procedure has also been considered for specific function forms of u in the neuroscience context in (Brookings *et al.*, 2014) wherein they set up an optimal search strategy applied to real data. The nudging strategy in general has been used in geosciences primarily for state estimation (Park, 2013). As shown in Toth et al. (2011) (Toth *et al.*, 2011) and Abarbanel et al. (2009) (Abarbanel, 2009), the control u acts to reduce conditional Lyapunov exponents.

The goal of DSPE is to define a high-dimensional cost functional which weakly constrains the estimated states to the system observations, and strongly constrains the estimates to the controlled model dynamics while penalizing the control. Without the control, the problem is explicitly formulated as a strong constraint 4D-Var. However, the basin of attraction for global minima along the optimization manifold is shallow. Also, while the minimization term itself is convex, the nonlinearities present in the model constraints generate a large degree of non-convexity in the solution manifold. The intended effect of the nudging term is to

smoothen the surface. Given that the system is so high dimensional and tightly coupled, formally visualizing this surface is not achievable for our parameter estimation problems.

In the DSPE framework, parameters and states at each point in time are taken on equal footing. Namely, the solution space of the cost function is $(L + 1)(N + 1) + D$ where D is the number of fixed parameters to infer and L is the number of dynamical variables. Additionally, we are solving for the control $u(t)$ at each point in time. The control is penalised quadratically in an effort to reduce the impact of it at the end of the optimization procedure. While having the control present enforces the data in the model equations, by minimizing it, one is attempting to recover back the minima subject to the uncontrolled model of the system. So, as $u \rightarrow 0$ over the course of the optimization, the physical system strong constraint is recovered. We note that in the results presented here, the control term was not fully eliminated by the end of the assimilation window. This may be due to intrinsic voltage-gated conductances present in the cell that are not included in our model, or other factors such as synaptic input or channel noise.

We must choose a particular transcription method to prescribe our equality constraints. We define our state vector as $x = (V, \bar{x})$ and our uncontrolled dynamics as:

$$\frac{dx}{dt} = f_x(x, \theta)$$

where we can separate out the terms with observations. We assume we only have observations of the voltage of one cell in one compartment (with natural generalizations to networks and multi-compartment descriptions):

$$\begin{aligned} \frac{dV}{dt} &= f_V(\bar{x}, V; \theta) \\ \frac{d\bar{x}}{dt} &= f_{\bar{x}}(\bar{x}, V; \theta). \end{aligned}$$

Then our controlled dynamics become

$$\begin{aligned} \frac{dV}{dt} &= f_V(\bar{x}, V; \theta) + u(V_{obs} - V) \\ \frac{d\bar{x}}{dt} &= f_{\bar{x}}(\bar{x}, V; \theta) \end{aligned}$$

where it is understood that $u(t)$ appears only at observational times.

We can formulate the constraints using either a multiple-shooting style approach or using collocation. We will assume measurements are taken uniformly at $t_k = t_0 + k\tau_{obs}$. High resolution measurements are preferred so that we can have control and knowledge of the system at basically every knot point. However, there are circumstances where we may not have data with that level of precision, or we may desire to downsample our data. For that reason, we will say that we have a set of times upon which our constraint equations are satisfied, namely $t_m = t_0 + m\tau_{col}$ where we simply require that the ratio of these time differences is a positive integer, $\frac{\tau_{obs}}{\tau_{col}} \in N$.

To reiterate, the constraints are what connect each of our time points $[t_m, t_{m+1}]$ to one another.

We use a direct collocation method due to the stability options afforded to us for our highly complex, nonlinear problem. With collocation, implementation of implicit methods is effectively as simple as explicit methods. We choose to use Hermite-Simpson collocation which approximates the set of discrete integrations using Simpson's rule. We introduce midpoints in this fashion $(x_{k+\frac{1}{2}})$, which are approximated using Hermite interpolation.

$$x_{k+1} - x_k = \frac{1}{6}h_k \left(f_k + 4f_{k+\frac{1}{2}} + f_{k+1} \right)$$

$$x_{k+\frac{1}{2}} = \frac{1}{2}(x_k + x_{k+1}) + \frac{h_k}{8}(f_k - f_{k+1})$$

where $f_k = f_x(x_k, \hat{\theta})$ and $\hat{\theta}$ is the present estimate of θ constant across our time window.

Here, we take the midpoint and endpoint conditions on equivalent footing for our constraints, $g(x) = 0$, in what is known as its "separated form". Therefore, we implement these equations so that $h_k = 2\tau_{col}$ based upon our previous notation, and we have LN equality constraints.

State and parameter bounds

Setting lower and upper bounds for the state and parameter estimates, $x^L \leq x \leq x^U$, can improve the performance of the DA algorithm. For the states, we specify that the voltage is within a plausible physiological range based on prior knowledge of the system and the variance in the observations. The gating variables are restricted to their dynamic range between 0 and 1. As for the parameters, it is difficult to know how tight the boundaries should be. As a rule of thumb, if it is possible to parameterise the model in a systematic and symmetric way, it may be easier to construct meaningful bounds. Also, it is advisable to keep the parameters within a bounding box which prevents blow-up of the dynamics such as divisions by zero. The maximal conductances are positive valued, and the sign of the slope for the steady-state gating functions should dictate if they are activating (positive) or inactivating (negative).

Background knowledge of the passive properties of the system, such as the capacitance and reversal potentials, can be informed from isolating step protocols by the electrophysiologist or voltage-clamp data if that is available.

Implementation

We have implemented 4D-Var in a framework with CasADi, (Andersson *et al.*, 2019), in MATLAB. The "cas" comes from "computer algebra system", in which the implementation of mathematical expressions resembles that of any other symbolic toolbox, and the "AD" for algorithmic (automatic) differentiation. These expressions are then easily used for generating derivatives by breaking the expressions into a number of atomic operations with explicit chain rules, with natural extensions to vector and matrix-valued functions. CasADi data types are all sparse matrices, and low-level scalar expressions (SX type) are stored as directed acyclic graphs where their numerical evaluation is conducted using virtual machines. For nonlinear programming problems, matrix expressions (MX type) are constructed to form the structure of the nonlinear program e.g. the collocation expression. The low-level expressions e.g. the differential equations are built using SX type to create a hierarchy of functions for evaluation efficiency and memory management. CasADi will generate the gradient and Hessian information through AD which are then passed to the solver of choice. We elect to solve the optimization problem with IPOPT (Interior Point OPTimize) (Wächter & Biegler, 2006). The high-dimensional linear algebra calculations are done using the linear solver MUMPS (MULTifrontal Massively Parallel sparse direct Solver) which is readily distributed with CasADi and interfaced with IPOPT.

Conductance-based model

An issue with the original version of the mouse SCN model (Sim & Forger, 2007; Belle *et al.*, 2009) is that the structure is asymmetric with huge ranges of parameter values, which creates complications when constructing our optimization problem. We aim to fit to current-clamp data of the *R. pumilio* using the same set of currents, but expressing their kinetics uniformly. Additionally, we separate the leak into sodium and potassium components to investigate the role each may play in altering the resting membrane potential of cells in day versus night, as was done in (Diekman *et al.*, 2013). Lastly, we will approximate the sodium activation as instantaneous, as has been done previously to reduce the dimensionality of the

SCN model (Sim & Forger, 2007). Conversely, we will allow the inactivation of sodium to have a wide range of permissible time constant values, as persistent sodium is known to play a role in maintaining the pace of firing (Harvey *et al.*, 2020). Thus, our sodium channel functionally plays the classical role of a transient sodium current in generating the upstroke of the action-potential, but also is possibly involved in governing certain sub-threshold properties. The full model is described by the following equations:

$$\begin{aligned}
 C \frac{dV}{dt} &= I_{app}(t) - I_{Na} - I_K - I_{Ca} - I_{LNa} - I_{LK} - I_H - I_A - I_{syne-E} - I_{syn-I} \\
 &= I_{app}(t) - g_{Na} m_{Na}^3 h_{Na} (V - E_{Na}) - g_K n^4 (V - E_K) - g_{Ca} m_{Ca} h_{Ca} (V - E_{Ca}) - g_{LNa} (V - E_{Na}) \\
 &\quad - g_{LK} (V - E_K) - g_H m_H (V - E_H) - g_A m_A^3 h_A (V - E_K) \\
 &\quad - g_{syne-E} s(t) (V - E_{syn-E}) - g_{syn-I} s(t) (V - E_{syn-I}) \\
 \\
 \frac{dq}{dt} &= \frac{q_{\infty}(V) - q}{\tau_q(V)}, \quad q = \{m_i, h_i, n\} \\
 q_{\infty}(V) &= \frac{1}{2} + \frac{1}{2} \tanh\left(\frac{V - v_q}{dv_q}\right) \\
 \tau_q(V) &= \tau_{q0} + \tau_{q1} \left(1 - \tanh^2\left(\frac{V - v_q}{dv_q}\right)\right)
 \end{aligned}$$

where C is membrane capacitance, V is membrane potential, $I_{app}(t)$ is the applied current, I are ionic currents, g are maximal conductances, E are reversal potentials, and q are gating variables with steady-state functions q_{∞} and time constants τ_q . The active conductance of a channel, G , is the product of its maximal conductance and gating variables, e.g. $G_{Na} = m_{Na}^3 h_{Na}$. The g_A and τ_{h_A} scaling factors used in Figures 6 and 7 are coefficients that multiply the maximal conductance parameter and time constant variable, respectively. The scaling factor for the ratio of potassium to sodium leak conductance used in Figures 7 and S4 is a coefficient that divides g_{LNa} and multiplies g_{LK} . We calculated the synaptic gating variable $s(t)$ from voltage-clamp recordings of post-synaptic currents in *R. pumilio* SCN neurons with the cells held at -70 mV. The synaptic currents I_{syne-E} and I_{syn-I} were not used in the DA procedure, and were only included in the model simulations shown in Figure 7A-B. The I_H and I_A currents were only included in the DA procedure and model simulations shown in Figures 6B-C and 7.

Downsampling

We utilized a downsampling strategy on the current-clamp data in order to facilitate the use of longer stretches of data without exceeding the computational limits on the size of the optimization problem that our computing resources can handle. We set a threshold of -20 mV for each action potential, and within a region of 30 ms on either side of when this threshold is hit, the full 25 kHz sampling is preserved. Outside of this window, the data used is downsampled by some factor. For the results presented here, we used a downsampling factor of 5 so that during the action potential the resolution is 25kHz and outside the time window of the action potential it is 5kHz. With this strategy, we can retain as many data points as possible during the action potential, which occurs on a much faster timescale than the membrane dynamics during the interspike interval and enables us to better fit the spike shape. We also used the full 25 kHz sampling for the 30 ms region immediately following the onset or offset of the depolarizing and hyperpolarizing pulses.

Multiple observations

A novel component of our DA approach is the use of multiple observations to inform a unified model for each cell's electrophysiology. We are restricted through a computational and memory budget with regard to our implementation on the amount of data we can use for each estimation. In a sense, we have a series of variational sub-problems solved

simultaneously which are connected through mutually shared parameters. We use symmetric current-clamp protocols which start with spontaneous activity, followed by either a depolarizing or hyperpolarizing step for 1s, and a subsequent return to spontaneous activity. We use a period of a few hundred ms prior to two different hyperpolarizing steps so as to access leak channel information and transient inactivation profiles. We use two similar segments from the return from hyperpolarizing steps to inform de-inactivation and activation time scales from rest. We use similar data for two responses to depolarizing steps to characterize the firing profiles and understand the limiting behavior for high-amplitude depolarizing pulses, including regular firing, firing with adaptation, or silence. We bias the data with a large segment (1500 ms) of data during spontaneous activity to reproduce the hallmark spontaneous activity and spike shape in our estimated models. In the problem construction shown by Figure S1, 4.5 seconds of data in total are used for the assimilation, amounting to around 36,000 time points after incorporating our downsampling strategy.

Acknowledgements

We would like to thank the members of the University of Manchester Biological Services Facility for their excellent assistance in colony maintenance and husbandry. We also thank Profs Luckman and Andy Randall for allowing us access to their electrophysiology equipment.

This work was funded by a Biotechnology and Biological Sciences Research Council (BBSRC) Industrial Partnership Award with Signify (BB/P009182/1) to R.J.L, and by grants from the BBSRC to MDCB (BB/S01764X/1) and to TMB (B/N014901/1), and the Wellcome Trust (210684/Z/18/Z) to R.J.L. This material is based upon work supported by grants from the National Science Foundation (DMS 155237), the US Army Research Office (W911NF-16-1-0584), and the US-UK Fulbright Commission to COD. MJM and COD gratefully acknowledge the financial support of the EPSRC via grant EP/N014391/1.

Author contributions: B.B.O, M.J.M, T.M.B, R.J.L, C.O.D and M.D.C.B conceived and designed research; B.B.O and M.D.C.B performed electrophysiology experiments; B.B.O performed data analysis; M.J.M and C.O.D performed mathematical modelling; B.B.O, M.J.M, T.M.B, R.J.L, C.O.D and M.D.C.B wrote the paper.

Figure 1

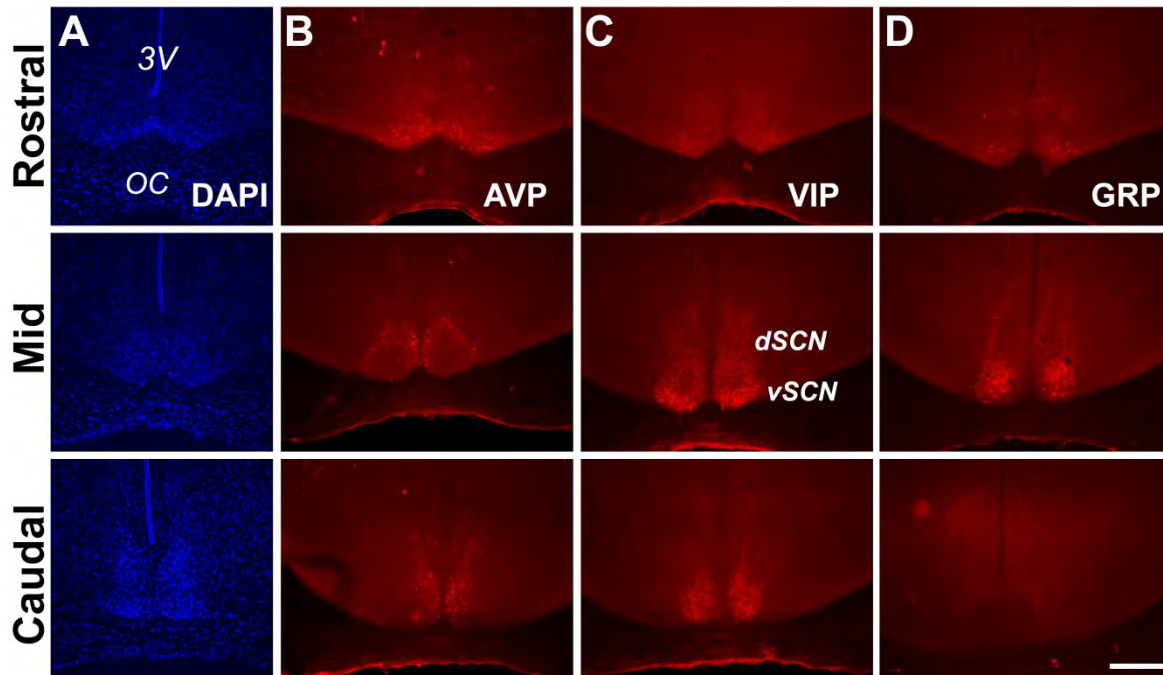


Figure 1. Anatomy and neuropeptidergic organization of the *Rhabdomys pumilio* SCN. (A) Coronal sections of the *R. pumilio* SCN taken across the rostro-caudal axis labelled with DAPI, and immunofluorescence for the main SCN neuropeptides: (B) Arginine-vasopressin (AVP), (C) Vasoactive intestinal peptide (VIP) and (D) Gastrin releasing peptide (GRP). 3V: third ventricle; OC: optic chiasm. dSCN: dorsal SCN, vSCN: ventral SCN. Labelling at the rostral level applies to mid and caudal aspects. Scale bar: 250 μ m.

Figure 2

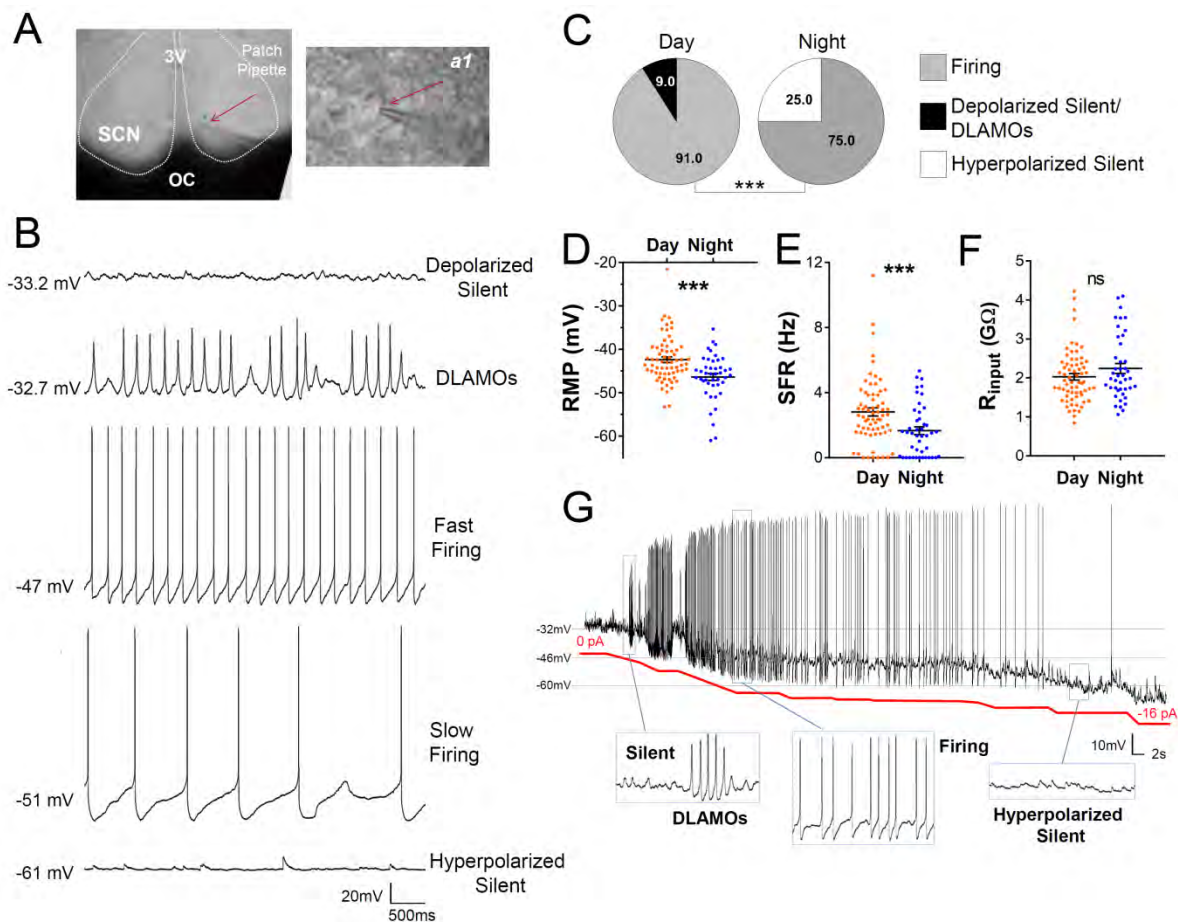


Figure 2. Diurnal changes in the spontaneous electrical activity of *Rhabdomys pumilio* SCN neurons. (A) Whole-cell patch clamp recording setup showing bright-field image of a SCN coronal brain slice. The SCN (delineated by white dotted lines) can be observed above the optic chiasm (OC), on either side of the third ventricle (3V). Patch pipette targeting a SCN neuron is indicated by the red arrow and magnified in inset (a1). (B) Representative current-clamp traces for each of the spontaneous excitability states recorded in *R. pumilio* SCN neurons (from top): highly depolarized-silent; depolarized low-amplitude membrane oscillations (DLAMOs); moderate resting membrane potential (RMP) with cells firing action potentials (APs) at high or low rate; and hyperpolarized-silent neurons. (C) Pie charts showing the percentages of SCN neurons in the different electrical states during the day and at night (** $p < 0.001$, Chi-Squared test). Mean RMP (D), spontaneous firing rate (SFR) (E) and input resistance (R_{input}) (F) of neurons recorded during the day (orange, $n=67$) and at night (blue, $n=44$). Data are expressed as mean \pm SEM with each dot representing an individual neuron. *** $p \leq 0.001$, Mann-Whitney U-test. (G) Manual hyperpolarization of hyperexcited SCN neurons elicits a range of electrical states. Silent cell resting at highly depolarized state could be driven to display DLAMOs, fire APs, and become hyperpolarized-silent by injection of progressive steps of steady-state hyperpolarizing currents (red line).

Figure 3

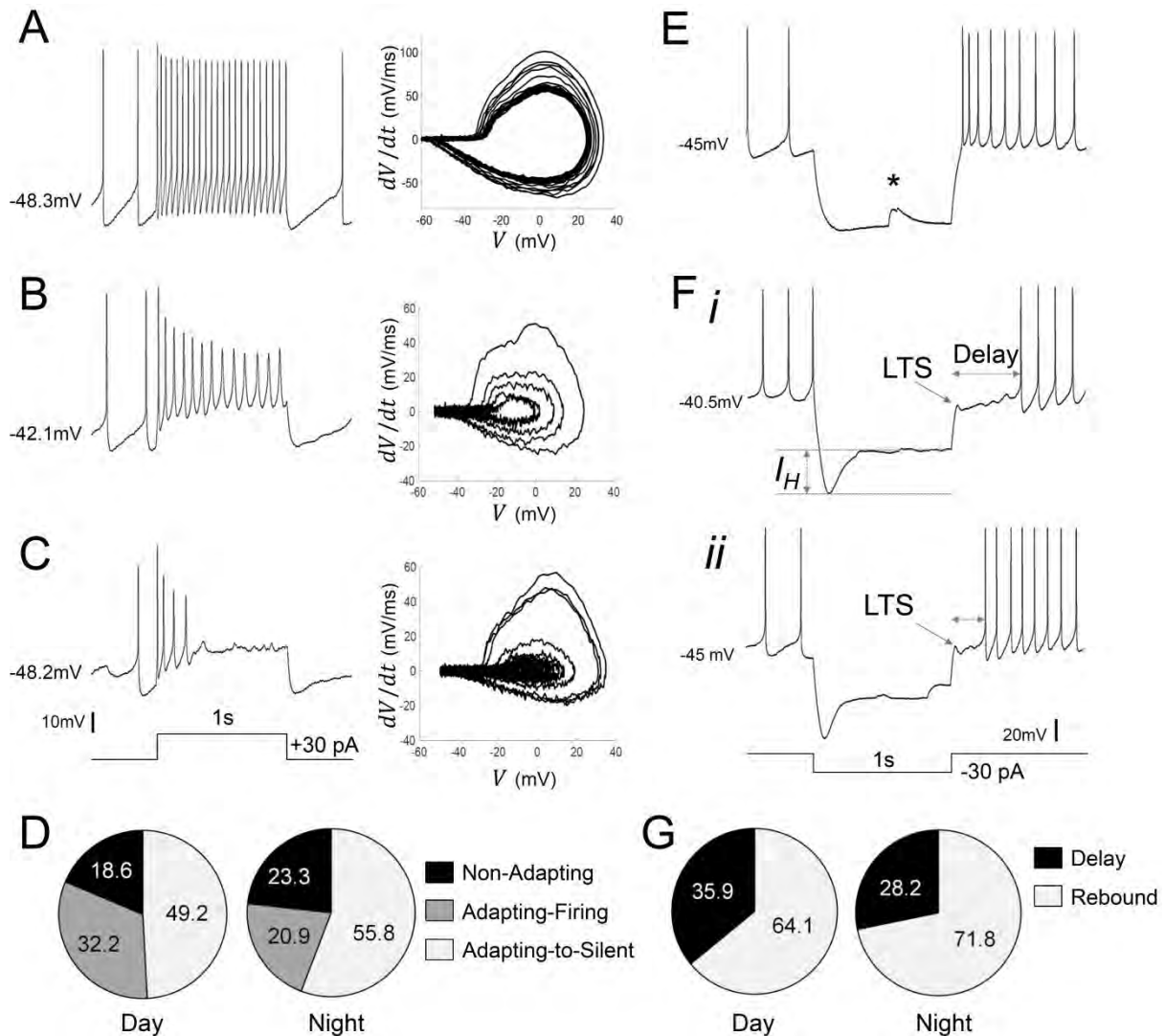


Figure 3. Diverse responses to depolarizing and hyperpolarizing current pulses in *Rhabdomys pumilio* SCN neurons. Representative current-clamp traces showing the different type of responses to a depolarizing pulse (1s, +30pA): (A) non-adapting; (B) adapting-firing; or (C) adapting-to-silent response. Phase-plot diagrams on the right of each panel (A, B, or C) show action potential (AP) velocity, trajectory and rate of frequency adaptation during the pulse for these neurons. (D) Pie charts showing the percentage of recorded neurons displaying each of these responses to depolarizing pulses during the day and at night. (E-F) Representative current-clamp traces showing the different type of responses to a 1s, -30pA hyperpolarizing pulse: (E) Type-A cells responded with a rebound spike upon termination of the pulse; (F) Type-B cells exhibited a rebound hyperpolarization which produced a delay-to-fire, following a LTS ((i-ii) long and short delay, respectively). (G) Pie charts showing the percentage of cells displaying a rebound spike or a delay-to-fire response during the day and at night. * indicates a spontaneous synaptic input. LTS: low threshold spike. I_H : inward membrane rectification or depolarizing “sag”.

Figure 4

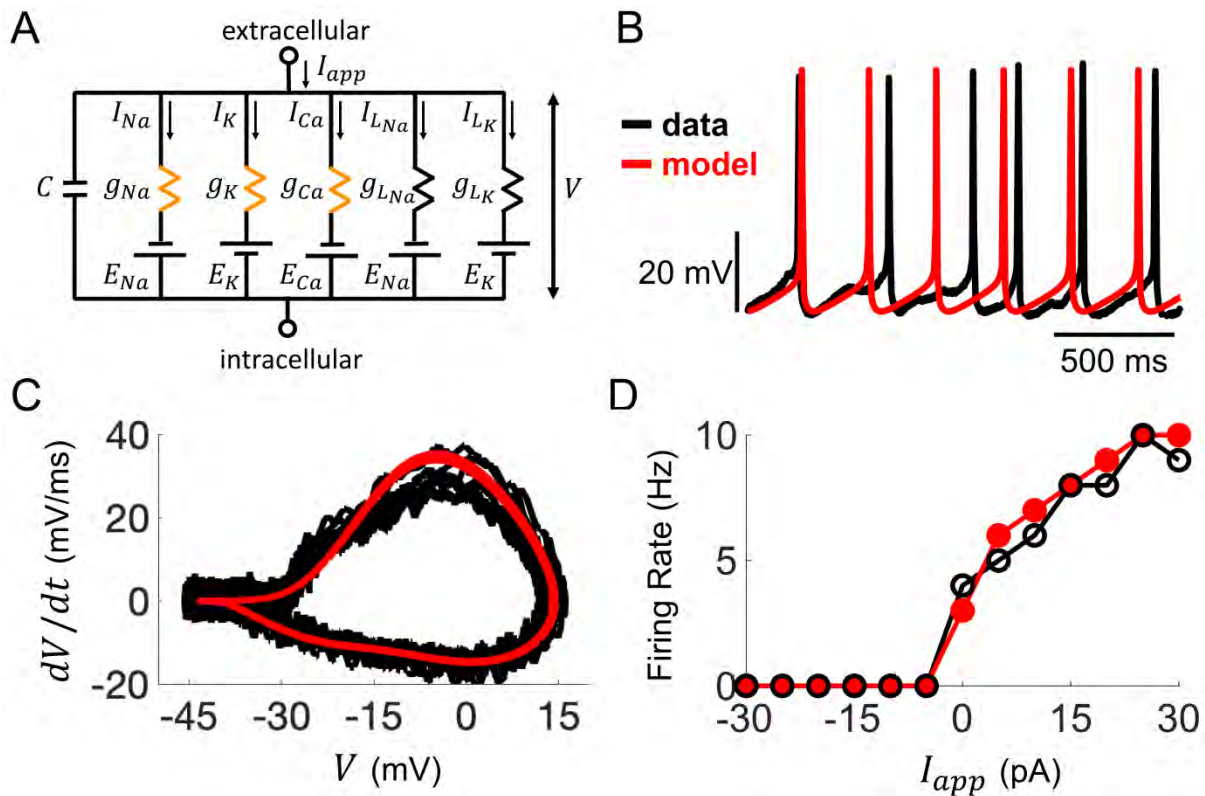


Figure 4. Computational modelling of *Rhabdomys pumilio* SCN neurons. (A) Schematic of conductance-based model for *R. pumilio* SCN neurons containing sodium (I_{Na}), calcium (I_{Ca}), potassium (I_K), and leak (I_{LNa} , I_{LK}) currents. Orange resistors (g_{Na} , g_{Ca} , g_K) indicate voltage-gated conductances, black resistors (g_{LK} , g_{LNa}) indicate passive leak conductances. (B) Voltage traces showing similarity in spontaneous firing of action potentials (APs) in the model (red) compared to a current-clamp recording from a *R. pumilio* SCN neuron (black). (C) Phase-plot of the derivative of voltage with respect to time (dV/dt) as a function of voltage (V) depicting the shape of APs in the model (red) and the current-clamp recording (black) during spontaneous firing. (D) Similarity in firing rate of the model (red) and current-clamp recordings (black) as a function of applied current (I_{app}).

Figure 5

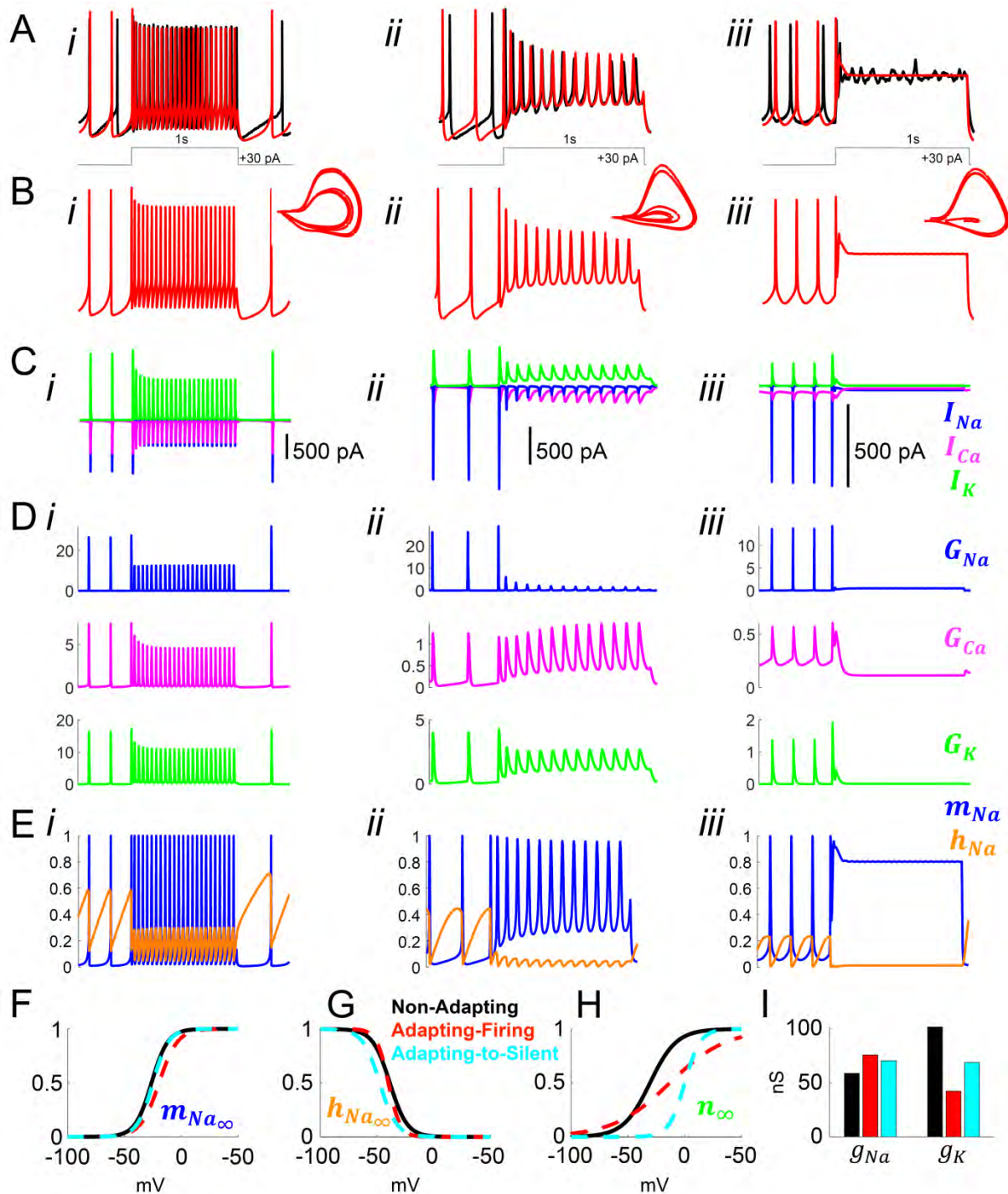


Figure 5. Model simulation of the responses to depolarizing pulses in *Rhabdomyus pumilio* SCN neurons and the underlying ionic mechanisms. (A-B) Voltage traces of models (red) and current-clamp recordings (black) during depolarizing pulses (1s, +30 pA) showing non-adapting (i), adapting-firing (ii), and adapting-to-silent (iii) responses. **(C)** Ionic currents sodium (I_{Na} , blue), calcium (I_{Ca} , magenta), and potassium (I_K , green) in the models during the non-adapting (i), adapting-firing (ii), and adapting-silent (iii) responses. **(D)** Ionic conductances for sodium (G_{Na} , blue), calcium (G_{Ca} , magenta), and potassium (G_K , green) in

the models during the non-adapting (*i*), adapting-firing (*ii*), and adapting-silent (*iii*) responses. **(E)** Sodium activation (m_{Na} , blue) and inactivation (h_{Na} , orange) gating variables in the models during the non-adapting (*i*), adapting-firing (*ii*), and adapting-silent (*iii*) responses. Ions cannot pass through the channel if it is closed ($m_{Na} = 0$) or inactivated ($h_{Na} = 0$); maximal current flows when the channel is fully open ($m_{Na} = 1$) and fully de-inactivated ($h_{Na} = 1$). Steady-state gating variables as a function of voltage in the non-adapting (black), adapting-firing (red), and adapting-to-silent (cyan) models for **(F)** sodium activation ($m_{Na\infty}$), **(G)** sodium inactivation ($h_{Na\infty}$), and **(H)** potassium activation (n_{∞}). The flattening of the n_{∞} curve in the adapting-firing model indicates that the channel is less activated at depolarized voltages than the non-adapting model (e.g. at -13 mV, the adapting-firing model is only half activated ($n_{\infty} = 0.5$), whereas the non-adapting model is almost fully activated ($n_{\infty} = 0.93$)). **(I)** Maximal conductance parameters g_{Na} and g_K in the non-adapting (black), adapting-firing (red), and adapting-to-silent (cyan) models. Notice that the maximal potassium conductance parameter is much smaller in the adapting-firing model ($g_K = 43$ nS) than in the non-adapting model ($g_K = 102$ nS).

Figure 6

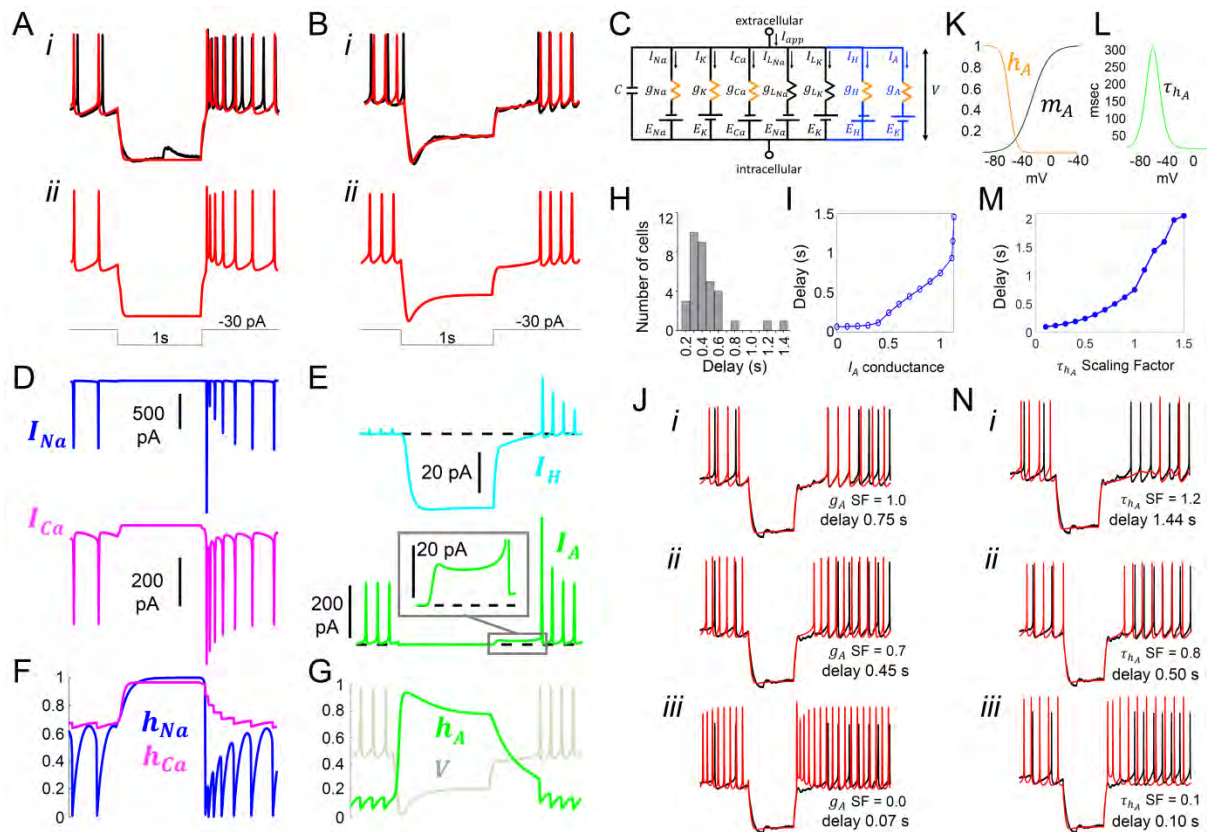


Figure 6. Model simulation of the responses to hyperpolarizing pulses in *Rhabdomy pumilio* SCN neurons and the underlying ionic mechanisms. (A-B) Voltage traces of models (red) and current-clamp recordings (black) during hyperpolarizing pulses (1s, -30 pA) showing rebound spiking of Type-A neurons (A) and delay responses of Type-B cells (B). **(C)** Schematic of conductance-based model for Type-B *R. pumilio* SCN neurons showing the addition of transient potassium (I_A) and hyperpolarization-activated (I_H) currents (blue). **(D)** Ionic currents for sodium (I_{Na} , blue) and calcium (I_{Ca} , magenta) in the model during the Type-A neuronal rebound spiking response. **(E)** Ionic currents I_H (cyan) and I_A (green) in the model during the delay response of Type-B neurons. **(F)** Sodium (h_{Na} , blue) and calcium (h_{Ca} , magenta) inactivation gating variables in the model during the Type-A neuronal rebound spiking response. **(G)** Transient potassium (I_A) inactivation gating variable (h_A , green) in the model during the delay response in Type-B neurons (voltage trace, V , is indicated in grey and is the same V -trace shown in B). **(H)** Histogram showing delay-to-fire latencies measured in Type-B cells. **(I)** Relationship between I_A conductance (g_A Scaling Factor) and delay-to-fire latencies in model of Type-B cells. **(J)** Data trace for a cell with a 0.75 s delay (black) overlaid with model voltage traces (red) with varied amounts of I_A conductance: (i) model of Type-B cell with g_A SF = 1 exhibiting a 0.75 s delay; (ii) Model from (i) with reduced I_A conductance (g_A SF = 0.7) exhibiting a reduced delay-to-fire latency; (iii) Model from (i) with no I_A current (g_A SF = 0), exhibiting rebound spiking, as in Type-A neurons. g_A SF: g_A Scaling Factor. **(K-L)** Gating variable functions for model I_A current: **(K)** steady-state activation (m_A , black), steady-state inactivation (h_A , orange), and **(L)** inactivation time constant (τ_{h_A} , green). **(M)** Relationship between the time constant of I_A inactivation and delay-to-fire latencies in model of Type-B cells. **(N)** Model simulations for I_A inactivation time constant scaling factors of 1.2 (i), 0.8 (ii) and 0.1 (iii). τ_{h_A} SF: τ_{h_A} Scaling Factor

Figure 7

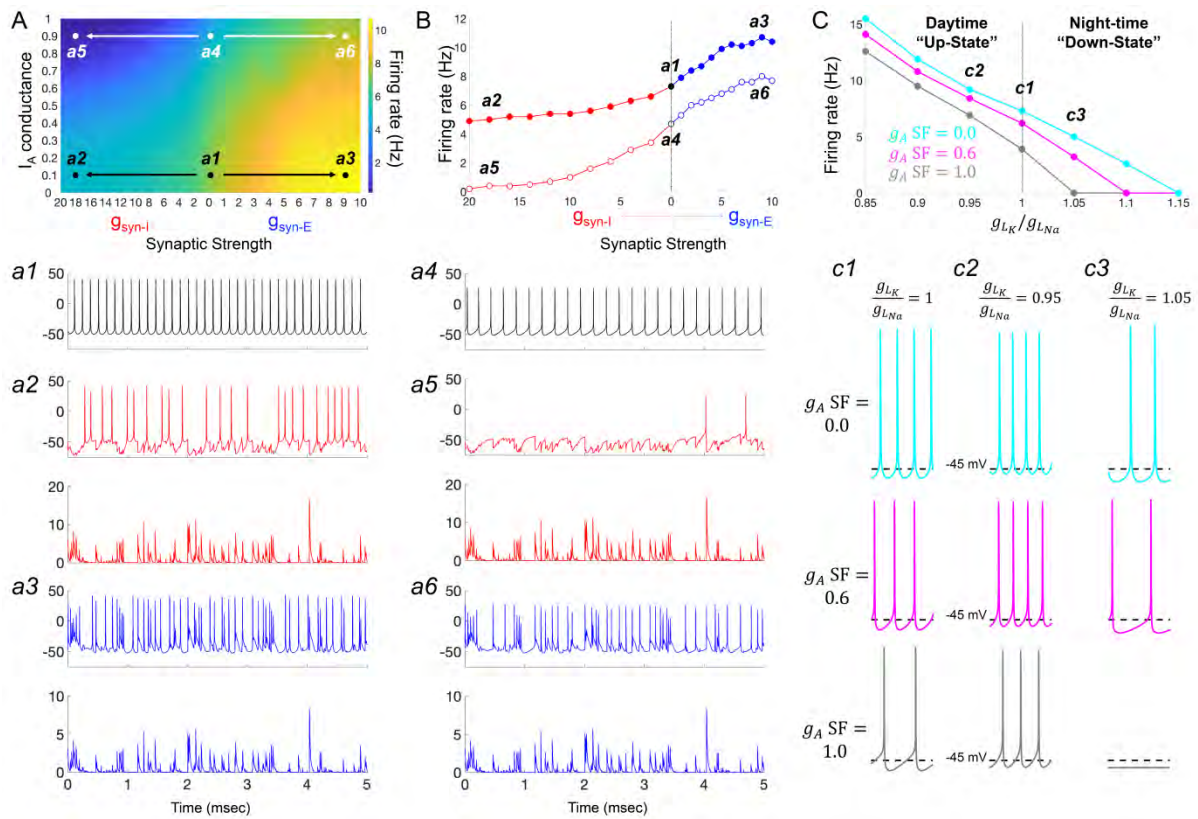


Figure 7. I_A conductances act to amplify extrinsic and intrinsic suppressive signals in the *Rhabdomyys pumilio* SCN. (A) Heatmap showing the overall effects of inhibitory (g_{syn-I} , red) and excitatory (g_{syn-E} , blue) physiological GABAergic synaptic conductances on firing frequency with increasing I_A conductances in the model *R. pumilio* SCN neurons. **(a1-a3)** Examples of firing activity in model cell with low I_A conductance (g_A SF = 0.1) and absence of GABAergic synaptic conductance (**a1**, $g_{syn-I} = g_{syn-E} = 0$ nS), high suppressive GABAergic synaptic conductance (**a2**, $g_{syn-I} = 18$ nS), or high excitatory GABAergic synaptic conductance (**a3**, $g_{syn-E} = 9$). **(a4-a6)** Examples of firing activity in model *R. pumilio* SCN neurons with high I_A conductance (g_A SF = 0.9) and absence of GABAergic synaptic conductance (**a4**, $g_{syn-I} = 0$ nS), high suppressive GABAergic synaptic conductance (**a5**, $g_{syn-I} = 18$ nS), or high excitatory GABAergic synaptic conductance (**a6**, $g_{syn-E} = 9$). **(B)** Firing rate as a function of inhibitory (g_{syn-I} , red) and excitatory (g_{syn-E} , blue) GABAergic synaptic conductances of different strength. Open and filled dots correspond to model cell with high (0.9) or low (0.1) I_A conductance (g_A SF), respectively. **(C)** Overall effect of intrinsic excitability states (scaling factor for the ratio of potassium leak current (g_{LK}) to sodium leak current (g_{LNa}) from 0.85 to 1.15) on firing frequency with increasing I_A conductances in the model cell (g_A SF = 0 (cyan), 0.6 (pink) and 1.0 (grey)). g_{LK}/g_{LNa} SF less than 1 corresponds to a daytime “up-state”, and a SF greater than 1 to a night-time “down-state”. **(c1)** Effect of I_A ($g_A = 0, 0.6$ and 1.0) on firing rate with nominal potassium/sodium leak current ratio (g_{LK}/g_{LNa} SF = 1). **(c2)** Effect of I_A (g_A SF = 0, 0.6 and 1.0) on firing rate with reduced potassium/sodium leak current ratio (g_{LK}/g_{LNa} SF = 0.95), representing daytime up-state. **(c3)** Effect of I_A (g_A SF = 0, 0.6 and 1.0) on firing rate with elevated potassium/sodium leak current ratio (g_{LK}/g_{LNa} SF = 1.05), representing night-time down-state. Notice that I_A amplifies the suppressive action of the low intrinsic excitability state (during down-state). SF: scaling factor.

Figure S1

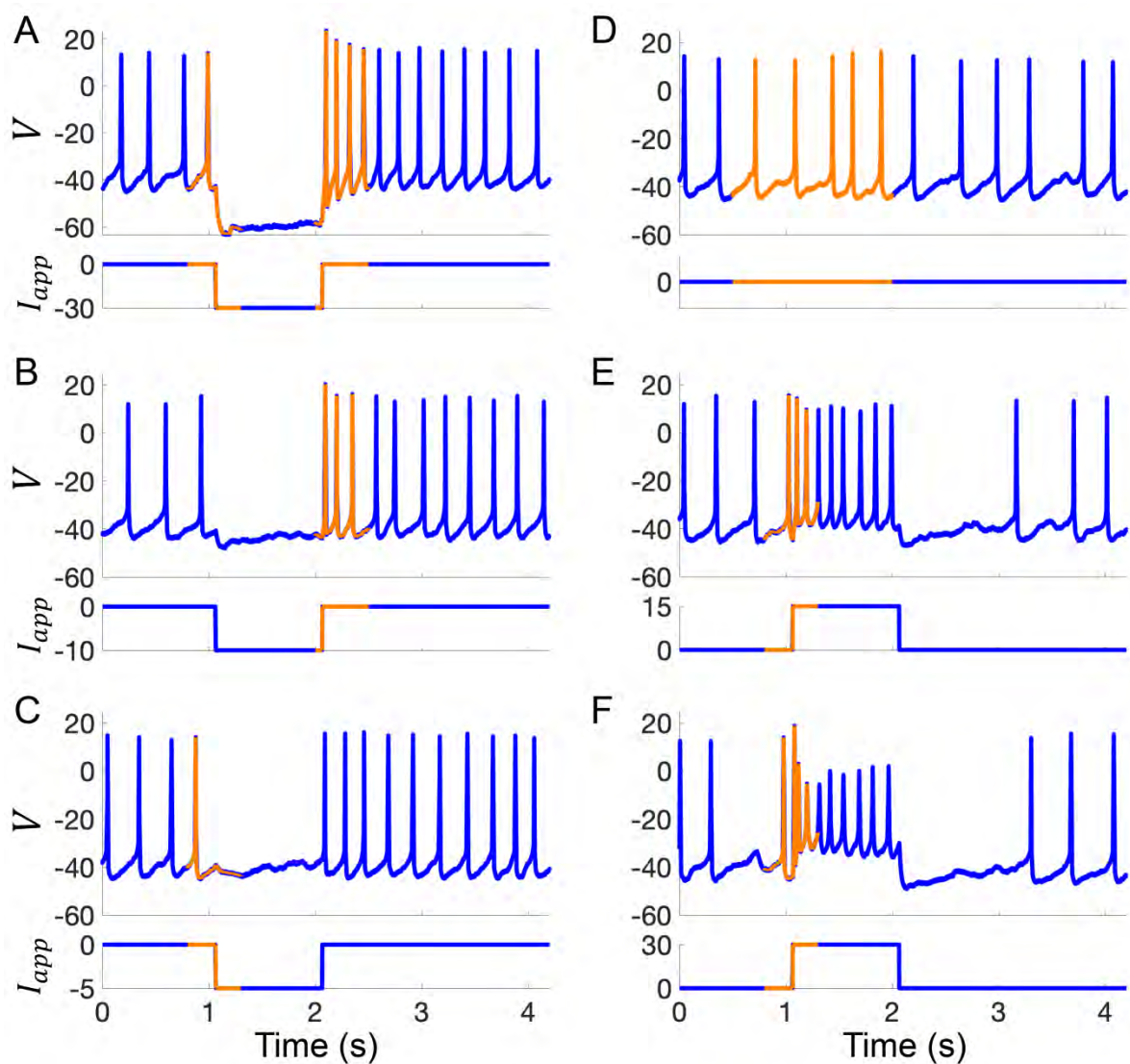


Figure S1. Example current-clamp traces used in data assimilation algorithm for building computational models of *Rhabdomys pumilio* SCN neurons. (A-F) Current-clamp recordings (blue) with the portion of the voltage trace used by the data assimilation algorithm (orange) to fit the model of rebound spiking in Type-A neuron shown in Figs. 4, 6A, and S2. **(A-C)** Hyperpolarizing current pulses. **(D)** Spontaneous activity. **(E-F)** Depolarizing current pulses.

Figure S2

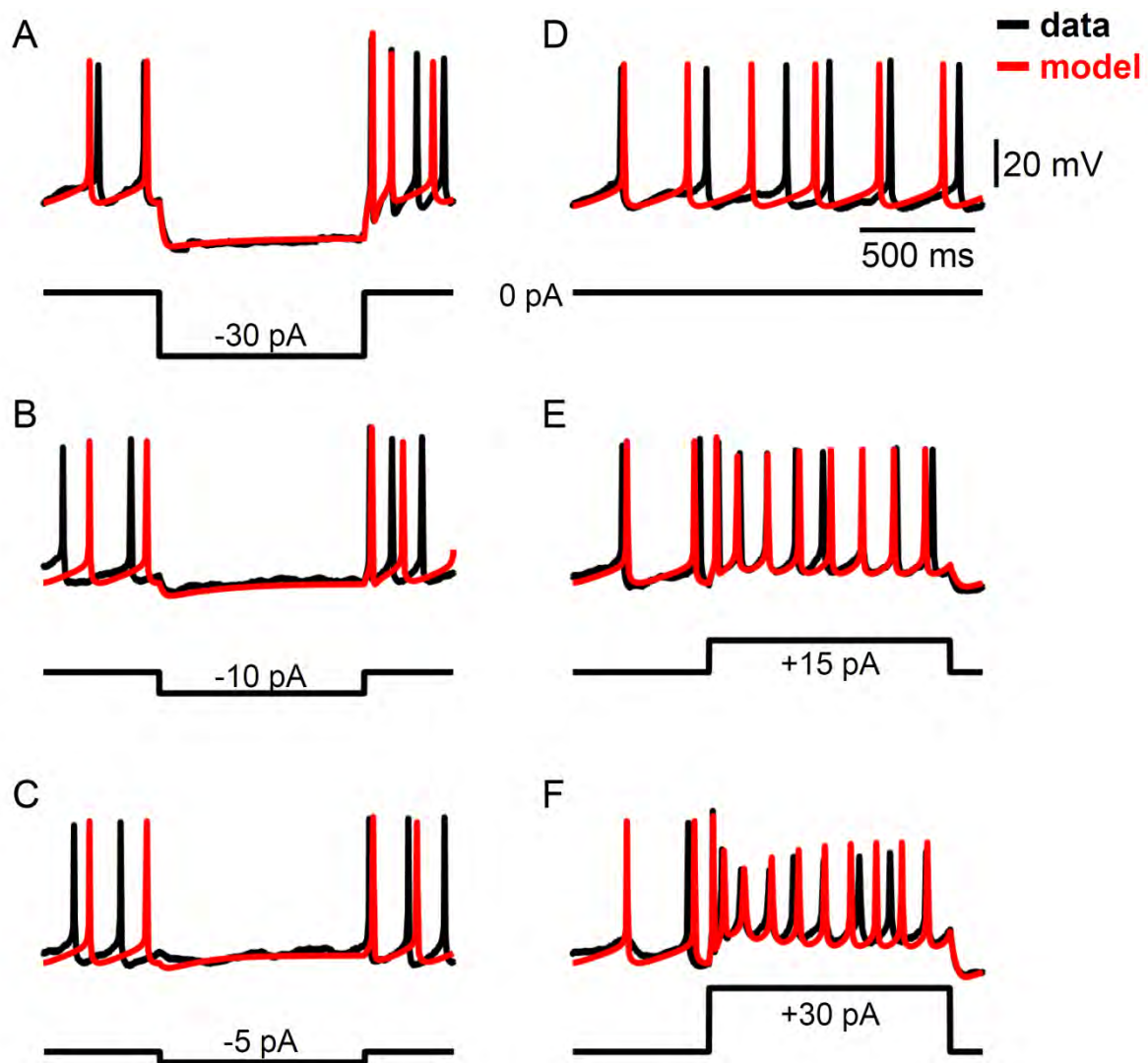


Figure S2. Example voltage traces for a computational model of *Rhabdomys pumilio* SCN neurons fit using a data assimilation algorithm. (A-F) Current-clamp recordings (black) and simulated voltage traces (red) from the model of rebound spiking in Type-A neurons shown in Figs. 4 and 6A using the portions of the data shown in Fig. S1. (A-C) Hyperpolarizing current pulses. (D) Spontaneous activity. (E-F) Depolarizing current pulses.

Figure S3

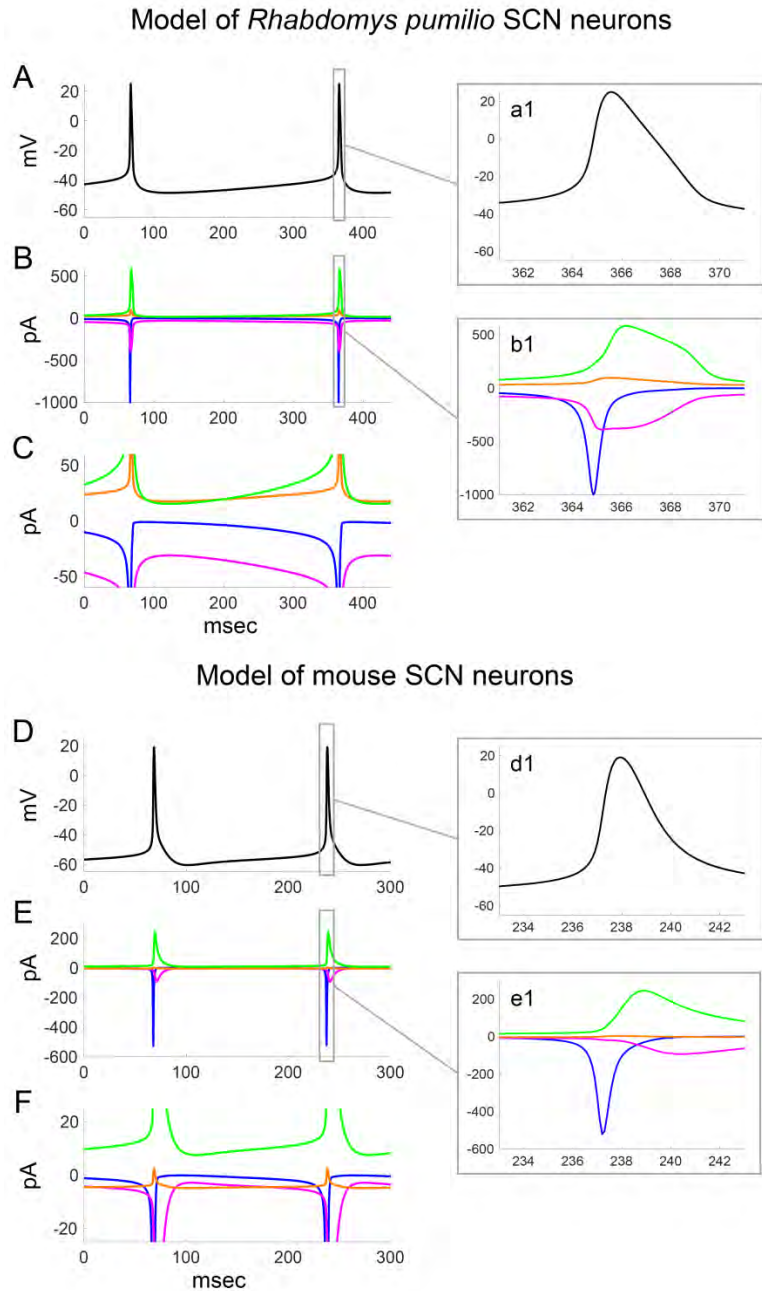


Figure S3. Ionic currents underlying action potential generation in computational models of *Rhabdomys pumilio* and mouse SCN neurons. (A) Voltage trace showing spontaneous firing in model of *R. pumilio* SCN neurons. **(a1)** Magnified view of second AP shown in (A). **(B)** Sodium (I_{Na} , blue), calcium (I_{Ca} , magenta), potassium (I_K , green), and leak ($I_{LK} + I_{LNa}$, orange) currents during the voltage trace shown in (A). **(b1)** Magnified view of currents during second AP shown in (A). **(C)** Same as (B), with y-axis scaled to emphasise the currents flowing during the interspike interval. **(D)** Voltage trace showing spontaneous firing in model of mouse SCN neurons. **(d1)** Magnified view of second AP shown in (D). **(E)** Sodium (I_{Na} , blue), calcium (I_{Ca} , magenta), potassium (I_K , green), and leak ($I_{LK} + I_{LNa}$, orange) currents during the voltage trace shown in (D). **(e1)** Magnified view of currents during second AP shown in (D). **(F)** Same as (E), with y-axis scaled to emphasise the currents flowing during the interspike interval.

Figure S4

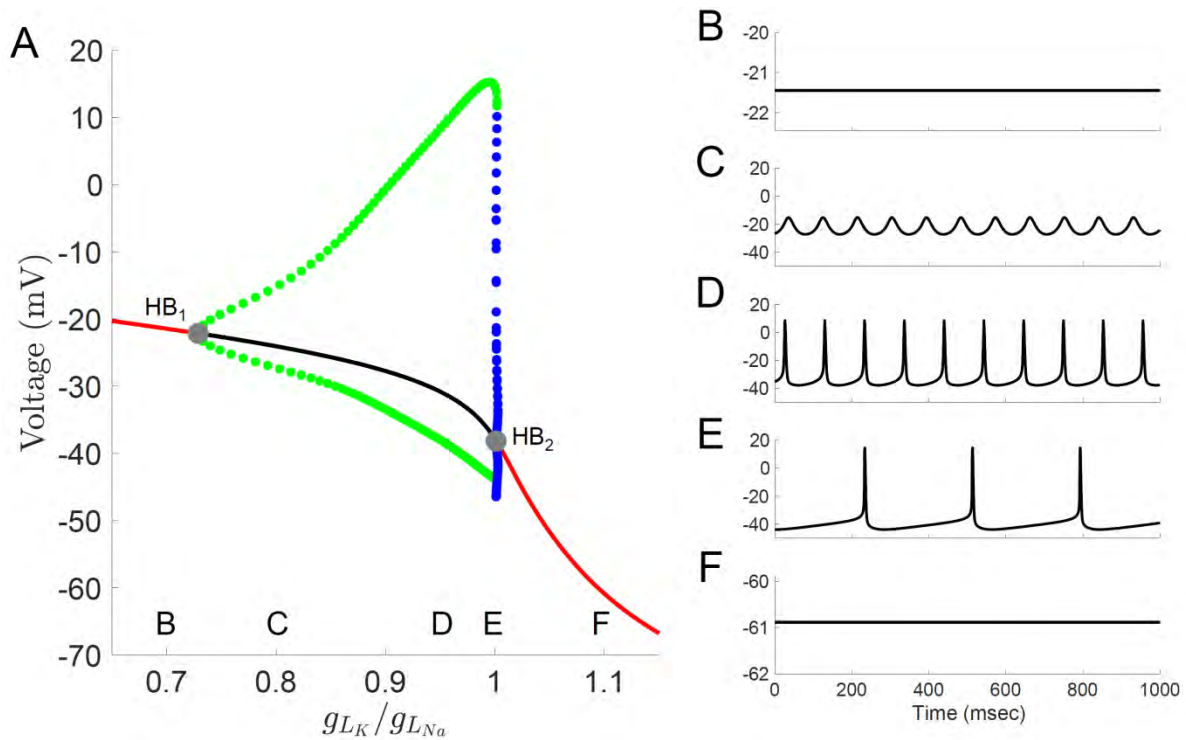


Figure S4. Bifurcation diagram for a computational model of *Rhabdomys pumilio* SCN neurons. (A) Voltage at steady-states and maximum/minimum voltage of oscillations for the model of rebound spiking in the Type-A neuron shown in Figs. 4, 6A, and S1-S3 with ratio of potassium leak current (g_{LK}) to sodium leak current (g_{LNa}) as the bifurcation parameter showing stable steady-states (black), unstable steady-states (red), stable periodic orbits (blue), and unstable periodic orbits (green). Stable periodic orbits correspond to spiking or DLAMOs. Transition from depolarized rest state to DLAMOs occurs through a supercritical Hopf bifurcation (grey dot HB_1) and transition from spiking to hyperpolarized rest state occurs through a subcritical Hopf bifurcation (grey dot HB_2). Model voltage traces showing each of the spontaneous excitability states: (B) highly depolarized-silent; (C) depolarized low-amplitude membrane oscillations (DLAMOs); moderate resting membrane potential (RMP) firing action potentials (APs) at high (D) or low rate (E); and hyperpolarized-silent neurons (F). According to the “bicycle model” proposed for the circadian regulation of electrical activity in mice and flies, a g_{LK}/g_{LNa} ratio scaling factor less than 1 corresponds to a daytime “up-state”, and a scaling factor greater than 1 to a night-time “down-state” (Flourakis *et al.*, 2015).

Figure S5

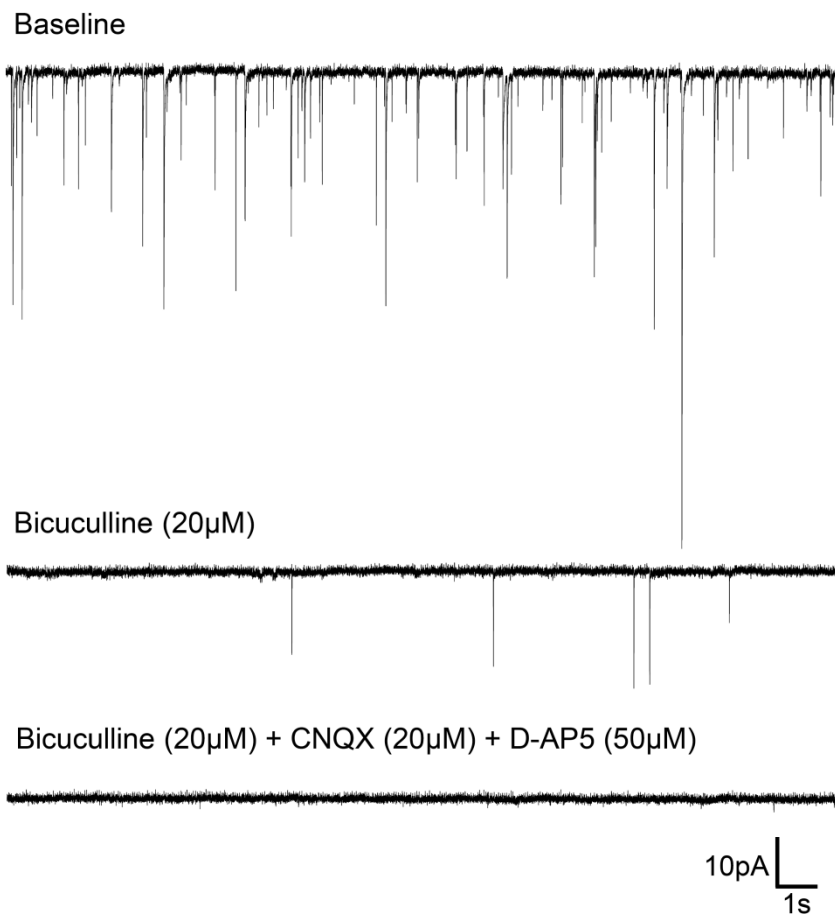


Figure S5. Spontaneous synaptic events in *Rhabdomys pumilio* SCN neurons. Representative trace from a SCN neuron (voltage-clamped at -70mV) showing post-synaptic currents (PSCs) under baseline conditions (top). Bath application of the GABA_A receptor blocker, Bicuculline (20 μ M), abolished most synaptic events (middle trace); all PSCs were blocked under the presence of Bicuculline (20 μ M) and specific glutamatergic receptor antagonists, CNQX (20 μ M) and D-AP5 (50 μ M) (bottom trace).

Table S1. Parameter values for the computational models of *Rhabdomys pumilio* SCN neurons.

Symbol	Parameter	Units	Base Model (Fig. 4, S1-S4)	Non-Adapting (Fig. 5Aii)	Adapting-Firing (Fig. 5Aiii)	Adapting-Silent (Fig. 5Aiii)	Type-A Rebound Spiking (Fig. 6A)	Type-B Delay (with IH) (Fig. 6B)	Type-B Delay (without IH) (Fig. 6i-N, 7)
C	whole-cell capacitance	pF	17.04	10.56	12.95	9.84	14.28	14.16	9.36
ENa	Na ⁺ reversal potential	mV	43.24	40.00	50.00	40.00	40.00	48.69	50
EK	K ⁺ reversal potential	mV	-100.00	-85.12	-100.00	-100.00	-80.00	-100.00	-100
Eca	Ca ²⁺ reversal potential	mV	123.89	130.00	130.00	130.00	130.00	130.00	87.69
EH	H-current reversal potential	mV	-	-	-	-	-	-40.00	-
gNa	INa maximal conductance	nS	88.58	58.81	75.92	70.50	90.70	53.27	500
gK	IK maximal conductance	nS	94.71	101.79	42.29	68.85	10.91	232.93	1.22
gCa	ICa maximal conductance	nS	5.13	13.08	4.17	3.74	6.02	7.86	2.01
gH	IH maximal conductance	nS	-	-	-	-	-	5.34	-
gA	IA maximal conductance	nS	-	-	-	-	-	16.23	300
gLNa	ILNa maximal conductance	nS	0.44	0.16	0.17	0.22	0.13	0.00	0.02
gLK	ILK maximal conductance	nS	7.62	1.19	0.39	0.99	0.93	1.74	1.9
vm_Na	INa half-activation	mV	-24.78	-26.18	-19.53	-24.94	-21.07	-23.61	-19.11
dvm_Na	INa activation slope	mV	17.63	14.47	16.24	13.78	22.61	18.72	25.27
vh_Na	INa half-inactivation	mV	-44.46	-38.75	-40.04	-47.67	-39.49	-32.87	-58.18
dvh_Na	INa inactivation slope	mV	-12.89	-15.24	-10.35	-15.03	-14.30	-10.10	-19.16
th0_Na	INa inactivation time constant baseline	msec	0.47	0.95	0.43	0.22	0.37	0.70	1.42
th1_Na	INa inactivation time constant baseline	msec	72.38	400.00	400.00	120.40	223.00	400.00	156.07
vht_Na	INa inactivation time constant half-inactivation	mV	-33.64	-69.63	-68.76	-37.73	-70.00	vh_Na	vh_Na
dvht_Na	INa inactivation time constant slope	mV	17.09	16.22	24.39	13.88	21.09	16.09	17.82
vn_K	IK half-activation	mV	-6.51	-30.62	-13.18	0.00	-45.23	0.00	-48.23
dvn_K	IK half-activation slope	mV	11.08	23.38	50.00	13.79	39.56	13.01	19.37
tn0_K	IK activation time constant baseline	msec	0.01	0.16	1.26	0.01	0.21	1.62	0.94
tn1_K	IK activation time constant baseline	msec	16.59	25.20	40.00	40.00	40.00	11.87	40
vnt_K	IK activation time constant half-activation	mV	-30.62	-24.31	-18.50	-52.33	-0.79	vn_K	vn_K
dvnt_K	IK activation time constant slope	mV	31.03	24.50	23.64	36.15	9.44	13.32	7.75
vm_Ca	ICa half-activation	mV	-40.00	0.00	0.00	0.00	-6.78	-15.32	-40
dvm_Ca	ICa half-activation slope	mV	50.00	26.19	23.79	36.36	27.23	32.05	50
tm0_Ca	ICa activation time constant baseline	msec	0.22	0.01	3.41	9.32	0.01	8.55	10
tm1_Ca	ICa activation time constant baseline	msec	3.11	5.66	17.63	0.01	40.00	0.01	3.82
vmt_Ca	ICa activation time constant half-activation	mV	-36.62	-40.72	-24.55	-70.00	-57.85	vm_Ca	vm_Ca
dvmt_Ca	ICa activation time constant slope	mV	10.66	13.92	12.85	5.00	5.00	50.00	50
vh_Ca	ICa half-inactivation	mV	-17.72	-18.32	0.00	-34.43	-19.20	-42.15	0
dvh_Ca	ICa half-inactivation slope	mV	-9.56	-50.00	-5.01	-17.49	-42.83	-34.07	-50
th0_Ca	ICa inactivation time constant baseline	msec	284.73	3.80	1.90	30.30	3.10	0.01	200
th1_Ca	ICa inactivation time constant baseline	msec	3000.00	400.00	400.00	74.50	1000.00	15.20	400
vht_Ca	ICa inactivation time constant half-activation	mV	-15.99	-57.20	-61.13	0.00	-36.25	vh_Ca	vh_Ca
dvht_Ca	ICa inactivation time constant slope	mV	6.99	21.10	32.22	5.00	22.14	33.89	31.2
vm_H	IH half-activation	mV	-	-	-	-	-	-80.00	-
dvm_H	IH half-activation slope	mV	-	-	-	-	-	-17.19	-
tm0_H	IH activation time constant baseline	msec	-	-	-	-	-	283.40	-
tm1_H	IH activation time constant baseline	msec	-	-	-	-	-	484.40	-
vmt_H	IH activation time constant half-activation	mV	-	-	-	-	-	vm_H	-
dvmt_H	IH activation time constant slope	mV	-	-	-	-	-	30.00	-
vm_A	IA half-activation	mV	-	-	-	-	-	-35.00	-28.54
dvm_A	IA activation slope	mV	-	-	-	-	-	25.00	25
vh_A	IA half-inactivation	mV	-	-	-	-	-	-55.00	-61.68
dvh_A	IA inactivation slope	mV	-	-	-	-	-	-25.00	-10
th0_A	IA inactivation time constant baseline	msec	-	-	-	-	-	1.00	11.6
th1_A	IA inactivation time constant baseline	msec	-	-	-	-	-	211.40	291.2
vht_A	IA inactivation time constant half-inactivation	mV	-	-	-	-	-	vh_A	vh_A
dvht_A	IA inactivation time constant slope	mV	-	-	-	-	-	23.62	14.05

References

- Abarbanel, H.D.I. (2013) *Predicting the Future. Completing Models of Observed Complex Systems*. Springer, New York, NY.
- Abarbanel, H.D.I.C., D.R. ; Farsian, R. ; Kostuk, M. (2009) Dynamical State and Parameter Estimation. *SIAM J Appl Dyn Syst*, **8**, 1341-1381.
- Abrahamson, E.E. & Moore, R.Y. (2001) Suprachiasmatic nucleus in the mouse: retinal innervation, intrinsic organization and efferent projections. *Brain Res*, **916**, 172-191.
- Aghajanian, G.K. (1985) Modulation of a transient outward current in serotonergic neurones by alpha 1-adrenoceptors. *Nature*, **315**, 501-503.
- Albers, H.E., Walton, J.C., Gamble, K.L., McNeill, J.K.t. & Hummer, D.L. (2017) The dynamics of GABA signaling: Revelations from the circadian pacemaker in the suprachiasmatic nucleus. *Front Neuroendocrinol*, **44**, 35-82.
- Allen, C.N., Nitabach, M.N. & Colwell, C.S. (2017) Membrane Currents, Gene Expression, and Circadian Clocks. *Cold Spring Harb Perspect Biol*, **9**.
- Alvado, L. & Allen, C.N. (2008) Tetraethylammonium (TEA) increases the inactivation time constant of the transient K⁺ current in suprachiasmatic nucleus neurons. *Brain Res*, **1221**, 24-29.
- Amarillo, Y., De Santiago-Castillo, J.A., Dougherty, K., Maffie, J., Kwon, E., Covarrubias, M. & Rudy, B. (2008) Ternary Kv4.2 channels recapitulate voltage-dependent inactivation kinetics of A-type K⁺ channels in cerebellar granule neurons. *J Physiol*, **586**, 2093-2106.
- Andersson, J.A.E., Gillis, J., Horn, G., Rawlings, J.B. & Diehl, M. (2019) CasADi: a software framework for nonlinear optimization and optimal control. *Mathematical Programming Computation*, **11**, 1-36.
- Atkinson, S.E., Maywood, E.S., Chesham, J.E., Wozny, C., Colwell, C.S., Hastings, M.H. & Williams, S.R. (2011) Cyclic AMP signaling control of action potential firing rate and molecular circadian pacemaking in the suprachiasmatic nucleus. *J Biol Rhythms*, **26**, 210-220.
- Bano-Otalora, B., Martial, F., Harding, C., Bechtold, D.A., Allen, A.E., Brown, T.M., Belle, M.D.C. & Lucas, R.J. (2020) Daytime light enhances the amplitude of circadian output in a diurnal mammal. *bioRxiv*, 2020.2006.2022.164194.
- Baranauskas, G. (2007) Ionic channel function in action potential generation: current perspective. *Mol Neurobiol*, **35**, 129-150.

- Belle, M.D., Diekman, C.O., Forger, D.B. & Piggins, H.D. (2009) Daily electrical silencing in the mammalian circadian clock. *Science*, **326**, 281-284.
- Belle, M.D., Hughes, A.T., Bechtold, D.A., Cunningham, P., Pierucci, M., Burdakov, D. & Piggins, H.D. (2014) Acute suppressive and long-term phase modulation actions of orexin on the mammalian circadian clock. *J Neurosci*, **34**, 3607-3621.
- Belle, M.D. & Piggins, H.D. (2017) Circadian regulation of mouse suprachiasmatic nuclei neuronal states shapes responses to orexin. *Eur J Neurosci*, **45**, 723-732.
- Belle, M.D.C. & Diekman, C.O. (2018) Neuronal oscillations on an ultra-slow timescale: daily rhythms in electrical activity and gene expression in the mammalian master circadian clockwork. *Eur J Neurosci*, **48**, 2696-2717.
- Bouskila, Y. & Dudek, F.E. (1995) A rapidly activating type of outward rectifier K⁺ current and A-current in rat suprachiasmatic nucleus neurones. *J Physiol*, **488 (Pt 2)**, 339-350.
- Brookings, T., Goeritz, M.L. & Marder, E. (2014) Automatic parameter estimation of multicompartmental neuron models via minimization of trace error with control adjustment. *J Neurophysiol*, **112**, 2332-2348.
- Burdakov, D., Alexopoulos, H., Vincent, A. & Ashcroft, F.M. (2004) Low-voltage-activated A-current controls the firing dynamics of mouse hypothalamic orexin neurons. *Eur J Neurosci*, **20**, 3281-3285.
- Burdakov, D. & Ashcroft, F.M. (2002) Cholecystokinin tunes firing of an electrically distinct subset of arcuate nucleus neurons by activating A-Type potassium channels. *J Neurosci*, **22**, 6380-6387.
- Collins, B., Pierre-Ferrer, S., Muheim, C., Lukacsovich, D., Cai, Y., Spinnler, A., Herrera, C.G., Wen, S., Winterer, J., Belle, M.D.C., Piggins, H.D., Hastings, M., Loudon, A., Yan, J., Foldy, C., Adamantidis, A. & Brown, S.A. (2020) Circadian VIPergic Neurons of the Suprachiasmatic Nuclei Sculpt the Sleep-Wake Cycle. *Neuron*, **108**, 486-499 e485.
- Colwell, C.S. (2011) Linking neural activity and molecular oscillations in the SCN. *Nat Rev Neurosci*, **12**, 553-569.
- Connor, J.A. & Stevens, C.F. (1971) Voltage clamp studies of a transient outward membrane current in gastropod neural somata. *J Physiol*, **213**, 21-30.
- de Jeu, M., Hermes, M. & Pennartz, C. (1998) Circadian modulation of membrane properties in slices of rat suprachiasmatic nucleus. *Neuroreport*, **9**, 3725-3729.

- Dewsbury, D.A. & Dawson, W.W. (1979) African four-striped grass mice (*Rhabdomys pumilio*), a diurnal-crepuscular murid rodent, in the behavioral laboratory. *Behavior Research Methods & Instrumentation*, **11**, 329-333.
- Diekman, C.O., Belle, M.D., Irwin, R.P., Allen, C.N., Piggins, H.D. & Forger, D.B. (2013) Causes and consequences of hyperexcitation in central clock neurons. *PLoS Comput Biol*, **9**, e1003196.
- Fleidervish, I.A., Friedman, A. & Gutnick, M.J. (1996) Slow inactivation of Na⁺ current and slow cumulative spike adaptation in mouse and guinea-pig neocortical neurones in slices. *J Physiol*, **493 (Pt 1)**, 83-97.
- Flourakis, M., Kula-Eversole, E., Hutchison, A.L., Han, T.H., Aranda, K., Moose, D.L., White, K.P., Dinner, A.R., Lear, B.C., Ren, D., Diekman, C.O., Raman, I.M. & Allada, R. (2015) A Conserved Bicycle Model for Circadian Clock Control of Membrane Excitability. *Cell*, **162**, 836-848.
- Gamble, K.L., Kudo, T., Colwell, C.S. & McMahon, D.G. (2011) Gastrin-releasing peptide modulates fast delayed rectifier potassium current in Per1-expressing SCN neurons. *J Biol Rhythms*, **26**, 99-106.
- Golowasch, J., Goldman, M.S., Abbott, L.F. & Marder, E. (2002) Failure of averaging in the construction of a conductance-based neuron model. *J Neurophysiol*, **87**, 1129-1131.
- Granados-Fuentes, D., Hermansteyne, T.O., Carrasquillo, Y., Nerbonne, J.M. & Herzog, E.D. (2015) IA Channels Encoded by Kv1.4 and Kv4.2 Regulate Circadian Period of PER2 Expression in the Suprachiasmatic Nucleus. *J Biol Rhythms*, **30**, 396-407.
- Granados-Fuentes, D., Norris, A.J., Carrasquillo, Y., Nerbonne, J.M. & Herzog, E.D. (2012) I(A) channels encoded by Kv1.4 and Kv4.2 regulate neuronal firing in the suprachiasmatic nucleus and circadian rhythms in locomotor activity. *J Neurosci*, **32**, 10045-10052.
- Hanna, L., Walmsley, L., Pienaar, A., Howarth, M. & Brown, T.M. (2017) Geniculohypothalamic GABAergic projections gate suprachiasmatic nucleus responses to retinal input. *J Physiol*, **595**, 3621-3649.
- Hannibal, J., Hundahl, C., Fahrenkrug, J., Rehfeld, J.F. & Friis-Hansen, L. (2010) Cholecystokinin (CCK)-expressing neurons in the suprachiasmatic nucleus: innervation, light responsiveness and entrainment in CCK-deficient mice. *Eur J Neurosci*, **32**, 1006-1017.
- Harvey, J.R.M., Plante, A.E. & Meredith, A.L. (2020) Ion Channels Controlling Circadian Rhythms in Suprachiasmatic Nucleus Excitability. *Physiol Rev*, **100**, 1415-1454.

- Hermansteyne, T.O., Granados-Fuentes, D., Mellor, R.L., Herzog, E.D. & Nerbonne, J.M. (2017) Acute Knockdown of Kv4.1 Regulates Repetitive Firing Rates and Clock Gene Expression in the Suprachiasmatic Nucleus and Daily Rhythms in Locomotor Behavior. *eNeuro*, **4**.
- Holmqvist, M.H., Cao, J., Hernandez-Pineda, R., Jacobson, M.D., Carroll, K.I., Sung, M.A., Betty, M., Ge, P., Gilbride, K.J., Brown, M.E., Jurman, M.E., Lawson, D., Silos-Santiago, I., Xie, Y., Covarrubias, M., Rhodes, K.J., Distefano, P.S. & An, W.F. (2002) Elimination of fast inactivation in Kv4 A-type potassium channels by an auxiliary subunit domain. *Proc Natl Acad Sci U S A*, **99**, 1035-1040.
- Huang, R.C., Peng, Y.W. & Yau, K.W. (1993) Zinc modulation of a transient potassium current and histochemical localization of the metal in neurons of the suprachiasmatic nucleus. *Proc Natl Acad Sci U S A*, **90**, 11806-11810.
- Itri, J.N., Vosko, A.M., Schroeder, A., Dragich, J.M., Michel, S. & Colwell, C.S. (2010) Circadian regulation of a-type potassium currents in the suprachiasmatic nucleus. *J Neurophysiol*, **103**, 632-640.
- Jackson, A.C., Yao, G.L. & Bean, B.P. (2004) Mechanism of spontaneous firing in dorsomedial suprachiasmatic nucleus neurons. *J Neurosci*, **24**, 7985-7998.
- Jerng, H.H., Kunjilwar, K. & Pfaffinger, P.J. (2005) Multiprotein assembly of Kv4.2, KChIP3 and DPP10 produces ternary channel complexes with ISA-like properties. *J Physiol*, **568**, 767-788.
- Jerng, H.H., Lauer, A.D. & Pfaffinger, P.J. (2007) DPP10 splice variants are localized in distinct neuronal populations and act to differentially regulate the inactivation properties of Kv4-based ion channels. *Mol Cell Neurosci*, **35**, 604-624.
- Jerng, H.H. & Pfaffinger, P.J. (2014) Modulatory mechanisms and multiple functions of somatodendritic A-type K (+) channel auxiliary subunits. *Front Cell Neurosci*, **8**, 82.
- Jerng, H.H., Qian, Y. & Pfaffinger, P.J. (2004) Modulation of Kv4.2 channel expression and gating by dipeptidyl peptidase 10 (DPP10). *Biophys J*, **87**, 2380-2396.
- Jeyaraj, D., Haldar, S.M., Wan, X., McCauley, M.D., Ripperger, J.A., Hu, K., Lu, Y., Eapen, B.L., Sharma, N., Ficker, E., Cutler, M.J., Gulick, J., Sanbe, A., Robbins, J., Demolombe, S., Kondratov, R.V., Shea, S.A., Albrecht, U., Wehrens, X.H., Rosenbaum, D.S. & Jain, M.K. (2012) Circadian rhythms govern cardiac repolarization and arrhythmogenesis. *Nature*, **483**, 96-99.
- Jung, H.Y., Mickus, T. & Spruston, N. (1997) Prolonged sodium channel inactivation contributes to dendritic action potential attenuation in hippocampal pyramidal neurons. *J Neurosci*, **17**, 6639-6646.

- Khaliq, Z.M. & Bean, B.P. (2008) Dynamic, nonlinear feedback regulation of slow pacemaking by A-type potassium current in ventral tegmental area neurons. *J Neurosci*, **28**, 10905-10917.
- Kimm, T., Khaliq, Z.M. & Bean, B.P. (2015) Differential Regulation of Action Potential Shape and Burst-Frequency Firing by BK and Kv2 Channels in Substantia Nigra Dopaminergic Neurons. *J Neurosci*, **35**, 16404-16417.
- Ko, C.H. & Takahashi, J.S. (2006) Molecular components of the mammalian circadian clock. *Hum Mol Genet*, **15 Spec No 2**, R271-277.
- Kuhlman, S.J. & McMahon, D.G. (2004) Rhythmic regulation of membrane potential and potassium current persists in SCN neurons in the absence of environmental input. *Eur J Neurosci*, **20**, 1113-1117.
- Liss, B., Franz, O., Sewing, S., Bruns, R., Neuhoff, H. & Roeper, J. (2001) Tuning pacemaker frequency of individual dopaminergic neurons by Kv4.3L and KChip3.1 transcription. *EMBO J*, **20**, 5715-5724.
- Maffie, J., Blenkinsop, T. & Rudy, B. (2009) A novel DPP6 isoform (DPP6-E) can account for differences between neuronal and reconstituted A-type K(+) channels. *Neurosci Lett*, **449**, 189-194.
- Meliza, C.D., Kostuk, M., Huang, H., Nogaret, A., Margoliash, D. & Abarbanel, H.D. (2014) Estimating parameters and predicting membrane voltages with conductance-based neuron models. *Biol Cybern*, **108**, 495-516.
- Moye, M.J. (2020) Data assimilation for conductance-based neuronal models. *Dissertations*, 1459.
- Mure, L.S., Le, H.D., Benegiamo, G., Chang, M.W., Rios, L., Jillani, N., Ngotho, M., Kariuki, T., Dkhissi-Benyahya, O., Cooper, H.M. & Panda, S. (2018) Diurnal transcriptome atlas of a primate across major neural and peripheral tissues. *Science*, **359**.
- Nadin, B.M. & Pfaffinger, P.J. (2010) Dipeptidyl peptidase-like protein 6 is required for normal electrophysiological properties of cerebellar granule cells. *J Neurosci*, **30**, 8551-8565.
- Park, S.K.X., L. (2013) *Data Assimilation for Atmospheric, Oceanic and Hydrologic Applications (Vol. II)*. Springer-Verlag Berlin Heidelberg, Berlin, Heidelberg.
- Patel, A.X., Murphy, N. & Burdakov, D. (2012) Tuning low-voltage-activated A-current for silent gain modulation. *Neural Comput*, **24**, 3181-3190.

- Paul, J.R., DeWoskin, D., McMeekin, L.J., Cowell, R.M., Forger, D.B. & Gamble, K.L. (2016) Regulation of persistent sodium currents by glycogen synthase kinase 3 encodes daily rhythms of neuronal excitability. *Nat Commun*, **7**, 13470.
- Pennartz, C.M., De Jeu, M.T., Geurtsen, A.M., Sluiter, A.A. & Hermes, M.L. (1998) Electrophysiological and morphological heterogeneity of neurons in slices of rat suprachiasmatic nucleus. *J Physiol*, **506 (Pt 3)**, 775-793.
- Reppert, S.M. & Weaver, D.R. (2002) Coordination of circadian timing in mammals. *Nature*, **418**, 935-941.
- Ruby, N.F. & Heller, H.C. (1996) Temperature sensitivity of the suprachiasmatic nucleus of ground squirrels and rats in vitro. *J Biol Rhythms*, **11**, 126-136.
- Rudy, B. (1988) Diversity and ubiquity of K channels. *Neuroscience*, **25**, 729-749.
- Rush, M.E. & Rinzel, J. (1995) The potassium A-current, low firing rates and rebound excitation in Hodgkin-Huxley models. *Bull Math Biol*, **57**, 899-929.
- Saito, Y. & Isa, T. (2000) Voltage-gated transient outward currents in neurons with different firing patterns in rat superior colliculus. *J Physiol*, **528 Pt 1**, 91-105.
- Sato, T. & Kawamura, H. (1984) Circadian rhythms in multiple unit activity inside and outside the suprachiasmatic nucleus in the diurnal chipmunk (*Eutamias sibiricus*). *Neurosci Res*, **1**, 45-52.
- Schoppa, N.E. & Westbrook, G.L. (1999) Regulation of synaptic timing in the olfactory bulb by an A-type potassium current. *Nat Neurosci*, **2**, 1106-1113.
- Schumann, D.M., Cooper, H.M., Hofmeyr, M.D. & Bennett, N.C. (2005) Circadian rhythm of locomotor activity in the four-striped field mouse, *Rhabdomys pumilio*: a diurnal African rodent. *Physiol Behav*, **85**, 231-239.
- Schwartz, W.J. (1991) SCN metabolic activity in vivo. In Klein, D.C.M., R.Y.; Reppert, S.M. (ed) *Suprachiasmatic Nucleus: The Mind's Clock*. Oxford University Press, New York, pp. 144-156.
- Shibata, R., Nakahira, K., Shibasaki, K., Wakazono, Y., Imoto, K. & Ikenaka, K. (2000) A-type K⁺ current mediated by the Kv4 channel regulates the generation of action potential in developing cerebellar granule cells. *J Neurosci*, **20**, 4145-4155.
- Sim, C.K. & Forger, D.B. (2007) Modeling the electrophysiology of suprachiasmatic nucleus neurons. *J Biol Rhythms*, **22**, 445-453.

- Smale, L. & Boverhof, J. (1999) The suprachiasmatic nucleus and intergeniculate leaflet of *Arvicanthis niloticus*, a diurnal murid rodent from East Africa. *J Comp Neurol*, **403**, 190-208.
- Sonoda, T., Li, J.Y., Hayes, N.W., Chan, J.C., Okabe, Y., Belin, S., Nawabi, H. & Schmidt, T.M. (2020) A noncanonical inhibitory circuit dampens behavioral sensitivity to light. *Science*, **368**, 527-531.
- Thomson, A.M. & West, D.C. (1990) Factors affecting slow regular firing in the suprachiasmatic nucleus in vitro. *J Biol Rhythms*, **5**, 59-75.
- Timothy, J.W.S., Klas, N., Sanghani, H.R., Al-Mansouri, T., Hughes, A.T.L., Kirshenbaum, G.S., Brienza, V., Belle, M.D.C., Ralph, M.R., Clapcote, S.J. & Piggins, H.D. (2018) Circadian Disruptions in the Myshkin Mouse Model of Mania Are Independent of Deficits in Suprachiasmatic Molecular Clock Function. *Biol Psychiatry*, **84**, 827-837.
- Toth, B.A., Kostuk, M., Meliza, C.D., Margoliash, D. & Abarbanel, H.D. (2011) Dynamical estimation of neuron and network properties I: variational methods. *Biol Cybern*, **105**, 217-237.
- van Oosterhout, F., Lucassen, E.A., Houben, T., vanderLeest, H.T., Antle, M.C. & Meijer, J.H. (2012) Amplitude of the SCN clock enhanced by the behavioral activity rhythm. *PLoS One*, **7**, e39693.
- Wächter, A. & Biegler, L.T. (2006) On the implementation of an interior-point filter line-search algorithm for large-scale nonlinear programming. *Mathematical Programming*, **106**, 25-57.
- Wen, S., Ma, D., Zhao, M., Xie, L., Wu, Q., Gou, L., Zhu, C., Fan, Y., Wang, H. & Yan, J. (2020) Spatiotemporal single-cell analysis of gene expression in the mouse suprachiasmatic nucleus. *Nat Neurosci*, **23**, 456-467.
- Yang, F., Feng, L., Zheng, F., Johnson, S.W., Du, J., Shen, L., Wu, C.P. & Lu, B. (2001) GDNF acutely modulates excitability and A-type K(+) channels in midbrain dopaminergic neurons. *Nat Neurosci*, **4**, 1071-1078.



Reentrainment of the circadian pacemaker during jet lag: East-west asymmetry and the effects of north-south travel



Casey O. Diekman^{a,b,*}, Amitabha Bose^{a,b}

^a Department of Mathematical Sciences, New Jersey Institute of Technology, Newark, NJ 07102 USA

^b Institute for Brain and Neuroscience Research, New Jersey Institute of Technology, Newark, NJ 07102 USA

ARTICLE INFO

Article history:

Received 12 May 2017

Revised 7 September 2017

Accepted 3 October 2017

Available online 4 October 2017

Keywords:

Biological rhythms

Entrainment

Circadian oscillator

Light-dark cycles

Poincaré map

Translatitudinal travel

ABSTRACT

The normal alignment of circadian rhythms with the 24-h light-dark cycle is disrupted after rapid travel between home and destination time zones, leading to sleep problems, indigestion, and other symptoms collectively known as jet lag. Using mathematical and computational analysis, we study the process of reentrainment to the light-dark cycle of the destination time zone in a model of the human circadian pacemaker. We calculate the reentrainment time for travel between any two points on the globe at any time of the day and year. We construct one-dimensional entrainment maps to explain several properties of jet lag, such as why most people experience worse jet lag after traveling east than west. We show that this east-west asymmetry depends on the endogenous period of the traveler's circadian clock as well as daylength. Thus the critical factor is not simply whether the endogenous period is greater than or less than 24 h as is commonly assumed. We show that the unstable fixed point of an entrainment map determines whether a traveler reentrains through phase advances or phase delays, providing an understanding of the threshold that separates orthodromic and antidromic modes of reentrainment. Contrary to the conventional wisdom that jet lag only occurs after east-west travel across multiple time zones, we predict that the change in daylength encountered during north-south travel can cause jet lag even when no time zones are crossed. Our techniques could be used to provide advice to travelers on how to minimize jet lag on trips involving multiple destinations and a combination of transmeridian and translatitudinal travel.

© 2017 Elsevier Ltd. All rights reserved.

1. Introduction

Circadian clocks have evolved to align biological functions with the 24-h environmental cycles conferred by the rotation of the earth (Johnson et al., 2003). In humans, a central circadian pacemaker coordinates various physiological rhythms so that they peak at the appropriate time of the day, such as the release of the sleep-promoting hormone melatonin in the evening and the wake-promoting hormone cortisol in the morning (James et al., 2007). The endogenous period of the human circadian oscillator in the absence of external time cues is not exactly 24 h (Czeisler et al., 1999). The period of the oscillator becomes 24 h under normal circumstances when exposed to natural environmental cycles, and a stable phase relationship between the oscillator and its environment is established: the oscillator is phase-locked or *entrained* to the external cycles (Wright et al., 2013). For circadian oscillators,

the strongest entraining signal is the daily light-dark (LD) cycle (Duffy and Wright, 2005). If entrainment is disrupted by a sudden shift in the phase of the LD cycle, for example due to rapid travel across time zones, then the phase of the circadian oscillator undergoes adjustments until phase-locking is reestablished and the oscillator is reentrained (Aschoff et al., 1975).

Jet lag is a collection of symptoms experienced after rapid transmeridian travel. These symptoms—such as insomnia, excessive daytime sleepiness, gastrointestinal disturbances, and general malaise—are not simply due to travel fatigue following a long flight, but rather are caused by misalignment of the traveler's internal circadian clock with the environmental cycles in the new time zone (Sack, 2009). Each year about 30 million US residents fly to overseas destinations (U.S. Citizen Travel to International Regions, 2017). For international business travelers, athletes, or government and military personnel, jet lag can impair judgment, hinder performance, or threaten public safety (Eastman and Burgess, 2009). Most travelers experience more severe jet lag after flying east than after flying west (Waterhouse et al., 2007), and a recent analysis of

* Corresponding author.

E-mail address: diekman@njit.edu (C.O. Diekman).

over 20 years of data from Major League Baseball games found that jet lag impairs performance more so after eastward than westward travel (Song et al., 2017). The conventional explanation for this directional asymmetry in jet lag severity is that since the human circadian clock typically has an endogenous period of greater than 24 h, it is easier to phase delay the clock in response to the phase delay of the LD cycle caused by westward travel than it is to phase advance the clock in response to the phase advance of the LD cycle caused by eastward (Eastman and Burgess, 2009). Reentrainment though phase adjustment in the same direction as the shift of the LD cycle is referred to as *orthodromic*. After long trips, some travelers reentrain *antidromically* or through phase adjustments in the opposite direction of the phase shift of the LD cycle, i.e. phase delays after traveling east and phase advances after traveling west (Arendt et al., 1987; Klein and Wegmann, 1977; Takahashi et al., 2001).

In this paper we use a mathematical model of the human circadian pacemaker, the Forger–Jewett–Kronauer (FJK) model (Forger et al., 1999), to explain the existence of east–west asymmetry in jet lag severity and the antidromic mode of reentrainment. The FJK model is a widely accepted model in the circadian literature that captures both phase and amplitude dynamics of daily core body temperature oscillations. It has been fit to experimental data on how light affects human circadian rhythms and has been used in several studies to design schedules that minimize jet lag (Dean et al., 2009; Serkh and Forger, 2014; Zhang et al., 2016). Consistent with a recent study employing a phase-only model (Lu et al., 2016), we find that the endogenous period of the circadian oscillator does influence east–west asymmetry. Differently than (Lu et al., 2016), however, we find that the period being greater than or less than 24 h is not the critical factor. Furthermore we show that daylength, and therefore the season of the year, affects whether eastward or westward travel is worse.

The medical definition of jet lag requires travel across time zones, implying that strictly north–south or translatitudinal travel within the same time zone cannot cause jet lag. We take a broader view of jet lag as symptoms resulting from any travel-induced misalignment of the circadian clock and the external LD cycle, and argue that the change in daylength experienced when traveling across latitudes (for example between the northern and southern hemispheres) in the summer or winter may disrupt entrainment. The question of whether purely north–south travel can result in significant misalignment has received very little attention in the literature. We find that in the FJK model, a difference in the daylength between departure and destination cities is enough to cause jet lag on the order of several days (depending on parameters) even with no change in time zone. Combining our findings on east–west travel with those on north–south travel, we also investigate travel that incorporates both of these directions. By considering a hypothetical case study involving travel between four cities located in North America, South America, Asia, and Australia, we show that the north–south component of travel can significantly add to or reduce reentrainment times even in cases where strict north–south travel itself incurs no jet lag.

The main tool we use to gain insights into the properties of jet lag is the *entrainment map*, a technique we recently introduced for calculating the LD-entrained solution of an oscillator subjected to external periodic forcing consisting of N hours of light and $24 - N$ h of darkness (Diekman and Bose, 2016). The method involved deriving a one-dimensional map, $\Pi(x)$, whose fixed points corresponded to stable or unstable entrained periodic solutions. We showed that the entrainment map yields more accurate predictions about the phase of the stable entrained solution than methods based on phase response curves. In Diekman and Bose (2016), we showed how the entrainment map for the two-dimensional Novak–Tyson model of the *Drosophila* molecular clock

(Tyson et al., 1999) depends on parameters of the model and how it can be used to determine regimes over which solutions entrain through phase advance or phase delay. The entrainment map was then applied to higher dimensional systems such as the three-dimensional Gonze et al. (2005) and the 180-dimensional Kim and Forger (2012) models of the mammalian molecular clock.

Here we build entrainment maps for the FJK model to explore various facets of reentrainment after travel. Travel can involve a change of time zone, such as eastward or westward travel, a change in photoperiod, such as northward or southward travel, or a combination of both, such as travel from North America to Australia. We show that reentrainment properties depend both quantitatively and qualitatively on key parameters including the endogenous period of the oscillator, the daylength, and the intensity of light. Using our methods, we can calculate reentrainment times for travel between any two locations on the globe, at any time of the year, and for any departure or arrival time. In doing so, we are able to explain that the east–west asymmetry of jet lag is a generic feature of the FJK model that is highly dependent on both the endogenous period of the traveler as well as the daylength. Using a generalization of the concept of neutral period introduced by Aschoff et al. (1975), we show that for different combinations of these two parameters, travel to the east can incur more jet lag than travel to the west or vice versa. In fact, because of seasonal changes in the daylength, for the same traveler a journey in one direction may be harder in the winter, while a journey in the opposite direction may be harder in the summer. Our findings are related, in part, to those of Herzog and collaborators (Bordyugov et al., 2015; Granada and Herzog, 2009; Schmal et al., 2015) who have characterized the phase of entrainment as a function of endogenous period, zeitgeber (external stimulus) strength, and photoperiod for several different circadian models using Arnold tongues and Arnold onions. The analysis of the entrainment map also provides insight into the different modes of reentrainment. Prior work using a model of the mammalian molecular clock identified a threshold separating orthodromic and antidromic modes of reentrainment, but did not explain what mathematical object might act as the threshold (Leloup and Goldbeter, 2013). Here we show that the unstable fixed point of the entrainment map can be used to predict the threshold that separates the two modes of reentrainment.

Contrary to what one might naively expect, we find that reentrainment time is relatively independent of departure or arrival time, and that the longest trips do not necessarily give rise to the longest reentrainment times. Instead, the worst-case trip is determined by the ordering and magnitude of the distance between the stable and unstable fixed points of the entrainment map, which themselves are dependent on the internal body clock and daylength. We find that for low light intensities, trips that place the traveler in a neighborhood of the unstable fixed point of the map will give rise to the longest reentrainment times. For higher light intensities, the longest reentrainment times still occur in a neighborhood of the unstable fixed point, but there is also the potential for dramatically short reentrainment times for certain trips within this neighborhood. These dramatically short reentrainment times are associated with amplitude suppression and a phase singularity, and have been observed previously in the FJK model at high light intensity (Serkh and Forger, 2014).

In this study, we consider the light level to be fixed at either low or high intensity (lux) across the entire photoperiod. Admittedly, this is not a light protocol that a traveler is likely to experience. However, the main purpose of our study is to provide a mathematical explanation for why certain features of jet lag arise, such as east–west asymmetry and different modes of reentrainment. This is most easily explained using single lux levels. As further discussed throughout the paper, we expect the mechanisms

that underlie our findings to continue to exist under more realistic light schedules.

2. Model and methods

2.1. The Forger, Jewett, and Kronauer (FJK) model

The FJK model (Forger et al., 1999) for the human circadian rhythm utilizes a Van der Pol type oscillator and is based on prior models of Kronauer and collaborators (Jewett and Kronauer, 1998; Kronauer, 1990). It is a three-dimensional model given by

$$\frac{dC}{dt} = \frac{\pi}{12} (A + B) \quad (1)$$

$$\frac{dA}{dt} = \frac{\pi}{12} \left(\mu \left(A - \frac{4}{3} A^3 \right) - C \left[\left(\frac{24}{0.99669 \tau_c} \right)^2 + kB \right] \right) \quad (2)$$

$$\frac{dn}{dt} = \gamma (\alpha [I] f(t) (1 - n) - \beta n) \quad (3)$$

$$B = G\alpha [I] f(t) (1 - n) (1 - 0.4C) (1 - 0.4A) \quad (4)$$

$$\alpha [I] = \alpha_0 \left[\frac{I}{I_0} \right]^p \quad (5)$$

The variable C represents core body temperature, A is a phenomenological auxiliary variable, and n models the phototransduction pathway through which light drives the circadian system. The variable B captures circadian modulation of the oscillator's sensitivity to light. All parameter values are positive. In particular, τ_c determines the period of the oscillator in constant darkness, I codes for the intensity of light, and μ is a stiffness parameter that is related to the rate of amplitude growth or decay after the oscillator is perturbed off of its limit cycle. We refer to $\mu = 0.23$, $k = 0.55$, $\gamma = 60$, $\beta = 0.0075$, $G = 33.75$, $\alpha_0 = 0.05$, $I_0 = 9500$, $p = 0.5$ with $I = 1000$ lux and $\tau_c = 24.2$ h as the canonical set of parameters.

The function $f(t)$ is the light stimulus. We are interested in three distinct situations: constant darkness (DD), in which we set $f(t) \equiv 0$; constant light (LL) in which $f(t) \equiv 1$; and a 24-h light/dark (LD) photoperiod in which the lights are on for N hours and off for $24 - N$ h. During the dark portion of the LD photoperiod $f(t) = 0$, while during the light portion $f(t) = 1$. In constant darkness, $dn/dt = -\beta n$, therefore $n \rightarrow 0$ and the parameter β controls the rate of decay. In constant light, $dn/dt = \gamma (\alpha (I) (1 - n) - \beta n)$ such that $n \rightarrow \alpha (I) / (\alpha (I) + \beta)$ with rate α_0 . Note that α_0 is an order of magnitude larger than β which implies that n approaches its maximum when the lights turn on faster than it approaches its minimum when the lights turn off.

The A and C -nullclines are given by

$$\mathcal{N}_A: C = \frac{\mu \left(A - \frac{4}{3} A^3 \right)}{\left(\frac{24}{0.99669 \tau_c} \right)^2 + kB} \quad (6)$$

$$\mathcal{N}_C: A = -B. \quad (7)$$

The nullcline \mathcal{N}_A is a cubic-shaped curve in the projection onto the $A - C$ space. During DD conditions, $B = 0$, and \mathcal{N}_C is a vertical line that intersects \mathcal{N}_A along its middle branch. This intersection corresponds to an unstable fixed point. Surrounding it is a stable periodic orbit, referred to as the DD limit cycle. The prefactors $\pi/12$ and 0.99669 that appear in (2), and the value of $\mu = 0.23$, were chosen such that the period of this limit cycle is very close to τ_c hours (Forger et al., 1999). The period of the DD limit cycle

is referred to as the endogenous period. The value of the roots of \mathcal{N}_A are $A = 0, \pm\sqrt{3}/2$ independent of τ_c . Increasing τ_c makes the A -nullcline have steeper left and right branches. This results in a decrease in the amplitude of dA/dt , thereby slowing down oscillations. As a result, the intrinsic period of the DD oscillator is an increasing function of τ_c . Under LL conditions, although n is constant, B depends on A and C . Using Eq. (4), and substituting into Eq. (7), yields a monotone increasing \mathcal{N}_C nullcline that continues to intersect \mathcal{N}_A along its middle branch. As a result, an LL limit cycle also exists. The period of the LL limit cycle is less than τ_c hours. The LL period is also an increasing function of τ_c , for the same reasons as the DD period. When the model is considered under LD conditions, depending on parameters, a periodic solution may exist. When the period of the solution matches that of the LD forcing (24 h), we call it an LD-entrained solution.

2.2. The entrainment map $\Pi(x)$

The entrainment map $\Pi(x)$ is a return map for initial conditions lying on a Poincaré section that return to it at a later time. A Poincaré section is a lower-dimensional slice (hyperplane) of the original phase space. Both in theory and in practice, we have freedom to choose the location of the section, provided that we know that a trajectory starting on it will return to it later in time. Because the FJK model uses a Van der Pol type oscillator, we have considerable knowledge of how trajectories evolve in phase space. For the sake of illustration, choose the Poincaré section, \mathcal{P} , at $A = 0$, with $A' < 0$, which yields a rectangle in the C and n space. Assume that an oscillator has an initial condition that lies on \mathcal{P} with $n = 0$ and the C value chosen as the value at the intersection with the DD limit cycle. Let x denote the number of hours since the lights last turned on. Evolve the trajectory under the flow until it again returns to \mathcal{P} . Call this time $\rho(x)$. The entrainment map $\Pi(x)$ is defined as the amount of time that has passed since the most recent onset of the lights. In Diekman and Bose (2016), we showed that $\Pi(x) = (x + \rho(x)) \bmod 24$, which yields a one-dimensional map. Because of the mod 24 operation, the map Π may have a discontinuity. The entrainment map has certain generic properties (Diekman and Bose, 2016): it maps the interval $[0, 24]$ onto itself, it has at most one point of discontinuity, it is increasing at each point of continuity, and it is periodic in that $\Pi(0^+) = \Pi(24^-)$. Moreover, it depends continuously on parameters of interest such as τ_c , N , and I .

A fixed point x^* of the entrainment map satisfies $\Pi(x^*) = x^*$. It corresponds to the situation where the trajectory has left \mathcal{P} x^* hours after the lights turned on, and then returns to \mathcal{P} exactly 24 h later when the lights have again most recently turned on x^* hours ago. The fixed point is stable if $|\Pi'(x^*)| < 1$ and unstable otherwise. We will show that over a wide range of parameters, there are typically two fixed points of the map, x_s which is stable, and x_u which is unstable. Whether the fixed points of the map correspond to actual stable and unstable periodic orbits of the system of Eqs. (1)–(3) is a delicate issue. A trajectory starting on the Poincaré section \mathcal{P} at $A = 0$ would have unknowns C , n , and x . A three-dimensional return map would track the values of the unknowns and return new values of C , n , and x when the trajectory returns to \mathcal{P} . The entrainment map however only tracks whether x has returned to its original value, not whether C and n have. As described below, the stable fixed point x_s of the map corresponds to a stable periodic orbit in all the cases we considered. The existence of the unstable fixed point of the map x_u has different implications depending on the light intensity. At low light intensity, the unstable fixed point corresponds to an unstable periodic orbit in the full phase space. x_u also demarcates a region in phase space that separates trajectories that reentrain through either phase advance or phase delay. At larger light intensities, there does not appear to be an unstable

periodic orbit that corresponds to x_u . Nonetheless this fixed point still separates the direction of reentrainment. x_u is also related to trajectories that can reentrain unusually fast. In the Appendix, we further elaborate on the mathematical correspondence between x_s , x_u , and dynamics of the full system of equations.

To explore various forms of jet lag, we will use a set of entrainment maps that are constructed with Poincaré sections corresponding to every half-hour. These sections are chosen by obtaining the LD-entrained solution numerically, and then dividing up this LD-entrained solution into half-hour time intervals, starting with $X = 0$ corresponding to lights on at a nominal choice of 7 AM. Radial Poincaré sections emanating from the origin ($A = 0, C = 0$) and passing through these half-hour marks are then constructed. The section is then extended to a rectangle by allowing n to vary between 0 and 1. We define $\Pi_X(x)$ to denote the map obtained by choosing the Poincaré section X hours from lights on. By construction of the map $\Pi_X(x)$, the stable fixed point x_s of the map occurs exactly at X , that is $x_s = X$, since 7 AM denotes both the time of lights on and $X = 0$. When we build an entrainment map using initial conditions that lie on the LD-entrained solution, then at a stable fixed point of the map all of the dependent variables C , n , and x return to their original values. In this case, the stable fixed point does correspond to a stable periodic solution.

We shall be interested in the transient time it takes a trajectory that has an initial condition that lies off of the LD-entrained solution to enter a neighborhood of it. Specifically, consider a Poincaré section taken along the LD-entrained solution X hours after the lights turn on. Take an initial condition that lies at the intersection of the LD-entrained solution and this Poincaré section, but with $x_0 \neq x_s, x_u$. In this case, the trajectory will not initially be entrained since the LD cycle will be offset by $|x_s - x_0|$ hours. This means that the first return time $\rho(x_0) \neq 24$. We will say that a trajectory is entrained if there exists a $k \geq 0$ such that $|\rho(x_j) - 24| < 0.5$ for $j \geq k$, where $x_j = \Pi(x_{j-1})$. Entrainment is said to occur on $(k + 1)$ th cycle. The total entrainment time is simply $\sum_{j=0}^k \rho(x_j)$. In terms of the map, $\Pi(x)$ entrainment is equivalent to $|\Pi(x_j) - x_s| < 0.5$.

3. Results

3.1. The LL, DD, and LD-entrained limit cycles of the FJK model

The DD limit cycle is obtained when $f(t) \equiv 0$. In this case, $B = 0$ and $dn/dt = -\beta n$, thus $n \rightarrow 0$. Since the DD limit cycle is restricted to $n = 0$, it can be found by solving the planar system given by Eqs. (1) and (2). Those equations are of standard Van der Pol oscillator type that possess a stable limit cycle. The A -nullcline is cubic, the C -nullcline is linear, and they intersect at an unstable fixed point on the middle branch. The DD trajectory encloses that unstable point. Similarly, the LL oscillator is obtained when $f(t) \equiv 1$. Now, $n \rightarrow \alpha[I]/(\alpha[I] + \beta)$ and B can be written in terms of A and C . So the model is again planar with a cubic nullcline and one that is monotone increasing. They intersect along the middle branch of the cubic, forming an unstable fixed point. For the canonical set of parameters (defined in Section 2.1), the period of the DD oscillator is τ_c , whereas the period of the LL oscillator (23.96 h) is less than τ_c .

In Fig. 1, we plot the DD, LL, and LD-entrained oscillations for $N = 12$ h, $I = 1000$ lux. Panel A shows the time traces of each of these oscillations, Panel B shows them in the 3-dimensional $A - C - n$ phase space, and Panel C shows them projected onto the $A - C$ phase plane. Note that the LD-entrained oscillation tracks towards the DD oscillation during darkness and towards the LL oscillation during light. The transition of the trajectory from DD to LL is fairly rapid, while that from LL to DD is relatively slow since β is small compared to α_0 . Hourly markings (open red or black circles)

are placed on the LD-entrained cycle where lights on corresponds to 7 AM and lights off to 7 PM.

In Fig. 2A and B, we plot $\rho(x)$ and $\Pi(x)$ for the canonical set of parameters using the $A = 0, A' < 0$ Poincaré section. The graph of $\rho(x)$ intersects the horizontal line corresponding to 24 h at two points, x_s and x_u . These points represent return times of exactly 24 h. Also note that because of periodicity $\rho(0^+) = \rho(24^-)$. The graph of $\Pi(x)$ intersects the diagonal at the fixed points x_s and x_u . The slope at the points of intersection determines the stability of these fixed points.

In Fig. 2C and D, we show two examples of reentrainment, both in the map and in simulations. The green trajectory in Panel C shows the cobweb diagram for a trajectory that starts with an initial condition that is less than x_u . The cobwebbed trajectory moves to the left with each iterate indicating a phase advancement. The corresponding green time trace in Panel D confirms this in its approach to the LD-entrained solution (solid black trace). The magenta trajectory in Panel C shows a trajectory that starts with an initial condition to the right of x_u , and entrains though phase delays as the iterates of the cobweb move to the right, over the discontinuity, before approaching x_s . The magenta trace in Panel D shows how the oscillator phase delays at each cycle until entrainment. Thus the unstable fixed point of the map x_u separates initial conditions of trajectories that entrain in direct simulations through phase advance or phase delay. What is particularly interesting about this agreement is the fact that we have found no evidence that an unstable periodic orbit actually exists for $I = 1000$ lux. Instead, the stable periodic orbit seems to be globally attracting. Locally near x_s and the stable periodic orbit, trajectories approach the fixed point by either advancing or delaying. Therefore there must be a structure elsewhere in phase space that separates trajectories that become phase advancing or phase delaying. We speculate that the unstable fixed point x_u of the map indicates where in phase space to look for such a structure. We provide further evidence for this conjecture in the Appendix; however, fully characterizing this structure mathematically is beyond the scope of this paper.

3.2. The dependence of $\Pi(x)$ on parameters

The entrainment map $\Pi(x)$ depends continuously on parameters. In particular, we are interested in how the map changes with variations in τ_c , N , and I . The dependence on parameters is qualitatively the same as what we found in our earlier study (Diekman and Bose, 2016) of the Novak-Tyson model of the molecular circadian clock in *Drosophila* (Novak and Tyson, 2008), and is consistent with general theories on the phase of circadian entrainment (Bordyugov et al., 2015). To understand this dependence, we vary one parameter at a time with the others set at their canonical values.

Consider first changes in the intrinsic period τ_c . Fig. 3A and B show how the maps $\rho(x)$ and $\Pi(x)$ depend on τ_c . The return time map $\rho(x)$ is a monotone function of the parameter τ_c . This has to do with how the A nullcline, \mathcal{N}_A , changes with τ_c . As discussed in Section 2.1, for both the DD and LL cases, the steepness of the right and left branches of the cubic increases with τ_c , leading to increases in the period of each of these oscillators (Fig. 3C and D). To illustrate this, consider the two extreme cases $\tau_c = 22.2$ h and 27.2 h with an initial condition of $x_0 = 18$. Fig. 3C shows the ensuing trajectories leaving the Poincaré section $A = 0$ projected onto the $A - C$ plane. Since $x_0 = 18$, the trajectories are initially subjected to six hours of darkness and thus they follow the corresponding DD dynamics. After six hours of evolution, the green trajectory ($\tau_c = 22.2$ h) is about an hour ahead of its magenta counterpart ($\tau_c = 27.2$ h). The green trajectory moves faster horizontally since its nullcline is further away. For the next 12 h, the trajectories evolve

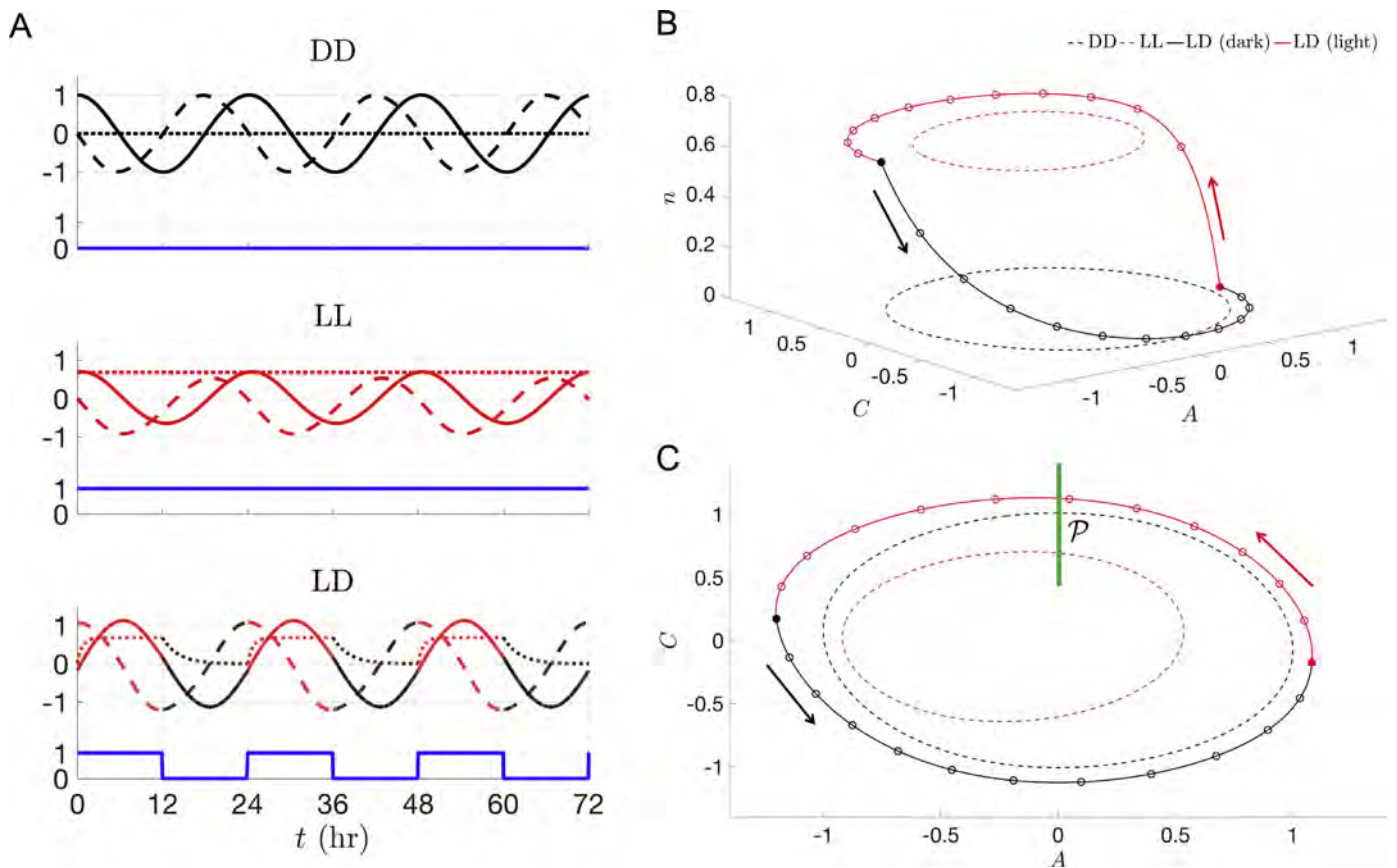


Fig. 1. FJK model DD, LL, and LD limit cycles for $\tau_c = 24.2$ h, $N = 12$ h, $I = 1000$ lux. (A) Time course of model variables in constant darkness (top), constant light (middle), and a 12:12 light-dark cycle (bottom). The variable C is shown as solid lines (black in DD, red in LL, and red/black in LD), the variable A as dashed lines, and the variable n as dotted lines. The light stimulus function $f(t)$ is shown as solid blue lines. The DD, LL, and LD limit cycles in the 3-dimensional $A-C-n$ phase space (B) and projected onto the 2-dimensional $A-C$ phase plane (C). A 1-dimensional projection of the Poincaré section \mathcal{P} at $A=0$ ($A' < 0$) is shown in green. (For interpretation of the references to color in this figure legend, the reader is referred to the web version of this article.)

under conditions of light, as shown in Fig. 3D. The $\tau_c = 22.2$ h trajectory moves further ahead of the other, now by about three hours. Again the green trajectory moves faster horizontally. Finally, for the last portion of their evolutions back to the Poincaré section, they evolve under darkness; Fig. 3C. In general, the dynamics of the LD-forced oscillator are determined by the LL limit cycle when the lights are on and by the DD limit cycle when the lights are off. Thus, independent of whether the LD-forced oscillator is in a current situation of lights on or off, its dynamics will always be slower when τ_c is greater. Therefore $\rho(x)$ will be larger for larger τ_c .

In Fig. 3B we show how $\Pi(x)$ depends on τ_c . Increasing τ_c causes the maps to shift up. This is a consequence of $\rho(x)$ being a monotone increasing function of τ_c . This causes the stable fixed point x_s to increase (and the unstable fixed point x_u to decrease). This means that individuals with slower intrinsic body clocks reach their maximum or minimum core body temperatures later in the day. The opposite is true when τ_c is decreased below 24.2 for individuals with faster than normal intrinsic body clocks. The maps shift down and the stable fixed point x_s decreases (and x_u increases). Note that as τ_c increases, the distance between x_s and x_u decreases. When τ_c becomes large enough, these two fixed points merge at a saddle-node bifurcation, implying the loss of entrainment and providing an upper bound on the range of entrainment. Similarly, when τ_c decreases and becomes too small, a different saddle-node bifurcation of these two fixed points occurs signifying the lower bound on the range of entrainment.

In Fig. 4A and B, we show how the entrainment map varies with changes in light intensity I (Panel A) and photoperiod (Panel B). Changing light intensity I has a pronounced effect on the shape of the maps, but less of an effect on the location of the stable and unstable fixed points (Fig. 4A). The increased concavity with stronger intensity light leads, in general, to faster entrainment (discussed in greater detail in Diekmann and Bose, 2016). The map becomes insensitive to increases in I above a certain point, with nearly complete overlap of the maps for $I = 100,000$ lux and above. This suggests that entrainment cannot be lost by increasing the light intensity too much. On the other hand, if the light intensity becomes too weak ($I \rightarrow 0$), then entrainment is lost through a saddle-node bifurcation as the maps move up and the stable and unstable fixed points collide. Changes to the photoperiod, $N:24-N$, are shown in Fig. 4B. An increase in N , meaning longer daylength, shifts the discontinuity of the map to the right because the portion of the map to the right of x_s gets shifted down. To the left of x_s , the opposite happens where an increase in N shifts the map up. Note that the distance between x_s and x_u decreases with N . This change in distance is a critical factor in explaining the east-west asymmetry of jet lag, as discussed in Section 3.4.

Information from entrainment maps can be used to construct plots that display the entrainment region as a function of two parameters, known as *Arnold tongues* or *Arnold onions*. In Fig. 4C and D, we show the stable phase of entrainment for different parameter pairs. The stable phase was determined by constructing an entrainment map at each set of parameter values, and then find-

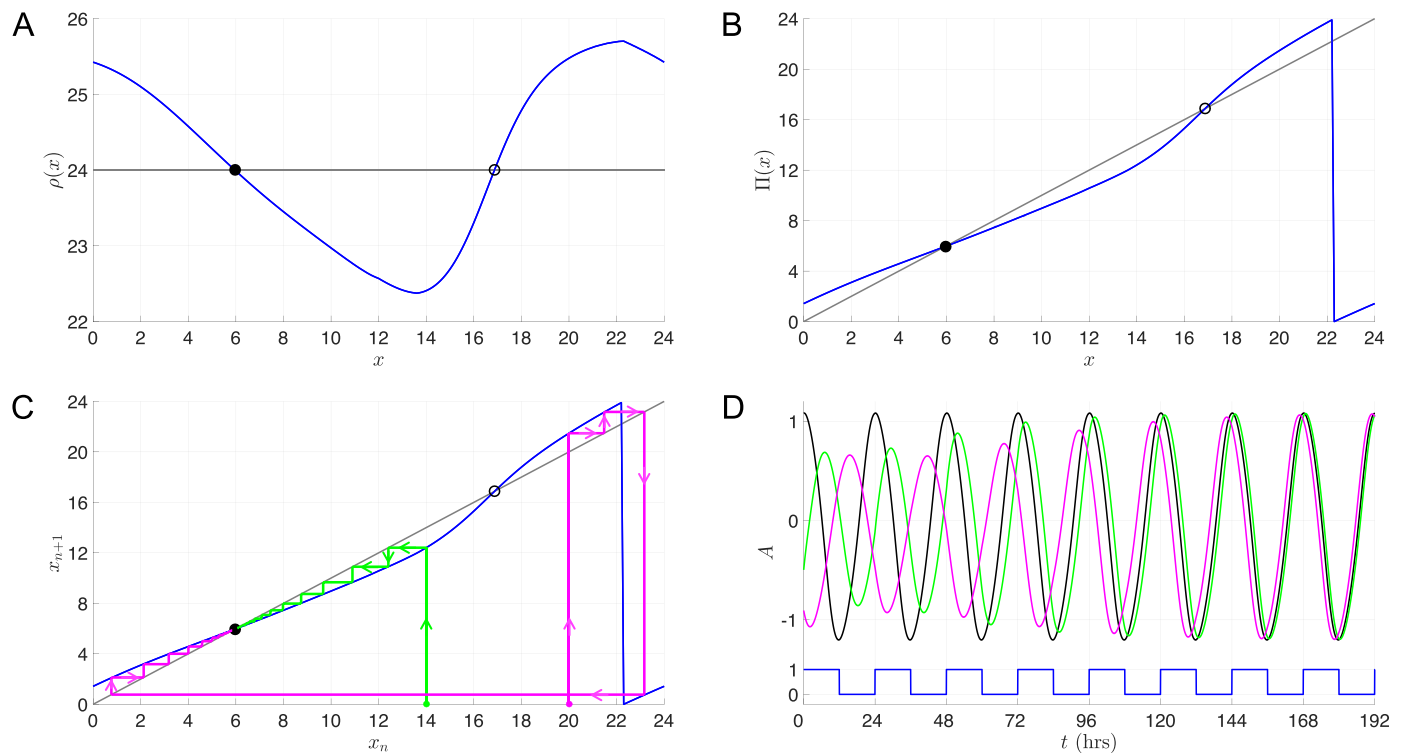


Fig. 2. Entrainment map and reentrainment simulations. Parameters: $\tau_c = 24.2$ h, $N = 12$ h, and $I = 1000$ lux. (A) $\rho(x) = 24$ at $x = 5.96$ (solid dot) and $x = 16.87$ (open dot). (B) These x values satisfy $\Pi(x) = x$ and correspond to stable and unstable fixed points, x_s and x_u , of the entrainment map. (C) Cobwebbing the entrainment map shows that x_u separates initial conditions that reentrain through phase advance (green) and phase delay (magenta). (D) Direct simulations for initial conditions lying on opposite sides of x_u showing reentrainment through phase advances (green) and phase delays (magenta) as predicted by the entrainment map. (For interpretation of the references to color in this figure legend, the reader is referred to the web version of this article.)

ing the location of the stable fixed point x_s . The Arnold tongue in Fig. 4C displays the entrainment region and stable entrained phase as a function of endogenous period τ_c and light intensity I for $N = 12$ h. The colored region of parameter space represents parameter pairs for which stable entrainment occurs, and curves of constant phase lie on curves of constant color. For illustrative purposes, the curve with $x_s = 6$ is shown in white. As I increases, curves of constant phase become almost vertical indicating that increasing light intensity does not significantly change the phase of entrainment (as noted in Fig. 4A). Horizontal slices of Fig. 4C show that the range of endogenous periods that lead to entrainment increases with intensity. These results are consistent with those of Bordyugov et al. (2015), who calculated Arnold tongues for a Kuramoto model as well as a variety of circadian models including the Gonze et al. (2005) and Relógio et al. (2011) models. The Arnold tongues for those models formed a V-shaped region in parameter space, similar to the parabola-shaped region that we find here for the FJK model. Our results are also consistent with the laboratory study of Wright et al. (2001), which found that humans could entrain to very low intensity light (1.5 lux) if the forcing period was exactly 24 h, but could not entrain if the forcing period was different than 24 h (specifically 23.5 or 24.6 h). The Arnold onion in Fig. 4D displays the entrainment region and stable entrained phase as a function of τ_c and N for $I = 1000$ lux. The curve with $x_s = 6$ is again shown in white. For a fixed endogenous period (vertical slice of figure), changes in the photoperiod can have large and counterintuitive effects on the stable phase. For example, with $\tau_c = 24.5$ h and $N = 8$ h, the stable phase $x_s < 6$. If N is either increased enough, or decreased enough, the stable phase becomes $x_s = 6$. Thus changes in entrained phase are not necessarily monotonic with respect to changes in photoperiod. This figure is qualitatively similar to Fig. 1B of Schmal et al. (2015) who

calculate Arnold onions for a host of models. The bottom tip of our onion is located at $\tau_c = 24$ h, corresponding to an endogenous period in constant darkness ($N = 0$) that is equal to the period of LD forcing that we used for $0 < N < 24$. The top tip of our onion is located at $\tau_c = 24.4$ h, which is close to the endogenous period in constant darkness that exhibits a 24-h period when placed in constant light ($N = 24$). The tilt of the onion to the right indicates that the FJK model is consistent with *Aschoff's Rule*, which states that $\tau_{LL} < \tau_{DD}$ for day-active animals. The Arnold onions in Schmal et al. (2015) are found by holding the endogenous period in constant darkness fixed at 24 h and varying the LD forcing period, whereas we vary the endogenous period in constant darkness and hold the LD forcing period fixed at 24 h. Thus their onions tilt to the left, rather than the right, for day-active animals.

3.3. Jet lag due to east-west travel

We now determine how long a traveler takes to reentrain after a change in time zone by computing, via direct simulation, reentrainment times for trips with a prescribed arrival time over a prescribed number of time zones (either east or west). We then use the entrainment map to explain the simulation results, as well as to explain the east-west asymmetry in jet lag.

Fig. 5 shows a schematic diagram of the 12:12 LD cycle across all time zones. The horizontal direction demarcates hourly intervals starting with 7 AM (defined as $X = 0$); the vertical direction demarcates hourly intervals corresponding to different time zones. The middle row of the diagram corresponds to the "home" time zone ($Z = 0$) while those lying above this row ($Z > 0$) correspond to travel to the east, and those below ($Z < 0$) correspond to travel to the west. In each row, the corresponding 12:12 LD cycle is shown such that lights turn on at 7 AM in the "destination" time zone. Each column shows the current position of the LD cycle in that

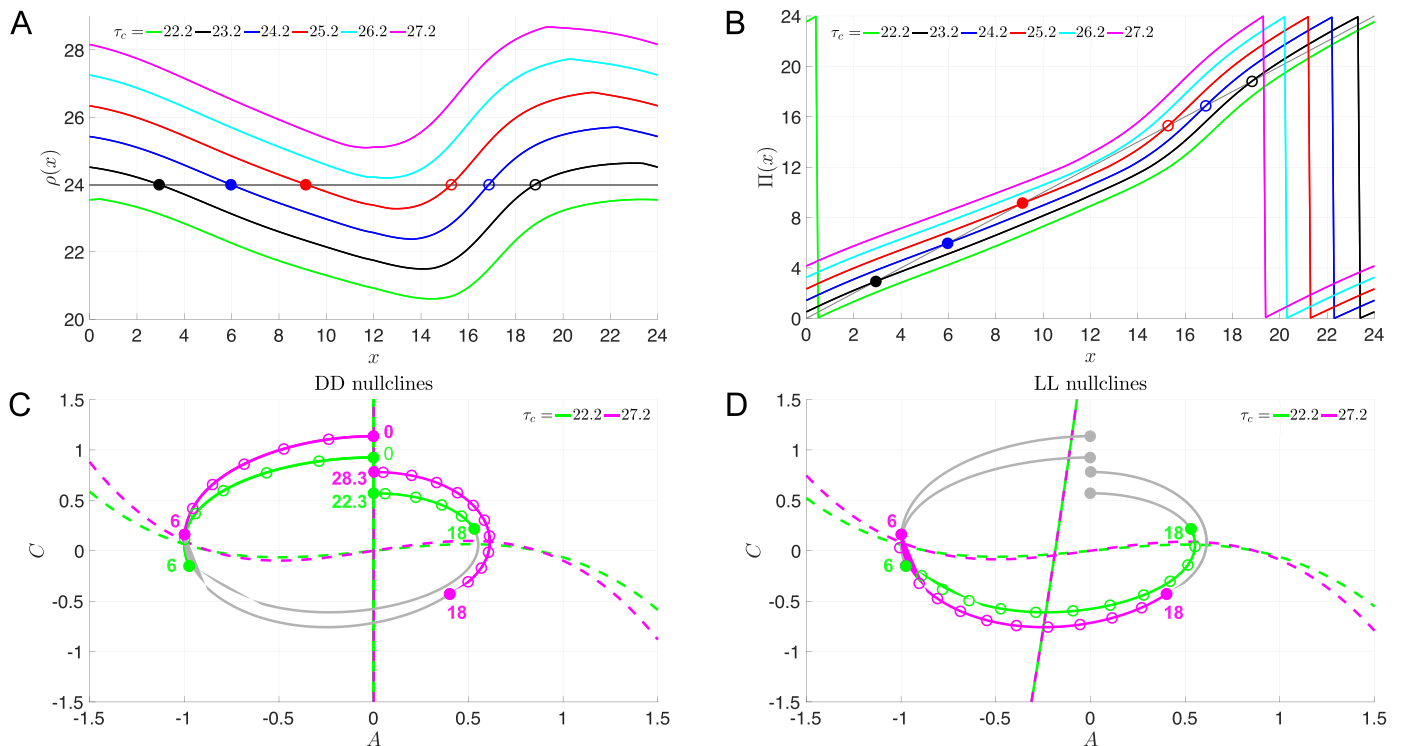


Fig. 3. Dependence of entrainment map on endogenous period τ_c . (A) $\rho(x)$ shifts up as τ_c increases and down as τ_c decreases. (B) $\Pi(x)$ shifts up and to the left as τ_c increases, causing the stable fixed point x_s (solid dots) to move to the right, implying that as intrinsic period increases the phase of entrainment becomes more delayed. The unstable fixed point x_u (open dots) move to the left. As τ_c decreases, $\Pi(x)$ and the fixed points move in the opposite manner. (C) and (D) Evolution of trajectories used in computation of $\rho(18)$. In (C), during the initial six hours of darkness the DD nullclines (dashed lines) are such that the $\tau_c = 27.2$ h oscillator moves slower than the $\tau_c = 22.2$ h oscillator; the green trajectory is ahead of the magenta. In Panel D, for the next 12 h of light, the LL nullclines (dashed lines) are such that the $\tau_c = 27.2$ h oscillator still moves slower than the $\tau_c = 22.2$ h oscillator when the lights are on. The final portions of their respective evolutions under darkness are shown in Panel C. Gray curves in each panel are copies of the colored curves in the opposite panels. In sum, the magenta trajectory moves slower than the green contributing to a larger $\rho(18)$ value and upward shift of the ρ map. For this figure $N = 12$ h and $I = 1000$ lux. (For interpretation of the references to color in this figure legend, the reader is referred to the web version of this article.)

zone. There are two natural ways to use this travel grid. One possibility is to assume that from departure, the traveler immediately tries to reentrain to the destination time zone (DTZ). The other is to assume that the traveler remains phase-locked to the home time zone (HTZ) throughout the duration of the trip and only begins to reentrain upon arrival at their destination. The former case is equivalent to studying the dynamics of a leaving time map, and the latter, the dynamics of an arrival time map. Both cases can be thought of as instantaneous travel time in that the traveler instantaneously switches from the HTZ to the DTZ. In what follows, let us take the latter interpretation of an arrival time map. Namely, we define the arrival time as the HTZ time when the destination is reached. For example, if one travels from New York to Los Angeles and arrives at 1 PM, this means they have arrived at 1 PM New York time (which corresponds to 10 AM Los Angeles time.)

In both the home and destination time zones, the 24-h LD forcing is identical, but phase shifted by Z hours. We construct a set of Poincaré maps associated with each arrival time X , denoted by $\Pi_X(x)$. An oscillator that is entrained in the home time zone to a value $x_s = \Pi_X(x_s)$ will also entrain to the same value x_s in the destination time zone if the Poincaré section is chosen at the same time location X along the LD-entrained cycle. In other words, the phase of entrainment to the LD cycle is the same, independent of the zone. Suppose the oscillator starts in its home time zone $Z = 0$ entrained to the 24-h LD forcing, i.e. with $x_0 = x_s$. Now consider an arrival HTZ time of X after travel of Z time zones. Upon arrival in the destination time zone, the oscillator will not be entrained to the 24-h LD forcing in the DTZ due to the shift in the LD cycle. For example, consider the blue dots and arrow in Fig. 5. The HTZ

arrival time in this case is 11 PM which corresponds to $X = 16$. Therefore $x_s = 16$. The trip consists of travel 11 time zones to the east, $Z = 11$. This corresponds to the vertical blue line and arrow pointing up. In the destination time zone, the DTZ time is 10 AM. Thus the traveler will be subjected to 9 h of light instead of the 8 h of darkness that was expected. Therefore in the DTZ, the oscillator will be phase shifted with regard to the LD cycle and will no longer be entrained. In effect, with regard to the Poincaré section at $X = 16$, the oscillator will have had its initial condition shifted to a new value $x_0 = 3$ and will need to reentrain toward $x_s = 16$. As another example, consider the case of $Z = -8$ and $X = 6$ shown by the red dot and arrow. This depicts travel 8 zones to the west arriving at 1 PM HTZ. The time in the destination zone is 5 AM DTZ. Thus the traveler will be subjected to 2 h of darkness in the destination time zone compared to the 6 h of light that it would have received in the home zone. Now, the oscillator must reentrain to $x_s = 6$ from an initial condition $x_0 = 22$.

We first calculate the reentrainment time by direct simulations assuming a 12:12 LD photoperiod. Define $R = 12 - X - Z$. The quantity R determines how much light or darkness to provide to the oscillator once in the destination time zone until the beginning of the next full 12 h of L or D. In the example of the travel shown in blue, $R = -15$ and we impose 9 h of light followed by 12 h of D. The various cases are summarized below:

- if $R \leq -12$: impose L for $24 + R$, then start 12:12 D:L (eastward travel)
- if $-12 < R \leq 0$: impose D for $12 + R$, then start 12:12 L:D (could be eastward or westward travel)

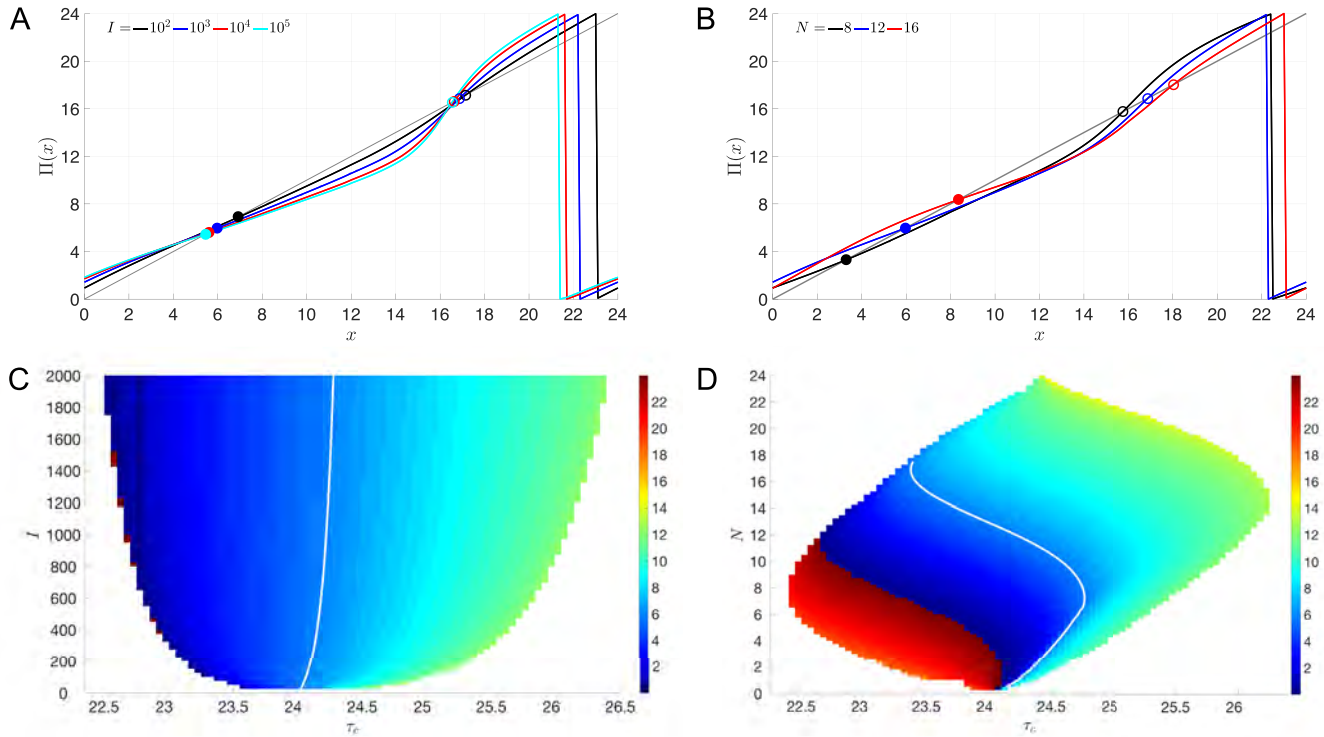


Fig. 4. Dependence of entrainment map on light intensity I and daylength N . (A) Concavity of the entrainment map increases as I is increased, implying that higher light intensity reduces the amount of time it takes an oscillator to reentrain following a phase shift of the LD cycle. The location of the stable fixed points x_s (solid dots) and unstable fixed points x_u (open dots) do not change much as I is varied. For this panel, $\tau_c = 24.2$ h and $N = 12$ h. (B) Stable fixed points of the entrainment map move to the right as N is increased, implying that as daylength increases the phase of entrainment becomes more delayed. The unstable fixed points also move as N is varied. For this panel, $\tau_c = 24.2$ h and $I = 1000$ lux. (C) Arnold tongue computed from entrainment map analysis displaying the entrainment region as a function of τ_c and I . Heatmap colors indicate the location of x_s , i.e. the stable phase of entrainment. The white contour line corresponds to $x_s = 6$. At the borders of the tongue, entrainment is lost through saddle-node bifurcation of x_s and x_u . For this panel, $N = 12$ h. (D) Arnold onion computed from entrainment map analysis displaying stable phases x_s within the entrainment region as a function of τ_c and N . For this panel, $I = 1000$ lux.

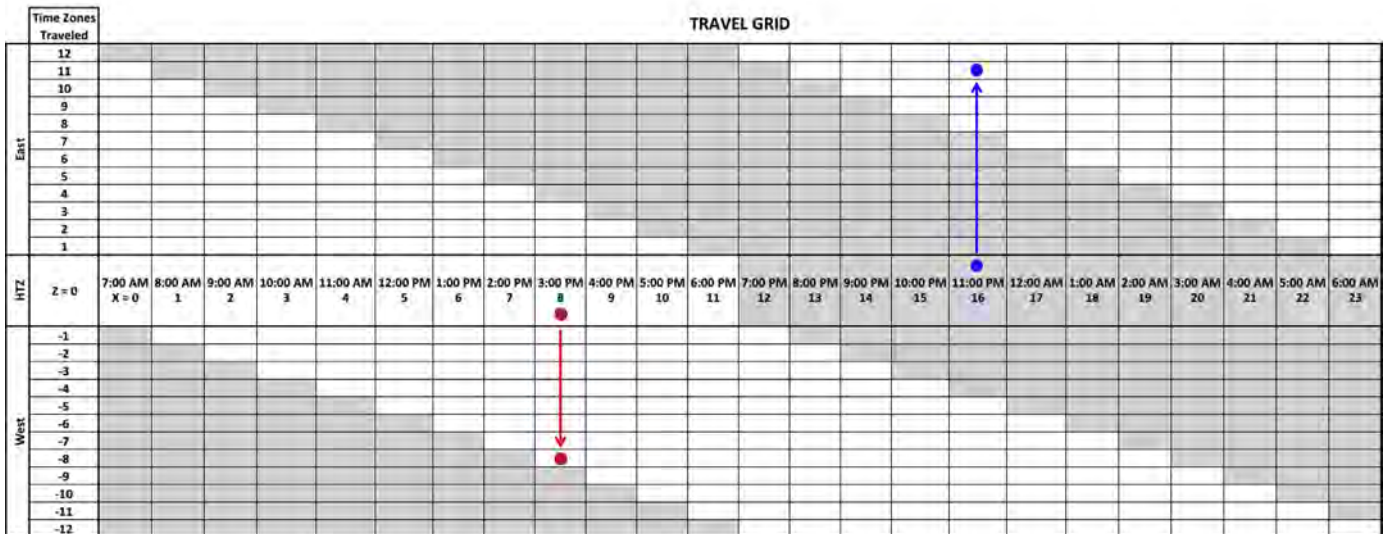


Fig. 5. Schematic diagram of 12:12 LD cycle across all arrival times X and number of time zones traveled Z . This travel grid can be used to easily visualize the offset of the LD cycle due to instantaneous travel and to identify the relationship between the home and destination time zones. The horizontal row in the middle of the grid at $Z = 0$ represents the home time zone (HTZ). The other rows represent destination time zones (DTZs) that lie east (west) for $Z > 0$ ($Z < 0$). The rows are broken up into one hour intervals. The shaded region in each row represents the times of darkness in that time zone relative to HTZ. The Poincaré section $X = 0$ is nominally chosen to correspond to 7 AM HTZ. The blue dots and arrow represent travel 11 time zones east with arrival at 11 PM HTZ and 10 AM DTZ. The red dots and arrow represent travel of 8 time zones west with arrival at 1 PM HTZ and 5 AM DTZ. The entrainment map's arrival time section X is defined with respect to HTZ. (For interpretation of the references to color in this figure legend, the reader is referred to the web version of this article.)

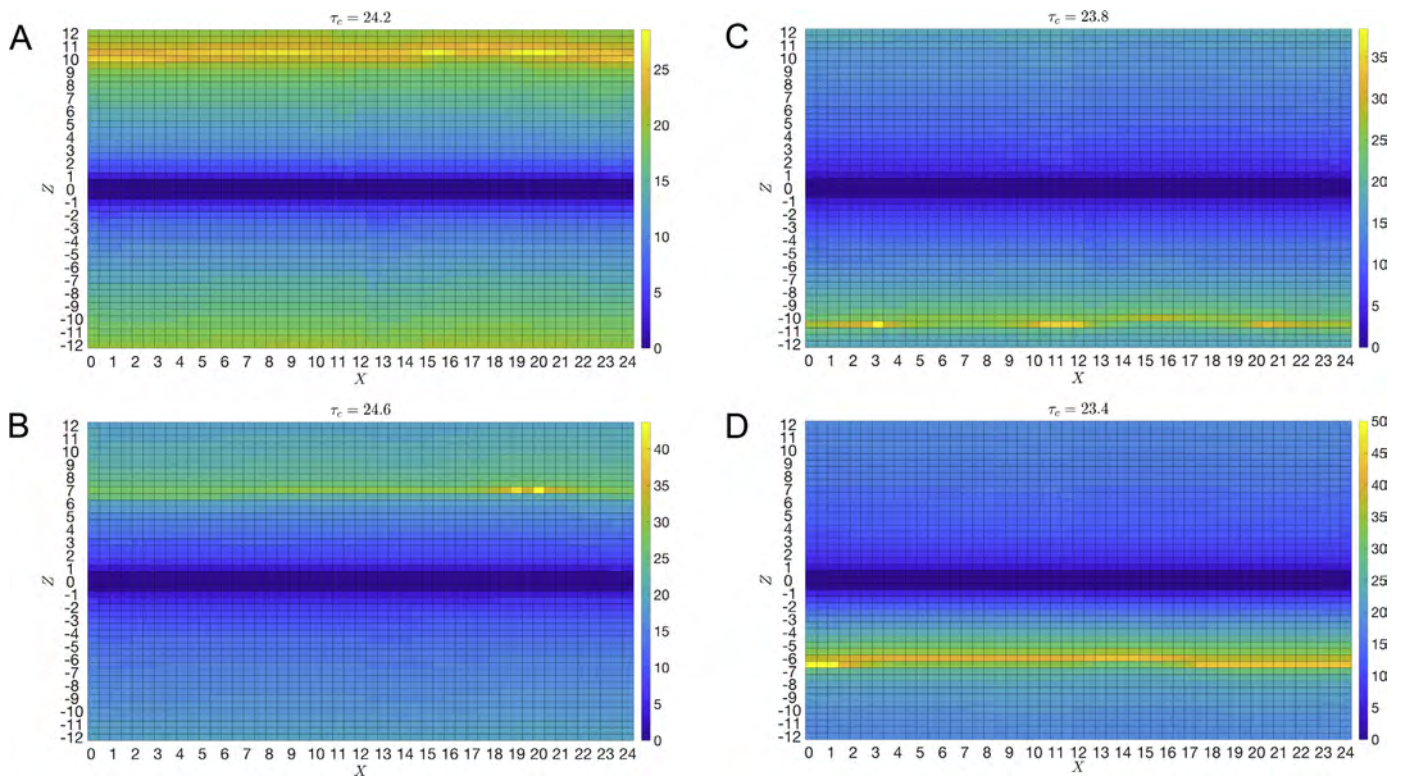


Fig. 6. Reentrainment times and worst-case jet lag from direct simulations across all arrival times X and number of time zones traveled Z . Light colors indicate longer reentrainment times. $Z > 0$ corresponds to eastward travel and $Z < 0$ to westward travel. In these simulations $N = 12$ h and $I = 100$ lux. (A) For the typical human intrinsic period of $\tau_c = 24.2$ h, the longest reentrainment times are for eastward trips of 10.5 time zones ($Z = 10.5$). (B) For a slower than typical intrinsic clock of $\tau_c = 24.6$ h (black), the worst jet lag is for eastward trips of 7 time zones ($Z = 7$). (C) For a faster than typical intrinsic clock of $\tau_c = 23.8$ h, the worst jet lag is for westward trips of 10.5 time zones ($Z = -10.5$). (D) For an even faster intrinsic clock of $\tau_c = 23.4$ h, the worst jet lag is for westward trips of 6.5 time zones ($Z = -6.5$).

- if $0 < R \leq 12$: impose L for R, then start 12:12 D:L (could be eastward or westward travel)
- if $12 < R \leq 24$: impose D for R – 12, then start 12:12 L:D (westward travel)

With direct simulations, the reentrainment time is calculated from the start of the above procedure until a stopping criterion is achieved; namely, we define reentrainment to have occurred when the magnitude of the time difference between the section crossings of the oscillator and a reference oscillator is less than 0.5 h. The reference oscillator is subjected to the same light-dark protocol as the traveler, but is by definition already entrained to the destination time zone. Thus the reference oscillator starts on the LD-entrained solution at the location given by $(X + Z) \bmod 24$.

To calculate the reentrainment time using entrainment maps, at each value X denoting the HTZ arrival time relative to 7 AM, we construct a Poincaré section along the LD limit cycle and define the return map Π_X as before. The fixed point of each map $\Pi_X(x)$ is by definition X . To calculate the appropriate initial condition with which to start iterations in the destination time zone, we determine the new phase relationship between the oscillator and the LD cycle of that time zone. To do so, compute $z_0 = X + Z$. If $0 \leq z_0 < 24$, then choose the initial condition $x_0 = z_0$. If $z_0 > 24$, then $x_0 = z_0 - 24$. If $z_0 < 0$, then $x_0 = z_0 + 24$.

3.3.1. Worst-case travel depends on endogenous period

In Fig. 6, we show entrainment time results over all possible HTZ arrival times (X) and trips (Z) for four different intrinsic periods τ_c . The light intensity was taken at the relatively low level of $I = 100$ lux, which is characteristic of indoor light. Fig. 6A corresponds to the typical endogenous human DD period of 24.2 h. The heatmap shows the reentrainment times with darker colors

indicating relatively short reentrainment times, and lighter colors indicating progressively longer times. In each case, the heatmap is asymmetric about $Z = 0$ indicating that reentrainment due to eastward travel can differ compared to westward travel. Indeed, for a $\tau_c = 24.2$ h oscillator, the longest reentrainment times occur for travel roughly 10 and 11 zones to the east. The reentrainment times are relatively insensitive to the arrival time. The remaining panels show the heatmaps for different τ_c . For $\tau_c = 24.6$ h (Fig. 6B), the worst trip shifts to smaller values of Z , meaning that shorter eastward trips are more difficult for individuals with slower body clocks. The right column shows the heatmap for individuals whose intrinsic clock is faster than normal, $\tau_c = 23.8$ h (Fig. 6C) and 23.4 h (Fig. 6D). Now observe that the worst reentrainment for these individuals occurs for trips to the west, instead of to the east. As the intrinsic clock speeds up, progressively shorter westward trips lead to longer reentrainment. For example at $\tau_c = 23.4$ h, a trip 6 h to the west is the worst.

The entrainment map can be used to explain these findings. In each case, the longest reentrainment time occurs when the travel places the oscillator's initial condition in a neighborhood of the unstable fixed point x_u . The location of x_u relative to x_s depends on τ_c . For example, when $\tau_c = 24.2$ h, we have found that $x_u \approx (x_s + 10.5) \bmod 24$, independent of arrival time. Thus travel of 10 or 11 h east would place the initial condition x_0 near the unstable fixed point. Specifically, if the Poincaré section is chosen at X , then $x_s = X$ and $x_u = (X + 10.5) \bmod 24$. Travel of $Z > 0$ time zones to the east would imply $x_0 = (X + Z) \bmod 24$, therefore $x_0 - x_u = Z - 10.5$. Thus if Z is either 10 or 11, then the initial condition x_0 lies within 0.5 of the unstable fixed point and will lead to very long reentrainment times. This is consistent with the heatmap shown in Fig. 6A.

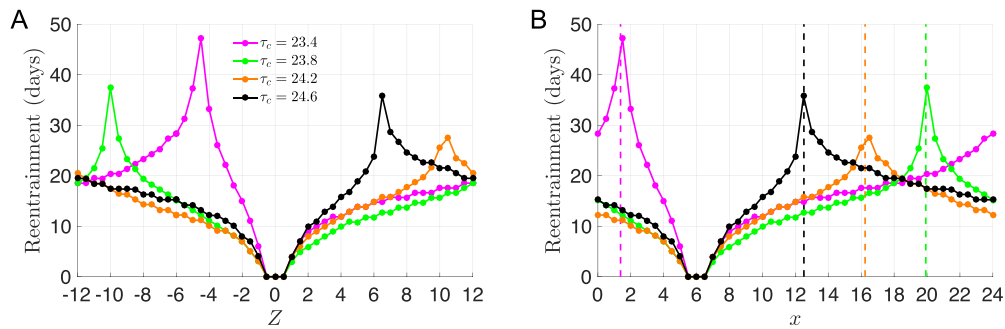


Fig. 7. Worst-case jet lag is explained by the unstable fixed point of the entrainment map. (A) Reentrainment times for the $X = 6$ column of the heatmaps in Fig. 6 (corresponding to an arrival time of 1 PM) computed by cobwebbing the analogous entrainment maps. The longest reentrainment times occur for trips of $Z = -4.5$ for $\tau_c = 23.4$ h (magenta), -10 for $\tau_c = 23.8$ h (green), 10.5 for $\tau_c = 24.2$ h (orange), and 6.5 for $\tau_c = 24.6$ h (black). The reentrainment times and Z value of these local peaks qualitatively agree with the longest reentrainment times found through direct simulation (the yellow hotspots in Fig. 6A–D). (B) Same data as (A), replotted with the horizontal axis in terms of x instead of Z . The local peaks in reentrainment time are at initial conditions near the location of the unstable fixed point x_u (dashed vertical lines) for each value of τ_c , indicating that the worst jet lag occurs after trips that put the traveler in the vicinity of x_u . (For interpretation of the references to color in this figure legend, the reader is referred to the web version of this article.)

Similarly, for different choices of τ_c , we find that the distance between x_u and x_s determines the travel distance and direction that leads to the longest reentrainment time. We illustrate this in Fig. 7 by plotting the reentrainment times derived from cobwebbing the map for a single arrival time $X = 6$, corresponding to one column of the heatmaps. Fig. 7A shows the reentrainment times centered around $Z = 0$ on the horizontal axis. This clearly shows how the worst travel changes as a function of τ_c , and that east-west asymmetry in jet lag exists over all τ_c values chosen. In Fig. 7B, we replot these reentrainment times converting the horizontal axis from Z to x . The dashed vertical lines show the location of x_u for the four different choices of τ_c . Recall that increasing τ_c moves the entrainment map up (Fig. 3B), and causes the unstable fixed point x_u to move to the left. For $\tau_c = 23.4$ h, $x_u \approx 1.5$ (dashed magenta line), and as τ_c increases x_u moves to the left through the $x = 0$ boundary and emerges through the $x = 24$ boundary at progressively leftward values (green, orange and black dashed lines). The longest reentrainment times predicted by the map are for travel of Z time zones that places the initial condition x_0 near x_u in each of these four cases. To find the worst-case trip, we find the value of $Z_D \in (-12, 12)$ that solves $x_u = (x_s + Z_D) \bmod 24$. In all cases the arrival time was held fixed at $X = 6$, implying $x_s = 6$. From the map, we found the values x_u to approximately equal 12.5, 16.5, 20, and 1.5 for $\tau_c = 24.6, 24.2, 23.8,$ and 23.4 h, respectively. Solving for the corresponding Z_D values yields 6.5, 10.5, -10 , and -4.5 respectively. These correspond to the worst possible trips being 6 h east, 10.5 h east, 10 h west, and 4.5 h west respectively, which are qualitatively consistent, and except for $\tau_c = 23.4$ h, quantitatively consistent with the reentrainment time heatmaps from direct simulation (Fig. 6). We call Z_D a *demarkation point*, since it separates trips that reentrain through phase advance or phase delay. Its properties will be further discussed in Section 3.5.

Fig. 6 indicates that the average amount of time it takes to reentrain after travel also depends on τ_c . For example, consider the 49 possible trips represented by $Z \in (-12, 12)$ in increments of 0.5, with the arrival time held fixed at $X = 6$. The median reentrainment times for these trips with $\tau_c = 24.6, 24.2, 23.8,$ and 23.4 h are 16.3, 13.3, 13.2, and 17.6 days, respectively. The longer median reentrainment times correspond to τ_c values closer to the bifurcation points at which entrainment is lost. Maps that are closer to bifurcation have less concavity, and therefore longer reentrainment times (Fig. 4A and Diekman and Bose, 2016). This finding is consistent with previous work showing that for a variation of the Poincaré oscillator, reentrainment times are longer near the borders of the Arnold tongue entrainment region than at the center (Granada and Herzel, 2009).

3.3.2. Quantifying the east-west asymmetry of jet lag

Fig. 8 shows a comparison of reentrainment times calculated using the map (empty circles) versus direct simulation (filled circles). In each case, the Poincaré section was chosen at $X = 6$. Reentrainment times for trips to the east (west) are shown in blue (red). The qualitative predictions of the entrainment map match those from the direct simulations. First, both methods show that trips to the east require longer reentrainment times than trips to the west for humans with average to slow body clocks. This is evidenced by the blue curves lying above the red curves in the two panels in the left column. The opposite is true for humans with fast body clocks as shown in the right column. These plots show that the extent of the east-west asymmetry found in reentrainment times depends critically on the endogenous period of the underlying DD oscillator. Second, the two methods yield results that are in very close agreement for westward travel of travelers with average to slow body clocks (Fig. 8A and B, red) and eastward travel for fast body clocks (Fig. 8C and D, blue). For travel in the opposite directions than these, the two methods quantitatively agree over many time zones, but there are intervals where they disagree. The place where the two methods quantitatively differ is when traveling to a time zone that lies in a neighborhood of the unstable fixed point. The predictions from the map for reentrainment for initial conditions that lie arbitrarily close to the unstable fixed point can become arbitrarily large. This is a consequence of the structure of piecewise monotone maps and the particular details of the entrainment map for FJK model. An arbitrarily large number of iterates are needed to leave a neighborhood of x_u if x_0 is chosen sufficiently close to it. In general, this leads to a map-based prediction that is larger than what is found in direct simulations, as seen by the larger peaks in the dashed curves than the solid curves in Fig. 8. In addition, for $\tau_c = 24.6$ and 23.4 h, the map-based predictions of the Z value corresponding to the worst-case reentrainment time are quantitatively different than the results from direct simulation (6.5 versus 7 h East for $\tau_c = 24.6$ h, and 4.5 versus 6 h West for $\tau_c = 23.4$ h), as further discussed in the Appendix.

Despite these differences, the map is useful to draw several conclusions. First, the sign and magnitude of the difference $x_u - x_s$ determines which direction of travel and over how many time zones leads to the worst jet lag. For those with a normal to slow intrinsic period, travel to the east will lead to the worst jet lag because the unstable fixed point x_u lies to the right of the stable one x_s . For those with a faster than normal intrinsic period, it is travel to the west that will lead to the worst jet lag. Second, the proximity of the initial condition x_0 in the destination time zone to x_u determines, in part, the length as well as the direction of reentrain-

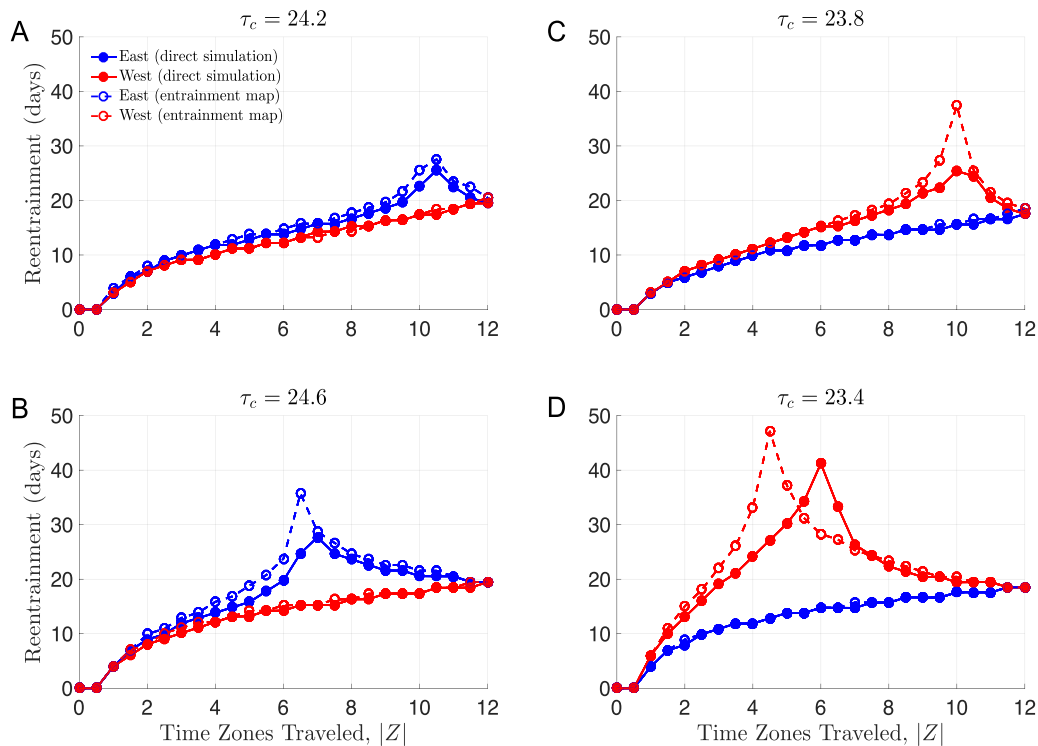


Fig. 8. East-West asymmetry of reentrainment times depends on intrinsic period τ_c . The reentrainment times for an arrival time of 1 PM obtained through direct simulation (solid lines and filled dots) qualitatively agree with the reentrainment times obtained by cobwebbing the analogous entrainment maps (dashed lines and open circles). (A) For $\tau_c = 24.2$ h, eastward trips (blue) take longer to reentrain from than westward trips (red). (B) For $\tau_c = 24.6$ h, eastward trips are worse than westward trips as in (A) but here the degree of asymmetry is increased. (C) For $\tau_c = 23.8$ h, westward trips take longer to reentrain from than eastward trips. (D) For $\tau_c = 23.4$ h, westward trips are worse than eastward trips as in (C) but here the degree of asymmetry is increased. (For interpretation of the references to color in this figure legend, the reader is referred to the web version of this article.)

ment (either through phase advance or delay). Since reentrainment times are quite sensitive to initial conditions in a neighborhood of x_u , we are hesitant to attribute too much importance to very long reentrainment times. We will further study the role of x_u in determining the direction of reentrainment in Section 3.3.3.

3.3.3. Orthodromic versus antidromic reentrainment

We now address the direction of reentrainment, and in particular the circumstances that lead to orthodromic versus antidromic reentrainment. Fig. 9 shows the regions of orthodromic and antidromic reentrainment for the four different choices of τ_c . For $\tau_c = 24.2$ h, antidromic reentrainment occurs when travel to the east causes the initial condition to lie in the interval $(x_u, 18)$. The lower bound of x_u is necessary to place the initial condition on the “opposite” side of x_u . The upper bound of 18 reflects that 12 is the maximum number of zones of eastward travel ($x_s + 12 = 18$). In this case, $x_u = 16.5$ and eastward trips of 10.5 zones or greater lead to antidromic reentrainment. All other trips in either direction are followed by orthodromic reentrainment (Fig. 9A). As τ_c increases to 24.6, the unstable fixed point x_u moves to the left, thus creating a larger interval $(x_u, 18)$ of antidromic reentrainment (Fig. 9B). The case for $\tau_c = 23.8$ h (Fig. 9C) is largely the same as $\tau_c = 24.2$ h, except that antidromy occurs for westward trips of 10 to 12 zones when x_0 lies in the interval $(18, x_u)$. For $\tau_c = 23.4$ h (Fig. 9D), x_u has moved to right, through the boundary at $x = 24$ to about 1.5. Thus the region of antidromy is the union of the intervals $(0, x_u)$ and $(18, 24)$. To summarize, antidromic reentrainment can occur when the number of time zones traveled is larger than the distance between x_s and x_u .

Antidromic reentrainment is typically regarded as leading to longer reentrainment times than orthodromic reentrainment (Arendt et al., 1987; Klein and Wegmann, 1977; Sack, 2010). Our

results suggest that while this is often true, it is not always the case. For example, consider eastward trips of 10 and 11 time zones for the $\tau_c = 24.2$ h oscillator with an arrival time of $X = 6$. The $Z = 10$ trip corresponds to $x_0 = 16$ and entrains orthodromically, whereas the $Z = 11$ trip corresponds to $x_0 = 17$ and entrains antidromically (Fig. 9A). In this case the orthodromic reentrainment takes longer (27.5 days) than the antidromic reentrainment (22.5 days); to see this compare the $Z = 10$ and $Z = 11$ data points in Fig. 7A. Furthermore, this orthodromic $Z = 10$ trip also has a longer reentrainment time than the corresponding 10-zone eastward trip for $\tau_c = 24.6$ h, which reentrains antidromically (21.5 days); to see this compare the orange and black $Z = 10$ data points in Fig. 7A. The possibility of antidromic reentrainment being faster than orthodromic reentrainment was also noted in a molecular model of the mammalian circadian clock (Leloup and Goldbeter, 2013). This feature is due to x_u creating a boundary that separates the x_0 values that reentrain through phase advances from those that reentrain through phase delays, and the fact that reentrainment times are sensitive to the distance between x_0 and this boundary.

To better understand the effect of photoperiod and intrinsic period on orthodromy/antidromy, we computed the differences in reentrainment times for the specific cases of trips made 10 time zones to the east and west ($|Z| = 10$) over a range of N and τ_c values. To simplify the argument, we choose the Poincaré section to lie at $X = 12$ for the different LD-entrained solutions that we will consider. This implies that $x_s = 12$. Antidromic reentrainment can only occur when the distance between x_s and x_u is less than 12. In Fig. 10 we show a heat map derived from cobweb simulations for trips 10 h to the east and west. We plot the difference of reentrainment times (east minus west). There are three principal features of this heat map. First is the solid black curve, which we call the *neutral period curve* for $|Z| = 10$, or NPC₁₀. The neu-

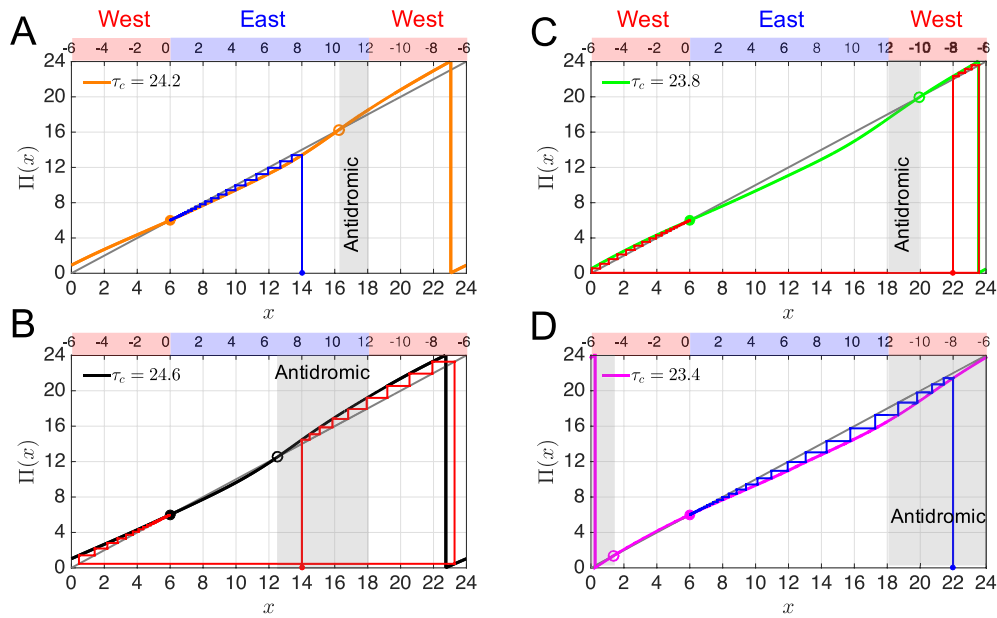


Fig. 9. Unstable fixed point of entrainment map controls whether reentrainment is orthodromic or antidromic. (A) After traveling 8 time zones east (a phase advance of the LD cycle), reentrainment occurs through phase advances and is therefore orthodromic if $\tau_c = 24.2$ h. The reentrainment time is 17.69 days. (B) The same trip as in (A) reentrains through phase delays and is therefore antidromic if $\tau_c = 24.6$ h. The reentrainment time is 24.64 days. (C) After traveling 8 time zones west (a phase delay of the LD cycle), reentrainment occurs through phase advances and is therefore orthodromic if $\tau_c = 23.8$ h. The reentrainment time is 19.31 days. (D) The same trip as in (C) reentrains through phase delays and is therefore antidromic if $\tau_c = 23.4$ h. The reentrainment time is 23.35 days.

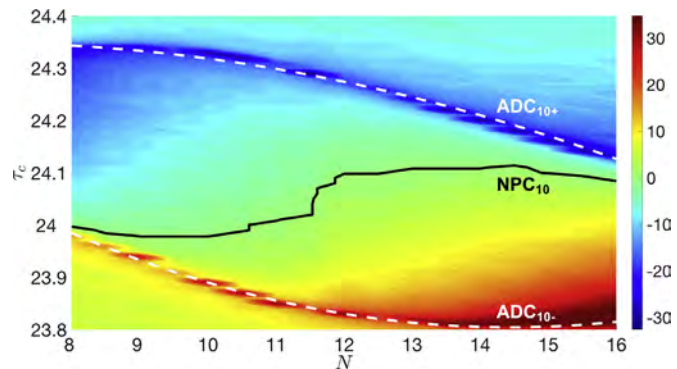


Fig. 10. East-West asymmetry and antidromic reentrainment depend on daylength N . Reentrainment times were determined by cobwebbing entrainment maps for eastward and westward trips of 10 time zones ($Z = \pm 10$) over a range of N and τ_c values with $I = 100$ lux and the stable fixed point held at $x_s = 12$. The colormap represents the degree of asymmetry in reentrainment times in units of days, and was calculated by subtracting the reentrainment time for $Z = 10$ from the reentrainment time for $Z = -10$. Therefore negative values correspond to (N, τ_c) pairs for which eastward travel is worse, and positive values to westward travel being worse. Along the black neutral period curve (NPC_{10}), reentrainment times are the same for eastward and westward travel. Along the upper dashed white curve (ADC_{10+}), the unstable fixed point is 10 h to the right of x_s , i.e. $x_u = 22$. Along the lower dashed white curve (ADC_{10-}), the unstable fixed point is 10 h to the left of x_s , i.e. $x_u = 2$. In between these antidromy curves all reentrainment is orthodromic; outside these curves all reentrainment is antidromic. Note that eastward travel is much worse than westward travel (dark blue colors) near ADC_{10+} , whereas westward travel is much worse than eastward travel (dark red colors) near ADC_{10-} . (For interpretation of the references to colour in this figure legend, the reader is referred to the web version of this article.)

tral period curve is a generalization of the concept of neutral period introduced by [Aschoff et al. \(1975\)](#). Points on NPC_{10} represent (N, τ_c) parameter pairs for which the reentrainment time after a trip 10 time zones east is identical to the reentrainment times for 10 zones to the west. For any parameter values that lie above the NPC_{10} , trips of 10 zones to the east are worse than 10 zones to the west. The other two important features of [Fig. 10](#) are the dark

blue and red regions of the heat map. These lie in a neighborhood of what we call the ADC_{10+} and ADC_{10-} antidromy curves. These curves correspond to parameter values at which $x_u - x_s = 10$ or -10 respectively. For parameter values that lie near ADC_{10+} (ADC_{10-}), trips 10 zones to the east (west) place the initial condition for reentrainment very close to the unstable fixed point x_u . Reentrainment times calculated from the map for such initial conditions are arbitrarily long. For parameter values between the two antidromy curves, reentrainment after a trip of 10 time zones is always orthodromic. But for eastward trips made with parameter values above the ADC_{10+} , reentrainment is antidromic. While for westward trips made with parameters below the ADC_{10-} curve, reentrainment is antidromic.

By studying a fixed horizontal slice of [Fig. 10](#), we can compare how a traveler's reentrainment times can differ as a function of the time of the year. For example, during the summer months the value N in the photoperiod is larger than 12, while during the winter it is less than 12. Thus the left $N = 8$ h edge of the graph corresponds to reentrainment during the winter and the right edge at $N = 16$ h corresponds to reentrainment during the summer. Consider the $\tau_c = 24.2$ h slice which shows that traveling east will be worse than west at all times of the year. The asymmetry is greater in the summer than in the winter. Furthermore in winter the reentrainment will be orthodromic; the parameter pair $(8, 24.2)$ lies below ADC_{10+} . In summer it will be antidromic; the parameter pair $(16, 24.2)$ lies above ADC_{10+} . For a person with a slower body clock, e.g. $\tau_c = 24.3$ h, eastward travel is still worse than westward all year-round and reentrainment is still orthodromic in winter and antidromic in summer, but now the east/west asymmetry is more severe in winter than summer. For someone with a fast body clock, e.g. $\tau_c = 23.9$ h, west is always worse than east, but more so in summer than winter. Here, reentrainment is antidromic in winter (since $(8, 23.9)$ lies below ADC_{10-}), and orthodromic in summer (since $(16, 23.9)$ lies above ADC_{10-}), which is the opposite relationship between season and the type of reentrainment as the other two τ_c values considered.

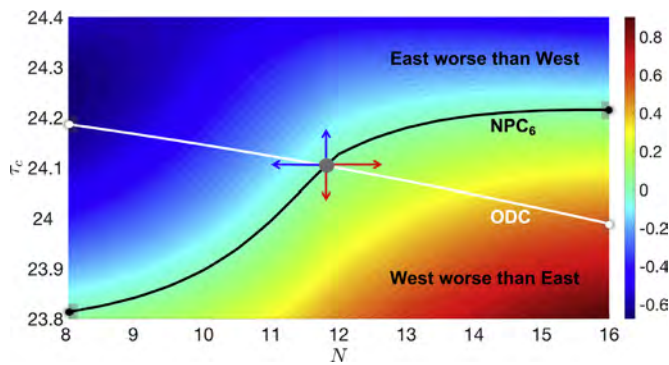


Fig. 11. East-West asymmetry persists in the absence of antidromic reentrainment. For entrainment maps over a range of N and τ_c values with $I = 100$ lux and the stable fixed point held at $x_s = 12$ (same maps as in Fig. 10), the first iterate of the maps was used as a surrogate for the reentrainment time following eastward and westward trips of 6 time zones ($Z = \pm 6$). The colormap represents the degree of asymmetry in the first iterate, and was calculated by subtracting $\Delta_{N,\tau_c}(6)$ from $\Delta_{N,\tau_c}(18)$; see text for definition of $\Delta_{N,\tau_c}(x_0)$. Negative values correspond to (N, τ_c) pairs for which eastward travel is worse, and positive values to westward travel being worse. Along the black neutral period curve (NPC₆), $\Delta_{N,\tau_c}(6) = \Delta_{N,\tau_c}(18)$ implying reentrainment times are the same for eastward and westward travel. Along the white orthodromy curve (ODC), the unstable fixed point is 12 h away from x_s (i.e. $x_u = 0 = 24$), and all reentrainment is orthodromic. At the intersection of the ODC and NPC₆ (the gray dot), reentrainment is both orthodromic and east-west symmetric. From this intersection point, increasing (decreasing) τ_c or decreasing (increasing) N introduces an asymmetry leading to worse jet lag for eastward (westward) travel; see text for a detailed explanation of this phenomenon based on properties of the entrainment map.

Note that the axes of the heatmap shown in Fig. 10 are τ_c and N , which are the same two parameters as the axes of the Arnold onion in Fig. 4D (albeit with the axes reversed). These two figures convey different information however. The Arnold onion shows how the stable entrained phase x_s changes with parameter variations. It does not contain information about the transient time it takes for trajectories to converge to the stable phase. The heatmap in Fig. 10, on the other hand, is constructed so that the stable phase is always at $x_s = 12$ for all parameter pairs. Thus it does not contain meaningful phase of entrainment information, but instead provides valuable information about reentrainment times.

3.4. Explaining the east-west asymmetry

As above, choose the Poincaré section to lie at $X = 12$ for the different LD-entrained solutions. Since x_s is fixed at 12, we can vary the location of x_u by changing τ_c and/or N . In general, increasing τ_c makes x_u decrease, while decreasing N makes x_u increase. By balancing N and τ_c appropriately, we define the *orthodromy curve* (ODC) as a monotone decreasing curve in $N - \tau_c$ space along which the distance $|x_u - x_s| = 12$; see the white curve in Fig. 11. To find this curve, we chose the values $N = 8, 12$, and 16 h and computed the corresponding τ_c values that led to $|x_u - x_s| = 12$. We then fit a quadratic curve through the ensuing three ordered pairs (the white and gray dots in Fig. 11); the resulting curve is quite linear, suggesting that three points is sufficient for approximating the shape of the ODC. The importance of the ODC is that an oscillator with parameters (N, τ_c) of a point chosen along the ODC can only experience orthodromic reentrainment, since it is not possible for a 12-h trip leaving from x_s to go beyond x_u in either direction.

Next we focus on six hour trips in either direction. We will use the first iterate of the entrainment map to help determine whether reentrainment after travel to the east is faster or slower than after travel to the west. Define $\Delta_{N,\tau_c}(x_0) = |\Pi(x_0) - x_0|$. This is the distance of the entrainment map from the diagonal for trips with initial condition x_0 for the choice (N, τ_c) . It measures the amount of phase advance or delay on the first iterate. A larger value in-

dicates a greater amount of phase change. We have found that a larger initial phase change ultimately leads to *shorter* reentrainment times. We shall use $\Delta_{N,\tau_c}(x_0)$ as a surrogate for comparison of actual reentrainment times. An eastward trip of 6 h corresponds to $x_0 = 18$ and a 6 h westward trip corresponds to $x_0 = 6$. Thus our convention is that for a particular ordered pair (N, τ_c) , if $\Delta_{N,\tau_c}(6) < \Delta_{N,\tau_c}(18)$, then reentrainment after a trip to the west is longer. If the inequality is switched, trips to the east lead to longer reentrainment.

Using this convention and computing at the left endpoint of the ODC, we find $\Delta_{8,24.1683}(6) > \Delta_{8,24.1683}(18)$. This implies that an eastward trip of 6 h is followed by longer reentrainment compared to a westward trip of 6 h. At the right endpoint of the ODC, we find that $\Delta_{16,23.9893}(6) < \Delta_{16,23.9893}(18)$ implying that westward trips take longer to reentrain from. By continuously varying N and τ_c along the ODC, there exists a unique value, found to be $N = 11.8116$, $\tau_c = 24.1035$, at which $\Delta_{11.8116,24.1035}(6) = \Delta_{11.8116,24.1035}(18)$, i.e. the distance from the map to the diagonal is the same for $x_0 = 6$ and 18 . We call this a neutral period point since it is a combination of photoperiod and intrinsic period for which reentrainment times are the same for the pair of initial conditions that lie a symmetric distance of 6 h away from the stable fixed point $x_s = 12$; see the gray dot in Fig. 11. We next computed the neutral period points along the vertical edges of the parameter space, finding them to be at $N = 8$, $\tau_c = 23.8133$ and $N = 16$, $\tau_c = 24.2147$ (black dots in Fig. 11). Since the maps depend continuously on N and τ_c , there exists a neutral period curve, NPC₆, in the $N - \tau_c$ space, that passes through these three neutral period points, along which 6 h trips in either direction lead to the same reentrainment time as determined from the condition $\Delta_{N,\tau_c}(6) = \Delta_{N,\tau_c}(18)$; see the black curve in Fig. 11.

The neutral period curve NPC₆ divides the parameter space into two distinct regions. Above NPC₆ (such as at the left endpoint of the ODC), reentrainment after eastward trips takes longer. Below NPC₆ (such as at the right endpoint of the ODC), reentrainment after westward trips takes longer. Note that NPC₆ must lie below the ODC for $N < 11.8116$ and above the ODC for $N > 11.8116$. To understand why, consider the neutral period point on the ODC where $N = 11.8116$, $\tau_c = 24.1035$. At this point $\Delta_{11.8116,24.1035}(6) = \Delta_{11.8116,24.1035}(18)$. Now consider a value of the parameters with the same N value but larger τ_c value. Since the entrainment map moves up as τ_c increases, the value $\Pi(6)$ will shift further away from the diagonal while the value $\Pi(18)$ will shift closer to the diagonal. This immediately implies for all $\tau_c > 24.1035$ that $\Delta_{11.8116,\tau_c}(6) > \Delta_{11.8116,\tau_c}(18)$, which implies that eastward travel is worse. Thus all such parameter pairs must lie on the same side of neutral period curve as the left endpoint of the ODC. Alternatively, for $\tau_c < 24.1035$, the map $\Pi(x)$ shifts down and $\Delta_{11.8116,\tau_c}(6) < \Delta_{11.8116,\tau_c}(18)$; westward travel is worse and all these parameter pairs must lie on the same side of NPC₆ as the right endpoint of the ODC. Together, this implies the following relationship between NPC₆ and the ODC: to the left of the intersection point of NPC₆ and the ODC, NPC₆ must lie below the ODC; whereas to the right of their intersection point, NPC₆ must lie above the ODC.

Several observations are in order. First, since NPC₆ intersects the ODC, our results show that east-west asymmetry does not require antidromic reentrainment. Indeed, along the ODC, all trips have orthodromic reentrainment. Roughly half of this curve lies to the left of the NPC where east is worse and the other to the right where west is worse. The results suggest that east-west asymmetry is a natural feature of the FJK model. Second, by considering various horizontal slices of the $N - \tau_c$ plane shown in Fig. 11 for fixed values of τ_c , we see that the duration of light N in the photoperiod is crucial for determining the direction and extent of asymmetry. In particular, as N is increased, westward travel takes increasingly longer to recover from. This suggests that, for example, individuals

with fast clocks will experience more jet lag after eastward trips than westward trips in the winter, whereas during the summer westward trips are worse. On the other hand, for individuals with slow clocks, eastward trips cause more jet lag than westward trips at all times of the year, since horizontal lines above $\tau_c = 24.2$ h lie to the left and above NPC_6 for all N .

3.5. Fast reentrainment and the phaseless set

Numerous experiments and models have found that a stimulus of a critical strength applied at a critical phase can suppress the amplitude of a circadian oscillator to nearly zero (Jewett et al., 1991; Sun et al., 2016; Ukai et al., 2007; Winfree, 1970). It has been suggested that driving the oscillator to this phaseless position, referred to as the “singularity”, could shorten reentrainment time by allowing the trajectory to take a “shortcut” in phase space (Serkh and Forger, 2014; Winfree, 1991). We show that in the FJK model, this shortcut can arise at both low and high light intensities. We will use the entrainment map to locate a set of initial conditions (critical phases) that allow trajectories to take this shortcut. For higher light intensities, this shortcut can be accessed from points on the LD-entrained solution by changing the light offset x by an appropriate amount, which can give rise to unusually fast reentrainment.

Consider higher intensity light with $I = 1000$ lux. In Fig. 12A, we reconstruct the heat map for $\tau_c = 24.2$ h using direct simulation. In comparison to Fig. 6A, note that now there is a band near $Z = 10$ and $Z = 11$ for which reentrainment times are much shorter than for nearby Z values. These are examples of trips for which reentrainment is much faster than would be expected. In addition, note that within this band, reentrainment depends on the arrival time much more sensitively than for the $I = 100$ lux case. For example, for $Z = 10$ arrival times near 7 AM incur shorter reentrainment than others. For $Z = 10.5$, arrival times from 12:30 PM to 5:30 PM have shorter reentrainment, while for $Z = 11$, arrival from 11:00 PM to 1:30 AM have quite short reentrainment times.

Recall the definition of the demarcation point $Z_D \in (-12, 12)$ which solves $x_u = (x_s + Z_D) \bmod 24$. For $\tau_c = 24.2$, $Z_D = 10.67$ as the unstable fixed point lies roughly 10.67 time zones to the east of the stable one. The demarcation point Z_D lies in the band of fast entrainment. Consider the Poincaré map fixed at $X = 6$ (1:00 PM), which has $x_s = 6$ and $x_u = 16.67$. Fig. 12B shows entrainment times for the $X = 6$ vertical column of the heat map, centered around $Z = 0$. Note that as $|Z|$ increases, entrainment times increase as would be predicted from the map. However as Z increases through 10, entrainment times suddenly begin to dip, reaching a local minimum at $Z = 10.46$ (which is near Z_D), then increasing until $Z = 11$ before beginning to fall again (gray shaded region of figure). The entrainment map predicts instead that the reentrainment times would show a local maximum, not a local minimum, in this neighborhood. In contrast, with $I = 100$ lux both the map and simulations show a local maximum in this neighborhood (Fig. 8A), which is why we chose to work with that light level in Sections 3.3 and 3.4.

To explain why there is fast entrainment, we identify a region of phase space that Guckenheimer (1975) calls a *phaseless set*. The easiest way to describe this set is to consider an unforced oscillator, say with $n=0$ which gives rise to the stable DD limit cycle. Every point on the DD limit cycle can be assigned a phase between 0 and τ_c . Now consider the $A-C$ phase plane. Following (Guckenheimer, 1975), we define a point to be phaseless if every neighborhood of that point intersects each isochron of the stable DD limit cycle. An isochron consists of the set of initial conditions that have the same asymptotic phase as a particular point on the DD limit cycle. In particular, two nearby initial conditions that lie in the phaseless set can have very different asymptotic phases. The

phaseless set lies in a region of phase space where the isochrons meet to form a pinwheel or a singularity. For any fixed value of n in the FJK model, including $n = 0$ (DD) or $n = 1$ (LL), this singularity lies in a neighborhood of the origin in $A-C$ space. A tubular neighborhood of the origin extending in the n direction can be considered as the generalization of the phaseless set for the periodically LD-forced FJK model. Trajectories that pass through this set deviate from the usual dynamics in that they do not stay close to the LL and DD limit cycles during the reentrainment process. Instead they take the aforementioned shortcut across phase space during reentrainment. Characteristics of these trajectories include amplitude suppression, an inability to predict whether the entrainment is strictly through advance or delay, and situations in which the phase of the trajectory cannot be clearly discerned on a cycle-by-cycle basis. What we have found in simulation is that travel to time zones in a neighborhood of the demarcation point Z_D , equivalently choosing an initial condition on the Poincaré section near x_u , leads to trajectories that enter the phaseless set and take a shortcut across phase space.

Fig. 12C–F shows the reentrainment process for the trajectories whose initial conditions lie in a neighborhood of x_u , $x_0 = 16.46$ (Panels C and D) and $x_0 = 16.68$ (Panels E and F). Both trajectories show amplitude suppression and take a shortcut across the projection onto the $A-C$ phase space; Panels C and E. The green dots in each of those panels indicate where the lights turned on in the current LD cycle. By the 4th cycle, both trajectories have reached a region of maximal suppression, but at the 5th cycle, the trajectory in Panel C emerges from that region in such a way that it quickly entrains to the correct phase (as shown by the red dot(s) on each of the panels). The trajectory in Panel E does not. From Panel D, one could argue that the trajectory entrains through phase advancing, but the entrainment in Panel F defies such characterization. In particular, the phase of this trajectory does not appear to be predictable on a cycle-by-cycle basis. What is common to the two trajectories in Panels D and F is that prior to entering the region of amplitude suppression (phaseless set), neither one seems to be systematically phase advancing or delaying. We comment further on this in the Appendix, where we show that a shortcut also exists in phase space at lower light intensities, but that this shortcut is not directly accessible through travel.

3.6. Jet lag due to north-south travel

The question of whether jet lag occurs due to north-south travel has received very little attention. Here we show that in fact there can be jet lag effects following long-distance north-south travel due to significantly different photoperiods between the departure and arrival locations. We show that these effects depend on the intrinsic period τ_c of the traveler, and that the direction of reentrainment (phase advance or phase delay) can be considered analogously to orthodromic and antidromic reentrainment due to east-west travel.

In modeling north-south travel and subsequent reentrainment, let N_{dep} be the number of hours of light in the departure city and N_{dest} be the number of hours of light in the destination city. We will make the following assumptions:

- Prior to and during the flight, the traveler remains entrained to the departure LD cycle ($N = N_{dep}$).
- Upon arrival at the destination, the traveler lies on a Poincaré section that intersects the LD-entrained solution ($N = N_{dep}$) of the departure city X_{dep} hours after the lights turned on in the departure city.
- This Poincaré section intersects the LD-entrained solution ($N = N_{dest}$) of the destination city at a location X_{dest} hours after the lights last turned on in the destination city.

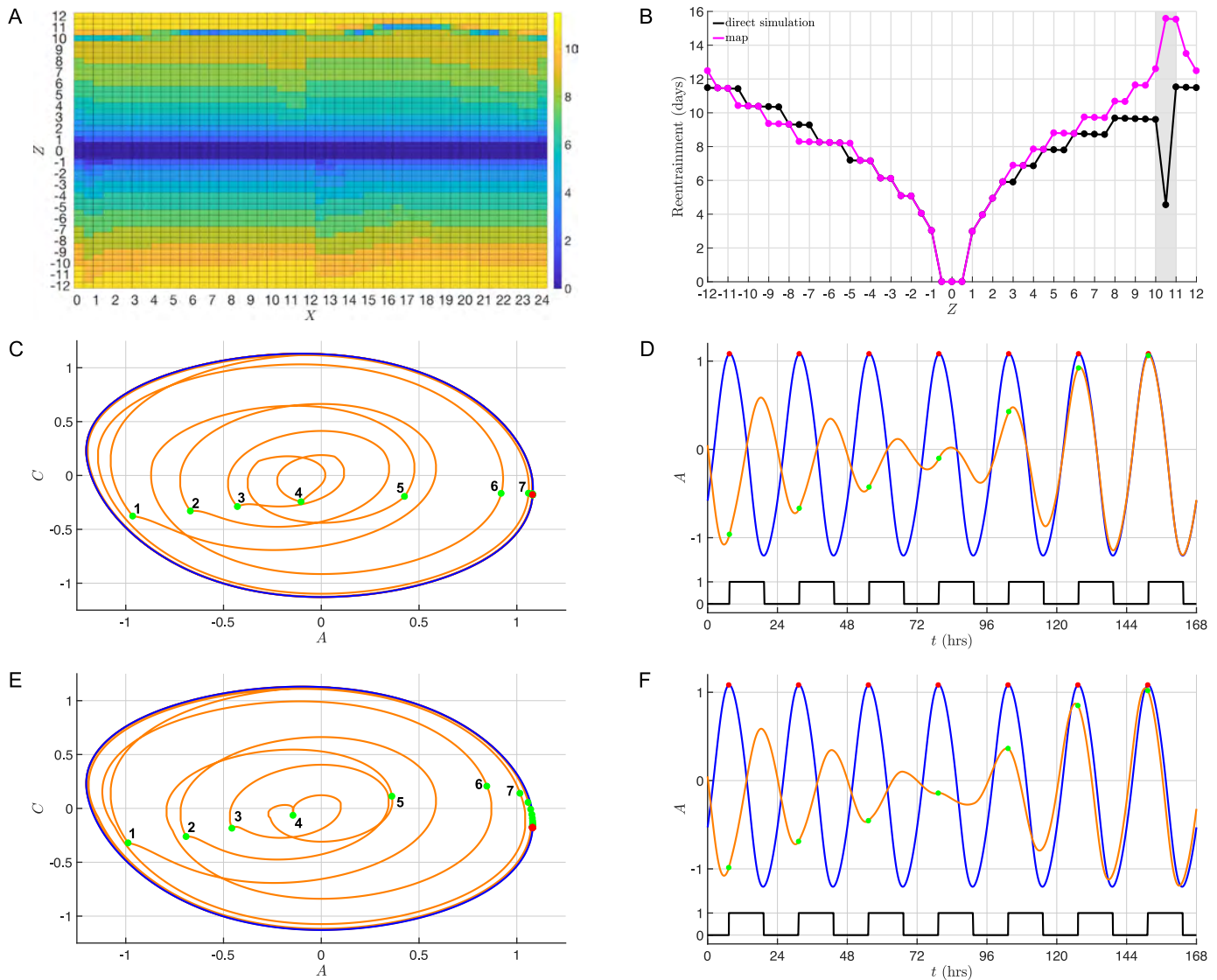


Fig. 12. Dramatically short reentrainment times are possible for travelers entering the phaseless set. (A) Heatmap of direct simulation reentrainment times (in days) for arrival times X and trips Z with $\tau_c = 24.2$ h, $N = 12$ h, and $I = 1000$ lux. There is a local minimum for eastward trips of 10.5 h ($Z = 10.5$). (B) Reentrainment times for $X = 6$ from direct simulation (black) and from cobwebbing the corresponding maps (magenta). The local minimum of reentrainment time observed in direct simulation corresponds to a local maximum predicted by the map, and occurs for trips that place the traveler in a region near the unstable fixed point of the map called the phaseless set (gray shading). (C–D) Phase plane trajectory (C) and time course (D) during reentrainment for $Z = 10.46$, which exhibits amplitude suppression and very fast reentrainment (4.5 days) for the traveler (orange). The green dots correspond to the location of the traveler when the lights turn on ($x = 0$), with labels indicating the first 7 cycles. The red dot is $x = 0$ for the reference oscillator (blue trajectory). (E–F) Phase plane trajectory (E) and time course (F) during reentrainment for $Z = 10.68$, which exhibits amplitude suppression but does not lead to very fast reentrainment (9.5 days). (For interpretation of the references to colour in this figure legend, the reader is referred to the web version of this article.)

- Upon arrival, in direct simulation, the traveler is subjected to the appropriate amount of light and/or dark to complete the current 24 h cycle and is then subjected to the destination LD cycle ($N = N_{dest}$).
- Upon arrival, the entrainment map is based on the Poincaré section X_{dest} and reentrainment time is calculated with an appropriate initial condition as described below.

To illustrate our findings we will work with a specific example: travel between New York City and Santiago, Chile on the Northern hemisphere's summer solstice. The reason for this choice is that at this time of the year, both cities lie in the same time zone and we do not have to adjust for east-west shifts. Below we will refer to the NYC LD-entrained solution and the Santiago LD-entrained solution. These solutions occur in our model for LD photoperiods of 15:9 ($N = 15$ h) and 10:14 ($N = 10$ h) respectively, with $I = 1000$ lux. This light intensity is characteristic of outdoor

light and provides a wider range of entrainment in τ_c than does 100 lux (Fig. 4C), which makes it easier to illustrate some of our findings in Sections 3.6 and 3.7.

On the northern solstice (June 20, 2016), the sun rose at 5:25 AM and set at 8:31 PM in New York City (day length of 15:05 h), whereas in Santiago, Chile the sun rose at 7:46 AM and set at 5:42 PM (day length of 9:56 h). For illustrative purposes we will take NYC to have an $N = 15$ h photoperiod with sunrise at 5:30 AM ($x = 0$) and sunset at 8:30 PM ($x = 15$), and Santiago to have an $N = 10$ h photoperiod with sunrise at 8 AM ($x = 0$) and sunset at 6 PM ($x = 10$).

The flight time from New York City to Santiago is roughly 13 h. Consider a leaving time of 10 AM from New York City with an arrival time of 11 PM in Santiago. Let us assume that the traveler is initially entrained to the NYC LD-entrained solution and remains so through the duration of the flight. Thus on arrival in Santiago, the traveler would be expecting 6.5 h of darkness, but instead re-

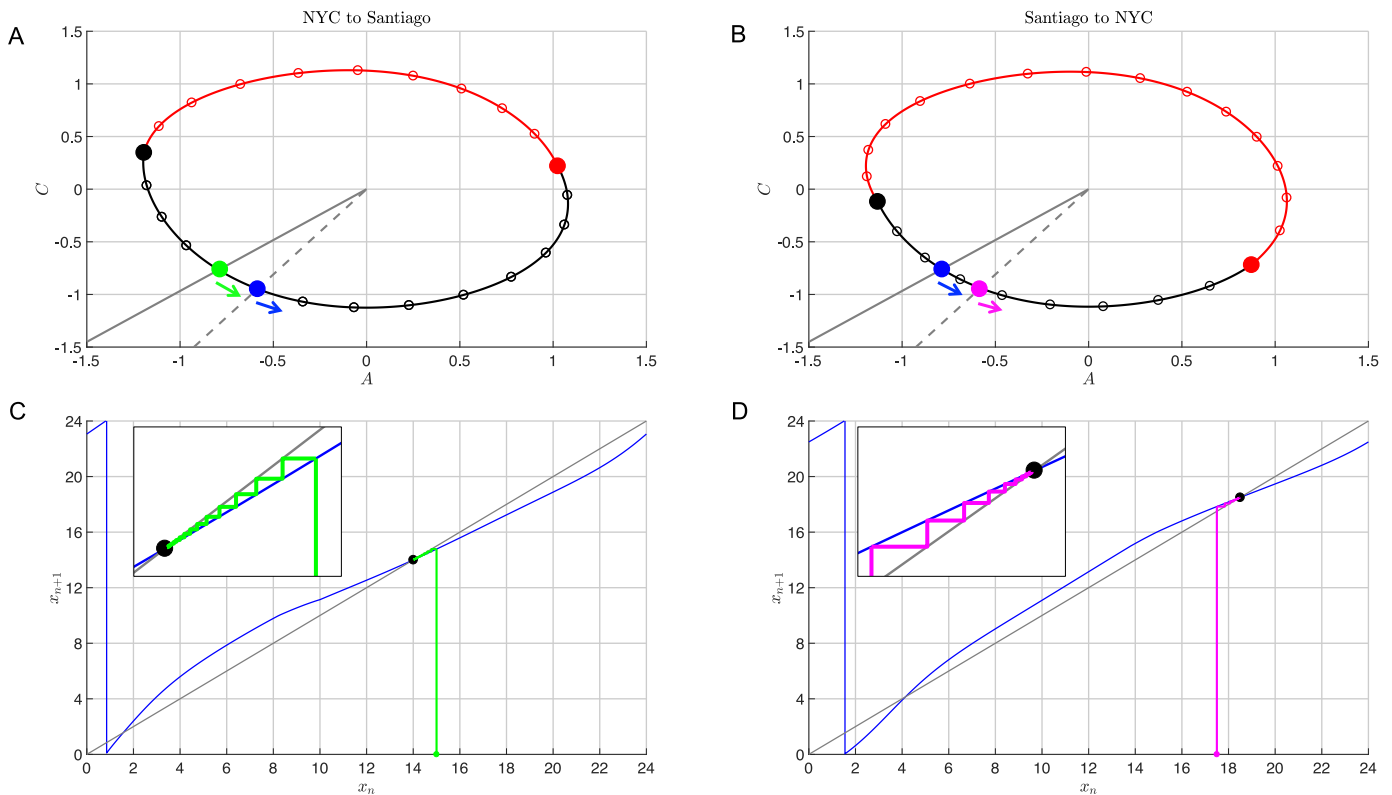


Fig. 13. Change in daylength due to north-south travel can cause jet lag. For all panels, $\tau_c = 24.2$ h and $I = 1000$ lux. (A) LD-entrained solution in Santiago on June solstice (photoperiod $N = 10$ h). The sun rises at 8 AM (red dot) and sets at 6 PM (black dot). The green dot represents a traveler from NYC that arrives in Santiago at 11 PM and is still entrained to the NYC LD cycle, where 11 PM corresponds to the $X_{NY} = 17.5$ section denoted by the solid gray line. The blue dot represents a reference oscillator already entrained to the Santiago LD cycle, where 11 PM corresponds to the $X_{SC} = 15$ section denoted by the dashed gray line. Therefore the traveler must reentrain and does so through phase advancing. (B) LD-entrained solution in NYC on June solstice (photoperiod $N = 15$ h). The sun rises at 5:30 AM (red dot) and sets at 8:30 PM (black dot). The magenta dot represents a traveler from Santiago that arrives in NYC at 11 PM and is still entrained to the Santiago LD cycle, where 11 PM corresponds to the $X_{SC} = 15$ section denoted by the dashed gray line. The blue dot represents a reference oscillator already entrained to the NYC LD cycle, where 11 PM corresponds to the $X_{NY} = 17.5$ section denoted by the solid gray line. Therefore the traveler must reentrain and does so through phase delaying. (C) Entrainment map for NYC to Santiago travel arriving at 11 PM. The stable fixed point is located at $x_s = 14.003$, which is where the $X_{NY} = 17.5$ section (solid gray line) intersects the $N = 10$ LD-entrained solution in (A). The initial condition is located at $x_0 = 15$, because upon arrival the traveler will experience 9 h of darkness before the sun rises. Cobwebbing the map yields reentrainment through phase advance (see inset), in agreement with direct simulation. (D) Entrainment map for Santiago to NYC travel arriving at 11 PM. The stable fixed point is located at $x_s = 18.496$, which is where the $X_{SC} = 15$ section (dashed gray line) intersects the $N = 15$ LD-entrained solution in (B). The initial condition is located at $x_0 = 17.5$, because upon arrival the traveler will experience 6.5 h of darkness before the sun rises. Cobwebbing the map yields reentrainment through phase delay (see inset), in agreement with direct simulation. (For interpretation of the references to colour in this figure legend, the reader is referred to the web version of this article.)

ceives 9 h of darkness since the sun does not rise until 8 AM. Thus at arrival, the traveler is not entrained to the Santiago $N = 10$ LD cycle. For now, consider a traveler with a normal internal clock of $\tau_c = 24.2$ h. At arrival, the traveler lies on the $X_{NY} = 17.5$ Poincaré section of the NYC LD-entrained solution. The intersection of this Poincaré section with the Santiago LD-entrained solution occurs for $X_{SC} = 14.005$. For travel from South to North, if a traveler leaves Santiago at 10 AM ($X_{SC} = 2$) and takes a 13-h flight, then arrival in NYC is at 11 PM which is $X_{SC} = 15$ and $X_{NY} = 18.946$. Panel A of Fig. 13 shows the $N = 10$ Santiago LD-entrained solution and Panel B shows the $N = 15$ NYC LD-entrained solution. In Panel B, the solid gray line is the projection of the Poincaré section onto the NYC LD-entrained solution at arrival corresponding to $X_{NY} = 17.5$. The projection of this same Poincaré section onto the Santiago LD-entrained solution at $X_{SC} = 14.005$ is shown in solid gray in Panel A. Similarly for travel from Santiago to NYC, the dashed gray lines correspond to the projection of the Poincaré section at arrival corresponding to $X_{SC} = 15$ of the Santiago LD-entrained solution and $X_{NY} = 18.946$ of the NYC LD-entrained solution.

The change in the stable entrained phase after north-south travel is already predicted by our earlier results concerning the Arnold onion and those of Schmal et al. (2015). North-south travel is equivalent to moving along a vertical slice of Fig. 4D. Knowing that there is a change in stable phase indicates that there may be

an associated time to reentrainment, which we can calculate by cobwebbing the appropriate entrainment map.

We first calculate reentrainment via direct simulation. Since the sun will come up in Santiago at 8 AM, we simulate 9 more hours of darkness starting with an initial condition corresponding to 11 PM on the NYC LD-entrained solution ($X_{NY} = 17.5$) and then begin 10:14 LD cycles. At the same time we also start a reference oscillator with initial conditions corresponding to 11 PM on the Santiago LD-entrained solution ($X_{SC} = 15$) and subject it to the same protocol. We keep track of the times that the trajectories cross the Poincaré section $X_{SC} = 14.005$, and when they cross within 0.5 h of each other we declare the traveler trajectory to be entrained. This procedure gives an entrainment time of 71.458 h (see * in Table 1). Note that travel from NYC to Santiago can be considered as a phase delay in the sense that at arrival at 11 PM, the traveler would expect the lights to turn on at the start of the next NYC-based LD cycle after 6.5 h. Instead the lights turn on at the beginning of the next SC-based LD cycle which occurs after 9 h. Thus the traveler is phase delayed with respect to lights on in the arrival time zone.

To compute entrainment time using the map, we build a $N = 10$ map with the Poincaré section at $X_{SC} = 14.005$ on the Santiago LD-entrained solution. Since arriving at 11 PM means there will be 9 more hours of dark before the 10:14 LD cycle begins, we cobweb the map using an initial condition of $x_0 = 15$. This proce-

Table 1
Reentrainment times for southward and northward travel with $\tau_c = 24.2$ h and $l = 1000$ lux.

	Direct simulation			Entrainment map				
	t	t_{ref}	$t_{ref} - t$	x_n	x_{n+1}	$x_s - x_{n+1}$	$\rho(x_n)$	$\Sigma\rho(x_n)$
NYC to Santiago	23.776	23.005	-0.772	15	14.780	-0.775	23.780	23.779
	47.598	47.005	-0.593	14.780	14.622	-0.617	23.842	47.621
	71.459*	71.005	-0.454	14.622	14.465	-0.460	23.843	71.465**
Santiago to NYC	24.3444	24.9960	0.6516	17.5	17.841	0.655	24.341	24.341
	48.5594*	48.9960	0.4366	17.841	18.040	0.456	24.199	48.540**

ture gives an entrainment time of 71.464 h (see ** in Table 1), which is in close agreement to the direct simulation result. Fig. 13C shows a cobweb diagram of the reentrainment process. The trajectory starts with $x_0 = 15$ and phase advances (moves to the left closer to the start of the LD cycle) towards the stable fixed point at $X_{SC} = 14.005$. Thus in this situation, although the travel from North to South is a phase delay, the reentrainment is antidromic through phase advancement. This is in contrast to the norm for east-west travel for which reentrainment is typically orthodromic, i.e. through phase delays when the travel yields a phase delay, and vice versa for advances. Thus, it is surprising that the “natural” mode of reentrainment for travel from north to south at the June solstice for a traveler with a normal body clock is antidromic.

For travel from south to north, if a traveler leaves Santiago at 10 AM ($X_{SC} = 2$) and takes a 13-h flight, then arrival in NYC is at 11 PM which is $X_{SC} = 15$ and $X_{NY} = 18.946$. Following a similar procedure as above, we simulate 6.5 h of darkness before starting 15:9 LD cycles. Through direct simulation the entrainment time is 48.56 h. Similarly, we build the $X_{NY} = 18.946$, $N = 15$ map and check reentrainment with an initial condition $x_0 = 17.5$. Reentrainment time using the map is found to be 48.54 h. Travel from south to north can be considered a phase advance since the traveler will experience the onset of the next LD cycle sooner in NYC than in SC. But, as noted from Fig. 13D, reentrainment is through phase delay. Thus this reentrainment is also antidromic. As seen from the above results, for $\tau_c = 24.2$ h traveling from photoperiods of $N = 10$ to $N = 15$ h incurs roughly the same reentrainment time (2 to 3 days) as traveling from $N = 15$ to $N = 10$ h.

In Fig. 14A we show reentrainment times calculated from direct simulation for travel between NYC and Santiago for τ_c ranging from 22.6 to 26 h. Note, as τ_c decreases, it takes longer to reentrain after the northbound Santiago to NYC trip than the southbound trip. The opposite is true as τ_c increases. Also observe that there are values of τ_c for which there is no jet lag, e.g. $\tau_c \approx 23, 24.7$.

As we change τ_c , both the NYC LD-entrained and SC LD-entrained solutions change in shape in phase space. This means that the locations of various Poincaré sections change. For arrival at 11 PM, while this still corresponds to lying on the section $X_{NY} = 17.5$, it means that the X_{SC} section changes. Fig. 14B shows the location of the X_{SC} section as a function of τ_c . It is parabolic shaped. What does not change is the location of the initial condition $x_0 = 15$ from which we check reentrainment time. For any fixed τ_c , the vertical distance between the dashed line at $x_0 = 15$ and the blue curve of section locations, which corresponds to the stable fixed points x_s for the respective maps, indicates the distance over which a trajectory would have to evolve in order to reentrain. Note that the curve of sections intersects $x_0 = 15$ at the values $\tau_c \approx 23$ and 24.7 . Thus the distance $|x_0 - x_s| < 0.5$ which means that the trajectory is already entrained. This explains why travel for nearby values of τ_c experience no jet lag. Similarly Fig. 14C shows the location of the X_{NY} section as determined from using the $X_{SC} = 15$ section. This curve is also parabolic shaped, but opens down. It intersects the line of initial conditions at $x_0 = 18$ at $\tau_c \approx 23$ and 24.7 as well.

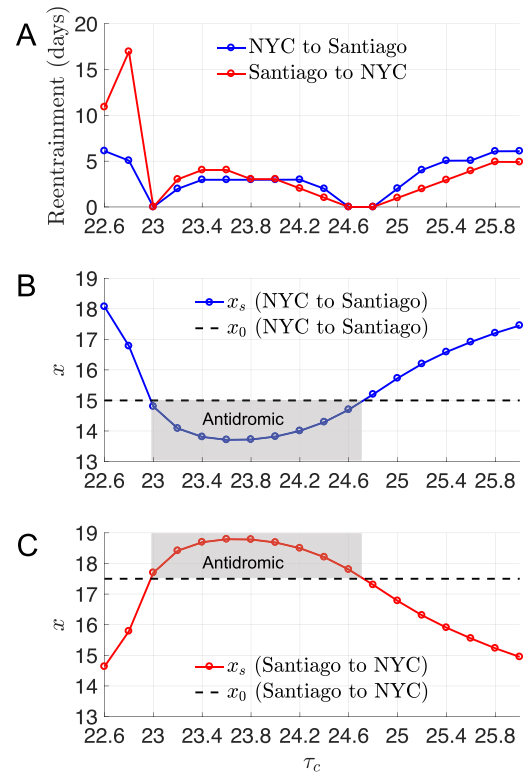


Fig. 14. Reentrainment following north-south travel depends on intrinsic period and is typically antidromic. (A) Jet lag due to north-south travel is most severe for extreme intrinsic periods (greater than 5 days for $\tau_c \leq 23$ and $\tau_c \geq 25.4$), with southbound travel (blue) being worse for slow intrinsic clocks and northbound travel (red) being worse for fast intrinsic clocks. (B) Location of stable fixed point x_s and initial condition x_0 for southbound travel as a function of τ_c . Severity of southbound jet lag in (A) reflects the distance between x_s and x_0 , with zero days of reentrainment required when x_0 is within 0.5 h of x_s , as is the case for $\tau_c = 23, 24.6$, and 24.8 h. For $23 \leq \tau_c \leq 24.6$, $x_s < x_0$, therefore reentrainment is through phase advances and is considered antidromic since southbound travel in the month of June is a phase delay of the LD cycle; see text for detailed explanation. (C) Location of stable fixed point x_s and initial condition x_0 for northbound travel as a function of τ_c . Severity of northbound jet lag in (A) reflects the distance between x_s and x_0 . For $23 \leq \tau_c \leq 24.6$, $x_s > x_0$, therefore reentrainment is through phase delays and is considered antidromic since northbound travel in June is a phase advance of the LD cycle. (For interpretation of the references to colour in this figure legend, the reader is referred to the web version of this article.)

For travel from NYC to Santiago, Fig. 14B shows that the curve of sections lies below $x_0 = 15$ for values lying between 23 and 24.7. This means that the stable fixed point lies to the left of the initial condition $x_0 = 15$. Thus reentrainment would occur through advance. However, for τ_c less than 23 or greater than 24.7, the stable fixed point x_s is to the right of $x_0 = 15$ so reentrainment is through phase delay. Since southward travel at the northern solstice is considered to be a delay, this reentrainment can be thought of as being orthodromic. Note that at the extreme values of τ_c , orthodromic reentrainment takes longer than the antidromic reentrainment that occurs for intermediate values $23 < \tau_c < 24.7$. In ad-

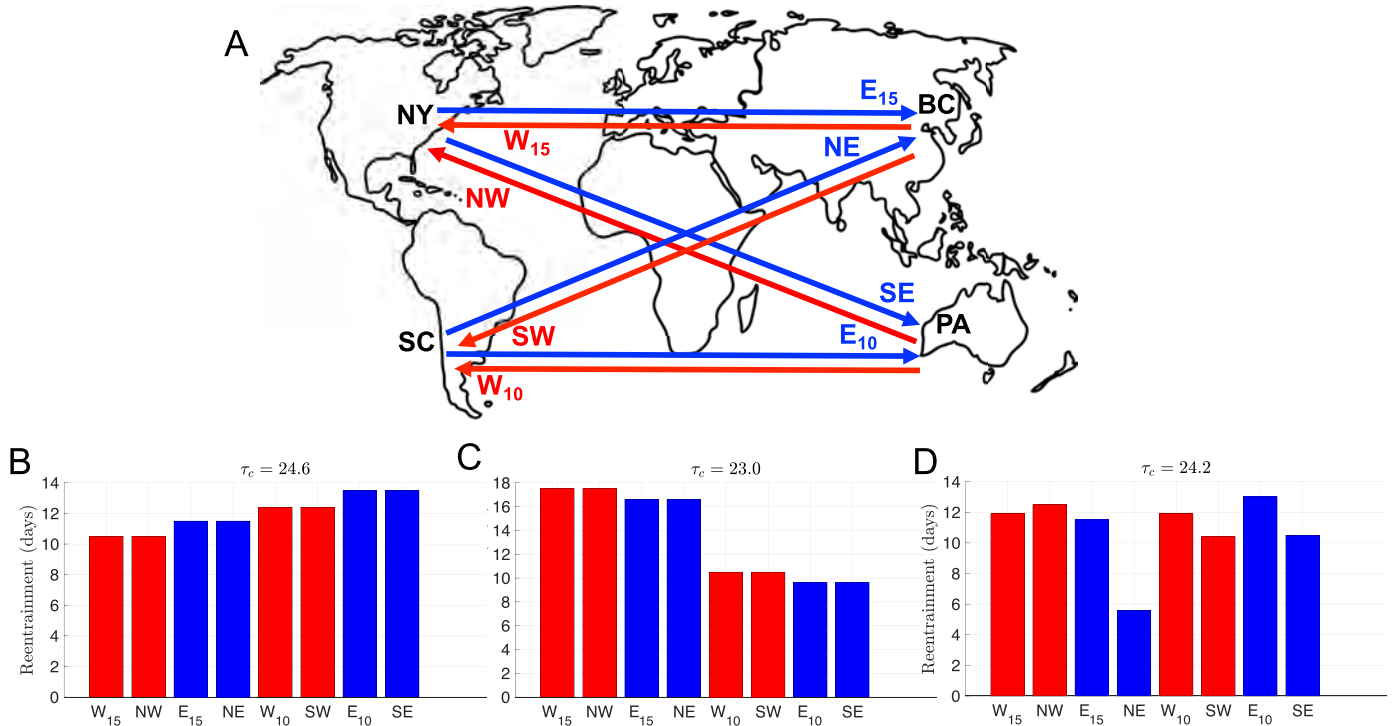


Fig. 15. Jet lag due to trips involving both north-south and east-west travel can be more or less severe than purely eastward or westward travel depending on intrinsic period and daylength. (A) Illustration of trips considered: pure eastward or westward travel between NYC and Beijing (E_{15}/W_{15}) and Santiago and Perth (E_{10}/W_{10}), travel between NYC and Perth (SE/NW), and travel between Santiago and Beijing (NE/SW). NYC and Santiago are 11 time zones away from Beijing and Perth. The trips are made on the June solstice when NYC/Beijing have 15 h of light and Santiago/Perth have 10 h of light. For these simulations we set $I = 1000$ lux. (B) Reentrainment times for $\tau_c = 24.6$ h. For $\tau_c = 24.6$ h, all reentrainment occurs through phase delays. Blue (red) bars correspond to eastward (westward) travel. See text for an explanation of the ordering of reentrainment times. (C) Reentrainment times for $\tau_c = 23.0$ h. In this case all reentrainment occurs through phase advances, and the ordering of reentrainment times is the opposite of the ordering for $\tau_c = 24.6$ h. (D) Reentrainment times for $\tau_c = 24.2$ h. In this case reentrainment can occur either through phase advance (E_{10}), phase delay (W_{15} , NW, W_{10} , SW, and SE), or fast reentrainment through the phaseless set (NE). (For interpretation of the references to colour in this figure legend, the reader is referred to the web version of this article.)

dition, for travel from Santiago to NYC, orthodromic reentrainment for $\tau_c < 23$ takes surprisingly long, on the order of 10 to 15 days. For small τ_c , the $N = 15$ entrainment map is closer to its bifurcation point than the $N = 10$ map. What this means is that the derivative of the map at the stable fixed point x_s^* is closer to one for the $N = 15$ map compared to the $N = 10$ map. The magnitude of this derivative controls the rate of attraction towards the fixed point. The closer it is to one, the slower the reentrainment. At the other extreme of $\tau_c = 26$ h, the $N = 10$ map is closer to bifurcation. The situation is reversed and southward trips take longer to reentrain from than northward trips.

3.7. Travel that is both east-west and north-south

Having separately considered jet lag due to east-west and north-south travel, we now consider travel that combines both east-west as well as north-south changes. The main point we would like to address is the extent to which changes in photoperiod synergistically add on to (or subtract from) jet lag due to pure eastward or westward travel. We will consider four different cities, New York City (NY), Santiago, Chile (SC), Beijing, China (BC) and Perth, Australia (PA); see Fig. 15A. The main reason to choose Beijing and Perth is that they lie in the same time zone and have the same photoperiods as New York City and Santiago respectively. We shall assume that on the June solstice, both NYC and Beijing have 15:9 photoperiods with sunrise at 5:30 AM and sunset at 8:30 PM. Santiago and Perth are both under 10:14 photoperiods with sunrise at 8:00 AM and sunset at 6:00 PM. Both Beijing and Perth are 11 time zones east of NYC and Santiago. We assume that the traveler stays entrained to the HTZ during travel. Initially, we will work

with two different periods of the intrinsic clock, $\tau_c = 23$ and 24.6 h. We choose these representative values because results from the prior section indicate that strict north-south travel for individuals with these clocks produces no jet lag. Thus an interesting question to explore is whether northeast and southeast (northwest and southwest) travel have different jet lag than pure eastward (pure westward) travel.

Fig. 15A shows the different directions of travel that we shall consider. The directions SE, SW, NE and NW are self-explanatory. The directions E_{10} , W_{10} , E_{15} and W_{15} refer to east-west travel under conditions of $N = 10$ h for travel between Santiago and Perth and $N = 15$ h for travel between NYC and Beijing. Fig. 15B shows reentrainment times for various modes of travel for $\tau_c = 24.6$ h with $I = 1000$ lux. There are effectively four pairs of reentrainment times:

$$W_{15} = NW < E_{15} = NE < W_{10} = SW < E_{10} = SE. \quad (8)$$

Below we shall explain why these pairs exist and why the ordering of reentrainment times follows this pattern. For now, note that SE travel has more jet lag than E_{15} , and SW travel has more jet lag than W_{15} . These results show how the change in photoperiod affects travel over different time zones. Consider the NYC, Beijing, Perth triangle. Travel from NYC to Beijing requires 11 days for reentrainment. Travel from Beijing to Perth requires zero days of reentrainment. Yet travel from NYC to Perth requires 13 days of reentrainment despite the fact that strict north-south travel incurs no jet lag. Fig. 15C shows reentrainment times for $\tau_c = 23.0$ h with $I = 1000$ lux. Here, as would be expected, the ordering of the reentrainment times is exactly the opposite than the larger τ_c case:

$$W_{15} = NW > E_{15} = NE > W_{10} = SW > E_{10} = SE. \quad (9)$$

What is different is the degree to which north-south travel affects jet lag, as illustrated by looking at the same travel triangle as above. Beijing to Perth still requires zero days of entrainment. Now E_{15} travel from NYC to Beijing requires 17 days for reentrainment, while the NYC to Perth travel only requires about 10 days to reentrain.

The reentrainment calculations for SE, SW, NE and NW travel combine the protocols that we had employed earlier to calculate reentrainment due to east-west or north-south travel. In particular, we choose Poincaré sections as for north-south travel, but now adjust the initial condition to take the change in time zone into consideration. For example, consider travel from NYC to Perth with arrival occurring at 10 AM Perth local time (DTZ). This corresponds to 11 PM NYC local time (HTZ). The traveler, by assumption, remains entrained to the NYC LD cycle. Thus at arrival in Perth, the traveler is at $X_{NY} = 17.5$. We compute where this Poincaré section intersects the $N = 10$ Perth LD-entrained solution, which occurs at $X_{PA} = 14.697$ for $\tau_c = 24.6$ h, and $X_{PA} = 14.803$ for $\tau_c = 23.0$ h. We build an entrainment map for the $N = 10$ LD-entrained solution and compute the reentrainment time with initial condition of $x_0 = 2$. We choose this initial condition because arrival at 10 AM in Perth where sunrise occurs at 8AM means that 2 h of light have already occurred. Travel that is SW, NE, or NW is handled analogously.

To understand why certain pairs of travel have the same reentrainment time, consider the result that $E_{10} = SE$. Above, we have already described the reentrainment protocol for SE travel. Now consider Santiago to Perth with arrival at 10 AM local Perth time (DTZ), which is 11 PM local Santiago time (HTZ). Now this corresponds to $X_{SC} = 15$. Our protocol for east-west travel dictates that we use $X_{PA} = 15$ and again choose $x_0 = 2$. Thus travel to Santiago from Perth (E_{10}) differs from NYC to Perth (SE) only to the extent that the entrainment maps being used are $X_{PA} = 15$ compared to $X_{PA} = 14.697$ (E_{10}) or 14.803 (SE). Both use the same initial condition $x_0 = 2$. Thus the reentrainment time to these two different, but relatively close fixed points is nearly identical. Similar arguments show why the other three pairs of travel have nearly identical reentrainment times.

To explain the ordering of reentrainment times, take the case $\tau_c = 24.6$ h, where we know that eastward travel is worse than westward travel. Thus $W_{10} < E_{10}$ and $W_{15} < E_{15}$. The reason that $E_{15} < W_{10}$ has to do with how far the $N = 15$ and $N = 10$ maps are from bifurcating. As τ_c increases, the fixed points of the $N = 15$ map bifurcate before those of the $N = 10$ map. Thus for $\tau_c = 24.6$ h the $N = 15$ map has a slope that is closer to one at its stable fixed point $x_s = 17.5$ than the $N = 10$ map at its stable fixed point $x_s = 10$. As stated in the previous section, entrainment times increase dramatically when the map is close to bifurcation. When $\tau_c = 23$ h, the $N = 10$ map is closer to bifurcating than the $N = 15$ map and this causes $W_{10} < E_{15}$ for this case. In fact for this case, the closeness of the map to bifurcation explains why the W_{15} reentrainment times are so much longer than the E_{10} times.

The choices of $\tau_c = 23.0$ and 24.6 h were taken because those were the ones at which strict north-south travel incurs no jet lag. The entrainment times for those two cases are anti-symmetric in their ordering. For a normal human traveler with $\tau_c = 24.2$ h, one might expect entrainment times to fall somewhere between those of the two specific cases. However, we would not expect the pairing of certain reentrainment times to continue to exist. Panel D of Fig. 15 confirms, in part, these observations. First, reentrainment times do generally lie between those of the two specific cases for each of the respective trips. Further, there is no pairing of entrainment times for certain trips since the Poincaré sections used to build the pairs, now, need not lie close to one another. We can explain the difference in reentrainment times within these pairs

using the maps for north-south travel with $\tau_c = 24.2$ h shown in Fig. 13.

Consider the pair W_{15} and NW, which reentrain according to similarly-shaped maps with $N = 15$ and $x_0 = 6.5$, where $x_s = 17.5$ (18.498) and $x_u = 3.048$ (4.144) for W_{15} (NW). Therefore both travelers reentrain through phase delays, however the NW traveler starts closer to x_u and has to cobweb further to get to x_s than does the W_{15} traveler. Thus the maps predict that NW will take longer to reentrain, which is consistent with the direct simulation results shown in Fig. 15D (12.5 versus 11.9 days).

Next consider the pair W_{10} and SW, which reentrain according to similarly-shaped maps with $N = 10$ and $x_0 = 4$, where $x_s = 15$ (14.003) and $x_u = 2.781$ (1.565) for W_{10} (SW). Again both travelers reentrain through phase delays, however the SW traveler starts further from x_u and does not have to cobweb as far to get to x_s as does the W_{10} traveler. Thus the maps predict that SW will take less time to reentrain, which is consistent with the direct simulation results (10.4 versus 11.9 days).

To summarize, we have found that NW travel incurs worse jet lag than W_{15} , whereas SW travel incurs less jet lag than W_{10} . In both cases the westward component of the travel leads to reentrainment through phase delay. What is different is that in the former case, the northbound component of the travel also requires the traveler to phase delay to reentrain to the shorter photoperiod, while in the latter case the southbound component requires the traveler to phase advance to reentrain to the lengthened photoperiod. For NW the change in time zone and change in photoperiod exacerbate each other leading to longer total reentrainment than pure westward travel in the northern hemisphere. For SW the change in time zone and change in photoperiod counteract each other leading to shorter total reentrainment time than pure westward travel in the southern hemisphere.

Now consider eastward travel, starting with the E_{10} and SE pair. These reentrain according to the $N = 10$ maps with $x_0 = 2$, where x_s and x_u are the same as for W_{10} and SW. Here the maps predict that the Santiago to Perth traveler reentrains through phase advances, but the NYC to Perth traveler reentrains through phase delays. Thus the change in photoperiod encountered by the SE traveler has moved the unstable fixed point enough that the southbound component of the travel reverses the direction of reentrainment with respect to pure eastward travel. Since the two travelers reentrain in different directions and thereby traverse different x values of the map, it is difficult to say which one will reentrain faster based solely on knowledge of the locations of x_s and x_u . However cobwebbing the map predicts that E_{10} reentrainment time will be longer than SE. These predictions regarding reentrainment times and directions are confirmed by the direct simulation results (13.0 days for E_{10} versus 10.5 days for SE).

Finally, consider the E_{15} and NE pair. These reentrain according to the $N = 15$ maps with $x_0 = 4.5$, where x_s and x_u are the same as for W_{15} and NW. Both travelers reentrain through phase delays, with the NE traveler starting closer to x_u and having to cobweb further to get to x_s than the E_{15} traveler. Thus the map predicts that NE will take longer to reentrain, however this is not what we find in direct simulation. Instead, the Santiago to Beijing traveler reentrains much more quickly (5.6 days) than the NYC to Beijing traveler (11.5 days), as shown in Fig. 15D. The reentrainment time for NE is shorter than predicted by the map due to the initial condition $x_0 = 4.5$ being very close to $x_u = 4.144$ and hence in the phaseless set of the NE map. As discussed in Section 3.5, with the higher intensity light level used for these simulations ($I = 1000$ lux), reentrainment times for initial conditions lying in the phaseless set can be dramatically short.

4. Discussion

For this study of jet lag, we chose the FJK model because it has been fit to human data on how light affects the circadian system (Forger et al., 1999; Jewett and Kronauer, 1998; Kronauer, 1990; Kronauer et al., 1999), has been extensively validated through experiments (Van Dongen, 2004), and has been used in “real-world” applications such as fatigue and performance modeling (Dean et al., 2007). Previous work employing the FJK model in the context of jet lag includes (Dean et al., 2009; Qiao et al., 2017; Serkh and Forger, 2014; Zhang et al., 2016), all of which used techniques from optimization or control theory to design light exposure schedules for the traveler to follow after reaching their destination in order to minimize reentrainment time. In our study, we assumed that the traveler will experience light according to the natural LD cycle in the destination and do not attempt to design alternative light exposure schedules. Instead, we systematically characterized how reentrainment depends on parameters such as the period of the endogenous circadian oscillator, the photoperiod and light intensity of the external LD forcing, the number of time zones crossed, the direction of travel, and the time of day at which the trip occurs.

The main mathematical tool that we used in this paper is the construction and analysis of a set of entrainment maps. These maps determine how the phase of light onset changes each time a trajectory passes through a prescribed Poincaré section of the phase space. Entrainment map analysis offers several advantages. First, the maps depend on parameters in predictable ways that yield important findings on how the dynamics of the full set of equations actually evolve. For example, we showed here how the maps depend on endogenous period τ_c , photoperiod N , and light intensity I . The parameter dependence was qualitatively similar to what we had found in an earlier study (Diekman and Bose, 2016) of circadian models (Gonze et al., 2005; Kim and Forger, 2012; Tyson et al., 1999), indicating that the map is capturing generic properties of circadian oscillators. Next, the fixed points of the entrainment map provide valuable information about the reasons for the underlying dynamics of circadian models. For example, when the map is constructed from a numerically obtained LD-entrained solution, then the stable fixed point of the map x_s corresponds to this stable limit cycle. The stability of x_s is easily determined by visual inspection of the slope of the map at x_s . The unstable fixed point of the map, x_u , can correspond to an actual unstable orbit of the system, but, as demonstrated here, this is dependent on other factors such as the light intensity. However, the unstable fixed point definitely provides evidence for a location in phase space where trajectories either reentrain through phase advance or delay. For instance, we located Z_D , a demarcation point, along the LD-entrained solution using information from x_u . Perhaps the biggest advantage of the map is that it simultaneously provides information about both the stable and unstable phases, as well as the time it takes initial conditions to converge to the stable phase through the cobweb procedure. This is in contrast to methods based on phase response curves or Arnold tongues/onions, which primarily give information about the stable phase but not the dynamics of the reentrainment process.

We used a combination of direct simulations and entrainment map analysis to obtain our results. In many cases, the map was used to organize and explain mathematically the results and observations obtained through direct simulations. Whereas in other cases, analysis of the map provided information that simulations alone would not likely have found. While discussed in more detail below, we would like to emphasize that the map was particularly helpful in identifying certain mathematical objects that play a key role in the FJK model. First, the map was used to find the existence of neutral period curves for different length trips. Using the first it-

erate of the map as a proxy for reentrainment times, we defined a neutral period point as an east or west trip for which the distance of the map from the diagonal is the same. This allowed us to explain the existence of the east-west asymmetry of jet lag. Next, the map explained which circumstances led to antidromic versus orthodromic reentrainment. Finally, the map revealed the existence of unstable periodic solutions for low light intensity. This led us to better understand the phase space structure of the full FJK model for all lux levels and to speculate about what geometric structure provides a separatrix-like effect for phase advancing versus phase delaying trajectories. Both of these latter two findings are related to the unstable fixed point of the map, which we discuss in more detail in the Appendix.

4.1. Neutral period and east-west asymmetry

Many travelers experience more severe symptoms of jet lag after traveling east than they do after traveling west (Sack, 2009; Waterhouse et al., 2007). The typical explanation for this asymmetry is that since the endogenous period of the human circadian clock is greater than 24 h, it is easier to phase delay the clock and entrain to the phase delay of sunrise/sunset that occurs following westward travel than it is to phase advance the clock and entrain to the phase advance of sunrise/sunset that occurs following eastward travel (Eastman and Burgess, 2009; Monk et al., 2000). Our analysis agrees with this explanation in general but adds an important distinction: while the directional asymmetry does depend on endogenous period, we find however that whether the endogenous period is greater than or less than 24 h is not the critical factor. Instead, we suggest it is a generic property of circadian limit cycle oscillators that there exists a “neutral” endogenous period for which equivalent advances or delays of the LD cycle (i.e. eastward or westward travel across the same number of time zones) will induce the same amount of jet lag. Clocks with an endogenous period greater than the neutral period suffer worse jet lag after eastward travel and those with an endogenous period less than the neutral period suffer worse jet lag after westward travel. The neutral period terminology was introduced by Aschoff et al. (1975), who studied the asymmetry effect in a variety of species and a mathematical model (Wever, 1966). We find that the neutral period depends on daylength and, as a result, we generalize this notion to a neutral period curve (see Figs. 10 and 11). For example, considering east/west trips of 6 time zones and $I = 100$ lux, we found the neutral period to be 24.2 under long days (15:9 photoperiod), 24 h for intermediate length days (11:13 photoperiod) and 23.9 under short days (10:14 photoperiod). Thus for a traveler with an endogenous period of 24.1 h, we predict that traveling east will be harder than west in the winter, but that traveling west will be harder than east in the summer, since for $I = 100$ lux these two cases correspond to parameter pairs that lie on opposite sides of the neutral period curve. While the existence of neutral period curves does not depend on light intensity, the shape of the NPC may be dependent on light intensity since a higher lux level increases the concavity of entrainment maps and leads to faster reentrainment. In turn, this may lead to different light intensity-dependent predictions regarding seasonal effects on the difficulty of travel.

In work related to the east-west asymmetry of jet lag, Lu et al. (2016) studied a macroscopic reduction of a globally coupled network of phase models. Their approach is to derive an ordinary differential equation for a complex-valued order parameter that governs whether or not the system is in an entrained or unentrained state. In their model, depending on parameters, this differential equation can have stable and unstable fixed points as well as limit cycle solutions. Lu et al. find that when the endogenous period is larger than 24 h, eastward trips take longer to reentrain

from then westward ones across the same number of timezones. They find the opposite to hold when the endogenous period is less than 24 h. In some sense, their model utilizes 24 h as a neutral period, independent of daylength.

4.2. Threshold separating orthodromic and antidromic reentrainment

After a small phase shift of the LD cycle a circadian oscillator will reentrain orthodromically, i.e. in the same direction as the shift. This corresponds to reentrainment through phase advances after short eastward trips and through phase delays after short westward trips. Longer transmeridian trips that constitute larger phase shifts of the LD cycle and can lead to antidromic reentrainment where travelers reentrain through phase delays after eastward travel or phase advances after westward travel (Arendt et al., 1987; Burgess et al., 2003; Klein and Wegmann, 1977; Takahashi et al., 2001). In a simulation study of a mammalian molecular clock model, Leloup and Goldbeter (2013) found a sharp threshold in the magnitude of the LD phase shift that separates orthodromic and antidromic reentrainment. They showed that phase shifts that put the traveler in the vicinity of this threshold result in very long reentrainment times, similar to what we find in the FJK model for lux levels corresponding to indoor light. Leloup and Goldbeter used phase response curve (PRC) analysis to roughly predict the location of this threshold, but stressed that using the PRC for this purpose is not straightforward and not very accurate. We have shown that the entrainment map, in particular the unstable fixed point of the map, provides an easy and accurate method of predicting the critical phase shift (or trip) that separates these two modes of reentrainment. Lu et al. (2016) find circumstances where the stable manifold of an unstable saddle fixed point determines whether solutions reentrain through phase advance or phase delay. The authors show this saddle fixed point merges with another fixed point as a parameter is varied. Interestingly, even after the bifurcation, the effect of the saddle is still present in separating phase advance versus phase delay. This is similar to what we find with the increase in the lux level ($I = 100$ increasing to $I = 1000$) causing the unstable fixed point of our map to no longer correspond to an actual unstable periodic orbit. Still, as demonstrated, we find that x_u separates out phase advancing versus phase delaying initial conditions even at high lux.

4.3. Aiming to enter the phaseless set as a strategy for minimizing jet lag

Our results show that as the light intensity is increased, reentrainment times decrease. This is consistent with previous simulation studies of the FJK model (Serkh and Forger, 2014). Moreover, we have shown that the FJK model exhibits the curious phenomenon of very fast entrainment for certain trajectories that pass through the phaseless set when the light intensity is large. For example, for travelers with an endogenous period of 24.2, trips that are roughly 10.5 h to the east place the traveler in a neighborhood of the unstable fixed point of the map. For low lux $I = 100$, this is the worst trip as this leads to the longest reentrainment time (roughly 25 days) compared to all other trips independent of arrival time; see Fig. 8. But once the lux is increased to 1000, the reentrainment time for this same trip is much shorter (on the order of 5 days) due to the “shortcut” that the trajectory takes through phase space; see Fig. 12. However, this seems to depend to some extent on arrival time, e.g. arriving at $X = 2$ instead of $X = 6$ will result in about 10 days of reentrainment. Thus our results suggest that a traveler may actually wish to intentionally make this “worst” trip, provided that the traveler can guarantee exposure to high lux levels during the reentrainment process and the correct arrival time.

Fast reentrainment through the phaseless set is characterized by a suppression of oscillation amplitude where the trajectory enters what is effectively a region of phases that converge at a phase singularity or pinwheel, a manifestation of the phaseless set. When the trajectory enters this pinwheel region, it has a chance of emerging with a phase that is much closer to the entrained phase than when it enters, thereby shortening the reentrainment time. When computing optimal light exposure schedules to reentrain the FJK model in minimum time, Serkh and Forger (2014) found several examples of optimal reentrainment that involved taking a shortcut across the limit cycle and reduction of oscillator amplitude in the middle of the schedule. Consistent with our results, Serkh and Forger only observed this phenomenon at high lux values. In Lu et al. (2016), there is a local minimum of reentrainment times exactly in a neighborhood of the “worst” trip. Though not discussed in their paper, this faster than expected reentrainment may also be related to trajectories taking shortcuts in phase space.

4.4. Jet lag due to north-south travel

The medical definition of jet lag—insomnia, excessive daytime sleepiness, or general malaise associated with transmeridian travel of at least two time zones—precludes the possibility of jet lag due to purely north-south travel (Sack, 2009). Indeed it has been explicitly stated that travel along the same meridian, for example Europe to southern Africa, causes no jet lag (Herxheimer and Waterhouse, 2003). However if one considers a broader definition, such as jet lag symptoms resulting from any travel that shifts the alignment of 24-h environmental cycles relative to the endogenous circadian clock (Song et al., 2017), then it seems plausible that the change in daylength encountered after long-distance translatitudinal travel in the summer or winter could induce jet lag-like effects. In our simulations of the FJK model, we find that it takes about 3 days for an oscillator with the average human endogenous period (24.2 h) to reentrain following travel from summer days with 15 h of light to winter days with 10 h of light, or vice versa. For circadian oscillators with long or short endogenous periods, the reentrainment time following such travel can be a week or more. We used the entrainment map to provide an explanation for these results by showing how the phase of entrainment (the stable fixed point of the map) is affected by daylength. The map and simulations also predict that the natural mode of reentrainment is antidromic, in that traveling from summer to winter constitutes a phase delay of the LD cycle but reentrainment occurs through phase advances. We are not aware of any field, laboratory, or computational studies that have thoroughly explored the question of reentrainment after translatitudinal travel. A review of jet lag by Waterhouse et al. (2007) notes that travel between hemispheres produces disorientation because of changes in natural lighting but does not elaborate further. In a field study with four human subjects, Hauty and Adams (1965a; 1965b; 1965c) included a north to south flight (from Washington, D.C. to Santiago, Chile) as a control to compare against east to west (Oklahoma City to Manila) and west to east (Oklahoma City to Rome) flights, in order to assess the effects solely attributable to a long flight versus effects due to changes in time zone. They found that all three flights produced a significant amount of subjective fatigue, but that the north-south flight did not cause a phase shift of circadian rhythms in physiological measurements such as rectal temperature and heart rate, whereas the other two flights did. However, the time of year that these flights took place is not reported in this study, and so it is possible that the flights were in spring or fall when the daylengths in D.C. and Santiago are similar. Moreover, the endogenous circadian period of the subjects was not reported, so it is difficult to compare their results to our predictions based on the FJK model.

Horses are the only species other than humans that are flown around the world for athletic competitions. The effect on equine physiology and performance of shifts in the LD cycle equivalent to travel across time zones has been assessed using thoroughbred racehorses kept in light-controlled stables (Tortonese et al., 2011). These studies found that horses are highly sensitive to light cues and rapidly adapt to phase shifts in the LD cycle. Surprisingly, athletic performance as measured by treadmill tests was actually enhanced following phase advances of the LD cycle simulating eastward travel. This enhancement was not attributed to an endogenous rhythm in athletic ability, but rather to masking effects of light and a timely rise in the hormone prolactin. In a commentary, the authors of this study note that horses have weak endogenous circadian rhythms but strong circannual biological rhythms (Tortonese and Short, 2012). The robust circannual clock may lead to slow adaptation in response to sudden changes in latitude, in contrast to the fast adaptation seen in response to simulated changes in longitude. Consistent with this prediction, racehorses subjected to simulated transequatorial flights exhibit negative effects on athletic performance (Domingo Tortonese, personal communication).

In our simulations of north-south travel, we have taken the photoperiod to be greater in the northern location ($N = 15$ h) than the southern location ($N = 10$ h) based on the duration of sunlight in the natural light-dark cycles at these latitudes at the selected time of year (June). However, the prevalence of electric lighting in modern society renders the duration of light that the circadian system is exposed to less dependent on the photoperiod of the natural light-dark cycle than it would be in the absence of artificial lighting (Skeldon et al., 2017). Despite the ability to control certain aspects of our light environment, there is still seasonal variation in the amount of light humans are exposed to in industrialized societies, with greater light exposure in the summer months than the winter months (Park et al., 2007). Furthermore, Thorne et al. (2009) found a seasonal effect on the time course of light exposure throughout the day. During the evening hours (5 PM–9 PM in their study), subjects were exposed to significantly more blue light in summer than in winter. Blue light is known to have a more potent phase shifting effect on the circadian clock than light at other wavelengths (Warman et al., 2003), and most artificial light sources contain less blue than natural light. Taken together, these observations suggest that modern humans are exposed to a longer duration of natural light in the summer, and therefore suddenly shifting from summer to winter (for example by traveling from NYC to Santiago in June) may reasonably be modeled as a reduction in N . Nevertheless, extensions of the entrainment map methodology to handle more realistic self-selected light exposure patterns would be useful for making quantitative predictions about the extent of north-south jet lag.

4.5. Traveling diplomat problem

The idea of minimizing reentrainment times has relevance for what we shall call the traveling diplomat problem. For example, the three most recent U.S. Secretaries of State traveled extensively during their tenures. John Kerry covered more than 1.3 million miles, Hillary Clinton visited 112 countries, and Condoleezza Rice made a total of 241 visits to foreign countries, all records within those categories (Chow and Kessler, 2013; Kelemen, 2016). The problem one can consider is analogous to a traveling salesman problem in which the salesman has to arrange travel to several locations so as to minimize total travel distance. In our scenario, a diplomat would seek to arrange his/her schedule to minimize jet lag. If a diplomat wished to visit a certain number of countries in the span of a certain number of days before returning home, could she arrange her travel to minimize her jet lag in each of the des-

tinuation cities and also upon return home? Or if she were to remain in each destination city until reentrained, before continuing to the next city, does an optimal path exist that minimizes total jet lag? Our results suggest that the diplomat could arrange her travel path to minimize jet lag. For example assuming a normal endogenous period of 24.2 h, if the diplomat were to travel between the four cities we studied, she would want to incorporate a NE component of travel; see Fig. 15. The loop NYC → Santiago → Beijing → Perth → NYC would cause her to have the least overall amount of jet lag. Santiago to Perth has 12 days of reentrainment, and Perth to Beijing 2 days, for a total of 14 days of reentrainment. But Santiago to Beijing has 5 days and Beijing to Perth 3 days, for a total of only 8 days of reentrainment. Thus by specifically including the NE component in her itinerary, she would minimize jet lag. The total number of reentrainment days for the NYC → Santiago → Beijing → Perth → NYC is 23 days. Another loop that has a relatively short reentrainment time is NYC → Perth → Beijing → Santiago → NYC which has 24 days of reentrainment. This loop has the advantage of two direct northward trips compared to the previous loop of two direct southward trips. This saves 2 days. Also, SE travel compared to NW travel saves 2 days. It is only because SW travel requires 5 more days of entrainment than NE that this loop is slightly worse than the previous. In comparison the loops NYC → Santiago → Perth → Beijing → NYC or NYC → Beijing → Perth → Santiago → NYC each lead to 28 days of jet lag. The example presented here is for a single daytime lux level, which is surely a simplification of what a diplomat or other traveler would likely experience. In reality, travelers would experience a variety of lux levels across their waking hours dependent on being exposed to indoor or outdoor light. As noted in our earlier results, higher lux levels lead to faster reentrainment but do not significantly affect the phase of the entrained solution. Thus we expect that even when a traveler experiences a more realistic light protocol than the single lux scenario presented here, there would still exist travel paths that minimize jetlag.

4.6. Future directions

There are several directions of further research that can be pursued. We plan to explore the effects of “social jet lag” where individuals stay up late on weekend nights, sleep in later the next day, and then return to their normal schedules for the work week (Crowley and Carskadon, 2010). This can be likened to taking a trip two or three hours west on a Friday night and returning home on Sunday night. Presumably, individuals who do this for several weeks in a row are not entrained to the daily light-dark cycle, but instead entrain to a more complicated weekly pattern (Smith and Eastman, 2012). Using the methods developed in this paper, we could study this problem by looking for a periodic solution, rather than a fixed point, of a set of composed entrainment maps. The added complication of using multiple maps arises as one must take into consideration the change of photoperiod that would occur due to staying up late and waking up late. We also plan to apply our methods to analyze night-shift work, which also involves periodic solutions of composed entrainment maps due to different light exposure and sleep schedules on weekdays versus weekends. Another situation where a periodic solution of the entrainment map would be relevant is for individuals who, because their endogenous period is too far from 24 h, are unable to entrain to LD forcing (Duffy and Wright, 2005). In all of these cases, the goal of our research would be to first find a stable periodic orbit of the entrainment map, and then find strategies (perturbations, perhaps of the light exposure) to move the individual closer to an entrained state.

The light-dark cycle is not the only external forcing that a circadian oscillator receives. For example, the effects of meals, exer-

cise, or taking melatonin can also be considered as external stimuli. We would like to generalize the entrainment map to incorporate multiple zeitgebers of this type. The main question to address is how a weaker, and perhaps conflicting, forcing signal would interact with the stronger light-dark forcing to determine entrainment properties. Another factor to consider is the entrainment of peripheral oscillators in tissues throughout the body by the suprachiasmatic nucleus (SCN), the master circadian pacemaker located in the hypothalamus. During jet lag, there can be internal desynchrony due to the SCN and peripheral oscillators reentraining at different rates or even in opposite directions, a phenomenon known as reentrainment by partition (Aschoff, 1978). Leise and Siegelmann (2006) studied reentrainment of a multistage computational model of the circadian system. Our approach would be to construct entrainment maps for each system component with some form of coupling among the maps. There is also significant coupling between the SCN and sleep-wake control centers in the brain (Vosko et al., 2010). Jet lag can desynchronize the circadian rhythm of the SCN and sleep-wake behavior. Models combining the circadian pacemaker and sleep-wake dynamics have been proposed (Gleit et al., 2013; Phillips et al., 2010; Skeldon et al., 2015), and one-dimensional maps for the circadian modulation of sleep have been developed (Booth et al., 2017; Nakao et al., 1997; Skeldon et al., 2014). An important future direction is to investigate the relationship between these maps and entrainment maps in the context of jet lag and other circadian rhythm sleep disorders.

Acknowledgments

We thank Somini Sengupta for helpful feedback regarding the traveling diplomat problem. This material is based upon work supported in part by the National Science Foundation [grant numbers DMS-1412877, DMS-1555237], and the U.S. Army Research Laboratory and the U.S. Army Research Office [contract/grant number W911NF-16-1-0584].

Appendix

In this Appendix, we further discuss the relationship between the fixed points x_s and x_u of an entrainment map and the dynamics of the forced FJK model. Given that we have considered many different entrainment maps, let us focus on the map constructed by taking a Poincaré section at $X = 6$ along the LD-entrained solution obtained for $\tau_c = 24.2$ h and $N = 12$ h. To construct the map, we choose initial conditions for A , C , and n that lie at the intersection of the Poincaré section and the LD-entrained solution and vary the value of the offset of the lights x between 0 and 24. The value $x_s = 6$ of the map therefore will correspond exactly to a periodic orbit of the FJK model because the trajectory returns to $X = 6$ after exactly 24 h and for this case the A , C , and n values return to their original values after 24 h. In general, when the entrainment map is constructed using a Poincaré section that intersects an LD-entrained solution and A , C , and n initial conditions at that intersection point, there is a direct correspondence between x_s and the stable LD-entrained solution.

The relationship of x_u to dynamic structures of the forced FJK model is more complicated. On one hand, we have found that the existence of a corresponding unstable periodic orbit depends on light intensity I . On the other hand, we have found that independent of light intensity, x_u corresponds to a structure in phase space that separates trajectories that phase advance or phase delay as they converge to the entrained solution. We explain both of these observations below.

First, consider low light intensity of $I = 100$ lux. For this case, $x_u = 16.24$. This means that the demarcation point predicted by our map is a journey given by $Z_D = 10.24$ time zones to the east.

In Fig. 16A, the projection of the stable LD-entrained solution onto the $A - C$ plane is plotted in solid red and black. The location $Z = 0$ and $X = 6$ (solid blue circle) coincide. The projection of the unstable periodic orbit is plotted in dashed red and black. Travel east corresponds to moving clockwise along the projection of the stable orbit to a location marked by an open blue circle on the LD-entrained solution. In terms of x , this value is called $\hat{x}_u = x_s - Z_D \text{ mod } 24$ and equals $x = 19.8$. The map predicts that this location along the LD-entrained solution separates trajectories that converge via phase delay or advance. Note that this interpretation is equivalent to the one given in Section 3.5 where the trajectory began on the Poincaré section with different light offset initial conditions taken in a neighborhood of x_u . Here we instead fix the light offset to be $x = 6$ and vary the initial conditions in a neighborhood of \hat{x}_u chosen by making a trip Z_D time zones on the LD-entrained solution. Panel A shows a stroboscopic map (solid dots) of different initial conditions projected onto the $A - C$ plane every 24 h. From each initial condition, we ran a simulation under 6 h of light, followed by 12 h of dark, and then 6 h of light before plotting the ensuing location of the trajectories, and then repeated. From just to the left of \hat{x}_u emanates a set of points, also in dark blue, that converge towards a point corresponding to $X = 6$ on the unstable periodic orbit. Thus these points lie on the stable manifold of the unstable periodic orbit! Finding this manifold without the insights provided by the entrainment map would have been extremely unlikely. The unstable periodic orbit appears to be a saddle with a stable manifold that is at least 2-dimensional. The saddle-like nature makes backward integration largely useless in locating the unstable periodic orbit. Instead it is the entrainment map that provided the clue on where to locate it in the full phase space. The initial conditions at $Z = 10$ and $Z = 11$ start on “opposite sides” of the stable manifold of the unstable orbit and are seen to produce a sequence of iterates that converge to $X = 6$ on the stable periodic orbit by phase advancing (green) or delaying (magenta); see Fig. 16B. In another set of simulations, we chose initial conditions very close to the solid blue separatrix on the LD-entrained solution and these also entrained by advance or delay depending on from which side of the stable manifold they originated (data not shown). Finally, observe the cyan set of dots that emanate from $X = 6$ on the unstable orbit and then converge to the stable LD-entrained solution at $X = 6$. The initial cyan dot that we chose as an initial condition was found in the following way. We located the value of (A^*, C^*, n^*) at which the unstable periodic orbit intersected the Poincaré section at $X = 6$ on the unstable orbit. We then perturbed the A and C values to $A^* - 0.00271035$ and $C^* + 0.01$, but kept $n = n^*$. Therefore after 24 h the n value returns to n^* . Thus all the cyan dots lie in the plane $n = n^*$. These points are seen in both Fig. 16A and B to take a shortcut across (through) phase space towards the stable LD-entrained solution. The trajectory is characterized by the fact that it neither phase advances or delays for the first few iterates until it undergoes amplitude suppression. After it reemerges to full amplitude it effectively has the correct phase of the LD-entrained solution. We suspect that these points lie on the strong stable manifold of the stable LD-entrained solution. We speculate that this strong stable manifold separates phase advancing or phase delaying trajectories, in general, independent of the light intensity I . The figure also shows points that initially lie close to the cyan points but then follow the more predictable advance (green) or delay (magenta).

Now consider Fig. 16C and D which show the corresponding plots for a higher light intensity of $I = 1000$ lux. For this case, $x_s = 6$ remains, but now $x_u = 16.68$. Thus the demarcation point is $Z_D = 10.68$ or $\hat{x}_u = 19.32$. Panel C shows the projection onto the $A - C$ plane and Panel D shows a few representative sequences of iterates in the three-dimensional phase space. The main difference to note is there is no unstable periodic orbit. Instead the sequence

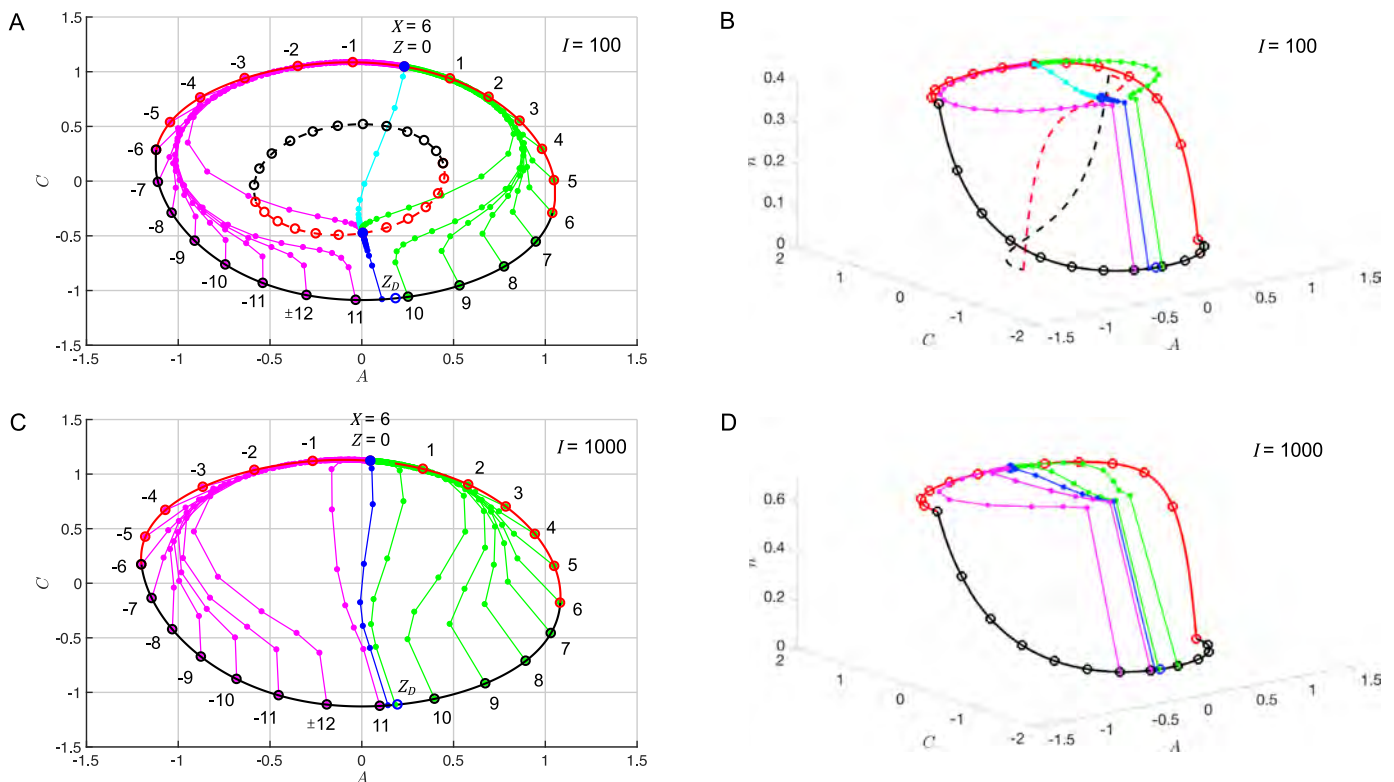


Fig. 16. Relationship between the unstable fixed point of entrainment map and dynamics of the FJK model. (A) Projection of stable LD-entrained solution (solid red/black lines) onto $A-C$ phase plane for $\tau_c = 24.2$ h, $N = 12$ h, and $l = 100$ lux. Simulations were performed starting from initial conditions on the LD-entrained solution at the hourly markings denoted by the open red and black circles with a light-dark protocol based on $x = 6$. Positions labeled with $Z > 0$ ($Z < 0$) correspond to travel Z time zones to the east (west). The reentrainment process is depicted by strobing the system every 24 h and plotting the location of the trajectory (solid green and magenta dots). These trajectories converge to $X = 6$ (solid blue circle) by either phase advance (green) or phase delay (magenta). The blue set of dots emanating from near the open blue circle ($Z_D = 10.24$) does not phase advance or delay, and converges to $x = 6$ on the unstable LD-entrained solution (dashed red and black lines, open circles red and black circles are hourly markings). These points lie on the stable manifold of the unstable periodic orbit, which serves to separate trajectories that entrain through phase advance and delay. The cyan dots are on a trajectory that starts near the unstable periodic orbit and takes a shortcut to converge to $X = 6$ on the stable LD-entrained solution, whereas nearby initial conditions converge to $X = 6$ by phase advancing or delaying. (B) Same objects as Panel A, plotted in the three-dimensional phase space A, C, n . (C) Projection of stable LD-entrained solution (solid red/black lines) onto $A-C$ phase plane for $\tau_c = 24.2$ h, $N = 12$ h, and $l = 1000$ lux. Unlike Panel A, here there is no unstable LD-entrained solution. The blue dots emanating from near $Z_D = 10.68$ are on a shortcut trajectory that exhibits amplitude suppression and converges to $X = 6$ unusually fast. Trajectories on either side of the blue trajectory converge to $X = 6$ through phase advance (green) or delay (magenta). (D) Same objects as Panel C, plotted in the three-dimensional phase space A, C, n . (For interpretation of the references to color in this figure legend, the reader is referred to the web version of this article.)

of dark blue dots that emanate from near Z_D converge directly to the stable LD-entrained solution at $X = 6$. The corresponding sequence behaves in the same way as the cyan sequence of Panel A. Nearby initial conditions also lead to a sequence of iterates that behave quite similarly to the blue one, which is in contrast to the $l = 100$ lux case. What we believe to be common between the two cases is that there exists a structure in phase space, perhaps the strong stable manifold associated with the point on the LD-entrained solution at $X = 6$, that separates phase advancing and phase delaying trajectories. What differs between the two cases appears to be that the shortcut is only accessible from the LD-entrained solution when an unstable periodic orbit does not exist. When it does, the stable manifold of the unstable periodic orbit appears to preclude the possibility of taking the shortcut and accessing the phaseless set. In summary, the entrainment map, and in particular, the unstable fixed point x_u and its corresponding demarcation point Z_D , provide a way to locate specific subspaces within the larger phase space that help organize the dynamics.

Finally, let us address the quantitative difference in the worst case travel between the map and direct simulation shown in Fig. 8D for $\tau_c = 23.4$ h, $l = 100$ lux. For this set of parameters, an unstable periodic orbit exists similar to the one shown in Fig. 16A and B. We believe that in direct simulation, the worst case travel $Z = -6$ is placing the trajectory very close to the stable manifold of the unstable orbit. In turn, this causes the entrainment time


to increase. We don't fully understand why the demarcation point Z_D predicted from the map is further from the actual demarcation value from the simulation for $\tau_c = 23.4$ h than it is for the other τ_c values shown in Fig. 8A–C. We believe, however, that is related to the fact that the system (and entrainment map) are closer to bifurcation for this τ_c value (see Fig. 9D) than it is for the others, and thus the unstable and stable limit cycles are quite close to one another in phase space.

References

- Arendt, J., Aldous, M., English, J., Marks, V., Arendt, J., Folkard, S., 1987. Some effects of jet lag and their alleviation by melatonin. *Ergonomics* 30, 1379–1393.
- Aschoff, J., 1978. Problems of re-entrainment of circadian rhythms: asymmetry effect, dissociation and partition. In: *Environmental Endocrinology*. Springer, pp. 185–195.
- Aschoff, J., Hoffmann, K., Wever, R., 1975. Re-entrainment of circadian rhythms after phase shifts of the zeitgeber. *Chronobiologia* 2, 23–78.
- Booth, V., Xique, I., Diniz Behn, C., 2017. A one-dimensional map for the circadian modulation of sleep in a sleep-wake regulatory network model for human sleep. *SIAM J. Appl. Dyn. Syst.* 16 (2), 1089–1112.
- Bordyugov, G., Abraham, U., Granada, A., Rose, P., Imkeller, K., Kramer, A., et al., 2015. Tuning the phase of circadian entrainment. *J. R. Soc. Interface* 12, 20150282.
- Burgess, H.J., Crowley, S.J., Gazda, C.J., Fogg, L.F., Eastman, C.I., 2003. Preflight adjustment to eastward travel: 3 days of advancing sleep with and without morning bright light. *J. Biol. Rhythms* 18 (4), 318–328.
- Chow, E., Kessler, G., 2013. On Official Business: A Look at Secretary of State Travel. *The Washington Post*, 24 Jan 2013 [accessed 29 April 2017]. Available from: http://www.washingtonpost.com/wp-srv/special/politics/secretary-of-state-travel/?tid=a_inl.

- Crowley, S.J., Carskadon, M.A., 2010. Modifications to weekend recovery sleep delay circadian phase in older adolescents. *Chronobiol. Int.* 27 (7), 1469–1492.
- Czeisler, C.A., Duffy, J.F., Shanahan, T.L., Brown, E.N., Mitchell, J.F., Rimmer, D.W., et al., 1999. Stability, precision, and near-24-hour period of the human circadian pacemaker. *Science* 284 (5423), 2177–2181.
- Dean, D.A., Fletcher, A., Hursh, S.R., Klerman, E.B., 2007. Developing mathematical models of neurobehavioral performance for the “real world”. *J. Biol. Rhythms* 22 (3), 246–258.
- Dean, D.A., Forger, D.B., Klerman, E.B., 2009. Taking the lag out of jet lag through model-based schedule design. *PLOS Comput. Biol.* 5 (6), E1000418.
- Diekman, C., Bose, A., 2016. Entrainment maps: a new tool for understanding properties of circadian oscillator models. *J. Biol. Rhythms* 31 (6), 598–616.
- Duffy, J.F., Wright, K.P.Jr., 2005. Entrainment of the human circadian system by light. *J. Biol. Rhythms* 20 (4), 326–338.
- Eastman, C.I., Burgess, H.J., 2009. How to travel the world without jet lag. *Sleep Med. Clin.* 4 (2), 241–255.
- Forger, D., Jewett, M., Kronauer, R., 1999. A simpler model of the human circadian pacemaker. *J. Biol. Rhythms* 14, 533–537.
- Gleit, R.D., Diniz Behn, C.G., Booth, V., 2013. Modeling inter-individual differences in spontaneous internal desynchrony patterns. *J. Biol. Rhythms* 28 (5), 339–355.
- Gonze, D., Bernard, S., Waltermann, C., Kramer, A., Herzog, H., 2005. Spontaneous synchronization of coupled circadian oscillators. *Biophys. J.* 89, 120–129.
- Granada, A.E., Herzog, H., 2009. How to achieve fast entrainment? the timescale to synchronization. *PLoS ONE* 23 (4), E7057.
- Guckenheimer, J., 1975. Isochrons and phaseless sets. *J. Math. Biol.* 1, 259–273.
- Hauty, G., Adams, T., 1965. Phase Shifts of the Human Circadian System and Performance Deficit During the Periods of Transition II. West-East Flight. Federal Aviation Agency, Office of Aviation Medicine.
- Hauty, G.T., Adams, T., 1965. Phase Shifts of the Human Circadian System and Performance Deficit During the Periods of Transition. I. East-West Flight. Federal Aviation Agency, Office of Aviation Medicine.
- Hauty, G.T., Adams, T., 1965. Phase Shifts of the Human Circadian System and Performance Deficit During the Periods of Transition. III. North-South Flight. Federal Aviation Agency, Office of Aviation Medicine.
- Herxheimer, A., Waterhouse, J., 2003. The prevention and treatment of jet lag. *BMJ Brit. Med. J.* 326 (7384), 296.
- James, F.O., Cermakian, N., Boivin, D.B., 2007. Circadian rhythms of melatonin, cortisol, and clock gene expression during simulated night shift work. *Sleep* 30 (11), 1427.
- Jewett, M., Kronauer, R., 1998. Refinement of a limit cycle oscillator model of the effects of light on the human circadian pacemaker. *J. Theor. Biol.* 192, 455–465.
- Jewett, M.E., Kronauer, R.E., Czeisler, C.A., 1991. Light-induced suppression of endogenous circadian amplitude in humans. *Nature* 350 (6313), 59.
- Johnson, C., Elliot, J., Foster, R., 2003. Entrainment of circadian programs. *Chronobiol. Int.* 20, 741–774.
- Kelemen, M., 2016. John Kerry Heads to Antarctica and to a New Travel Record. NPR Parallels. 8 Nov 2016 [accessed 29 April 2017]. Available from: <http://www.npr.org/sections/parallels/2016/11/08/501153007/john-kerry-heads-to-antarctica-and-to-a-new-travel-record>.
- Kim, J., Forger, D., 2012. A mechanism for robust circadian timekeeping via stoichiometric balance. *Mol. Syst. Biol.* 8, 630.
- Klein, K., Wegmann, H., 1977. Circadian performance rhythms: experimental studies in air operations. In: Mackie, R. (Ed.), *Vigilance: Theory, Operational Performance and Physiological Correlates*. Plenum, New York, pp. 111–131.
- Kronauer, R., 1990. A quantitative model for the effects of light on the amplitude and phase of the deep circadian pacemaker, based on human data. In: Horne, J. (Ed.), *Sleep '90, Proceedings of the Tenth European Congress on Sleep Research*. Pontenagel Press, Dusseldorf, pp. 306–309.
- Kronauer, R.E., Forger, D.B., Jewett, M.E., 1999. Quantifying human circadian pacemaker response to brief, extended, and repeated light stimuli over the photopic range. *J. Biol. Rhythms* 14 (6), 501–516.
- Leise, T., Siegelmann, H., 2006. Dynamics of a multistage circadian system. *J. Biol. Rhythms* 21, 314–323.
- Leloup, J., Goldbeter, A., 2013. Critical phase shifts slow down circadian clock recovery: implications for jet lag. *J. Theor. Biol.* 333, 47–57.
- Lu, Z., Klein-Cardena, K., Lee, S., Antonsen, T.M., Girvan, M., Ott, E., 2016. Resynchronization of circadian oscillators and the east-west asymmetry of jet-lag. *Chaos* 26 (9), 094811.
- Monk, T.H., Buysse, D.J., Carrier, J., Kupfer, D.J., 2000. Inducing jet-lag in older people: directional asymmetry. *J. Sleep Res.* 9 (2), 101–116.
- Nakao, M., Sakai, H., Yamamoto, M., 1997. An interpretation of the internal desynchronizations based on dynamics of the two-process model. *Methods Inf. Med.* 36 (4–5), 282–285.
- Novak, B., Tyson, J., 2008. Design principles of biochemical oscillators. *Nat. Rev. Mol. Cell Biol.* 9, 981–991.
- Park, D.H., Kripke, D.F., Cole, R.J., 2007. More prominent reactivity in mood than activity and sleep induced by differential light exposure due to seasonal and local differences. *Chronobiol. Int.* 24 (5), 905–920.
- Phillips, A.J., Chen, P., Robinson, P., 2010. Probing the mechanisms of chronotype using quantitative modeling. *J. Biol. Rhythms* 25 (3), 217–227.
- Qiao, W., Wen, J.T., Julius, A., 2017. Entrainment control of phase dynamics. *IEEE Trans. Automat. Control* 62 (1), 445–450.
- Relógio, A., Westermark, P.O., Wallach, T., Schellenberg, K., Kramer, A., Herzog, H., 2011. Tuning the mammalian circadian clock: robust synergy of two loops. *PLoS Comput. Biol.* 7, E1002309.
- Sack, R., 2009. The pathophysiology of jet lag. *Travel Med. Infect. Dis.* 7, 102–110.
- Sack, R.L., 2010. Clinical practice. jet lag. *N. Engl. J. Med.* 362 (5), 440–447.
- Schmal, C., Myung, J., Herzog, H., Bordyugov, G., 2015. A theoretical study on seasonality front. *Neurology* 6, 94.
- Serkh, K., Forger, D., 2014. Optimal schedules of light exposure for rapidly correcting circadian misalignment. *PLOS Comput. Biol.* 10, E1003523.
- Skeldon, A.C., Derks, G., Dijk, D.J., 2015. Modelling changes in sleep timing and duration across the lifespan: changes in circadian rhythmicity or sleep homeostasis? *Sleep Med. Rev.* 28, 96–107.
- Skeldon, A.C., Dijk, D.J., Derks, G., 2014. Mathematical models for sleep-wake dynamics: comparison of the two-process model and a mutual inhibition neuronal model. *PLoS ONE* 9 (8), E103877.
- Skeldon, A.C., Phillips, A.J., Dijk, D.J., 2017. The effects of self-selected light-dark cycles and social constraints on human sleep and circadian timing: a modeling approach. *Sci. Rep.* 7, 45158.
- Smith, M.R., Eastman, C.I., 2012. Shift work: health, performance and safety problems, traditional countermeasures, and innovative management strategies to reduce circadian misalignment. *Nat. Sci. Sleep* 4, 111–132.
- Song, A., Severini, T., Allada, R., 2017. How jet lag impairs major league baseball performance. *Proc. Natl. Acad. Sci. USA* 114 (6), 1407–1412.
- Sun, M., Wang, Y., Xu, X., Yang, L., 2016. Dynamical mechanism of circadian singularity behavior in neurospora. *Physica A* 457, 101–108.
- Takahashi, T., Sasaki, M., Itoh, H., Yamadera, W., Ozone, M., Obuchi, K., et al., 2001. Re-entrainment of the circadian rhythms of plasma melatonin in an 11-h eastward bound flight. *Psychiatry Clin. Neurosci.* 55 (3), 275–276.
- Thorne, H.C., Jones, K.H., Peters, S.P., Archer, S.N., Dijk, D.J., 2009. Daily and seasonal variation in the spectral composition of light exposure in humans. *Chronobiol. Int.* 26 (5), 854–866.
- Tortorese, D., Short, R., 2012. Biological rhythms, jetlag and performance in thoroughbred racehorses. *Equine. Vet. J.* 44 (4), 377–378.
- Tortorese, D.J., Preedy, D.F., Hesketh, S.A., Webb, H.N., Wilkinson, E.S., Allen, W.R., et al., 2011. Experimental jetlag disrupts circadian clock genes but improves performance in racehorses after light-dependent rapid resetting of neuroendocrine systems and the rest-activity cycle. *J. Neuroendocrinol.* 23 (12), 1263–1272.
- Tyson, J., Hong, C., Thron, C., Novak, B., 1999. A simple model of circadian rhythms based on dimerization and proteolysis of PER and TIM. *Biophys. J.* 77, 2411–2417.
- Ukai, H., Kobayashi, T.J., Nagano, M., Masumoto, K.h., Sujino, M., Kondo, T., et al., 2007. Melanopsin-dependent photo-perturbation reveals desynchronization underlying the singularity of mammalian circadian clocks. *Nat. Cell Biol.* 9 (11), 1327–1334.
- U.S. Citizen Travel to International Regions, 2017. Database: U.S. Department of Commerce, International Trade Administration. National Travel and Tourism Office. 20 October 2017 31 Jan 2017 [accessed 29 April 2017]. Available from: <http://travel.trade.gov/view/m-2016-0-001/>.
- Van Dongen, H., 2004. Comparison of mathematical model predictions to experimental data of fatigue and performance. *Aviat. Space Envir. Med.* 75 (3), A15–A36.
- Vosko, A.M., Colwell, C.S., Avidan, A.Y., 2010. Jet lag syndrome: circadian organization, pathophysiology, and management strategies. *Nat. Sci. Sleep* 2, 187–198.
- Warman, V.L., Dijk, D.J., Warman, G.R., Arendt, J., Skene, D.J., 2003. Phase advancing human circadian rhythms with short wavelength light. *Neurosci. Lett.* 342, 37–40.
- Waterhouse, J., Reilly, T., Atkinson, G., Edwards, B., 2007. Jet lag: trends and coping strategies. *Lancet* 369 (9567), 1117–1129.
- Wever, R., 1966. The duration of re-entrainment of circadian rhythms after phase shifts of the zeitgeber a theoretical investigation. *J. Theor. Biol.* 13, 187–201.
- Winfree, A., 1991. Circadian rhythms. resetting the human clock. *Nature* 350, 18.
- Winfree, A.T., 1970. Integrated view of resetting a circadian clock. *J. Theor. Biol.* 28 (3), 327–374.
- Wright, K.P.Jr., Hughes, R.J., Kronauer, R.E., Dijk, D.J., Czeisler, C.A., 2001. Intrinsic near-24-h pacemaker period determines limits of circadian entrainment to a weak synchronizer in humans. *Proc. Natl. Acad. Sci. U S A* 98 (24), 14027–14032.
- Wright, K.P.Jr., McHill, A.W., Birs, B.R., Griffin, B.R., Rusterholz, T., Chinoy, E.D., 2013. Entrainment of the human circadian clock to the natural light-dark cycle. *Curr. Biol.* 23 (16), 1554–1558.
- Zhang, J., Qiao, W., Wen, J.T., Julius, A., 2016. Light-based circadian rhythm control: entrainment and optimization. *Automatica* 68, 44–55.

Magnesium Regulates the Circadian Oscillator in Cyanobacteria

Young M. Jeong,^{*} Cristiano Dias,[†] Casey Diekman,^{‡§} Helene Brochon,^{*} Pyonghwa Kim,^{*} Manpreet Kaur,^{*} Yong-Sung Kim,^{||} Hye-In Jang,[¶] Yong-Ick Kim^{*,§,1} 

^{*}Department of Chemistry and Environmental Science, New Jersey Institute of Technology, Newark, NJ, USA, [†]Department of Physics, New Jersey Institute of Technology, Newark, NJ, USA, [‡]Department of Mathematical Sciences, New Jersey Institute of Technology, Newark, NJ, USA, [§]Institute for Brain and Neuroscience Research, New Jersey Institute of Technology, Newark, NJ, USA, ^{||}Department of Physics, Applied Physics, and Astronomy, Rensselaer Polytechnic Institute, Troy, NY, USA, [¶]School of Cosmetic Science and Beauty Biotechnology, Semyung University, Jecheon, Republic of Korea.

Abstract The circadian clock controls 24-h biological rhythms in our body, influencing many time-related activities such as sleep and wake. The simplest circadian clock is found in cyanobacteria, with the proteins KaiA, KaiB, and KaiC generating a self-sustained circadian oscillation of KaiC phosphorylation and dephosphorylation. KaiA activates KaiC phosphorylation by binding the A-loop of KaiC, while KaiB attenuates the phosphorylation by sequestering KaiA from the A-loop. Structural analysis revealed that magnesium regulates the phosphorylation and dephosphorylation of KaiC by dissociating from and associating with catalytic Glu residues that activate phosphorylation and dephosphorylation, respectively. High magnesium causes KaiC to dephosphorylate, whereas low magnesium causes KaiC to phosphorylate. KaiC alone behaves as an hourglass timekeeper when the magnesium concentration is alternated between low and high levels in vitro. We suggest that a magnesium-based hourglass timekeeping system may have been used by ancient cyanobacteria before magnesium homeostasis was established.

Keywords circadian clock, KaiC, phosphorylation, hourglass, autokinase, PhoQ

INTRODUCTION

Almost all organisms on earth have adapted to environmental cycles by developing their own time-keeping system, a circadian clock, to predict daily changes. The simplest circadian model system is found in cyanobacteria, a single-celled organism. The central oscillator of the cyanobacterial circadian clock is composed of only 3 proteins, KaiA, KaiB, and KaiC (Golden and Canales, 2003). Because oscillations continue without transcriptional-translational feedback

loops (Tomita et al., 2005), the cyanobacterial circadian clock can be reconstituted in vitro by mixing those 3 proteins and adenosine 5'-triphosphate (ATP) with magnesium ions (Nakajima et al., 2005). KaiC undergoes rhythmic autophosphorylation and autodephosphorylation with a 24-h period in the presence of both KaiA and KaiB (Iwasaki and Kondo, 2004). These autokinase and autophosphatase activities in KaiC are regulated by the conformation of the A-loop, which is known as a day/night switch located in the C-terminus of KaiC (residues 487-519; Kim

1. To whom all correspondence should be addressed: Yong-Ick Kim, Department of Chemistry and Environmental Science, New Jersey Institute of Technology, 161 Warren St., Newark, NJ 07102, USA; e-mail: ykim@njit.edu.

et al., 2008). Without KaiA and KaiB, KaiC alone undergoes dephosphorylation in the *in vitro* reaction because the default conformation of the A-loop is the “buried” state (Kim et al., 2008). The A-loop changes its conformation from the buried to the “exposed” state by binding KaiA (Kim et al., 2008; Vakonakis and LiWang, 2004). When the A-loop is in the exposed conformation, kinase activity is predominant and KaiC is phosphorylated. KaiA keeps the A-loop in the exposed conformation by binding the A-loop with differential affinity, while KaiB returns the A-loop to a buried conformation by sequestering KaiA far from the A-loop (Snijder et al., 2017; Tseng et al., 2017). At the active site of KaiC, S431 and T432 residues are phosphorylated and dephosphorylated sequentially over the daily cycle (Nishiwaki et al., 2007; Rust et al., 2007). Because the active site is distal from the A-loop, the kinase and phosphatase activity of KaiC may be regulated by an allosteric effect that changes the conformation of the active site. Currently, the mechanism acting downstream of the A-loop is unknown. In this study, we found that magnesium is a key element regulating the kinase and phosphatase activity of KaiC as a downstream regulatory element of the A-loop. Based on our findings, we suggest a possible direction of the evolution of the cyanobacterial circadian oscillator in cyanobacteria.

MATERIALS AND METHODS

Cloning, Protein Purification, and Expression

Cloning and purifications were performed essentially as described previously (Kim et al., 2015; Kim et al., 2012). The KaiC E318D protein expression plasmid was generated using the site-directed mutagenesis method.

Structure Analysis of KaiC Hexamer

Every structure analysis was performed with UCSF Chimera (Pettersen et al., 2004). Distance measurements between O^{Glu} and O^{Thr} were performed with the “Structure Analysis” function in UCSF Chimera.

In Vitro Assay of KaiC Phosphorylation

All assays were performed essentially as described previously (Kim et al., 2015) with the following modification: ethylenediaminetetraacetic acid (EDTA) was completely removed for all reactions that were performed without KaiA. The magnesium concentration was modified as indicated in the main text. Disodium

ATP (initial concentration: 1 mM), rather than MgATP, was used for all *in vitro* reactions to avoid the addition of magnesium ions from another source.

Molecular Dynamics Simulation of KaiC Hexamer

All-atom molecular dynamics simulations were performed using GROMACS version 5.1. The Charmm36 force field was used to account for the different interactions between the atoms of the system that comprised the KaiC protein in the hexameric state solvated with 60,000 to 70,000 TIP3P water molecules. For the initial conformation of the KaiC hexamer, we used its experimentally resolved crystal structure (i.e., PDB ID: 1U9I), wherein positions of each atom of residues 14–497 of KaiC were given. We also studied a variant of this experimental structure in which the A-loop (residue 489–497) was deleted from the PDB entry. The latter mimics the exposed conformation of the A-loop, in which KaiC becomes phosphorylated. Moreover, to study the effects of magnesium, 2 sets of simulations were performed for these 2 initial conformations: one with magnesium ions and the other without them. The initial location of the magnesium atoms was indicated in the PDB structure. The net charge of the system was neutralized by adding Na and Cl ions to the solvent.

The 4 systems examined in this study underwent energy minimization as well as equilibration in the NVT ensemble for 10 ns at 300 K, with heavy atoms of the protein restrained to their initial positions via 1000 kcal mol⁻¹Å⁻² springs. The leap-frog algorithm with a time step of 2 fs was used to integrate the equations of motion, and the neighbor list was updated every 10 steps. A Lennard-Jones cutoff of 1.0 nm was used. Electrostatics were treated using the smooth particle mesh Ewald method with a grid spacing of 0.13 nm and a 1.0 nm real-space cutoff. The production run was performed in the NPT ensemble (1 atm and 300 K), in which the temperature was controlled using the *v*-rescale thermostat ($\tau_T = 0.1$ ps) and the pressure was controlled using the Parrinello-Rahman barostat ($\tau_P = 1$ ps). The total simulation time of the production runs was 50 ns.

Hourglass Timer In Vitro

The KaiC (3.4 μ M, 2 mL)-alone reaction mixture was prepared with the modified *in vitro* reaction buffer (150 mM NaCl, 20 mM Tris-HCl, 5 mM MgCl₂, pH = 8.0). The reaction mixture was incubated at 30 °C for 16 h to completely dephosphorylate KaiC. The incubated reaction mixture was passed through a spin desalting column (Zeba spin desalting column,

Fisher Scientific, Waltham, MA) at $100 \times g$ for 3 min. The protein concentration was measured using the Bradford protein assay kit and adjusted by concentrating it with a spin concentrator (Vivaspin 2, Millipore, Burlington, MA). The reaction mixture was incubated at 30°C for 12 h for phosphorylation. During the incubation, 20 μL of the reaction mixture was mixed with sodium dodecyl sulfate–polyacrylamide gel electrophoresis (SDS-PAGE) loading dye every 2 h for 12 h. Then, 5 μL of highly concentrated magnesium solution in the modified *in vitro* reaction buffer was added for dephosphorylation and continuously incubated at 30°C for 12 h. Sampling was performed in the same manner. The removal and addition of magnesium were performed repeatedly for 2 days to simulate light/dark alterations in magnesium concentration. After collecting all the reaction samples, SDS-PAGE was performed with the previously reported method to analyze the phosphorylation state of KaiC (Kim et al., 2015). The KaiB and KaiC reaction mixture for testing the hourglass timer was performed in the same manner as the KaiC-alone reaction mixture.

Mathematical Modeling of Hourglass Timer

Our mathematical model of magnesium-dependent phosphorylation and dephosphorylation cycles of KaiC in the absence of KaiA and KaiB is based on the Rust model of ordered multisite phosphorylation for the KaiABC oscillator (Rust et al., 2007). The model is a 3-dimensional system of ordinary differential equations that captures the temporal dynamics of KaiC in 4 different forms: unphosphorylated (U), singly phosphorylated at the T432 site (T), singly phosphorylated at the S431 site (S), and doubly phosphorylated at both the S431 and T432 sites (D). Our model equations are as follows:

$$\begin{aligned}\frac{dT}{dt} &= k_{UT}U + k_{DT}D - k_{TU}T - k_{TD}T \\ \frac{dS}{dt} &= k_{US}U + k_{DS}D - k_{SU}S - k_{SD}S \\ \frac{dD}{dt} &= k_{TD}T + k_{SD}S - k_{DT}D - k_{DS}D \\ U &= [\text{KaiC}] - T - S - D \\ k_{XY} &= k_{XY}^B + (k_{XY}^M - k_{XY}^B)f([\text{Mg}]) \\ f([\text{Mg}]) &= \frac{[\text{Mg}]^n}{(K_A)^n + [\text{Mg}]^n}\end{aligned}$$

where k_{XY} are the rate constants for transitions from state X to state Y , $[\text{KaiC}] = 3.4 \mu\text{M}$ is the concentration of KaiC, $[\text{Mg}]$ is the concentration of magnesium, K_A is the concentration at which the effect of magnesium on the transition rates is half-maximal, and n is the

Hill coefficient. Because the total amount of KaiC is conserved, $[\text{KaiC}]$ is constant and U can be obtained algebraically from the amounts of the other phosphoforms. The transition rates consist of baseline rates k_{XY}^B in the absence of magnesium and k_{XY}^M at high magnesium concentrations. If $k_{XY}^M > k_{XY}^B$ ($k_{XY}^M < k_{XY}^B$), then magnesium promotes (inhibits) that transition. We fit these baseline rates assuming first-order kinetics for the 2 limiting cases of high and low magnesium concentrations, respectively. First, suppose that $[\text{Mg}]$ is sufficiently high such that the magnesium effect has saturated, that is, $f([\text{Mg}]) \approx 1$ and $k_{XY} \approx k_{XY}^M$. These experimental conditions are similar to those indicated in figure 2B of Rust et al. (2007), in which autonomous dephosphorylation of KaiC was observed after removing KaiA. Thus, we used the parameters that Rust et al. estimated from those data, namely, $k_{TU}^M = 0.21$, $k_{SU}^M = 0.11$, $k_{DS}^M = 0.31$, and $k_{DT}^M = k_{UT}^M = k_{US}^M = k_{SD}^M = k_{TD}^M = 0 \text{ h}^{-1}$. Second, suppose $[\text{Mg}] = 0$ and $k_{XY} = k_{XY}^B$. By fitting our experimental data on the autonomous phosphorylation of KaiC in the absence of magnesium (Suppl. Fig. S1), we obtained the parameters $k_{TU}^B = 0.5412$, $k_{SU}^B = 0.0530$, $k_{DS}^B = 0.1853$, $k_{DT}^B = 0$, $k_{UT}^B = 0.3623$, $k_{US}^B = 0.0267$, $k_{SD}^B = 0.0601$, and $k_{TD}^B = 0.1269 \text{ h}^{-1}$. These parameters were found by minimizing the total least-squares error between the model and data for T-KaiC, S-KaiC, and ST-KaiC using MATLAB's constrained nonlinear optimization routine *fmincon* with the default interior point algorithm. We set parameter lower bounds of 0 and initial parameter guesses equal to the values of $k_{XY}^0 + k_{XY}^A$ given in Rust et al. (2007).

To determine the remaining parameters K_A and n , we fit the model to the experimental hourglass data. In the simulations, we set $[\text{Mg}] = 0 \text{ mM}$ during the light periods and to the values 0.05, 0.1, 0.5, 1.0, and 5.0 mM during the dark periods. We used *fmincon* to minimize the total least-squares error between the model and data for P-KaiC. With an initial guess of $K_A = 0.43$ and $n = 2$, the optimized parameters were $K_A = 0.0298$ and $n = 1.1470$. Setting $n = 1$ and optimizing K_A alone yields $K_A = 0.0256$ and less than a 1% increase in the error function. We selected the more parsimonious model with Michaelis-Menten kinetics for magnesium ($n = 1$) and show the hourglass simulation results for $K_A = 0.0256$.

Adenosine diphosphate (ADP) inhibits the kinase reaction involved in KaiC phosphorylation, and periodic changes in the ATP/ADP ratio can entrain the KaiABC oscillator (Rust et al., 2011). To incorporate the effect of the ATP/ADP ratio into our model, we followed Rust's model (Rust et al., 2011) and added a multiplicative term to the transition rates for the phosphorylation (but not the dephosphorylation) reactions:

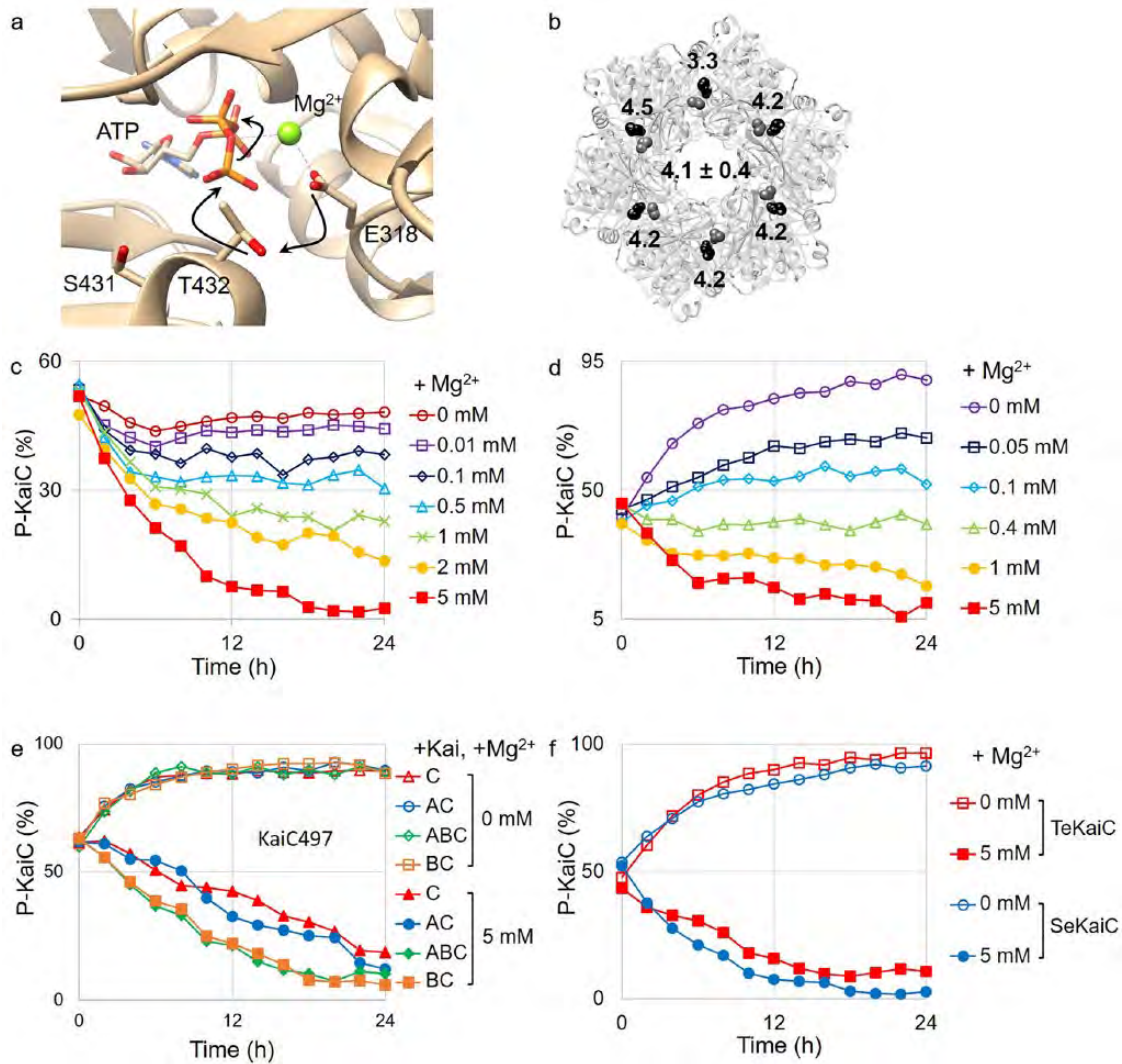


Figure 1. Magnesium regulates the phosphorylation and dephosphorylation of KaiC. (a) Crystal structure of an active site in the KaiC hexamer (PDB ID: 1U9I). The phosphate group on ATP was removed for clearance. Black arrows indicate the electron movements in the phosphorylation transfer reaction. The oxygen atom in E318 and the oxygen atom in T432 are labeled on the crystal structure of the KaiC hexamer. Black represents E318, and gray represents T432. (b) Distances (in angstroms, Å) between the oxygen atom in E318 and the oxygen atom in T432 are labeled on the crystal structure of the KaiC hexamer. Black represents E318, and gray represents T432. (c) Phosphorylation state of KaiC in the in vitro reaction with many different magnesium concentrations. Magnesium concentrations are labeled on the right of the graph. (d) Phosphorylation state of KaiC in the absence of ethylenediaminetetraacetic acid with many different magnesium concentrations. Magnesium concentrations are labeled on the right of the graph. (e, f) Phosphorylation state of the KaiC mutant and other species of cyanobacteria. Open markers indicate the absence of magnesium. Closed markers indicate the presence of magnesium (5 mM). KaiC497 was mixed with KaiC497 alone (▲), KaiA (•), KaiB (●), and KaiA and KaiB (◆) (e). Phosphorylation state of KaiC from *Thermosynechococcus elongatus* (TeKaiC) and from *Synechococcus elongatus* (SeKaiC) (f).

$$k_{XY} = \frac{[ATP]}{[ATP] + K_{rel}[ADP]} \left(k_{XY}^B + (k_{XY}^M - k_{XY}^B) f([Mg]) \right)$$

where $XY = UT, US, SD$, and TD , and $K_{rel} = 1$ is the relative affinity for ADP versus ATP in the kinase reactions. Because darkness leads to a drop in the ATP/ADP ratio, we simulated an hourglass experiment with ATP = 100%/ADP = 0% during the light periods when magnesium is absent and ATP = 30%/ADP = 70% during the dark periods when magnesium is present.

RESULTS

Magnesium Ions Are Necessary for the Dephosphorylation of KaiC

To obtain insight into how the allosteric effect of the A-loop induces a conformational change in the active site of KaiC phosphorylation, we analyzed the crystal structure of the KaiC hexamer from a cyanobacterium, *Synechococcus elongatus*. The E318 residue in the active site is known as a catalytic base,

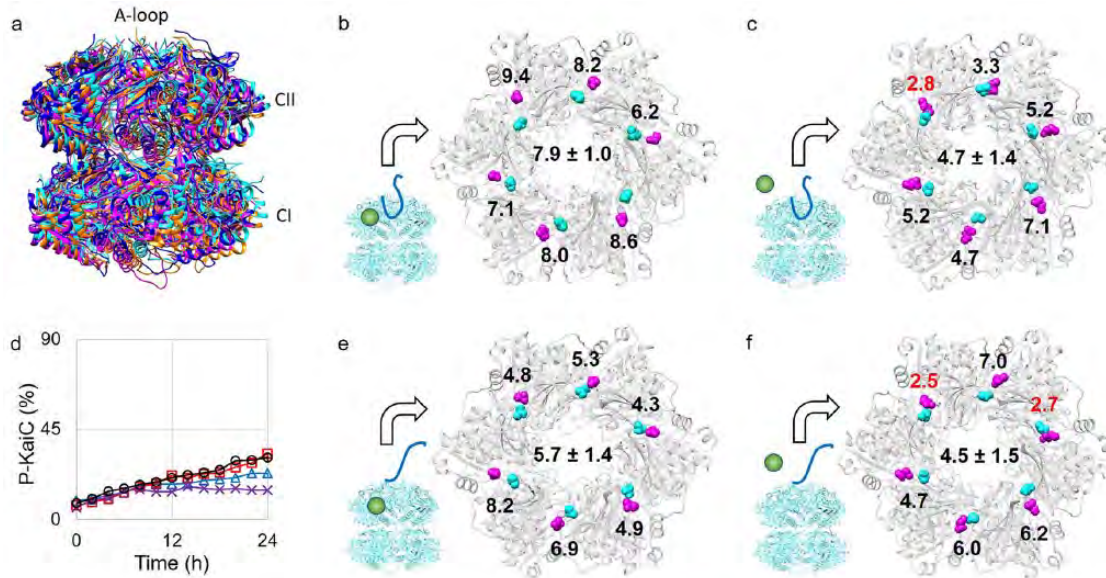


Figure 2. Molecular dynamics (MD) simulations of the KaiC hexamer. (a) Four MD simulation structures are superimposed. The “buried” conformations are shown in magenta (with magnesium) and cyan (without magnesium). The “exposed” conformations are shown in orange (with magnesium) and blue (without magnesium). The 3 domains of KaiC are labeled at the position. (b,c,e,f) MD simulation structures of the KaiC hexamer. Magenta represents E318, and cyan represents T432. The distances (in angstroms, Å) between the oxygen atom in E318 and the oxygen atom in T432 are labeled on the structure. Distances shorter than 3 Å are labeled in red. The average distance of all 6 subunits is labeled at the center of the structure. The combinations of the A-loop conformation and magnesium (see the cartoon representations) were the buried conformation with magnesium (b), the buried conformation without magnesium (c), the exposed conformation with magnesium (e), and the exposed conformation without magnesium (f). (d) Phosphorylation state of KaiC E318D. Four different reaction mixtures were prepared to measure the phosphorylation state: KaiC alone (Δ), KaiC and KaiA (\square), KaiC and KaiB (\times), KaiC, KaiA, and KaiB (\circ).

which activates T432 for the phosphoryl transfer reaction by taking a proton from the hydroxyl group in T432 (thereafter H^{Thr} ; Hayashi et al., 2004; Valiev et al., 2003). In the active form of the KaiC hexamer, a magnesium ion holds E318 to prevent free rotation and movement, which are necessary to activate T432 for the phosphoryl transfer reaction (Fig. 1a). All distances between the oxygen atom in the carboxyl group of the E318 side chain (thereafter O^{Glu}) and the oxygen atom in the hydroxyl group of the T432 side chain (thereafter O^{Thr}) in the 6 subunits of the KaiC hexamer are longer than the hydrogen bonding distance (~ 3 Å; Fig. 1b). With these distances and structural restrictions, E318 is unable to activate T432 for the phosphoryl transfer reaction in the presence of magnesium. We hypothesized that the O^{Glu} can move or rotate freely in the absence of magnesium and can activate T432 for the phosphoryl transfer reaction by taking the H^{Thr} . To test this hypothesis, *in vitro* reactions with KaiC alone were established with various magnesium concentrations, and the KaiC phosphorylation state of each reaction was monitored. In general, KaiC alone is dephosphorylated in the reconstituted *in vitro* reaction, which has a comparatively high (5 mM) magnesium concentration (Kim et al., 2008; Nakajima et al., 2005). In the KaiC-alone *in vitro* reaction with

various magnesium concentrations, the intensity of the dephosphorylation was reduced when the magnesium concentration was decreased, ultimately reaching a minimum in the absence of magnesium (Fig. 1c; Supplemental Fig. S2a). Although KaiC did not show phosphorylation under these reaction conditions, the phosphatase activity disappeared completely in the absence of magnesium. Therefore, KaiC needs magnesium to be dephosphorylated and is possibly a magnesium-dependent phosphatase, which uses magnesium as a reaction center (Shi, 2009).

EDTA Inhibits the Phosphorylation of KaiC in the Absence of KaiA and Magnesium

Because KaiC alone did not show phosphorylation in the absence of magnesium, we hypothesized that at least one of the components in the reaction mixture possibly inhibits the kinase activity of KaiC. For the original *in vitro* oscillator developed by Kondo (Nakajima et al., 2005), EDTA is used as a metal chelator; however, EDTA is not present as a natural component in cyanobacteria. We removed EDTA from the *in vitro* reaction to determine whether the kinase activity was recovered. In the absence of magnesium and EDTA, KaiC was

phosphorylated to the same level as that observed when KaiC was incubated with KaiA in vitro (Fig. 1d; Supplemental Fig. S2b). KaiC was still dephosphorylated with higher magnesium concentrations in the absence of EDTA. The removal of EDTA did not affect the dephosphorylation of KaiC. To confirm the inhibition of kinase activity by EDTA, we added different concentrations of EDTA to the KaiC-alone in vitro reactions in the absence of magnesium. The intensity of the phosphorylation was decreased by increasing the EDTA concentration in the reaction mixture (Supplemental Fig. S3). Therefore, the deficiency of magnesium turns on the kinase activity of KaiC, while EDTA inhibits its kinase activity.

Magnesium Regulation of KaiC Phosphorylation Is Universal

KaiC497 is a KaiC mutant with 23 residues (residues 497-519) deleted from the A-loop, maintaining a dephosphorylation state even in the presence of KaiA due to the lack of the KaiA binding site (Kim et al., 2008). We checked the phosphorylation level of KaiC497 to test the magnesium regulation of KaiC phosphorylation in this mutant. KaiC497 alone spontaneously dephosphorylates with a high magnesium concentration while phosphorylating without magnesium (Fig. 1e; Supplemental Fig. S4). The addition of KaiA or KaiB did not affect KaiC phosphorylation at either concentration. Therefore, the magnesium regulation of KaiC phosphorylation is a downstream regulatory element of the A-loop for the phosphorylation and dephosphorylation of KaiC.

We also tested the magnesium effect with another cyanobacterial species, *Thermosynechococcus elongatus*, which is mainly used for the structural study of the cyanobacterial circadian clock (Chang et al., 2015; Vakonakis and LiWang, 2004). Again, KaiC from *T. elongatus* behaves in the same manner as that from *S. elongatus* (Fig. 1f; Supplemental Fig. S5). Therefore, the magnesium regulation of KaiC phosphorylation can be considered a universal mechanism shared by the 2 species.

Molecular Dynamics Simulation Reveals That E318 Activates T432 for the Phosphorylation of KaiC in the Absence of Magnesium

To provide structural insight into the effect of magnesium on the regulation of KaiC phosphorylation, we performed molecular dynamics simulations of the crystal structure of the KaiC hexamer, which has the A-loop in the buried conformation. The overall backbone conformation of KaiC did not significantly change in the simulations performed with

or without magnesium (Fig. 2a; Supplemental Fig. S6). However, the distances between O^{Glu} and O^{Thr} were significantly longer than 3 Å when the simulations were performed with magnesium (Fig. 2b; Supplemental Fig. S7a). In the simulations performed without magnesium, 1 of the 6 pairs of O^{Glu}-O^{Thr} distances was found to be sufficiently short (less than ~3 Å) to allow O^{Glu} to interact with H^{Thr} (Fig. 2c; Supplemental Fig. S7b). This interaction enables T432 to be activated for phosphorylation. Thus, these molecular dynamics simulations suggest that magnesium interacts with O^{Glu} and keeps it away from H^{Thr}, which leads to the suppression of KaiC phosphorylation. In contrast, in the absence of magnesium, O^{Glu} can move and/or rotate more freely toward H^{Thr}, which enables residue T432 to be activated for phosphorylation.

The molecular dynamics simulations reveal that certain O^{Glu}-O^{Thr} distances are shorter than 3 Å but longer than 2 Å in the absence of magnesium. We hypothesized that if E318 is mutated to D318, this mutant would not be able to activate T432 for phosphorylation because of the shortness of the side chain. Indeed, KaiC E318D cannot phosphorylate in the absence of magnesium (Fig. 2d; Supplemental Fig. S8). Interestingly, the addition of KaiA cannot activate the kinase activity of KaiC E318D (Fig. 2d; Supplemental Fig. S8). Therefore, the O^{Glu}-O^{Thr} distance is an important factor for KaiC phosphorylation and is regulated by magnesium.

Magnesium Is a Downstream Regulator of the A-Loop Conformation in the Circadian Oscillation of KaiC Phosphorylation

We hypothesized that magnesium regulation of KaiC phosphorylation is correlated with the conformation of the A-loop. A molecular dynamics simulation of KaiC was previously reported with an exposed A-loop conformation that is mimicked by removing the entire A-loop (residue 487 to 518) from KaiC (Egli et al., 2013). When the A-loop is in the exposed conformation, the flexibility of the 422-loop in KaiC is increased in the presence of magnesium, but the distance information between O^{Glu} and O^{Thr} has not been reported (Egli et al., 2013). To understand the relationship between the A-loop conformation and magnesium regulation, we performed molecular dynamics simulations with an A-loop deletion mutant KaiC in both the presence and absence of magnesium. As in the simulations performed with the A-loop, the overall backbone conformation of KaiC did not significantly change in the absence of the A-loop (Fig. 2a; Supplemental Fig. S6). All O^{Glu}-O^{Thr} distances were longer than 3 Å in the presence of magnesium (Fig. 2e; Supplemental Fig. S7c). In contrast, the distances in the 2 subunits were

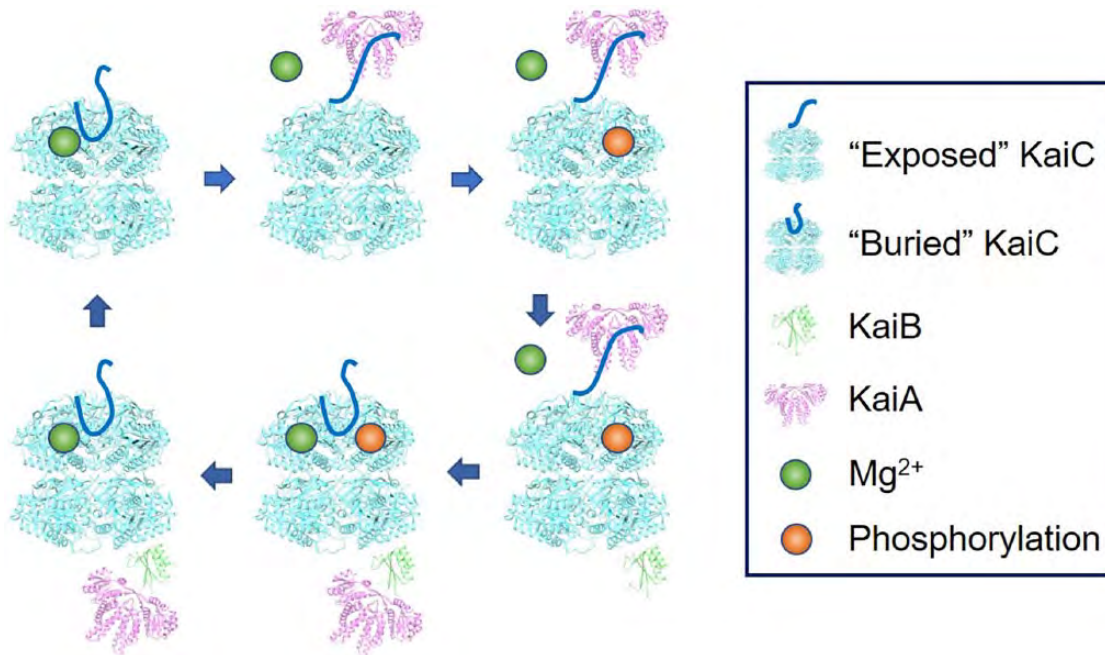


Figure 3. Molecular mechanism of the circadian oscillator in cyanobacteria. KaiC is fully dephosphorylated, the A-loop (solid line) is “buried,” and the magnesium ion is bound on E318 in the active site (upper left). KaiA is bound to the A-loop to keep it in the “exposed” conformation, and magnesium is released from the active site (upper center). KaiC is fully phosphorylated (upper right). KaiB is bound on the CI domain of KaiC to sequester KaiA from the A-loop (lower right). A-loop turns to the buried conformation by dissociation of KaiA, and magnesium is bound on E318 in the active site (lower center). KaiC is fully dephosphorylated (lower left), and KaiB and KaiA are dissociated from KaiC (upper left).

shorter than 3 Å in the absence of magnesium (Fig. 2f; Supplemental Fig. S7d). We suggest that this rare chance for activation helps explain why phosphorylation in the cyanobacterial circadian oscillator is so slow. These results also suggest that the distances between O^{Glu} and O^{Thr} were significantly affected not by the conformation of the A-loop but by the presence or absence of magnesium (Fig. 2b, c, e, and f). However, the conformation of the A-loop does enhance the probability of phosphorylation in the absence of magnesium, as we found more subunits that were within the hydrogen bonding distance when the A-loop was in the exposed conformation (Fig. 2f) than in the buried conformation (Fig. 2e). The average $O^{\text{Glu}}-O^{\text{Thr}}$ distance of all subunits was the shortest when the A-loop was exposed in the absence of magnesium (Fig. 2f) and the longest when the A-loop was buried in the presence of magnesium (Fig. 2b). Therefore, the phosphorylation and dephosphorylation of KaiC is regulated by the presence or absence of magnesium, which is an effect downstream of the A-loop conformation.

We tested this finding using the KaiC E487A mutant, which shows constitutive phosphorylation without KaiA (Kim et al., 2008). The A-loop conformation in the mutant KaiC seems to stay exposed by breaking the H-bond network formed between the A-loops in the KaiC hexamer (Kim et al., 2008). The

binding affinity of the regulatory magnesium ion should be significantly lower in this mutant, keeping KaiC in the hyperphosphorylated state even in a high magnesium concentration. To test this hypothesis, we constructed the *in vitro* reaction with KaiC E487A in a high magnesium concentration. Indeed, KaiC E487A was able to stay hyperphosphorylated in 20 mM magnesium (Supplemental Fig. S9).

The possible molecular mechanism of KaiC phosphorylation is proposed in Figure 3. When the A-loop in KaiC is exposed by binding KaiA, magnesium is released from the active site of KaiC, and O^{Glu} moves and rotates toward H^{Thr} to activate T432 for the phosphoryl transfer reaction (Fig. 3). While the A-loop is buried after sequestration of KaiA by KaiB, magnesium is tightly bound to O^{Glu} , making it unable to activate T432 for phosphorylation, and KaiC undergoes dephosphorylation (Fig. 3).

The Circadian Oscillator Has Possibly Evolved from an Hourglass to a Self-sustained Oscillator in Cyanobacteria

This magnesium regulation of KaiC phosphorylation enables the construction of an hourglass-type *in vitro* reaction with KaiC alone that is suggestive of the evolutionary trajectory of the circadian clock in

cyanobacteria. Previous genetic analysis indicated that KaiC is the oldest protein among the oscillator components and that KaiB and KaiA were added later, respectively (Dvornyk et al., 2003; Tauber et al., 2004). Based on the evolutionary information of the oscillator components, a reasonable hypothesis was proposed: the prokaryotic timekeeping system evolved from an hourglass timer to a self-sustained oscillator in response to selective pressures (Johnson et al., 2017; Ma et al., 2016). Before the appearance of KaiB or KaiA, day/night alterations of the environment caused the phosphorylation state of KaiC to oscillate as an hourglass. In other organisms, magnesium concentration is altered by the natural light/dark cycle and provides feedback to the circadian clock (Feeney et al., 2016). Thus, we hypothesized that the KaiC-alone timekeeping system may operate as an hourglass timer driven by the influx and efflux of magnesium, assuming the magnesium concentration was altered by an environmental signal such as the light/dark cycle in the ancient cyanobacteria. If we assume that the environmental magnesium concentration in the habitat of cyanobacteria oscillated daily as a result of evaporation during the day and condensation during the night, then the KaiC-alone hourglass could have been used as a timekeeping system in the ancient cyanobacteria before establishing the current magnesium homeostasis system.

To test the possibility of an hourglass timer *in vitro*, we constructed an *in vitro* reaction with KaiC alone. By altering the magnesium concentration every 12 h, KaiC showed a robust phosphorylation and dephosphorylation cycle with a 24-h period, although the variation of magnesium concentrations (0.5-5 mM) was somewhat greater than that observed under the physiological condition (Fig. 4a; Supplemental Fig. S10). We still observed the phosphorylation and dephosphorylation cycle in the low magnesium concentration range (0.05-0.1 mM), although the amplitude was significantly decreased compared with that of the KaiABC oscillator. Simulations of a mathematical model of KaiC alone (see the Materials and Methods section) can reproduce the hourglass timer (Fig. 4b). In cyanobacteria, light alters ADP concentration (Rust et al., 2011; Simons, 2009) in addition to magnesium concentration. Increasing ADP can induce dephosphorylation of KaiC in cyanobacteria and entrain the self-sustained KaiABC circadian oscillator (Rust et al., 2011). This ADP effect may enhance the amplitude of the phosphorylation rhythm in the hourglass timer by inducing robust dephosphorylation at night. When we applied the ADP effect in simulations of the mathematical model of the KaiC-alone hourglass timer, robust oscillations were observed across the entire range of magnesium

concentrations (Fig. 4c). The existence of the hourglass timer provides evidence for the hypothesis that the molecular evolution of the cyanobacterial circadian clock started from a KaiC-alone hourglass timer. To further test steps along an evolutionary path to an oscillator, we constructed an *in vitro* reaction with KaiB and KaiC, which was proposed to be a damped oscillator (Johnson et al., 2017). Many different magnesium concentrations were screened for the signature of a damped oscillator, but all the phosphorylation patterns were similar to the KaiC-alone reaction (Supplemental Fig. S11). The *in vitro* reaction with KaiB and KaiC also behaved as an hourglass timer (Fig. 4d; Supplemental Fig. S12). It is possible that the KaiBC timekeeping system in each species may be at a different stage of evolution. Thus, whether the mechanism is an hourglass timer, a damped oscillator, or a self-sustained oscillator is species-dependent. In this study, we found an hourglass KaiBC timer using both KaiB and KaiC from *S. elongatus*, but a KaiBC damped oscillator might be discovered using KaiB and KaiC from a different species of bacterium. Finally, we checked the magnesium effect on the self-sustained circadian oscillator composed of KaiA, KaiB, and KaiC with many different magnesium concentrations. In the self-sustained oscillator, KaiC phosphorylation was observed as a stable oscillation with a circadian period (~24 h) over a wide range of magnesium concentrations (Fig. 4e; Supplemental Fig. S13).

DISCUSSION

We successfully demonstrate the phosphorylation of wild-type KaiC without KaiA. Until now, it was believed that KaiC needed KaiA or a mutation on the A-loop to undergo phosphorylation (Kim et al., 2008; Nishiwaki et al., 2004). Because of this limitation, although the KaiC-alone hourglass was proposed before as a major step in the evolutionary pathway of the circadian oscillator, no experimental proof was reported (Axmann et al., 2009; Ma et al., 2016). We present a possible pathway for the evolution by removing EDTA, an unnatural reagent commonly used in reactions, from the hourglass reaction mixture. The inhibition of the phosphorylation of KaiC by EDTA was not observed in the presence of KaiA. Currently, the detailed mechanism of the inhibition of kinase activity by EDTA is unknown. We thought that the examination of the A-loop conformation could serve as a basis for elucidating the effect of EDTA on KaiC phosphorylation.

The general consensus on the mechanism of the phosphoryl-transfer reaction is that the magnesium ion acts as a cofactor to neutralize the negative charges

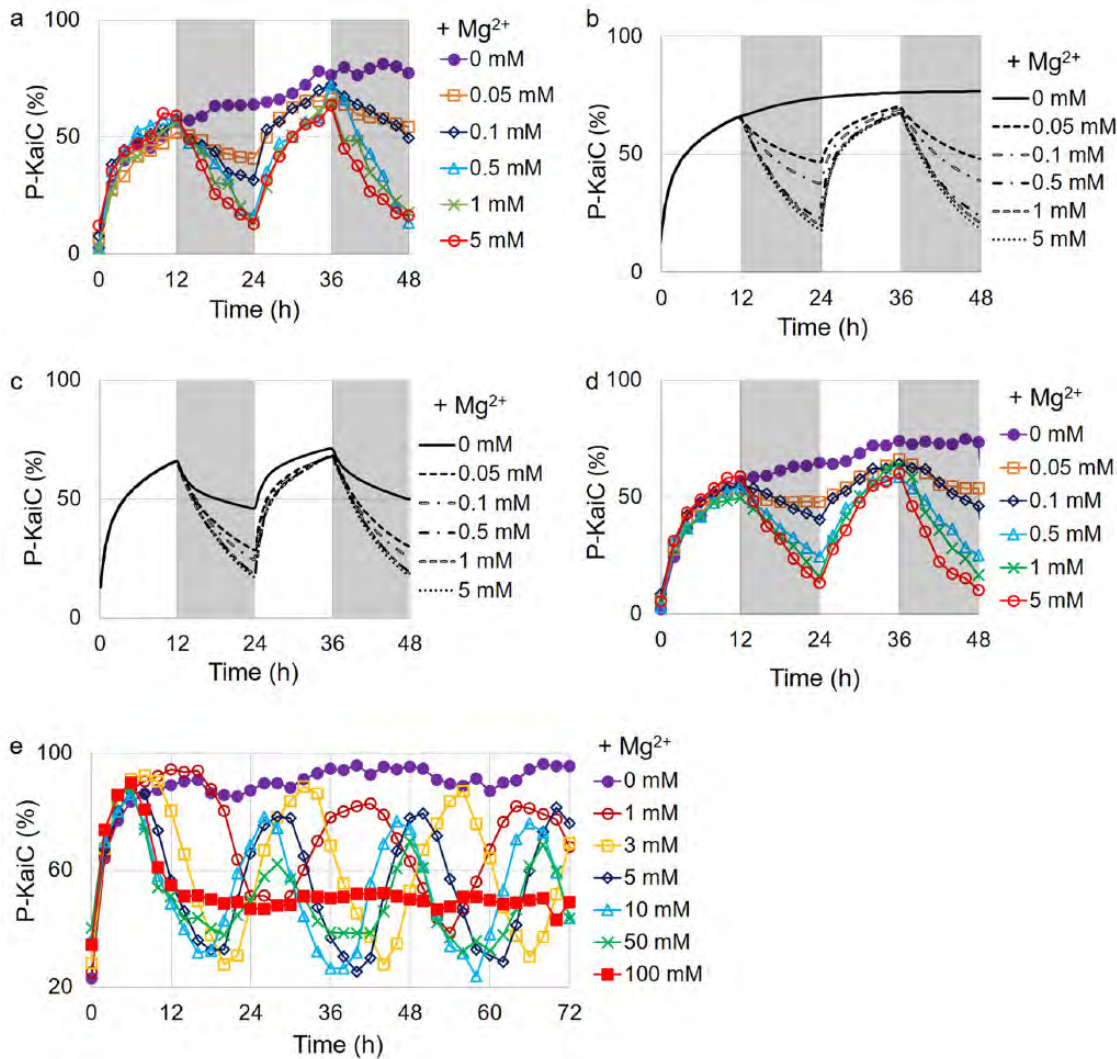


Figure 4. Molecular evolution of the circadian clock in cyanobacteria. (a) Hourglass timer of KaiC alone in vitro. The magnesium concentration was altered every 12 h (low in white and high in gray). The magnesium concentrations in gray are labeled on the right of the graph. (b) Simulations of a mathematical model of the hourglass KaiC timer. All other features are the same as those in (a). (c) Simulations of a mathematical model of the hourglass KaiC timer with ATP/ADP effect. All other features are the same as those in (b). (d) Hourglass-type oscillation of KaiBC in vitro oscillator. All other features are the same as those in (a). (e) Magnesium effect on the KaiABC self-sustained oscillator. Magnesium concentrations are labeled on the right of the graph.

on the γ -phosphate of ATP to facilitate the nucleophilic phosphoryl-transfer reaction. Our findings on the activation of KaiC kinase activity run counter to this general behavior. However, there are other examples of bacterial autokinases that respond in a similarly unusual way to changes in magnesium concentration. In PhoQ, which is involved in magnesium homeostasis in bacteria, the autokinase and the autophosphatase activities are predominant in low and high magnesium concentrations, respectively (Montagne et al., 2001). Although the detailed reaction mechanism at the atomic level is not yet elucidated, the magnesium ion regulates the autokinase activity of PhoQ in the same way as KaiC. In either case, the addition of EDTA inhibits the autophosphorylation in low

magnesium concentration (Castelli et al., 2000). Therefore, we cannot exclude the possibility that a trace amount of magnesium ions from the impurities of the reagents may act as a cofactor for the phosphoryl-transfer reaction. EDTA may strip magnesium ions from the active sites, resulting in the inhibition of kinase activity. Indeed, 2 magnesium ions are found within some KaiC crystal structures. One is located at the same position that we are claiming here as a “regulatory magnesium,” and the other is located near the γ -phosphate of ATP (Supplemental Fig. S14). However, even if the kinase activity is inhibited in absolute zero magnesium concentration, our findings here are still valid because absolute zero magnesium is impossible in cyanobacteria.

The magnesium concentration in cyanobacteria may be affected by fluctuating environmental conditions such as evaporation and condensation, because cyanobacteria can live even in the small amount of moisture found in a desert. Although magnesium concentration did not have a large effect on the self-sustained period, it is still possible that day/night magnesium alternations play a role in entraining the KaiABC oscillator because small changes in the self-sustained period can have a large effect on the entrained phase (Granada et al., 2013). We also hypothesize that signaling pathways other than magnesium, such as quinone signaling through KaiA (Kim et al., 2012), evolved to enable effective entrainment of the self-sustained oscillator. For example, CikA, a major input pathway protein (Kaur et al., 2019; Schmitz et al., 2000), directly interacts with the KaiABC oscillator to entrain circadian rhythms in cyanobacteria (Tseng et al., 2017). The step-by-step evolution from an hourglass timer permitted the development of a robust and entrainable circadian clock system in this single-celled organism.

CONCLUSION

Until recently, adding KaiA was the only way to activate the kinase activity of wild-type KaiC. We found that magnesium regulates KaiC phosphorylation downstream of the A-loop conformation, which is the master regulator of KaiC phosphorylation. By modulating magnesium concentration, the phosphorylation state of KaiC can be regulated without KaiA and KaiB. In ancient cyanobacteria, the KaiC-alone hourglass timekeeping system, which evolved before the current homeostasis system was established, may be used for the regulation of gene expression in the fluctuating magnesium environment. The current self-sustained circadian oscillator possibly evolved from the KaiC-alone hourglass controlled by magnesium.

ACKNOWLEDGMENTS

We thank Hana Nim for insightful discussions, Dr. Carl Johnson and Daniel Kim for critical comments, and Alejandra Lopez-Diaz, Brianna Porr, and Neha Thati for technical assistance. This work was supported by a New Jersey Institute of Technology start-up grant and a faculty seed grant awarded to Y. I. Kim and the National Science Foundation grants DMS-1412877 and DMS-1555237 and the U.S. Army Research Office grant W911NF-16-1-0584 awarded to C. Diekmann.


CONFLICT OF INTEREST STATEMENT

The authors have no potential conflicts of interest with respect to the research, authorship, and/or publication of this article.

NOTE

Supplemental material is available for this article online.

ORCID ID

Yong-Ick Kim  <https://orcid.org/0000-0001-5491-616X>

REFERENCES

- Axmann IM, Duhring U, Seeliger L, Arnold A, Vanselow JT, Kramer A, and Wilde A (2009) Biochemical evidence for a timing mechanism in prochlorococcus. *J Bacteriol* 191:5342-5347.
- Castelli ME, Garcia Vescovi E, and Soncini FC (2000) The phosphatase activity is the target for Mg²⁺ regulation of the sensor protein PhoQ in Salmonella. *J Biol Chem* 275:22948-22954.
- Chang YG, Cohen SE, Phong C, Myers WK, Kim YI, Tseng R, Lin J, Zhang L, Boyd JS, Lee Y, et al. (2015) Circadian rhythms: a protein fold switch joins the circadian oscillator to clock output in cyanobacteria. *Science* 349:324-328.
- Dvornyk V, Vinogradova O, and Nevo E (2003) Origin and evolution of circadian clock genes in prokaryotes. *Proc Natl Acad Sci U S A* 100:2495-2500.
- Egli M, Pattanayek R, Sheehan JH, Xu Y, Mori T, Smith JA, and Johnson CH (2013) Loop-loop interactions regulate KaiA-stimulated KaiC phosphorylation in the cyanobacterial KaiABC circadian clock. *Biochemistry* 52:1208-1220.
- Feeney KA, Hansen LL, Putker M, Olivares-Yanez C, Day J, Eades LJ, Larrondo LF, Hoyle NP, O'Neill JS, and van Ooijen G (2016) Daily magnesium fluxes regulate cellular timekeeping and energy balance. *Nature* 532:375-379.
- Golden SS and Canales SR (2003) Cyanobacterial circadian clocks—timing is everything. *Nat Rev Microbiol* 1:191-199.
- Granada AE, Bordyugov G, Kramer A, and Herzel H (2013) Human chronotypes from a theoretical perspective. *PLoS One* 8:e59464.
- Hayashi F, Itoh N, Uzumaki T, Iwase R, Tsuchiya Y, Yamakawa H, Morishita M, Onai K, Itoh S, and Ishiura M (2004) Roles of two ATPase-motif-containing

- domains in cyanobacterial circadian clock protein KaiC. *J Biol Chem* 279:52331-52337.
- Iwasaki H and Kondo T (2004) Circadian timing mechanism in the prokaryotic clock system of cyanobacteria. *J Biol Rhythms* 19:436-444.
- Johnson CH, Zhao C, Xu Y, and Mori T (2017) Timing the day: what makes bacterial clocks tick? *Nat Rev Microbiol* 15:232-242.
- Kaur M, Ng A, Kim P, Diekman C, and Kim Y-I (2019) CikA modulates the effect of KaiA on the period of the circadian oscillation in KaiC phosphorylation. *J Biol Rhythms* 34:218-223.
- Kim YI, Boyd JS, Espinosa J, and Golden SS (2015) Detecting KaiC phosphorylation rhythms of the cyanobacterial circadian oscillator in vitro and in vivo. *Methods Enzymol* 551:153-173.
- Kim YI, Dong G, Carruthers CW Jr, Golden SS, and LiWang A (2008) The day/night switch in KaiC, a central oscillator component of the circadian clock of cyanobacteria. *Proc Natl Acad Sci U S A* 105:12825-12830.
- Kim YI, Vinyard DJ, Ananyev GM, Dismukes GC, and Golden SS (2012) Oxidized quinones signal onset of darkness directly to the cyanobacterial circadian oscillator. *Proc Natl Acad Sci U S A* 109:17765-17769.
- Ma P, Mori T, Zhao C, Thiel T, and Johnson CH (2016) Evolution of KaiC-dependent timekeepers: a proto-circadian timing mechanism confers adaptive fitness in the purple bacterium *Rhodospseudomonas palustris*. *PLoS Genet* 12:e1005922.
- Montagne M, Martel A, and Le Moual H (2001) Characterization of the catalytic activities of the PhoQ histidine protein kinase of *Salmonella enterica* serovar Typhimurium. *J Bacteriol* 183:1787-1791.
- Nakajima M, Imai K, Ito H, Nishiwaki T, Murayama Y, Iwasaki H, Oyama T, and Kondo T (2005) Reconstitution of circadian oscillation of cyanobacterial KaiC phosphorylation in vitro. *Science* 308:414-415.
- Nishiwaki T, Satomi Y, Kitayama Y, Terauchi K, Kiyohara R, Takao T, and Kondo T (2007) A sequential program of dual phosphorylation of KaiC as a basis for circadian rhythm in cyanobacteria. *EMBO J* 26:4029-4037.
- Nishiwaki T, Satomi Y, Nakajima M, Lee C, Kiyohara R, Kageyama H, Kitayama Y, Temamoto M, Yamaguchi A, Hijikata A, et al. (2004) Role of KaiC phosphorylation in the circadian clock system of *Synechococcus elongatus* PCC 7942. *Proc Natl Acad Sci U S A* 101:13927-13932.
- Pettersen EF, Goddard TD, Huang CC, Couch GS, Greenblatt DM, Meng EC, and Ferrin TE (2004) UCSF Chimera—a visualization system for exploratory research and analysis. *J Comput Chem* 25:1605-1612.
- Rust MJ, Golden SS, and O'Shea EK (2011) Light-driven changes in energy metabolism directly entrain the cyanobacterial circadian oscillator. *Science* 331:220-223.
- Rust MJ, Markson JS, Lane WS, Fisher DS, and O'Shea EK (2007) Ordered phosphorylation governs oscillation of a three-protein circadian clock. *Science* 318:809-812.
- Schmitz O, Katayama M, Williams SB, Kondo T, and Golden SS (2000) CikA, a bacteriophytochrome that resets the cyanobacterial circadian clock. *Science* 289:765-768.
- Shi Y (2009) Serine/threonine phosphatases: mechanism through structure. *Cell* 139:468-484.
- Simons MJ (2009) The evolution of the cyanobacterial post-translational clock from a primitive "phoscillator." *J Biol Rhythms* 24:175-182.
- Snijder J, Schuller JM, Wiegard A, Lossl P, Schmelling N, Axmann IM, Plitzko JM, Forster F, and Heck AJ (2017) Structures of the cyanobacterial circadian oscillator frozen in a fully assembled state. *Science* 355:1181-1184.
- Tauber E, Last KS, Olive PJ, and Kyriacou CP (2004) Clock gene evolution and functional divergence. *J Biol Rhythms* 19:445-458.
- Tomita J, Nakajima M, Kondo T, and Iwasaki H (2005) No transcription-translation feedback in circadian rhythm of KaiC phosphorylation. *Science* 307:251-254.
- Tseng R, Goularte NF, Chavan A, Luu J, Cohen SE, Chang YG, Heisler J, Li S, Michael AK, Tripathi S, et al. (2017) Structural basis of the day-night transition in a bacterial circadian clock. *Science* 355:1174-1180.
- Vakonakis I and LiWang AC (2004) Structure of the C-terminal domain of the clock protein KaiA in complex with a KaiC-derived peptide: implications for KaiC regulation. *Proc Natl Acad Sci U S A* 101:10925-10930.
- Valiev M, Kawai R, Adams JA, and Weare JH (2003) The role of the putative catalytic base in the phosphoryl transfer reaction in a protein kinase: first-principles calculations. *J Am Chem Soc* 125:9926-9927.

The E3 ubiquitin ligase adaptor *Tango10* links the core circadian clock to neuropeptide and behavioral rhythms

Jongbin Lee^{1,2,3,6}, Chunghun Lim^{1,3,6}, Tae-Hee Han^{1&}, Tomas Andreani¹, Matthew Moyer^{4#}, Jack Curran¹, Eric Johnson⁵, William L. Kath⁵, Casey O. Diekman⁴, Bridget C. Lear¹, and Ravi Allada^{1,7,*}

¹ Department of Neurobiology, Northwestern University, Evanston, Illinois 60208

² Department of Biological Sciences, Korea Advanced Institute of Science and Technology, Daejeon 34141, Republic of Korea

³ School of Life Sciences, Ulsan National Institute of Science and Technology, Ulsan 44919, Republic of Korea

⁴Department of Mathematical Sciences, New Jersey Institute of Technology, Newark, New Jersey 07102

⁵Department of Engineering Sciences and Applied Math, Northwestern University, Evanston, Illinois 60208

⁶These authors contributed equally

⁷Lead Contact

[&]Current affiliation: Eunice Kennedy Shriver National Institute of Child Health and Human Development, National Institute of Health, Bethesda, Maryland 20892

[#]Current affiliation: Department of Quantitative Pharmacology & Pharmacometrics (QP2) at Merck & Co. Inc., Kenilworth, New Jersey 07033

^{*}Correspondence: r-allada@northwestern.edu (R.A.)

Summary

Circadian transcriptional timekeepers in pacemaker neurons drive profound daily rhythms in sleep and wake. Here we reveal a molecular pathway that links core transcriptional oscillators to neuronal and behavioral rhythms. Using two independent genetic screens, we identified mutants of *Transport and Golgi 10 (Tango10)* with poor behavioral rhythmicity. *Tango10* expression in pacemaker neurons expressing the PDF neuropeptide is required for robust rhythms. Loss of *Tango10* results in elevated PDF accumulation in nerve terminals even in mutants lacking a functional core clock. TANGO10 protein itself is rhythmically expressed in PDF terminals. Mass spectrometry of TANGO10 complexes reveals interactions with the E3 ubiquitin ligase *Cullin-3 (Cul3)*. *Cul3* knockdown phenocopies *Tango10* mutant effects on PDF independent of the core clock gene *timeless*. Patch clamp electrophysiology in *Tango10* mutant neurons demonstrates elevated spontaneous firing due potentially due to reduced voltage-gated Shaker-like potassium currents. We propose that *Tango10/Cul3* transduces molecular oscillations from the core clock to neuropeptide release important for behavioral rhythms.

Introduction

Circadian (~24 h) clocks govern almost all aspects of behavior and physiology across the animal kingdom. These overt daily behavioral rhythms are driven by oscillatory transcriptional feedback loops whose components are modified by phosphorylation and ubiquitination. In *Drosophila*, the CLOCK(CLK)-CYCLE(CYC) heterodimer activates transcription from *period (per)* and *timeless (tim)* promoters (Allada et al., 1998; Rutila et al., 1998). PER and TIM feedback to inhibit CLK-CYC activity and

suppress their own transcription. CLK-CYC also activates activator *Par Domain Protein-1e* and repressor *vri* (*vri*) which feedback to control *Clk* transcription (Cyran et al., 2003; Glossop et al., 2003). Post-transcriptional control of core clock components also plays a crucial role in sustaining molecular clocks (Kojima et al., 2011; Lim and Allada, 2013a, b; Lim et al., 2011; Lim et al., 2007b; Zhang et al., 2013). Phosphorylation of clock proteins modulates their subcellular localization, activity, and susceptibility to ubiquitin-dependent degradation (Grima et al., 2012; Grima et al., 2002; Ko et al., 2002; Koh et al., 2006; Peschel et al., 2009; Peschel et al., 2006).

Core clock oscillations in about 150 networked pacemaker neurons are responsible for discrete aspects of rhythmic behavior. Of special importance are just 10 Pigment Dispersing Factor (PDF) expressing pacemaker neurons (small ventral lateral neurons; sLN_v) which are critical for free running behavioral rhythms. The sLN_v act as master pacemakers in constant darkness, synchronizing the circadian phase of molecular clocks among PDF and non-PDF expressing groups of clock neurons, including the dorsal lateral neurons (LN_d) and the PDF- sLN_v. Loss of PDF or its receptor result in dramatically reduced free running rhythmicity, highlighting the crucial role of this neuropeptide (Hyun et al., 2005; Im et al., 2011; Lear et al., 2005b; Lin et al., 2004; Mertens et al., 2005; Peng et al., 2003; Renn et al., 1999; Stoleru et al., 2005).

The circadian clock also regulates multiple aspects of pacemaker neural output. Clock regulation promotes rhythmic accumulation of PDF levels (Park et al., 2000) in part through *vri* regulation and the sodium leak channel *narrow abdomen* (*na*) (Blau and Young, 1999; Gunawardhana and Hardin, 2017; Lear et al., 2005a). In addition, the clock also regulates daily structural rhythms in the sLN_v axonal

terminals, including changes in arborization and fasciculation (Fernandez et al., 2007). Structural plasticity rhythms may be mediated by clock transcriptional regulation of *vri*, *Mef2/Fas2*, and *Puratrophin-1-like (Pura)* (Abruzzi et al., 2011; Blanchard et al., 2010; Gunawardhana and Hardin, 2017; Petsakou et al., 2015; Sivachenko et al., 2013). Changes in structural plasticity appear to contribute to behavior under different environmental conditions likely through changes in sensory inputs (Fernandez et al., 2020; Petsakou et al., 2015). However, oscillations in structural plasticity or PDF levels are likely not essential for rhythmic behavior, as strains that lack these rhythms often retain strong behavioral rhythmicity (Blanchard et al., 2010; Kula et al., 2006; Petsakou et al., 2015; Sivachenko et al., 2013), suggesting other mechanisms play a role.

Circadian neurons also exhibit daily rhythms in excitability (Cao and Nitabach, 2008; Flourakis et al., 2015; Sheeba et al., 2008), which may be mediated in part by clock regulation of the sodium leak channel regulator *Nlf-1* and the calcium-dependent potassium channel *Slowpoke* (Ceriani et al., 2002; Fernandez et al., 2007; Flourakis et al., 2015). Notably, acute or chronic hyperexcitation of PDF neurons elevates PDF levels and enhances defasciculation of the sLNv terminals (Herrero et al., 2020; Nitabach et al., 2006; Sivachenko et al., 2013), while acute silencing has opposing effects (Depetris-Chauvin et al., 2011), indicating that changes in clock neuron excitability can affect PDF levels and sLNv morphology. Clock and excitability dependent arborization changes depend on PDF/PDFR, highlighting the critical role for this neuropeptide (Gunawardhana and Hardin, 2017; Herrero et al., 2020). Here we demonstrate that TANGO10-CUL3 defines a novel circadian output pathway important for regulating pacemaker neuron excitability and PDF levels. Loss

of TANGO10-CUL3 severely disrupts free-running rhythmic behavior highlighting its crucial role in neuronal output.

Results

Loss of the BTB adaptor Tango10 strongly reduces free-running rhythms

Identification of novel clock mutants has been an essential strategy to understand how genetic components shape circadian behaviors and clock-relevant physiology. As part of a genetic screen (Pfeiffenberger and Allada, 2012), we identified a P-element insertion allele of *Tango10* (*Tango10^{GG}*) that strongly reduces behavioral rhythmicity, comparable to the strongest clock mutants reported (Figure 1A,B; Figure S1, Table S1). *Tango10^{GG}* head extracts do not express detectable TANGO10 protein, consistent with a strong or complete loss of function allele (Figure 1C). Females trans-heterozygous for *Tango10^{GG}* and chromosomal deletions of the *Tango10* locus display poor rhythmic power similar to hemizygous male flies (Figure 1D; Table S1). Importantly, excision of the P element or transgenic expression of a genomic *Tango10* construct fully reverts/rescues the circadian arrhythmicity of *Tango10^{GG}* mutants (Figure 1E; Table S2).

We independently identified a novel mutant through an X chromosome ethyl methanesulfonate mutagenesis screen for disruptions in circadian and sleep behaviors. We named this mutant *busy run* (*bsr*), based on a Korean word meaning ‘diligent’ and pronounced as [bu:zirʌn]. *bsr* mutants display arrhythmic locomotor behavior in constant darkness comparable to *Tango10^{GG}* mutants (Figure 1A, Table S1). Complementation tests revealed that neither *Tango10^{GG}* nor genomic deletions

spanning the *Tango10* locus rescue *bsr* mutant phenotypes in trans-heterozygous females (Figure 1D; Table S2), suggesting that *bsr* might be a recessive mutant allele of *Tango10*. To assess this possibility, we compared the coding sequences of *Tango10* in wild-type and *bsr* mutants. Indeed, we found a missense mutation in *bsr* mutants that converts phenylalanine at the position of amino acid 462 to leucine (P462L) within the third coding exon of *Tango10* (Figure 1B, Figure S2A). Sequence alignments reveal strong conservation of this residue among TANGO10 homologs including human (Figure S2B), implicating its significance in the structure, stability or function of TANGO10 proteins. Consistent with this hypothesis, we find that TANGO10 proteins are barely detectable in head extracts of *bsr* mutants (Figure 1C). Finally, a genomic transgene harboring a wild-type *Tango10* locus fully rescues the circadian phenotypes in *bsr* mutants (Figure 1E; Table S2). Taken together, these genetic data convincingly demonstrate that *Tango10* is a novel clock gene whose importance for sustaining high-amplitude rhythms is comparable to core clock genes.

***Tango10* functions in PDF neurons to control free-running rhythms**

To determine the anatomical requirements for *Tango10*, we employed GAL4-UAS to express wild-type *Tango10* cDNA in *Tango10^{GG}* mutants in specific tissues and stages. We find that adult-specific *Tango10* induction using the RU486 inducible GeneSwitch system either pan-neuronally or ubiquitously (*elav-geneswitch*GAL4 or *daughterless-geneswitch*GAL4, respectively) restores robust behavioral rhythms in *Tango10* mutants, indicating that *Tango10* functions in adult neurons (Figure 2A; Table S3). In contrast, *Tango10* expression in all (*tim*GAL4) or subsets of (*Clk*GAL4-8.0, *pdf*GAL4) circadian pacemaker neurons, does not rescue *Tango10* mutant rhythms (Figure 2B; Table S4). The lack of rescue using circadian drivers cannot be

attributed to overexpression, as *Tango10* overexpression of *Tango10* in a wild-type background does not reduce rhythmicity (Table S4).

To narrow down the anatomical locus necessary for *Tango10*-dependent clocks, we combined broader Gal4 rescue with different Gal80 transgenes to block GAL4 induction in defined subsets of neurons. We used the broadly expressing GAL4, *30YGAL4* (Yang et al., 1995), which robustly rescues rhythmicity in *Tango10* mutants (Figure 2B, Table S4). *30Y*-driven *Tango10* rescue is blocked using the pan-neuronal *elavGAL80*, confirming a neuronal *Tango10* requirement (Figure 2C, Table S4). *30Y* is notably active in mushroom body neurons (Yang et al., 1995) yet the MB-specific GAL80, *247-Gal80* does not block rescue. On the other hand, blocking *30y* specifically in PDF neurons did substantially suppress rescue of behavioral rhythms. Thus, *Tango10* function in PDF neurons is necessary to drive free running rhythms (Figure 2C; Table S4).

To validate the necessity of *Tango10* in PDF neurons, we silenced endogenous *Tango10* expression in the select neurons by RNA interference (RNAi) and examined effects on circadian locomotor rhythms. We first confirmed that pan-neuronal expression of the *Tango10* RNAi transgene effectively depletes endogenous TANGO10 proteins in fly head extracts, indicating RNAi efficacy and neuronal TANGO10 expression (Figure S3). We further found that *Tango10* depletion in PDF neurons, but not in mushroom body neurons, leads to behavioral arrhythmicity, comparable to that of *Tango10* mutants (Figure 2D; Table S4). Taken together, these data demonstrate that *Tango10* in PDF neurons is necessary for robust rhythmicity in circadian locomotor behavior.

Loss of Tango10 function selectively affects small LN_v PER and TIM oscillations

Daily rhythmic expression of clock proteins underlies circadian locomotor behavior. We thus examined the daily expression of core clock proteins PER and TIM as a measure of molecular clocks. Immunoblotting of adult head extracts at circadian time (CT) 3 and CT15 showed comparable levels of PER and TIM between wild-type and *Tango10* mutants (Figure S4). We also evaluated PER and TIM rhythms in LD in individual groups of circadian pacemaker neurons: PDF⁺ sLN_v and lLN_v and PDF⁻ LN_d and 5th sLN_v (Figure 3). PER and TIM oscillations were evident in all groups of neurons in both wild-type and *Tango10* mutants (Figure 3). Moreover, in most of those groups, levels and oscillation amplitude were comparable between wild-type and *Tango10* mutants, although modest time-dependent changes in protein levels are consistent with a small phase delay in *Tango10* mutants (Figure 3). *Tango10* sLN_v exhibit the most prominent effects with a modest ~30% reduction in peak PER levels (2.5x oscillation in wild-type and 1.9x in *Tango10*) and a ~60% reduction in TIM levels, although TIM levels still oscillate significantly (~3x; Figure 3). Thus, while peak levels are reduced in the sLN_v especially in TIM, both PER and TIM oscillations are still evident.

Loss of Tango10 dramatically elevates PDF levels in clock neuron terminals

The finding of largely intact molecular oscillations suggests that *Tango10* may function to regulate the output of PDF neurons. The molecular clock is thought to transmit timing information in part via the daily rhythm in the circadian neuropeptide PDF. To assess *Tango10* effects on PDF, we examined PDF accumulation at the dorsal axonal terminals of the sLN_v. Wild-type sLN_v display robust PDF rhythms with the peak levels 2 h after lights-on in LD cycle (i.e., zeitgeber time 2; lights-on at ZT0; lights-off at ZT12) (Figure 4A,B) (Park et al., 2000). *Tango10* mutant sLN_v,

however, displayed constitutively high levels of PDF at their axon terminals, dampening PDF rhythms (Figure 4A,B). To address whether these PDF phenotypes are via changes in TIM, we generated double mutants of *Tango10* and *tim⁰¹* and examined PDF expression. We found that loss of *Tango10* results in elevated PDF levels even in a *tim* null mutant background (Figure 4C), indicating a clock-independent role for *Tango10* in the regulation of PDF rhythms.

We next examined the subcellular localization of TANGO10 to determine how it might exert its effects on PDF. Unfortunately, our anti-TANGO10 antibody failed to detect endogenous TANGO10 proteins in whole-mount brains by immunostaining. We thus expressed transgenic TANGO10 proteins with an HA epitope-tag in order to visualize expression in PDF neurons. We confirmed that the *Tango10-HA* transgene strongly rescues *Tango10* mutant rhythms indicating it is functional (Figure 5A). When expressed in PDF neurons, transgenic TANGO10-HA exhibits punctate localization in the axonal tract and terminals of sLN_v neurons (Figure 5B). We observe partial colocalization between PDF and TANGO10-HA expression in the sLN_v terminals, with TANGO10 exhibiting somewhat broader localization (Figure 5B). Moreover, our quantitative analysis revealed robust TANGO10 rhythms at axonal terminals of sLN_v in LD cycles (Figure 5C,D; peak ZT 10, trough ZT 22). These data suggest that rhythmic TANGO10 expression in the dorsal terminals may contribute to rhythmic PDF levels.

Proteomic analysis identifies CUL3 as a TANGO10-interacting partner

Multiple sequence alignments indicate that BTB/POZ and BACK domains implicated in protein-protein interactions are well conserved among TANGO10 homologs (Figure S2B,C). Accordingly, we performed proteomic analyses of

immunoprecipitated TANGO10 protein complexes from fly heads to identify factors mediating *Tango10*-dependent clock function *in vivo*. We first confirmed that a C-terminal triple FLAG tag does not interfere with wild-type *Tango10* function as pan-neuronal expression of the FLAG-tagged TANGO10 rescues behavioral phenotypes in *Tango10* mutants (Table S5). We expressed FLAG-tagged TANGO10 either in clock cells using *timGAL4* or in all postmitotic neurons using *elavGAL4*. The protein complex associating with FLAG-tagged TANGO10 was then affinity-purified by immunoprecipitation at ZT10 and ZT22 and analyzed by mass spectrometry. To identify “hits”, we looked for proteins that were detected in at least two of the four samples but not present in GAL4/+ controls nor in immunoprecipitation of the clock translation factor TWENTY-FOUR (Lim and Allada, 2013a). This strategy revealed 21 overlapping hits from independent proteomic analyses (Table S6). Interestingly, an E3 ligase *Cullin-3* (*Cul3*) was identified as one of the overlapping hits present in both *timGAL4* samples and one out of two *elavGAL4* samples. CUL3 has been proposed to play a role in TIM ubiquitination, contributing to high-amplitude TIM cycling and behavioral rhythms (Grima et al., 2012; Guo et al., 2014; Szabo et al., 2018). TANGO10 and CUL3 co-immunoprecipitate from *Drosophila* S2 cells when transiently transfected. (Figure 6A). We also observed that endogenous CUL3 co-immunoprecipitates with *timGAL4* driven FLAG-tagged TANGO10 further confirming their *in vivo* interactions (Figure 6B). Taken together, these data suggest that TANGO10 and CUL3 form a protein complex to sustain circadian rhythms.

***Cul3* depletion phenocopies the behavioral rhythms and PDF levels of *Tango10* mutants**

To assess *Cul3* function in PDF neurons, we employed *pdf*GAL4 driven *Cul3* RNAi. We find that *Cul3* depletion in PDF neurons severely dampens DD locomotor rhythms (Figure 6C; Table S7), consistent with a prior report (Grima et al., 2012). We next determined if *Cul3*, like *Tango10*, similarly affects PDF levels and find that PDF levels are constitutively high in the axon terminals of *Cul3*-depleted sLNv (Figure 6D,E), phenocopying the effects of *Tango10* mutants. Given the proposed links between CUL3 and TIM, we assessed *Cul3* effects in a *tim* null background (*tim*⁰¹) and find elevated PDF levels similar to what we observe for *Tango10* mutants (Figure 6D,E), supporting a *tim*-independent role of *Cul3* downstream of the clock on PDF. Given the similarity of *Cul3* and *Tango10* phenotypes, we hypothesize that CUL3 employs TANGO10 as an adaptor downstream of the molecular clock to drive PDF and behavioral rhythms.

Loss of Tango10 increases firing rate and depolarizes membrane potential

PDF levels in axonal terminals are also dependent on neuronal excitability (Herrero et al., 2020; Nitabach et al., 2006). To investigate the impact of a *Tango10* mutation on excitability, we performed whole-cell patch electrophysiology on the PDF-expressing large LNv (ILNv). ILNv electrophysiology has been well-studied as their position near the surface of the brain and large soma makes them more accessible compared to other fly clock neurons. We find that *Tango10* mutant ILNv exhibit increased excitability compared to wild-type (Figure 7A). Firing frequency of *Tango10* ILNv neurons is significantly higher compared to wild-type ILNv (Figure 7B). The increase in firing rate of *Tango10* ILNv is linked to a more depolarized membrane potential (Fig 7C, $p < 0.01$). Input resistance of ILNv neurons was measured using a hyperpolarizing current injection protocol, with no significant difference found

between wild-type and *Tango10* (Figure 7D). Cell capacitance was determined from a current step measured in voltage-clamp mode, with *Tango10* ILNv neurons found to have a significantly lower capacitance compared to wild-type during morning hours (Figure 7E). Nonetheless, the finding of elevated excitability in *Tango10* mutant neurons is consistent with a role in neuronal output.

4AP-sensitive I_A potassium current is significantly reduced in *Tango10* mutant ILNv

To investigate which ion channels could be mediating the difference in *Tango10* mutant ILNv, we used voltage clamp electrophysiology. We observed a voltage-gated outward current with fast and slow inactivating components (Figure 8A). We noted that the fast, but not slow, inactivating component was reduced in *Tango10* mutants (Figure 8A-C). We then used pharmacology to block subsets of potassium channels to further resolve the mechanisms underlying *Tango10* hyperexcitability. Whole-cell currents were recorded in the presence of TTX to block sodium channels, before repeating the same voltage-clamp protocol while adding TEA to block voltage-gated potassium channels. The TEA-sensitive current was calculated by subtracting the currents measured in the two conditions (Figure 8D). No significant differences were found in the TEA-sensitive current between wild-type and *Tango10* (Figure 8E). To further interrogate potassium channel currents the same voltage-clamp protocol was performed with the further addition of 4AP to the solution, with the 4AP-sensitive current again calculated using subtraction of the currents evoked in the two conditions. Isolating the 4AP-sensitive current revealed a significant reduction in *Tango10* ILNv neurons, (Figure 8D,8F). The inactivation kinetics and

pharmacological specificity of this current identifies a reduced Shaker-like (I_A) current in *Tango10* mutants.

To determine if reductions in I_A current can explain the increased firing rate observed in *Tango10* mutants, we developed a new mathematical model of ILNv electrophysiology (Table S8). Our model builds on the Smith model of ILNv neurons (Smith et al., 2019) which includes an inward sodium current, an inward calcium current, a leak current, and four outward potassium currents: fast inactivating A-type currents Shaker and Shal, and slow or non-inactivating currents Shab and Shaw. In the Smith model, the potassium current parameters were fit to voltage-clamp data isolating these currents in ILNv neurons, whereas the sodium and calcium current parameters were taken from a previously published model of mammalian circadian clock neurons (Sim and Forger, 2007). For our model, we retained the Smith model potassium current parameters, but refit the sodium and calcium current parameters to current-clamp data from ILNv neurons using data assimilation, a state and parameter estimation technique for optimally combining dynamical models with observations (see Methods). This approach yielded a model that closely matches the firing rate and action potential shape observed in recordings from WT LNV neurons (Figure 8G, S5, S6). We then simulated the model with reduced values of the maximal conductance parameter for the Shaker and Shal currents. We found that a 30% reduction in Shaker/Shal currents can reproduce the increased firing rate phenotype of the *Tango10* mutants (Figure 8G-H).

To experimentally test the contribution of the TEA-sensitive and 4AP-sensitive currents on ILNv neurophysiology, we measured the effects of pharmacological application of the respective drugs upon resting membrane potential, measured in the presence of TTX. Application of TEA resulted in a small

depolarization of membrane potential (~1-2mV), both at morning and evening, with no difference observed between *Tango10* and wild-type (Fig S7A,B). However, application of 4AP caused a larger depolarization (~5-10mV) in wild-type ILNv, with a significantly smaller response in *Tango10* ILNv evident in the evening (Figure S7A,C) providing further evidence for a reduction of the 4AP-sensitive current in *Tango10* ILNv neurons. Interestingly, *Shal* gene expression and current levels are more elevated in the evening consistent with these 4-AP effects (Kula-Eversole et al., 2010; Smith et al., 2019).

Discussion

To discover genes involved in circadian behavior, we performed two large scale genetic screens: one P-element candidate based and the other an unbiased chemical mutagenesis. These divergent approaches independently identified mutants of *Transport and Golgi 10 (Tango10)*, highlighting its pivotal role. These mutants profoundly disrupt free running rhythmicity. Moreover, loss of *Tango10* results in dramatic accumulation of PDF in clock neuron terminals and loss of PDF accumulation rhythms. These effects persist in the absence of a functioning core clock. To better understand the molecular mechanisms by which *Tango10* functions we analyzed TANGO10 complexes using immunoprecipitation and mass spectrometry and found interactions with the E3 ubiquitin ligase *Cullin-3 (Cul3)* and *Cul3* knockdown also results in similar PDF accumulation effects. Patch clamp electrophysiology of PDF neurons demonstrates increased excitability and reduction of Shaker-like potassium currents suggesting that *Cul3/Tango10* effects are via elevated excitability. TANGO10 protein levels also oscillate in these terminals, suggesting they contribute to cellular rhythms. Taken together, this study reveals a

critical ubiquitin-proteasome pathway by which temporal information is conveyed to cellular and behavioral outputs (Figure S8).

This work highlights a novel neuronal output pathway with remarkably robust effects on free-running circadian rhythms. Loss of *Tango10* with two independent alleles results in a substantial reduction in rhythmic power (~ 95% reduction in P-S for the GG allele). Independent alleles were discovered in two phenotype-driven screens. The strength of the rhythmicity phenotype is in contrast with those previously reported for loss-of-function alleles of other putative output genes. Much of the prominent work examining output in circadian neurons has focused on fasciculation/defasciculation of axonal arbors (Petsakou et al., 2015; Sivachenko et al., 2013). While the gold standard loss-of-function genetics (e.g., RNAi or dominant negative manipulations) have profound consequences on rhythmic fasciculation neural states (see Figure 1C in Petsakou et al. 2015) they have limited effects on the crucial functional output of these neurons, circadian behavior (see Figure 4D, Rho1DN, Petsakou et al. 2015 and Table 2 pdf>Mef2 RNAi; Sivachenko et al. 2013). The only studies that have observed large circadian behavioral phenotypes as a result of loss-of-function genetic manipulations are those targeting the PDF neuropeptide itself as well as subunits of the ion channel NARROW ABDOMEN and its regulator NLF-1, which function via excitability (Flourakis et al., 2015; Lear et al., 2013; Renn et al., 1999). Our finding that *Tango10* has profound effects on free running rhythmicity indicates it defines a special pathway crucial for free-running rhythmicity.

Using cell-type specific genetic rescue and quantitative immunofluorescence, we demonstrate that *Tango10* effects on rhythmicity map to just ~20 clock neurons expressing the neuropeptide PDF. RNAi knockdown specifically in the LNV disrupts free running rhythmicity, and LNV expression is required for robust rescue of the

Tango10 rhythmicity phenotype. Moreover, the clock-independent effects of TANGO10 and CUL3 on PDF expression levels map to the PDF-positive LN_v, as elevated PDF levels are observed when RNAi knockdown of either gene is restricted to the PDF neurons (Figure 6B, data not shown). Additionally, the effects of TANGO10 and CUL3 effects on the molecular clock are mainly observed in the sLN_v group and not other pacemaker neuron groups (Figure 3, Grima et al. 2012). Taken together, our data indicate a critical functional requirement for TANGO10-CUL3 in the PDF-positive LN_v to promote molecular and behavioral rhythmicity.

We have demonstrated that *Tango10* likely functions in concert with the E3 ubiquitin ligase *Cul3*, thus defining a role for protein ubiquitination in neuronal output. Proteomic and co-immunoprecipitation experiments indicate that CUL3 and TANGO10 interact *in vivo*. Loss of *Tango10* or *Cul3* function in PDF neurons causes comparable arrhythmicity. Moreover, decreased *Tango10* or *Cul3* function also results in similar molecular phenotypes, including clock-independent elevation of PDF levels. Ubiquitination can serve as a signal for protein degradation and/or traffic proteins to the cell membrane (Foot et al., 2017; Gschweidl et al., 2016). It will be of interest to examine the function of other TANGO10-interacting proteins as potential enzymatic targets of this complex.

Under this model (Figure S8), core clock effects observed may be secondary to *Tango10*-mediated effects on excitability/PDF. In most pacemaker neurons and in whole heads, PER and TIM oscillations are largely intact in *Tango10* mutants. We did observe modest reductions in peak PER levels and more robust reductions in TIM specifically in the sLN_v. Interestingly, these sLN_v phenotypes are very similar to those observed after *Cul3* impairments (Grima et al., 2012). This prior study proposed that CUL3 ubiquitinates TIM, targeting it for degradation. Yet loss of putatively

TIM-degrading *Cul3* results in a *decrease* in peak TIM levels in clock neurons (Figure 2, Grima et al 2012), inconsistent with a direct role in degrading TIM. Moreover, reduction of *Cul3* on its own in vivo does not alter TIM ubiquitination (Szabo et al., 2018).

We believe that our data suggest that these effects are instead due to elevated excitability/PDF signaling. Acute increases in excitability lead to acute reductions in TIM but not PER (Guo et al., 2014). Chronic activation of LNV clock neurons (via expression of the bacterial sodium channel NaChBac) results in reductions in peak levels of the CLK activated transcription factor PDP1 (Nitabach et al., 2006). This effect is comparable to the reduction in peak levels in CLK-activated PER and TIM seen in *Tango10* (Figure 3). *Cul3* has previously been shown to be required for excitation-dependent reductions in TIM (Guo et al., 2014). One possibility is that knockdown of *Cul3*, like *Tango10*, elevates excitability and thus, additional excitation may not be able to further drive down TIM levels. In addition, PDF signaling is also known to feedback and regulate PER and/or TIM levels. The finding that PDF effects of *Tango10* and *Cul3* are evident even in a *tim⁰¹* further cements the notion that core clock effects may be a secondary consequence of its excitability/PDF effects and not due to direct effects on the core clock or TIM. It is worth noting that a *clockwork orange* allele (*cwo^{B9}*) with comparable effects on PER and TIM oscillation amplitude in the sLNV retain more robust rhythms than observed with *Tango10* (Richier et al., 2008), suggesting the core clock effects are not sufficient for the behavioral phenotype.

We hypothesize that the primary effects of *Tango10* are on excitability which in turn regulates PDF levels in the terminals (Figure S8). *Tango10* mutant lLNV exhibit an increased firing rate, possibly due to reductions in I_A current. Electrical

activation of the LNV via NaChBac or TrpA1 each result in elevated PDF, as seen in *Tango10* or *Cul3* reductions (Herrero et al., 2020; Nitabach et al., 2006). Activity-induced increases in PDF may be further sustained by PDF release and PDFR feedback signaling (Herrero et al., 2020).

Our finding of reduced I_A currents in *Tango10* mutants suggest they are a key target for mediating LNV excitability and behavior. Reduction of I_A currents elevates ILNV firing rates and alters the timing of sleep onset (Feng et al., 2018; Smith et al., 2019). We have developed a new computational model for the ILNV that more faithfully recapitulates in vivo activity and this model demonstrates that the changes in I_A observed in *Tango10* can explain the elevated firing rates. The *Shal* transcript expression and current activity are time-dependent peaking in the evening hours suggesting a role in mediating clock control of neuronal excitability (Kula-Eversole et al., 2010; Smith et al., 2019). These results are consistent with time-dependent effects of I_A inhibition in the evening (Figure S7). One possibility is that TANGO10 expression may enhance *Shal* currents in the evening. These effects may be conserved in mammals as reduction in I_A currents also more strongly elevate firing rates at night in the suprachiasmatic nuclei and alter circadian behavior (Granados-Fuentes et al., 2012; Hermansteyne et al., 2017). I_A has also been observed to exhibit time-dependence (Itri et al., 2010). It will be of interest to test the hypothesis that reductions in I_A current may result from reduced ubiquitination of *Shaker/Shal* ion channels or their regulators.

In summary, we demonstrate a novel role for the BTB adapter TANGO10 in regulating LNV excitability and PDF signaling to promote circadian rhythmicity (Figure S8). Our behavioral, molecular and electrophysiological data support a primary role for CUL3-TANGO10 in increasing K current activity to decrease

excitability. These effects on excitability can in turn regulate PDF signaling and levels to affect rhythmic behavior. Molecular clock effects may be downstream or independent of changes in excitability. Future studies will be required to determine whether CUL3/TANGO10 plays a broader role in other neuropeptidergic neurons, particularly in circadian output circuits.

Figure Legends

Figure 1. Loss of Tango10 disrupts behavioral rhythms. (A) Average activity profiles of wild-type and *Tango10* mutant strains during 4 days LD (white and gray background) followed by 7 days DD (gray background). white: light conditions, gray: dark conditions. n=34-59. (B) Schematic diagrams of the *Tango10* transcript and mutations. Untranslated regions are marked as black boxes and coding sequences are shown as white boxes. The *Tango10^{GG}* mutant strain contains a P-element insertion within a coding exon (exon 2) while *Tango10^{bsr}* contains an EMS-mediated missense mutation in exon 3 (P426L), marked with an asterisk. (C) Protein extracts from wild-type, *Tango10* mutant, and heterozygous flies blotted with Rat anti-TANGO10 and anti-Synapsin as loading control. GG indicates *Tango10^{GG}* mutant while *bsr* refers to the *Tango10^{bsr}* mutant. Representative images shown. (D-E) Locomotor rhythmicity, as determined by Chi-squared periodogram analysis over 7 days of constant darkness. Error bars indicate SEM. (D) Complementation rhythmicity data from adult female strains as indicated. Df1 refers to *Df(1)ED7147* while Df2 refers to *Df(1)BSC722* (n=8-51). Statistical significance determined one-way ANOVA followed by Dunnett's comparison test, with comparisons made to wild-type control (**P<0.02, *P<0.05). (E) Excision and genomic rescue rhythmicity data from the adult male strains indicated. ΔGG indicates precise (#5,#6) or mock (#1,#3) excision strains. [*Tango10*#1] and [*Tango10*#2] indicate *Tango10* genomic rescue transgenes (n=12-71). Statistical comparisons made using one-way ANOVA followed by Dunnett's test (excision) or two-way ANOVA followed by Tukey's multiple comparison test (genomic rescue). Asterisks indicated significant difference from corresponding mutant (*Tango10^{GG}* or *Tango10^{bsr}*) (** p < 0.02).

Figure 2. Tango10 expression in PDF neurons and adult stage-specific expression are important for sustaining rhythmic behavior. (A-D) Assessment of behavioral rhythmicity in *Tango10* mutant, rescue, and RNAi strains, as determined using chi-squared periodogram analysis. GG indicates *Tango10*^{GG} mutant allele. Error bars indicate SEM. (A) Adult-specific expression of Tango10 in *Tango10*^{GG} mutants, using *elav-GeneSwitch*GAL4 (Elav GS) and *daughterless-GeneSwitch*GAL4 (Da GS). Flies in which *Tango10* expression is induced in adulthood (RU486) exhibit increased behavioral rhythmicity compared to ethanol (EtOH) fed flies (n= 8-22). Statistical significance determined by Student's t-test (**P<0.02). (B) *30Y*Gal4 restored rhythmicity of *Tango10*^{GG} mutants in contrast to circadian Gal4s including *Pdf*GAL4, *tim*GAL4, and *Clk8.0*GAL4 (*Clk*GAL4; n=19-79). Statistical significance between Gal4 crossed lines and iso31 crossed control was determined by Student's t-test (**P<0.02) (C) Elav- and Pdf-Gal80 blocked the rescue of rhythmicity by *30Y*Gal4 driven Tango10 expression (n=15-39). Statistical significance of GAL80 compared to control (*30Y*Gal4 mediated Tango10 expressed flies) was determined by one-way ANOVA with Dunnett's multiple comparisons test. (**P<0.02, N.S. : Not Significant) TANGO10 : *uas-Tango10* (D) RNAi- depletion of Tango10 in clock neurons phenocopies *Tango10*^{GG} mutants. *Dicer2*(DCR) was combined with Gal4s to increase RNAi efficiency (n=32-44). Statistical significance was determined by Student t-test between RNAi and Gal4 heterozygous controls (**P<0.02).

Figure 3. Clock oscillations are dampened in s-LNvs in *Tango10* mutants.

Intensity of PER (A) and TIM (B) in confocal images of brains were normalized to

averaged signal intensity of wild-type at zeitgeber time (ZT), normalized to average wild-type (WT) signal within each experiment. 7-9 hemispheres were imaged for each time-point per genotype per experiment, n=2 experiments. Wild-type and *Tango10* measurements were compared at each time-point using Student's t-test (* p < 0.05, ** p < 0.02). l-LNvs : large-ventral lateral neurons, s-LNvs: small-ventral lateral neurons, 5th: PDF negative LNv, LNds : dorsal lateral neurons (C-D) Representative confocal images of s-LNvs in wild-type (C) and *Tango10* mutants (D). Proteins are labeled as follows: PER(red), PDF(blue), TIM(green).

Figure 4. Loss of *Tango10* results in elevated PDF independent of *timeless*

function. (A) Representative Z-stacked maximum intensity projection images of PDF staining in dorsal terminals of sLNv under LD conditions. WT refers to wild-type, GG indicates *Tango10^{GG}* mutant. ZT indicates Zeitgeber Time. (B) Quantification of PDF intensity in dorsal projection of s-LNvs from Z-stacked images. Section images were stacked as maximum intensity projection. Integrated densities above threshold were measured and normalized to averaged measurement of wild type and *Tango10* mutants at ZT2 (set as 1). Normalized value from two experiments (N=7~13 per genotype at each time point) were combined and samples were compared by Student's t-test at each time point (* p < 0.05, **p < 0.02). (C) Representative images of and quantitation of PDF signal in dorsal projections of s-LNvs of *tim⁰¹* and *Tango10^{GG}* *tim⁰¹* at ZT15. GG; *tim⁰¹*: *Tango10^{GG}*; *tim⁰¹*. Quantification of PDF images in dorsal projections performed as in Figure 4B, except normalized to *tim01* ZT 15 (average set to 1; n=22-24). Genotypes compared by Student t-test, (**P<0.02).

Figure 5. Transgenic Tango10 protein localizes to and oscillates in PDF neuron dorsal terminals. (A) Rescue of behavioral rhythmicity using UAS-*Tango10HA* construct vs. wild-type (WT) in *Tango10^{GG}* mutants (GG) using *30YGAL4*, analyzed over 7 days DD using Chi-squared periodogram analysis. Student's t-test, $P < 0.001$ (***). (B) Confocal images of a representative *pdfGAL4* UAS-*Tango10HA* brain colabeled for PDF (green) and TANGO10-HA (red) in the sLNv dorsal terminals at ZT15. (C-D) *PdfGAL4* driven TANGO10-HA cycles in the s-LNv dorsal projections. (C) Quantification of HA and PDF signal, performed as in Fig 4. ZT = Zeitgeber Time, gray area of chart indicates dark phase while white area indicates light phase. PDF intensity at ZT2 was set to 1 in three independent experiments. Sample size were 27-38 at each time point. Tango10-HA cycling was detected by one-way ANOVA followed by Turkey's post hoc test ($p < 0.01$). (D) Representative max projection images of TANGO10-HA staining at the timepoints indicated from *pdfGAL4* UAS-*Tango10HA* brains.

Figure 6. Depletion of TANGO10 interactor CUL3 in PDF neurons phenocopies *tim*-independent PDF expression phenotype observed in *Tango10* mutants. (A-B) Co-immunoprecipitation of CUL3 and TANGO10 in *Drosophila* tissues. (A) Representative Western blots of input and immunoprecipitation (IP) samples from S2 cells transfected with CUL3-V5 and/or TANGO10-HA as indicated. (B) Western blot analysis of input and IP samples of adult head extracts upon transgenic expression of FLAG-tagged TANGO10 using *timGAL4*, compared to *timGAL4*/ wild-type (WT) control, assayed by anti-FLAG and anti-CUL3. CUL3 is detected in input blots as well as IP blots for samples in which TANGO10-FLAG is co-transfected. A non-specific band (NS) is observed in both IP samples independent of TANGO10-FLAG

transfection, but the size of this band is larger than CUL3. (C) *Cul3* depletion in circadian neurons including PDF+ cells induces decreased rhythmicity. *Cul3* RNAi refers to NIG strain 11861R-2, pDCR2: *PdfGal4*, Uas-dicer2, tDCR2: *timGal4*, Uas-dicer2. Power of rhythmicity determined using Chi-squared periodogram. Statistical significance determined by Student t-test compared to Gal4 heterozygous control (**P<0.02). (D-E) PDF intensity in dorsal lateral projection of LNvs increased by *Cul3* depletion in PDF neurons at Zeitgeber Time 14 (ZT14) and is independent from *timeless*. PD2: *PdfGal4* UAS-dicer2. (D) PDF signal analyzed similarly to data in Figure 4C. Relative values from two experiments were averaged. *Cul3* depletion in PDF neurons has a significant effect.: Two-way ANOVA, $F(1, 56) = 27.33$, $P < 0.0001$. There was no effect of *tim*⁰¹ in Tukey's multiple comparisons test, whereas *pdfGAL4* UAS-Dcr2 *Cul3* RNAi is significantly different from RNAi control in both *tim*⁺ and *tim* mutant backgrounds (* $p < 0.05$, ** $p < 0.02$). (E) Representative PDF staining images of dorsal projection of LNvs in *Cul3* depleted flies and RNAi controls in a *tim*⁺ or *tim*⁰¹ background at ZT14.

Figure 7. Loss of *Tango10* increases excitability in PDF neurons. (A)

Representative current-clamp recordings at ZT0~4 (top) and ZT8~12 (bottom) of wild-type (WT) (left) and *Tango10*^{GG} (right). (B) Summary bar graphs showing mean firing rate of WT (n = 18 at ZT0~4; n = 21 at ZT8~12) and *Tango10*^{GG} mutant (n = 19 at ZT0~4; n = 19 at ZT8~12). (C) Summary bar graphs showing mean membrane potential (MP) of WT (n = 18 at ZT0~4; n = 21 at ZT8~12) and *Tango10*^{GG} (T10) mutants (n = 19 at ZT0~4; n = 19 at ZT8~12). Values are means ± SEM. **P < 0.01 by Student's t-test. (D) Input resistance was measured in current clamp from the voltage response to hyperpolarizing current steps. No difference was found between

WT and *Tango10* at both morning and evening (Student's t-test). (E) Cell capacitance of *Tango10^{GG}* l-LNv neurons is significantly lower than WT at morning hours (** $p < 0.02$) but not evening ($p = 0.11$), as determined by Student's t-test.

Figure 8. Decreased I_A current in *Tango10* mutants may underlie increased firing rate. (A-C) A) Whole-cell current traces induced by step pulse to potentials between -120 and +100 mV with 10 mV increment in WT (top) and *Tango10^{GG}* mutant (bottom). Pulse protocols for recording whole-cell currents (inset). (B and C) I-V show mean whole-cell current densities for the peak current (IK fast; fig B) and the late portion (IK slow; fig C) of the current of lLNv in WT ($n = 14$ at ZT0~4; $n = 12$ at 8~12) and *Tango10* mutant ($n = 17$ at ZT0~4; $n = 13$ at ZT8~12). The amplitude of $I_{K_{fast}}$ current was significantly lower in lLNv from *Tango10* mutant compared with wild-type (two-way ANOVA, $p < 0.0001$). (Cont ZT0~4 vs. Mutant ZT0~4, Cont ZT8~12 vs. Mutants ZT8~12; $P < 0.05$ by Two-Way ANOVA; $\#P < 0.05$, Tukey's HSD test). (D-F) TEA-sensitive and 4AP-sensitive current in WT and *Tango10* mutant. (D) TEA-sensitive outward current (top traces) and 4AP-sensitive outward current (bottom traces), respectively. (E) I-V show mean TEA-sensitive current densities of lLNv in WT ($n = 7$ at ZT0~4; $n = 6$ at 8~12) and *Tango10* ($n = 5$ at ZT0~4; $n = 7$ at ZT8~12). (F) I-V show mean 4AP-sensitive current densities of lLNv in WT ($n = 7$ at ZT0~4; $n = 6$ at 8~12) and *Tango10^{GG}* mutants ($n = 5$ at ZT0~4; $n = 7$ at ZT8~12). The amplitude of 4AP-sensitive current was significantly lower in lLNv from *Tango10* mutant compared with wild-type animal (two-way ANOVA, $p < 0.0001$). (Cont ZT0~4 vs. Mutant ZT0~4, Cont ZT8~12 vs. Mutants ZT8~12; $P < 0.05$ by Two-Way ANOVA; $\#P < 0.05$, Tukey's HSD test). (G) Simulations of mathematical models of WT (top trace, firing rate ~ 1 Hz) and *Tango10* mutant

(bottom trace, firing rate ~ 4 Hz) in l-LNv neurons. (H) Firing rate of model as a function of the percentage reduction in Shaker/Shal current, with red dot (30% reduction) and gray dot (0% reduction) corresponding to the *Tango10* and WT models shown in (G), respectively.

Acknowledgements

This work was supported by NINDS R01NS106955 and Simons Foundation/SFARI 735135 to R.A., National Science Foundation DMS 155237 and a US-UK Fulbright Commission award to C.O.D, and Department of Defense W911NF-1-6-1-0584 to R.A. and C.O.D. MJM and COD also gratefully acknowledge the financial support of the EPSRC via grant EP/N014391/1.

STAR METHODS

RESOURCE AVAILABILITY

Lead Contact

Further information and requests for resources and reagents should be directed to and will be fulfilled by the Lead Contact, Ravi Allada (r-allada@northwestern.edu).

Materials Availability

Drosophila strains and antibodies generated in this study are available upon request.

EXPERIMENTAL MODEL AND SUBJECT DETAILS

***Drosophila* strains**

All flies used this study were raised at 25° C, 60% humidity with standard cornmeal food under 12hr:12hr light-dark cycles. Behavioral assays and immunostaining utilized male flies except for complementation assays performed in females. Proteomic and co-immunoprecipitation used a mix of males and females. *w¹¹¹⁸* (iso31) was used as a wild-type strain (Bloomington Drosophila Stock center, 5905). *Tango10^{GG}* (aka *Tango10^{GG01371}*) and *Tango10* deficiency strains were also obtained from the Bloomington Stock Center (stock numbers 12775 (*Tango10^{GG01371}*), 9171 (*Df(1)ED7147*), and 26574 (*Df(1)BSC722*)). The *Tango10^{GG}* rhythmicity phenotype was initially identified from a screen for putative loss-of-function mutations covering 1015 genes (Pfeiffenberger and Allada, 2012). *Tango10^{bsr}* was isolated as part of an EMS mutagenesis screen in which F1 progeny of mutagenized *w¹¹¹⁸* males X C(1)DX females were assayed for locomotor behavioral phenotypes (Bokel, 2008). *Tango10^{GG}* excision strains were generated using P-element transposition. The following *Tango10* transgenic flies were generated through embryo injection by BestGene (Chino Hills, CA): UAS-*Tango10* (no tag), UAS-*Tango10-HA*, UAS-*Tango10-3XFLAG*. *Tango10* RNAi (strain 103920) and UAS-Dcr2 strains were obtained from Vienna Drosophila Stock Center. *Cullin-3* RNAi was obtained from NIG-FLY stock center (11861R-1). Elav-Gal4 (Lin and Goodman, 1994), Pdf-Gal4 (Renn et al., 1999), tim-Gal4 (Kaneko and Hall, 2000), Clk4.1-Gal4 (Zhang et al., 2010), 30Y-Gal4 (Yang et al., 1995), 247-Gal4 (Zars et al., 2000), Elav-Gal80 (Rideout et al., 2010), Pdf-Gal80 (Stoleru et al., 2004), 247-Gal80 (Krashes et al., 2007), *tim⁰¹* (Sehgal et al., 1994), *per⁰¹* (Konopka and Benzer, 1971), Elav-GeneSwitch (Osterwalder et al., 2001), and Da-GeneSwitch (Tricoire et al., 2009) were described previously.

Cell lines.

Drosophila Schneider 2 cells (S2-R+) (*Drosophila* Genomics Resource Center), which are derived from Oregon R late embryonic stage male tissue, were cultured in Shields and Sang M3 Insect Medium (Sigma aldrich) containing 10% FBS and 1% Penicillin-Streptomycin at 25°C.

METHOD DETAILS

Fly locomotor analysis

Drosophila locomotor behavioral assays were performed as described previously (Lim et al., 2007a). Briefly, crosses and strains were raised at 25° C and individual progeny were loaded into tubes containing 1% agar, 5% sucrose food and monitored using the DAM (*Drosophila* activity monitor, Trikinetics) system under 5 days of 12 hour light: 12 hour dark cycle followed by 7 days of constant darkness (DD) at 25° C. Period was calculated from chi square periodogram using Clocklab (Actimetrics). Rhythmic power of individual fly was calculated from Power-significance (P-S) and averaged in each genotype, and percent rhythmic was defined as percentage of flies with P-S value ≥ 10 . For GeneSwitch crosses, 1-3 day old flies were maintained on standard *Drosophila* food supplemented with 250 μ M RU486 in EtOH or EtOH alone for 5 days. Flies were then loaded into agar-sucrose behavior tubes, again containing either RU486 or EtOH, and activity was monitored using the DAM system as above.

Plasmids

The coding region of Tango10 was subcloned from DGRC, HL07962 into modified pAc5.1 (untagged, 3X-HA, or 3X-FLAG tags). Constructs were then subcloned into

pUAS-C5 for generation of transgenic strains. The Tango10 genomic locus, spanning 2969 bp upstream and 435bp downstreams of the transcript region, was subcloned into pCasper vector. A 3X HA tag was cloned in between the c-terminus of Tango10 and the 3' untranslated region. The Cul3-V5 expression vector was described previously (Pfeiffenberger and Allada, 2012).

Antibody generation

Rat anti-TANGO10 antibodies were generated using full length GST-Tango10 (Cocalico Biologicals). Mouse anti-TANGO10 antibodies were generated using AKMVWGEDVP as epitope (Abmart).

Immunohistochemistry

Flies aged \geq 5 days old were entrained at least 2 days before dissection.

Immunostaining was performed as in (Lim et al., 2011). Fly brains were dissected at the indicated time and fixed in 4% formaldehyde in PBS for 30 min at room temperature (RT). Brain samples were blocking with 5% normal goat serum in 0.3% triton X-100 in PBS for 30min in RT. Primary antibodies were diluted in PBST containing 5% normal goat serum and incubated in 4°C overnight. Binding with secondary antibodies in PBST was done in 4°C overnight. Samples were mounted using Vectashield (Vector Labs). The antibodies used for immunostaining were as follows: anti-mouse-PDF C7 (1:800, DSHB), anti-rabbit-PER (1:200, gift from EY.Kim), anti-guinea pig-TIM (1:5000,(Barbagallo et al., 2010)), anti-rat-HA (1:2000, Sigma-Aldrich), anti-rabbit-PDF (1:2000, gift from Choe) Alexa488, Alexa 594, Alexa 647 conjugated secondary antibodies (Invitrogen) were diluted as 1:800.

Imaging was performed by confocal microscopy using a Nikon C2 or Zeiss LSM780 confocal microscope system.

Quantification of immunostaining

Images were processed using NIH ImageJ. Images of dorsal projections of sLNv were Z-stacked as maximum intensity projection. Z-stacked images were thresholding and integrated density of dorsal terminals were measured and averaged for each genotype. Quantification of PER, TIM in clock cells was performed as described previously (Lim et al., 2011).

S2 cell culture

The Drosophila S2 cells were grown in Shields and Sang M3 Insect Medium (Sigma-Aldrich) containing 10% FBS and 1% Penicillin-Streptomycin. The expression plasmids were transiently transfected using effectene (Qiagen) followed by manufacturer's protocol. Cell were harvested at 72hr post transfection.

Immunoprecipitation

Fly heads or S2 cell were lysed in T300 buffer (25mM Tris-Cl pH 7.5, 300mM NaCl, 10% glycerol, 1mM EDTA, 0.5% Nonidet P-40, 1mM dithiothreitol, 1mM phenylmethylsulfonyl fluoride). After centrifugation, the same volume of T0 (without NaCl from same recipe of T300) was added to lysates and bound to Flag beads or V5 beads (Sigma-Aldrich) for 1hr 30min in 4°C. Beads-bound protein was eluted by boiling with SDS sample buffer after 3 washes.

Western blot

For immunoblotting of heads extract, 40 heads of male flies were collected and frozen at indicated time. Heads were homogenized with T300 buffer and protein samples were loaded onto acrylamide gels. Proteins were transferred on nitrocellulose membranes (GE health) and the membranes incubated with rat anti-Tango10 (Fig1), mouse anti-Tango10 (Fig S3), mouse anti-Synapsin (Developmental Studies Hybridoma Bank 3C11), rat anti-GE-1 (Eulalio et al., 2007), mouse anti-CUL3 (BD Biosciences 611848), mouse anti-V5 (ThermoFisher), rat anti-HA (Sigma Aldrich), rabbit anti-PER (Stanewsky et al., 1997), guinea pig anti-TIM (Lim et al., 2007b), mouse anti-Actin (Developmental Studies Hybridoma Bank, JLA20), and anti-Flag. The blots were detected using ECL prime (GE Healthcare). Quantitations were performed using Image J from two separate experiments (Figure S4).

Proteomics

Triple Flag tagged Tango10 expressed S2 cells and fly heads (*tim Gal4/UAS-Tango10-3xFlag, elav Gal4/Y; UAS-Tango10-3xFlag/+*) were harvested and immunoprecipitated with Flag beads at ZT 10 or ZT 22, as in (Lim and Allada, 2013a), with n=1 experiment per timepoint for each GAL4. Bound proteins were eluted using 3xFlag peptides (Sigma). The eluted solution were subject to LC-MS/MS and data analysis by the Northwestern Proteomics Core Facility. The proteomics hits were identified from analysis using Proteome Discoverer software ver 1.3 (Thermo Scientific), with hits for each GAL4 defined as proteins identified from either or both timepoints. Proteins identified in any GAL4-only controls were excluded. Proteins identified in proteomic analysis of Flag tagged TWENTY-FOUR (TYF) in fly heads (Lim and Allada, 2013a) were also removed from the hit list to improve specificity.

Electrophysiology

Brains from adult male *Drosophila* were removed from their heads in ice-cold control recording solution (in mM: 101 NaCl, 1 CaCl₂, 4 MgCl₂, 3 KCl, 5 glucose, 1.25 NaH₂PO₄, and 20.7 NaHCO₃, pH 7.2, 250 mOsm). The connective tissue, air sacs, and trachea were removed with fine forceps. No enzymatic treatment was used to avoid removing ion channels from the cell surface. Brains were then transferred to a recording chamber and held ventral side up with a harp slice grid. Brains were allowed to rest in continuously flowing oxygenated saline (95% oxygen and 5% carbon dioxide) for at least 10 min and no more than 2 h before recording. Perfusion with oxygenated saline was continued throughout the recording period. Time of recording is used to determine Zeitgeber Time (ZT).

Whole brain electrophysiology experiments were performed on an Ultima two-photon laser scanning microscope (Bruker, former Prairie Technologies, Middleton, WI) equipped with galvanometers driving a Coherent Chameleon laser. Fluorescence was detected via photomultiplier tubes. Images were acquired with an upright Zeiss Axiovert microscope with a 40×0.9 numerical aperture water immersion objective at 512 pixels × 512 pixels resolution and 1-μm steps. Current-clamp and voltage-clamp recordings were performed with thick-walled borosilicate glass electrodes (1B150F-4; World Precision Instruments) ranging in resistance 10–14 MΩ filled with internal solution containing the following (in mM): 102 K-gluconate, 0.085 CaCl₂ 1.7, MgCl₂, 17 NaCl, 0.94 EGTA, 8.5 HEPES, 4 Mg-ATP, 0.3 Tris-GTP, and 14 phosphocreatine (di-tris salt), pH 7.2, 235 Osm. To visualize the recorded cell, Alexa Fluor 594 biocytin (10μM) was added into the intracellular solution. Recordings were made using Axopatch 200B patch-clamp amplifier, digitized with a

Digidata 1320 A, and acquired with pCLAMP software (Axon Instruments, Union City, CA).

To determine firing frequency from current-clamp data, action potentials (APs) were detected by applying a median filter to the data, after which a set of biologically feasible thresholds were applied and used to count peaks in the signal. The most robust peaks were selected using the threshold that corresponded to the maximal voltage difference without changing the number of detected peaks. To assess membrane potential from current-clamp data, a 10th percentile windowed filter was applied and the membrane potential was estimated as the average of this filtered signal. See also (E.M. Johnson and W.L. Kath, Program No. 432.19, Society for Neuroscience, 2019).

Mathematical Modeling of ILNv Electrophysiology

Our conductance-based model is based on the Smith model of LNv neuron electrophysiology (Smith et al., 2019) and includes a voltage-gated sodium current (I_{Na}), a voltage-gated calcium current (I_{Ca}), four voltage-gated potassium currents (I_{Kv1} , I_{Kv2} , I_{Kv3} , I_{Kv4}), a sodium leak current ($I_{leak,Na}$) and a potassium leak current ($I_{leak,K}$):

$$\begin{aligned}
 C \frac{dV}{dt} = & I_{app} - g_{Na} m_{Na}^3 h_{Na} (V - E_{Na}) \\
 & - g_{Ca} m_{Ca} h_{Ca} (V - E_{Ca}) \\
 & - g_{Kv1} m_{Kv1}^4 h_{Kv1} (V - E_K) - g_{Kv2} m_{Kv2}^4 (V - E_K) \\
 & - g_{Kv3} m_{Kv3}^4 h_{Kv3} (V - E_K) - g_{Kv4} m_{Kv4}^4 h_{Kv4} (V - E_K) \\
 & - g_{leak, Na} (V - E_{Na}) - g_{leak, K} (V - E_K)
 \end{aligned}$$

$$x_{\infty}(V) = \frac{1}{1 + e^{-\frac{V-V_h}{k}}}$$

$$\tau_x(V) = Amp \times e^{-\frac{V-V_{\max}}{\sigma}}$$

The potassium channels Shaker, Shab, Shaw, Shal are the *Drosophila* orthologues of the mammalian Kv1, Kv2, Kv3, and Kv4 channels, respectively. For the Smith model, these four potassium currents were fit to voltage-clamp data from ILNv neurons to characterize the kinetic parameters associated with their steady state activation, x_∞ , and time constants, τ_x . However, in the Smith model the kinetic parameters of the sodium and calcium currents were used unaltered from a previously published model of mammalian suprachiasmatic nucleus (SCN) neurons (Sim and Forger, 2007).

Simulations of the Smith model show a discrepancy with our LNV recordings in terms of action potential amplitude and shape (Figure S6), presumably due to misspecified sodium and calcium kinetics. To address this issue, we employed data assimilation (DA) to fit the parameters of the sodium and calcium currents from current-clamp recordings from LNV neurons. Data assimilation is a technique for obtaining optimal state and parameter estimates for dynamical models directly from observations. DA was originally developed for numerical weather prediction but has recently been utilized in neuroscience applications (Moye and Diekman, 2018; Schiff, 2012). Here we used an implementation of a variational DA algorithm previously applied to fit models to current-clamp data from SCN neurons, see (Bano-Otalora et al., 2020) for a detailed description of our implementation and its mathematical representation. This approach can simultaneously estimate the mean trajectory of the state variables (V , m , h) and parameters of our model. To simplify the optimization problem, we assume a more stable form of the rate kinetics:

$$x_\infty(V) = \frac{1}{2} + \frac{1}{2} \tanh\left(\frac{V - vx}{d vx}\right)$$

$$\tau_x(V) = \tau_{x0} + \tau_{x1} \left(1 - \tanh^2\left(\frac{V - vxt}{d vxt}\right)\right)$$

for $x = m_{\text{Na}}, h_{\text{Na}}, m_{\text{Ca}}, h_{\text{Ca}}$. For m_{Ca} , the time constant is assumed to be voltage-independent, i.e. $\tau_x(V) = \tau_{x0}$. We are estimating each of the parameters in these equations in addition to the maximal conductances $g_{\text{Na}}, g_{\text{Ca}}, g_{\text{leak, Na}}, g_{\text{leak, K}}$. The Smith model has a single leak current, but here we separate the leak into sodium and potassium components as in previous SCN models (Diekman et al., 2013; Flourakis et al., 2015).

In variational DA, a very high-dimensional optimization problem is constructed where each model state variable, parameter, and time point adds one dimension. The fact that each time point included increases the dimension of the optimization problem, combined with the high sampling rate (10 kHz) required for current-clamp experiments to accurately capture action potential waveforms, means that only a relatively small amount of data (a few seconds at most) can be assimilated before the optimization problem becomes too large to be solved. To increase the amount of information contained in these short windows of data, previous work with DA and conductance-based models have utilized current-clamp recordings performed with complex time-varying stimuli (Meliza et al., 2014) or a series of current pulses (Bano-Otalora et al., 2020). In this work, we are able to fit models with DA in the absence of input currents to stimulate the neuron, i.e. using spontaneous firing activity alone.

Since LNV neurons fire slowly, there may only be one or two action potentials present in the short window of data that can be used for DA due to constraints on the size the optimization problem that can be solved. Thus, rather than using a raw voltage trace as the data for the DA algorithm, we elected to use an average AP waveform obtained from multiple APs in a current-clamp recording (Figure S7A). We extracted 30 APs from this trace and aligned them at the time point where the voltage crossed a spike threshold of -35 mV (Figure S7B). We then computed the mean membrane potential

across these aligned APs at each point in time for a window of 350 ms prior to and 400 ms after the threshold crossing. This average AP waveform was then used as the data (observations) for our DA algorithm. To our knowledge, the use of an average AP waveform as the observations is a novel contribution to DA methodology for constructing models of slow spontaneously firing neurons. We ran our DA algorithm starting from over 100 different initial conditions to select the parameters for the WT model (Figure S6 and Table S8). MATLAB code to perform simulations of the model is available at ModelDB (<https://senselab.med.yale.edu/modeldb/>).

References

- Abruzzi, K.C., Rodriguez, J., Menet, J.S., Desrochers, J., Zadina, A., Luo, W., Tkachev, S., and Rosbash, M. (2011). *Drosophila* CLOCK target gene characterization: implications for circadian tissue-specific gene expression. *Genes & development* 25, 2374-2386.
- Allada, R., White, N.E., So, W.V., Hall, J.C., and Rosbash, M. (1998). A mutant *Drosophila* homolog of mammalian Clock disrupts circadian rhythms and transcription of period and timeless. *Cell* 93, 791-804.
- Bano-Otalora, B., Moye, M.J., Brown, T.M., Lucas, R.J., Diekman, C.O., and Belle, M.D.C. (2020). Daily electrical activity in the master circadian clock of a diurnal mammal. *bioRxiv*, 2020.2012.2023.424225.
- Barbagallo, B., Prescott, H.A., Boyle, P., Climer, J., and Francis, M.M. (2010). A dominant mutation in a neuronal acetylcholine receptor subunit leads to motor neuron degeneration in *Caenorhabditis elegans*. *J Neurosci* 30, 13932-13942.
- Blanchard, F.J., Collins, B., Cyran, S.A., Hancock, D.H., Taylor, M.V., and Blau, J. (2010). The transcription factor Mef2 is required for normal circadian behavior in *Drosophila*. *J Neurosci* 30, 5855-5865.
- Blau, J., and Young, M.W. (1999). Cycling vrilie expression is required for a functional *Drosophila* clock. *Cell* 99, 661-671.
- Bokel, C. (2008). EMS screens : from mutagenesis to screening and mapping. *Methods Mol Biol* 420, 119-138.
- Cao, G., and Nitabach, M.N. (2008). Circadian control of membrane excitability in *Drosophila melanogaster* lateral ventral clock neurons. *The Journal of neuroscience : the official journal of the Society for Neuroscience* 28, 6493-6501.
- Ceriani, M.F., Hogenesch, J.B., Yanovsky, M., Panda, S., Straume, M., and Kay, S.A. (2002). Genome-wide expression analysis in *Drosophila* reveals genes controlling circadian behavior. *J Neurosci* 22, 9305-9319.
- Cyran, S.A., Buchsbaum, A.M., Reddy, K.L., Lin, M.C., Glossop, N.R., Hardin, P.E., Young, M.W., Storti, R.V., and Blau, J. (2003). vrilie, Pdp1, and dClock form a second feedback loop in the *Drosophila* circadian clock. *Cell* 112, 329-341.
- Depetris-Chauvin, A., Berni, J., Aranovich, E.J., Muraro, N.I., Beckwith, E.J., and Ceriani, M.F. (2011). Adult-specific electrical silencing of pacemaker neurons uncouples molecular clock from circadian outputs. *Curr Biol* 21, 1783-1793.
- Diekman, C.O., Belle, M.D., Irwin, R.P., Allen, C.N., Piggins, H.D., and Forger, D.B. (2013). Causes and consequences of hyperexcitation in central clock neurons. *PLoS Comput Biol* 9, e1003196.
- Eulalio, A., Behm-Ansmant, I., Schweizer, D., and Izaurralde, E. (2007). P-body formation is a consequence, not the cause, of RNA-mediated gene silencing. *Mol Cell Biol* 27, 3970-3981.
- Feng, G., Zhang, J., Li, M., Shao, L., Yang, L., Song, Q., and Ping, Y. (2018). Control of Sleep Onset by Shal/Kv4 Channels in *Drosophila* Circadian Neurons. *J Neurosci* 38, 9059-9071.
- Fernandez, M.P., Chu, J., Villella, A., Atkinson, N., Kay, S.A., and Ceriani, M.F. (2007). Impaired clock output by altered connectivity in the circadian network. *Proc Natl Acad Sci U S A* 104, 5650-5655.
- Fernandez, M.P., Pettibone, H.L., Bogart, J.T., Roell, C.J., Davey, C.E., Pranevicius, A., Huynh, K.V., Lennox, S.M., Kostadinov, B.S., and Shafer, O.T. (2020). Sites of Circadian Clock Neuron Plasticity Mediate Sensory Integration and Entrainment. *Curr Biol* 30, 2225-2237 e2225.

Flourakis, M., Kula-Eversole, E., Hutchison, A.L., Han, T.H., Aranda, K., Moose, D.L., White, K.P., Dinner, A.R., Lear, B.C., Ren, D., *et al.* (2015). A Conserved Bicycle Model for Circadian Clock Control of Membrane Excitability. *Cell* 162, 836-848.

Foot, N., Henshall, T., and Kumar, S. (2017). Ubiquitination and the Regulation of Membrane Proteins. *Physiol Rev* 97, 253-281.

Glossop, N.R., Houl, J.H., Zheng, H., Ng, F.S., Dudek, S.M., and Hardin, P.E. (2003). VRILLE Feeds Back to Control Circadian Transcription of Clock in the Drosophila Circadian Oscillator. *Neuron* 37, 249-261.

Granados-Fuentes, D., Norris, A.J., Carrasquillo, Y., Nerbonne, J.M., and Herzog, E.D. (2012). I(A) channels encoded by Kv1.4 and Kv4.2 regulate neuronal firing in the suprachiasmatic nucleus and circadian rhythms in locomotor activity. *J Neurosci* 32, 10045-10052.

Grima, B., Dognon, A., Lamouroux, A., Chelot, E., and Rouyer, F. (2012). CULLIN-3 controls TIMELESS oscillations in the Drosophila circadian clock. *PLoS Biol* 10, e1001367.

Grima, B., Lamouroux, A., Chelot, E., Papin, C., Limbourg-Bouchon, B., and Rouyer, F. (2002). The F-box protein slimb controls the levels of clock proteins period and timeless. *Nature* 420, 178-182.

Gschweidl, M., Ulbricht, A., Barnes, C.A., Enchev, R.I., Stoffel-Studer, I., Meyer-Schaller, N., Huotari, J., Yamauchi, Y., Greber, U.F., Helenius, A., and Peter, M. (2016). A SPOPL/Cullin-3 ubiquitin ligase complex regulates endocytic trafficking by targeting EPS15 at endosomes. *eLife* 5, e13841.

Gunawardhana, K.L., and Hardin, P.E. (2017). VRILLE Controls PDF Neuropeptide Accumulation and Arborization Rhythms in Small Ventrolateral Neurons to Drive Rhythmic Behavior in Drosophila. *Curr Biol* 27, 3442-3453 e3444.

Guo, F., Cerullo, I., Chen, X., and Rosbash, M. (2014). PDF neuron firing phase-shifts key circadian activity neurons in Drosophila. *eLife*, e02780.

Hermansteyne, T.O., Granados-Fuentes, D., Mellor, R.L., Herzog, E.D., and Nerbonne, J.M. (2017). Acute Knockdown of Kv4.1 Regulates Repetitive Firing Rates and Clock Gene Expression in the Suprachiasmatic Nucleus and Daily Rhythms in Locomotor Behavior. *eNeuro* 4.

Herrero, A., Yoshii, T., Ispizua, J.I., Colque, C., Veenstra, J.A., Muraro, N.I., and Ceriani, M.F. (2020). Coupling Neuropeptide Levels to Structural Plasticity in Drosophila Clock Neurons. *Curr Biol*.

Hyun, S., Lee, Y., Hong, S.T., Bang, S., Paik, D., Kang, J., Shin, J., Lee, J., Jeon, K., Hwang, S., *et al.* (2005). Drosophila GPCR Han is a receptor for the circadian clock neuropeptide PDF. *Neuron* 48, 267-278.

Im, S.H., Li, W., and Taghert, P.H. (2011). PDFR and CRY signaling converge in a subset of clock neurons to modulate the amplitude and phase of circadian behavior in Drosophila. *PLoS One* 6, e18974.

Itri, J.N., Vosko, A.M., Schroeder, A., Dragich, J.M., Michel, S., and Colwell, C.S. (2010). Circadian regulation of a-type potassium currents in the suprachiasmatic nucleus. *J Neurophysiol* 103, 632-640.

Kaneko, M., and Hall, J.C. (2000). Neuroanatomy of cells expressing clock genes in Drosophila: transgenic manipulation of the period and timeless genes to mark the perikarya of circadian pacemaker neurons and their projections. *J Comp Neurol* 422, 66-94.

Ko, H.W., Jiang, J., and Edery, I. (2002). Role for Slimb in the degradation of Drosophila Period protein phosphorylated by Doubletime. *Nature* 420, 673-678.

Koh, K., Zheng, X., and Sehgal, A. (2006). JETLAG resets the *Drosophila* circadian clock by promoting light-induced degradation of TIMELESS. *Science* 312, 1809-1812.

Kojima, S., Shingle, D.L., and Green, C.B. (2011). Post-transcriptional control of circadian rhythms. *J Cell Sci* 124, 311-320.

Konopka, R.J., and Benzer, S. (1971). Clock mutants of *Drosophila melanogaster*. *Proc Natl Acad Sci U S A* 68, 2112-2116.

Krashes, M.J., Keene, A.C., Leung, B., Armstrong, J.D., and Waddell, S. (2007). Sequential use of mushroom body neuron subsets during *drosophila* odor memory processing. *Neuron* 53, 103-115.

Kula, E., Levitan, E.S., Pyza, E., and Rosbash, M. (2006). PDF cycling in the dorsal protocerebrum of the *Drosophila* brain is not necessary for circadian clock function. *J Biol Rhythms* 21, 104-117.

Kula-Eversole, E., Nagoshi, E., Shang, Y., Rodriguez, J., Allada, R., and Rosbash, M. (2010). Surprising gene expression patterns within and between PDF-containing circadian neurons in *Drosophila*. *Proceedings of the National Academy of Sciences of the United States of America* 107, 13497-13502.

Lear, B.C., Darrach, E.J., Aldrich, B.T., Gebre, S., Scott, R.L., Nash, H.A., and Allada, R. (2013). UNC79 and UNC80, Putative Auxiliary Subunits of the NARROW ABDOMEN Ion Channel, Are Indispensable for Robust Circadian Locomotor Rhythms in *Drosophila*. *PLoS One* 8, e78147.

Lear, B.C., Lin, J.M., Keath, J.R., McGill, J.J., Raman, I.M., and Allada, R. (2005a). The ion channel narrow abdomen is critical for neural output of the *Drosophila* circadian pacemaker. *Neuron* 48, 965-976.

Lear, B.C., Merrill, C.E., Lin, J.M., Schroeder, A., Zhang, L., and Allada, R. (2005b). A G protein-coupled receptor, groom-of-PDF, is required for PDF neuron action in circadian behavior. *Neuron* 48, 221-227.

Lim, C., and Allada, R. (2013a). ATAXIN-2 activates PERIOD translation to sustain circadian rhythms in *Drosophila*. *Science* 340, 875-879.

Lim, C., and Allada, R. (2013b). Emerging roles for post-transcriptional regulation in circadian clocks. *Nat Neurosci* 16, 1544-1550.

Lim, C., Chung, B.Y., Pitman, J.L., McGill, J.J., Pradhan, S., Lee, J., Keegan, K.P., Choe, J., and Allada, R. (2007a). Clockwork orange encodes a transcriptional repressor important for circadian-clock amplitude in *Drosophila*. *Current biology : CB* 17, 1082-1089.

Lim, C., Lee, J., Choi, C., Kilman, V.L., Kim, J., Park, S.M., Jang, S.K., Allada, R., and Choe, J. (2011). The novel gene twenty-four defines a critical translational step in the *Drosophila* clock. *Nature* 470, 399-403.

Lim, C., Lee, J., Choi, C., Kim, J., Doh, E., and Choe, J. (2007b). Functional role of CREB-binding protein in the circadian clock system of *Drosophila melanogaster*. *Mol Cell Biol* 27, 4876-4890.

Lin, D.M., and Goodman, C.S. (1994). Ectopic and increased expression of Fasciclin II alters motoneuron growth cone guidance. *Neuron* 13, 507-523.

Lin, Y., Stormo, G.D., and Taghert, P.H. (2004). The neuropeptide pigment-dispersing factor coordinates pacemaker interactions in the *Drosophila* circadian system. *J Neurosci* 24, 7951-7957.

Meliza, C.D., Kostuk, M., Huang, H., Nogaret, A., Margoliash, D., and Abarbanel, H.D. (2014). Estimating parameters and predicting membrane voltages with conductance-based neuron models. *Biol Cybern* 108, 495-516.

Mertens, I., Vandingenen, A., Johnson, E.C., Shafer, O.T., Li, W., Trigg, J.S., De Loof, A., Schoofs, L., and Taghert, P.H. (2005). PDF receptor signaling in *Drosophila* contributes to both circadian and geotactic behaviors. *Neuron* 48, 213-219.

Moye, M.J., and Diekman, C.O. (2018). Data Assimilation Methods for Neuronal State and Parameter Estimation. *J Math Neurosci* 8, 11.

Nitabach, M.N., Wu, Y., Sheeba, V., Lemon, W.C., Strumbos, J., Zelensky, P.K., White, B.H., and Holmes, T.C. (2006). Electrical hyperexcitation of lateral ventral pacemaker neurons desynchronizes downstream circadian oscillators in the fly circadian circuit and induces multiple behavioral periods. *J Neurosci* 26, 479-489.

Osterwalder, T., Yoon, K.S., White, B.H., and Keshishian, H. (2001). A conditional tissue-specific transgene expression system using inducible GAL4. *Proc Natl Acad Sci U S A* 98, 12596-12601.

Park, J.H., Helfrich-Forster, C., Lee, G., Liu, L., Rosbash, M., and Hall, J.C. (2000). Differential regulation of circadian pacemaker output by separate clock genes in *Drosophila*. *Proc Natl Acad Sci U S A* 97, 3608-3613.

Peng, Y., Stoleru, D., Levine, J.D., Hall, J.C., and Rosbash, M. (2003). *Drosophila* free-running rhythms require intercellular communication. *PLoS Biol* 1, E13.

Peschel, N., Chen, K.F., Szabo, G., and Stanewsky, R. (2009). Light-dependent interactions between the *Drosophila* circadian clock factors cryptochrome, jetlag, and timeless. *Curr Biol* 19, 241-247.

Peschel, N., Veleri, S., and Stanewsky, R. (2006). Veela defines a molecular link between Cryptochrome and Timeless in the light-input pathway to *Drosophila*'s circadian clock. *Proc Natl Acad Sci U S A* 103, 17313-17318.

Petsakou, A., Sapsis, T.P., and Blau, J. (2015). Circadian Rhythms in Rho1 Activity Regulate Neuronal Plasticity and Network Hierarchy. *Cell* 162, 823-835.

Pfeiffenberger, C., and Allada, R. (2012). Cul3 and the BTB adaptor insomniac are key regulators of sleep homeostasis and a dopamine arousal pathway in *Drosophila*. *PLoS Genet* 8, e1003003.

Renn, S.C., Park, J.H., Rosbash, M., Hall, J.C., and Taghert, P.H. (1999). A pdf neuropeptide gene mutation and ablation of PDF neurons each cause severe abnormalities of behavioral circadian rhythms in *Drosophila*. *Cell* 99, 791-802.

Richier, B., Michard-Vanhee, C., Lamouroux, A., Papin, C., and Rouyer, F. (2008). The clockwork orange *Drosophila* protein functions as both an activator and a repressor of clock gene expression. *Journal of biological rhythms* 23, 103-116.

Rideout, E.J., Dornan, A.J., Neville, M.C., Eadie, S., and Goodwin, S.F. (2010). Control of sexual differentiation and behavior by the doublesex gene in *Drosophila melanogaster*. *Nat Neurosci* 13, 458-466.

Rutila, J.E., Suri, V., Le, M., So, W.V., Rosbash, M., and Hall, J.C. (1998). CYCLE is a second bHLH-PAS clock protein essential for circadian rhythmicity and transcription of *Drosophila* period and timeless. *Cell* 93, 805-814.

Schiff, S.J. (2012). *Neural control engineering : the emerging intersection between control theory and neuroscience* (Cambridge, MA: MIT Press).

Sehgal, A., Price, J.L., Man, B., and Young, M.W. (1994). Loss of circadian behavioral rhythms and per RNA oscillations in the *Drosophila* mutant timeless [see comments]. *Science* 263, 1603-1606.

Sheeba, V., Gu, H., Sharma, V.K., O'Dowd, D.K., and Holmes, T.C. (2008). Circadian- and light-dependent regulation of resting membrane potential and spontaneous action potential firing of *Drosophila* circadian pacemaker neurons. *Journal of neurophysiology* 99, 976-988.

Sim, C.K., and Forger, D.B. (2007). Modeling the electrophysiology of suprachiasmatic nucleus neurons. *J Biol Rhythms* 22, 445-453.

Sivachenko, A., Li, Y., Abruzzi, K.C., and Rosbash, M. (2013). The transcription factor Mef2 links the *Drosophila* core clock to Fas2, neuronal morphology, and circadian behavior. *Neuron* 79, 281-292.

Smith, P., Buhl, E., Tsaneva-Atanasova, K., and Hodge, J.J.L. (2019). Shaw and Shal voltage-gated potassium channels mediate circadian changes in *Drosophila* clock neuron excitability. *J Physiol* 597, 5707-5722.

Stanewsky, R., Frisch, B., Brandes, C., Hamblen-Coyle, M.J., Rosbash, M., and Hall, J.C. (1997). Temporal and spatial expression patterns of transgenes containing increasing amounts of the *Drosophila* clock gene period and a lacZ reporter: mapping elements of the PER protein involved in circadian cycling. *J Neurosci* 17, 676-696.

Stoleru, D., Peng, Y., Agosto, J., and Rosbash, M. (2004). Coupled oscillators control morning and evening locomotor behaviour of *Drosophila*. *Nature* 431, 862-868.

Stoleru, D., Peng, Y., Nawathean, P., and Rosbash, M. (2005). A resetting signal between *Drosophila* pacemakers synchronizes morning and evening activity. *Nature* 438, 238-242.

Szabo, A., Papin, C., Cornu, D., Chelot, E., Lipinszki, Z., Udvardy, A., Redeker, V., Mayor, U., and Rouyer, F. (2018). Ubiquitylation Dynamics of the Clock Cell Proteome and TIMELESS during a Circadian Cycle. *Cell Rep* 23, 2273-2282.

Tricoire, H., Battisti, V., Trannoy, S., Lasbleiz, C., Pret, A.M., and Monnier, V. (2009). The steroid hormone receptor EcR finely modulates *Drosophila* lifespan during adulthood in a sex-specific manner. *Mechanisms of ageing and development* 130, 547-552.

Yang, M.Y., Armstrong, J.D., Vilinsky, I., Strausfeld, N.J., and Kaiser, K. (1995). Subdivision of the *Drosophila* mushroom bodies by enhancer-trap expression patterns. *Neuron* 15, 45-54.

Zars, T., Fischer, M., Schulz, R., and Heisenberg, M. (2000). Localization of a short-term memory in *Drosophila*. *Science* 288, 672-675.

Zhang, L., Chung, B.Y., Lear, B.C., Kilman, V.L., Liu, Y., Mahesh, G., Meissner, R.A., Hardin, P.E., and Allada, R. (2010). DN1(p) circadian neurons coordinate acute light and PDF inputs to produce robust daily behavior in *Drosophila*. *Current biology : CB* 20, 591-599.

Zhang, Y., Ling, J., Yuan, C., Dubruille, R., and Emery, P. (2013). A role for *Drosophila* ATX2 in activation of PER translation and circadian behavior. *Science* 340, 879-882.

Supplemental Figure Legends

Figure S1. A reverse genetics screen identifies *Tango10* as a novel circadian gene.

The *Tango10*^{GG} rhythmicity phenotype was identified from a locomotor behavior screen of 1297 putative loss-of-function mutations covering 1015 genes (Pfeiffenberger et al 2012). Average rhythmic power was determined using Chi-squared periodogram analysis over 7 days constant darkness. Strains were binned based on average rhythmic power values, as indicated on the X axis +/- 5. *Tango10*^{GG} mutants exhibited an average rhythmic power < 10.

Figure S2. *busyrun* contains a mutation in a conserved residue of the TANGO10

BTB-BACK domain protein. (A) Sequence analysis of the EMS-induced mutant strain *Tango10*^{busyrun} identifies a missense C->T mutation corresponding to a P-> L substitution at amino acid 462 in comparison to a wild-type (WT) strain, *iso31* (B) Clustal W alignment of TANGO10 orthologs demonstrates strong conservation of P462 among other animals. (C) Protein domain analysis through Pfam identifies both BTB (BR-C, ttk, and bab) and BACK (BTB and C-terminal-Kelch) domains in *Drosophila* TANGO10.

Figure S3. RNAi induced depletion of TANGO10 in Adult Heads. Western blot analysis of adult head extracts from the strains indicated (Elav-GAL4, UAS-Dcr2, and/ or UAS-*Tango10* RNAi). Blots were probed with mouse anti-Tango10 and rat anti-GE-1.

Figure S4. Loss of *Tango10* does not alter PER or TIM levels in whole heads. (A)

Western blot analysis of adult head extracts in DD conditions. GG refers to

Tango10^{GG} mutants and WT refers to wild-type strain. CT indicates circadian time. (B-D) Quantification of (B) TANGO10, (C) PER, and (D) TIM levels performed using Image J from two independent experiments. Protein intensity is normalized to actin controls. Normalized value of WT at CT3 set as 1. Statistical comparison made using two-way ANOVA followed by Tukey's post-hoc test. (B) No significant interaction is detected between genotypes and timepoint. Significant differences were observed between WT and *Tango10^{GG}* at CT3 and CT15 (** $p < 0.02$) but no differences found between timepoints within genotype ($p \geq 0.50$). (C) No significant interactions detected in PER levels between genotypes and timepoints ($p \geq 0.46$). (D) No significant interactions detected in TIM levels between genotypes and timepoints ($p \geq 0.36$).

Figure S5. Simulations comparing a previously published LNv model and our newly developed LNv model to current-clamp data. (A) Top panel: Simulation of the Smith et al (2019) model of LNv neurons (magenta) and a current-clamp trace (black) from a WT l-LNv neuron recorded at ZT 2. Bottom panel: Simulation of our newly developed LNv model (magenta) and the same current-clamp trace shown in the top panel (black). B) Phase-plane trajectory diagram showing dV/dt versus V for the simulations of the Smith model (magenta, left panel), our new model (magenta, right panel), and the current-clamp trace (black) shown in (A).

Figure S6. Current-clamp recordings used in data assimilation (DA) procedure to estimate l-LNv model parameters. (A) Current-clamp trace from a WT l-LNv neuron recorded at ZT 2. B) Alignment of all the action potentials for the recording

shown in (A). C) Action potential waveform used in the DA algorithm obtained by averaging the aligned APs shown in (B).

Fig S7. Membrane depolarization of l-LNv by potassium channel blockers is diminished in *Tango10* mutants. A) Representative current clamp traces of l-LNv neurons showing the membrane potential responses to the potassium channel blockers TEA and 4AP (with TTX blocking sodium channels). Application of TEA alone results in a small membrane depolarization (~1-2mV), while the further addition of 4AP causes a larger depolarization (5 – 10 mV). B) Resting Membrane Potential (RMP) was measure before (Bf) and after (At) application of channel blockers (*left panel*). Application of TEA alone does not result in a significantly different membrane potential response between WT and *Tango10* (*right panel*). C) Application of 4AP results in larger membrane depolarization (*left panel*; * P<0.05, ** P<0.001; paired t-test), but this response was significantly lower in *Tango10* mutant l-LNv neurons (*right panel*; Cont ZT8~12 vs. Mutant ZT0~4, Cont ZT8~12 vs. Mutants ZT8~12; * P<0.05 One-way ANOVA, Tukey's HSD test)

Fig S8. TANGO10 and CUL3 link the core circadian clock to neuronal output and behavioral rhythmicity. Model for TANGO10/CUL3 circadian function, highlighting core clock regulation of TANGO 10 expression, TANGO10 regulation of excitability via Shaker/Shal currents, PDF expression, and impact on behavioral rhythmicity. We propose that the effects of TANGO10/CUL3 on PDF and/or the core circadian clock may be indirect via effects on excitability.

Supplemental Tables

Genotype	Period	Power	%R	n
+/+	24.1 ± 0.1	54 ± 7	88	32
GG/+	24.2 ± 0.2	53 ± 4	92	51
GG/GG	21.0 ± 0.0	2 ± 1**	11	18
bsr/+	24.4 ± 0.2	58 ± 5	94	49
bsr/bsr	24.3 ± 0.6	16 ± 10*	38	8
GG/bsr	24.2 ± 1.6	6 ± 1**	19	37
Df(1)ED7147/+	24.6 ± 0.1	74 ± 10	80	40
Df(1)ED7147/GG	14.5 ± n/a	2 ± 1**	10	10
Df(1)ED7147/bsr	25.2 ± 1.3	5 ± 2**	23	26
Df(1)BSC722/+	24.5 ± 0.1	64 ± 7	78	50
Df(1)BSC722/GG	33.0 ± n/a	2 ± 1**	6	17
Df(1)BSC722/bsr	24.1 ± 1.0	6 ± 1**	27	37

Table S1. Homozygous or trans-heterozygous *Tango10* mutants exhibit disrupted rhythms. Chi squared periodogram analysis of DD locomotor rhythmicity from adult females with the genotypes indicated. Power refers to power-significance measurement %R indicates percent rhythmic, defined as flies with power ≥ 10 . ‘+’ indicates wild-type, GG indicates *Tango10*^{GG} allele, while bsr indicates *Tango10*^{bsr} allele. *Df(1)ED7147* and *Df(1)BSC722* chromosomes are deficient for the *Tango10* locus. Error measurements are SEM. Statistical comparisons to wild-type control made using one-way ANOVA followed by Dunnett’s multiple comparison (* p < 0.05, **p < 0.02).

Genotype	Period	Power	%R	n
P-element excision				
+	23.8 ± 0.1	84 ± 4	96.6	59
GG	24.8 ± 2.0	3 ± 1 ^{††}	16.1	31
ΔGG#5 (precise excision)	24.1 ± 0.3	77 ± 8 ^{**}	100.0	32
ΔGG#6 (precise excision)	24.3 ± 0.1	83 ± 10 ^{**}	96.2	26
ΔGG#1 (excision control)	25.6 ± 2.2	8 ± 3	33.3	12
ΔGG#3 (excision control)	25.0 ± 1.0	4 ± 2	18.8	16
Genomic rescue				
[Tango10#1]	23.7 ± 0.0	81 ± 7	96.8	31
[Tango10#2]	23.6 ± 0.0	111 ± 7	100.0	32
GG	23.7 ± 0.4	9 ± 3 ^{††}	23.5	34
GG+[Tango10#1]	23.6 ± 0.1	73 ± 6 ^{**}	94.3	35
GG+[Tango10#2]	23.9 ± 0.1	87 ± 6 ^{**}	100.0	36
bsr	24.7 ± 0.7	17 ± 4 ^{††}	42.9	56
bsr+[Tango10#1]	23.8 ± 0.1	74 ± 5 ^{**}	100.0	71
bsr+[Tango10#2]	23.8 ± 0.1	58 ± 5 ^{**}	92.1	63

Table S2. P-element excision or genomic rescue restores rhythmicity to

Tango10^{GG}. Chi squared periodogram analysis of DD locomotor rhythmicity from adult females with the genotypes indicated. Power refers to power-significance measurement %R indicates percent rhythmic, defined as flies with power ≥ 10 . ‘+’ indicates wild-type, GG indicates *Tango10^{GG}* allele, while bsr indicates *Tango10^{bsr}* allele. ΔGG indicates precise (#5,#6) or mock (#1,#3) excision of *Tango10^{GG}*.

[*Tango10#1*] and [*Tango10#2*] indicate *Tango10* genomic rescue transgenes.

Statistical comparisons made using one-way ANOVA followed by Dunnett’s test

(excision) or two-way ANOVA followed by Tukey's multiple comparison test (genomic rescue). Asterisks indicated significant difference from corresponding mutant (*Tango10^{GG}* or *Tango10^{bsr}*) (** p < 0.02) or from wild-type control (†† p < 0.02) for one-way ANOVA data. Error measurements are SEM.

Genotype	Period	Power	%R	n
GG; ElavGS U-Tango10: EtOH	23.5 ± 0.5	5 ± 2	11	19
GG; ElavGS U-Tango10: RU486	23.5 ± 0.1	45 ± 8***	82	22
GG; Da GS U-Tango10: EtOH	NA	1 ± 1	0	8
GG; Da GS U-Tango10: RU486	24.4 ± 0.2	98 ± 18***	92	13

Table S3. Restoring Tango10 expression specifically in the adult stage rescues rhythmicity. Rhythmic power (Power - Significance) of locomotor behavior for Tango10 mutants following adult specific rescue using pan-neuronal (ELAV GS) or pan-cellular (DA GS) induction of UAS-*Tango10* expression (U-Tango10), as induced by RU486 of GeneSwitch (GS) GAL4. Error indicates SEM . Asterisks indicate significant difference from EtOH control (***) P<0.001) as determined using Student's t-test. %R indicates percent rhythmic, defined as flies with power >=10.

Genotype	Period	Power	%R	n
Rescue				
GG; U-Tango10/+	24.2 ± 0.9	15 ± 4	58	19
GG;PdfGal4/+; U-Tango10/+	25.1 ± 0.3	21 ± 3	73	33
GG; timGal4/+; U-Tango10/+	26.2 ± 0.6	14 ± 2	58	33
GG;;U-Tango10 / Clk4-1MGal4	24.3 ± 0.4	8 ± 2	26	19
GG;;U-Tango10/ 30yGal4	24.0 ± 0.1	87 ± 8**	100	34
30Y GAL4 rescue plus GAL80				
GG;;30yGAL4/+	24.6 ± 1.2	8 ± 2	29	24
GG; 30yGAL4/ U-Tango10	23.9 ± 0.2	55 ± 5	95	39
GG;ElavGAL80/+;30yGAL4/ U-Tango10	24.7 ± 0.3	13 ± 2**	49	39
GG; PdfGal80/+; 30yGAL4/ U-Tango10	22.6 ± 0.5	25 ± 4**	87	15
GG; 247Gal80/+; 30yGAL4/ U-Tango10	24.0 ± 0.2	64 ± 7	93	28
Overexpression				
U-Tango10/+	23.5 ± 0.0	92 ± 12	93	14
pdfGal4+	24.4 ± 0.1	69 ± 12	79	24
pdfGal4/+; U-Tango10/+	24.9 ± 0.1**	71 ± 7	96	24
timGal4+/+	25.1 ± 0.1	81 ± 10	93	27
timGal4/+ U-Tango10/+	25.5 ± 0.1**	71 ± 9	96	24
Clk4.1GAL4/+	23.6 ± 0.0	132 ± 8	100	32
Clk4.1GAL4/ U-Tango10	23.7 ± 0.1	142 ± 8	100	31

30YGal4/+	23.8 ± 0.1	91 ± 10	100	20
30YGal4/ U-Tango10	23.7 ± 0.1	121 ± 6**	100	28
RNAi				
ElavGAL4;; U-Dcr2/+	24.0 ± 0.1	78 ± 6	100	37
U-Dcr2/+; 247GAL4/+	23.7 ± 0.0	121 ± 5	100	36
timGAL4/+; U-Dcr2/+	24.3 ± 0.0	76 ± 6	100	38
PdfGAL4 U-Dcr2/+	24.3 ± 0.1	72 ± 7	97	32
ElavGAL4;Tango10 RNAi/+; U-Dcr2/+	23.1 ± 0.3	22 ± 3**	63	38
U-Dcr2/ Tango10 RNAi; 247GAL4/+	23.5 ± 0.0	125 ± 5	100	39
timGAL4/ Tango10 RNAi; U-Dcr2/+	24.6 ± 0.3	13 ± 2**	42	38
PdfGAL4 U-Dcr2/ Tango10 RNAi	23.4 ± 0.5	16 ± 3**	50	44

Table S4. Tango10 function is necessary but not sufficient in pacemaker neurons

for locomotor rhythmicity. Chi squared periodogram analysis of DD locomotor rhythmicity from the genotypes indicated. ‘+’ indicates wild-type, GG refers to Tango10 GG allele, U-Dcr2 indicates UAS-Dicer2, U-Tango10 indicates UAS-Tango10, and *Tango10* RNAi refers to VDRC strain #103920. Power refers to power-significance measurement %R indicates percent rhythmic, defined as flies with power ≥ 10 . Statistical comparisons made between rescue, overexpression, or RNAi and corresponding control using Student’s T-test (** $p < 0.02$).

Genotype	Period	Power	%R	n
GG ElavGAL4; (+)	-	2 ± 1	0	9
GG ElavGAL4; U-Tango10- FLAG/+	23.7 ± 0.1	59 ± 6**	92	38
GG ElavGal4; U-Tango10 WT/+	23.9 ± 0.2	64 ± 5**	95	79
ElavGAL4; U-Tango10-FLAG/+	23.5 ± 0.1	62 ± 7**	92	38

Table S5. Flag tagged Tango10 rescues rhythmicity in *Tango10^{GG}* mutants. Chi squared periodogram analysis of DD locomotor rhythmicity from the genotypes indicated. GG refers to *Tango10^{GG}* allele, U-Tango10-FLAG refers to UAS-Tango10-3XFLAG tagged construct. Power refers to Power-Significance, %R indicates percent of flies with Power ≥ 10 . SEM included for Period and Power measurements. Asterisks indicate significant different from GG ElavGAL4 using one-way ANOVA followed by Tukey's post-hoc test (** $p < 0.02$).

	elavGAL4 ZT10	elavGAL4 ZT22	timGAL4 ZT10	timGAL4 ZT22
Cyt-c1	43.6	40.5	127.5	84.5
Droj2	51.8	50.2	136.1	269.3
RpS14a	103.8	35.8	62.8	198.8
sta	54.3	71.2	57.4	114.3
Cul3	-	115.5	46.6	249.9
Pdh	-	90.3	54.1	201.0
Rab5	-	42.7	94.3	85.3
CG5028	-	146.9	33.6	104.8
bdl	58.2	-	-	69.4
GlyS	50.4	-	-	82.9
ND-49	63.0	-	-	71.7
Rpn1	41.0	-	-	44.8
CG42540	-	59.4	91.8	-
Dic1	-	44.4	-	88.3
Mcad	-	68.0	-	134.1
Mlp84B	-	47.1	-	51.8
Rpn12	-	23.3	-	53.0
Rpt3	-	31.7	-	69.1
Rpt4	-	33.9	-	104.2
Scsalphal	-	44.9	-	105.4
wal	-	52.2	-	116.0

Table S6. The E3 Ligase CUL3 physically interacts with TANGO10 protein in vivo. List of protein scores for putative TANGO10 interactors from mass spectrometry analysis of FLAG-tagged TANGO10 using either *elavGAL4* or *timGAL4* at both ZT10 and ZT 22, as determined using Proteome Discoverer software (ThermoFisher). Fly heads from Gal4 heterozygotes were used as controls. The hits from FLAG-tagged twenty-four (TYF) proteomics were also excluded from the list to increase TANGO10-specificity. Proteins listed are those present in at least one *elavGAL4* sample and at least one *timGAL4* sample but no negative controls.

Genotype	Period	Power	%R	n
PdfGAL4 U-Dcr2/+	24.6 ± 0.1	131 ± 8	97	33
PdfGAL4 U-Dcr2/+; CUL3 RNAi/+	24.5 ± 0.4	39 ± 5**	77	44
timGAL4/+; U-Dcr2/+	24.2 ± 0.2	118 ± 13	88	26
timGAL4/+; U-Dcr2/ CUL3 RNAi	23.7 ± 0.4	13 ± 4**	38	8

Table S7. *Cul3* RNAi mediated depletion in circadian neurons disrupts

locomotor rhythmicity. Chi squared periodogram analysis of DD locomotor rhythmicity from the genotypes indicated. U-dcr2 indicates UAS-Dcr2, CUL3 RNAi refers to NIG strain 11861R-2. Power refers to periodogram power-significance. Error indicates SEM, %R refers to percent rhythmic, defined as flies with Power \geq 10. Power measurements compared between GAL4/RNAi and GAL4/+ controls using Student's t-test (** p < 0.02).

Symbol	Parameter	Units	Value
C	whole-cell capacitance	pF	3.70
Ena	Na ⁺ reversal potential	mV	52.00
Eca	Ca ²⁺ reversal potential	mV	132.00
EK	K ⁺ reversal potential	mV	-90.00
gNa	INa maximal conductance	nS	100.00
gCa	ICa maximal conductance	nS	4.64
gKv1	IKv1 maximal conductance	nS	2.35
gKv2	IKv2 maximal conductance	nS	0.86
gKv3	IKv3 maximal conductance	nS	0.22
gKv4	IKv4 maximal conductance	nS	0.10
gLNa	ILNa maximal conductance	nS	0.14
gLK	ILK maximal conductance	nS	1.00
vm_Na	INa half-activation	mV	-41.41
dvm_Na	INa activation slope	mV	7.43
tm0_Na	INa activation time constant baseline	msec	0.01
tm1_Na	INa activation time constant baseline	msec	32.15
vmt_Na	INa activation time constant half-inactivation	mV	-60.45
dvmt_Na	INa activation time constant slope	mV	5.00
vh_Na	INa half-inactivation	mV	-53.78
dvh_Na	INa inactivation slope	mV	-5.00
th0_Na	INa inactivation time constant baseline	msec	0.54
th1_Na	INa inactivation time constant baseline	msec	0.95
vht_Na	INa inactivation time constant half-inactivation	mV	-42.97
dvht_Na	INa inactivation time constant slope	mV	5.00
vm_Ca	ICa half-activation	mV	-44.91
dvm_Ca	ICa half-activation slope	mV	12.85
tm0_Ca	ICa activation time constant baseline	msec	1.21
vh_Ca	ICa half-inactivation	mV	-80.00
dvh_Ca	ICa half-inactivation slope	mV	-26.94
th0_Ca	ICa inactivation time constant baseline	msec	4.01
th1_Ca	ICa inactivation time constant baseline	msec	40.00
vht_Ca	ICa inactivation time constant half-activation	mV	-66.51
dvht_Ca	ICa inactivation time constant slope	mV	5.00
vm_Kv1	IKv1 half-activation	mV	-34.18
dvm_Kv1	IKv1 half-activation slope	mV	9.75
tm0_Kv1	IKv1 activation time constant baseline	msec	0.00
tm1_Kv1	IKv1 activation time constant baseline	msec	1.79
vmt_Kv1	IKv1 activation time constant half-activation	mV	-4.07
dvmt_Kv1	IKv1 activation time constant slope	mV	73.88
vh_Kv1	IKv1 half-inactivation	mV	-93.19
dvh_Kv1	IKv1 inactivation slope	mV	-54.49
th0_Kv1	IKv1 inactivation time constant baseline	msec	0.00
th1_Kv1	IKv1 inactivation time constant baseline	msec	22.19
vht_Kv1	IKv1 inactivation time constant half-inactivation	mV	35.81
dvht_Kv1	IKv1 inactivation time constant slope	mV	52.04
vm_Kv2	IKv2 half-activation	mV	-29.69
dvm_Kv2	IKv2 half-activation slope	mV	10.49
tm0_Kv2	IKv2 activation time constant baseline	msec	0.00
tm1_Kv2	IKv2 activation time constant baseline	msec	30.72
vmt_Kv2	IKv2 activation time constant half-activation	mV	-63.69
dvmt_Kv2	IKv2 activation time constant slope	mV	28.54
vm_Kv3	IKv3 half-activation	mV	-57.30
dvm_Kv3	IKv3 half-activation slope	mV	14.63
tm0_Kv3	IKv3 activation time constant baseline	mV	0.00
tm1_Kv3	IKv3 activation time constant baseline	mV	0.03
vmt_Kv3	IKv3 activation time constant half-activation	mV	20.03
dvmt_Kv3	IKv3 activation time constant slope	mV	238.58
vh_Kv3	IKv3 half-inactivation	mV	-25.82
dvh_Kv3	IKv3 inactivation slope	mV	-2.50
th0_Kv3	IKv3 inactivation time constant baseline	msec	0.00
th1_Kv3	IKv3 inactivation time constant baseline	msec	154.83
vht_Kv3	IKv3 inactivation time constant half-inactivation	mV	159.82
dvht_Kv3	IKv3 inactivation time constant slope	mV	167.10
vm_Kv4	IKv4 half-activation	mV	-48.63
dvm_Kv4	IKv4 half-activation slope	mV	7.65
tm0_Kv4	IKv4 activation time constant baseline	msec	0.00
tm1_Kv4	IKv4 activation time constant baseline	msec	0.05
vmt_Kv4	IKv4 activation time constant half-activation	mV	-74.86
dvmt_Kv4	IKv4 activation time constant slope	mV	61.54
vh_Kv4	IKv4 half-inactivation	mV	-43.05
dvh_Kv4	IKv4 inactivation slope	mV	-1.73
th0_Kv4	IKv4 inactivation time constant baseline	msec	0.00
th1_Kv4	IKv4 inactivation time constant baseline	msec	44.52
vht_Kv4	IKv4 inactivation time constant half-inactivation	mV	-66.24
dvht_Kv4	IKv4 inactivation time constant slope	mV	180.11

Table S8. Parameter values for ILNv electrophysiology modeling

Figure 1

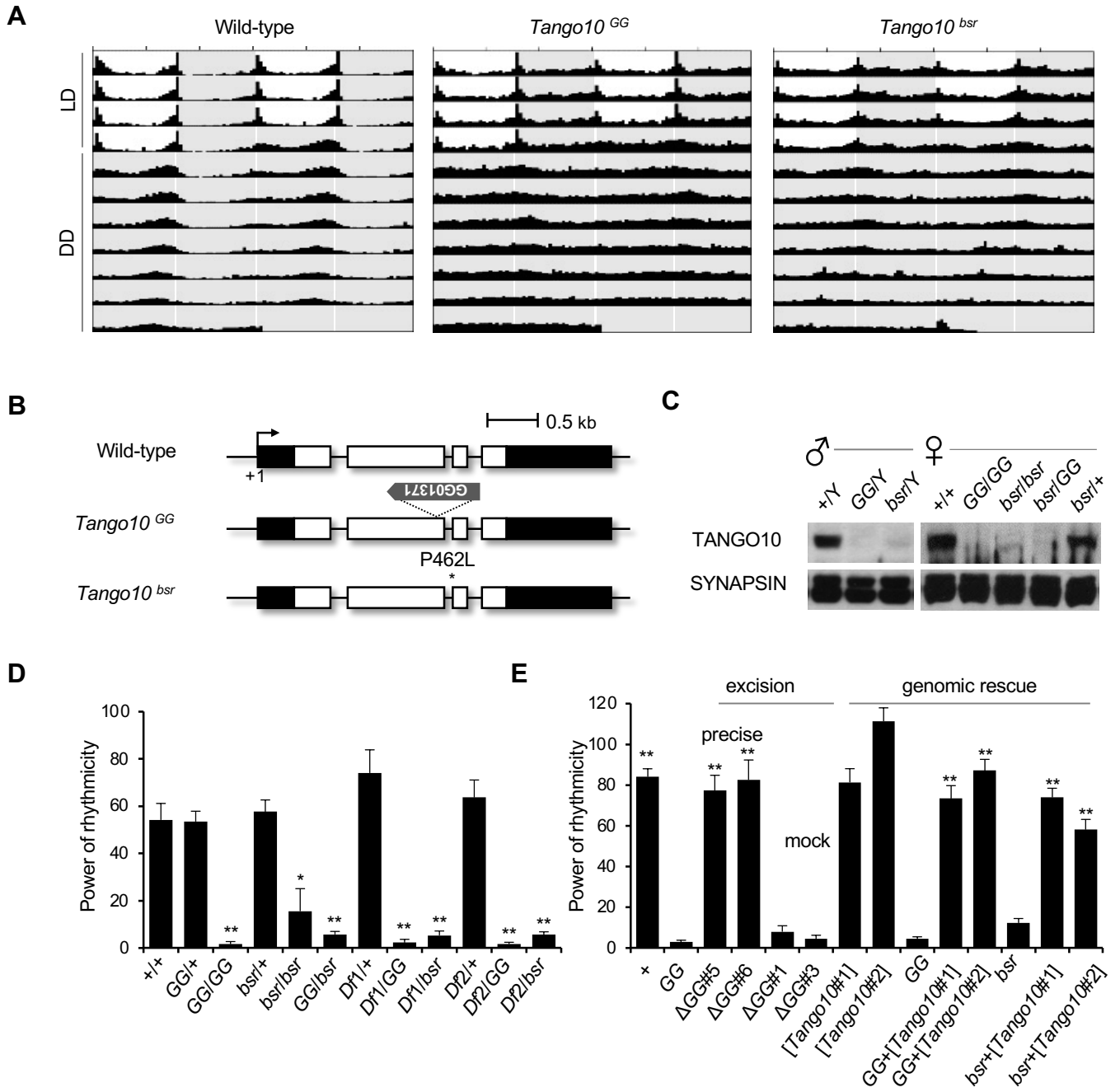


Figure 2

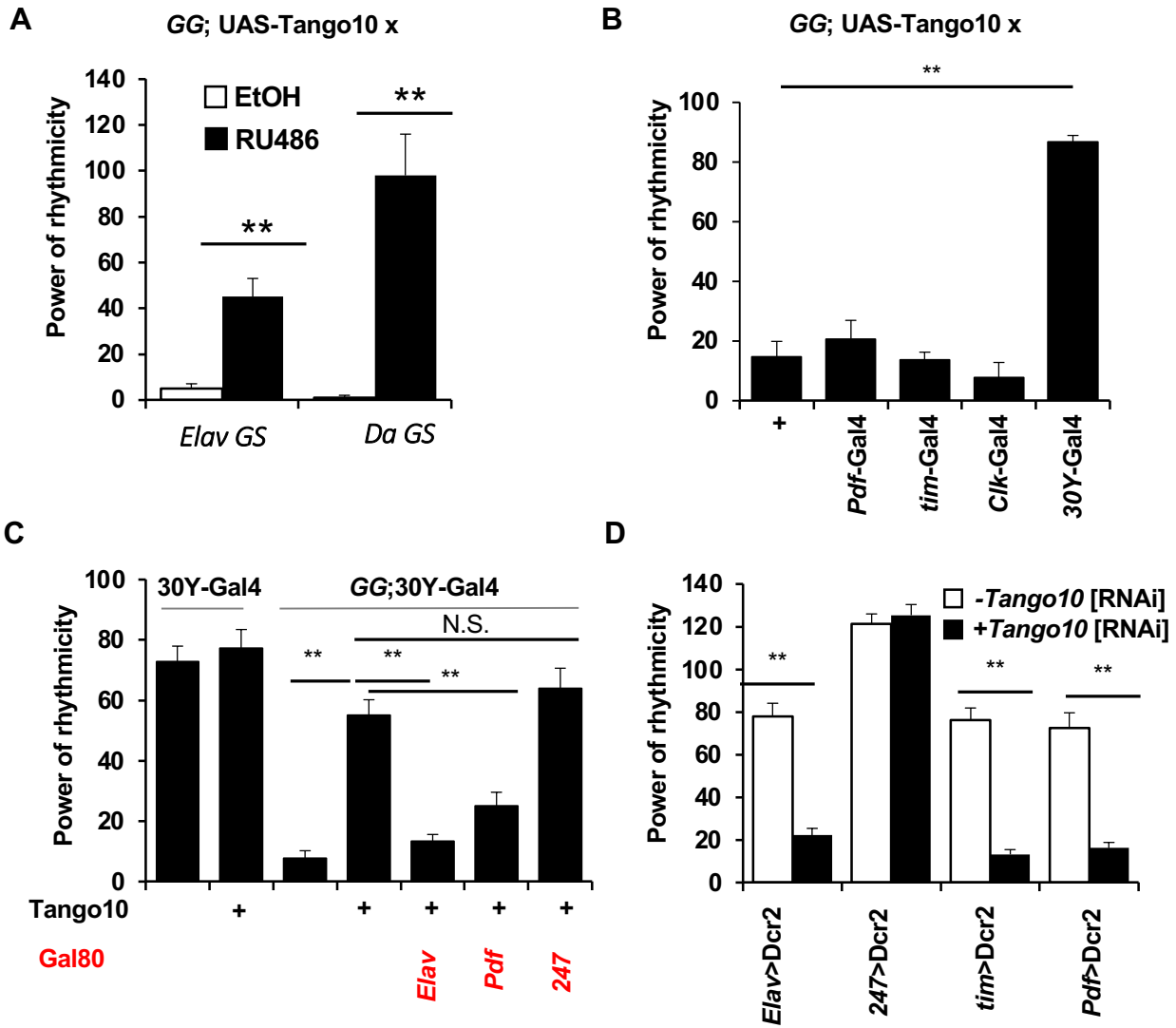


Figure 3

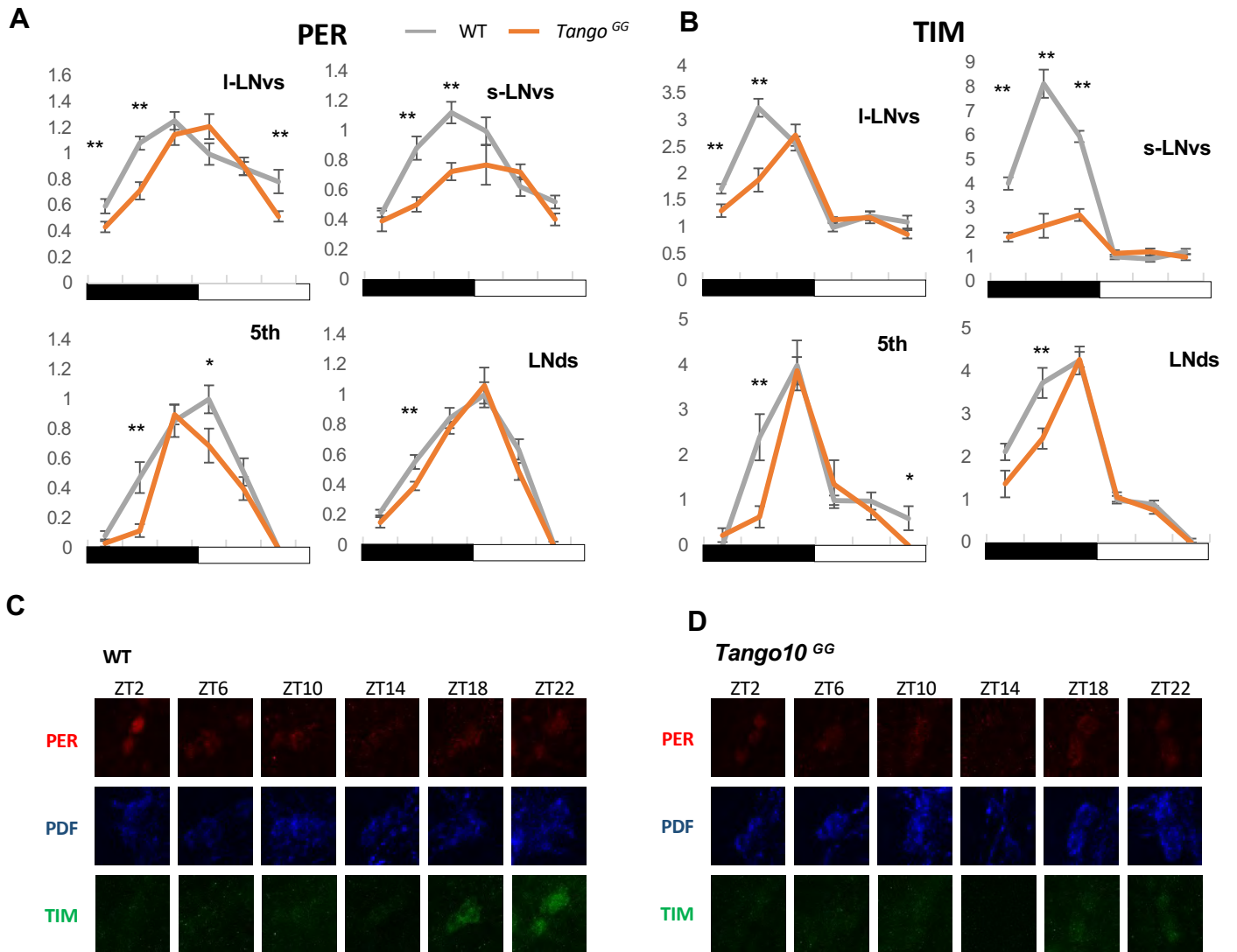


Figure 4

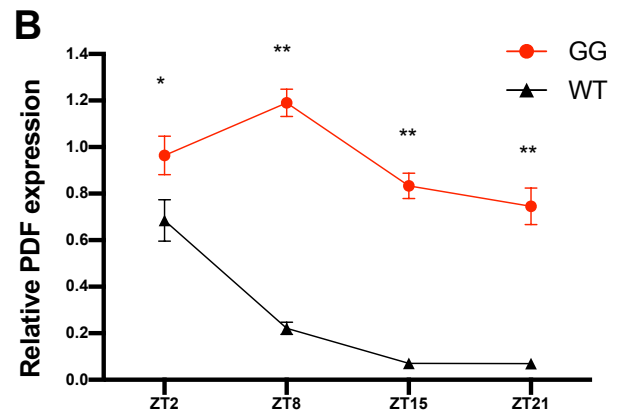
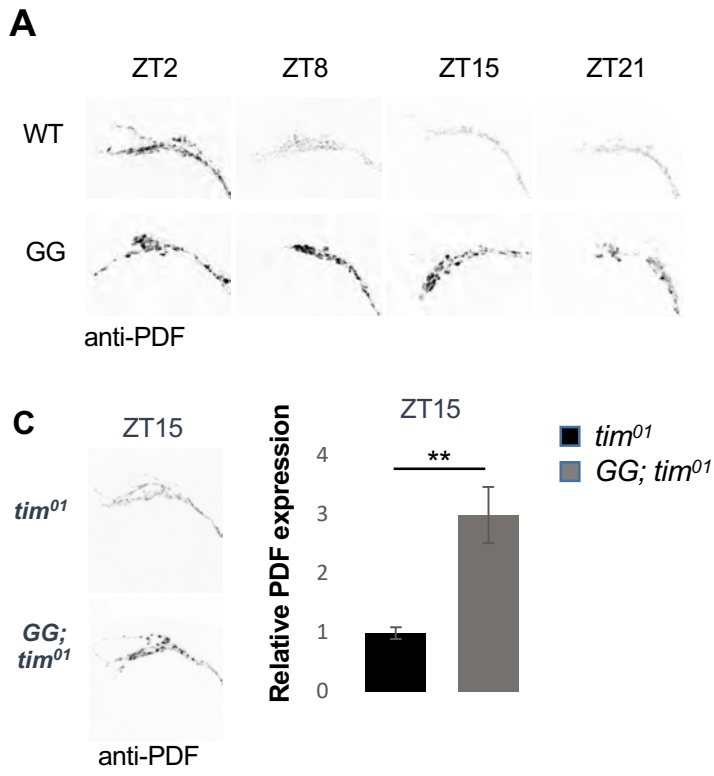


Figure 5

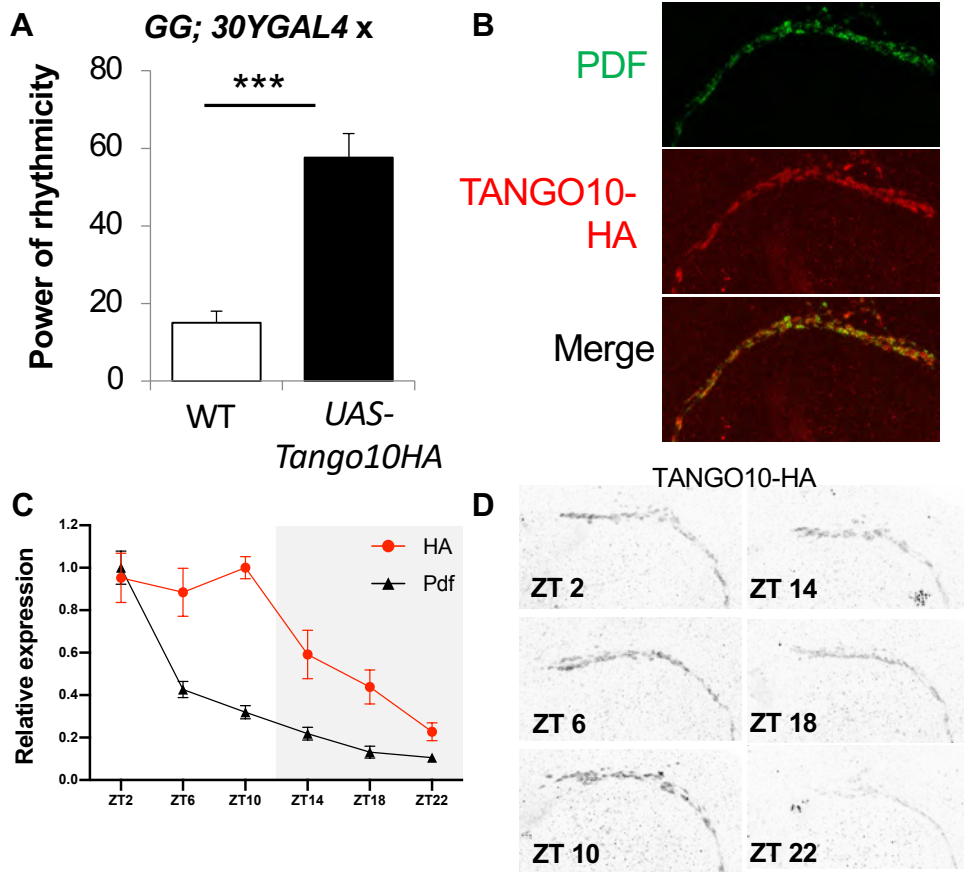


Figure 6

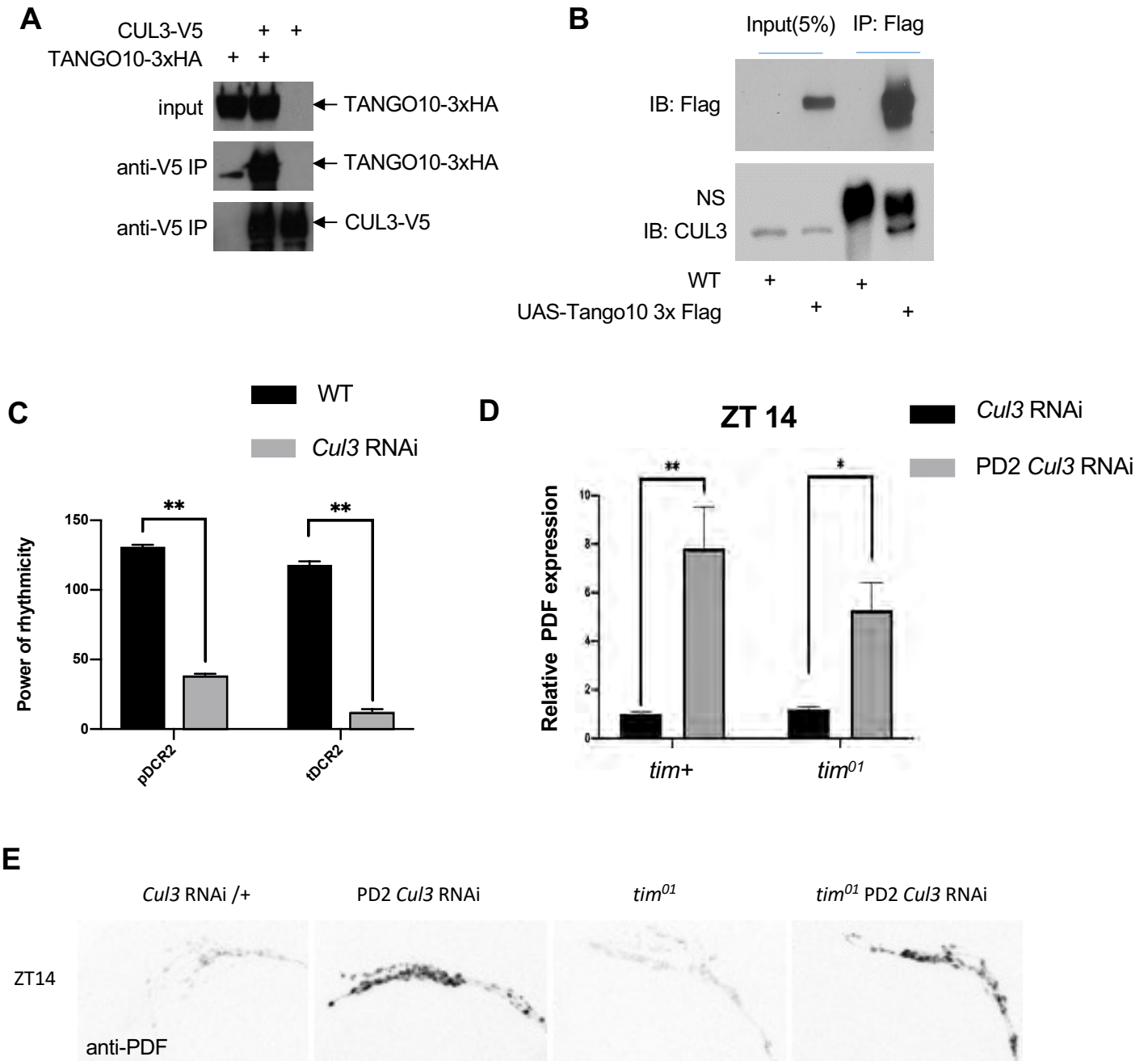


Figure 7

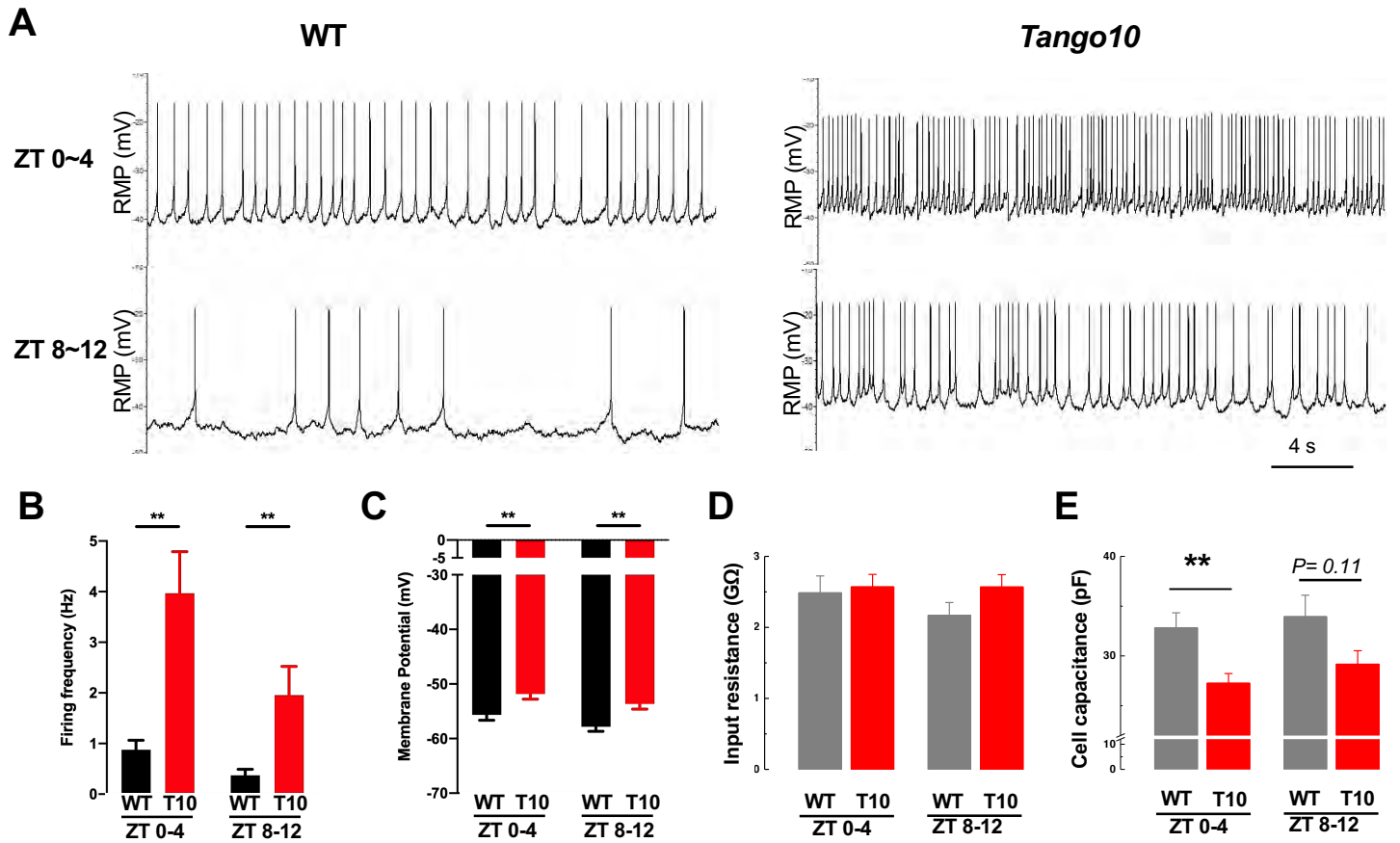


Figure 8

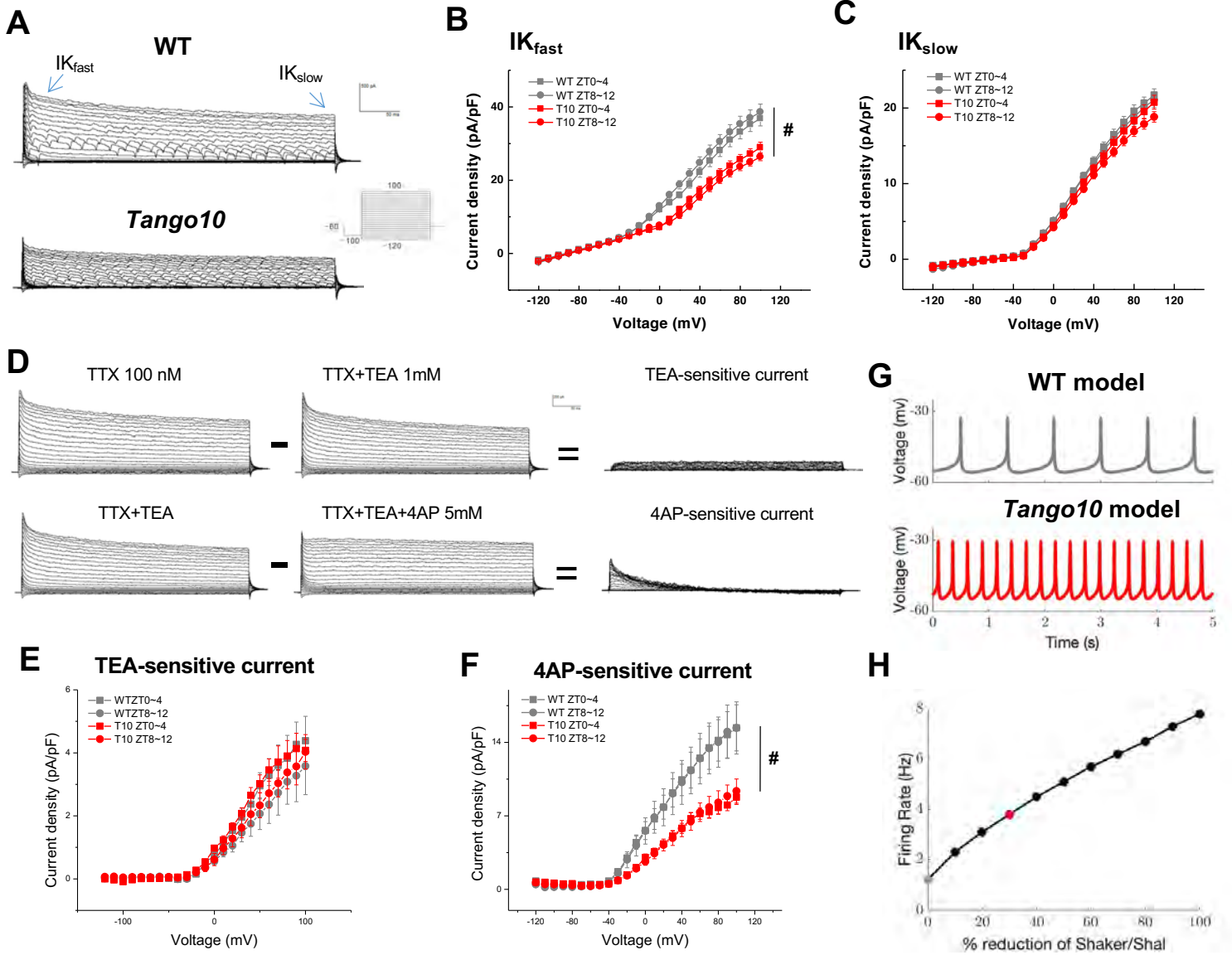


Figure S1

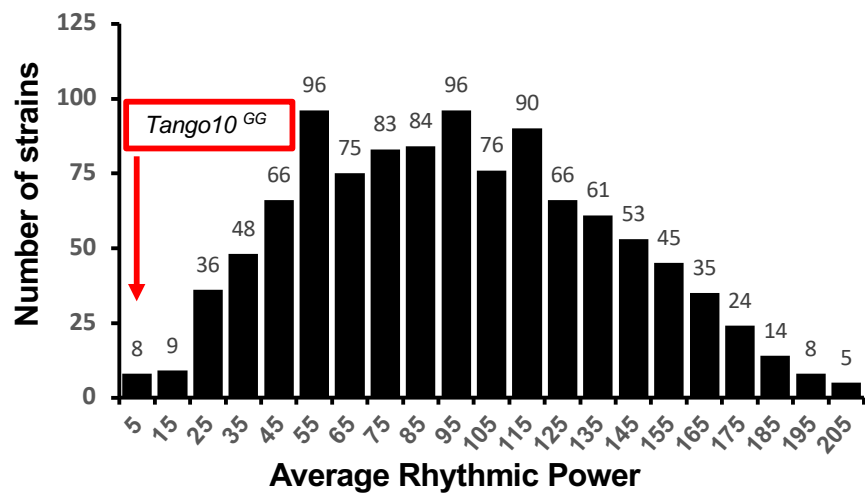


Figure S2

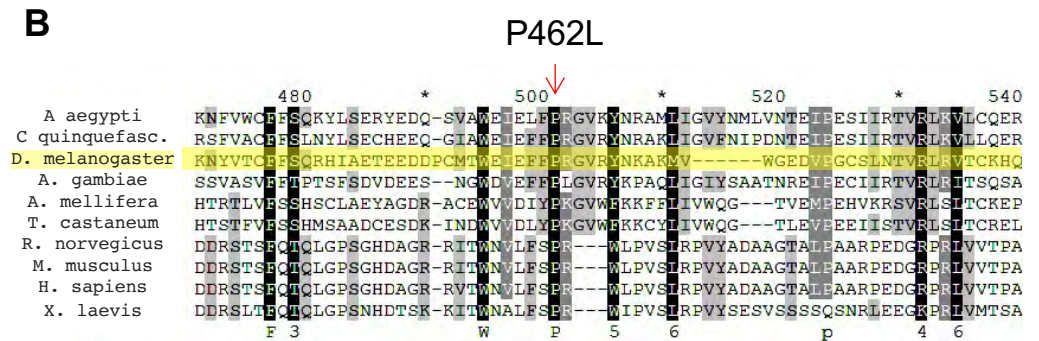
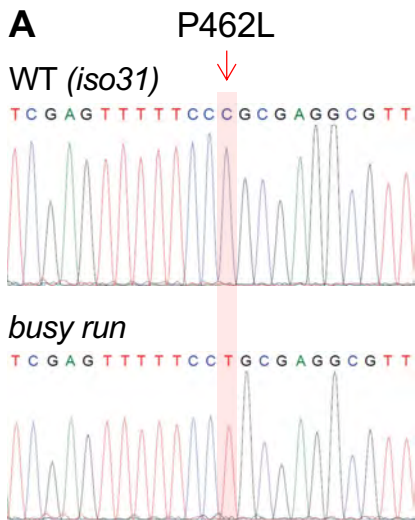


Figure S3

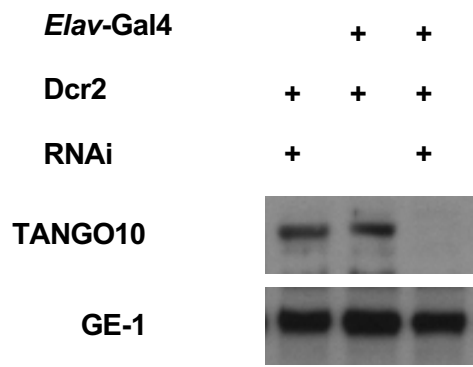


Figure S4

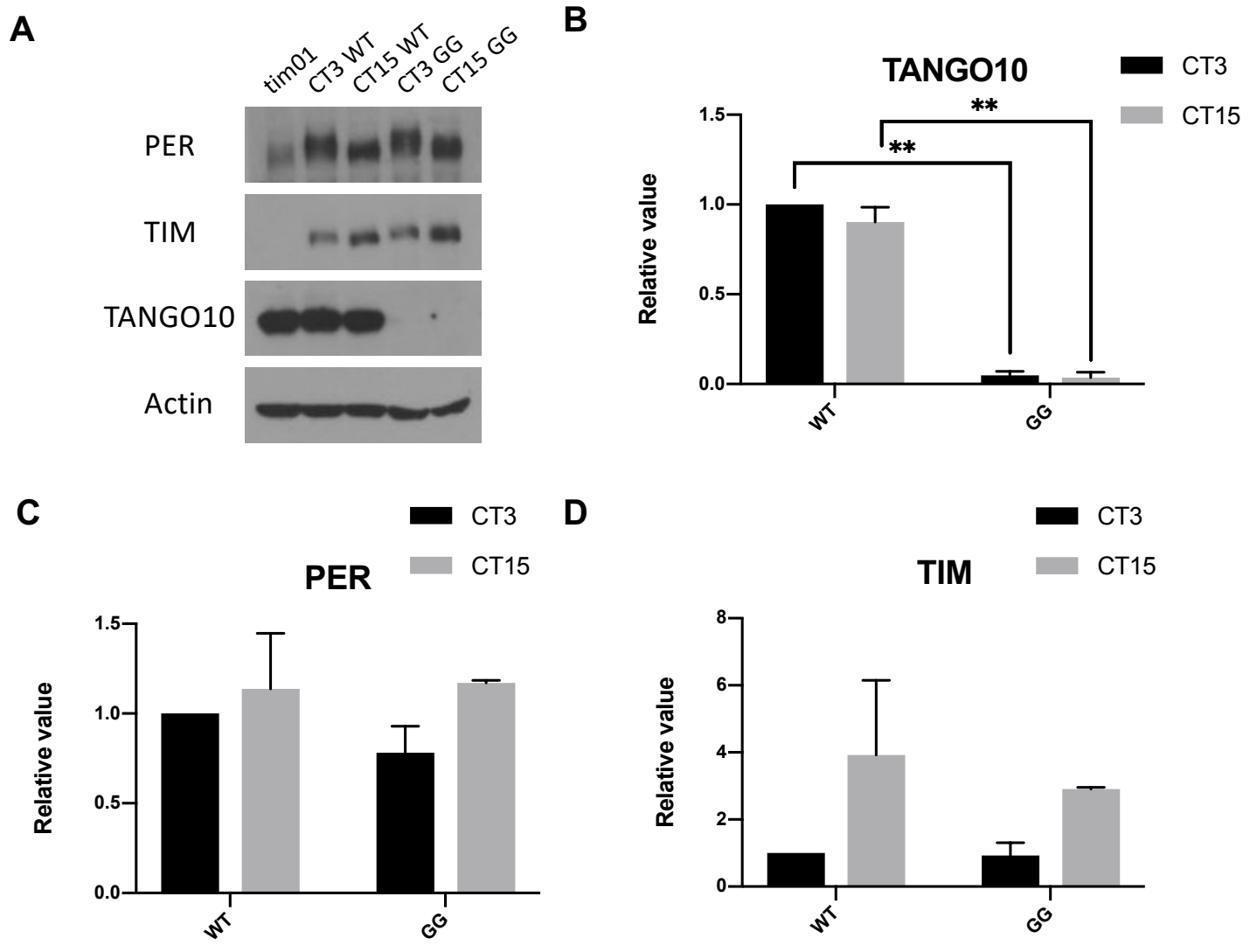


Figure S5

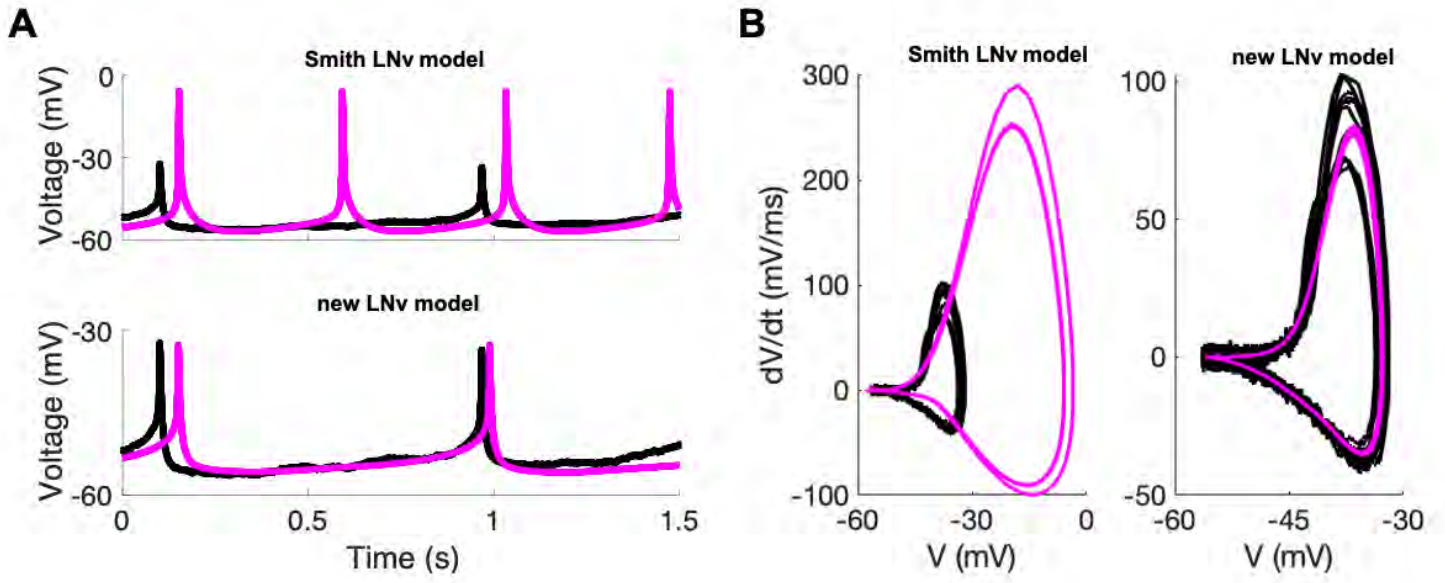


Figure S6

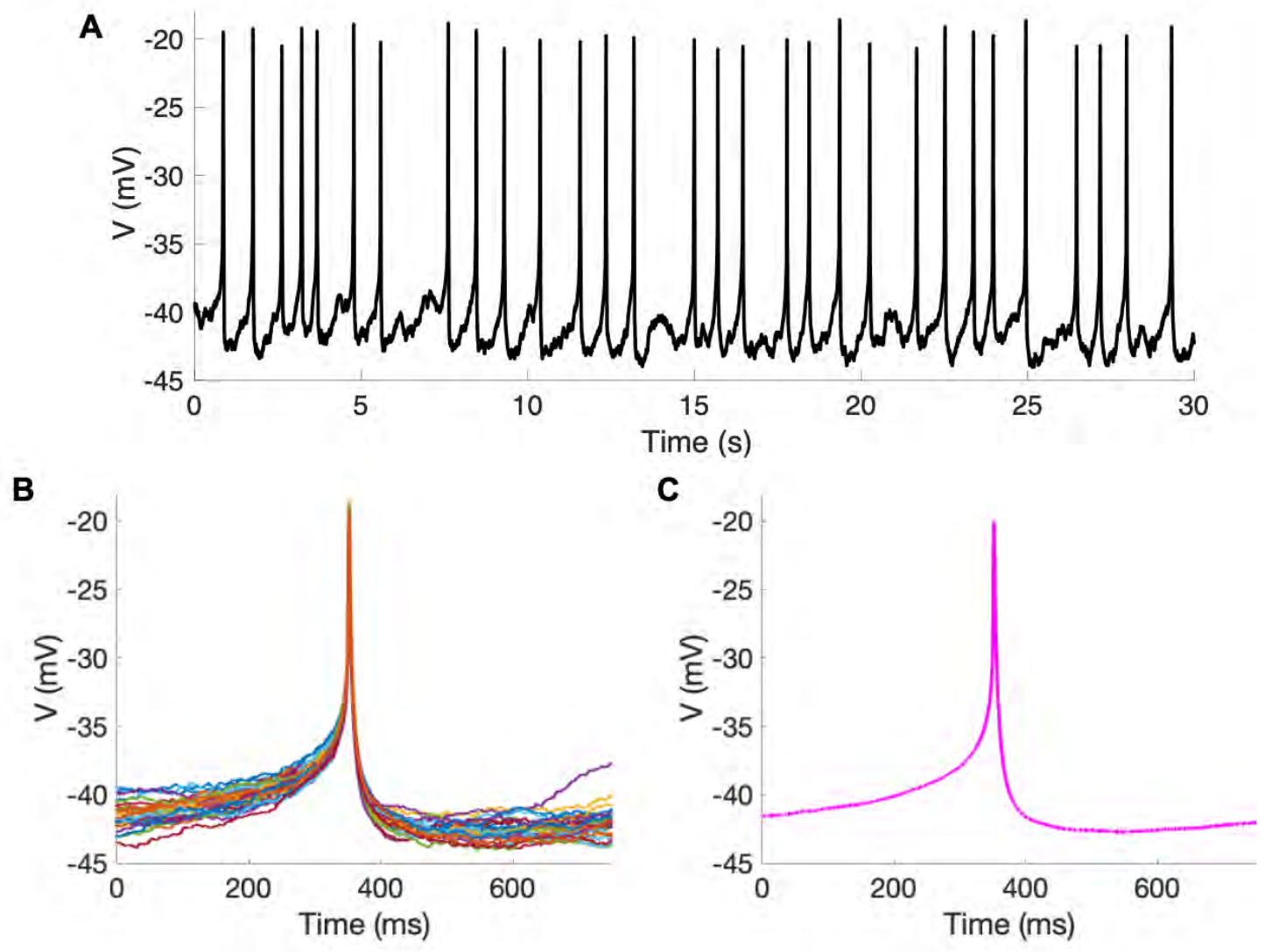


Figure S7

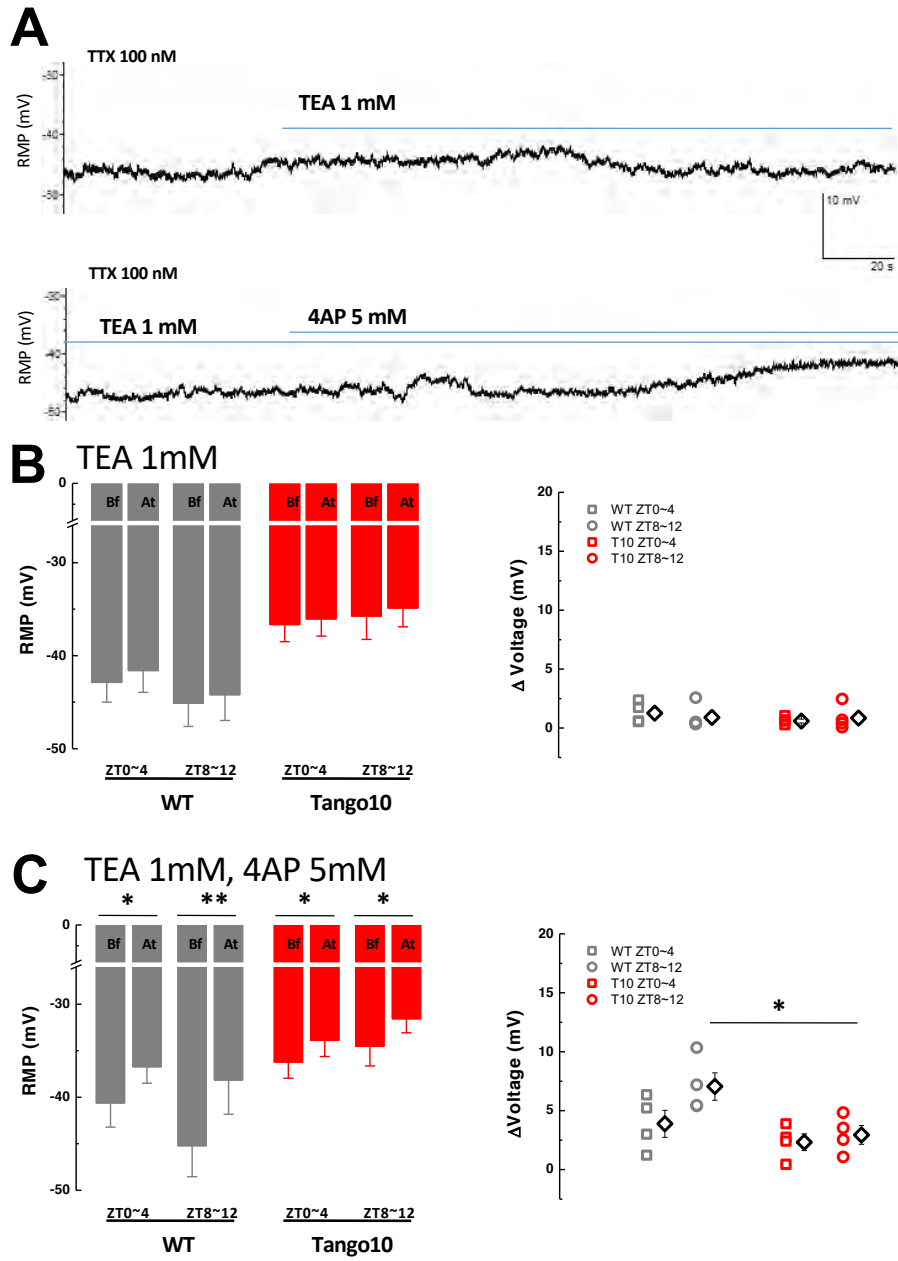
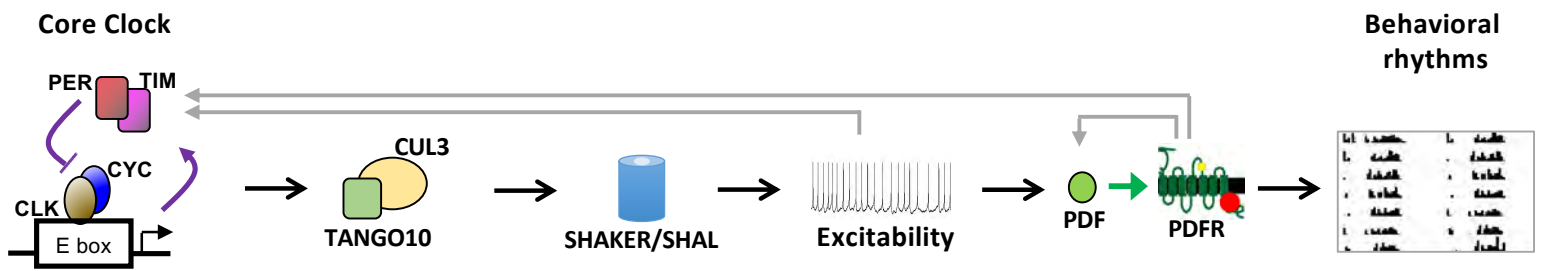


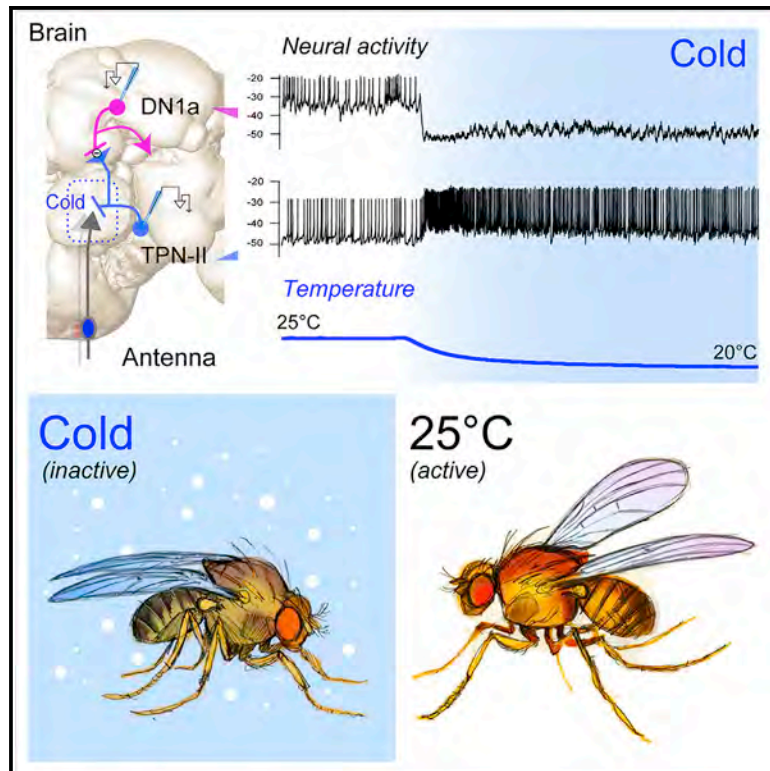
Figure S8



Current Biology

A Circuit Encoding Absolute Cold Temperature in *Drosophila*

Graphical Abstract



Authors

Michael H. Alpert, Dominic D. Frank, Evan Kaspi, ..., Ravi Allada, Alessia Para, Marco Gallio

Correspondence

marco.gallio@northwestern.edu

In Brief

Alpert et al. uncover a specialized circuit, from sensory neurons to higher brain centers that processes information about absolute cold temperature in *Drosophila*. This circuit directly connects thermosensory neurons of the antenna with circadian and sleep centers in the brain, adapting sleep and activity specifically to cold conditions.

Highlights

- The fly antenna contains 3 types of cold-activated sensory neurons
- Cold cells converge on “cold” domain of the brain thermosensory map
- Second-order TPN-IIs relay absolute cold, below *D. melanogaster*'s favorite 25°C
- TPN-IIs inhibit DN1a circadian neurons, adapting sleep to cold/dark conditions



Article

A Circuit Encoding Absolute Cold Temperature in *Drosophila*

Michael H. Alpert,^{1,2} Dominic D. Frank,^{1,2} Evan Kaspi,¹ Matthieu Flourakis,¹ Emanuela E. Zaharieva,¹ Ravi Allada,¹ Alessia Para,¹ and Marco Gallio^{1,3,*}

¹Department of Neurobiology, Northwestern University, Evanston, IL 60208, USA

²These authors contributed equally

³Lead Contact

*Correspondence: marco.gallio@northwestern.edu

<https://doi.org/10.1016/j.cub.2020.04.038>

SUMMARY

Animals react to environmental changes over timescales ranging from seconds to days and weeks. An important question is how sensory stimuli are parsed into neural signals operating over such diverse temporal scales. Here, we uncover a specialized circuit, from sensory neurons to higher brain centers, that processes information about long-lasting, absolute cold temperature in *Drosophila*. We identify second-order thermosensory projection neurons (TPN-IIs) exhibiting sustained firing that scales with absolute temperature. Strikingly, this activity only appears below the species-specific, preferred temperature for *D. melanogaster* (~25°C). We trace the inputs and outputs of TPN-IIs and find that they are embedded in a cold “thermometer” circuit that provides powerful and persistent inhibition to brain centers involved in regulating sleep and activity. Our results demonstrate that the fly nervous system selectively encodes and relays absolute temperature information and illustrate a sensory mechanism that allows animals to adapt behavior specifically to cold conditions on the timescale of hours to days.

INTRODUCTION

Changes in temperature influence animal behavior on both short (seconds to minutes) and long (hours to days and weeks) timescales. Rapid changes in the external temperature are transformed by the nervous system into the percepts of heating and cooling and used to quickly predict and avoid potentially dangerous thermal extremes. Meanwhile, sustained thermal conditions below or above the optimal range (perceived as cold or hot, respectively) trigger specific long-term behavioral and autonomic responses, including shivering or sweating; changes in sleep/wake patterns; and seasonal adaptations, such as hibernation or aestivation. Little is known on how these responses, happening on vastly different temporal scales, are orchestrated in the brain starting from the activity of peripheral thermosensory neurons.

The debate on how absolute temperature and temperature change are encoded in the nervous system is an old one and one that is central to our understanding of how sensory stimuli are processed on different timescales. Having observed robust adaptation as a result of prolonged exposure to cold temperature in humans, in the 1800s, Weber argued that only temperature changes and not absolute temperature stimulate thermosensory neurons [1]. In 1950, Hensel and Zotterman rebuked this notion, presenting data from cold receptors of the skin that showed a burst of firing in response to cooling but also persistent activity in response to stable cold [2]. This led to the idea that temperature change and absolute temperature information could be extracted from the complex activity of sensory neurons [3], but this has been difficult to prove experimentally in the

absence of specific assays and reagents that would allow one to dis-entangle transient from persistent signals.

Recent advances in microscopy and the availability of activity indicators have made it possible to systematically characterize the responses to temperature simultaneously in large numbers of neurons of the mouse trigeminal ganglion (innervating the oral cavity) [4] and dorsal horn of the spinal cord (receiving input from neurons innervating the skin) [5]. The results revealed an unanticipated complexity—with multiple functionally distinct classes of responses characterized by different adaptation properties and thresholds of activation. However, it is fair to say that, even after more than 200 years of work in this area, we still do not understand how information about temperature change and absolute temperature may be differentially extracted from the activity of sensory neurons at the periphery and relayed to the brain to trigger the appropriate responses.

Drosophila flies are small poikilothermic animals and are characterized by robust temperature-evoked behavior and a numerically simpler nervous system. On account of these advantages, work in the fruit fly is providing fundamental insights into the basic principles of temperature sensing and processing in the brain.

In flies, rapid temperature changes are detected by thermosensory neurons residing in the last antennal segment, the arista [6]. Each arista contains three thermosensory sensilla, each housing one hot- and one cold-activated cell. Much like their mammalian counterparts, antennal thermosensory receptor neurons (TRNs) respond to the preferred temperature stimulus (cooling for cold-activated TRNs, etc.) with activity that generally



scales with stimulus intensity. Non-preferred stimuli instead cause a decrease in intracellular calcium [6] and firing rates [7].

From their origin at the periphery, the axons of hot- and cold-activated TRNs of the arista converge onto a brain region called the posterior antennal lobe (PAL), where they form adjacent “hot” and “cold” glomeruli, defining a simple sensory map for the central representation of external temperature [6]. Next in line, second-order thermosensory projection neurons (TPNs) collect information from the PAL glomeruli and target higher brain centers involved in the processing of both innate and learned behavior [8, 9].

Interestingly, TPN cell types are characterized by different response dynamics to temperature stimuli: “fast-adapting” cells respond rapidly but transiently to the onset of a temperature change, and “slow-/non-adapting” TPNs are characterized by persistent activity [8, 9]. Differences in TPN adaptation dynamics are potentially very significant, as fast-adapting TPNs may relay temperature change signals, while slow-adapting cells are well positioned to relay information about absolute temperature.

How are temperature change and absolute temperature signals encoded in the activity of TPNs, relayed to higher brain circuits, and used to inform behavior happening on timescales ranging from milliseconds to seconds to days and weeks?

Here, focusing on cold responses, we set out to identify the source and significance of the persistent activity observed in slow-adapting TPNs. Our ultimate goal was to understand how the thermosensory system may process information about absolute temperature and how this information may be used to drive behavior happening on the appropriate timescales.

Our work leads to the identification of a circuit that functions as a conduit for information about absolute temperature in the cold range. This circuit displays persistent activity that scales with temperature, but only at absolute temperatures lower than the fly’s favorite $\sim 25^{\circ}\text{C}$, and directly targets higher brain centers involved in the control of sleep and activity, adjusting fly behavior specifically to cold conditions.

RESULTS

A Thermosensory PN Displays Persistent Activity in Response to Extended Cold Steps

To systematically study the adaptation dynamics of TPNs, we focused on two cold-activated TPN cell types previously described as fast and slow adapting (TPN-I and II in Figure 1A, identified by expression of the drivers VT19428 and R60H12, respectively) [8]. We designed a stimulation protocol that consists of a rapid temperature change ($\sim 2^{\circ}\text{C}/\text{s}$) followed by extended stable cold conditions (1–15 min), again followed by a rapid return to baseline. As before, we initially chose as the baseline the fly’s preferred temperature of 25°C and stimulus parameters (rate of change and temperatures ranges) reasonably close to what a fly may encounter in the environment. We then used two-photon calcium imaging and recorded TPN responses to temperature stimulation by targeting expression of the transgenic calcium indicator GCaMP to each cell type (i.e., under the control of selective drivers) [8].

Our results demonstrate that calcium levels in fast-adapting VT19428 TPNs quickly return to baseline after an initial

cooling-induced spike (TPN-I; Figure 1B). In contrast, R60H12 TPNs (TPN-II) respond to a cold temperature step with an initial calcium spike that accompanies the onset of cooling and that is followed by a rapid decrease to a plateau. The levels of intracellular Ca^{2+} do not return to baseline for as long as the temperature remains in the cold range (Figure 1C), supporting the notion that these cells may not adapt at all under conditions of persistent cold.

Calcium levels do not allow one to estimate the firing rate of a neuron in stable conditions. To obtain a more direct readout of TPN-II’s action potential firing under conditions of persistent cold, we next developed a method to perform two-photon guided patch-clamp electrophysiology by targeting TPN-II’s using GFP expression as a guide (again under the control of the selective driver R60H12-Gal4) [8].

Our patch clamp results confirmed and expanded what we had observed using calcium imaging. The firing rate of non-adapting TPN-II’s showed little or no evidence of adaptation; rather, TPN-II’s sustained a remarkably stable level of activity for the entire duration of the cold step. Only when the temperature started returning to baseline, TPN-II’s firing rate decreased, followed by a small inflection in membrane potential (Figures 1D and 1E; note that heating steps caused little response in TPN-II’s; Figures 1F and 1G). Protracted patch-clamp recordings further demonstrated that TPN-II’s display little or no adaptation even to extended cold stimuli (~ 25 min; Figures 1H–1J).

TPN-II Activity Correlates with Absolute Temperature in the Cold Range

Our next goal was to determine whether the persistent activity of non-adapting TPN-II’s at stable cold conditions indeed scales proportionally with (and may therefore contain information about) “absolute” temperature rather than correlate with other stimulus statistics, such as the magnitude of the initial cooling change (Δt).

To address this question, we designed temperature steps that either differed in the absolute temperature reached at stable conditions (different $|t|$, same Δt) or in the magnitude of the temperature change the preparation experiences on the way to the same stable conditions (different Δt , same $|t|$).

Our data show that the firing rate of non-adapting TPN-II’s at stable conditions (persistent activity) correlates with absolute temperature rather than with stimulus history (Figure 2). Remarkably, although an initial action potential burst (dynamic activity) was invariably observed in response to cooling (Figures 2A–2D), persistent activity (i.e., “plateau” firing rates above baseline firing) only appeared when the absolute temperature stabilized at temperatures lower than 25°C (Figures 2B, 2D, and 2E), i.e., lower than the preferred temperature for *Drosophila melanogaster*. Even when challenged with prolonged stimuli involving multiple cooling steps, static activity only emerged below 25°C (Figure 2F), and only in this range, firing rates correlated well with absolute temperature (Figures 2G and 2H).

These observations suggest that the non-adapting activity of TPN-II’s may indeed encode information about absolute temperature below the preferred range for *D. melanogaster*, i.e., in what can be described as cold temperature for the fly.

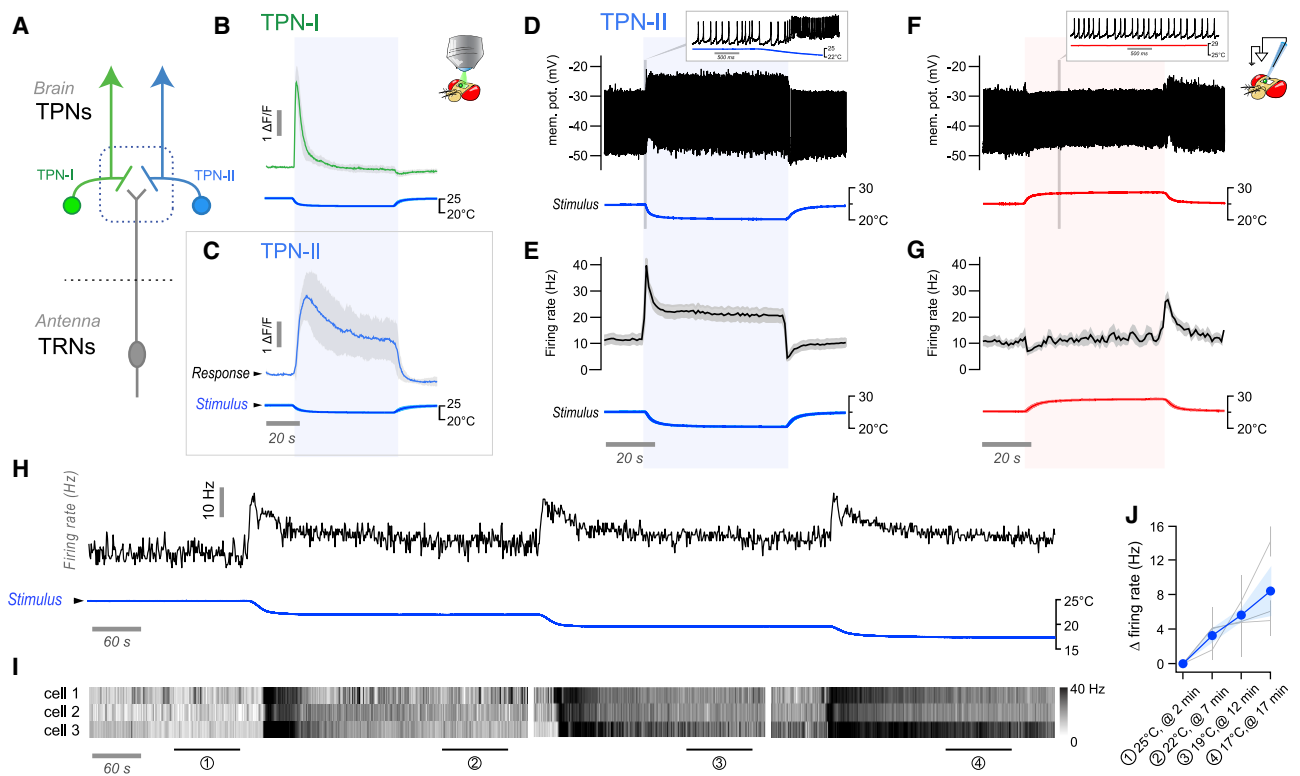


Figure 1. Identification of Thermosensory Projection Neurons Characterized by Non-adapting Responses

(A) Thermosensory projection neurons (TPNs) receive synaptic input from antennal thermoreceptors (TRNs).
 (B and C) Two-photon calcium imaging with GCaMP demonstrates significant differences in the adaptation of (B) type-I fast-adapting and (C) type-II slow/non-adapting TPNs to a cold temperature step (~1 min; $\Delta F/F$ traces are averages of B: 14 cells/3 animals, C: 5 cells/3 animals, \pm SD; stimulus trace is an average of the experiments \pm SD).
 (D–G) Two-photon guided patch-clamp electrophysiology reveals that TPN-II's firing is indeed non-adapting.
 (D) Representative whole-cell current clamp recording from a TPN-II in response to a cold step (~5°C; 1 min). Inset shows x axis expansion during cooling.
 (E) Firing rate histogram for TPN-II's responses to cold (9 animals/9 cells, 3 trials per cell were averaged in each experiment; $n = 9$ cells \pm SEM; temperature [temp.] trace: average [av.] of 9, \pm SEM).
 (F and G) TPN-II's are not significantly modulated by heat.
 (F) Representative whole-cell current-clamp recording from a TPN-II in response to a hot step (~5°C; 1 min). Inset shows x axis expansion.
 (G) Firing rate histogram for TPN-II's responses to hot (5 cells/4 animals, \pm SEM; temp. trace av. of 5, \pm SEM).
 (H–J) TPN-II's firing does not return to baseline even for extended cooling steps.
 (H) (Top) Representative recording from a TPN-II subjected to extended cooling steps.
 (I) Pseudo-colored spike rate histogram of 3 cells in response to a cooling stimulus similar to that in (H) (~20 min recordings; 3 Δ t steps as in H; responses aligned to stimuli).
 (J) Quantification (gray lines, mean \pm SD for individual cells calculated in regions corresponding numbered bars in I; blue line/shading, mean \pm SEM firing rate across cells; same 3 cells as in I).

The PAL Cold Glomerulus Is Independently Targeted by Distinct Populations of Thermosensory Neurons

Our results raise a number of important questions: where does this absolute cold temperature signal originate (at the sensory layer or within TPNs)? And what may be the behavioral significance of such a persistent cold-evoked activity in the fly brain? We set out to address each question in turn.

First, we re-evaluated the contribution of the sensory neurons of the antenna to TPN-II cold responses. Consistent with previous observations [8, 9], acute resection of the antennal nerve completely abolished TPN-II responses (Figure S1), suggesting that all cold-evoked activity originates in thermosensory neurons of the antenna (rather than within TPN-II's, and see below).

We reasoned that any sensory input into TPN-II's would have to come from neurons innervating the cold glomerulus of the PAL

(harboring the post-synaptic terminals of TPN-II's; Figures 3A and 3B) and screened a collection of Gal4 lines for drivers that would allow us to identify and selectively manipulate sensory input to this TPN cell type.

We discovered that at least 3 cell types independently target the cold glomerulus of the PAL: (1) the well-known TRNs of the arista [6] (labeled by a selective driver in Figures 3C and 3D); (2) a new population of sensory neurons that innervate chamber one of the sacculus, a structure previously shown to be involved in olfaction and humidity sensing [10, 11] (labeled by a selective driver in Figures 3E and 3F); and (3) an unusual cell type that expresses the broad sensory co-receptor IR25a and that resides on the surface of the antennal nerve (note that the terminals of this cell type within the PAL are clearly visible after external ablation of the antenna, i.e., as a result of degeneration of antennal

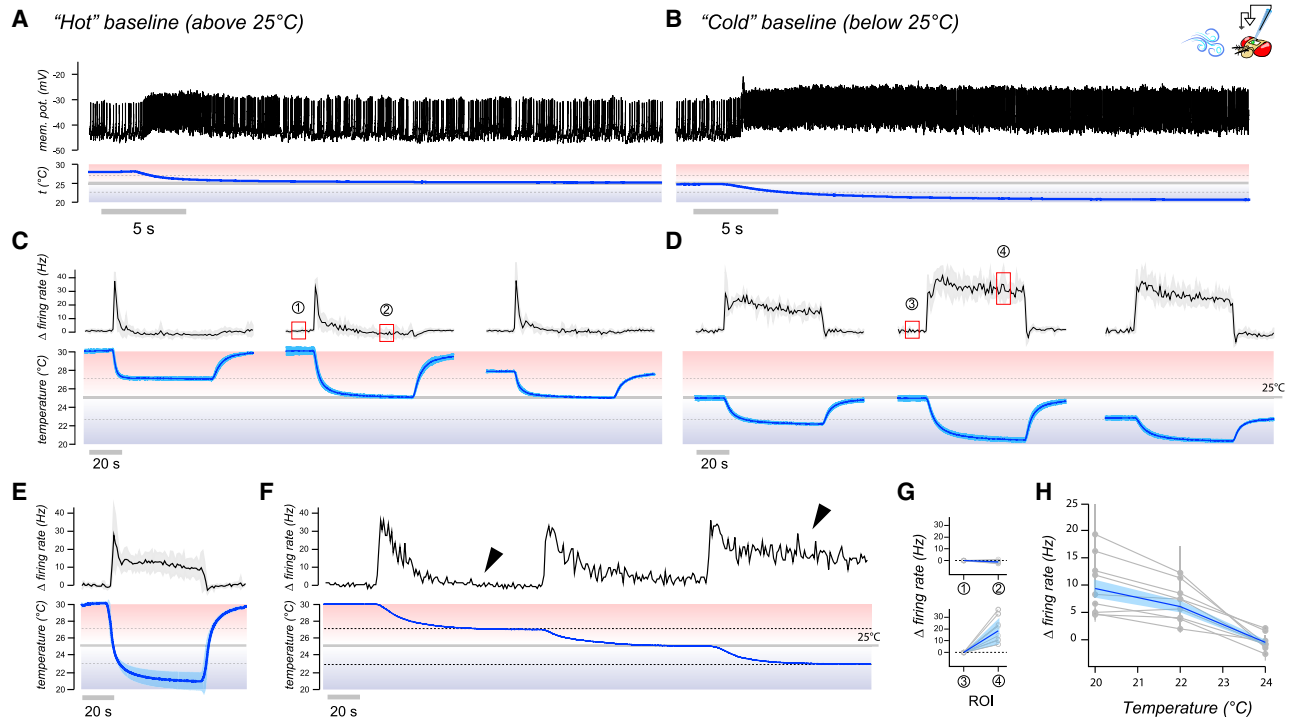


Figure 2. TPN-II Neurons Encode Absolute Temperature in the Cold Range

(A–F) Sustained firing of TPN-IIs depends on absolute temperature rather than stimulus history.

(A and B) Representative whole-cell current-clamp recording from a TPN-II in response to a cold step starting from a baseline temperature (A) above or (B) below 25°C (see also Figure S1).

(C and D) Firing rate histograms from TPN-II in response to cooling steps of different sizes (Δt) and settling on distinct absolute temperatures (C) above or (D) below 25°C (gray line), showing that persistent activity only appears in the cold range (below 25°C; 4 cells/4 animals, \pm SD; temp. trace av. of 4, \pm SD).

(E) Sustained firing in response to a large stimulus starting at 30°C and settling to ~20°C (3 cells/3 animals, av. \pm SD; temp. trace av. of 3, \pm SD).

(F) Representative response to a complex stimulus showing persistent firing below 25°C (gray line).

(G) Quantification of firing rates corresponding to numbered regions of interest (ROIs) in (C) and (D) (top: 10 cells/8 animals; bottom: 9 cells/9 animals).

(H) Quantification of TPN-II firing rate changes at stable temperatures below 25°C (readings were taken after ~1 min at each temp.; 9 cells/9 animals).

In (G) and (H), responses from the same cell are connected; colored lines and shading are population averages \pm SD (G) or \pm SEM (H); gray dots in (H) are averages of 3 repeats/cell/condition \pm SD; note that an f-test demonstrates a significant relationship between firing rates and temperature; $p < 0.05$.

afferents; Figures 3G and 3H). The location of this cell is similar to that of the previously described “anterior cell” neurons [12], and we therefore refer to it as the anterior cold cell (ACc) (Figure 3H, inset; see Figure S2 for further characterization of this unusual sensory neuron).

The observation that additional sensory cell types (besides the arista TRNs) [6] converge onto the cold glomerulus of the PAL was unexpected: we have previously described cold-responding sensory neurons innervating sensilla located in chamber two of the sacculus, but these neurons are part of an “hygrosensory triad” (composed of a dry-, humid-, and cold-activated cell innervating the same sensillum) and project to a distinct region of the PAL (the “column” or VP1 glomerulus) [10, 11]. The results of two-color two-photon microscopy instead suggest extensive intermingling between TPN-II dendrites, the terminals of chamber one sacculus neurons, and those of arista TRNs within the cold glomerulus of the PAL (Figures 3I–3O). Finally, we were surprised to find an additional “internal” temperature receptor within the head capsule (ACc; see above), which also selectively innervates the cold glomerulus. Our results confirm that each of these cell types independently innervates the cold glomerulus

indeed selectively responds to cold temperature stimuli (see below).

Multiple Pre-synaptic Drives Shape the Activity of TPN-IIs

Our next goal was to determine whether each of the sensory neurons innervating the cold glomerulus indeed provides direct synaptic drive to TPN-II. To test for connectivity, we employed activity-dependent, synaptic GFP reconstitution across synaptic partners (syb:GRASP) [13].

Our results suggest that each sensory cell population makes direct functional connections with TPN-II second-order neurons (Figures 3P–3R). Using selective drivers, we could directly demonstrate synaptic GFP reconstitution between chamber one sacculus neurons and TPN-IIs (Figure 3P). We have been so far unable to identify a driver only active in ACc neurons; to test for ACc:TPN-II connectivity, we used R77C10-Gal4—a driver active in both the arista cold-activated TRNs and ACc neurons. Robust GFP reconstitution using this line confirmed that one or both of these cell types indeed forms synapses with TPN-IIs (Figure 3Q; see [8, 9] for arista TRNs:TPN-II

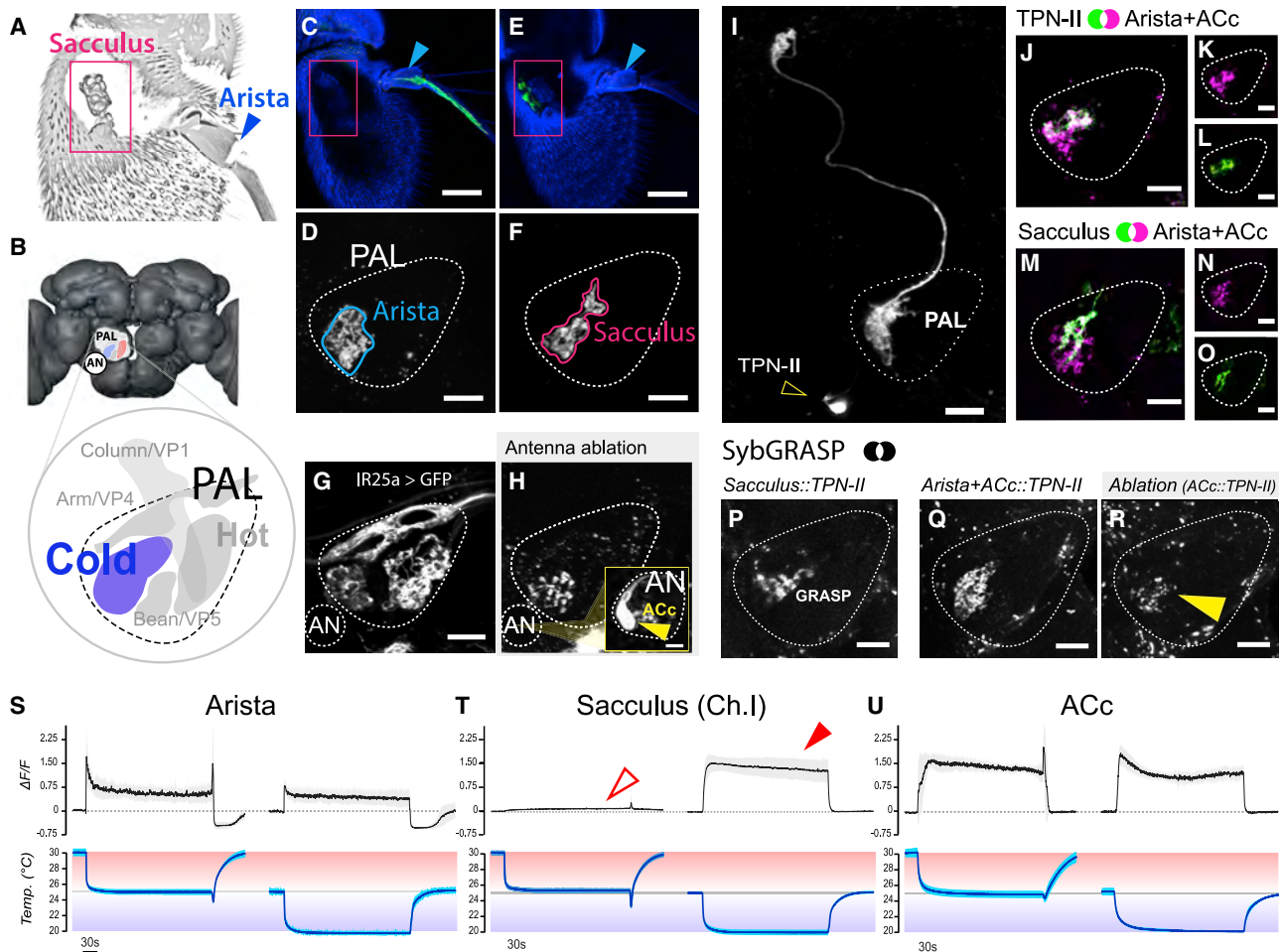


Figure 3. Three Distinct Populations of Peripheral Cold-Sensing Neurons Drive the Activity of TPN-IIs

(A) Confocal micrograph of the fly antenna showing the location of the sacculus (pink box) and arista (blue arrow).
 (B) 3D model of the fly brain showing the location of the posterior antennal lobe (PAL) and PAL glomeruli (inset; the glomerulus innervated by cold cells is shown in blue, additional glomeruli are annotated with standard nomenclature).
 (C–H) Selective drivers identify distinct sensory neuron populations targeting the cold glomerulus.
 (C and D) A selective driver for arista cold cells labels (C) cell bodies in the arista and (D) their PAL termini.
 (E and F) A selective driver for cold cells of the sacculus labels (E) cell bodies innervating chamber I of the sacculus and (F) their termini in the PAL (C and E are confocal micrographs of the whole antenna; blue, cuticle autofluorescence, green, GFP; scale bars, 50 μm ; D and F are single two-photon slices; scale bars, 10 μm).
 (G and H) Antenna ablation demonstrates the existence of an unusual “internal” cold receptor also innervating the PAL.
 (G) IR25a-Gal4 > UAS-GFP labels many of the antennal sensory neurons innervating PAL glomeruli.
 (H) A week following antennal resection, all antennal afferents have degenerated, revealing anterior cold cell (ACc) termini in the PAL. The fluorescent signal can be traced to one/two cell bodies located on the edge of the antennal nerve (AN) (inset; scale bar, 10 μm ; see also Figure S2).
 (I–O) Extensive overlap between TPN-II dendrites with both arista/ACc and sacculus termini in the PAL.
 (I) A selective split-Gal4 driver reveals TPN-II’s anatomy (two-photon z stack).
 (J–O) Two-color two-photon micrograph illustrating spatial overlap between (J–L) TPN-II dendrites (green) and Arista/ACc termini (magenta, single z slice) and between (M–O) sacculus (green) and arista/ACc termini (magenta).
 (P–R) Synaptobrevin GRASP confirms synaptic connectivity between TPN-IIs and (P) sacculus and (Q) arista/ACc; the fact that the syb:GRASP signal in (Q) persists a week post-antenna ablation (R) shows ACc also connects to TPN-IIs.
 (S–U) Two-photon Ca^{2+} imaging shows sacculus neurons exclusively respond in the cold range. Response profiles of (S) arista, (T) chamber I sacculus, and (U) ACc neuron termini in response to cooling steps in the hot (bottom, above 25°C, red) or cold (bottom, below 25°C, blue) range are shown.
 (S) Arista neurons show both a transient peak in response to cooling and a persistent Ca^{2+} elevation in both conditions.
 (T) Sacculus cold cells only respond when the temperature drops below 25°C (arrows).
 (U) ACc neurons show persistent signals both above and below 25°C.
 (S–U) show averages of 4 animals \pm SD. In all PAL panels, scale bars are 10 μm .

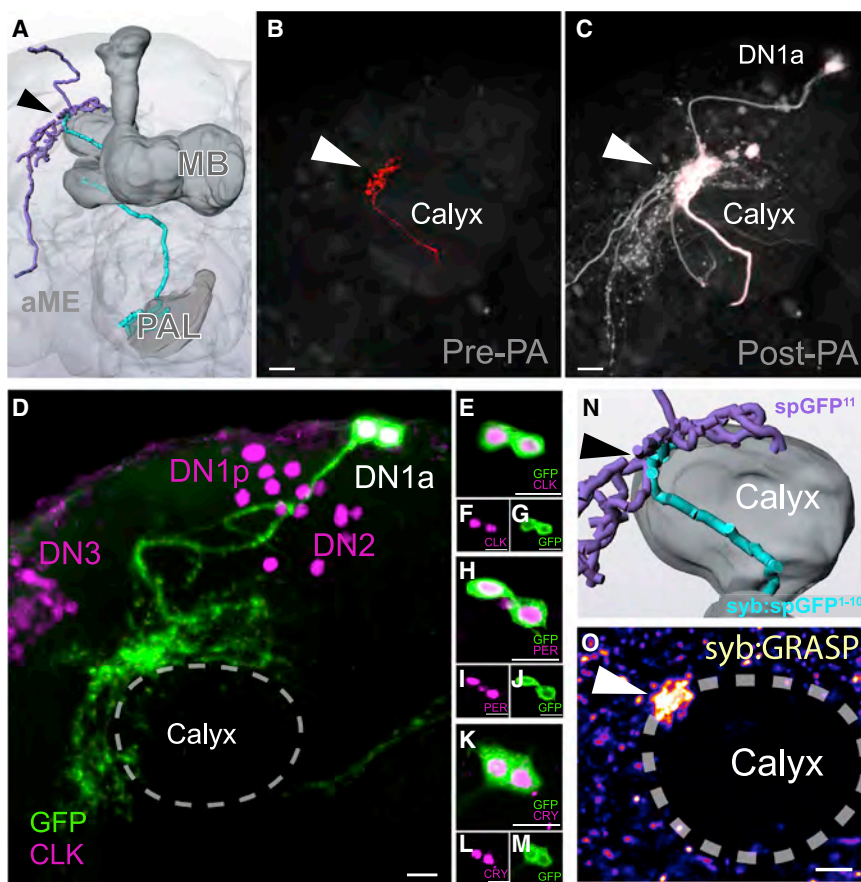


Figure 4. TPN-II Target the DN1a Group of Dorsal Neurons, Part of the Circadian Clock Network

(A) 3D reconstruction of the TPN-II (blue)-DN1a (purple) connection, at the edge of the mushroom body (MB) calyx.

(B and C) Photolabeling with PA-GFP reveals DN1as are candidate targets for TPN-II. For this experiment, (B; pre-photoactivation) TPN-II termini are targeted by independent labeling with TdTomato, although PA-GFP is expressed broadly. Following targeted photoactivation at 720 nm, (C; white) PA-GFP diffuses to label TPN-II targets.

(D–M) DN1as are identifiable by anatomy and because they express a combination of molecular clock components. Here, (D) DN1as were labeled by GFP expression (green, under the control of a selective driver) and immunostained using an anti-Clock antibody (CLK, purple; confocal z stack of a whole-mount fly brain; note that CLK also labels DN1p, DN2, and DN3).

(D–G) DN1as were labeled by GFP expression (green, under the control of a selective driver) and immunostained using an anti-Clock antibody (CLK, purple). (E) is an enlargement from panel (D) centered on DN1as; (F) purple channel, (G) green channel. (D–G, confocal z stack of a whole-mount fly brain; note that CLK also labels DN1p, DN2, and DN3).

(H–M) DN1as also express (H–J) period (anti-PER, purple) and (K–M) cryptochrome (anti-CRY, purple; in all panels, scale bar, 10 μ m).

(N and O) Syb:GRASP demonstrates mono-synaptic connectivity between TPN-II and DN1as.

(N) Enlargement of a 3D reconstruction showing predicted point of synaptic contact.

(O) Synaptic GFP reconstitution is observed between TPN-II and DN1a neurons at the edge of the mushroom body calyx (pseudocolored two-photon stack).

connectivity). Moreover, significant syb:GRASP signal persisted even a week following antenna ablation (i.e., following degeneration of antennal afferents; Figure 3R). This result suggests that ACc neurons are also independently connected to TPN-II.

Chamber I Sacculus Neurons Selectively Respond to Absolute Cold

Next, we asked which—if any—of these cold-sensing cell types may contribute the absolute cold temperature signal recorded in TPN-II. To address this question, we designed a stimulation protocol whereby the temperature is stepped down by $\sim 5^{\circ}\text{C}$ either from a baseline of 25°C or, alternatively, from a hot baseline of 30°C . In this setup, we expect that cells responding to absolute cold (rather than cooling) would only respond to the stimulus starting at the 25°C baseline and dipping into temperatures that are below the fly's favorite range (i.e., cold temperatures).

To test for temperature responses, we again used two-photon calcium imaging, measuring calcium transients at the PAL terminals of each cell type by selective targeting of GCaMP. Our results clearly demonstrate that, although the calcium responses of all three cell types appear to have non-adapting components, only the chamber one sacculus neurons exclusively respond to cold, but not to cooling (Figures 3S–3U).

Together with the results of connectivity experiments, this observation suggests that all three sensory cell types may

contribute to shape TPN-II's responses to temperature but that the absolute cold temperature signal recorded in TPN-II is relayed by chamber one neurons of the sacculus.

Interestingly, although calcium transients in the terminals generally correlate well with synaptic release, the activity recorded in TPN-II does not appear to be a simple summation of the activity of these pre-synaptic cell types, suggesting additional processing is likely to occur at this synapse.

TPN-II Have Selective Targets in the Fly Brain

What is the behavioral significance of this persistent, cold temperature activity relayed by sensory neurons of the sacculus and prominently recorded in specialized second-order neurons of the thermosensory system?

Although many second-order neurons of the thermosensory system (TPNs) share common higher brain targets (such as the calyx of the mushroom body, lateral horn, and posterior lateral protocerebrum) [8, 9], non-adapting TPN-II exclusively innervate a microglomerulus at the edge of the calyx [8] (Figure 4A). We reasoned that this anatomy may underlie selective connectivity in the brain and that revealing TPN-II's synaptic targets may illuminate circuits that utilize specifically cold temperature information to process behavior happening on slow timescales.

Therefore, we used two-photon guided conversion of photo-activatable GFP (PA-GFP) [14] to identify TPN-II's cellular

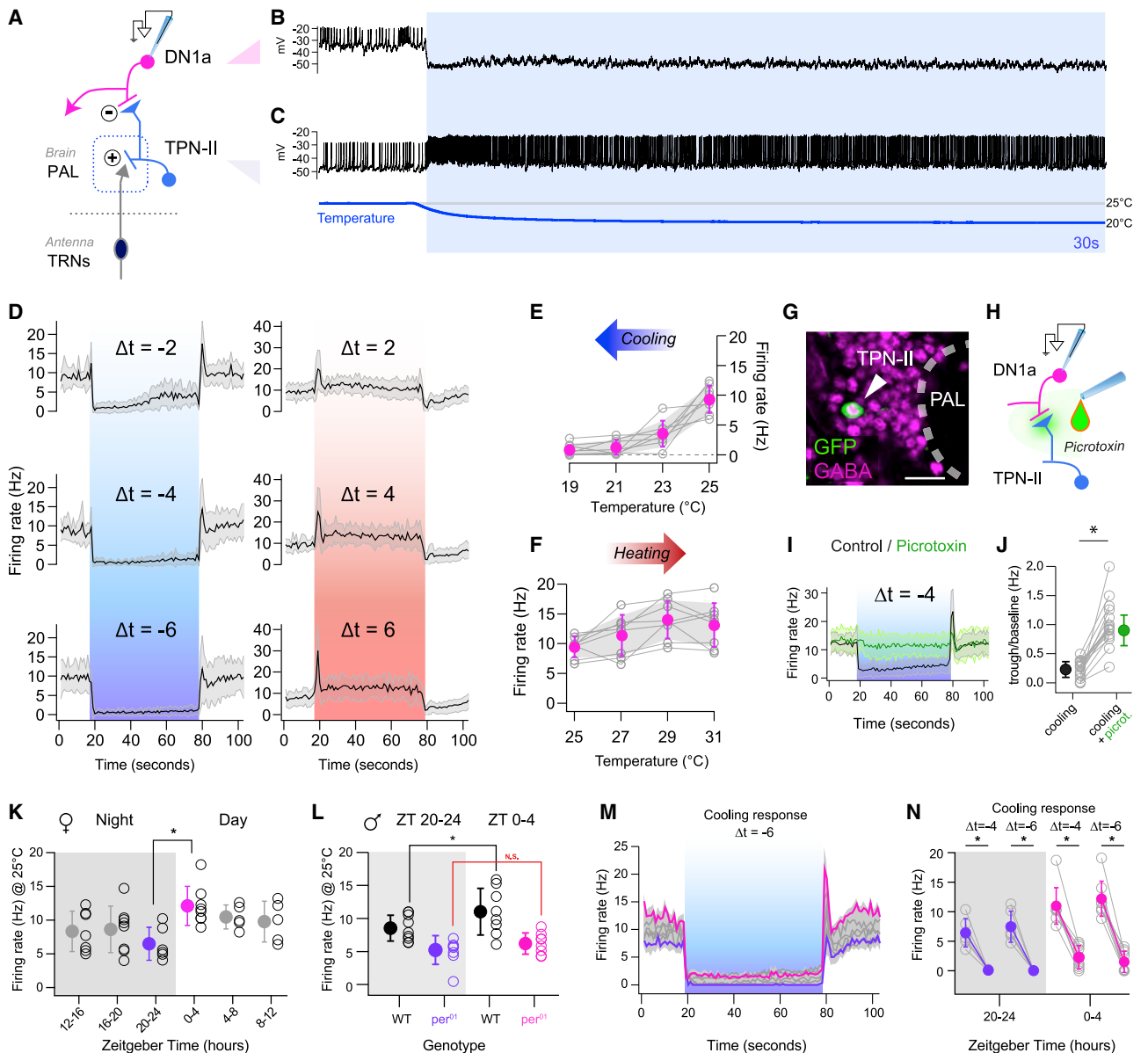


Figure 5. TPN-IIs Robustly Inhibit DN1a Activity in Cold Conditions through GABA Release

(A) Schematic representation of the circuit, including cold thermosensory neurons (TRNs) (dark blue), TPN-IIs (light blue), and DN1as (pink).
 (B and C) DN1a firing is persistently silenced by cold, correlating with TPN-II activation.
 (B and C) Representative whole-cell current-clamp recording (B) from a DN1a neuron and (C) from a TPN-II in response to a cold step (recorded independently).
 (D) Average firing rate histograms for DN1as challenged with cooling steps of different amplitude show robust silencing even for small stimuli (blue boxes; $\Delta t = -2$, $\Delta t = -4$, $\Delta t = -6$; 8 cells/7 animals; av. \pm SD). Note that corresponding heating stimuli produce an initial burst in activity but modest persistent modulation (red box, right; $\Delta t = 2$, $\Delta t = 4$, $\Delta t = 6$; 9 cells/8 animals; av. \pm SD).
 (E and F) Quantification of firing rates at plateau for (E) cold and (F) hot steps as in (D) (gray lines connect responses from the same cell; colored dots, averages \pm SD).
 (G) Whole-mount immunostaining showing that TPN-II (labeled by expression of GFP, white arrow) expresses the inhibitory neurotransmitter GABA (anti-GABA, pink, scale bar 10 μ m).
 (H–J) GABA release mediates cold inhibition of DN1as.
 (H) Schematic of the experiment.
 (I) Average firing rate histograms of DN1a in response to a $\Delta t \sim -4^\circ\text{C}$ cooling before (black) and after (green) application of the GABA receptor antagonist, picrotoxin (100 μM ; 13 cells/13 animals; av. \pm SD), showing that GABA receptor blockade abolishes cold inhibition of DN1as.
 (J) Quantification of (I) as trough-to-baseline ratio of firing rate (in first 10 s after cooling), before (black) and after application of picrotoxin (green). Gray circles connected by lines represent individual neurons; filled circles, population av. \pm SD; * $p < 0.05$ in a paired, one-tailed t test.

(legend continued on next page)

targets. First, we engineered flies where PA-GFP was constitutively expressed throughout the brain (under the control of *syb-Gal4*) and the TPN-II terminals were selectively labeled by a red fluorescent protein (Figure 4B). Then, using the red fluorescence as a guide, we photo-converted PA-GFP exclusively in a volume tightly overlapping the TPN-II axon terminals and traced the labeled neurites of next-order neurons as they became illuminated by diffusion of the photo-converted fluorophore (Figure 4C).

Our results reveal that prominent targets of R60H12 cold-activated TPNs are two distinctive neurons that have been previously described as components of the circadian network in the *Drosophila* brain (Figures 4C and 4D). The 1a cluster of “dorsal neurons” (DN1a) is part of a network of DNs that express key circadian gene products, such as clock and period (Figures 4D–4J). DN1as are defined by their unique anatomy (including projections to the accessory medulla) and by the fact that they are among a small group of DN1s that express cryptochrome [15] (Figures 4K–4M). Importantly, DN1as are indeed direct synaptic targets of TPN-IIs, as demonstrated by synaptic GRASP (Figures 4N and 4O).

DN1a Neurons Are Directly Inhibited by TPN-IIs in Cold Conditions

What is the effect of cold temperature on DN1a activity? Given TPN-II's firing rates are elevated in cold conditions and scale proportionally with cold temperature, we expected TPN-IIs to drive similar activity in the post-synaptic DN1as. Instead, cold temperature all but shut down activity in this cell type (Figures 5A–5C).

Using temperature steps of different magnitude (and patch-clamp electrophysiology as described above), we observed that a cooling step as small as 2°C was sufficient to nearly silence DN1as (from an initial baseline of nearly 10 Hz) and that the firing of this cell type was essentially completely silenced at temperatures 4°C or 6°C below the 25°C baseline (Figures 5D and 5E). As expected, and consistent with the properties of TPN-IIs, DN1a's inhibition by cold temperature was very persistent (showing limited recovery in stable cold conditions) and depended on the presence of the antennae (Figure S3).

In contrast to strong responses to cold, DN1as demonstrated little persistent modulation by heat (i.e., when the temperature was stepped above the 25°C range; Figures 5D and 5F). This is again consistent with the limited response recorded from TPN-IIs in the hot range. Interestingly, we did observe a rapid, heating-induced burst in DN1a firing that could not be directly correlated with the responses of the pre-synaptic TPN-IIs (Figure 5D; compare with Figures 1F and 1G). This observation

suggests an additional (albeit transient) heating-evoked drive to DN1a.

The fact that DN1as are powerfully silenced (rather than activated) by cold temperature and at the same time are synaptic targets of cold-activated TPN-IIs suggests that TPN-IIs may be inhibitory projection neurons. Indeed, immunohistochemistry demonstrated that TPN-IIs express the inhibitory neurotransmitter GABA (Figure 5G), and bath application of the GABA_A-receptor antagonist picrotoxin abolished cold inhibition of DN1as (Figures 5H–5J).

Together, our results suggest that cold-activated TPN-IIs directly inhibit the activity of the clock neuron cluster DN1a, through a GABA-ergic synapse, in cold conditions. Because clock neurons can exhibit endogenous (clock-regulated) rhythms in activity, we next tested the possibility that activity rhythms may also shape the firing profile of DN1as, perhaps gating the effect of cold temperature on DN1a activity.

DN1as Have Clock-Regulated Rhythms in Activity but Are Invariably Inhibited by Cold

Previous work has demonstrated that “posterior” DN1s (DN1ps) possess endogenous mechanisms to modulate firing rates in a time-of-day-dependent fashion [16]. To test whether DN1as may display similar properties, we recorded their activity at different times of day and night. Our recordings suggest that, as for DN1ps, DN1as also possess time-of-day-dependent modulation, with higher firing rates during the first part of the day (zeitgeber time 0 [ZT0]–4; ~12 Hz) as compared to the last time point of the night (ZT20–24; ~6 Hz; Figure 5K). These activity rhythms are present in both females and males (Figures 5K and 5L) and are regulated by the molecular clock, as they were abolished in *per*⁰¹ mutants (Figure 5L). Higher rates of DN1a firing in the morning may reflect an important role for these cells in the regulation of morning activity and/or in the night-to-day sleep/wake transition. Interestingly, notwithstanding these rhythms of activity, cold steps of 4°C or 6°C (from a baseline of 25°C) were effective in significantly reducing DN1a activity at all time points tested (Figures 5M and 5N). Hence, in the absence of other external stimuli, cold temperature should be effective in silencing DN1a activity at all times of day and night.

Cold Temperature Has Both an Acute and Persistent Effect on Fly Activity and Sleep

What is the functional significance of this powerful cold inhibition of DN1a? The DN1ps have been abundantly implicated in the regulation of sleep, including the onset and extent of the afternoon “siesta” flies enjoy in hot days [17–19], as well as the regulation of sleep patterns in cold days [20]. At least one previous

(K) Baseline firing rates of DN1as at 25°C measured during different times of day (white) and night (gray). Firing rates from different cells (black circles) were grouped in 4-h bins (filled circles; mean ± SD). Morning rates (pink) were significantly higher than evening ones (purple; *n* = 39 cells/32 animals; **p* < 0.05; unpaired one-tailed *t* test).

(L) Circadian rhythms of DN1a firing are absent in *per*⁰¹ mutants. Nighttime and daytime firing rates of DN1as at 25°C recorded from wild-type (WT) (**p* < 0.05; unpaired one-tailed *t* test) and period mutant flies are shown (*per*⁰¹; NS, not significant difference; unpaired one-tailed *t* test; black circles are individual cells; filled circles indicate av. ± SD; *n* = 35 cells/21 animals; recordings are from +/Y and *per*⁰¹/Y male flies).

(M and N) DN1as are inhibited by cooling at all ZTs.

(M) Mean firing rate of DN1as in response to a cooling step (blue box, from 25°C; individual gray traces represent averages; ZTs as in L; ZT20–24 and ZT0–4 are colorized as in K; envelope: ±SEM, *n* = 40 cells/32 animals).

(N) Quantification of change in firing frequency in response to different cooling steps (from 25°C) during the night (ZT20–24, purple) and day (ZT0–4, pink; gray circles connected by lines indicated individual cells; filled circles indicate mean ± SD; **p* < 0.05; paired one-tailed *t* test; 14 cells/10 animals; see also Figure S3).

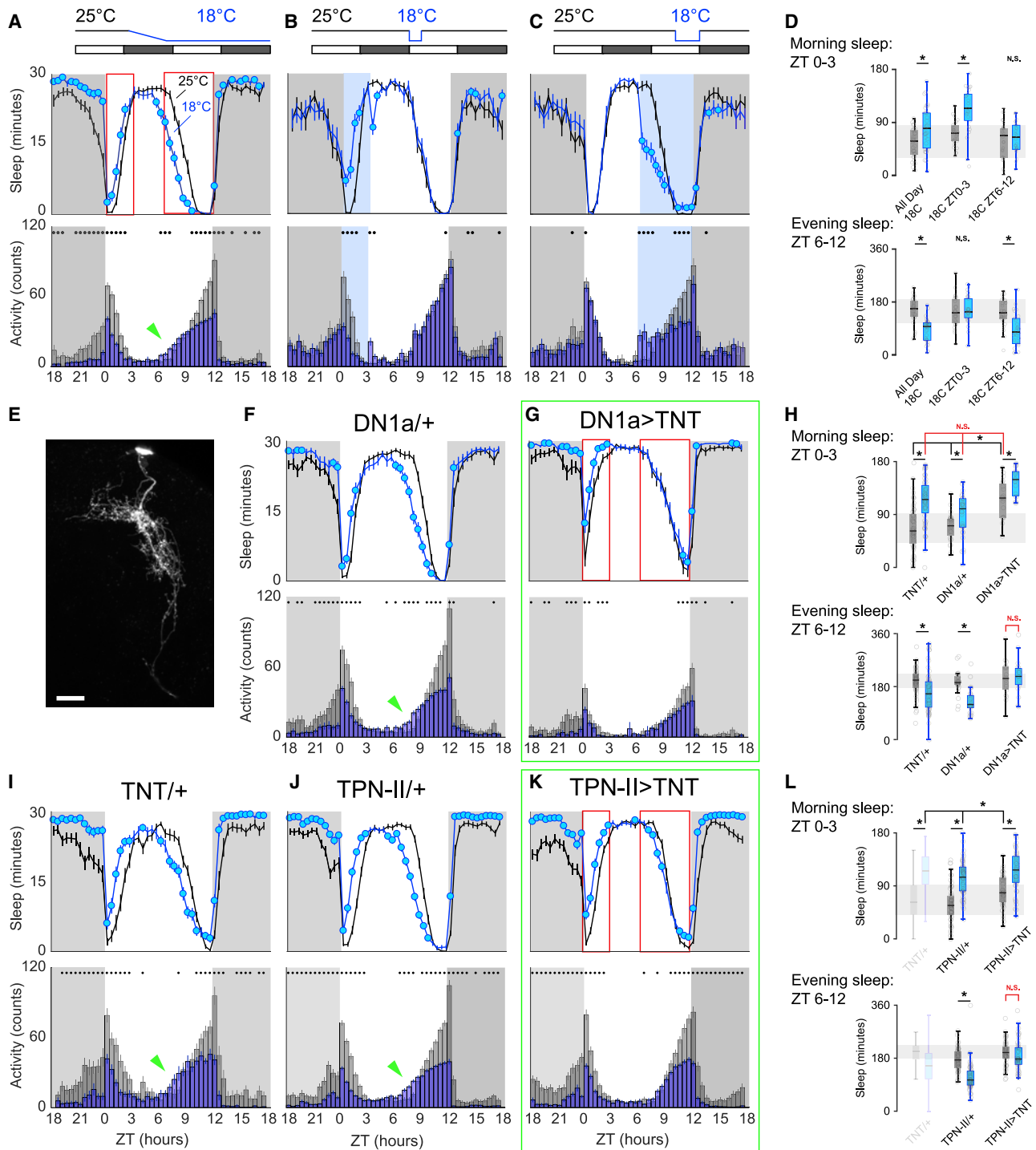


Figure 6. Genetic Silencing of Either DN1a or TPN-II Perturbs Normal Daytime Sleep Restructuring by Cold

In wild-type flies, cold temperature has both acute and persistent effects on daytime activity and sleep. In (A), (F), (G), and (I)–(K), activity and sleep were quantified in 30-min bins in 2 consecutive days per condition (B and C: 1 day/condition). Schematics on top illustrate the experimental design. Data plots represent sleep (above) and activity bar graphs (below) and are averages \pm SEM across days and across individual flies; filled circles in sleep plots and black dots above activity bars indicate time points that are significantly different between cold (18°C, blue) and 25°C (gray) conditions ($p < 0.05$; paired two-sided *t* test); dark shades indicate lights off (night); ZT, zeitgeber time.

(A) In wild-type animals, cold conditions increase morning sleep and suppress morning activity (ZT0–3); in contrast, cold reduces both sleep and activity in the evening (ZT6–12). Moreover, the onset of evening sleep is advanced (green arrowhead in A). As a result, the net effect of cold is an advancement of daytime sleep. (B) Morning cold (ZT0–3) rapidly suppresses activity and increases sleep; following the return to 25°C, sleep and activity quickly return to normal levels.

(legend continued on next page)

publication suggests that DN1as may also be involved in the regulation of daytime sleep [21].

Here, our goal was to test the possibility that DN1as may be directly involved in the regulation of activity and sleep by temperature and that their powerful inhibition by cold may be of significance for the regulation of activity/sleep patterns in persistent cold conditions. Unlike previous studies, our experiments could be guided by knowledge of the specific thermal range that modulates DN1a's activity via connections with the antennal TRNs/TPN-II circuit (Figure 6).

At the normal rearing temperature of 25°C (and under 12 h light:12 h dark, or LD, cycles), fly behavior is characterized by peaks of activity corresponding to the late night-early morning transition ("morning peak") and to the end of the day ("evening peak"; see Figure 6A, gray bar graph). Fly sleep is generally defined as inactivity that persists for 5 min or longer [22, 23], and as such, most of fly sleep occurs at night, yet flies (male flies in particular) [24] also display a prominent mid-day siesta (Figure 6A, black plot)—perhaps to avoid potentially hot/dry conditions in the mid-day [25].

Cold temperature (18°C) has both an acute and persistent effect on fly activity and sleep: cold conditions rapidly suppress morning activity (and increase morning sleep; Figure 6A, blue bar graphs and lines). Activity in the evening is also reduced; in addition, the onset of evening activity is advanced (arrow in bar graph, Figure 6A). The overall effect of cold on daytime sleep is that the siesta is advanced to earlier time points—potentially an adaptation to the fact that cooler conditions normally accompany the seasonal shortening of days (Figure 6A, blue plot; see also [26]).

Interestingly, this acute shift in siesta sleep can be ascribed to independent and reversible effects of cold temperature on sleep in the morning and evening: in LD conditions, a defined 3 h cold step in the morning *increases* sleep (but, following return to 25°C, fly behavior returns to normal; Figure 6B), although a similar defined cold step in the evening *decreases* sleep (Figure 6C; see Figure 6D for quantifications).

Silencing DN1a Output Mimics Cold Conditions

Are DN1as involved in the restructuring of daytime sleep in response to cold temperature? To test the potential involvement of DN1as (and TPN-IIIs) in this process, we first developed genetic reagents to selectively target each cell type for genetic silencing. Starting from broader drivers, we created intersectional split-Gal4 lines narrowly active in either DN1as (Figure 6E) or non-adapting TPN-IIIs (see Figure 3I and STAR Methods for details). Next, we used these drivers to express a transgenic

blocker of synaptic transmission (tetanus toxin light chain) [27] and monitored the effect of this manipulation on sleep and activity.

Remarkably, genetic silencing of DN1a's output at 25°C partially mimicked cold conditions: under LD cycles, the onset of siesta sleep was advanced even at 25°C, resembling the response to cold conditions observed in controls (Figures 6G and 6H; see Figures 6F and 6I for controls). This suggests that reducing the output of DN1as in the morning may be a key mechanism for daytime siesta sleep advancement by cold temperature. Interestingly, blocking DN1a's output also prevented the plastic remodeling of sleep by cold temperature in the evening (ZT6–12). This time, constitutive block of DN1a output produced a stable (i.e., temperature-independent) sleep profile more similar to the control's 25°C conditions, as DN1a > tetanus toxin light chain (TNT) flies did not reduce the amount of evening sleep in response to cold (Figures 6G and 6H).

As cold temperature suppresses DN1a firing in both morning and evening (Figure 5), this observation is incompatible with simple models, in which silencing DN1a invariably results in more sleep, irrespective of time of day. Instead, our results suggest that the appropriate timing and extent of DN1a activity may be crucial for the dynamic regulation of daytime sleep patterns and for their plastic adaptation to changes in the external temperature.

Next, we tested the potential impact of TPN-II silencing. Our previous results suggest that TPN-IIIs provide powerful inhibitory drive to DN1as in cold conditions. Consistent with this, silencing TPN-II's output had no effect on sleep at 25°C. After a shift to 18°C, siesta sleep of TPN-II > TNT flies advanced normally. Interestingly, constitutive block of TPN-II's output again prevented sleep restructuring in the evening, producing a stable sleep profile similar to that of DN1a > TNT flies (Figures 6K and 6L; compare to Figures 6G and 6H).

The fact that reducing the output of inhibitory neurons (TPN-IIIs) had the same (rather than the opposite) effect on evening sleep to that obtained by silencing their targets (DN1as) is again consistent with the notion that the dynamics of DN1a activity (rather than their net output at a given time point) may be important to determine the appropriate pattern of daytime sleep, so that locking the system in one state may produce similar effects.

Notably, the overall daytime sleep profile of TPN-II > TNT flies at 18°C was remarkably similar to that of DN1a > TNT flies at 25°C (both in the morning and evening; compare Figure 6K, blue plot with Figure 6G, black plot). This daytime sleep profile

(C and D) Evening cold (C; ZT6–12) decreases sleep so that, together, morning and evening effects recapitulate all day cold conditions (n = 31 animals in A, 26 in B and C; see D for quantifications).

(E) A split-Gal4 driver allows selective targeting of DN1as (shown driving GFP; two-photon z stack; scale bar, 20 μm).

(F–L) Silencing DN1as or TPN-IIIs using selective split-Gal4s perturbs sleep restructuring by cold temperature.

(F, I, and J) Control genotypes (n = 30 in F; n = 61 in I; n = 62 in J).

(G) Silencing DN1as by expression of tetanus toxin light chain (TNT) partially mimics cold conditions, producing flies that sleep more in the morning even at 25°C and that fail to restructure their afternoon sleep in response to cold (n = 19 animals).

(K and L) Silencing (K) TPN-II output with TNT also produces flies that fail to restructure afternoon sleep in response to cold (n = 52 animals; see H and L for quantifications; in all boxplots, box edges: 25th and 75th percentiles; thick lines: median; whiskers: data range; gray dots: individual data points/flies; *p < 0.05 in paired two-sided t test comparing 25°C versus 18°C within genotype or two-way ANOVAs with a Bonferroni correction for multiple comparisons across genotypes/temperatures).

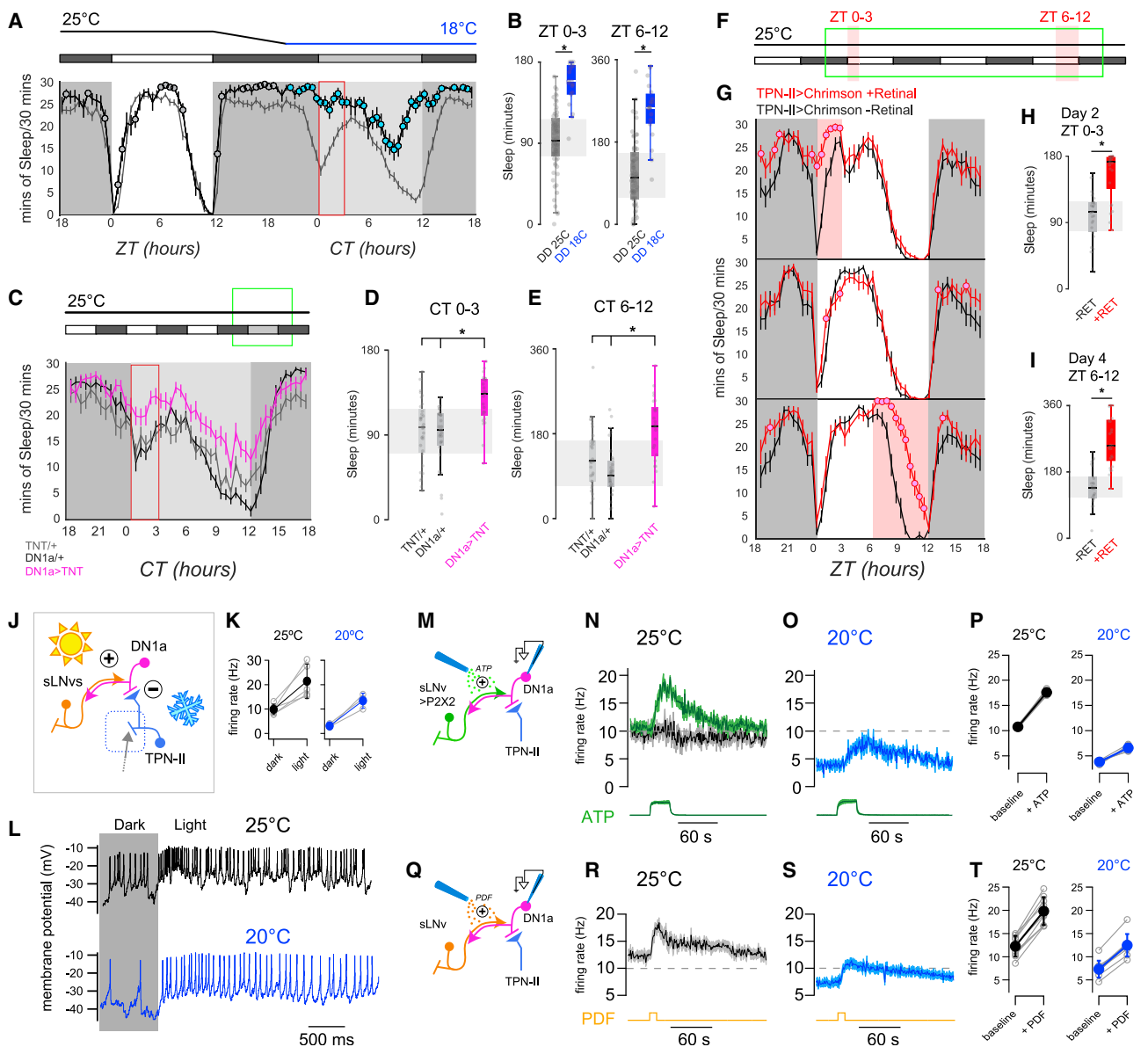


Figure 7. Sleep and DN1a Activity Are Modulated by the Opposing Pushes of Light and Cold Temperature

(A and B) Cold and dark synergize to increase sleep across the day.

(A) (Top) Behavioral protocol used to evaluate sleep on flies entrained in 12 h light-dark (LD) cycles (white box: day [lights on]; black box: night [lights off]; gray box: subjective day [lights off]). (Bottom) Sleep plot for two independent groups of control (wild-type) flies during a single LD day at 25°C and in the following dark day at either 18°C (blue line; n = 19 animals, ±SEM) or 25°C is shown (gray line; N = 19 animals, ±SEM; filled circles indicate time points that are significantly different between conditions; p < 0.05; unpaired two-sided t test).

(B) Quantification of total sleep in the indicated intervals (box edges: 25th and 75th percentiles; thick lines: median; whiskers: data range; gray dots: individual data points/flies; *p < 0.05 in unpaired two-sided t test).

(C–E) In the dark, suppressing DN1a output by TNT expression mimics cold conditions, increasing sleep across the day.

(C) (Top) Behavioral protocol. (Bottom) Sleep in DN1a > TNT flies (orange trace; n = 25 animals), UAS-TNT/+ (gray; n = 32 animals) and DN1a-Gal4/+ flies is shown (black; n = 31 animals; all traces are av. ± SEM; circles, significantly different from both controls in two-way ANOVA; p < 0.05).

(D and E) Quantification of total sleep in the indicated intervals for genotypes in (C) (box edges: 25th and 75th percentiles; thick lines: median; whiskers: data range; gray dots: individual data points/flies; *p < 0.05; two-way ANOVA with a Bonferroni correction for multiple comparisons across genotypes).

(F–I) Optogenetic activation of TPN-II produces an acute increase in sleep.

(F) Protocol used (3 consecutive days represented top to bottom); red shading indicates optogenetic activation.

(G) Sleep pattern of TPN-II > Chrimson flies fed all-trans retinal (red trace; 25 animals) or control food (black; 27 animals—note that retinal is essential for Chrimson function; traces: av. ± SEM; circles, significantly different from controls in two-sided t tests; p < 0.05).

(H and I) Quantification of total sleep in the indicated intervals (H) ZT0–3 on day 2 and (I) ZT6–12 on day 4 (box edges: 25th and 75th percentiles; thick lines: median; whiskers: data range; gray dots: individual data points [flies]; *p < 0.05; unpaired, two-sided t test).

(legend continued on next page)

may perhaps represent a default state of the system that results from manipulations that disconnect it from external temperature drive.

Despite this potentially complex interaction, our results suggest that the circuit composed of inhibitory TPN-ILs and DN1a plays a key role in mediating the restructuring sleep and activity patterns in cold conditions.

Dark and Cold Synergize to Suppress Morning Wakefulness

In the environment, the seasonal arrival of cold temperatures is often accompanied with darker conditions and shorter days. Next, we tested the potential impact of light on DN1a function and fly behavior in the cold. Under light/dark cycles in constant cold (LD at 18°C), control flies robustly wake up at the first appearance of light (“lights on”) but quickly return to sleep within 60–90 min (Figure 6); our results also demonstrate that, at 25°C, blocking DN1a output significantly increases morning sleep, partially mimicking cold conditions (Figures 6G and 6H). Interestingly, when switched to constant dark/cold conditions (DD at 18°C), control animals nearly fail to wake up in the morning altogether (Figure 7A, blue line; see Figure 7B for quantification). Blocking the output of DN1as mimics this effect of cold, so that—in the absence of a light signal—most DN1a > TNT flies fail to wake up in the morning even at 25°C (Figures 7C–7E). Optogenetic activation of TPN-ILs was sufficient to reproduce this effect, generating animals that largely ignore the lights on signal in the morning (Figures 7F–7H; note that, in dark conditions, cold temperature also produces a significant increase in evening sleep, an effect reproduced by DN1a silencing and optogenetic activation of TPN-ILs; Figures 7F, 7G, and 7I).

Hence, light and cold have powerfully antagonistic effects on morning wakefulness. Based on these results, we tested the interaction of light and temperature in regulating DN1a firing rates.

DN1as Directly Integrate Light and Cold Temperature Signals

Ample evidence suggests that DN1a activity may be directly or indirectly modulated by light. For example, DN1as express the blue light receptor cryptochrome [15] and, in the larva, are known

targets of light-responsive ventral lateral neurons (LNvs) (a core component of the clock circuit) [28]. Importantly, the “small” LNvs or sLNvs have been described as master regulators of morning activity [29] and have been suggested to form reciprocal connections with DN1as [21].

Our results suggest that indeed DN1as respond to light as well as to sLNv signaling. First, we observed light responses in DN1a (Figures 7J–7L; see [29]). Next, we showed that “artificial” activation of sLNvs using P2X2 results in an increase of DN1a firing (Figures 7M and 7N). Finally, we recorded an increase in firing rates in DN1as upon focal application of the neuropeptide pigment dispersing factor (PDF) (normally expressed by sLNvs [30] and for which DN1as express the cognate receptor PDF receptor [PDFR] [31]; Figures 7Q and 7R).

Strikingly, light exposure, artificial sLNv activation, and PDF application were each able to partially overcome cold inhibition of DN1as (Figures 7K, 7L, 7O, 7P, 7S, and 7T), suggesting that light and/or LNv signaling (through PDF release) could drive DN1as even in cold conditions and explaining the dominant effect of light in setting the beginning of daytime activity.

Together, our results demonstrate functional connectivity between sLNvs and DN1as and suggest that DN1a activity is shaped by signals from the circadian clock and modulated by the opposing pushes of light and cold temperature, dynamically shifting the pattern of daytime sleep to better adapt to changing environmental conditions.

DISCUSSION

In this work, we uncover a complete circuit, from sensory neurons to circadian and sleep centers, that processes information about absolute cold temperature to exert influence on fly behavior in the timescale of minutes to hours to days.

The circuit we describe is composed of sensory neurons of the antenna (including newly identified thermosensory neurons only active in the cold) and of specialized second-order thermosensory projection neurons of the PAL and provides persistent inhibition to the DN1a cluster of circadian neurons to adapt sleep/activity patterns specifically to cold conditions.

Our data show that “absolute temperature” and “temperature change” signals can be extracted by second-order neurons from

(J) Circuit schematic including TPN-ILs (light blue), DN1as (pink), and sLNvs (orange).

(K and L) DN1as are excited by light.

(K) Light produces robust increases in firing rate at 25°C (black) and at 20°C (blue; gray circles connected by lines represent individual cells; filled circles are av. ± SD; *p < 0.05; paired one-tailed t test).

(L) Representative whole-cell recordings from a single DN1a neuron before and during light stimulation (yellow box) at 25°C (black) or 20°C (blue).

(M–P) Artificial activation of sLNvs drives fire rate increases in DN1a and can overcome cold inhibition.

(M) Experiment schematic. sLNvs express the exogenous ATP receptor P2X2 and can be activated by pressure ejection of ATP (20 mM, green), while patch clamp records activity in DN1a (pink).

(N) ATP (20 mM, green) can drive an increase in DN1a firing at 25°C in animals in which sLNvs express P2X2 (green trace, 4 cells/animals), but not in control animals (driver without the receptor, gray/black trace; 6 cells/4 animals).

(O) ATP can also overcome cold inhibition of DN1as (4 cells/4 animals av. ± SEM; the green trace at the bottom of N and O is Alexa Fluor 594 fluorescence, a dye included as a marker in the ATP solution; arbitrary fluorescence units ± SEM).

(P) Quantification of (N) and (O) (gray circles connected by lines represent individual cells; filled circles are av. ± SD; *p < 0.05; paired one-tailed t test).

(Q–T) The neuropeptide PDF can increase DN1a firing to overcome inhibition in the cold.

(Q) Experiment schematic. PDF is pressure ejected (50 μM, yellow), while patch clamp records activity in DN1a (pink).

(R–T) PDF can drive an increase in DN1a firing both at (R) 25°C or (S) 20°C (9 cells/6 animals av. ± SD; the yellow line at the bottom of R and S represent the approximate time of the PDF puff).

(T) Quantification of (R) and (S) (gray circles connected by lines represent individual cells; filled circles are av. ± SD; *p < 0.05; paired one-tailed t test; all experiments were done at ZT 0–8).

the activity of peripheral thermoreceptors and demonstrate that persistent signaling in sensory circuits mediates long-lasting changes in behavior, beyond the rapid responses that are generally well understood. Moreover, our results illustrate how the fly nervous system selectively encodes and relays absolute cold temperature information to adapt behavior specifically to cold conditions.

What may be the significance of this sensory mechanism for the animal's natural behavior? Thermal conditions are well known to exert long-lasting changes in physiology and behavior, but due to the pervasive nature of temperature itself, such changes do not necessarily require input from a sensory circuit. For example, on the timescale of days and weeks, cold temperature promotes the alternative splicing of clock genes [26, 32], directly affecting the dynamics of the molecular clock. The sensory mechanism we discover here allows the animal to respond both rapidly and persistently to cold conditions. Such a mechanism may be important to bridge the gap between behavioral responses on the timescale of minutes to hours and biochemical changes that may take days to fully set in (and may be difficult to reverse).

In a small poikilotherm, cold (the range of temperature below the optimal species-specific value determined by the biochemistry of the animal) profoundly impacts motility and the ability to process stimuli. Cold temperature can quickly render a fly unable to move rapidly or fly away [33], and it is well known that larger insects, such as bumble bees, have evolved adaptations to ensure that their internal temperature is sufficient to support flight once they leave the hive [34]. We speculate that, for example, it may be adaptive for a fly to “sleep in” on a cold, dark morning until the conditions are met for it to warm up sufficiently as to rapidly avoid predation. If cold conditions indeed persist, the new sleep/wake pattern may become further reinforced by stable biochemical/molecular changes and become part of a new seasonal pattern of activity.

Following up on the TPN-II targets, our work also identifies DN1a neurons as a key node for the integration of sensory information with internally regulated drives for rest and activity. We show that DN1as are powerfully and persistently inhibited by cold temperature but also that they have clock-regulated rhythms of activity, respond to light, and receive excitatory drive from sLNvs (which are part of the endogenous pacemaker and are in turn also activated by light) [35]. Together, our results demonstrate how information about external conditions (light and temperature) is directly relayed to a circadian/sleep center in the brain and integrated with internal drives to adapt sleep and wake cycles to changing external conditions.

Our results open a window on the temporal structure of sensory signaling in the fly thermosensory system and reveal how—even within sensory modality—distinct neural circuits can operate on different temporal scales to drive appropriate behavioral responses.

STAR★METHODS

Detailed methods are provided in the online version of this paper and include the following:

- KEY RESOURCES TABLE
- RESOURCE AVAILABILITY

- Lead Contact
- Materials Availability
- Data and Code Availability
- EXPERIMENTAL MODEL AND SUBJECT DETAILS
 - Fly Strains
- METHOD DETAILS
 - Characterization of Gal4, LexA and split-Gal4 drivers
 - Electrophysiology
 - Immunohistochemistry
 - Fluorescence Microscopy and Image Analysis
 - Antennae Anatomy
 - Ablation of Antennae
 - Calcium Imaging
 - Circadian Behavioral Experiments
- QUANTIFICATION AND STATISTICAL ANALYSIS
 - Detection of Action Potentials
 - Temperature
 - Time of Day Cellular Effects
 - Cellular Effects of Light
 - Pressure Ejected Chemicals
 - Calcium Imaging
 - Circadian Behavior

SUPPLEMENTAL INFORMATION

Supplemental Information can be found online at <https://doi.org/10.1016/j.cub.2020.04.038>.

ACKNOWLEDGMENTS

We thank Meghana Holla, Eilene Ni and David Kocoj for assistance, Evdokia Menelaou for help with spike analysis, Graham Robinson for graphical abstract artwork, and Lindsey Macpherson, Tiffany Schmidt, Bridget Lear, Clark Rosenzweig, and members of the Gallio lab for comments on the manuscript. Work in the Aallada Lab is supported by NIH grant R01NS106955 and the US Department of the Army grant W911NF-1-6-1-0584P00001. Work in the Gallio lab is supported by NIH grant R01NS086859, the Pew Scholars Program in the Biomedical Sciences, and a McKnight Technological Innovations in Neuroscience Award (to M.G.). M.H.A. was supported by training grant NIH T32HL007909, and D.D.F. was supported by NIH F31NS093873.

AUTHOR CONTRIBUTIONS

M.G., M.H.A., and D.D.F. designed the study, analyzed the data, and wrote the paper with critical input from all authors; M.H.A. performed all recordings with initial assistance from M.F. and Ca²⁺ imaging for F1. D.D.F. performed circuit mapping, Ca²⁺ imaging (F3), and anatomy. E.K. performed and analyzed sleep and activity recordings with assistance from M.H.A. E.E.Z. performed immunohistochemistry. A.P. assisted with recombinant and transgenic reagents. R.A. provided critical expertise.

DECLARATION OF INTERESTS

The authors declare no competing interests.

Received: February 27, 2020

Revised: March 31, 2020

Accepted: April 16, 2020

Published: May 21, 2020

REFERENCES

1. Weber, E.H., (1842). *Handwörterbuch der Physiologie: 1* (Friedrich Vieweg und Sohn).

2. Hensel, H., and Zotterman, Y. (1951). The persisting cold sensation. *Acta Physiol. Scand.* 22, 106–113.
3. Hensel, H. (1974). Thermoreceptors. *Annu. Rev. Physiol.* 36, 233–249.
4. Yarmolinsky, D.A., Peng, Y., Pogorzala, L.A., Rutlin, M., Hoon, M.A., and Zuker, C.S. (2016). Coding and plasticity in the mammalian thermosensory system. *Neuron* 92, 1079–1092.
5. Ran, C., Hoon, M.A., and Chen, X. (2016). The coding of cutaneous temperature in the spinal cord. *Nat. Neurosci.* 19, 1201–1209.
6. Gallio, M., Ofstad, T.A., Macpherson, L.J., Wang, J.W., and Zuker, C.S. (2011). The coding of temperature in the *Drosophila* brain. *Cell* 144, 614–624.
7. Budelli, G., Ni, L., Berciu, C., van Giesen, L., Knecht, Z.A., Chang, E.C., Kaminski, B., Silbering, A.F., Samuel, A., Klein, M., et al. (2019). Ionotropic receptors specify the morphogenesis of phasic sensors controlling rapid thermal preference in *Drosophila*. *Neuron* 101, 738–747.e3.
8. Frank, D.D., Jouandet, G.C., Kearney, P.J., Macpherson, L.J., and Gallio, M. (2015). Temperature representation in the *Drosophila* brain. *Nature* 519, 358–361.
9. Liu, W.W., Mazor, O., and Wilson, R.I. (2015). Thermosensory processing in the *Drosophila* brain. *Nature* 519, 353–357.
10. Enjin, A., Zaharieva, E.E., Frank, D.D., Mansourian, S., Suh, G.S., Gallio, M., and Stensmyr, M.C. (2016). Humidity sensing in *Drosophila*. *Curr. Biol.* 26, 1352–1358.
11. Frank, D.D., Enjin, A., Jouandet, G.C., Zaharieva, E.E., Para, A., Stensmyr, M.C., and Gallio, M. (2017). Early integration of temperature and humidity stimuli in the *Drosophila* brain. *Curr. Biol.* 27, 2381–2388.e4.
12. Hamada, F.N., Rosenzweig, M., Kang, K., Pulver, S.R., Ghezzi, A., Jegla, T.J., and Garrity, P.A. (2008). An internal thermal sensor controlling temperature preference in *Drosophila*. *Nature* 454, 217–220.
13. Macpherson, L.J., Zaharieva, E.E., Kearney, P.J., Alpert, M.H., Lin, T.Y., Turan, Z., Lee, C.H., and Gallio, M. (2015). Dynamic labelling of neural connections in multiple colours by trans-synaptic fluorescence complementation. *Nat. Commun.* 6, 10024.
14. Datta, S.R., Vasconcelos, M.L., Ruta, V., Luo, S., Wong, A., Demir, E., Flores, J., Balonze, K., Dickson, B.J., and Axel, R. (2008). The *Drosophila* pheromone cVA activates a sexually dimorphic neural circuit. *Nature* 452, 473–477.
15. Benito, J., Houl, J.H., Roman, G.W., and Hardin, P.E. (2008). The blue-light photoreceptor CRYPTOCHROME is expressed in a subset of circadian oscillator neurons in the *Drosophila* CNS. *J. Biol. Rhythms* 23, 296–307.
16. Flourakis, M., Kula-Eversole, E., Hutchison, A.L., Han, T.H., Aranda, K., Moose, D.L., White, K.P., Dinner, A.R., Lear, B.C., Ren, D., et al. (2015). A conserved bicycle model for circadian clock control of membrane excitability. *Cell* 162, 836–848.
17. Guo, F., Yu, J., Jung, H.J., Abruzzi, K.C., Luo, W., Griffith, L.C., and Rosbash, M. (2016). Circadian neuron feedback controls the *Drosophila* sleep–activity profile. *Nature* 536, 292–297.
18. Lamaze, A., Öztürk-Çolak, A., Fischer, R., Peschel, N., Koh, K., and Jepson, J.E. (2017). Regulation of sleep plasticity by a thermo-sensitive circuit in *Drosophila*. *Sci. Rep.* 7, 40304.
19. Parisky, K.M., Agosto Rivera, J.L., Donelson, N.C., Kotecha, S., and Griffith, L.C. (2016). Reorganization of sleep by temperature in *Drosophila* requires light, the homeostat, and the circadian clock. *Curr. Biol.* 26, 882–892.
20. Yadlapalli, S., Jiang, C., Bahle, A., Reddy, P., Meyhofer, E., and Shafer, O.T. (2018). Circadian clock neurons constantly monitor environmental temperature to set sleep timing. *Nature* 555, 98–102.
21. Fujiwara, Y., Hermann-Luibl, C., Katsura, M., Sekiguchi, M., Ida, T., Helfrich-Förster, C., and Yoshii, T. (2018). The CCHamide1 neuropeptide expressed in the anterior dorsal neuron 1 conveys a circadian signal to the ventral lateral neurons in *Drosophila melanogaster*. *Front. Physiol.* 9, 1276.
22. Hendricks, J.C., Finn, S.M., Panckeri, K.A., Chavkin, J., Williams, J.A., Sehgal, A., and Pack, A.I. (2000). Rest in *Drosophila* is a sleep-like state. *Neuron* 25, 129–138.
23. Shaw, P.J., Cirelli, C., Greenspan, R.J., and Tononi, G. (2000). Correlates of sleep and waking in *Drosophila melanogaster*. *Science* 287, 1834–1837.
24. Huber, R., Hill, S.L., Holladay, C., Biesiadecki, M., Tononi, G., and Cirelli, C. (2004). Sleep homeostasis in *Drosophila melanogaster*. *Sleep* 27, 628–639.
25. Chen, W.F., Low, K.H., Lim, C., and Edery, I. (2007). Thermosensitive splicing of a clock gene and seasonal adaptation. *Cold Spring Harb. Symp. Quant. Biol.* 72, 599–606.
26. Majercak, J., Sidote, D., Hardin, P.E., and Edery, I. (1999). How a circadian clock adapts to seasonal decreases in temperature and day length. *Neuron* 24, 219–230.
27. Sweeney, S.T., Broadie, K., Keane, J., Niemann, H., and O’Kane, C.J. (1995). Targeted expression of tetanus toxin light chain in *Drosophila* specifically eliminates synaptic transmission and causes behavioral defects. *Neuron* 14, 341–351.
28. Collins, B., Kane, E.A., Reeves, D.C., Akabas, M.H., and Blau, J. (2012). Balance of activity between LN(v)s and glutamatergic dorsal clock neurons promotes robust circadian rhythms in *Drosophila*. *Neuron* 74, 706–718.
29. Stoleru, D., Peng, Y., Agosto, J., and Rosbash, M. (2004). Coupled oscillators control morning and evening locomotor behaviour of *Drosophila*. *Nature* 431, 862–868.
30. Helfrich-Förster, C. (1995). The period clock gene is expressed in central nervous system neurons which also produce a neuropeptide that reveals the projections of circadian pacemaker cells within the brain of *Drosophila melanogaster*. *Proc. Natl. Acad. Sci. USA* 92, 612–616.
31. Shafer, O.T., Kim, D.J., Dunbar-Yaffe, R., Nikolaev, V.O., Lohse, M.J., and Taghert, P.H. (2008). Widespread receptivity to neuropeptide PDF throughout the neuronal circadian clock network of *Drosophila* revealed by real-time cyclic AMP imaging. *Neuron* 58, 223–237.
32. Martin Anduaga, A., Evantal, N., Patop, I.L., Bartok, O., Weiss, R., and Kadener, S. (2019). Thermosensitive alternative splicing senses and mediates temperature adaptation in *Drosophila*. *eLife* 8, e44642.
33. Lehmann, F.O. (1999). Ambient temperature affects free-flight performance in the fruit fly *Drosophila melanogaster*. *J. Comp. Physiol. B* 169, 165–171.
34. Heinrich, B. (1972). Energetics of temperature regulation and foraging in a bumblebee, *Bombus terrestris* kirby. *J. Comp. Physiol.* 77, 49–64.
35. Li, M.T., Cao, L.H., Xiao, N., Tang, M., Deng, B., Yang, T., Yoshii, T., and Luo, D.G. (2018). Hub-organized parallel circuits of central circadian pacemaker neurons for visual photoentrainment in *Drosophila*. *Nat. Commun.* 9, 4247.
36. Schindelin, J., Arganda-Carreras, I., and Frise, E. (2012). Fiji: an open-source platform for biological-image analysis. *Nat. Methods* 9, 676–682.
37. Rothman, J.S., and Silver, R.A. (2018). NeuroMatic: an integrated open-source software toolkit for acquisition, analysis and simulation of electrophysiological data. *Front. Neuroinform.* 12, 14.
38. Rush, B.L., Murad, A., Emery, P., and Giebultowicz, J.M. (2006). Ectopic CRYPTOCHROME renders TIM light sensitive in the *Drosophila* ovary. *J. Biol. Rhythms* 21, 272–278.

STAR★METHODS

KEY RESOURCES TABLE

REAGENT or RESOURCE	SOURCE	IDENTIFIER
Antibodies		
chicken polyclonal anti-GFP	Abcam	Cat# ab13970, RRID:AB_300798
donkey polyclonal anti-mouse Alexa 594	Abcam	Cat# ab150105, RRID:AB_2732856
chicken polyclonal anti-GFP	Abcam	Cat# ab13970, RRID:AB_300798
rat monoclonal anti-Elav	Developmental Studies Hybridoma Bank	Cat# Rat-Elav-7E8A10 anti-elav, RRID:AB_528218
mouse monoclonal anti-Repo	Developmental Studies Hybridoma Bank	Cat# 8D12 anti-Repo, RRID:AB_528448
rabbit anti-Per	Gift from R. Allada & M. Rosbash	N/A
rabbit anti-Cry	Gift from R. Allada	N/A
donkey polyclonal anti-chicken Alexa 488	Jackson ImmunoResearch Labs	Cat# 703-545-155, RRID:AB_2340375
donkey polyclonal anti-rabbit Alexa 594	Jackson ImmunoResearch Labs	Cat# 711-585-152, RRID:AB_2340621
donkey polyclonal anti-chicken Alexa 488	Jackson ImmunoResearch Labs	Cat# 703-545-155, RRID:AB_2340375
rabbit polyclonal anti-GABA	Millipore Sigma	Cat# A2052, RRID:AB_477652
goat anti-rat DyLight 594	NovusBio	Cat# NBP1-76096, RRID:AB_11023227
goat polyclonal anti-CLK (dC-17)	Santa Cruz Biotechnology	Cat# sc-27070, RRID:AB_638555
rabbit polyclonal anti-dsRED	Takara Bio	Cat# 632496, RRID:AB_10013483
donkey polyclonal anti-goat Alexa 568	Thermo Fisher Scientific	Cat# A-11057, RRID:AB_2534104
Chemicals, Peptides, and Recombinant Proteins		
Adenosine 5'-triphosphate magnesium salt	Millipore Sigma	Cat. # A9187; CAS: 74804-12-9
Pigment dispersing factor (PDF) peptide	Gift from R. Allada; Genscript	N/A
Alexa Fluor 594 Hydrazide	Thermo Fisher Scientific	Cat. # A10438
all trans-Retinal	Millipore Sigma	Cat. # R2500; CAS: 116-31-4
picrotoxin	Tocris	Cat. # 1128; CAS: 124-87-8
Experimental Models: Organisms/Strains		
<i>D. melanogaster: IR25a Gal4</i>	Bloomington Drosophila Stock Center	BDSC: 41728; Flybase: FBti0148895
<i>D. melanogaster: R49B06 Gal4</i>	Bloomington Drosophila Stock Center	BDSC: 50409; Flybase: FBti0136309
<i>D. melanogaster: R49B06 LexA</i>	Bloomington Drosophila Stock Center	BDSC: 52707; Flybase: FBti0155964
<i>D. melanogaster: R25B07 AD</i>	Bloomington Drosophila Stock Center	BDSC: 70144; Flybase: FBti0188065
<i>D. melanogaster: R25B07 LexA</i>	Bloomington Drosophila Stock Center	BDSC: 54125; Flybase: FBti0155514
<i>D. melanogaster: R77C10 Gal4</i>	Bloomington Drosophila Stock Center	BDSC: 39958; Flybase: FBti0138389
<i>D. melanogaster: R77C10 DBD</i>	Bloomington Drosophila Stock Center	BDSC: 69705; Flybase: FBti0191888
<i>D. melanogaster: R60H12 AD</i>	Bloomington Drosophila Stock Center	BDSC: 70761; Flybase: FBti0188587
<i>D. melanogaster: VT032805 DBD</i>	Bloomington Drosophila Stock Center	BDSC: 75119; Flybase: FBti0193574
<i>D. melanogaster: R49A06 Gal4</i>	Bloomington Drosophila Stock Center	BDSC: 50401; Flybase: FBti0136298
<i>D. melanogaster: R23E05 Gal4</i>	Bloomington Drosophila Stock Center	BDSC: 49029; Flybase: FBti0134061
<i>D. melanogaster: R23E05 AD</i>	Bloomington Drosophila Stock Center	BDSC: 70601; Flybase: FBti0188021
<i>D. melanogaster: R92H07 DBD</i>	Bloomington Drosophila Stock Center	BDSC: 70004; Flybase: FBti0192102
<i>D. melanogaster: 20XUAS-IVS-GCaMP6f</i>	Bloomington Drosophila Stock Center	BDSC: 42747; Flybase: FBti0151345
<i>D. melanogaster: 20XUAS-IVS-jGCaMP7f</i>	Bloomington Drosophila Stock Center	BDSC: 79031; Flybase: FBti0199863
<i>D. melanogaster: 20XUAS-IVS-CsChrimson.mVenus</i>	Bloomington Drosophila Stock Center	BDSC: 55135; Flybase: FBti0160803
<i>D. melanogaster: 13XLexAop-IVS-jGCaMP7f</i>	Bloomington Drosophila Stock Center	BDSC: 80914; Flybase: FBti0202387
<i>D. melanogaster: AOP.Syb.spGFP [1–10], UAS.spGFP [11]</i>	Bloomington Drosophila Stock Center	BDSC: 64315; Flybase: FBti0180566; FBti0180561
<i>D. melanogaster: 10XUAS-IVS-mCD8::GFP</i>	Bloomington Drosophila Stock Center	BDSC: 32186; Flybase: FBst0032186

(Continued on next page)

Continued

REAGENT or RESOURCE	SOURCE	IDENTIFIER
<i>D. melanogaster</i> : UAS-TNT	kind gift from M. Rosbash	N/A
<i>D. melanogaster</i> : LexAop-P2X2	kind gift of O. Shafer	N/A
<i>D. melanogaster</i> : 13XLexAop-TdTomato	kind gifts from V. Ruta and B. Noro	N/A
<i>D. melanogaster</i> : UAS-C3PA	kind gifts from V. Ruta and B. Noro	N/A
<i>D. melanogaster</i> : UAS-SPA	kind gifts from V. Ruta and B. Noro	N/A
<i>D. melanogaster</i> : Synaptobrevin-Gal4	kind gifts from V. Ruta and B. Noro	N/A
<i>D. melanogaster</i> : w ¹¹¹⁸ CS	kind gifts of R. Allada	N/A
<i>D. melanogaster</i> : per ⁰¹	kind gifts of R. Allada	N/A
<i>D. melanogaster</i> : VT003226 Gal4	Vienna Drosophila Resource Center	N/A
Software and Algorithms		
MAT LAB	The Mathworks	http://www.mathworks.com
Fiji	[36]	http://fiji.sc
Pclamp (Clampex software v.9.2.1.9)	Axon Instruments/Molecular Devices	https://www.moleculardevices.com/
Igor Pro v.6.37	Wavemetrics, Inc.	https://www.wavemetrics.com/
Neuromatic v2.6i plug-in for Igor Pro	[37]	http://www.neuromatic.thinkrandom.com/
Axograph v.1.70	Axograph	https://axograph.com/

RESOURCE AVAILABILITY**Lead Contact**

Further information and requests for reagents should be directed to and will be fulfilled by the Lead Contact, Marco Gallio (marco.gallio@northwestern.edu).

Materials Availability

This study did not generate new unique reagents. Requests of fly stocks should be directed to and will be fulfilled by the Lead Contact, Marco Gallio (marco.gallio@northwestern.edu).

Data and Code Availability

All data are available in the main text or the supplementary materials. Further information and requests for data and code should be directed to and will be fulfilled by the Lead Contact, Marco Gallio (marco.gallio@northwestern.edu).

EXPERIMENTAL MODEL AND SUBJECT DETAILS**Fly Strains**

Drosophila melanogaster strains were reared on cornmeal agar medium under 12:12 LD cycles at 25°C. Stocks were obtained from Bloomington *Drosophila* Stock Center (BDSC) or Vienna *Drosophila* Resource Center (VDRC). The following stocks were used: IR25a Gal4 (BDSC 41728), R49B06 Gal4 (BDSC 50409), R49B06 LexA (BDSC 52707), R25B07 AD (BDSC 70144), R25B07 LexA (BDSC 54125), R77C10 Gal4 (BDSC 39958), R77C10 DBD (BDSC 69705), R60H12 AD (BDSC 70761), VT032805 DBD (BDSC 75119), R49A06 Gal4 (BDSC 50401), VT003226 Gal4, R23E05 Gal4 (BDSC 49029), R23E05 AD (BDSC 70601), R92H07 DBD (BDSC 70004), 20XUAS-IVS-GCaMP6f (BDSC 42747), 20XUAS-IVS-jGCaMP7f (BDSC 79031), 20XUAS-IVS-CsChrimson.mVenus (BDSC 55135), 13XLexAop-IVS-jGCaMP7f (BDSC 80914), 13XLexAop-TdTomato, UAS-C3PA, UAS-SPA and synaptobrevin-Gal4 (kind gifts from V. Ruta and B. Noro), AOP.Syb:spGFP [1–10], UAS.spGFP [11] (BDSC 64315) PDF-LexA and Per⁰¹ (kind gifts of R. Allada), AOP-P2X2 (kind gift of O. Shafer), 10XUAS-IVS-mCD8::GFP (BDSC 32186) UAS-TNT (kind gift from M. Rosbash). A full description of genotypes used in each figure can be found in Table S1. Male flies were used for all behavioral experiments. In Figure 5, electrophysiological recordings were performed on males and females, separately, as indicated; all other recordings were performed on males. A full description of genotypes used in each figure can be found in Table S1. A full list of fly lines can be found in the Key Resources Table.

METHOD DETAILS**Characterization of Gal4, LexA and split-Gal4 drivers**

In addition to sacculus chamber I neurons, R25B07-LexA expresses in the lateral horn, subesophageal ganglia, and a single olfactory glomerulus in the antennal lobe. R77C10-Gal4 is active in arista cold cells, the ACc, and subesophageal ganglia. IR25a-Gal4 expresses in ACc, and a detailed description of antennal sensory neurons in this line can be found in Enjin et al., 2016. R25B07

AD \cap R77C10 DBD is active in 2-3 cold cells of the arista. R60H12 AD \cap VT032805 DBD expresses in TPN-IIIs, weakly in subesophageal ganglia, and a pair of cells in the ventral nerve cord. R92H07 AD \cap R23E05 DBD is active in DN1as and no other neurons in the brain.

Electrophysiology

Whole-cell patch clamp electrophysiology experiments were performed on 2-3 days old flies. Flies (generally females, except for *per⁰¹* mutants and controls) were anaesthetized by brief cold exposure in an ice bath ($\sim 0^{\circ}\text{C}$) for ~ 1 min. Using a dissection microscope (Nikon SMZ1000), a small window in the head cuticle was opened and the underlying perineural sheath was gently removed using fine forceps (Moria Surgical). Brain tissue was exposed while maintaining connectivity with peripheral antennae, and bathed in artificial hemolymph (AHL) solution containing the following (in mM): 103 NaCl, 3 KCl, 26 NaHCO₃, 1 NaH₂PO₄, 8 trehalose dihydrate, 10 dextrose, 5 TES, 4 MgCl₂, adjusted to 270-275 mOsm. For experiments, 1.5 mM CaCl₂ was included and the solution was continuously bubbled with 95% O₂ 5% CO₂ to pH 7.3 and perfused over the brain at a flow rate of 1-2 mL/min. To target neurons for patching under the 2-photon microscope, Gal4 lines expressing GFP for neuron targeting were excited at 840 nm and detected using a photomultiplier tube (PMT) through a bandpass filter (490-560 nm) using an Ultima 2-photon laser scanning microscope (Bruker, formerly Prairie Technologies). The microscope is equipped with galvanometers driving a Coherent Chameleon laser and a Dodt detector was used to visualize neural tissue/somata. Images were acquired with an upright Zeiss Examiner.Z1 microscope with a Zeiss W Plan-Apochromat 40 \times 0.9 numerical aperture water immersion objective at 512 pixels \times 512 pixels resolution using PrairieView software v. 5.2 (Bruker). Current clamp recordings were performed with pipettes pulled (Sutter P-97) using borosilicate capillary tubes (WPI Cat # 1B150F-4) with open tip resistances of 20 ± 3 M Ω filled with internal solution containing the following (in mM): 140 K-aspartate, 1 KCl, 1 EGTA, 10 HEPES, 4 Mg-ATP, 0.5 Na₃-GTP, pH 7.3, 265 mOsm. To visualize the electrode and fill the cell after recording to confirm GFP co-localization, Alexa Fluor 594 Hydrazide (5 μM ; Thermofisher Scientific Cat. # A10438) was added into the intracellular solution, excited using the 2-photon microscope at 840 nm, and detected with a second PMT through a bandpass filter (580-630 nm). Recordings were made using Axopatch 200B patch-clamp amplifier and CV203BU headstage (Axon Instruments), lowpass filtered at 2 KHz, scaled to a 20x output gain, digitized with a Digidata 1320 A, and acquired with Clampex software v.9.2.1.9 (Axon Instruments).

Temperature stimulation

For temperature stimulation, preparations were continuously perfused with Ca²⁺-containing AHL (as described above). AHL was gravity fed through a 3-way valve (Lee company, part # LHDA1231315H) and flow rate was adjusted through a flow regulator. Following the valve, temperature was precisely regulated through 2 in-line solution heater/coolers (Warner, cat. # SC-20) in parallel with by a dual channel bipolar temperature controller (Warner Instruments, CI⁻200A). Excess heat produced by each SC-20 Peltier was dissipated through a liquid cooling system (Koolance, Cat. # EXT-1055). To circumvent changes in resistivity and voltage offsets from changing the temperature of the bathing solution, the reference Ag-Cl pellet electrode was placed in an isolated well adjacent to the recording chamber (Warner Instruments, Cat. # RC-24N), filled with identical AHL and connected via a borosilicate capillary tube filled by 2% agar in 3 M KCl. The bath temperature was precisely recorded using a custom Type T thermocouple with 1cm exposed tip (Physitemp, Cat. # T-384A) connected to a thermometer (BAT-12, Physitemp) with an analog output connected to the digitizer and sampled at 10 kHz. The tip of thermocouple was threaded through a borosilicate capillary tube and precisely placed near the antennae using a micromanipulator (MP-225, Sutter Instruments).

Time of Day Electrophysiology Experiments

Flies were reared on a 12:12 L:D cycle at 25°C. Experiments were performed on female flies 2-3 days post-eclosion and recordings were binned in 4 hr intervals according to Zeitgeber Time (ZT). For ZT0-12 recordings a white LED was used during the dissection, whereas during ZT 12-24, red light was used instead in otherwise complete darkness. The baseline firing rate was established and taken from an average of the firing rate in the first 1-2 min after break-in and the establishment of whole cell configuration. Mean firing rate (Hz) \pm SD are reported for each bin. An unpaired 1-tailed t test was used to test for significant differences in firing rate between night (ZT 20-24) and day (ZT 0-4). For experiments in a *per⁰¹* background, Gal4 lines expressing GFP were crossed to female *per⁰¹*; as *per* maps to the X chromosome, only male progeny were used for experiments.

Light stimulation

Flies were reared on a 12:12 L:D cycle at 25°C and dissected using white light. Experiments were performed on female flies 2-3 days post-eclosion at ZT 0-8 with intact eyes. Whole cell recordings were established using 2-photon illumination at 840 nm. Flies were then left in darkness at 25°C until stimulated from below using the microscope condenser halogen lamp (Sunlite Q100). A light intensity of ~ 430 lux was measured through the recording chamber using a Digital lux meter (# LX1330B, Dr. Meter). Flies were then cooled to 20°C for several minutes and then stimulated again with the condenser light. To quantify the change in firing rate from light stimulation, a baseline period of ~ 30 s was averaged and compared to the peak response elicited upon light exposure.

Pressure ejection of chemicals

For focal application of ATP (20 mM in AHL) or PDF peptide (50 μM in AHL, GenScript), solutions were backfilled into a borosilicate capillary tube (WPI) connected to a TTL-triggerable PV830 Pneumatic PicoPump (WPI). Alexa 594 Hydrazide (5 μM) was included to confirm and record the fluorescence intensity and time course of the ejected solution. Pipettes were pulled using a P-97 puller (Sutter) to open tip resistances of 5-10 M Ω and precisely positioned using a micromanipulator (Sutter MP-225) near DN1a projections. Constant pressure (5 psi) was maintained for the duration of the stimulus. For ATP experiments, controls were performed in Gal4 lines expressing GFP only.

Immunohistochemistry

Staining of fly brains was performed essentially as previously described [6]. Briefly, brains of young (3-5d old) male and female flies were dissected in cold PBS or artificial hemolymph and fixed in 4% PFA. Blocking was performed in PBSBT (PBS, 0.2% Triton X-100, 3% BSA) and samples were incubated overnight at 4°C with the appropriate dilution of primary antibody in PBSBT. The following day, samples were washed and incubated for 3hr with fluorescently tagged secondary antibody diluted to the appropriate concentration in PBSBT. The following antibodies were used: chicken anti-GFP (Abcam #ab13970), rabbit anti-dsRED (Clontech #632496), rabbit anti-GABA (1:200, Sigma #A2052), goat anti-CLK (dC-17) (1:500, Santa Cruz Biotechnology #sc-27070), rabbit anti-Per (1:5000, a gift from the Allada lab), rabbit anti-Cry (1:50, a gift from the Allada lab [38]), donkey anti-chicken Alexa 488 (1:250, Jackson ImmunoResearch #703-545-155), donkey anti-rabbit Alexa 594 (1:250, Jackson ImmunoResearch #711-586-152), donkey anti-goat Alexa 568 (1:250, Invitrogen #A-11057). For staining of antennal nerves to characterize ACc, the following antibodies were used: rat anti-Elav (1:50, Hybridoma Bank #Rat-Elav-7E8A10 anti-elav), goat anti-rat DyLight 594 (1:500, NovusBio #NBP1-76096), mouse anti-Repo (1:50, Hybridoma Bank #8D12 anti-Repo), donkey anti-mouse Alexa 594 (1:500, Abcam #ab150105), chicken anti-GFP (1:500 Abcam #ab13970), donkey anti-chicken Alexa 488 (1:500, Jackson ImmunoResearch #703-545-155).

Fluorescence Microscopy and Image Analysis

Confocal imaging of antennae and immunofluorescent-stained brains was performed on a Zeiss LSM 510 confocal microscope equipped with Argon 450-530nm, Helium-Neon 543nm, and Helium-Neon 633 nm lasers and a Zeiss LCI Plan-Neofluar/0.8 DIC Imm Corr 25x objective at 512x512 pixel resolution. Two-photon imaging of GFP-, TdTomato-, and sybGRASP-labeled neurons was performed on a Prairie Ultima two-photon microscope with a Coherent Chameleon Ti:Sapphire laser tuned to 945nm, GaAsP PMTs and an Olympus 40X 0.9NA water immersion objective at 512x512 pixel resolution and 1X or 2X optical zoom. Maximum projections were obtained from stacks taken at 1 μ m steps. Images were processed in Fiji.

Antennae Anatomy

Large online collections of Gal4 driver lines (Janelia Farm FlyLight initiative, Vienna *Drosophila* Resource Center ViennaTile) were visually screened to identify driver lines putatively active in sensory neurons innervating the PAL. Drivers were crossed to 10XUAS-IVS-mCD8::GFP and the antennae of the resulting progeny examined under confocal microscopy. Antennae of young flies were dissected and collected in cold artificial hemolymph and mounted in artificial hemolymph or Vectashield.

Ablation of Antennae

Male and female flies were collected shortly after eclosion and anesthetized on ice, fine forceps were used to gently pluck the antennae from the flies. Removal of the entire third segment and arista was confirmed visually. Imaging experiments in the PAL were conducted 7-10 days post-ablation.

Calcium Imaging

Calcium imaging of temperature stimuli was performed essentially as previously described [6, 8]. Gal4 driver line males were crossed to virgin GCaMP females (see [STAR Methods Key Resources Table](#) for a complete list of genotypes) and progeny used for imaging experiments 3-5 days post-eclosion. Dissections and temperature stimuli were performed as described above in AHL continuously bubbled with 95% O₂ 5% CO₂. Images were acquired at 256x256 or 512x512 pixels resolution at a rate of 4 Hz on a Prairie Ultima two-photon microscope with a Coherent Chameleon Ti:Sapphire laser tuned to 945nm.

Circadian Behavioral Experiments

All flies were reared at 25°C in 12 hr light: 12 hr dark (LD) conditions. Male flies (3-5 days old) were loaded into 65mm x 5mm tubes containing 5% sucrose 2% agar food medium. Locomotor activity was recorded using the *Drosophila* Activity Monitoring System (DAMS, Trikinetics) in 1 minute intervals. Temperature, light and humidity were controlled using a DR-36NL incubator (Percival Scientific). To suppress synaptic output of DN1a split Gal4 (R23E05 AD \cap R92H07 DBD) and TPN-II split Gal4 (R60H12 AD \cap VT032805 DBD), males were crossed to virgin UAS-TNT females, and male progeny were assayed.

Optogenetic Stimulation

All-*trans* retinal powder (RET, Sigma-Aldrich) was mixed with ethanol to prepare a 100mM stock solution. 1mL of stock was then mixed with 250mL of molasses and cornmeal medium to produce 400 μ M food. Flies were reared on this medium, and then transferred to 400 μ M retinal 5% sucrose 2% agar medium for data collection using the DAMS. Control food was prepared using the same volume of ethanol. To optogenetically activate TPN-II, TPN-II split Gal4 (R60H12 AD \cap VT032805 DBD) males were crossed to virgin UAS-CsChrimson females, and male progeny were assayed in a DigiTherm incubator (Trikinetics). For time-delimited optogenetic activation (i.e., to minimize CsChrimson activation by the standard white incubator light), we covered the light tubes with \sim 488 nm polyester film (Rosco #R375) to produce 210 lux blue light. Flies were reared on blue light 12:12 LD cycles at 25°C and behavior was assayed in the same incubator. For sleep analysis (Figures 7G–7I), flies were entrained to blue-LD cycles for 4 days, with red light stimulation from ZT0-3 on day 2, and ZT6-12 on day 4. Constant red light (4800 lux) was produced using 3 symmetrically-placed high-power 660nm LEDs (M660L3 or M660L4, Thorlabs) mounted on heat sinks. The angle and height of the LEDs were adjusted to ensure uniform illumination. Lux measurements were made using a Digital lux meter (# LX1330B, Dr. Meter).

QUANTIFICATION AND STATISTICAL ANALYSIS

Detection of Action Potentials

Membrane potential recordings were made in current clamp mode sampled at 10 kHz. Data was analyzed offline using Axograph and Igor Pro. Action potentials (spikes) were detected using custom scripts in Igor Pro using Neuromatic v2.6i plug-in [37]. A first derivative transformation was performed on the membrane potential trace defining dV/dt . Then a constant dV/dt threshold was used to detect individual spikes. Peristimulus time histograms (PTH) of firing rate were made by binning detected spikes in 1 s bins, defining spikes/s (Hz). In experiments in which single trials from individual cells were averaged, the line and shading indicate the mean firing rate (Hz) \pm SD. For experiments in which multiple sweeps were performed at a given stimulus temperature, average PTH were calculated per cell; the line and shading indicate the mean firing rate (Hz) \pm SD; then across cells the line and shading indicate the mean firing rate (Hz) \pm SEM. For figure panels using pseudocolored histograms to show firing rates for extended temperature stimuli, an image matrix representing the firing rates (in 1 s bins) was imported into ImageJ.

Temperature

In experiments in which single trials from individual cells were averaged, the line and shading indicate the mean temperature ($^{\circ}\text{C}$) \pm SD. For experiments in which multiple sweeps were performed at a given stimulus temperature, the line and shading indicate the mean temperature ($^{\circ}\text{C}$) \pm SD across cells. To test for a significant relationship between temperature and firing rate for TPN-II, a *f*-test was performed and significance (*) defined as $p < 0.05$.

Time of Day Cellular Effects

An unpaired 1-tailed *t* test was used to test for significant differences in firing rate between night (ZT 20-24) and day (ZT 0-4) for WT or *per⁰¹* flies. A paired 1-tailed *t* test was used to test for significant decreases in firing rate of different magnitude cooling steps between night (ZT 20-24) and day (ZT 0-4). Significance (*) was defined as $p < 0.05$.

Cellular Effects of Light

A paired, 1-tailed *t* test was used to test for significant differences in firing rate between darkness and light conditions, both at 25°C and then at 20°C .

Pressure Ejected Chemicals

PTHs were calculated and the lines and shading represent the mean firing rate \pm SEM. To confirm statistical significance between baseline firing and baseline + ATP/PDF, a paired 1-tailed *t* test was used and significance (*) defined as $p < 0.05$.

Calcium Imaging

Delta F/F analysis was carried out using custom MAT LAB scripts. To calculate change in fluorescence we used the formula $\Delta F/F = (F_t - F_0)/F_0$, where F_0 is the baseline fluorescence determined by averaging frames before stimulus onset and F_t is the fluorescent value at a given time. Circular regions of interest (ROIs) of constant area were drawn manually, as appropriate, using the overlaid averaged image as a guide. Representative stimulus and $\Delta F/F$ response pairs were used to generate average traces in MATLAB. Values across individual trials were averaged and the standard deviation was determined for each time point.

Circadian Behavior

Sleep was defined as ≥ 5 consecutive minutes of inactivity. Activity and sleep analysis was performed using MATLAB 2016a software (Mathworks). Sleep is displayed in 30 minute bins represented as mean \pm SEM. For 25°C - 18°C behavior comparisons, (Figures 6A, 6D, and 6F-6L), flies were entrained for 4 days to 12:12 LD at 25°C , then gradually transferred to 18°C during the 4th night (9 hr -0.8°C/hr linear cooling ramp, ZT12-21) for 3 additional days. 25°C activity and sleep data are the mean of 2 days before cooling, and 18°C data are the mean of 2 days after cooling. For cold step experiments (Figures 6B-6D), flies were entrained in 12:12 LD at 25°C for 3 days. On the subsequent day, the temperature was stepped to 18°C from ZT 0-3 (0.35°C/min); after a day of recovery, the temperature was stepped to 18°C from ZT 6-12 (0.35°C/min). Quantifications are made between the pulse day and the preceding non-pulse day at 25°C . To test for significance differences of both sleep and activity at 25°C versus 18°C (Figures 6A-6D and 6F-6L), two-sided paired *t* tests were used. When comparing sleep across genotypes (Figures 6H and 6L), statistical significance was determined using a 2-way Analysis of Variance (ANOVA) with a post hoc Bonferroni test for multiple comparisons. For Figures 7A-7E, flies were entrained for 3 days 12:12 LD at 25°C , then transferred to constant darkness (DD) for one day at 25°C , or transferred to DD following a 9hr cooling ramp to 18°C (-0.8°C/hr). Because comparisons were made from different cohorts of flies (Figures 7A and 7B), two-sided unpaired *t* tests were used to test for significance differences in sleep. When comparing sleep across genotypes (Figures 7D and 7E), statistical significance was determined using a 2-way Analysis of Variance (ANOVA) with a post hoc Bonferroni test for multiple comparisons. For optogenetic experiments, a two-sided unpaired *t* test was used to test for significant differences in sleep between RET+ versus RET- flies (Figures 7G-7I).

A feature extraction method for noisy electrophysiology data. E. M. JOHNSON*; W. L. KATH.
Society for Neuroscience Annual Meeting 2019

Extraction of features such as action potential peaks or widths, and determining how they change under different conditions, is an essential component of analyses of electrophysiological data. Current methods range from using simple voltage thresholds to more complicated wavelet decompositions, but all perform relatively poorly when applied to noisy or low-resolution data. Furthermore, many of these methods require user input or refinement of algorithm parameters, making them ill-suited for large data sets. A suite of tools for robustly extracting features automatically from electrophysiological data has been developed using the Python programming language. The tools in this package make use of the statistics of the data themselves to estimate algorithm parameters, minimizing user intervention while remaining robust to noise. To demonstrate the use of these methods, we have applied them to a set of electrophysiological recordings of DN1 “clock” neurons in *Drosophila* (from Flourakis [Cell, 1162 (2015)]) to determine electrophysiological features that are coupled to the circadian rhythm.